UNIVERSITY OF
PLYMOUTH

NUMERICAL MODELLING OF EXTREME WAVES: THE ROLE OF NONLINEAR WAVE-WAVE INTERACTIONS

by

THOMAS VYZIKAS

A thesis submitted to the University of Plymouth
in partial fulfilment for the degree of

DOCTOR OF PHILOSOPHY

School of Engineering

2018

τρικυμία < τρι- + -κυμία < κῦμα (trici'mia)

Ancient word for a sequence of three high waves;
the commonly observed shape of extreme waves.
In modern times, it refers to a rough sea state.

Acknowledgements

A PhD is a long, life-changing journey of trying to push one's personal limits, and achieve a tiny contribution to human knowledge, by slightly expanding its frontiers and maybe putting another stepping stone for those to come.

A PhD is a marathon with many sprints. It has struggles and disappointments. 99 failures before 1 success, which is enough though to make it worth it. It is a constant effort to compete at global level and keep the standards high.

A PhD is a privilege to be in a stimulating and dynamic environment, among creative people. It gives opportunities to develop skills in identifying problems, searching for solutions, making hypotheses, exploring them in different ways and collaborating with many disciplines. This process is far beyond acquiring a qualification or being trained on some advanced techniques

For this personal, educational and professional experience, I am grateful to my supervisors: Deborah Greaves, Dave Simmonds and Christophe Maisondieu. In particular, Deborah, who despite her numerous duties, was supportive from the first moment that welcomed me in the team and throughout the long period that I was working remotely, allowing me to explore different routes. Crucial was the support of Christophe, who did his best to invite me in Ifremer, which had a huge impact on the course of the present work.

Moreover, I would like to especially acknowledge Marc Prevosto, whose input was vital and made me love the maths again and appreciate the value of analytical methods. The support of Alan Tassin with the-after-5pm programming sessions was crucial for achieving operational codes. The correspondence and the advice of some of the developers of the methods and models was very important to better understand the principles and details. For that, I especially thank D. Stagonas, E. Buldakov, O. Gramstad, P. H. Taylor, G. Ducrozet and M. Benoit. Also, I would like to thank all my colleagues and friends in the University of Plymouth, Ifremer and the European Research Council EA, who, in their own way each, helped me complete this work.

Apart from the great psychological encouragement, the practical support of my sister Melpomeni for the artwork and the proofreading, together with Helena's input, were vital for achieving high quality of the manuscript. Also, my forever Plymouth flatmate Erwin Bergsma, the beloved Italian Al. Al. and the excellent paella cook Carlos, were always there and happy to remind me to submit! Of course, words are not enough to describe the support of my family, especially my parents Giannis and Fotini, who almost learnt sign language in order to be silent and not to interrupt my studying. My

aunts, Koula, Tasitsa and Vlasia, made my trips back home a delicious weight-gaining time.

Last but not least, the "ticket" for the PhD journey was financially covered mainly by the INTERREG IV A FP7 European project MERiFIC (Marine Energy in Far Peripheral and Island Communities) and the School of Engineering of the University of Plymouth. My research visit in Ifremer was supported by the internship grant of Ifremer, Erasmus + and LabexMER.

Abstract

Numerical Modelling of Extreme Waves:
The Role of Nonlinear Wave-Wave Interactions

Thomas Vyzikas

The real monsters of the ocean, extreme waves, haunted mariners since the early days of human activities in the sea. Despite having caused numerous accidents and casualties, their systematic study began only in 2000s. Many mechanisms have been proposed to simulate these rare but catastrophic events, with the most prominent being wave focusing. This is connected to the NewWave theory, which has been used extensively in experimental and numerical modelling. However, the majority of the studies fail to capture the distinguishing characteristics of extreme waves, due to the inherent high nonlinearity of the problem and shortcomings of the modelling practice, but also due to inadequate knowledge of the underlying physics. Overcoming these issues is unquestionably necessary for understanding extreme waves and including them in the engineering design practice.

The nonlinearity of the problem lies upon the nonlinear wave-wave interactions, which violate the fundamental linear assumptions of NewWave and pose challenges to numerical models. The present work aims at contributing in both understanding the nature of nonlinear wave-wave interactions during the formation of extreme wave events, and examining the applicability and performance of numerical solvers via their systematic validation with state-of-the-art techniques that give new insights into the problem. A range of phase-resolving and phase-averaged models are employed to cover different scales and examine the undergoing physical processes.

Through the study of limiting breaking unidirectional dispersive wave groups in finite water depth, it is demonstrated that the free-wave spectrum undergoes considerable transformation and a large portion of energy is transferred to higher and lower harmonics. These effects can be attributed to the action of near-resonant and bound nonlinearities, which have however robust mathematical description. As such, a large part of the thesis is devoted to analytical methods towards establishing an efficient integrated framework for estimating extreme wave profiles, going beyond the classic NewWave.

Overall, the present work is a balance of physics and numerics to tackle parts of the challenging problem of extreme waves and improve safety at sea.

Author's declaration

At no time during the registration for the degree of Doctor of Philosophy has the author been registered for any other University award without prior agreement of the Doctoral College Quality Sub-Committee.

Work submitted for this research degree at the University of Plymouth has not formed part of any other degree either at the University of Plymouth or at another establishment.

The following external institutions were visited for consultation purposes:

Ifremer, Centre Bretagne, France

Relevant scientific seminars and conferences were regularly attended at which work was often presented. Three papers were published in refereed journals.

Word count for the main body of this thesis: **78, 000**

Signed: _____

Date: _____

Publications:

Vyzikas, T., Stagonas, D., Buldakov, E. and Greaves, D. (2017). *The evolution of free and bound waves during dispersive focusing in a numerical and physical flume*, Coastal Engineering 132, pp. 95-109.
DOI: doi:10.1016/j.coastaleng.2017.11.003.

Vyzikas, T., Greaves, D. (2018), *Chapter 8: Numerical Modelling, Book: Wave and Tidal Energy*, Wiley-Blackwell publishing, pp. 289-363. ISBN-10: 1119014441.

Vyzikas, T., Deshoulières, S., Giroux, O., Barton, M. and Greaves, D. (2017). *Numerical study of fixed Oscillating Water Column with RANS-type two-phase CFD*

model, Renewable Energy 102, Part B, pp. 294-305.
DOI: doi:10.1016/j.renene.2016.10.044.

Vyzikas, T., Deshoulières, S., Barton, M., Giroux, O., and Greaves D. and Simmonds, D. (2017). *Experimental investigation of different geometries of fixed oscillating water columns devices*, Renewable Energy 104, pp. 248-258.
DOI: doi:10.1016/j.renene.2016.11.061.

Vyzikas, T., Greaves, D., Simmonds D., Maisondieu C., Smith H. and Radford L. (2014). Best practice report: Task 3.4.4 of WP3 from the MERiFIC project: *Application of numerical models and codes*. University of Plymouth, February 2014.

Conference proceedings:

Vyzikas, T., Prevosto, M., Maisondieu, C., Tassin, A. and Greaves, D. (2018). *Reconstruction of an extreme wave profile with analytical methods*, Proc. of IWWWFB33: 33rd International workshop for water waves and floating bodies, 4-7 April 2018, Guidel-Plages, France.

Vyzikas, T., Stagonas, D., Buldakov, E. and Greaves, D. (2015). *Efficient numerical modelling of focused wave groups for freak wave generation*, Proc. of ISOPE-2015: 25th Int. Ocean and Polar Eng. Con., 21-26 June 2015, Kona, Hawaii.

Vyzikas, T., Stagonas, D., Buldakov, E. and Greaves, D. (2014). *On the simulation of focused waves with OpenFOAM & waves2Foam*, Proc. of Coastlab14: 5th Int. conf. on the application of physical modelling to port and coastal protection, Vol. 2, pp. 237-282, 29 September - 2 October 2014, Varna, Bulgaria.

Vyzikas, T., Ransley, E., Hann, M., Magagna, D., Greaves, D., Simmonds, D., Magar V. and Conley D. (2013). *Integrated Numerical Modelling System for Extreme Wave Events at the Wave Hub Site*, Proc. of the ICE conf.: Coasts, Marine Structures and Breakwaters 2013, 18-20 September 2013, Edinburgh, U.K..

Vyzikas, T., Greaves, D., Simmonds, D., Ransley, E. and Brown, S. (2013). *Shape optimization of perforated caissons for wave energy harnessing*, Proc. of the 6th PanHellenic conf. of Marine Structures, 10-14 November 2013, Athens, Greece.

Posters and oral presentations:

Alberello, A., **Vyzikas, T.**, et al. (2017). Poster:*Simulation of the Peregrine Breather with a Multi-Layer Non-Hydrostatic Model*, European Geosciences Union General Assembly (EGU), Vienna, Austria, 23-28 April 2017.

Vyzikas, T., et al. (2015). Poster:*Experimental and numerical analysis of OWCs*, 2^{nd} PRIMaRE conference, Penryn, UK, 16-17 June 2015.

Vyzikas, T., et al. (2014). Poster:*Simulating focused waves with OpenFOAM*, 1^{st} PRIMaRE conference, Plymouth, UK, 4-5 June 2014.

Vyzikas, T., et al. (2014). Poster:*Focusing wave groups with OpenFOAM*, Inore Symposium, La Vega, Spain, 11-17 May 2014.

Vyzikas, T. . Oral presentation: *Integrated numerical modelling of a wave tank*, 4^{th} UK Marine Technology Postgraduate Conference, University College London, UK, 11-12 June 2013.

Vyzikas, T., et al. (2013). Poster:*Composite modelling for MRE*, Inore Symposium, Pembrokeshire, UK, 12-18 May 2013.

Vyzikas, T. . Oral presentation: *Composite Modelling of an extreme wave event in the Wave Hub site*, Marine Operation MERiFIC Workshop, University of Plymouth, UK, 26-27 March 2013.

Contents

List of Figures

List of Tables

Nomenclature

Abbreviations

1D; 2D; 3D	One-, two-, three-, dimensional
3G	Third Generation
AM	Amplitude matching location
AR	Aspect Ratio
BDF	Backward difference scheme
BEM	Amplitude matching location
BF	Benjamin-Feir
BFI	Benjamin-Feir Index
BST	Bateman-Swan-Taylor model
CCD	Charge Coupled Device (CCD camera)
CF	Crest Focused
CFD	Computational Fluid Dynamics
COAST	Coastal, Ocean And Sediment Transport laboratory (UoP)
controlDict	Control dictionary in OpenFOAM
COSMHOS	High order spectral (HOS) method code
CPU	Central Processing Unit
DIA	Discrete Interaction Approximation
DNO	Dirichlet to Neumann Operator

DNS	Direct Numerical Simulation
ECN	Ecole Centrale de Nantes
EDL	Edinburgh Designs Ltd.
FAR	Fatal Accident Rate
FBI	Full Boltzmann Integral
FDM	Finite Difference Method
FEM	Finite Element Method
FFT	Fast Fourier Transform
FSI	Fluid-Structure Interaction
FVM	Finite Volume Method
GKE	General Kinetic Equation
GMD	Generalized Multiple DIA
GPU	Graphics Processing Unit
GSE	Garden Sprinkler Effect
GUI	Graphical User Interface
HF	High Frequency (radars)
HFA	Hydrostatic Front Approximation
HOBEM	High Order Boundary Element Method
HOS	High Order Spectral
HOST	High Order Spectral method Tank
HPC	High Performance Computer
IFFT	Inverse Fast Fourier Transform
IG	Infragravity
ILU	Incomplete L unit lower triangular and U upper triangular
IOWAGA	Integrated Ocean Waves for Geophysical and other Applications

JONSWAP	Joint North Sea Wave Project
KE	Kinetic Equation
LDA	Laser Doppler Anemometry
LES	Large Eddy Simulation
LHEEA	Laboratory in Hydrodynamics, Energetics and Atmospheric Environment (ECN)
LTA	Lumped Triad Approximation
MERiFIC project	Marine Energy in Far Peripheral and Island Communities
MI	Modulation Instability
MNLSE	Modified Nonlinear Schrödinger Equation
MPI	Message Passing Interface
MRE	Marine Renewable Energy
MULES	Multi-dimensional Limiter for Explicit Solution
MWL	Mean Water Level
N.I.	Numerical Inlet
NASA	National Aeronautics and Space Administration
NCEP	National Centers for Environmental Prediction
NetCDF	Network Common Data Form
NL	Nonlinear
NLSE	Nonlinear Schrödinger Equation
NLSWE	Nonlinear Shallow Water Equations
NOAA	National Oceanic and Atmospheric Administration
NSE	Navier-Stokes Equations
NWT	Numerical Wave Tank
OpenFOAM	Open source Field Operation and Manipulation

OpenMP	Open Multi-Processing
OpenMPI	Open Message Passing Interface
OWC	Oscillating Water Column
PAE	Phase Averaged Equation
PDEs	Partial Differential Equations
PF	Phase Focal
PFS	Potential Flow theory (solvers)
PIV	Particle Image Velocimetry
PM	Pierson-Moskowitz
QALE-FEM	Quasi Arbitrary Lagrangian-Eulerian Finite Element Method
RANS	Reynolds Averaged NSE
SCM	Self-Correcting Method
SPH	Smoothed Particle Hydrodynamics
SWAN	Simulating WAves Nearshore model
SWASH	Simulating WAves till Shore model
SWE	Shallow Water Equation
SWEET	Spectral Wave Evolution in the ECN Tank
SWENSE	Spectral Wave Explicit Navier-Stokes Equations
SWL	Still Water Level
SWOT	Strengths, Weaknesses, Opportunities, Threats analysis
TF	Trough Focused
TSA	Two-Scale Approximation
UCL	University College London
USSR	Union of Soviet Socialist Republics
VoF	Volume of Fluid Method

WAM	WAve Modelling model
WG	Wave Gauge
WM	Wavemaker
WRT	Webb-Tracy-Resio method
WW3	WAVEWATCH III model
ZE	Zakharov Equation

Symbols

A	Coefficients at integrals that correspond to the second order bound waves (Krasitskii)
A	Wave action (WW3)
A_{Th}	Linearly predicted amplitude of focused wave
A_f	Total area of computational cell face (OpenFOAM)
A_w	Wet area of computational cell face (OpenFOAM)
A_i, B_i, C_i	Parameters to define the order of the wavemaker (HOS)
$alphaC_o$	Courant number at the interface of the fluids (OpenFOAM)
a_j	Scaling parameter for the energy of the JONSWAP spectrum (HOS)
$B_p(k_i,k_j)$, $B_m(k_i,k_j)$	Coefficients second order theory
B_{ij}	Coefficients of Fifth order approximation as hyperbolic functions of kd
B	Coefficients at integrals that correspond to the third order bound waves (Krasitskii)
B_{mn}	Transformation of the flow variables in the Fourier space (HOS)
$b(k,t)$	Generalized complex amplitude spectrum of free waves in the transformed space (GKE)
b_i^*	Complex conjugate of $b(k,t)$ for wave component i
$b(k)$	Auxiliary variable for amplitude spectrum in $\kappa-$space (Krasitskii)
C	Proportionality constant given by tuning of the source term in DIA (WW3)
C_o	Courant number
C_i	Wave action
C_n	Wave action spectrum with n components (GKE)
Cg_i	Wave group celerity for every component i
C_i	Wave phase celerity for component i

c_f	Bottom friction (SWASH)
c_g	Group velocity (WW3)
$\mathbf{c}_g$	Vector of group velocity (WW3)
c_θ	Propagation velocity in $\theta-$ space (spectral modelling)
c_σ	Propagation velocity in $\sigma-$ space, accounting for shift in the relative frequency due to depth and currents (spectral modelling)
$D\mathbf{k}_i$	Area of a bin of component i in the wavenumber vector place (GKE)
$D(\theta)$	Directional distribution of the energy density spectrum (JONSWAP)
Dk	Wavenumber increment in the $\kappa-$grid
Dt	Timestep in GKE
$D_p(k_i,k_j)$, $D_m(k_i,k_j)$	Coefficients second order theory
Dx	Spatial resolution in $x-$plane (Linear theory)
D_{ij}	New variables of Fifth order approximation
Dx	Spatial resolution / distance increment of wave profile
D	Factor for the effect of water depth in DIA (WW3)
d	Water depth
df	Frequency increment
$dx, \quad dy, \quad dz$	Dimensions of computational cells (OpenFOAM)
E	Total energy of the wave field (WW3)
F	Variance density spectrum (WW3)
$\hat{F}$	Fourier transform (Krasitskii)
$F(\omega)$	Frequency discretization of the energy density spectrum (HOS)
f_i	Frequencies of wave component i
f_{mean}	Mean frequency of the spectrum

f_p	Peak frequency
$f-$space	Frequency / Fourier space
f_r	Relative frequency (WW3)
f_a	Absolute frequency (WW3)
$G(\theta)$	Directional spreading of the energy density spectrum (HOS)
G	Coupling coefficient in Boltzmann integral (WW3)
g	Gravitational acceleration
H	Wave height
H_s	Significant wave height calculated from the standard deviation of the surface elevation
$H_{1/3}$	Significant wave height calculated from zero-crossing analysis (highest third of the waves)
H_{m0}	Significant wave height calculated from zeroth spectral moment in deep water
H_{max}	Maximum wave height
H_s^{orig}	H_s calculated from the full timeseries of the focused wave
$H_s(t)$	A time dependent H_s used for investigations in the GKE
H_s^{PF}	H_s calculated from the compacted timeseries at Phase Focal location (GKE)
$H^{(n)}$	Hamiltonian of order n
H_{rms}	Root mean square of wave height
$\tilde{H}$	Total energy (Hamiltonian) of the wave field (GKE)
$\tilde{H}$	Canonically transformed Hamiltonian (Krasitskii)
h	Water depth of the domain (HOS)
h_k	Thickness of layer k (SWASH)
K	Number of layers at the $\sigma-$transformed grid (SWASH)
k_i	Wavenumber of wave component i

k_p	Wavenumber of wave component of peak frequency
k	Wavenumber vector
L	Wavelength
L_a	Characteristic length scale for Reynolds number
L_p	Wavelength of the peak-frequency component
L_{mean}	Wavelength of component of mean frequency
L_x	Total length of the domain (HOS)
L_y	Beam length of the numerical domain (HOS)
$[L]$, $[T]$	Normalised space and time scales (HOS)
$M(k)$ $N(k)$	Transformation variables (Krasitskii)
m_n	n^{th} moment of the energy density spectrum
m	Order of HOS
N	Number of components / sinusoidal waves
N	Number of spectral modes (HOS)
$N1$	Number of modes in $x-$direction (HOS)
$N2$	Number of modes in $y-$direction (HOS)
$N3$	Number of modes at the wavemaker (HOS)
$\tilde{N}$	Total wave action of the wave field (GKE)
NR	Non-resonant wave interactions
N_d	Larger modes of expansion of spectral space that equal zero (HOS)
$N(k,\theta)$	Action density spectrum (WW3)
N_i	Wave action density of wave component i (WW3)
n_s	Number of segments in WRT (WW3)
$O(\varepsilon^{-i})$	Time scale evolution of a wave field based on steepness

$O(\Delta t^i)$	Truncation error of Taylor expansion at order i
$P(s_i)$	Product term at a point on the locus in WRT (WW3)
$\tilde{\mathbf{P}}$	Total momentum of the wave field (GKE)
p_o	Total pressure (OpenFOAM)
p	Pressure (OpenFOAM)
p^*	Pseudo-dynamic pressure (OpenFOAM)
p_h	Hydrostatic part of pressure (SWASH)
$q(k)$	Variable for linear dispersion (Krasitskii)
q_b	Non-hydrostatic pressure at the bottom (SWASH)
$q(x,z,t)$	Non-hydrostatic pressure (normalised by the density) (SWASH)
q	Non-hydrostatic part of pressure (SWASH)
q_k	Hydrodynamic pressure (SWASH)
R	Resonant wave interactions
R_i	Introduced coefficient for transformations of variables in Fourier space (Krasitskii)
Re	Reynolds number
$S(\omega)$	Energy density spectrum
S	Timeseries of the surface elevation (four wave decomposition)
S^H	Imaginary part of the Hilbert transform of the timeseries of S
$S(f)$	Frequency-energy density spectrum
$S(k)$	Wavenumber-energy density spectrum
$SD(\eta(t))$	Standard deviation function of surface elevation
S_{nl}	Source term in spectral models for the nonlinear four-wave interactions
ψ_i	Phase of wave component i (Linear theory)
S_{ij}	Stokes coefficients (Fifth order approximation)

S_{tot}	The source terms (WW3)
S_{in}	Source term for wave generation by the wind input (WW3)
S_{ds}	Source term for energy dissipation (whitecapping) (WW3)
S_{ice}	Source term for wave-ice interactions (WW3)
S_{bot}	Source term for wave-bottom interactions (WW3)
S_{db}	Source term for depth-induced (WW3)
S_{tr}	Source term for triad wave-wave interactions (WW3)
S_{sc}	Source term for wave scattering by the bottom (WW3)
S_{ref}	Source term for wave reflection by shorelines or floating objects (WW3)
S_{xx}	User defined source terms (WW3)
s_i	Coordinates of segments in WRT (WW3)
s	Coordinate in the direction θ (WW3)
T_p	Peak wave period
$T_{1,2,3,4}$	Coupling coefficient for the KE, which corresponds to the coefficient $\tilde{V}^{(2)}_{0,1,2,3}$ Krasitskii (1994)
T_m	Mean wave period
$T(\mathbf{k}_1, \mathbf{k}_3)$	Function for the WRT (WW3)
t	Time
U_r	Ursell number
U, Z, V, E, Γ	Krasitskii's auxiliary coefficients
$\mathbf{U}$	Uniform velocity of the current (WW3)
U_c	Uniform velocity in depth (calculated with SWE assumption)
$\mathbf{U}$	Velocity vector (OpenFOAM)
$\mathbf{U}_r$	Relative compression velocity at the free surface (OpenFOAM)
u	Horizontal velocity component (OpenFOAM)

$\overline{u}_x$	Horizontal velocity averaged in the vertical (Boussinesq)
u_{mag}	Velocity magnitude
u_x	Horizontal velocity
u_z	Vertical velocity
$u(x,t)$	Depth averaged horizontal flow velocity (SWASH)
u_k	Horizontal velocity defined at the middle of the computational cell (SWASH)
u_{in}	Corrected value of incident velocity in sponge layer (SWASH)
v	Velocity component normal to the NWT (OpenFOAM)
v_t	Eddy viscosity (SWASH)
W	Vertical velocity at the free surface (HOS)
w	Vertical velocity component (OpenFOAM)
w_r	Weighting function in relaxation zone (OpenFOAM)
w_s	Vertical velocity at the free surface (SWASH)
w_b	Vertical velocity at the bottom (SWASH)
w_k	Vertical velocity defined at the middle of the computational cell (SWASH)
$\mathbf{X}$	Position vector (OpenFOAM)
$x, \quad y, \quad z$	Cartesian coordinates
$\mathbf{x}$	Location vector in horizontal plane
$xlen$	Length of computational domain in the $x-$direction (HOS)
α_i	Amplitude of wave component i
$\alpha(f_i)$	Amplitude of wave component i in the frequency-energy spectrum $S(f)$
$\alpha(k)$, $\alpha^*(k)$	Canonically conjugate variables for amplitude spectrum in $\kappa-$space (Krasitskii)

$\alpha_f(k)$	Amplitude spectrum of free waves in $\kappa-$space (Krasitskii) (Krasitskii)
β	Parameter controlling directionality of spectrum (HOS)
β_{1234}	Stokes drift coefficient (GKE)
γ_i	Scalar field of the fluid phase fraction (OpenFOAM)
γ	Peak enhancement factors of the JONSWAP spectrum
γ	Surface tension parameter (Krasitskii)
Δt	Time step (HOS)
Δ_{12}^{34}	Difference among angular frequencies ω_i for interacting wave quadruplet (GKE)
ΔX	Displacement of the wave paddle (OpenFOAM)
δ_{12}^{34}	Kronecker delta for interacting wave quadruplet (GKE)
δ	Function in Fourier transformations (Krasitskii)
δt	Maximum time step allowed by C_o (OpenFOAM)
ε_i	Arbitrary phase of wave component i (Second order theory)
ε	Wave steepness
$\zeta(\mathbf{x},t)$, $\eta(\mathbf{x},t)$	Vertical displacement of the free surface (Krasitskii)
$\zeta(x,t)$	Free surface elevation measured from the SWL (SWASH)
ζ_{in}	Target value of incident free surface elevation in sponge layer (SWASH)
η_R	Surface elevation of the incoming wave to the boundary
η_c	Crest elevation
η	Free surface elevation
$\eta(x,t)$	Free surface elevation as a function of space and time (Linear theory)
η_L	Linear wave profile (Fifth order approximation)

η_{LH}	Hilbert transform of linear wave profile (Fifth order approximation)
η_{2-}	Global set-down of the free surface elevation calculated by second order theory (approximation)
$\eta_H(x)$	Hilbert transform of the spaceseries of the surface displacement (Creamer)
$\eta_{NL}(k)$	Nonlinear amplitude spectrum (Creamer)
$\eta(x)$	Vertical displacement of the free surface for unidirectional waves (Krasitskii)
$\eta(k)$	Complex amplitude spectrum in $\kappa-$space (Krasitskii)
η_R	Real part of complex amplitude spectrum in $\kappa-$space (Krasitskii)
η_I	Imaginary part of complex amplitude spectrum in $\kappa-$space (Krasitskii)
$\hat{\eta}(k)$	Hamiltonian form of vertical displacement of the free surface after the canonical transformations (Krasitskii)
$\theta_{1234}(t)$, β_{1234}	Parameters in the GKE
$\theta(k)$	Phase of wave components in $\kappa-$space (Krasitskii)
θ-scheme	Parameter to select between Crank-Nicolson scheme and first-order backward Euler scheme (SWASH)
θ	Direction of wavenumber k (WW3)
θ	Function for the WRT (WW3)
$\kappa-$space	Wavenumber space
κ_c	Curvature of the interface of the fluids (OpenFOAM)
λ_{nl}	Constant shape parameter in DIA (WW3)
μ_{eff}	Efficient dynamic viscosity (OpenFOAM)
μ	Molecular dynamic viscosity (OpenFOAM)
μ_t	Turbulent viscosity (OpenFOAM)
ρ	Density of the fluid

$\Sigma\alpha_i$	Amplitude sum of focused waves
σ	Spectral variance
σ_τ	Surface tension coefficient (OpenFOAM)
$\sigma-$	$\sigma-$transformed vertical grid (SWASH)
σ	Wave frequency altered by the current velocity (WW3)
σ_{SD}	Standard deviation
τ_{ij}	Turbulent stresses (SWASH)
ϕ_i	Phase of wave component i
$\phi_s(x)$	Velocity potential for unidirectional waves (Krasitskii)
ϕ_{add}	Additional potential for the wavemaker (HOS)
ϕ_{spec}	Potential in the original computational domain for the wavemaker (HOS)
$\hat{\phi}_s(k)$	Hamiltonian form of velocity potential after the canonical transformations (Krasitskii)
$\tilde{\phi}(x,t)$	Velocity potential at the free surface (HOS)
ψ_i	Phase of wave component (OpenFOAM)
$\psi(\mathbf{x},t)$, $\phi_s(\mathbf{x},t)$	Velocity potential (Krasitskii)
$\tilde{\phi}$	velocity potential at the free surface elocity potential at the free surface
Ψ	Arbitrary flow variable, e.g., velocity, surface elevation, pressure.
Ψ_{com}	Calculated value of flow variable by the governing equations for the fluid
Ψ_{trg}	Target value of flow variable by the governing equations for the fluid
ψ_m	Spectral space for the expansion of the velocity potential (HOS)
ω_i	Angular frequency of wave component i
ω_p	Angular frequency of wave component of peak frequency

ω	Absolute angular frequency of wave component (WW3)

Chapter 1

Introduction

THIS work examines the nonlinear wave-wave interactions occurring during the dispersive focusing of NewWave-type wave groups. Using a newly developed focusing methodology, a range of numerical models are validated against experimental results and they are later employed to identify the role of wave-wave interactions during the formation of extreme waves. Analytical models are then used to try to reproduce these interactions in a stochastic approach towards suggesting an improved representation for NewWave profiles. The Introduction explains the rationale of the work, the research route followed and the structure of the Thesis.

The work context

The development of human civilization is strongly bonded with settlements at coast and activities at sea. Nowadays, apart from the large ocean trade routes, other exploitation activities, such as offshore drilling, keep expanding and new, more sustainable solutions, such as offshore wind, wave and tidal energy, have emerged. The increased need for energy and shorter navigation routes is pushing the offshore and shipping industry into harsher environments, e.g., the Arctic (Bitner-Gregersen et al., 2014). At the same time, Marine Renewable Energy (MRE) devices require energetic envi-

ronments for high energy yield (Boudière et al., 2013). The issue in both cases is that marine structures and vessels must withstand greater operational environmental loads, with the dominant being that of waves. Supposing that the wave height can be predicted based on the environmental forcings and factors, e.g., wind and bathymetry, the problem simply reduces to calculating the corresponding structural parameters to ensure the safety of the crew and integrity of the structure. However, many accidents have been reported due to abnormally high and unexpected waves. Mariners had built legends around these monster waves, but solid evidence for the existence of extreme waves came with analysis of field data. Systematic research activity in the topic only started two decades ago and there is still no consensus in the scientific community even about the basic aspects of extreme waves (Bitner-Gregersen and Gramstad, 2015). The findings so far suggest that extremes are rare, local events in space and time, of high steepness and nonlinearity. As such, the inclusion of extremes in the engineering design process remains an untackled and challenging task. Moreover, since the risk of extremes is higher in energetic sea states (Christou and Ewans, 2014), investments in the MRE sector are delayed due to uncertainties. As a consequence, the sector develops slowly and wave energy is not considered viable at present unless it is subsidized (Astariz and Iglesias, 2015). Nevertheless, there are emerging synergetic ideas combining energy generation and coastal protection (Abanades et al., 2014; Vyzikas et al., 2017a) or collocation with wind farms (Pérez-Collazo et al., 2015).

Wave-wave interactions

One of the major physical processes taking place during the formation of extreme waves is nonlinear wave-wave interactions, which redistribute the energy in the wave spectrum. Despite their complexity and sometimes ambiguous effects, wave-wave interactions have a robust mathematical description, referring to a six-fold Boltzmann integral (Hasselmann, 1962). Among the different suggested generation mechanisms of extreme waves, phase focusing of the energetic components of the spectrum is

the best validated with field data (Christou and Ewans, 2014). During the focusing process, considerable changes were shown to occur at the underlying free-wave spectrum, which can be associated with nonlinear resonant wave-wave interactions, and, at the same time, bound wave interactions become strong, increasing the steepness of the group. The combination of explicit mathematical description of wave-wave interactions and focusing as generation mechanism opens a window for studying extreme waves purely analytically.

On the downside, the computational effort required to solve explicitly for all the possible wave-wave interactions makes can be considerable, hindering their application in operational models and engineering practice. Moreover, on one hand, the exact role of wave-wave interactions during the focusing process is not fully understood, and on the other hand, wave focusing may not be the only mechanism that contributes to extreme wave generation, with other environmental factors being potentially important, e.g., currents and bathymetry. A way to mitigate these uncertainties is by blending as much physics as possible in the solution and accounting for wave-wave interactions implicitly. This can be achieved through the numerical modelling of the hydrodynamical equation.

The state of the art in modelling of extreme waves

The development and use of numerical models for solving the hydrodynamical equations have expanded dramatically during the last two decades. Models vary from fully nonlinear computational fluid dynamics (CFD) codes that are accurate and computationally expensive, to more approximate[1], but efficient models, such as nonlinear shallow water equations (NLSWE) and potential flow solvers (PFS). On determining the most appropriate shape of extreme waves, the best established and validated method is the NewWave theory (Tromans et al., 1991). According to it, the most likely shape of an extreme wave in the ocean can be given by the autocorrelation function of the cor-

[1] Approximate in a sense that they can simulate only weakly nonlinear problems, without accounting for phenomena of high turbulence, such as wave breaking and green water effects.

responding energy spectrum, or simply speaking, by a focused wave group. NewWave offers a very convenient approach to simulate deterministic extreme waves without the need for random simulations, making it ideal for expensive models and physically limited experimental facilities (Stagonas et al., 2018).

Nevertheless, considerable discrepancies may occur during the focusing of waves due to nonlinearities, causing unexpected transformations of the wave group and partial loss of control over the simulated signal. To mitigate this, focusing methodologies that correct the signal for the nonlinearities have been developed, but commonly, discrepancies persist for wave groups of high steepness. Important consequences refer to missing the maximum impact of an extreme wave on the examined structure and to suboptimal validation of models against experimental results. However, the recently developed focusing methodology of Stagonas et al. (2014), used in the present study, provides accurate focusing of up to breaking wave groups and excellent comparisons between models and experiments, which is essential for additional studies with numerical models. The new methodology is based on the separation of harmonics of the wave group, which also gives a good insight of the undergoing wave-wave interactions (Vyzikas et al., 2018b).

The first objective: validation of models

Aiming at creating confidence in the use of skilled solvers for interaction of extreme waves and marine structures, the first step was to ensure accurate simulation of the NewWave-type groups in a skilled CFD solver, namely OpenFOAM, which corresponds to solution path "1" in Figure 1.1. Initial attempts with empirical methods for the correction of the signal revealed discrepancies between OpenFOAM and experiments (Vyzikas et al., 2013), which were not expected since the solver could theoretically account for the physics of the problem. After identifying that the issue was on the boundary conditions, it was decided to test the new focusing methodology of Stagonas et al. (2014) in order to correct the input signal. Indeed, the first numerical results

showed excellent comparison with the experiments -far beyond the state of the art (Chen et al., 2014)- and demonstrated clearly the harmonics' structure of the spectrum (Vyzikas et al., 2014b).

However, the issue with the focusing methodology is that it is based on iterative corrections of four phase shifts of the wave group, inducing considerable computational burden for a high resolution numerical wave tank (NWT) in CFD. Thus, it was decided to check the applicability of the focusing method on other more efficient solvers, namely NLSWE (SWASH) and PFS (HOS-NWT), which could be potentially used for the iterations before the CFD model, as demonstrated in the solution path "2-2a" in Figure 1.1. The initial results with SWASH showed that although the model could accurately simulate extreme waves, there were noticeable differences between the boundary conditions of SWASH and OpenFOAM, hindering their potential integration (Vyzikas et al., 2015). Nevertheless, it was demonstrated for the first time that approximate, computationally efficient solvers can have such impressive performance. Thus, their thorough and systematic validation for the challenging problem of extreme waves became the first objective of the present work, which corresponds to solution path "2-2b" in Figure 1.1. It is noted that coupling of the models with domain decomposition techniques (Paulsen et al., 2014a) was not attempted, since the objective was to correct the signal for the nonlinearities in order to achieve accurate focusing and not to design an overall computationally efficient NWT.

Along with the accurate focusing of the waves, the focusing methodology can offer unique insights in the spectral transformation due to the underlying wave-wave interactions, provided that the locations of the correction of the signal are selected strategically in order to observe the natural evolution of the spectrum. This allowed for the first time to obtain the accurate evolution of the free-wave spectrum and the emergence of bound harmonics up to fourth order (Vyzikas et al., 2018b).

The fortunate outcome of this part of the work, presented in Chapter 3, is a range of well-validated open-source NWTs designed in the fully nonlinear CFD model Open-

FOAM, the operational NLSWE model SWASH and the very efficient PFS-based high order spectral model HOS-NWT. Moreover, thanks to the four-wave harmonic decomposition method, the nonlinear wave-wave interaction processes could be identified, isolated and examined as they evolve towards the formation of an extreme wave.

Phase-averaged Vs Phase-resolving approach

Being able to track the evolution of the constituents of the energy spectrum in phase-resolving NWTs until the moment of the formation of the extreme wave (zero phases), a natural question raises whether the observed spectral transformation can be reproduced stochastically, i.e., without assigning phases to the wave components of the spectrum. This is common approach for examining spectral evolution at large scales with phase-averaged, aka spectral, models. Thanks to their computational efficiency, spectral models are routinely used for wave forecasting at ocean and regional scales. Spectral modelling is based on the energy balance equations with source terms to account for the nonlinear physical processes, including nonlinear wave-wave interactions.

To examine if the source terms can reproduce similar evolution of the spectrum, a custom set-up of WAVEWATCH-III (WW3) was prepared at similar timescales as the experiment. The available four-wave resonant interaction source terms, which are approximations of the Boltzmann integral, were tested in order to capture the evolution of the free-wave spectrum. An insuperable barrier was that these approximations account only for the interaction of directional waves, which are the most important in the ocean, but yield no spectral evolution for unidirectional waves, such as the NewWave groups simulated in phase-resolving models. At the moment of exploring the potential alternatives, Gramstad and Babanin (2016) published their first results using an improved version of source terms that include near-resonant interactions for unidirectional waves. To present, still this source term has not been implemented in the public distribution of WW3. A challenging path was thus taken, trying to program independently the near-resonant interactions stochastically with the General Kinetic Equation

(GKE). The literature on the topic is very recent and very limited, forcing the author to go through many potential pitfalls before reaching an operational code.

Using the custom-made GKE code, many ways were explored to obtain the expected free-wave spectral evolution. An alternative way to obtain the evolved free wave spectrum refers to envelope equations, but their limitations in spectral bandwidth and steepness of the waves pose considerable constraints, as discussed in Section 2.1.7. Despite not reaching exactly the one of the experiment, good agreement was observed through a suggested methodology that practically "marries", to an extent, phase-averaged and phase-resolving models. The road is of course long before making any generalizations and concrete statements.

The research hypothesis

Where can phase-resolving NWTs, NewWave theory, focusing methodology and analytical solutions of source terms lead?

At this stage, well-validated NWTs became available to simulate extreme waves and a phase-averaged equation (GKE) that can predict the free-wave spectrum. According to the theory, the bound wave nonlinearities are uniquely defined by the free-wave spectrum (Holthuijsen, 2007). This implies that if a method to calculate the bound interactions based on the evolved free-wave spectrum of GKE exists, the extreme wave profile for a given spectrum can be potentially estimated with purely analytical methods. This is explored in the solution path "3" in Figure 1.1. The final result should be comparable with that of phase-resolving NWTs, provided that the expansion to high orders is accurate.

The expected gain from this process is that there is no need for running numerical models and correcting the signal with iterations, since the extreme wave profile can be calculated by time marching the solution of the GKE and adding high order bound nonlinearities of the evolved free-wave harmonics. This process is demonstrated in

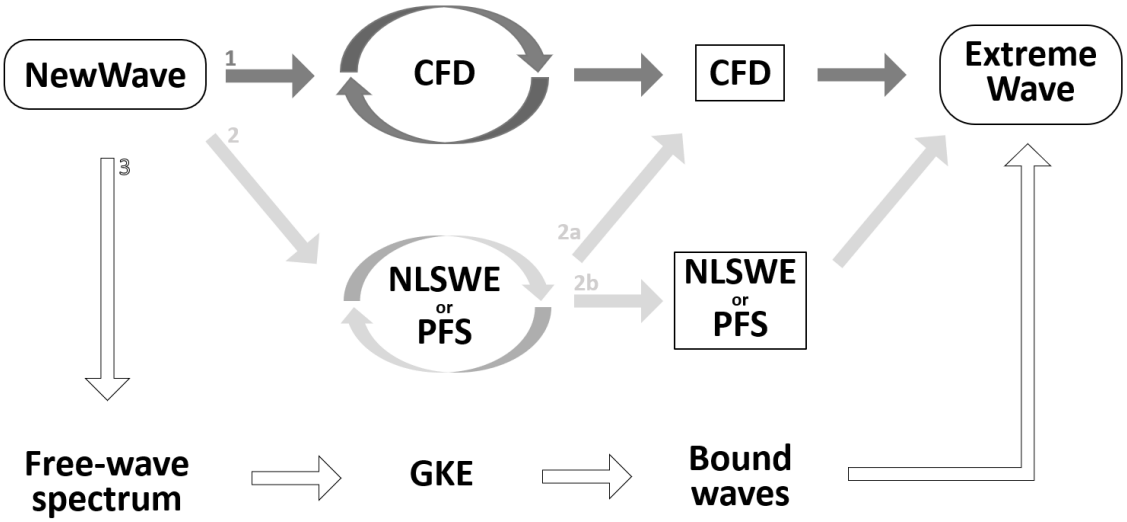

Figure 1.1: Different ways of calculating an extreme wave profile based on a given spectrum. Curved boxes, oval arrows and rectangulars represent the starting/ending point, iterations with focusing methodology and final run in the NWTs, respectively.

Chapter 5, where linear theory is compared with four high order methods to reconstruct the extreme wave profile.

Scientific Hypothesis: NewWave theory can provide a realistic profile of extreme waves, if the evolved free-wave spectrum is used with nonlinear bound harmonics.

As discussed, there are several ways to model an extreme wave profile, i.e., using phase-resolving or phase-averaged methods combined with analytical methods. The routes to reproduce an extreme wave profile are shown in the schematic of Figure 1.1.

The tools used to approach the different elements of the problem are:

(i) OpenFOAM with waves2Foam (Jacobsen et al., 2012) and IHFOAM (Higuera et al., 2013a) wave generation and absorption boundary conditions for high-fidelity CFD simulations of focused waves.

(ii) SWASH and HOS-NWT for computationally efficient phase-resolving simulations of focused waves.

(iii) HOS-ocean for computationally efficient Monte Carlo-type simulations the for verification of the GKE.

(iv) WW3 for exploring the source terms for four-wave interactions in phase-averaged models.

(v) The GKE for solving the four-wave near-resonant interactions.

(vi) Analytical methods for reconstructing the extreme wave profile: linear theory, second order theory, fifth order expansion, Creamer transform and static Krasitskii.

The methods to correct and analyse the signal into harmonics were the focusing methodology of Stagonas et al. (2014) and the four-wave decomposition method, respectively.

Challenges and risks

The present work is formulated around a fundamental pre-assumption that during the dispersive focusing of NewWave-type groups the evolution of the free-wave spectrum is governed by resonant / near-resonant four-wave nonlinear interactions. Although this is the only mechanism that is known to change the dispersive properties of free waves and there has been evidence for that since the work of Baldock et al. (1996) for this type of problem, there is no solid proof that this is a valid or the only possible mechanism (Johannessen and Swan, 2003). It was also stated that there had been no existent theories to describe the changes in the free-wave regime (Johannessen and Swan, 2001). In fact, the present work attempts to give an answer by explicitly solving for the four-wave interactions via the GKE. Similarly, the role, or more specifically the strength, of bound nonlinearities during the formation of NewWave-type extreme waves is not clear. Overall, the impact of bound and resonant nonlinearities is an open debate. This is discussed in Chapter 2.

Assumption: The free-wave spectrum changes due to near-resonant wave-wave interactions occurring during the dispersive focusing of the wave group.

The major challenge that this work faces is that it tries to connect phase-averaged and phase-resolving methods for nonlinear wave-wave interactions during the formation of extreme waves. From a modelling point of view, these methods are seen almost always independently and used at different scales and for different purposes. Finding equivalent spectral parameters between the two methods is one of the main objectives of the present study. From a theoretical point of view, there are two main "schools" in the modelling of extreme waves: modulation instabilities and dispersive focusing. These two physical processes are based on different principles and employ different modelling and analysis techniques. The issue is that the literature coming from these two research communities is often contradictory and it might be an one-way road to select one of the two approaches. Here, dispersive focusing is used thanks to its practical advantages and recent evidence that it occurs in nature (Christou and Ewans, 2014; Fedele et al., 2016).

Another challenge, from a practical perspective, is that since newly developed methods are implemented in the present work, the literature is often limited. For phase resolving models, the use of the focusing methodology provided for the first time highly accurate focusing and clear view of the harmonic structure of the wave. This was not possible with other methods used in the literature until recently. The consequence is that inaccuracies in focusing and discrepancies between models and experiments were commonly interpreted as different physics or limitations of the models, see e.g., Katsardi and Swan (2011) and Higuera et al. (2015), respectively. Thus, direct comparisons with previous studies can be often misleading. Additionally, the fact that only open-source models were used for the present work should not be underestimated, since all the adaptations were made manually and with limited provided support.

Other practical issues refer to the GKE. Since it was suggested very recently (Gramstad

and Stiassnie, 2013; Gramstad and Babanin, 2016), the literature is limited or practically non-existent when examining the short-term evolution of the spectrum. Moreover, the programming of the method and its coefficients are far from trivial, which in combination with the limited literature makes it hard to find potential errors. Similar is the case for some of the techniques of reconstructing the wave profile, where literature is little and often within a different context.

Mitigation strategy: integrated approach

The aforementioned challenges are mitigated with a modelling practice that employs the most appropriate tools for each problem. This is in-line with the composite modelling approach suggested in order to minimize uncertainties and increase efficiency (Sutherland and Barfuss, 2011)[2]. As such, numerical models, experiments and theories should act complementary, and in competition, for offering opportunities on holistic further developments. This can be part of an optimized balanced approach within the context of composite modelling, in order to obtain a more complete view of the problem.

Under this principle, physical modelling is routinely employed to validate the phase-resolving NWTs of the present work, before any further use. Moreover, experiments are used to find the onset of wave breaking. This is because numerical models may induce discrepancies due to the modelling of turbulence, for example the selection of different turbulence models for wave breaking in OpenFOAM (Brown et al., 2016), the heavy bore-like parameterization in SWASH and the complete neglection of turbulence in HOS-NWT.

Numerical models are used to gain better insight in the evolution of the wave groups thanks to the possibility of obtaining measurements of the flow variables at any time and location. Phase-resolving models are also used to verify analytical methods, for example Monte Carlo simulations are employed to verify the GKE in order to miti-

[2] A strengths-weaknesses-opportunities-threats (SWOT) analysis for MRE modelling problems is found in (Vyzikas et al., 2014a).

gate the issue of limited literature. Also, the validity and performance of the analytical methods to reconstruct the extreme wave profile are benchmarked against numerical simulations.

Analytical methods are used to obtain an insight in the underlying physical processes, thanks to the fact that these get a mathematical description and can be studied separately (Babanin et al., 2012). The benefit of understanding the physics of the problem is that the verified analytical methods can be then used to put the problem in a general physical context or to be part of approximate models in order to improve the solution.

The wide range of models, methods and techniques of the present work create an "artillery" of tools that can approach the problem of extreme waves from different angles, scales and physics. Validation of phase-resolving models is performed against experimental simulations that replicate real oceanic extreme waves under controlled conditions. Verification of the stochastic approach of the GKE is performed using Monte Carlo simulations after calibrating its parameters. The analytical methods of computing the free surface are verified against fully nonlinear simulations. The combination of models' validation, verification and calibration (Roache, 1998) aims at confirming the initial hypothesis of the thesis that a fully nonlinear wave profile can be approached by analytical methods.

Limitations

Part of the composite modelling method is the good understanding of the associated limitations in order to avoid any pitfalls. Thus, it should be noted that in the present study only unidirectional waves up to their breaking limit were tested. As explained in Chapter 2, directional wave groups entail different dynamics and level of nonlinearity. Also, the focusing methodology cannot be applied beyond the breaking point and it has not been tested for directional waves and varying bathymetry.

Beyond these limitations, there is confidence that the results of the present work have

general applicability because i) Very steep wave groups are tested to their breaking limit, which is the most challenging case in terms of nonlinearity. ii) Wave groups of different steepness are used, demonstrating excellent performance at different degrees of nonlinearity. iii) There are practically no bandwidth limitations, since broadbanded spectra are used. iv) The wave groups are tested in finite intermediate water depth, without the limitations of no influence of the bottom (deep water assumption), nor the weakened dispersion (shallow water assumption). v) The resonant wave interactions are even more relevant in directional spectral evolution, which prepares the ground for application of the present approach in realistic directional seas.

Novelties - Contribution

The present work aimed at advancing the modelling practice of focused waves and contributing to the better understanding of the physical processes during the formation of extreme waves. This was facilitated with the broad tool-set that was prepared during the research course. The main novel achievements are:

1. Identification of the role of nonlinear wave-wave interactions during dispersive focusing of NewWave-type groups.

2. Implementation of the focusing methodology for the first time in numerical models.

3. Validation of phase-resolving NWTs in OpenFOAM, SWASH and HOS-NWT for NewWave-type extreme waves.

4. Intercomparison of different types of NWTs and boundary conditions under exactly the same conditions.

5. Demonstration of a solution strategy for phase-averaged modelling of extreme waves with the GKE.

6. Consistent demonstration of the concept of using original and evolved free-wave spectra in analytical models for computing the wave profile.

7. Implementation and development of new methods for reconstructing extreme wave profiles.

8. Demonstration of an integrated approach for reproducing extreme wave profiles with known error margins.

Thesis outline

To help gaining an overview and an overall perspective of the present work, the scope, tools-methods and objectives are summarized in Figure 1.2. "**What**": The main objective is to provide a framework to study extreme waves numerically and analytically, potentially using an integrated approach among well-validated solvers and methods. "**How**": To achieve the objective, the nonlinear wave-wave interactions during the formation of extreme waves are examined using NewWave-type groups in physical and numerical wave tanks, and analytical theories are explored to reproduce the observed spectral changes. "**Why**": The vision is to improve the understanding of the formation of extreme waves and to suggest tools and methodologies with known error margins towards a more accurate estimation of extreme waves. This can contribute to preventing accidents at sea, de-risking the MRE sector and designing improved coastal defence structures. With the climate change increasing the storminess at sea and causing sea level rise, more extremes with potentially greater impacts should be anticipated (Bitner-Gregersen and Gramstad, 2015), which makes the present work very timely.

The presentation of the work is structured in four main chapters and complementary material is given in the Appendices. The necessary background knowledge for following the present work is included in Chapter 2, which is accompanied with Appendix A. These chapters are an amalgamation of an extensive literature review of almost 400 papers that concern numerical modelling of water waves, nonlinear wave-wave interac-

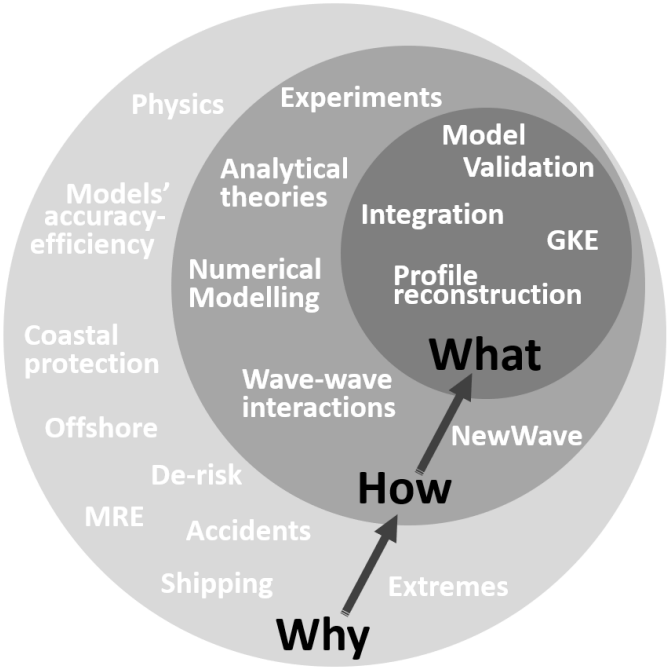

Figure 1.2: Research principles, concept and tools.

tions, extreme waves and focusing methodologies. Appendix A explains the rationale behind selecting the numerical tools in the present study and provides general information about the numerical solvers, their application, as well as the design of NWTs for focused waves. The numerical modelling part of the work starts in Chapter 3, where the validation of the models is performed against experimental or published results. Details on the design of the NWTs are presented there. The results of Chapter 3 are used to examine the spectral evolution of the wave group, as presented in Chapter 4. The core of the scientific hypothesis is explored in that chapter, through the equivalence between the phase-averaged and phase-resolving approach. The outcome of this method is the evolved free-wave spectrum from the GKE, which is used along with the original and extracted free-wave spectrum from the phase-resolving modelling for reconstructing the extreme wave profile in Chapter 5. Five different methods are examined in that chapter, which take the frequency domain result and transform it to the time domain wave profile by also including high order harmonics. The performance of the methods is examined and the error against the fully nonlinear simulation is found.

As such, the objective of the present work to suggest an integrated method with known error for estimating an extreme wave profile is fulfilled.

Chapter 2

Background

THIS Chapter of the Thesis is dedicated to providing the necessary background knowledge for the topics addressed in the subsequent chapters. It includes basic physical and mathematical concepts, as well as the state of the art in the current understanding and methodologies for examining extreme wave phenomena. This field covers from well-established theories, e.g., numerical modelling, to active research topics, where consensus has not been reached yet. As such, techniques and methods that were not finally used in the present work are also discussed in order to give a broader frame of the problem.

2.1 Numerical modelling of water waves

2.1.1 Introduction to wave modelling

The modelling of water waves is a very broad field, which includes various analytical models and numerous mathematical techniques. Wave modelling begun with the classical works of Airy and Stokes in the middle of the 19^{th} century, when analytical solutions for regular waves were given, e.g., Linear, Second order waves etc, covering

a wide range of water depths and wave steepness, as seen in Figure 2.1[1]. Linear theory provides a linearized solution for gravity water waves propagating at a constant water depth and in a inviscid, irrotational and incompressible fluid. It is valid of long waves of small amplitude and the surface elevation is assumed to follow a sinusoidal form ($\eta(x,t) = \alpha\cos(kx - \omega t + \phi)$, where k: wavenumber, ω: angular frequency, t: time and phi: phase), as seen in Figure 2.2, where the basic characteristics of a wave (H, α and L) are shown. Second order theory is derived from linear theory and it is quadratic in the wave amplitude (Holthuijsen, 2007).

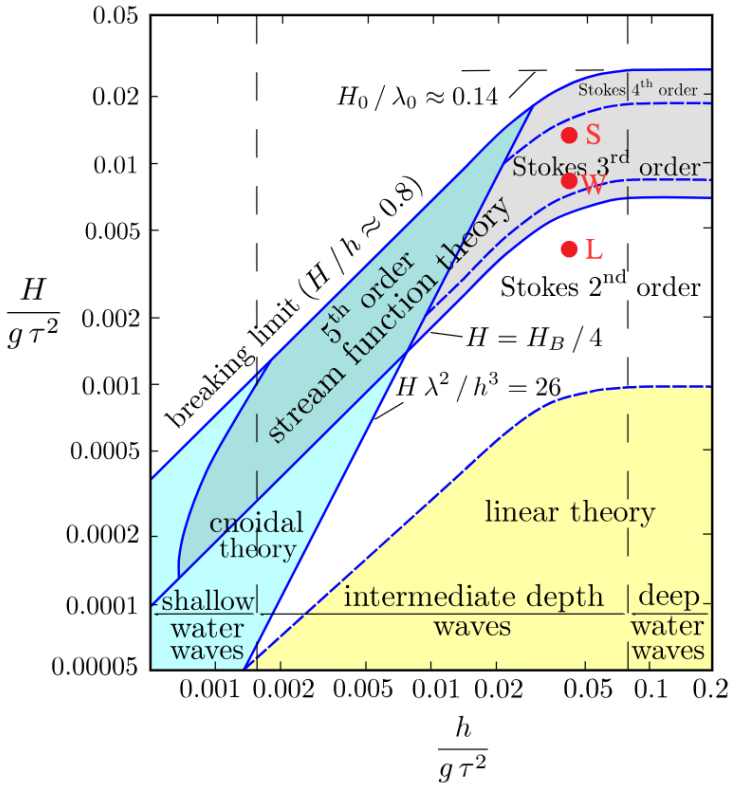

Figure 2.1: Regular wave theories and their applicability according to the water depth (h) and the steepness determined by the wave height (H) and the wave period (τ) (Le Méhauté, 1976). The red dots denote the linear (L), weakly-nonlinear (W) and strongly nonlinear (S) wave groups used later in this study. Courtesy: Kraaiennest (2009). This figure is free to distribute under Attribution-ShareAlike 3.0 Unported (CC BY-SA 3.0).

Developments in wave modelling took place in the first half of the 20^{th} century, but

[1]NB: The extreme waves examined in this study via NewWave groups are not regular waves to be placed in the diagram of Le Méhauté (1976).

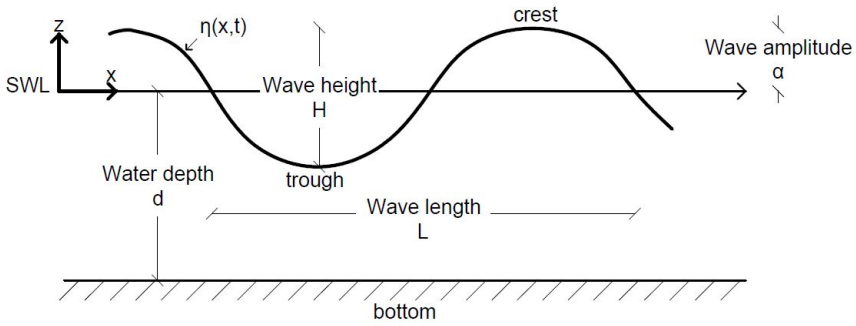

Figure 2.2: Basic characteristics of wave a wave form.

the most important progress was made during the Second World War for naval operations, where attention was given to wind-wave and wave-wave interactions at various time and spatial scales, as well as to wave breaking. Still, at that stage research was mostly based on visual observations. Systematic experimental research begun in the 60s with the works of Hasselmann, Benjamin & Feir, Zakharov and Longuet-Higgins which was supported by more sophisticated instrumentation and analysis techniques (Adcock and Taylor, 2014; Babanin et al., 2012). At present, effort is put in better understanding specific physical processes, e.g., atmosphere-wave interactions, and providing solid mathematical descriptions for building numerical models, or tackling unresolved issues, such as the formation and forecasting of extreme waves. Numerical modelling is nowadays a pillar of research in oceanography, where models operate on larger scales based on parameterizations of physical phenomena, and on short scales examining specific physical or engineering problems, with the so-called Numerical Wave Tanks (NWTs), which level of accuracy, simply speaking, is proportional to their computational cost (Schmittner et al., 2009). Large scale spectral models can be employed for hindcasting, nowcasting or forecasting, if they aim at modelling a past, real-time or future event, respectively. In general, they show very good agreement with the field measurements for the bulk properties of the wave field, such as the significant wave height (H_s) and the peak period (T_p), but simulating rapidly changing conditions, for instance, cyclones, is more challenging (Adcock and Taylor, 2014). NWTs are computational phase-resolving domains for the simulation of specific wave characteristics,

wave transformation and fluid-structure interaction problems, such as overtopping and impact of breaking waves, that, numerically, can only be assessed via the solution of the hydrodynamical equations (Fernández et al., 2014). To a large extent, the results provided by even the most accurate and sophisticated NWTs are subject to the applied boundary conditions, which are specified by the fundamental regular wave theories, such as linear, second order, Cnoidal, Stokes V, or irregular wave theories commonly considered as a superposition of regular waves (Zhao et al., 2009). Despite the tremendous progress in numerical modelling, which led the research from empiricism to robust wave analysis, large errors can be induced through the selection of the governing equations and the numerical techniques for their integration. Good review papers on wave models for different applications are Liu and Losada (2002) and Cavaleri et al. (2007), while lists of state-of-the-art commonly used solvers are included in the works of Vyzikas et al. (2014a), Higuera et al. (2015) and Vyzikas and Greaves (2018).

The selection of the most appropriate method depends on the physics, scale, resources and engineering interest in the problem. The models can be grouped in different ways, with the most common being phase-averaged and phase-resolving (Benoit et al., 2015), depending on whether they deal with the wave dynamics globally, in a statistical sense, or on a wave-to-wave basis, capturing the exact time history of the water surface elevation. The problem of wave modelling belongs to the general topic of fluid dynamics, as waves are in practice oscillatory flows. Another way to classify the models, used in more engineering-oriented applications, is in exact and approximate models depending on the integration used to solve the equations (Bitner-Gregersen and Gramstad, 2015). The former category includes Navier-Stokes Equations (NSE), Potential Flow theory Solvers (PFS) and Nonlinear Shallow Water Equations (NLSWE), while the latter includes for example Nonlinear Schrödinger Equation (NLSE) and Zakharov Equation (ZE), which are derived under the assumption of weak nonlinearity. The literature is very extended in the topic, including the recent books of Lin (2008) and Holthuijsen (2007), as well as the author's contributions in the report of the MERiFIC project (Vyzikas et al., 2014a) and the chapter of a book (Vyzikas and Greaves, 2018),

where the main focus is on MRE applications, including also lists of commonly used solvers. In the present section, only a short description is provided for some of the basic equations for solving water wave problems. For the NSE, PFS, NLSWE, ZE and phase-averaged models, the latter commonly referred to as spectral models, specific details and solving techniques are discussed in the sections for the corresponding solvers used in the present work, namely OpenFOAM, HOS, SWASH, GKE and WW3, in Sections A.1, A.3, A.2, 4.3 and A.4, respectively.

A graphical representation of the applicability of the wave models is shown in Figure 2.3. Of course, such presentation is simplistic and may ignore variations of the models that extend the validity of each approach. What is clear from the graph is that the NSE (CFD) can handle the full flow complexity of the examined problem, while analytical Stokes models and approximate models are valid only for narrow-banded spectra. NLSWE and Bousinesq models have been added to the graph by the author, correctly placed between ZE and second order theory in terms of steepness, noting that the bandwidth limitation is less relevant for these type of models. This figure should be considered in combination with the more detailed Table A.1.

The largest part of the present work is dedicated to the modelling of extreme waves, which has two inherent challenges: i) high nonlinearity, sometimes beyond the capabilities of approximate solvers, and ii) the randomness of the problem, since as it will be discussed later, extreme waves can appear locally in space and time from a chaotic background. As such, their modelling varies from random simulations with low-accuracy but efficient solvers, e.g., ZE, linear and second order solvers, where extremes "naturally" emerge, to precise and computational expensive modelling, e.g., PFS and NSE, for deterministic analysis of a single wave event using wave focusing techniques (Vyzikas et al., 2013).

For the description of the mathematical approaches for wave modelling that follows, it is out of the scope of the present thesis to re-introduce the derivation of the equations, since they can be found in numerous works, e.g., in Lin (2008); Holthuijsen (2007);

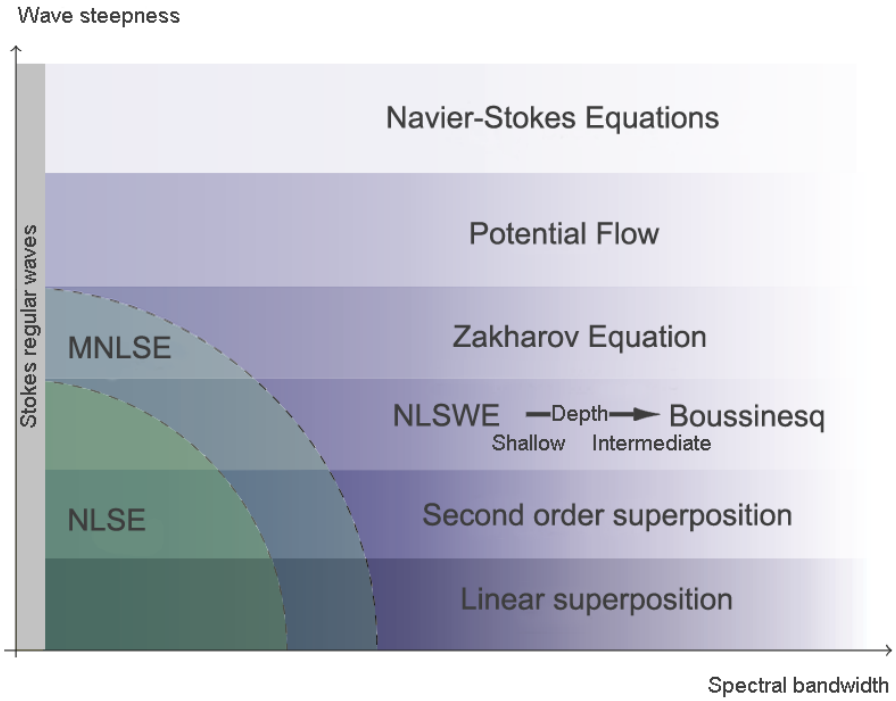

Figure 2.3: Validity range of the wave theories and models according to the nonlinearity, namely the steepness (ratio of the wave amplitude to wave length) and spectral bandwidth (modified figure from (Bitner-Gregersen and Gramstad, 2015)).

Versteeg and Malaskekera (2007); Ferziger and Peric (2002); Lin (2008) and Holthuijsen (2007), including those of the author Vyzikas et al. (2014a); Vyzikas and Greaves (2018). This short description aims at providing an overview of the methods, the rationale for the selection of some of them and relevant applications in previous works, mainly concerning extreme waves.

2.1.2 Navier-Stokes Equations

The NSE are the fundamental equations of fluid mechanics, referring to the momentum equations in the three dimensions. The compressible form of the NSE is given in the tensor form in Equation 2.1 for the $x-$ direction (Versteeg and Malaskekera, 2007). Similar expressions can be derived for the $y-$ and $z-$ direction.

$$\frac{\partial \rho u}{\partial t} + \nabla(\rho u \mathbf{u} - \nabla(\mu \nabla u) = -\frac{\partial p}{\partial x} + \left[\nabla(\mu \nabla \cdot \mathbf{u}) + \frac{\partial}{\partial} \lambda \nabla \mathbf{u}\right] \tag{2.1}$$

where ∇ is the divergence, u is the velocity in the $x-$ direction, **u** the vector of the velocity, p is the pressure, μ is the dynamic viscosity and λ is the viscosity that relates the stresses to the volumetric deformation. The terms in brackets have small contributions.

Nowadays, NSE solvers are commonly referred to as Computational Fluid Dynamics (CFD) solvers, and they can also incorporate heat transfer and chemical reactions. Theoretically, CFD solvers are powerful tools that can simulate very complex phenomena with minimum approximation. The price for this is the computational cost, which can become unbearable, even for modern High Performance Computer (HPC) facilities. NSE are the only solvers that can implicitly account for viscous and highly nonlinear turbulent effects through Direct Numerical Simulations (DNS), and they are often used as the ground truth for the validation of other more simplified models or for understudying the underlying physics (Greaves, 2010). The best-established approach to integrate the NSE in the computational domain is the Eulerian (on a mesh), but also Lagrangian approaches, such as the Smoothed Particle Hydrodynamics (SPH) method, have emerged (Vyzikas and Greaves, 2018) and demonstrated good performance for practical engineering applications, e.g., for overtopping (St-Germain et al., 2014). Nevertheless, SPH methods are at an earlier stage of development than traditional Eulerian approaches (Higuera et al., 2013b). Due to the computational burden, the modelling of turbulence is approximated for practical applications by relating the Reynolds stresses to the mean flow characteristics or by spatial filtering of the vortices, as discussed below. Despite these approximations, CFD solvers are the most expensive models and, still, they do not constitute common practice in operational engineering applications (Liu and Losada, 2002). Nonetheless, since CFD is considered as a cutting-edge method in many sectors, from aerospace to naval engineering and beyond, rapid developments are expected through the contributions from the various communities that will expand its use (CFD-Online, 2018).

Regarding the modelling of water waves, CFD is employed for simulations with high nonlinearity, including very steep and over-turning waves, as well as the interaction of waves with complex structures or when violent effects, such as green water and splashing, are expected (Lin, 2008). Nonetheless, even theoretically simpler cases, such as the flow around cylinders, can result in complex flow fields (Chaplin et al., 1997) that may not be well resolved by simpler models than CFD. Similar conclusions were reached by the recent experimental study of Swan and Sheikh (2015), where the complexity of the local flow characteristics around a cylinder interacting with incident waves was highlighted as a result of the nonlinear interactions of scattered and incident waves, as well as due to the runup and wash-down on the faces of the cylinder. CFD models are also used for the calculation of the structural loads or the response of the structure, either by being coupled with structural solvers or by calculating the fluid forces through the integration of the kinematics on the surface of the body. Advanced models can include the full aeroelastic response of the structure and capture dynamic effects, such as ringing (see Section 2.3.5). The high computational cost of CFD models hinders their use in large spatial scales where the transformation of the waves, e.g. shoaling, refraction, diffraction, takes place. For this reason, coupling techniques have been proposed, where the propagation of the waves from the far field to the vicinity of the region of high nonlinearity is performed by cheaper models (Paulsen et al., 2014a; Bredmose et al., 2016; Yan et al., 2015). Such highly nonlinear effects include for example wave breaking, which can be realistically simulated only by CFD models (Liu and Losada, 2002). Nevertheless, attention should be given to select the most appropriate turbulence model (Brown et al., 2016). Moreover, regarding extreme waves, the simulation of random sea states with NSE for capturing extreme waves is practically impossible, due to the high computational cost, and deterministic approaches, such as the NewWave theory (presented in Section 2.4) are often employed (Bunnik et al., 2008).

The modelling of turbulence

O. Reynolds in 1883 Reynolds (1883) observed that the particles of the fluid can move in an orderly or in a chaotic manner depending on the characteristics of the flow. These two types of flow regimes are called laminar and turbulent and they can be determined by the âĂIJReynolds numberâĂİ ($Re = \rho \frac{uL_a}{\mu}$, where rho is the density, u the velocity, L_a the characteristic length scale and μ the dynamic viscosity of the fluid.), which is the ratio of the inertial forces that cause disturbance to the fluid particles, over the viscous forces that restrain them to move along certain paths (Douglas et al., 2005). Laminar flows are characterized by relatively low fluid velocities, with fluid particles moving along the flow streamlines and retaining their relative positions. Turbulent flows are characterized by continuous and random fluctuations of the velocity and the pressure, exhibiting a chaotic and unsteady behaviour. Turbulence is associated with vortices that have three dimensional structures of different scales. An important consequence of turbulence is the energy dissipation, since the mechanical energy of the fluid is transformed to internal energy or heat (Ferziger and Peric, 2002). The transition from laminar to turbulent flows occurs when the velocity of the fluid is increased, causing the Re to exceed a certain threshold, called the critical Re. The numerical modelling of turbulence is performed with NSE solvers by considering appropriate mathematical models to calculate the Reynolds stresses and close the set of equations for the flow variables. It is noted that, so far, there is not a generally valid and efficient universal mathematical model for turbulence, due to the complexity of the problem (MARNET CFD, 2002). Nevertheless, the most commonly applied methods in CFD for engineering applications are the Reynolds-Averaged Navier-Stokes (RANS) equations with appropriate turbulence closure models and the Large-Eddy simulation (LES) (Versteeg and Malaskekera, 2007). RANS modelling is based on the time-averaging of the governing equations by splitting the flow variables into mean and instantaneous fluctuating components. The time averaging eliminates the latter unsteady components and expresses them via their mean values and the Reynolds stresses that are calculated by

appropriate turbulent models, such as for example the well-known two-equation models $\kappa-\varepsilon$ and $\kappa-\omega$. LES modelling is based on the principle that turbulent flows include eddies of different scales that have different behaviour: the small eddies are isotropic, while the large eddies are anisotropic and depend on the local geometry of the domain. LES employs a spatial filter to separate the large from small eddies. Only the large eddies are resolved, while the small eddies are filtered out and their effects are taken into account by a sub-grid-scale (SGS) stresses model (Versteeg and Malaskekera, 2007).

When the viscosity of the fluid can be neglected, the flow is characterized as inviscid and the effects of turbulence vanish. Under these considerations, the NSE are simplified to the Euler equation by eliminating the terms that contain μ and λ in Equation 2.1 (Versteeg and Malaskekera, 2007). The Euler equation is used in potential flow models by considering also irrotationality. A classic example of an inviscid flow is the flow around a wing.

The treatment of the free surface: the VoF method

The modelling of water waves is a subcategory of free surface flows. Numerically, the challenge is to compute accurately the position of the free surface, a task which requires additional robust algorithms. Two possible methods to achieve this are interface tracking methods, such as moving meshes, front tracking schemes and particle tracking methods (e.g., SPH), and interface capturing methods, such as the Volume of Fluid (VoF) and the Level Set (Greaves, 2010). An up-to date description is given in (Ransley, 2015). The most well-known CFD codes, namely OpenFOAM, Star CCM+ and Ansys CFX, use VoF. Nevertheless, very good results for ocean waves have been also achieved recently with the Level Set method used in REEF3D (Bihs et al., 2017).

According to the VoF method, which is used in this study, each cell of the computational mesh at a given time is assigned with a value of the fluid fraction (γ_i) between 0 and 1. This additional scalar (γ_i) expresses the proportion of water in the computational cell. If the cell is "wet" containing only water, the value of the fluid fraction is 1, while

it becomes 0 when the cell does not contain any water. Any values between 0 and 1 indicate the interface of air and water, i.e. the free surface. To compute the interface, the VoF method consists of two basic elements: an algorithm for finding the new location of the volume fraction in time and an algorithm for reconstructing the interface (Greaves, 2010). The governing Equations of the flow are solved simultaneously for the two fluids, and thus, the algorithm for the volume fraction results in an additional advection equation (see Section A.1.2).

In the present study, a RANS two-phase flow CFD solver, as described in Section A.1, is used for replicating experimental results for very steep nearly breaking NewWave-type waves. The high nonlinearity of the examined problem can be captured by using a CFD model, while the cost is kept to the minimum with the use of focused waves.

2.1.3 Potential flow theory

PFS can be derived from the NSE by assuming irrotational and inviscid flow (Bredmose et al., 2006), and thus, they are used for applications with negligible turbulence. Under these assumptions, the continuity equation for an incompressible fluid can be expressed as the Laplace equation (Equation 2.2) for the velocity potential, as explained in (Lin, 2008).

$$\nabla^2\phi + \frac{\partial^2\phi}{\partial z^2} = 0 \tag{2.2}$$

For the simulation of free surface problems additional dynamic and kinematic boundary conditions are included for calculating the location of the free surface and the fluid particle velocity at that location. Since the Laplace equation is linear, the difficulty -but also the interesting physical behaviours of the PFS- in the solution process arises from the nonlinear boundary conditions of the free surface (Onorato et al., 2013). Boundary Element Methods (BEM) are commonly used in PFS (Yan et al., 2015) and classic examples of applications refer to flows around airfoils. PFS is the second most

"skilled" category of solvers for handling nonlinear fluid flows, and despite having a significantly reduced computational cost compared to CFD solvers, it requires considerable resources (Vyzikas and Greaves, 2018). PFS are widely used in industry, since they can handle highly nonlinear problems, with the main limitations referring to flow separation and boundary layers, due to the irrotationality assumption. Within the framework of water waves, PFS can be employed for studies of wave propagation and transformation over complex bathymetries, nonlinear wave-wave interactions and weak interaction of waves with large structures. On the other hand, PFS cannot be used to simulate realistic wave breaking, green water effects and wave interaction with small bodies (Lin, 2008).

PFS are routinely used in wave research (Westphalen et al., 2008), in particular as part of coupled modelling systems with CFD solvers and for the simulation of extreme waves. An example for the former is the code OceanWave3D, which has been coupled with OpenFOAM (Paulsen et al., 2014a) after it was validated against experimental results for nearly breaking waves (Paulsen et al., 2013b). Similarly, high order BEM NWTs were used by Ning et al. (2008) and Ning et al. (2009b) to simulate regular and focused wave groups in finite and infinite water depth. For the latter, the Quasi Arbitrary Lagrangian-Eulerian Finite Element Method (QALE-FEM) was used to simulate the extreme Draupner wave (Adcock et al., 2011) and was also compared with OpenFOAM and experimental results for the interaction of focused waves with cylinders, showing very good performance (Yan et al., 2015)[2]. Thanks to the nature of water waves that can be considered as a summation of sinusoidal Fourier components, attractive pseudo-spectral models have been suggested to increase the computational efficiency of PFS using FFT algorithms (Taylor and Swan, 2000; Cavaleri et al., 2007). Another way to increase efficiency is by configuring the solvers for GPU architecture, as done for OceanWave3D that is used producing statistics of extreme waves in the DeRisk project (De-risked extreme wave loads for offshore wind energy) (Bredmose

[2]In the study of Yan et al. (2015) the PFS seems to have a much better performance than that of the CFD model, but, according to the author, there seems to be a crude mistake in the numerical parameters selected in OpenFOAM, leading to this unorthodox conclusion.

et al., 2016).

In the present study, since very steep but not breaking waves are considered, PFS can be employed. Exploiting further their advantage of computational efficiency, a pseudo-spectral model HOS-NWT is used to study deterministic focused waves and the HOS-ocean model for random wave simulations to determine the spectral evolution, as discussed in Section A.3.

2.1.4 Nonlinear Shallow Water Equations

The shallow water approximation of waves can be used when the horizontal length scales of the wave propagation are much greater than the vertical. Such examples include the propagation of the waves in shallow water, the modelling of tsunamis, tides, storm surges as well as river flows Shallow water equations (SWE) are used, apart from stand-alone solvers, as a model to approximate piston-type wavemakers in NWTs (Zhang et al., 2007; Higuera et al., 2013a). In such cases, the movement of the water particles takes place mainly in the horizontal dimension and the vertical accelerations are negligible. Under this consideration, the NSE can be integrated along the water depth assuming uniform velocity distribution in the horizontal, as well as small velocity in the vertical, and hydrostatic vertical pressure gradients (Holthuijsen, 2007). The set of the SWE consists of the mass conservation equation (Equation 2.3a) and the momentum conservation equations (Equations 2.3b and 2.3c), which are derived for negligible Coriolis, frictional and viscous forces (Moler, 2011):

$$\frac{\partial \eta}{\partial t} + \frac{\partial (\eta u)}{\partial x} + \frac{\partial (\eta v)}{\partial y} = 0 \tag{2.3a}$$

$$\frac{\partial (\eta u)}{\partial t} + \frac{\partial}{\partial x}(\eta u^2 + \frac{1}{2} g \eta^2) + \frac{\partial (\eta uv)}{\partial y} = 0 \tag{2.3b}$$

$$\frac{\partial (\eta v)}{\partial t} + \frac{\partial (\eta uv)}{\partial x} + \frac{\partial}{\partial y}(\eta v^2 + \frac{1}{2} g \eta^2) = 0 \tag{2.3c}$$

where η is the total fluid column height, u and v is the fluidâĂŹs horizontal velocity in

the x and y direction, respectively, averaged across the vertical column and g is the acceleration due to gravity.

SWE are very computationally efficient, thanks to their depth-averaged approximation. However, as it becomes apparent, this induces a considerable limitation for practical applications, restricting the use of these models from intermediate and deep water regimes. Moreover, in their original form, SWE ignore wave dispersion effects and for some applications, other models, such as the Boussinesq equations, are preferred. To overcome the aforementioned constraints, nonlinear versions of the SWE were developed leading to NLSWE models. These approaches are based on non-hydrostatic pressure assumption and divide the computational domain in layers of uniform horizontal velocities (Stelling and Duinmeijer, 2003). NSWE solvers have demonstrated very good performance for simulating dispersive regular waves, wave propagation over immersed obstacles and focused waves (Vyzikas et al., 2015), as discussed in Section A.2. Nevertheless, NLSWE cannot handle overturning waves, for which CFD models are required (Jacobsen et al., 2012), and they can only approximate breaking as a moving bore (The SWASH Team, 2017).

In the present work, since no overturning waves are considered, the NLSWE model SWASH is tested for steep focused wave groups -to the best of the author's knowledge, for the first time- using a high resolution flexible layers' grid and a non-hydrostatic pressure assumption, as discussed in Section A.2.

2.1.5 Boussinesq

The original Boussinesq equations (Boussinesq, 1872) were developed in order to model the propagation of nonlinear waves in intermediate water depth, where the ratio of water depth to wavelength is $d/L \approx 0.5$ and wave dispersion still holds, while nonlinear effects, such as shoaling cannot be neglected. Similarly to SWE, Boussinesq equations are depth-averaged with a constant horizontal velocity component along the vertical dimension. However, in contrast to SWE, the vertical velocities vary along the

water column, being calculated by the nonlinear balance equations, and as such, there is a vertical acceleration of the fluid flow (Holthuijsen, 2007). The original Boussinesq equations were derived for horizontal sea bed and expressions for non-horizontal bottom were later given by Peregrine (1967):

$$\frac{\partial \eta}{\partial t} + \frac{\partial}{\partial x}[(d+\eta)\overline{u}_x] = 0 \tag{2.4a}$$

$$\frac{\partial \overline{u}_x}{\partial t} + \overline{u}_x \frac{\partial \overline{u}_x}{\partial x} + g\frac{\partial \eta}{\partial x} = \frac{1}{2}d\frac{\partial^3(d\overline{u}_x)}{\partial t \partial x^2} - \frac{1}{6}d^2\frac{\partial^3(d\overline{u}_x)}{\partial t \partial x^2} \tag{2.4b}$$

where $\overline{u}_x$ is the vertically averaged horizontal velocity.

The original Boussinesq equations are valid when both frequency dispersion and nonlinearities in the wave propagation are considered weak and in fact have the same order of magnitude. This limits their applicability in intermediate water depth, since in deep water, waves are fully dispersive and at very shallow water, dispersion weakens and nonlinearity becomes more important (Liu and Losada, 2002).

In their original form, Boussinesq equations were used to simulate propagation in intermediate water and long waves, for example, seiches that should be taken into account in port designing (Kofoed-Hansen et al., 2005, 2001; Giese et al., 1998). Many versions of Boussinesq models have been proposed, the so-called modified Boussinesq equations, which aim at expanding the applicability of these models, by including energy dissipation effects for wave breaking, and with appropriate modifications to become able to simulate surf-zone effects. To present, Boussinesq equations are still widely used for operational engineering applications in coastal areas and sometimes as part of an integrated modelling system (Liu and Losada, 2002), e.g., switching from Boussinesq to NLSWE at the onset of wave breaking (Whittaker et al., 2017). A review of the developments of Boussinesq models was written recently by Brocchini (2013).

In the present work, Boussinesq models were not used, although well tested open-source numerical models, such as FUNWAVE (Shi et al., 2012) and COULWAVE (Lynett et al., 2008), are available. Instead, SWASH was preferred as a weakly nonlin-

ear model, thanks to its better performance, wider applicability and greater operational capacity, as explained in Section A.2. Nevertheless, it appears that Boussinesq models have similar behaviour to NLSWE for focused waves, as seen by comparing Figure 6 in Stagonas et al. (2014) with Figure 3.10 of the present work.

2.1.6 Zakharov equation

The Zakharov equation (ZE) was derived considering the Hamiltonian representation of surface waves, according to the assumption of weak nonlinearity (Zakharov, 1968), which is valid for deep water waves taking the form of Equation 2.5:

$$\frac{\partial \eta}{\partial t} = \frac{\delta E}{\delta \phi_s}, \quad \frac{\partial \phi_s}{\partial t} = -\frac{\delta E}{\delta \eta} \tag{2.5}$$

where η is the free surface elevation, E is the energy of the fluid and ϕ_s is the velocity potential at the free surface.

The flow is considered inviscid and irrotational, and thus, the velocity potential can be expressed by the Laplace equation. After an appropriate canonical transformation, the flow variables can be found by the so-called integro-differential equations.

As explained later in Section 5.5.1, the Hamiltonian expression of water surface, puts ocean waves in the general physical problem of the propagation of waves in nonlinear dispersive media. The ZE used in most of the numerical models nowadays is based on the derivation of up to five-wave interactions (or truncation to lower order), as suggested by Krasitskii (1994), who managed to obtain a conservative form of the Hamiltonian through the symmetrical coefficients that he proposed for various combinations of wavenumbers. ZE-based numerical models can simulate high order wave-wave interactions without the spectral bandwidth constraints of the NLSE (Kharif and Pelinovsky, 2003; Dysthe et al., 2003).

ZE is used mainly in research to study the spatial and temporal transformation of the wave field due to nonlinear wave-wave interactions. ZE models are time resolving

(Gramstad and Stiassnie, 2013), but they also serve as the basis to derive the phase-averaged Kinetic Equation for the long-term evolution of random wave fields (Krasitskii, 1994). In its phase resolving version, the ZE is used to study the effects of modulation instabilities (MI) that may lead to the emergence of rogue waves and to deduce general statistical properties of random wave fields by direct numerical simulations, since it is the most accurate weakly nonlinear model for such purposes (Kharif and Pelinovsky, 2003). In practice, ZE is used in computational efficient high order spectral (HOS) methods, by selecting the nonlinear HOS order at 3 or 4[3], with order 1 referring to linear simulation (Alam, 2014; Slunyaev et al., 2013) and 6 to a fully nonlinear simulation Slunyaev et al. (2011). A considerable advantage of the integro-differential approach is that the physical processes of the wave-wave interactions can be isolated by including and excluding the corresponding integrals in the ZE, as noted by Gibson and Swan (2007), who used ZE to examine the spectral evolution of directionally spread focused wave groups. It was shown that ZE had excellent agreement with the fully nonlinear BST model.

In the present study, ZE is used in phase-resolving Monte Carlo simulations with the HOS-ocean model of order 3 for estimating the spectral evolution of random realisations of a wave field as well as in a phase-averaged approach for the GKE, as shown in Sections 3.4 and 4.3. Moreover, ZE was used in a less conventional approach with Krasitskii's coefficients to estimate a nonlinear wave profile (see Section 5.5).

2.1.7 Nonlinear Schrödinger Equation

NLSE describes the evolution of wave fields as modulations of the waves, in the form of envelope equations, which is possible when the surface elevation and the velocity are associated in a convenient way that allows the governing equations to take that simple form (Slunyaev et al., 2011). The evolution complex wave envelope in space and time is given by Equation 2.6 (Onorato et al., 2013):

[3]Most of the literature suggests that nonlinear order M=3 corresponds to the ZE, with some exceptions such as Alam (2014) and Kharif and Pelinovsky (2003).

$$i\left(\frac{\partial A}{\partial t}+c_g\frac{\partial A}{\partial x}\right)-\frac{\omega_0}{8k_0^2}\frac{\partial^2 A}{\partial x^2}-\frac{1}{2}\omega_0 k_0^2|A|^2A=0 \tag{2.6}$$

where A is the complex wave envelope, k_0 is the wave number of the carrier wave, g the gravity acceleration and $c_g=\frac{\partial\omega}{\partial k}$ is the group velocity.

The envelope approach, despite being approximate, was shown to be very powerful for simulating waves of considerable steepness (Slunyaev et al., 2013), but at the same time these models may miss the steepest waves in a wave nonlinear field (Onorato et al., 2013). NLSE can be derived by the NSE, with the hypothesis of inviscid irrotational flow and weak nonlinearity (Bitner-Gregersen and Gramstad, 2015), similarly to ZE integrals (Trulsen et al., 2000), but with additional assumptions of narrow spectral bandwidth and infinite water depth (Trulsen et al., 2001). NLSE are derived through power series expansion of the slowly varying fields of the free surface elevation and velocity potential (Onorato et al., 2013). The additional assumptions refer to narrowbandness and deep water depth . The original NLSE are of third order of wave steepness and spectral bandwidth (Shemer and Dorfman, 2008), and are thus called cubic NLSE. The expansion to fourth order was suggested by Dysthe (1979), in the so-called "Dysthe" equation. Other variations of modified NLSE (MNLSE) have been also proposed attempting to increase the applicability of this approach (Dysthe et al., 2003). A necessary requirement to model nonlinearly a wave field with NLSE is the accurate knowledge of the free-wave spectrum Trulsen et al. (2001), since the method is based on the exact linear dispersion.

The main advantage of the NLSE (or MNLSE) is their simplicity and computational efficiency, which expanded their use among the research community (Trulsen et al., 2000). Provided that the spectrum is narrowbanded and the waves are weakly nonlinear, the NLSE has demonstrated very good ability in capturing the dynamics of the wave field, namely the four-wave interactions, as well as complex phenomena, such as the modulation, aka side-band, instability for the generation of rogue waves (Onorato et al., 2013). MNLSE have been recently applied to simulate directionally spread extreme

waves spotted in random simulations (Adcock et al., 2016) and measured timeseries of extreme wave profiles from a platform, showing good performance but inability to capture the large crests (Slunyaev et al., 2013). On the downside, NLSE are limited by their inherent assumptions of weak nonlinearity, narrowbandness and infinite water depth (Shemer and Dorfman, 2008). Additionally, the method may also suffer from energy leakage to high wavenumbers and subsequent violation of the initial bandwidth assumption (Trulsen et al., 2000; Taylor and Swan, 2000). This leakage can cause spurious wiggles in front of the examined wave group due to high nonlinearity, indicating an important limitation of the MNLSE for simulating large steep waves (Adcock and Taylor, 2016b,a).

In the present study, where very steep broadbanded wave groups are simulated, it was decided not to employ a NLSE-based model. Nevertheless, the MNLSE approach merits future investigation especially for problems of MI, for which preliminary work of the author indicated that CFD models cannot handle efficiently.

2.1.8 Phase-averaged models

The numerical modelling approaches for water waves presented in the previous sections were based on the description of a wave field through individual waves components obeying rigorous equations of wave theories and fluid motion, and are characterized as phase-resolving models (Yang et al., 2017). However, when the properties of individual waves are not concerned or large scales should be simulated, a random wave field can be described in a statistical sense through a phase-averaged approach (Lin, 2008). As such, instead of solving hydrodynamic equations, the waves are regarded as energy distributed over a spectrum analysed in frequencies and directions, which changes due to forcing terms that represent the various physical processes. This consideration is sufficient to determine the most important characteristics of a wave field (Monbaliu and Lefèvre, 2005) and leads to the mathematical description of the energy balance equation for phase-averaged models or to the wave action equa-

tion, which can account for the presence of ambient currents (Holthuijsen, 2007). The energy balance equation is a conservation relation, which balances the effects of the forcing terms with a corresponding transformation of the energy spectrum. The basic formulation of the wave action equation used in spectral models is given by Equation 2.7:

$$\frac{\partial N}{\partial t} + \frac{\partial c_{g,x} N}{\partial x} + \frac{\partial c_{g,y} N}{\partial y} + \frac{\partial c_{\theta} N}{\partial \theta} + \frac{\partial c_{\sigma} N}{\partial \sigma} = \frac{S}{\sigma} \tag{2.7}$$

where $A \equiv E/\sigma$ is the wave action, N and S are functions of $(\sigma, \theta; x, y, t)$, representing the action density spectrum and the source terms in the action balance equation respectively. $c_{g,x}$ and $c_{g,y}$ refer to the propagation velocities in $x-$ and $y-$ space respectively, which account for the shoaling effect. c_{θ} is the propagation velocity in $\theta-$ space, accounting for depth induced and current induced refraction. c_{σ} is the propagation velocity in $\sigma-$ space, accounting for shift in the relative frequency due to the effect of depth and current variations.

In phase-averaged modelling, it is considered that wave energy propagates according to the linear dispersion relation. The basic assumption is that the wave field changes in scales much larger than the individual wavelengths and wave periods, which dictates a slow evolution of the wave field. The effects of the physical processes and the nonlinearities are introduced via the forcing, aka source, terms. There are processes that have a robust mathematical description through the source terms, such as the four-wave interactions, but there are also other processes that refer to phase-related phenomena, e.g., reflection and diffraction, or to highly nonlinear phenomena that are vaguely understood or poorly mathematically described, such as wind-wave interactions and wave breaking (Cavaleri et al., 2007). For such processes, the source terms rely on heavy parameterizations (Rijnsdorp et al., 2017). Therefore, phase-averaged models are expected to perform less well for rapidly changing conditions and at the nearshore areas, where nonlinear effects and local characteristics become important (Rijnsdorp et al., 2014). The unrivalled advantage of phase-averaged models is their

computational efficiency, which makes it possible to simulate the random nature of the waves at large spatial and temporal scales. Phase-averaged models find application at hindcasting and forecasting, as well as at wave resource characterization studies (Yang et al., 2017). They are also used as part of integrated modelling systems for propagating the wave spectrum from the far oceanic field to the region of interest, where they provide the boundary conditions for phase-resolving or highly-skilled models (Guimarães et al., 2015). Regarding extreme waves, since these phenomena are phase related, phase-averaged models cannot directly account for them. However, thanks to the fact that the probabilities of extreme wave emergence have shown to be associated to spectral characteristics, e.g., kurtosis, spectral models can indicate potential high probabilities for extreme waves at certain regions or weather conditions (Janssen, 2005; Mori, 2012; Bitner-Gregersen and Gramstad, 2015), acting as a warning system, or be used to analyse the sea state when accidents related to extreme waves have been encountered (Prevosto and Bouffandeau, 2002; Adcock et al., 2011).

In the present work, where the spectral changes during the focusing of wave groups have been thoroughly explored, direct associations with phase-averaged models were identified. The relevant source terms for four-wave interactions and triads have been tested in WW3 (see Section A.4), but, since at their present form the source terms cannot account for near-resonant wave-wave interactions in 1D, the GKE was programmed separately. Nevertheless, future work, which can expand the present methodology in 2D, could include WW3 or a similar model as a part of modelling system for analysing extreme waves.

2.2 Wave-wave interactions

In this section, the generation mechanisms of free and bound waves are discussed, along with the effects of instabilities, directionality and generation of spurious waves in physical and numerical wave tanks. The understanding of these effects is crucial not

only for the interpretation of the wave dynamics, but also for the accurate estimation of the impact of the waves on structures needed for engineering purposes (Zang and Taylor, 2010; Swan and Sheikh, 2015).

2.2.1 Bound and resonant nonlinearities

In a linear consideration of a wave field, the wave components do not exchange energy through their interactions, but propagate independently according to the linear dispersion relation. As such, the spectrum of the waves remains constant, but the spatial and temporal shape of the wave group can change due to the fact that longer waves propagate faster than shorter waves (Arena and Fedele, 2005). In reality, water is a nonlinear medium and wave interactions that transfer energy among the waves take place as a natural physical process, which can be enhanced by environmental factors, such as the wind, current and water depth. These interactions redistribute the energy in the wave spectrum by generating harmonics, which are dependent on the initial-fundamental frequencies of the wave spectrum, or new wave components that propagate independently, called bound and free waves, respectively (Lin, 2008). This nonlinearity of the wave field adds considerable complication, but opens a window to study very interesting aspects on the behaviour of water waves. In particular, nonlinearity is an inherent characteristic of the large waves, however there is not a consensus yet to what extent and how it is related with the emergence of extreme waves in the ocean (Adcock and Taylor, 2014). Compared with other nonlinear processes though, wave-wave interactions have a robust mathematical description within the resonance theory (Cavaleri et al., 2007) and are also discussed in the context of the Hamiltonian expression of the waves in the work of West and Brueckner (1987). Before continuing the discussion about the nonlinear wave-wave interactions, some basic definitions are given:

- Free waves: obey the linear dispersion relation, propagating independently.

- Bound waves: phase-locked to the free waves, propagating with the celerity of the wave group.
- Resonant interactions: nonlinear wave-wave interactions between three or four free wave components that create new free wave components. Exact conditions for the frequencies and wavenumbers, which take the mathematical form of a linear resonator, must apply (Phillips, 1960).
- Bound interactions: nonlinear wave-wave interactions among pairs of free waves that generate bound harmonics.
- Near-resonant interactions: similar to resonant interactions, but the exact conditions are not satisfied. Important for the generation of free wave in long-crested seas as well as numerical and physical flumes.
- Non-resonant interactions: depending on the context, they may refer to bound, near-resonant interactions or BF instabilities.

Bound interactions

Bound nonlinearities refer to the generation of new harmonics at higher and lower frequency bands than the original free waves of the spectrum. These bound harmonics propagate with the same celerity as the free waves and their phases are related to the free (linear) waves. The understanding of the formation and the mathematical description of the super- and sub-harmonics started with the pioneering works of Longuet-Higgins and Stewart (1960), Longuet-Higgins (1978a) and Longuet-Higgins (1978b), who used PFS as a starting point for the analysis that was based on the eigen-functions and steepness of the waves. High order bound waves are generated at multiple integers of the frequencies of free waves, referring to second, third, fourth etc harmonics. At half of the free wave frequencies, bound long waves are generated, aka as low frequency or infragravity (IG) waves. The manifestations of the bound waves are local for the high order (super-)harmonics, which cause narrower and higher crests and flatter

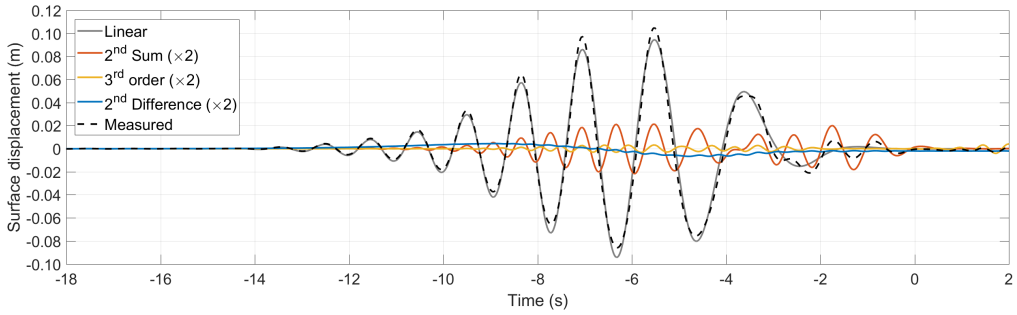

Figure 2.4: Harmonic analysis of a focused wave group used in the present study, demonstrating the bound wave structure. The amplitude of bound waves is doubled.

and shallower troughs when added to the a linear wave signal, and more global for the long bound waves (sub-harmonics), which cause a decrease of the mean water level (MWL) especially beneath wave trains (Fedele and Tayfun, 2009)[4]. An example of the effects bound waves on the wave group in seen in Figure 2.4, where the amplitude of bound waves was doubled for better visibility. The long wave structure of the 2^{nd} difference harmonic under the wave group is evident. Since bound waves are phase-locked to the free wave and thus, they do not propagate with their linearly predicted celerity, it becomes clear that they are uniquely defined by the free-wave spectrum and they do not influence the dynamics of the wave evolution (Onorato et al., 2013; Bitner-Gregersen and Gramstad, 2015). It is noted however that it is not straight-forward to distinguish which waves are free and bound from a single measurement (Walker et al., 2004; Holthuijsen, 2007), and harmonic separation techniques (see Section 2.4.5) and multiple recordings at subsequent measurements are needed (Vyzikas et al., 2018b).

At second order, the calculation of the bound waves for a regular wave was given by Stokes second order theory (Stokes, 1847) as perturbation expansion, and for realistic broadbanded spectra was given by Sharma and Dean (1981) as a summation of any possible combination of free interacting components. The inclusion of bound waves causes a vertical asymmetry of the wave profile (Walker et al., 2004; Taylor et al., 2006), which strength depends on the local wave steepness (Taylor and Swan, 2000; Baldock

[4]Although a set-down is observed in laboratory experiments beneath wave groups, a set-up is also plausible in crossing seas, i.e., wave systems coming from different directions, and has been associated with the emergence of extreme waves (Adcock et al., 2011).

et al., 1996) and the initial amplitude sum of the wave group (Johannessen and Swan, 2001; Vyzikas et al., 2018b) as well as the relative frequencies and the directions of the interacting components (Adcock et al., 2011). Second order theory provides a more realistic representation of a wave field than linear theory and it is often used for direct numerical simulations to deduce statistics of the exceedance probabilities (Forristall, 2000). However, the second order contributions may not be sufficient to account for the largest transient waves (Gibson and Swan, 2007). Instead, the perturbation expansion can be considered at higher orders, which have progressively lower contribution to the wave profile (Hann et al., 2014). Their effect is mostly important for unidirectional waves (Adcock, 2017). As such, for regular waves, the initially single-peak spectrum at the wavemaker becomes multi-peak as the waves propagate in the nonlinear medium (Zhao et al., 2009).

The bound interactions are also known as "triad-wave" interactions, because two waves of frequencies f_1 and f_2 interact to transfer energy to waves at higher or lower frequency $f_3 = |f_1 \pm f_2|$ (Holthuijsen, 2007). Triad-wave interactions, generally speaking, are only important in shallow water, where the corresponding resonance of the wavenumbers is permitted, due to the weakening of the dispersion of the waves that results in the transition from four-wave to triad-wave interactions, as predicted by Hasselmann's theory (Cavaleri et al., 2007). This was also observed in the experimental and numerical study of Shemer et al. (2007), who suggested that for a given steepness of a unidirectional wave group the strength of triads decreases with increasing depth. Triads can develop in short timescales, pumping energy from the free-wave spectrum to higher and lower harmonics (Ris, 1997), which shows similarities to the spectral evolution of the focused wave in the present study. In general, the propagation of waves in shallow water induces additional complexity in physical terms, such as shoaling, self-self interactions, energy transfers from free waves to bound and vice versa (Liang et al., 2015; Holthuijsen, 2007). A particularly interesting phenomenon with considerable consequences in the wave dynamics in the coastal regions is the release of IG waves, which occurs when the wave groups break on the beach and the coupling of

the long waves that are locked to the group is destroyed (Cavaleri et al., 2007).

Resonant interactions

The resonant interactions occur between free waves that satisfy the exact resonant conditions among wave numbers, which for three interacting components that generate a fourth component take the form of the so called four-wave or quadruplet interaction: $k_1 + k_2 = k_3 + k_4$ and $\omega_1 + \omega_2 = \omega_3 + \omega_4$, where k_i and ω_i refer to the wavenumber vector and angular frequency of a wave component i (Janssen, 2003). These conditions satisfy the famous "8 pattern" of Phillips (1960), seen in Figure 2.5, without any limitations for the bandwidth (Trulsen et al., 2000). This generation of new wave components redistributes the energy along the frequencies and directions of the spectrum, altering also the dispersive properties, namely the amplitudes and phases, of the original free waves (Gibson and Swan, 2007). The visualisation of the resonant interactions in a wave tank can be realised with a diamond wave pattern, which can be created by two wave groups coming from different directions, that interacts with another free wave in order to generate a fourth wave, as described by Holthuijsen (2007) and seen in Figure 2.6. The problem of resonant interactions was initially studied by Phillips (1960) and shortly later two fundamental processes of the wave evolution where this theory applies were identified: i) The instability of wave trains, aka BF instability[5] (Benjamin and Feir, 1967), and ii) the long-term evolution of a wave field towards an equilibrium condition for the spectrum (Holthuijsen, 2007), taking the form of a Boltzmann integral (Hasselmann, 1962). The timescales of these two processes differ significantly, with BF instabilities taking place within 5-10 wave periods and the long-term evolution occurring over 100-1000 wave periods, referring to as BF and Hasselmann scales, respectively. In the framework of ocean modelling, four-wave interactions are one of the dominant processes that dictate the wave evolution in deep water (Gramstad and Stiassnie, 2013). It is worth noting that four-wave interactions are energy conservative

[5]Strictly speaking, BF instability is caused by non-resonant interactions (Janssen, 2003).

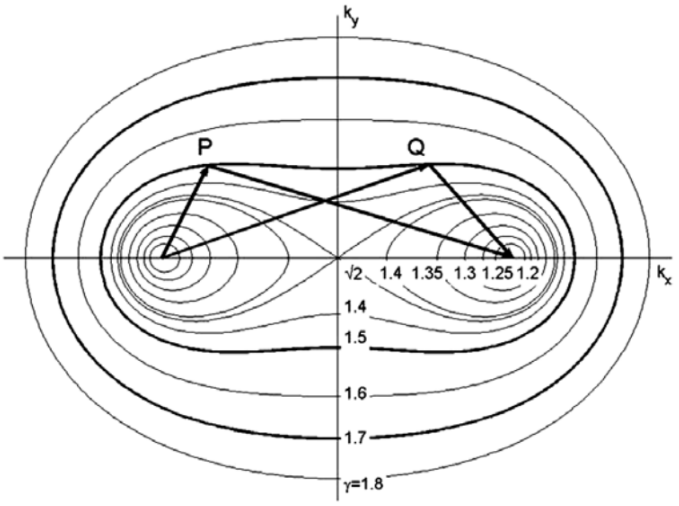

Figure 2.5: Eight pattern interaction that satisfies the resonance conditions for the four wave numbers and angular frequencies (Phillips, 1960). Permission to reproduce this figure has been granted by Cambridge University Press.

and their action only redistributes the energy within the wave spectrum (Holthuijsen, 2007). The wave groups studied in the present work do not satisfy the criteria for BF instabilities, nor for the long-term evolution at the Hasselmann scale. Nevertheless, the patterns are similar to those of resonant and bound interactions and effort is put to explore the sources of these changes. This problem has puzzled other researchers in similar studies (Johannessen and Swan, 2003).

The modelling of the wave dynamics at long timescales requires the inclusion of resonant nonlinear interactions for the accurate description of the wave field. However, although resonant interactions are important for the evolution of the wave group, they seem to play little role on the wave crest statistics (Socquet-Juglard et al., 2005), which appear to be influenced mainly by the contributions of the bound nonlinearities (Dysthe et al., 2008). Nonetheless, other local properties of the waves can be affected by resonant interactions (Latheef and Swan, 2013). This is supported by the present work, which shows that the inclusion of the evolved free-wave spectrum does not increase the crest elevation, but affects the shape of the wave group and its height (see Chapter 5).

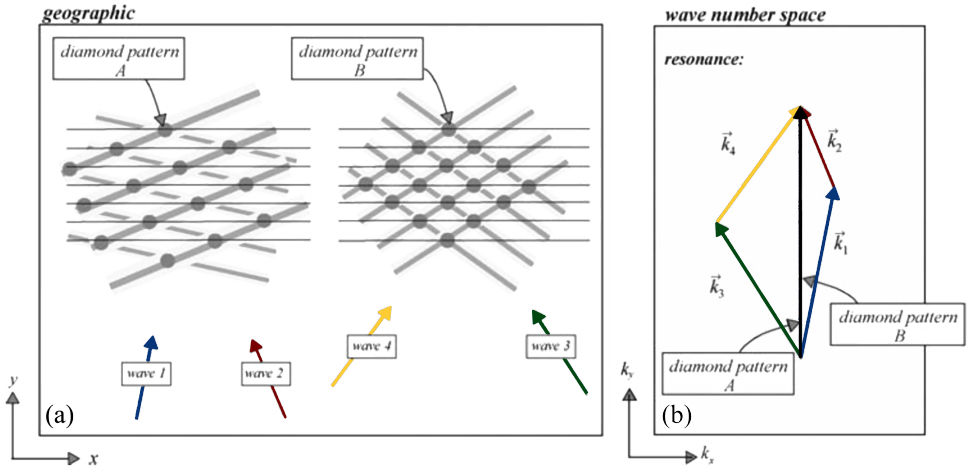

Figure 2.6: (a) The pattern created on the free surface due to the interaction of four waves travelling at different directions and (b) the resonance condition among the four wavenumbers (Holthuijsen, 2007). Permission to reproduce this figure has been granted by Cambridge University Press.

In the context of extreme waves, there is still an ongoing debate to which extent resonant interactions are relevant to extreme wave dynamics at short scales and in realistic ocean conditions (without BF instabilities) (Adcock et al., 2015). For the case of laboratory focused wave groups, rapid widening of the free-wave spectrum is observed[6], which causes important changes to the amplitudes of the free waves (Baldock et al., 1996; Ning et al., 2009b), and its effects seem to be more pronounced for unidirectional wave groups. This conclusion suggests that extreme waves in the field may be more likely to occur in swell-dominated sea states (Gibson and Swan, 2007). Therefore, there exist similarities for the nonlinear wave-wave interactions between focused waves and oceanic waves (Christou and Ewans, 2011a). In real ocean, the strength of these interactions can be high enough to generate extreme waves that can even break in the deep water (Lara et al., 2011). Another manifestation of the resonant nonlinearities in focused wave groups is the nonlinear downshifts of the focal location, which can be tackled with appropriate correction methodologies, as described in Section 2.4.4.

The study of the exact effects of the resonant / near-resonant interactions is an ac-

[6]It is important to distinguish between the rapid broadening of the free-wave spectrum at the BF timescale and the broadening of the total spectrum due to bound high order nonlinearities that occur very close to the focal point. This is well demonstrated in Section 4.1.1.

tive field of research with new literature often contradicting the existing conceptions (Aubourg and Mordant, 2015; Haudin et al., 2016; Bonnefoy et al., 2016; Aubourg et al., 2017).

2.2.2 Spurious waves

In this section, spurious waves are briefly discussed because they often cause discrepancies in the comparisons between physical and numerical models, as well as potential miscalculations in engineering design parameters, e.g., overtopping. Spurious waves are erroneous artificial waves commonly caused by deficiencies of the wave generation conditions in physical and numerical wave tanks. The main types of spurious waves are: i) Free sub- and super-harmonics, which are the most relevant for the case of focused waves and are discussed in detail below; ii) Free local disturbance waves, aka evanescent standing modes, which are created in the vicinity of the wavemaker, due to the mismatch between the shape of the face of the wavemaker and the real profile of the horizontal velocities of progressing waves (Zhang et al., 2007). Evanescent modes decay exponentially in short distance downstream of the wavemaker, disappearing at distance shorter than a wavelength or 3-5 times the water depth (Shemer et al., 2007; Orszaghova et al., 2014). The decay length from the wavemaker can be found using $\phi = \sum_{n=0}^{\infty} c_n Z_n z \exp^{-m_n x}$ for $n \geq 1$, which relates the velocity potential (ϕ) with the vertical distance from the free surface (z) for n wavenumbers, as discussed in the work of Keaney (2015); iii) Free displacement long waves, referred to as seiching, generated due to the abrupt initial movement of the wave paddle from its mean position (Baldock et al., 1996). .

The generation of spurious free sub- and super-harmonics is caused due to the linear transfer function of the wavemaker (Zang and Taylor, 2010), or the linear boundary conditions at the inlet in a NWT, which attempt to introduce linear waves in a nonlinear medium. However, even for moderate steepness, second order effects are not negligible, and linear theory is not adequate to describe the free surface elevation and

kinematics of the waves. Unavoidably, to satisfy the nonlinearity of the medium, second order bound waves are naturally created (Chaplin, 1996), but likewise, their free counterparts are also produced to cancel them at the inlet, having equal amplitudes but opposite phases (Jacobsen et al., 2012). Downstream of the wavemaker, the erroneous second order free waves become apparent, since their propagation has different dynamics than the rest of the wave group. The spurious sub-harmonics travel faster than the wave group and create an artificial preceding surge (Whittaker et al., 2017), which may also affect the shape of the wave group at relatively short distance from the wavemaker (Orszaghova et al., 2014; Vyzikas et al., 2018b). Another common issue is the dissipation of these long waves, which are not always effectively absorbed or destroyed at the outlet and they can be reflected, creating a sloshing effect in the wave tank (Orszaghova et al., 2014). On the other hand, the free spurious super-harmonics, travel with a lower celerity than the rest of the wave group, and they are eventually separated from it a few wavelengths downstream of the wavemaker. Therefore, they do not usually cause any issues at the region of interest, especially in the case of focused wave groups, provided that the focal point is sufficiently far from the wavemaker. An intuitive comparison between the evolution of spurious free and bound waves in relation to the group dynamics is given by Vyzikas et al. (2018b), where it is also discussed that different wavemakers cause different spurious waves, which can explain some of the discrepancies between numerical and experimental results found in many studies, e.g., Bredmose et al. (2016); Ning et al. (2009b); Westphalen et al. (2012). From an engineering design point of view, the spurious long waves have been reported to cause considerable overestimation of the overtopping and the runup of NewWave-type wave groups (Orszaghova et al., 2014).

To suppress the spurious effects of linear wave generation, high order theories have been proposed that give a better estimation of the free surface dynamics and kinematics at the wavemaker. The most commonly used correction to the wavemaker's signal is the second order theory of Schäffer (1996), which was based on the analysis of Barthel et al. (1983). Second order theory was shown to be relatively successful in

eliminating the spurious long wave in experiments (Whittaker et al., 2017), but it had less impressive performance for the high frequency spurious waves (Orszaghova et al., 2014). In NWTs, second order wave generation (Higuera et al., 2013a) and third order corrections to the wavemaker's movement (Ducrozet et al., 2012a) have been applied with success, as discussed in Section A.3.3.

2.2.3 Benjamin-Feir instability

Early experimental observations of unstable Stokes waves in the '60s started puzzling researchers about the nature of these instabilities that were not expected according to conventional theories. This phenomenon was explained by the fathers of the MI, Benjamin and Feir (Benjamin and Feir, 1967) in the West, and, at the same time, independently by Zakharov (1968) in the USSR. An interesting historical review is given by Zakharov and Ostrovsky (2009), where applications of the BF instabilities to other fields, e.g., electromagnetic waves, are discussed (see also Onorato et al. (2013) for more applications). Here, a brief presentation of the BF instabilities is given because they are non-resonant nonlinear wave-wave interactions that have been associated with extreme waves.

The BF instability refers to the disintegration of regular wave trains with an initial perturbation, which can exponentially grow drawing energy from the surrounding waves (Adcock and Taylor, 2014). The simplest case to observe the effect of the BF instability is the interaction of a high amplitude carrier wave at frequency ω with two low amplitude side band waves at frequencies $\omega \pm \Delta\omega$, where $\frac{\Delta\omega}{\omega} < \sqrt{2}k\alpha$, with k and α being the wavenumber and wave amplitude respectively, that exchange energy according to weak modulations (Zakharov and Ostrovsky, 2009). These types of wave groups are called breathers and they have been extensively used to study MI, attempting to understand the mechanism of rogue waves' formation (Fedele and Tayfun, 2009; Kharif and Pelinovsky, 2003). BF instabilities can result in isolated waves of more than three times the initial amplitude of the wave group, at a timescale of $(k\alpha)^2$ wave periods (Dysthe

et al., 2008), which is commonly after 10-30 wavelengths of propagation. This can be a considerable limitation for short physical flumes and computationally expensive NWTs (Bitner-Gregersen and Gramstad, 2015). Moreover, it is noted that BF instability it can appear only under certain conditions: i) The wave field should be sufficiently narrow-banded, with a BF index $BFI > 1$. BFI is defined as the ratio: $BFI = 2(k_p\sigma)/(\Delta\omega/\omega_p)$, where k_p and ω_p are the wavenumber and angular frequency of the component of the peak frequency and σ the spectral variance (Janssen, 2003); ii) The waves should be dispersive. Consequently, they should propagate in deep water of $kd > 1.363$, where d is the depth (Benjamin and Feir, 1967); iii) The wave field should be sufficiently long-crested (Dysthe et al., 2008).

The aforementioned conditions pose important limitations to the emergence of BF instabilities in real ocean, which is mostly characterized by broadbanded directionally spread energy spectra, or in coastal areas of finite water depth (Fedele et al., 2016). However, conditions for BF instabilities can be encountered at the initial stages of a wind-generated wave field or when the wind conditions change suddenly (Janssen, 2003) and during typhoons (Mori, 2012). As such, spectral parameters, namely the kurtosis and skewness, are often used to characterise sea states with high probabilities for extreme waves (Bitner-Gregersen and Gramstad, 2015)[7], which are more common in transitional stages of wave fields (Socquet-Juglard et al., 2005).

To conclude, in a random realistic wave field BF instability effect ceases (Taylor and Swan, 2000), but it is still an open debate which of the two competing mechanisms (energy focusing or non-resonant interactions) are mostly responsible for extreme waves in nature (Fedele et al., 2016). This discussion continues in Section 2.3.

[7] According to the author, the popularity of this approach is partially related to the convenience in associating easily estimated spectral parameters to the probability of extreme waves, compared to more robust mechanisms, such as focusing, that occur however randomly.

2.2.4 Directionality

Directionality is an important parameter that controls the evolution and the properties of wave fields, being an inherent characteristic of real ocean waves that is often neglected in 1D laboratory experiments (Taylor and Swan, 2000; Dysthe et al., 2008). The inclusion of directional spread has considerable effects on resonant and bound wave interactions, spectral evolution, steepness and crest statistics. This section serves also as a "disclaimer" that the findings of the present study refer only to unidirectional wave groups and generalisations should be made with caution, since directionality may affect the wave interactions in focused waves significantly (Johannessen and Swan, 2001). It is also noted that the spectral distribution of the free waves affects the wave-wave interactions and subsequently the shape of the wave group and the onset of breaking (Chaplin, 1996; Stagonas et al., 2018).

A first effect of directionality is the weakening of the bound nonlinearities. Numerical simulations and experiments have shown that long-crested large waves have a bound harmonic structure that exceeds second order (Vyzikas et al., 2018b; Christou and Ewans, 2014), while directionally spread waves can be adequately described by second order theory (Latheef and Swan, 2013; Johannessen and Swan, 2001). The consequence of this is that realistic seas can be described by second order statistical distributions (Forristall, 2000; Tayfun, 1980), but unidirectional seas may show considerable departures for the largest waves with low probabilities of occurrence[8]. Regarding the low-frequency bound wave, it is always expressed as a set-down in following seas, but it can be considered negligible in directional seas (Forristall, 2000). The bound nonlinearity of the directionally spread wave groups reduces their steepness and more energy is required before they break. Thus, limiting breaking directional wave groups can reach higher elevations than the equivalent uni-directional groups (Johannessen and Swan, 2001).

[8] It is noted however that crossing seas can also give very large waves, if they are separated by specific angles (Onorato et al., 2013), which can explain the positive long bound wave structure observed in the famous Draupner wave (Taylor et al., 2006; Adcock et al., 2011).

Regarding resonant interactions, the wave evolution in 2D demonstrates fundamental changes, since the wave energy is not "trapped" in 1D and the exact resonance conditions can be satisfied (Phillips, 1960). Therefore, pronounced spectral changes can occur, with four-wave interactions spreading energy to large angles or creating bimodal spectra (Gagnaire-Renou et al., 2010). In ocean models, the resonant interactions control the long-term spectral evolution at the Hasselmann scale (Gramstad and Stiassnie, 2013; Gramstad and Babanin, 2016; Benoit, 2006). In directional focused waves, the nonlinear wave interactions can cause concentration of energy in the mean direction, long-crested behaviour towards focusing and movement of the highest crest at the front of the wave group (Adcock and Taylor, 2014). Such effects can result in a "wall of water" shape (Adcock et al., 2016) that persists for longer time than predicted by linear theory (frozen profile) (Adcock et al., 2015).

2.2.5 A note on the kinematics

A wave field is characterised both from the surface dynamics and the kinematics. The latter is particularly important for engineering purposes because they determine the loading of the structure, commonly through the use of the Morison's equations (Chaplin et al., 1997) or by integrating the measured pressure on the surface of the structure (Ransley, 2015). Similarly to surface dynamics, kinematics are also influenced by the nonlinear wave-wave interactions and subsequently by the steepness, dispersion and directionality (Forristall, 2002). In brief, the linear Airy theory calculates the waves at the MWL and it fails to calculate accurate kinematics above the MWL, especially for realistic waves. Thus, empirical extrapolation techniques are used, such as the Wheeler stretching, which however are not based on the hydrodynamics' principles (Trulsen et al., 2001).

Accurate calculation of the kinematics can be achieved by PFS and CFD solvers, but, operational models for kinematics require both computational efficiency and expansion to higher order. Such an example is the stochastic second order approach of Alberello

et al. (2016). Moreover, there are challenges in obtaining accurate kinematics from point measurements in the field, because the waves have to be considered unidirectional (Slunyaev et al., 2011). In laboratory, kinematics can be studied thoroughly, but it is also challenging to obtain the velocity profile along the water column with conventional point measurements, e.g., using LDA (Johannessen, 2010), because they require many repetitions. Alternatively, the Particle Image Velocimetry (PIV) technique can be used that instantly maps the full velocity field (Santo et al., 2017). Other challenges that are relevant to the kinematics is the accurate prediction of the Stokes drift and the return flow, which become particularly relevant for focused wave groups in tanks (Taylor and Swan, 2000).

In the present work, comparisons for the kinematics are not included, however, preliminary studies with experimental results measured with PIV showed good agreement. Nonetheless, by comparing the propagation of the wave group at different locations and obtaining similar results everywhere in the flume, confidence is gained that the kinematics are correctly reproduced in the NWTs. Instead, when comparisons are performed only at a single location, the measured elevation may be an outcome of intercancellations of different processes, e.g., incident and reflected waves, which can result in different kinematics.

2.3 Extreme Waves

In this section, a brief but multilateral review of extreme waves is given after consulting a broad literature. This covers the period from early observations to the most recent reviews and findings, and it comes from different research teams, which approach the problem with different methods and for different objectives. Some main outcomes are:

- Extreme waves are not as rare as initially thought, and solid evidence brought them from maritime folklore to engineering studies.
- Full consensus of the main aspects of extreme waves, such as definition, proba-

bility of occurrence, generation mechanisms, most appropriate way of modelling, has not been reached yet, making the study of extreme waves an exciting field of research.

- There are two main "schools" for the generation of extremes: MI and dispersive focusing, which use different modelling tools, referring to envelope and hydrodynamic equations, respectively.
- Recent analyses of field data proved that dispersive focusing is a valid mechanism for extreme wave generation in the real ocean.

2.3.1 Definition

A common definition of extreme waves has not been generally agreed yet by the scientific community (Haver, 2000; Cavaleri et al., 2012; Onorato et al., 2013). Many terms are also used indistinguishably in scientific publications, such as rogue, freak and extreme, or in everyday language, e.g., giant and monster, to refer to extreme waves (Bitner-Gregersen and Gramstad, 2015). In the present work, the term "extreme" is used to refer to such very large waves. Nevertheless, there is a consensus that extremes refer to events that are not expected for the considered sea state and thus, they should be characterized in relation to the surrounding wave field (Adcock and Taylor, 2014). However, what makes a large wave be characterized as extreme is something ambiguous and for decades researchers try to see whether extremes are rare members of the normal population of waves or they form another population governed by different physics (Haver, 2004). A quantitative criterion that is commonly used is the ratio of the crest height (η_c) and/or maximum wave height (H_{max}) over the H_s, as seen in Equation 2.8 (Haver, 2000). The threshold for these ratios is set based on the length of the record where the extremes are observed, here considered 20 min. However, these thresholds should not be considered as strict criteria, because they are mostly empirical and there is no particular change in the physics beyond them (Christou and Ewans, 2011b). Moreover, these criteria should not be necessarily used together, be-

cause this may exclude extreme distortions of the free surface, e.g., deep troughs, that do not comply with both of the conditions (Christou and Ewans, 2011b). Thus, other criteria based on steepness and statistics may be also used. It is noted that based on this definition, extreme waves can also be of very small amplitude if they appear in a calm sea (Onorato et al., 2013; Bitner-Gregersen and Gramstad, 2015). For this reason, when analysing field data, other criteria can be included that are related to the design wave for the examined structure in order to focus on meaningful extreme waves (Vyzikas et al., 2013).

$$\frac{\eta_c}{H_s} > 1.25 \quad \text{and/or} \quad \frac{H_{max}}{H_s} > 2 \tag{2.8}$$

It becomes apparent that the definition of Equation 2.8 is not ideal. On a more generic approach, extreme waves can be considered those waves that are not part of our understanding, statistical distributions and engineering design practice. In this framework, extremes can refer to the outliers of the models presently used, namely the Rayleigh distribution with second order corrections (Haver, 2000). Usually, they are observed as single kick-outs at the tails of the statistical distributions (Christou and Ewans, 2011b). It is noted, however, that extremes occur more frequently than the exceedance probabilities from the statistical models would allow for (Taylor and Swan, 2000). A consequence is that extremes are perceived as unexpected events of high steepness and asymmetry, and thus, inherent nonlinearity, being much larger for the given sea state than linear thoery would predict (Kharif and Pelinovsky, 2003; Christou and Ewans, 2014). Theoretically, using more advanced models could capture more of the nonlinear characteristics of the extremes or the environmental factors that contribute to their generation. Therefore, as our understanding and tools improve, more rogue events may fall into the category of classic very large waves (Haver, 2004). Indeed, recent analysis suggests that extreme waves are rare events of the normal statistical population (Christou and Ewans, 2014). This process of "de-rogueing" will eventually make extreme waves part of the engineering design process, decreasing the number of acci-

dents that they cause. Towards this direction, efforts should be made to collect reliable field and laboratory measurements (Onorato et al., 2013) and combine them with numerical models in order to be able to predict the emergence of extremes (Alam, 2014).

2.3.2 From myth to reality

The existence of giant waves that appear out of nowhere and swallow ships has been always part of mariners tails (Bitner-Gregersen and Gramstad, 2015), creating a legend and mystery around extreme waves. In anecdotal evidence, extreme waves are commonly referred to as "walls of water", "holes in the sea" and "three sisters" (Kharif and Pelinovsky, 2003) as well as "mad dogs" in coastal waters (Tsai et al., 2004). A common characteristic is that extreme events seemed to appear suddenly without any warning and to be much larger than the surrounding waves, and to persist for some wave periods having a "frozen profile" (Haver, 2000). Also, in many cases they seemed to propagate in an oblique direction to the sea state, posing a greater threat to navigation (Adcock and Taylor, 2014). Although these descriptions do not offer precise characteristics for a systematic study of extreme waves, they do capture some general features of extreme waves, such as the high vertical asymmetry and nonlinearity (Fernández et al., 2014). The hard evidence for the existence of extremes comes from measurements at fixed structures (Christou and Ewans, 2014), usually oil platforms, and wave buoys (Liu and Pinho, 2004). These measurements show that extremes may be less rare than initially thought (Dysthe et al., 2008) and certainly far from being simply legends of mariners, who are in fact likely to encounter a few rogue waves in their career (Adcock and Taylor, 2014). A photograph of a rogue wave taken from a ship is shown in Figure 2.7 demonstrating how the rogue event stands out from the surrounding sea.

The understudying of these monster waves is crucial for the safety at sea, because they pose a real threat to shipping and offshore industry (Slunyaev et al., 2011; Fernández et al., 2014). Compared to large waves that occur in storms, extremes can happen in

Figure 2.7: Rogue wave off of Charleston, South Carolina. Photo courtesy: National Weather Service USA.

a relative mild sea, which makes them in particularly dangerous, since they are not anticipated. Public media became interested in the topic after many accidents associated with extreme waves were reported: for example, at passenger ships, such as Queen Elisabeth II (1995), Caledonia Star*[9] (2000), Bremen (2000), Explorer (2005), Voyager (2005), Norwegian Dawn (2005), Louis Majesty* (2010) and MS Marco Polo (2014), as well as at oil platforms, such as the 30 installation in the Gulf of Mexico during the Hurricane Katrina (2005) (Bitner-Gregersen and Gramstad, 2015), and the Ekofisk and Frigg fields in the North Sea. Accidents were also reported for semi-submersibles (Veslefrikk B and Ocean Ranger), oil tankers (MV Derbyshire in 1980), liners (Queen Elizabeth in 1943 (Haver, 2000), Queen Mary* (1942) and RMS Etruria* (Adcock and Taylor, 2014)) and super-carriers (22 losses between 1969-1994, 12 of them near the Agulhas Current at the South Coast of Africa) (Kharif and Pelinovsky, 2003)[10]. Damages were also reported at offshore wind turbines due to extreme runup and loading

[9]For the cases marked with *, the extreme waves were reported to be in an angle compared to the mean sea direction, supporting the argument that extremes can be generated by crossing seas (Adcock and Taylor, 2014), which makes it more easily to roll a vessel (Bitner-Gregersen and Gramstad, 2015).

[10]An unofficial database of extreme wave encounters can be found in the wiki page: https://en.wikipedia.org/wiki/List_of_rogue_waves and in the chronicles of Liu (2007).

(Bredmose and Jacobsen, 2011). The encounter of extreme waves with vessels and structures usually results in catastrophic consequences and human losses. Thus, extremes should be taken into account in the design process, as discussed in Section 2.3.4, and not simply be considered as a part of the error in the Fatal Accident Rate (FAR) (Haver, 2000).

The first extreme wave to be recorded and studied extensively was the famous Draupner wave, aka New Year Wave, that was measured on 1/1/1995 in the North Sea at the Draupner platform, with its wave height reaching 26 m in a sea state of $H_s = 12$ m. The recorded free surface elevation is shown in Figure 2.8. Its crest elevation was also abnormally high (18.5 m). The probability of observing such an event may be as low as $1 : 10^5$ waves (Haver, 2000; Walker et al., 2004). Thorough analysis of the recording of the Draupner wave revealed that the low frequency bound harmonic was causing a set-up instead of a set-down, as it would be expected for large unidirectional waves. Initially, it was speculated that this abnormal feature might have been an intrinsic characteristic of extreme waves (Taylor et al., 2006), but further analysis demonstrated that the Draupner wave probably occurred in a crossing sea state, where the bound subharmonics can be positive. Moreover, meteorological data support the existence of two sea systems of different directions. The force measurement[11] on the platform is also consistent with this hypothesis. In addition, it is unlikely that the Draupner wave was caused by BF instabilities, due to the directionality of the sea state and the finite depth of the region (70 m) (Adcock et al., 2011). The Draupner wave has been topic for numerous studies and the "holy grail" for experimentalists and numerical modellers to replicate, commonly failing to capture the largest crest, probably due to the unidirectional approach (Schmittner et al., 2009).

Apart from the Draupner wave, the analysis of field measurements revealed evidence of extreme waves in many locations, such as the North Sea, the Sea of Japan and the Gulf of Mexico (Mori, 2012). The most comprehensive study to present is that of

[11] On the contrary, the interpretation of Trulsen et al. (2001) is that the response of the structure suggests unidirectional sea.

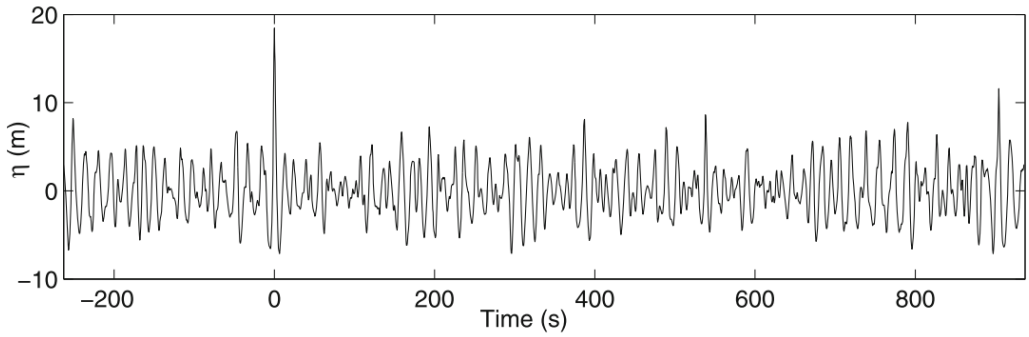

Figure 2.8: Timeseries of the free surface elevation recorded at Draupner platform on 1/1/1995, containing the New Year Wave at time $t = 0$ s (Adcock, 2017). Permission to reproduce this figure has been granted by Springer International Publishing.

Christou and Ewans (2014), where 121 million individual waves were analysed from 22 different offshore installations and, after following a strict data quality control methodology, more than 3,500 extremes were identified. The study aimed at determining the characteristics of the extremes and potential generation mechanisms. Important outcomes are that extremes are not uncommon compared to Foristall statistical distributions and occur also in moderately steep sea states and in intermediate water. Their only common characteristic is the constructive phasing (focusing) of the most energetic wave components.

It is worth noting that despite the fact that extreme waves were first observed by mariners and oceanographers, they comprise a natural phenomenon that can be found in other media than water, which puts them in a general context of nonlinear physics. Other fields in which active research is undertaken on extreme waves are hydrodynamics, electrodynamics, nonlinear optics and convection theory. The applications refer to many topics ranging from molecular dynamics to cosmology (Zakharov and Ostrovsky, 2009). Common applications refer to superfluid Helium, optical fibers, capillary waves, plasma waves, Bose-Einsteins condensates and acoustic turbulence, but still the question on how to connect them all and achieve a universal description remains open (Onorato et al., 2013). Any analogies, however, should be made with caution, considering the particularities of the medium. For example, infinitely high water waves cannot be realised due to the dissipation mechanism of breaking (Babanin et al., 2012).

2.3.3 Generation mechanisms

Probably the most crucial part in advancing the understanding of extreme waves is explaining their generation mechanisms. Unfortunately, in many cases the literature is contradictory (Cavaleri et al., 2012) and the two main streams, i.e., MI and dispersive focusing, find arguments to prove each other invalid. The present work mainly focuses on the latter mechanism, which is supported by the latest literature (Christou and Ewans, 2014; Fedele et al., 2016). In this section, both mechanisms are discussed along with other possible environmental factors, such as the bathymetry, wind and presence of currents, and spectral parameters, namely, the directionality, steepness, skewness-kurtosis and spectral width.

Environmental factors: Despite the fact that extremes are more frequent at certain ocean areas, they have been observed worldwide (Bitner-Gregersen and Gramstad, 2015). Regarding the water depth, extremes have been encountered both in deep and shallow water (Kharif and Pelinovsky, 2003), but for the latter, waves are less dispersive, which decreases the possibility of MI (Bitner-Gregersen and Gramstad, 2015). Thus, in shallow water, instead of MI, linear-type focusing is expected (Kharif and Pelinovsky, 2003). The water depth, however, can play an important role in concentrating the wave energy at certain locations by refraction due to underwater topography[12] (Adcock and Taylor, 2014; Dysthe et al., 2008; Socquet-Juglard et al., 2005). The spatial focusing caused by bathymetry is considered a separate generation mechanism, which is well understood within the linear theory framework (Kharif and Pelinovsky, 2003). A similar mechanism causing spatial focusing due to refraction is the presence of currents (Yan et al., 2015). Ambient currents can interact in a linear sense with the waves, causing change of their direction and their celerity as a Doppler-type shifting. However, in ocean, currents have sheared profiles, and nonlinear interactions with waves can be strong, changing the properties of the wave field (Adcock and Taylor, 2014). Currents increase the steepness of oppositely propagating waves causing extreme waves or

[12] Such "hot-spots" of energy have been suggested for wave energy converters (Dysthe et al., 2008).

being even able completely block the waves (Kharif and Pelinovsky, 2003). Many accidents due to extreme waves have been reported in areas where the presence of currents is strong. The most famous is the Agulhas current at the south-east coast of Africa (Socquet-Juglard et al., 2005) and the Bermuda triangle (Adcock and Taylor, 2014). It should be noted that MI effects (Bitner-Gregersen and Gramstad, 2015) as well as dispersive focusing (Buldakov et al., 2015) can occur and potentially be enhanced by the presence of currents. Regarding the effect of the wind, since the energy for the waves to grow is provided by the wind, it would appear intuitively possible that continuous feeding of energy from the wind could cause extreme waves. However, the findings so far are inconclusive (Adcock and Taylor, 2014). Nevertheless, the presence of strong winds can be an indirect generation mechanism for extremes. The wind field affects the wave age and, accordingly, the steepness of the sea state (Christou and Ewans, 2014). Thus, in cases when wind starts blowing or changes direction, it is possible that nonlinearity increases and the spectrum becomes temporarily narrowbanded creating the right conditions for MI (Adcock and Taylor, 2014). On the other hand, it is also possible that the wind effect neutralizes the MI (Alam, 2014).

Spectral parameters: As discussed in Section 2.2.3, some spectral parameters, namely the bandwidth, directionality, skewness and kurtosis, can cause or hinder MI. The analysis of field data of Christou and Ewans (2014), however, showed that extreme waves do not have any particular skewness. Moreover, kurtosis does not seem to have a correlation with the likelihood of extreme waves, rather than simply indicating the presence of high waves by definition. On the other hand, the same analysis showed that there is a weak correlation between the presence of extremes and the spectral bandwidth, with narrowbandness increasing the probabilities of extremes. Even clearer is the correlation for the steepness, with extreme waves mainly being encountered in stormy sea states of high mean steepness, defined as $\frac{2\pi}{g}\frac{H_s}{T_m}$, where T_m the mean wave period. To an extent, this could be expected, since high steepness can cause beyond second order wave interactions. Furthermore, Christou and Ewans (2014) examined different spectral shapes, finding no trends for extremes in unimodal or bimodal spectra. Last

but not least, the directional spreading is a parameter that can be related to extremes: with decreasing directionality, MI increases (Alam, 2014) and, at the same time, the bound wave structure becomes more pronounced leading to departures from second order theory, as discussed in Section 2.2.4.

MI has been suggested as one of the main mechanisms for extreme wave generation (Kharif and Pelinovsky, 2003) that causes nonlinear self-focusing to the deep water waves (Onorato et al., 2013), as observed in many numerical and experimental works. However, as explained in Section 2.2.3, realistic sea conditions do not satisfy the criteria for MI especially the narrow directional spreading (Haver, 2004; Bitner-Gregersen and Gramstad, 2015). Moreover, the randomness of the wave field is broadly believed to limit MI (Taylor and Swan, 2000; Deng et al., 2016; Adcock, 2017)[13], but at the same time, this argument is used to disprove the theory of spontaneous dispersive focusing in real ocean (Socquet-Juglard et al., 2005). On the other hand, it was suggested that MI effects are possible in crossing seas, where extreme waves can be created (Cavaleri et al., 2012; Bitner-Gregersen and Gramstad, 2015). MI is certainly an active topic of research and, since it can be predicted by spectral parameters and the BFI, it could be useful in forecasting extremes using spectral models (Dysthe et al., 2008; Zhao et al., 2009). However, the latest studies of oceanic extreme waves have demonstrated that MI ceases in real ocean and dispersive focusing is the most likely generation mechanism (Christou and Ewans, 2014; Fedele et al., 2016; Benetazzo et al., 2017). This gives a concrete basis to the present work.

Lastly, the most widely accepted generation mechanism is discussed: dispersive focusing, also referred to as temporal focusing (Bitner-Gregersen and Gramstad, 2015; Deng et al., 2016). The principle is that, due to the dispersive nature of the waves, fast/long waves may coincide with slow/short waves creating local high concentration of energy. This constructive interference of free-wave components (Fedele et al., 2016) is well described by linear theory. For more than two decades now, linear superposition

[13]There exist cases, however, that show that the amplification caused by BF instabilities is not destroyed in random fields (Kharif and Pelinovsky, 2003).

of waves, with appropriate tuning of the phases in order to create focused waves, is widely used in experiments (Chaplin, 1996; Baldock et al., 1996), expanding the early findings of Longuet-Higgins on chirps (Dysthe et al., 2008) and setting the basis for the broad use of the NewWave theory in physical and numerical tanks (Section 2.4.1). However, if in fact dispersive focusing was the only mechanism for extreme wave generation, the probability of extremes could be directly defined by the probability of certain phasing among the waves (Bitner-Gregersen and Gramstad, 2015). In reality, extreme waves are more frequent than predicted in Gaussian seas, i.e., sea states where the amplitudes of the waves follow Rayleigh distributions, which can be partially explained by the nonlinear effect of the strong bound wave structure (Onorato et al., 2013). In contrast to MI, dispersive focusing can also occur in a random background (Hunt, 2003; Dysthe et al., 2008). Moreover, appropriate controlling of the phases of the wave components can produce extreme waves of various forms that resemble extremes recorded in the field (Kharif and Pelinovsky, 2003). Nevertheless, it is noted that mechanisms that cause dispersive focusing in the ocean have not been identified (Dysthe et al., 2008) and the randomness of a real wave field may destroy the dispersive focusing (Kharif and Pelinovsky, 2003). New evidence that leans the debate in favour of the occurrence of dispersive focusing came with the extensive study of (Christou and Ewans, 2014), where it was demonstrated that a common characteristic of extreme waves is the phases coherence of the most energetic components of the spectrum[14]. These findings were also supported by the analysis of Fedele et al. (2016).

To summarize, from all the generation mechanisms discussed, it becomes clear that extreme waves are associated with high local energy concentration (Dysthe et al., 2008). In nature it is likely that these mechanisms coexist and amplify each other.

[14]This aspect could be also observed in normal large waves, but the trend was considerably more evident for extreme waves.

2.3.4 Statistics and uncertainties

A crucial step for incorporating extreme waves in the engineering design process is the estimation of their statistical distributions in order to select a design wave with the appropriate return period. The most commonly used statistical distributions are: the Rayleigh, Weibull, Forristall and Tayfun distributions (Bitner-Gregersen and Gramstad, 2015). The Rayleigh distribution is based on linear theory and assumes that the wave field is sufficiently narrowbanded and unidirectional (Fedele and Tayfun, 2009). Due to the inherent nonlinearity of realistic ocean waves, which makes their crests higher and steeper, and the troughs shallower, deviations were observed for the Rayleigh distribution (Longuet-Higgins, 1980) resulting in positive skewness (Fedele and Tayfun, 2009). To account for these effects the generic two-parameter Weibull distribution was proposed. Forristall (1978) suggested specific parameters for the Weibull distribution after fitting it to field measurements from the Gulf of Mexico. Later, Forristall (2000) performed random numerical simulations of directional waves using second order theory and suggested new parameters to the Weibull distribution. At present, this is considered the state-of-the-art distribution in engineering practice that was shown to fit well field observations (Bitner-Gregersen and Gramstad, 2015). Another statistical distribution that was derived using second order theory was proposed by Tayfun (1980), which is valid for long-crested narrowbanded wave fields (Fedele and Tayfun, 2009). A more recent second order model was suggested by Arena and Fedele (2005) for unidirectional seas and by Fedele and Tayfun (2009), as a generalization to the Tayfun distribution. The exceedance probability of a crest elevation in relation to the H_s of the sea state is shown in Figure 2.9 (Forristall, 2000; Tayfun, 1980). It can be seen that for high exceedance probabilities (small crests) the distributions are almost identical, but for low exceedance probabilities ($< 10^{-3}$) (high crests) Rayleigh distributions predict smaller crests than the second order distributions. Moreover, adding directionality to the wave field (Forristall 3D), decreases the wave crest elevation for the same sea state (Forristall 2D).

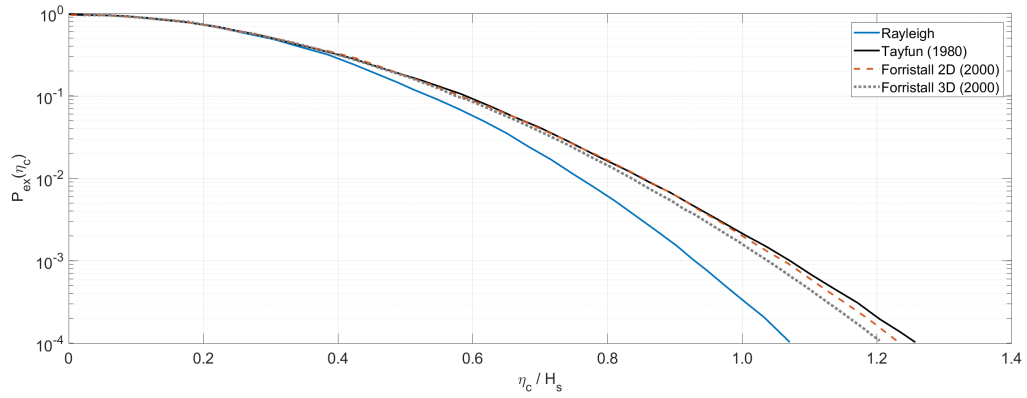

Figure 2.9: Commonly used statistical distribution of exceedance probabilities of crest elevation (η_c) compared to H_s (Bitner-Gregersen and Gramstad, 2015).

As far as extreme waves are concerned, at the beginning, it was not clear if they had to be treated as a different statistical population (Haver, 2000) or if they were instrument errors or statistical flukes (Bitner-Gregersen and Gramstad, 2015; Dysthe et al., 2008). However, recent field analysis shows that they are rare occurrences of the normal population (Christou and Ewans, 2014), emerging as kick-outs at the tails of the statistical distributions. Being naturally nonlinear events, extremes deviate in general from the linear and second order distributions. To capture them, theoretically, higher than second order statistics, i.e., statistics of second order waves, can be produced by running high order nonlinear numerical models, as for example in Adcock (2017) and Socquet-Juglard et al. (2005). Similarly, physical experiments require a high number of realizations to produce robust statistics (Latheef and Swan, 2013), which is a challenging task even if all the other uncertainties for long experimental runs, such as reflections and repeatability issues, are minimized. These concerns become even more important when considering that extreme waves are rare and a large number of simulations is required to produce robust statistics (Adcock and Taylor, 2014). An option would be to analyse vast amounts of field records, potentially from different locations. However, in the field, conditions are not controlled and the measurements are intermittent or refer to different sea states. The latter violates the very hypotheses of all theoretical models, namely the stationariness and ergodicity of the wave field. Especially in transitional

sea states, where extreme appear, the hypothesis of a stationary field even for short periods of time, e.g, 20 min field records, is questionable (Adcock and Taylor, 2014). Similarly, the assumptions of narrowbandness and small directionality of the Rayleigh and Tayfun models deserve attention when referring to realistic ocean waves (Kharif and Pelinovsky, 2003). Last but not least, an issue when extreme waves are present in short wave records is that they may alter temporarily the spectral characteristics on the one hand (Bitner-Gregersen and Gramstad, 2015), and on the other hand, create a coherence in the phases, which may not be anymore considered uncorrelated to satisfy homogeneity (Adcock and Taylor, 2014).

Despite the previous concerns for analysing the statistical properties of extremes with Rayleigh and second order distributions, this is a necessary starting step, since they are widely used in the design practice. The analysis of field data of Christou and Ewans (2014) concluded that in general extreme waves are underpredicted by the Rayleigh distribution and overpredicted by Forristall distribution. This finding contradicts to an extent the perception that extremes fit in higher than second order statistics (Taylor and Swan, 2000), which can be the case mainly for unidirectional seas (Latheef and Swan, 2013). The introduction of directional spreading brings the statistics back to the second order statistical model (Latheef and Swan, 2013) (apart from the case of shallow water (Forristall, 2000)), because it both weakens the bound wave structure and any potential MI effects. On the contrary, increasing steepness may cause departures from theoretical distributions (Adcock, 2017), to the point where the limiting mechanism of wave breaking is activated (Latheef and Swan, 2013)[15]. Another aspect to consider, which is commonly neglected by the statistical distributions that mainly refer to crest statistics, is the wave height. It was shown that linear models may severely underestimate the crest distributions, but they can predict well the wave height distributions (Dysthe et al., 2008).

[15]It is worth noting that when sea states have similar steepness, directional spreading has little influence on the exceedance probabilities (Latheef and Swan, 2013), which justifies the rationale of the present study to make comparisons with different works only among limiting breaking wave groups (see e.g., (Johannessen and Swan, 2003))

From the previous discussion, it is clear that further work is needed to obtain better insight into the properties of extreme waves and their probabilities of occurrence. Undoubtedly, field data is considered the gold standard with the least bias, and naturally the starting point to obtain reliable information should be their analysis. However, before putting blind trust in field observations, some limitations of the measuring apparatus are discussed that may induce considerable uncertainties in the recording of extreme waves. To begin with, in the past, due to technological limitations, only averaged spectral parameters were stored, which, of course, do not provide information about individual waves and as such, extremes were not recorded (Bitner-Gregersen and Gramstad, 2015). Modern measuring apparatus records the timeseries, but in some cases, the measurements suffer from low sampling rate, which may miss the steep shape of extreme waves and underestimate their crest (Forristall, 2000; Whittaker et al., 2016). Thus, for extreme events, which are rare and populate the tail of the statistical distribution (Latheef and Swan, 2013), low sampling rate can induce considerable uncertainties (Trulsen et al., 2001). There are also important physical limitations on the measuring apparatus. For example, wave buoys follow a Lagrangian motion on the free surface and, as a result, they are dragged by the waves passing more time on the crest than on the troughs, measuring an artificial set-up (Whittaker et al., 2016) and, also, they are known to move laterally off the highest crests, missing the maximum elevation (Adcock and Taylor, 2014; Christou and Ewans, 2014; Benetazzo et al., 2017) and the high order nonlinearities (Forristall, 2000). The most accurate way to record extreme waves is with radar and laser altimeters, and wave staff mounted on fixed structures. Important issues in these cases are the potential wave-structure interaction effects (Adcock and Taylor, 2014) and the errors due to sea spray from wave breaking, which is expected to overestimate the crests (Bitner-Gregersen and Gramstad, 2015; Dysthe et al., 2008). To make the situation more complicated, there is sometimes lack of information about the sensitivity of the sensors, and the maintenance and calibration of the apparatus is suboptimal (Christou and Ewans, 2011a). For these reasons, quality control should be applied to the data, sometimes combined

with visual checks, where the human experience and interpretation can be valuable (Christou and Ewans, 2014). To give an indication of the errors and uncertainties in recording extreme waves, only 16% of the measurements passed the quality control in the study of Christou and Ewans (2014). Other observable physical effects, such as damages on the structure (Dysthe et al., 2008), or measured loading on the structure could be useful in confirming the presence of an extreme wave, as it was done for the Draupner wave (Adcock et al., 2011). New promising measuring technologies refer to satellites and radars that can provide spatio-temporal information (Dysthe et al., 2008) and are expected to identify more extremes than classical point recording (Benetazzo et al., 2017). Nevertheless, concerns have been expressed for the accuracy of these methods tested (Onorato et al., 2013), since they are based on linear assumptions for processing of the images and consider large length scales (≈ 100 m) (Bitner-Gregersen and Gramstad, 2015).

To conclude, it is not trivial to produce reliable statistics for extreme waves (Christou and Ewans, 2014). There is still not a consensus about the probability of occurrence of rogue waves (Bitner-Gregersen and Gramstad, 2015) and whether a quasi-linear or second order model is enough to include them (Adcock and Draper, 2015; Ardhuin and Roland, 2013). At present, for a single location in the ocean, a large extreme wave is expected in every $\approx 10^5$ waves (Christou and Ewans, 2014), while when a region is considered instead of a point this probability increases (Benetazzo et al., 2017). Moreover, considering that the climate change is expected to increase the steepness in the ocean, the probabilities of extremes may rise in the future (Bitner-Gregersen and Gramstad, 2015).

2.3.5 Design practice

After presenting the basic properties of extreme waves, this section discusses how extremes can be incorporated in the engineering practice and for what problems they are expected to have an important contribution.

According to the classic engineering approach, a structure is supposed to withstand the environmental loading that it may experience during its lifetime, which is determined by the return period of this loading, commonly amplified by a safety factor to account for uncertainties. The issue with extreme waves is that neither their exceedance probabilities are known with confidence, nor the additional nonlinearities, which pose challenges in defining their return period and safety factors, respectively (Haver, 2000). Another important issue is that the loading due to waves of progressively increasing crest heights may not be a "well-behaved" problem. In practice this means that if the crest height increases beyond a certain threshold, the integrity of the structure can be put at risk because some of its members, which were not designed for direct wave impact, e.g., upper decks of vessels or platforms, may be directly exposed to it (Haver, 2004). Moreover, even in the cases that there may be high correlation between the crest heigh and the load that the structure experiences, this, almost certainly, is not an one-to-one relation (Haver, 2004), due to directionality effects or to shape variation of the waves, which can cause different response to different structures (Adcock and Draper, 2015). Therefore, to which extent a wave is considered dangerous for a structure is case specific. The same also applies for the exceedance probabilities of the loads which depend on the environment that the structure is expected to operate at, e.g., a ship should be designed for the magnitude and type (including wave-currents) of extreme waves that it may face at any of its sailing routes[16], while a platform is designed for the potential extremes of its particular location (Bitner-Gregersen and Gramstad, 2015). Thus, knowing the statistical properties of extreme events for the survivability of marine structures is essential (Ewans and Buchner, 2008; Latheef and Swan, 2013; Yan et al., 2015).

Supposing that the exceedance probabilities of extreme waves are known, what remains to estimate the loads is the wave kinematics, which can be determined from a wave theory or calculated numerically, as mentioned in Section 2.2.5. The kinematics

[16]Certification permits indicate the geographical areas and maximum distance in the ocean that ships are allowed to sail, see e.g., DNV-GL certifications (Bitner-Gregersen and Gramstad, 2015).

can then be used by sophisticated fluid-structure interactions solvers, or, as commonly done in engineering practice, by empirical formulae (Morison's equations). The popularity of the Morison's equations for monopiles and members of jacket platforms lies on its simplicity, because only the relative dimension of the structure to the wavelength and the Keulegan-Carpenter number (K-C) are required to determine the flow regime (viscous drag, unsteady inertia, linear diffraction). The K-C is found by the incident wave-induced velocity in absence of the structure (Swan and Sheikh, 2015). However, this approach does not account for nonlinear effects and it may fail for transient extreme waves (Bredmose et al., 2016) and when the presence of the structure influences considerably the velocity field (Bredmose et al., 2006; Bredmose and Jacobsen, 2011). To calculate the incident velocity, regular waves are used (Chaplin et al., 1997; Forristall, 2000) under the assumption of weak nonlinearity and narrowbandness of the spectrum, which are questionable for extreme waves (Bitner-Gregersen and Gramstad, 2015). Due to the inherent nonlinearity of large waves, linear models for the wave kinematics are avoided and nowadays, second order and Stokes V theories are often employed. On considering regular waves, the advantage is that crest height is consistent with that of the design wave. However, the directionality, crossing seas and irregularity of the sea state, are neglected (Forristall, 2000; Bitner-Gregersen and Gramstad, 2015).

Lastly, some specific design aspects related to extreme waves are discussed. For the design of offshore structures, the problem becomes "bad-behaved" when there is wave slamming on the deck, which is not designed to withstand such horizontal pulse loads. Slamming can be catastrophic, leading to the collapse of the structure. For this reason, an "air-gap" should always be maintained between the highest expected crest and the deck (Haver, 2000; Swan and Sheikh, 2015)[17]. At least partially, the required air-gap can be estimated by including high order harmonics in the wave profile (Adcock, 2017). Similarly, extreme wave crests should be accounted for the design of other structures, so that their sensitive members, e.g., blades of offshore wind turbines and upper decks

[17] Increasing the air-gap results in considerable cost of the initial investment. Thus, accurate estimation and modelling of the extreme waves is crucial for balancing risk Vs safety (Christou and Ewans, 2014).

of ships, are not exposed to direct wave impact (Adcock and Taylor, 2014). As mentioned, the flow around cylinders is complex, resulting in runup, secondary load cycles and scattered waves (Chaplin et al., 1997), which are relevant for monopile foundations of offshore structures. The runup can reach higher elevations than the wave crest and can impact the underdeck of an oil platform or the inspection platform of wind turbines (Bredmose and Jacobsen, 2011). An issue with the runup can also be the high velocities, which result in additional loading (Swan and Sheikh, 2015). Something which was examined only recently is the impact on the underdeck away from the monopile by an extreme crest that can be created by the interaction of incident and scattered waves from the structure (Swan and Sheikh, 2015). Similar issues arise when examining complex, but more realistic, support structures consisting of more than one monopiles whose interaction with waves causes wave trapping effects (Bai et al., 2014). Other phenomena of important role for the survivability of structures are the "springing" and "ringing" effects, referring to linear resonance response and to nonlinear burst-like dynamic response due to resonance, respectively (Chaplin et al., 1997). Conventional monopiles have higher eigen-frequency than the main wave spectrum[18]. However, the higher harmonic structure of extreme waves may increase the bandwidth of the spectrum and match the eigen-frequency of the structure (Fitzgerald et al., 2012). Ringing can be catastrophic due to the potentially strong excitation of the structure, but also because of the fatigue that eventually induces (Paulsen et al., 2014a). It should be noted that most computational tools at present consider rigid structures and thus, the structural deflection due to ringing is not properly accounted (Bredmose et al., 2013). Apart from the offshore industry, extreme waves can cause excessive runup and overtopping at coastal structures, which can cause a civil threat due to flooding (Orszaghova et al., 2014; Whittaker et al., 2016, 2017).

At present, extreme waves are not included neither in the design process, nor in the certifications (Bitner-Gregersen and Gramstad, 2015). Nevertheless, this should be

[18]Nevertheless, the tendency of increasing the size of offshore wind turbines can lead to structures with lower natural frequencies (Bredmose et al., 2016), which can resonate to frequencies close to the f_p.

revised soon, because climate change is expected to increase the frequency and intensity of extremes. Moreover, the predicted sea level rise will put the coastal structures at higher risk (Whittaker et al., 2017) and effectively decrease the air-gap of offshore platforms. From an operational point of view, the ultimate goal, especially for the shipping industry, would be to create an efficient warning system for extreme waves as a part of weather forecasting services (Bitner-Gregersen and Gramstad, 2015).

2.4 The NewWave theory and focusing methodologies

2.4.1 Introduction to the NewWave theory

As discussed in Section 2.3, extreme waves may appear randomly in a sea state, but pose a threat to the survivability of marine structures. As such, they should be taken into account in the design process. The obvious issue is to overcome the randomness of the ocean surface and to find a representative wave form that appropriately describes the crest height and shape of extreme waves. Regular waves with appropriately selected characteristics are commonly used in the design practice (see Section 2.3.5), but this approach induces discrepancies for surface dynamics and kinematics when compared with realistic random simulations (Tromans et al., 1991). Nonlinear Monte Carlo simulations may seem as an alternative, however the computational cost is considerable. These considerations set the rationale that led Tromans et al. (1991) to suggest a new deterministic model to describe the largest waves in the sea: the NewWave theory. Thanks to its convenience, needing a single simulation for the expected largest wave, NewWave has been extensively used in physical and numerical modelling as a method to examine the representative extreme wave (Stagonas et al., 2014). At present, NewWave is the state of the art for deterministic simulations of extreme waves and its applicability keeps expanding to regimes and problems that was not initially formulated for, as discussed in this section.

The form of the NewWave theory used nowadays is based on the formulation of Tro-

mans et al. (1991), but the mathematical principle had been given two decades earlier. First, Lindgren (1970) used the Slepian model for representing stochastically a random Gaussian surface and suggested that the average shape of a large wave can be approximated by the scaled covariance function of the wave field. Later, Boccotti (Boccotti, 1982, 1983) applied the asymptotic form of Lindgren (1970) to individual large waves in a random sea state, demonstrating that the average shape of the largest wind-generated waves in the ocean can be expressed by the scaled autocorrelation function of the underlying random process. Probably the most important outcome of Boccotti's work is the connection between the local properties of large waves and the global properties of the sea state (Gibbs and Taylor, 2005). Independently of Lindgren's work, Phillips et al. (1993) extended the work of Boccotti to include both temporal and spatial wave profile (Tucker, 1999). Lindgren's theory remained practically unused for 20 years (Tucker, 1999), but finally, Tromans et al. (1991) introduced this principle to offshore engineering problems, which became known as the NewWave theory (Taylor and Swan, 2000). Since then, the literature on the topic of the origins and applications of NewWave keeps growing (Johannessen and Swan, 2001; Adcock and Draper, 2015), including verification with field data (Taylor and Williams, 2004; Jonathan and Taylor, 1997) and numerical simulations (Tucker, 1999), as also done in the present work.

In mathematical terms, the average shape of the random ocean surface is $\eta(\tau) = \alpha\rho(\tau) + g(\tau)$, where α is the crest elevation, ρ the autocorrelation function of the ocean surface elevation, τ the time lapse of the crest occurrence at t_o and $g(\tau)$ a parameter for a non-stationary Gaussian process ρ proportional to the Fourier transform of the surface energy spectrum. Thus, by definition $\eta(\tau)$ is a linear process without bandwidth approximations (Tromans et al., 1991). $g(\tau)$ has zero mean and standard deviation at some distance away from the crest, being independent of α, but with increasing α, the term $\alpha\rho(\tau)$ becomes dominant and $\eta(\tau) \approx \alpha\rho(\tau)$. Therefore, for the largest waves, the process converges to a Gaussian one and the NewWave theory for a given energy density spectrum $S(\omega)$ is expressed by Equation 2.9 for the wave components i of the

spectrum.

$$\eta(x,t) = A\frac{\sum_{i=1}^{N} S(\omega_i)\cos(kx-\omega_i t)}{\sum_{i=1}^{N} S(\omega_i)} \tag{2.9}$$

where A is the scaling factor, which equals the sum of the amplitudes of the wave components of the spectrum.

The convenience of NewWave becomes now apparent, since the average shape of an extreme wave in a considered sea state can be directly obtained by Equation 2.9. The kinematics can be calculated in a similar way (Tromans et al., 1991; Tucker, 1999). However, it is underlined that NewWave is a probabilistic theory, which is based on linear, Gaussian assumptions (homogeneity), and it was initially tested for unidirectional sea states in deep water (Tromans et al., 1991). Thus, for long-duration storms, the stationary assumption of the Gaussian process may not be valid, nor the linear assumption, if the steepness of the sea is high (Whittaker et al., 2016). Despite these assumptions for its derivation, the recent examination of field wave measurements from intermediate/shallow water by Whittaker et al. (2016) demonstrated the applicability NewWave beyond deep water and even for non-Gaussian distributions of waves in coastal areas. Similarly, the present study also contributes to the validation of NewWave for intermediate water depth (Vyzikas et al., 2018b). However, it is worth noting again that NewWave is valid for the largest crests (Tucker, 1999) and variability of the wave profile with increasing distance from the peak of the timeseries can be observed (Adcock and Taylor, 2014), which is also to an extent demonstrated in the present work through the comparison between the theoretical (NewWave) and extracted evolved linear harmonics in Chapter 5.

In practice, the autocorrelation function of NewWave takes the form of a crest focused wave (zero phases) (Christou and Ewans, 2014), which is extensively used for deterministic physical and numerical modelling (Vyzikas et al., 2013; Whittaker et al., 2016), resembling also well the transient character of large waves in the ocean that have local

high energy concentration (Gibbs and Taylor, 2005). As already observed in the original study (Tromans et al., 1991), NewWave provides more accurate kinematics than Stokes V theory and it was recently shown to be valid until the point of wave breaking (Adcock and Taylor, 2014; Buldakov et al., 2017). NewWave was also used to approximate the famous Draupner wave (Walker et al., 2004; Taylor et al., 2006), and other extreme waves measured in the field, achieving impressive agreements (Fedele et al., 2016; Benetazzo et al., 2017). The expansion of NewWave in directional seas was examined by Arena et al. (2008) and was applied later in other studies (Adcock and Draper, 2015). An advantage of the envelope shape of NewWave is that its phasing can be used to study variations of the shape of extreme waves and the corresponded resulted loading (Adcock and Draper, 2015), which is elaborated in the appendix of Vyzikas et al. (2018b) and applied to measure the maximum possible runup on a beach (Whittaker et al., 2017) and overtopping (Orszaghova et al., 2014).

Overall, the NewWave theory is a valuable and practical tool for ocean and coastal engineering applications. Differences between the average shape of extreme waves and the NewWave profile do exist, but they are not considered important in terms of the design process (Tucker, 1999).

2.4.2 Practical advantages of NewWave

The simplicity of the NewWave theory is certainly a good reason to use it for engineering applications, but there are also other important practical advantages that made NewWave popular in the research community. As mentioned, probably the greatest achievement of NewWave is that it connects the parameters of a random sea state with the local deterministic characteristics of the largest expected waves (Taylor and Swan, 2000).

From a modelling point of view, the localized character of a NewWave group in space and time, creating a compact wave packet, has several advantages. In laboratories, where the physical dimensions of the tanks are limited, the NewWave theory helps

creating the desired wave event at the location of interest (Stagonas et al., 2018), while minimizing spurious effects, such as reflections that can substantially change the results (Forristall, 2002; Whittaker et al., 2016). In random sea simulations, spurious effects are harder to spot, considerably more difficult to remove and they may build up over time (e.g., sloshing) (Paulsen et al., 2013b; Orszaghova et al., 2014). This also favours the use of focused wave groups to check the quality and repeatability of the produced experimental results as well as for calibration purposes (Latheef and Swan, 2013). Moreover, especially in physical experiments, there are limitations at the number of locations that measurements can be taken, which may result in missing extreme events in random seas that appear spontaneously in space and time. To mitigate this with random simulations, a large number of simulations should be performed for sufficiently long duration (Walker et al., 2004; Ning et al., 2009b; Stagonas et al., 2014; Whittaker et al., 2017). The latter raises again the problem of spurious effects, while the former is subject to the availability and the cost of the facilities. In numerical modelling, the major issue, especially for sophisticated solvers such as CFD, is the computational cost (Taylor and Swan, 2000; Bredmose and Jacobsen, 2010). Even on modern HPCs, random sea simulations may require weeks or months for a CFD solver, which makes it prohibitive to perform a large number of simulations. On the other hand NewWave has the advantage of requiring only a single simulation of relatively short duration.

In physical terms, compared to conventional engineering practice, NewWave overcomes the suboptimal representation of the kinematics of regular wave theories, and consequently the induced structural loads, offering a more realistic representation of extreme wave loading (Bredmose and Jacobsen, 2010; Chen et al., 2014). This is in particular relevant for the burst excitation due to ringing, where the continuously propagating regular waves hinder the realistic response of the structure compared to an isolated event (Chaplin et al., 1997). Furthermore, being a deterministic event, NewWave allows for better control of the phases, which in practice means that extreme waves of different phase shifts can be generated to study the response of the structure towards the definition of its design wave (Whittaker et al., 2017; Vyzikas et al., 2018b)

and to apply harmonics separations methods (Chen et al., 2014) to investigate the influence of individual harmonics. Moreover, instead of representing extreme waves in isolation, NewWave-type groups can be embedded in irregular sea states in order to obtain more realistic conditions with other background processes (Whittaker et al., 2016; Hunt, 2003).

Overall, the use of NewWave groups for the study of extreme waves offers a simple, inexpensive, quick alternative compared to random simulations with better control of the whole modelling process (Orszaghova et al., 2014; Chen et al., 2014). NewWave is broadly used and good experience has been built (Orszaghova et al., 2014) and the ground to overcome its shortcomings has been prepared.

2.4.3 Beyond the NewWave

As discussed in Section 2.4.1, the NewWave theory assumes linearity and homogeneity (Gaussianity) of the wave field. However, especially energetic sea states, where extreme waves are more likely to occur, are better described by second order models that include bound waves (see Section 2.3.4). This initial shortcoming, however, offers the basis to improve NewWave by adding bound nonlinearities, because the linear dynamics of the NewWave still hold and bound waves can be calculated using the known free-wave regime (Taylor and Swan, 2000). The extension of NewWave to second order was suggested by Arena and Fedele (2005) with analytical expressions and Monte Carlo simulations for confirming the statistics of the problem. Arena and Fedele (2005) also included the kinematics and the directionality in their study of NewWave groups. Vyzikas et al. (2018b) also examined NewWave groups, including the element of the evolution of the free-wave spectrum, which, as observed earlier by Johannessen and Swan (2003), can alter considerably the wave profile.

Higher than second order bound nonlinearities may be present in extreme waves, such as the Draupner wave, where a bound wave structure of up to fifth order was identified (Walker et al., 2004). Similar observations are made in the present work for the nearly

breaking wave group (see Section 3.3.5). The high order bound wave structure was confirmed in recent spatio-temporal analysis of field data, with the second order bound waves being dominant (Benetazzo et al., 2017). That study demonstrated remarkable agreement between the normalized profile of the measured extreme waves and the NewWave profile, enhanced by bound nonlinearities, irrespectively of the specific characteristics of the wave spectrum, even when that was bi-modal. As such, Benetazzo et al. (2017) provided sound evidence that realistic extreme waves have the universal characteristics of the NewWave theory and can be modelled as focused waves with bound harmonics. To do this, it is vital to know the free-wave spectrum, which is not trivial to extract from field records (Jonathan and Taylor, 1997; Walker et al., 2004; Whittaker et al., 2016).

The present work aims to go beyond the linear NewWave theory by suggesting a method to account for both the resonant and bound nonlinearities and provide a more accurate representation of extreme waves. To achieve that, the free waves are calculated using an advanced method for the separation of harmonics and the GKE, while the bound harmonics are computed using a range of analytical methods.

2.4.4 Focusing methodologies

In practice, the NewWave theory takes the form of a focused wave group. Focusing occurs due to the dispersive nature of waves. Thus, if the phases of the wave components are appropriately chosen at the wave inlet, with short waves being generated before the longer ones, constructive interference of the components of the group can be achieved at the desired focal location (crest focused wave). However, when waves propagate in nonlinear media, their dispersive properties may change. Focusing methodologies are techniques developed to cancel the nonlinear effects that cause downshifts to the focusing location with subsequent discrepancies in the modelling of NewWave-type groups, see e.g., Westphalen et al. (2008); Ning et al. (2009b); Zhao et al. (2009). Commonly, these methodologies refer to iterative corrections of the dis-

persive characteristics of the wave group. A brief historical outline of the development of these techniques is discussed here and interesting reviews of focusing methods can be found in the works of Sun et al. (2008), Fernández et al. (2014), Alford and Maki (2015) and Deng et al. (2016).

The backbone of most focusing methods is linear theory, which is used for the backward propagation of the waves from the focal location to the wave inlet as part of the iteration process or at least as an initial guess of the phases before the first correction. From the early '90s to present, many different techniques have been developed to correct the phases or the phases and amplitudes of the wave components of the spectrum, or the entire signal at once. In relevant reviews, focusing methods are commonly presented chronologically, but here they are grouped in categories according to their operating principle.

No correction: In some cases, the application of a focusing methodology is either infeasible or not necessary. When examining directionally focused waves, the initial phases at the wave inlet can be determined by backward propagation from the focal point using linear or second order theory (Johannessen and Swan, 2001, 2003; Gibbs and Taylor, 2005; Gibson and Swan, 2007; Adcock and Taylor, 2016a). However, it is not trivial to determine the wavenumber vectors and correct the signal from point measurements in the tank. In such cases, if the observed maximum crest is at a different location and time, due to nonlinear interactions, a crude remedy is the re-definition of the focal location or the time-shifting of the timeseries. Another reason not to correct the signal is because this is taken from a record in the experiment, where it was already corrected using a focusing method (Vyzikas et al., 2013). Discrepancies may be observed in this case, most likely due to the different specific characteristics of the wavemaker. Correction may not be necessary also when the signal is initiated very far from the focal location. In this case, the initial linear or second order boundary conditions at the wavemaker are assumed to be valid, since the wave group is well dispersed and no steep waves are included (Johannessen and Swan, 2003; Katsardi and Swan,

2011). However, such an approach may not be feasible for experimental facilities with limited physical dimensions or different dynamics can occur, e.g., BF instabilities or resonant Hasselmann scale effects, that may corrupt the focusing mechanism (Katsardi and Swan, 2011). It should be noted that a focusing methodology is not needed if the steepness of the wave group is too small to trigger nonlinear effects, but in this case one can hardly refer to the focused group as an extreme wave.

Trial and error: In many cases, instead of using an automated approach to correct the dispersive characteristics of the wave group, empirical corrections are applied until the produced timeseries approach the desired one. Such examples can be found in the work of Ning et al. (2009b); Ransley et al. (2013); Vyzikas et al. (2013); Hann et al. (2014) and Hu et al. (2014). Provided that the wave group is not very steep, these methods can be effective, but they also may end up being time consuming (Vyzikas et al., 2013). The use of second order wave generation in combination with a trial and error correction method can improve the results (Ning et al., 2008). Nevertheless, considerable discrepancies from the target focal location and time can occur, resulting in shifting of the results. Since trial and error methods do not have a solid mathematical description and are based on the experience of the modeller, they are considered less sophisticated than the methods that follow.

Linear theory: Linear theory is the best-established method used for iterative corrections. Its convenience lies on the simplicity and the consistency between the linear transport functions of most wave paddles. What distinguishes the different methodologies in this category is the part of the signal that is corrected. First, Rapp and Melville (1990) used linear theory to find the phases of the waves at the wave paddle. This method was also used by Baldock et al. (1996), who reported shortcomings due to nonlinearities and underlined the importance of eliminating any reflections at the examined location. Chaplin (1996) formulated the approach of Rapp and Melville (1990) into an iterative correction method for the wavemaker control signal. Chaplin's approach is the basis for most of the focusing methodologies used at present. Chaplin (1996) and

Chaplin et al. (1997) corrected the wavemaker's control signal by applying the exact opposite phase shift to each wave component obtained by FFT of the measured signal. The method was shown to improve the results, but still some discrepancies due to reflections and bound waves could not be removed. Despite that, the method could converge and help predicting with better accuracy the timing of the focusing event. It is noted, however, that the method was used on a narrowbanded spectrum, where the bound waves can be easily isolated. The next development was suggested by Schmittner et al. (2009), who extended the method of Chaplin by including iterative corrections to the amplitudes in the frequency domain in order to match both the amplitudes (α) and phases (ϕ) of the components to the target values. For the amplitude correction a scaling factor (s) was used to accelerate the convergence, as seen in Equation 2.10. This method was tested in different laboratory facilities with computer-controlled wave paddles to replicate the field measurements of the Draupner wave. Overall, the method could improve the accuracy of the generated wave record, but considerable discrepancies were observed at the highest crest. Schmittner et al. (2009) also showed that the correction methodology did not have to deal with the complex transport functions of the paddles and it did not depend on the selection of the initial phases. It was also noted that the amplitudes were found harder to correct.

$$\phi_{new} = \phi_{old} - 2(\phi_{trg} - \phi_{rec}) \quad \text{and} \quad \alpha_{new} = \alpha_{old} \cdot s \cdot \left(\frac{\alpha_{trg}}{\alpha_{rec}} \right) \tag{2.10}$$

where the subscripts new, old, rec, trg refer to the corrected, previous, recorded, target values, respectively.

A similar method for combined phase-amplitude corrections of the entire measured signal was used by Deng et al. (2016), who also observed discrepancies at the higher harmonics for steep wave groups.

In the present study, the focusing methodology of Stagonas et al. (2014) is used, which relies on a similar principle for correcting both the phases and amplitudes. However, as explained in Section 2.4.5, the novelty of the method is that it is applied only on the

free-wave spectrum extracted from the four-phase harmonic decomposition and thus, handles the generated nonlinearities in a more effective way. This idea was also applied by Ducrozet et al. (2016a), who, however, used only the two-phase decomposition method and could not effectively correct the high frequency wave components.

Nonlinear solvers: Nonlinear models can be used as a preliminary step in order to correct the input signal for physical experiments or other more expensive NWTs. For the first case, the so called self-correcting method (SCM), as revisited by Fernández et al. (2014), was suggested for adjusting both the amplitudes and phases of the wave components (see Equation 2.11) of the spectrum in a PFS model, before using the corrected signal in the physical tank. The method can be combined with second order generation if the steepness of the wave group is high. An advantage is that the complex transform function of the paddles are not accounted in the SCM, but the most important aspect is that the method can be applied in cases of uneven seabed topography, at the vicinity of the structures and at fully reflective walls as well as to model tsunamis. The phases were seen to play the most important role in the focusing process, while amplitudes were proven harder to be corrected effectively. As with every other method, the issue is the emerging nonlinearities that increase with the steepness of the wave group, which result in some observable discrepancies referring to the loss of symmetry at focus and to nonlinear shifts. Despite these deficiencies, this method interesting for testing focused waves in realistic bathymetries and near structures.

$$\phi_{new} = \phi_{old} \pm |\phi_{trg} - \phi_{rec}| \quad \text{and} \quad \alpha_{new} = \alpha_{old} \left(\frac{\alpha_{trg}}{\alpha_{rec}} \right) \tag{2.11}$$

For the second case, a promising method that uses a high order correction theory for the phases of the wave components was proposed by Alford and Maki (2015). Instead of using only linear theory to find the phases at the focal location, a pseudo-third-order phase shift is applied, essentially to account for the effects of resonant interactions. The method is called "pseudo", because it does not calculate the third order interactions, but instead it uses a third order dispersion relation. It should be

noted that this method does not require iterations, since the phase shift is calculated only once. The overall performance of this technique is satisfactory, but discrepancies can be observed when compared with fully nonlinear simulations as the steepness of the wave group increases.

As discussed, the objective of the focusing methodologies is the correction of the dispersive variables (amplitudes and phases) of the wave components. Theoretically, these can only be altered by resonant/near-resonant wave-wave interactions, and, in principle, bound waves are irrelevant in the process. However, most of the focusing methods do not make the distinction between the free and bound parts of the spectrum and correct it all together. Correcting bound waves based on the linear dispersion relation and including them in the wave generation (most of the times as free waves) inevitably leads to discrepancies. Thus, according to the author, correcting the full spectrum is the main deficiency of previous works, which is tackled here with the focusing methodology of Stagonas et al. (2014).

2.4.5 The new methodology for focusing waves

Application of the methodology

The methodology for focusing wave groups used in the present study was proposed by Stagonas et al. (2014) and applied in a number of studies by the developers and the author, such as in Vyzikas et al. (2014b) (first time in a numerical model), Vyzikas et al. (2015) (comparison between CFD and NLSWE), Buldakov et al. (2015) (Lagrangian solver including sheared currents), Buldakov et al. (2017) (breaking waves), Vyzikas et al. (2018b) (evolution of harmonics) and Stagonas et al. (2018) (breaking waves in CFD). Recently, it was compared with other focusing methods by independent researchers (Wang et al., 2017), showing the best performance.

The new methodology is an iterative correction process of the amplitudes and phases of the wave components of the spectrum until they match the desired target values. The

corrections of the amplitudes and phases can be performed at different locations depending on the scope of the study, allowing for examination of specific properties of the wave group, e.g., dispersion (Vyzikas et al., 2018b). The distinguishing characteristic of the new method is that the corrections of phases and amplitudes are performed only for the components of the extracted free-wave spectrum. To the best of the author's knowledge this is the first method to correct only the linearised harmonics. To achieve high accuracy in extracting the linearised harmonics, the focusing method is combined with a four-wave decomposition technique, which is elaborated later in Section 2.4.5.

The steps for applying the focusing method are:

(i) The target amplitude spectrum is defined and the desired locations for the amplitude and phase corrections, namely AM and PF, respectively, are determined. Moreover, the focal time is selected, usually as half of the repeat time of the periodic signal. The latter is determined by the frequency increment (df) between two consecutive wave components and should be selected small enough so that the produced periodic wave groups do not overlap.

(ii) Wave groups of different phase shifts are generated at the wave paddle. For a four-wave decomposition, four wave groups with phase shifts of 0, $\pi/2$, π and $3\pi/2$ are used to generate crest focused (CF), positive slope, trough focused (TF) and negative slope focused waves at the PF location, respectively. For the first run, the linear dispersion relation can be used to backwards propagate the signal from PF to the wavemaker, as a best guess. An example is given in Figure 2.10, where the contraction of the wave group towards focusing is also evident.

(iii) The linearised harmonic is extracted using a suitable linear combination of the four wave groups measured at PF, according to the four-wave decomposition (see Equation 2.13) in the frequency domain after performing FFT of the measured signals.

(iv) The phases and amplitudes of the wave components of the linearised harmonic

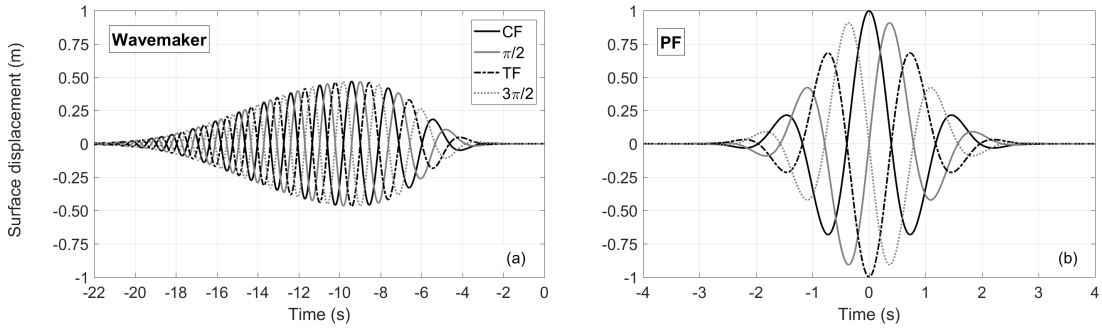

Figure 2.10: Timeseries of the normalized free surface elevation of four wave groups of different phases at the wavemaker (a) and at the PF location (b).

are corrected using Equation 2.12. It is noted that the correction of α and ϕ can be performed at different locations.

$$\alpha_{in}^{i+1} = \alpha_{in}^{i} \times \alpha_{trg}/\alpha_{out}^{i} \quad \text{and} \quad \phi_{in}^{i+1} = \phi_{in}^{i} - (\phi_{trg} - \phi_{out}^{i}) \tag{2.12}$$

where $\alpha_{in}, \alpha_{out}, \alpha_{tgt}$ are the input, measured and target amplitudes of the components of the spectrum respectively and $\phi_{in}, \phi_{out}, \phi_{tgt}$ are input, measured and target phases of the components respectively.

(v) The corrected signal for the wavemaker is calculated: the phases of wave components of the corrected linearised spectrum are found by propagating backwards the signal from PF to the wavemaker using the linear dispersion relation. The corrected amplitudes of the components are not altered according to linear theory, being the same at AM and the wavemaker.

(vi) The process is repeated iteratively from step ii to v until the target values for α and ϕ match the target values within the desired accuracy.

Advantages and shortcomings

The combination of correcting only the free-wave spectrum and the four-wave decomposition method for extracting accurately the free-wave harmonics give many comparative advantages to this focusing methodology. The use of the linear harmonic is considered a natural choice, since: a) the linear dispersion relation is used to propagate backwards the signal from PF to the wavemaker; b) in most cases the transfer functions of the wavemaker are linear and when second order generation is used (Stagonas et al., 2018), it is based on the free-wave spectrum; c) the nonlinear harmonics are uniquely defined by the free-wave spectrum. As mentioned, it is not consistent to use the full nonlinear spectrum to perform linearised corrections, which seems to be the main issue with other focusing methodologies. The correction of only the free-wave spectrum makes this methodology very accurate for focusing very steep waves up to their breaking limit, without showing decrease of the quality of focusing with increasing wave steepness, as almost all the other methods do. Moreover, the focusing event takes place at exactly the desired location and time and there is no need for manual time-shifting of the results or redefinition of the focusing location, as commonly done for other methods. Thanks to the accuracy of extracting the free-wave spectrum from the recording, this methodology can correct any type of spectra and it is not limited to narrowbanded spectra with unrealistic theoretical distributions, such as tophat or constant steepness (Fernández et al., 2014).

From a practical point of view, the focusing methodology is simple to apply, because it requires only one recording location, provided that the α and ϕ corrections are performed at the same location. Working experience with the methodology showed that it is always convergent, assuming that the linear harmonic remains the leading order. In most cases, only 2-5 corrections are needed to correct the signal. The methodology is applied independently in NWTs and physical flumes, preventing any deficiencies of one being inherited to the other. It can be seen as a self-calibration method for the wavemaker, which cancels any particularities of the wave generation, allowing

for obtaining very good agreement between different facilities and numerical models. Moreover, previous studies reported inability of reproducing the desired focused wave in long facilities, due to nonlinearities (Shemer et al., 2007). This is not an issue for the present methodology, which was also tested in the long flume of HR Wallingford and by the author for longer propagation distances in NWTs (unpublished work). Furthermore, issues related to the accuracy of focusing for decreasing mesh resolution were reported in other works (Bredmose and Jacobsen, 2011), however, the present method demonstrates good accuracy almost irrespectively of the grid resolution (see Figure 3.16). Overall, the methodology can correct efficiently and effectively almost any type of wave group. Additionally, because the signal is corrected to match a desired phase distribution and amplitude spectrum and not until symmetry or the highest crest is observed, the entire correction process can be fairly automated. Nevertheless, human experience can help avoid any pitfalls. For example a tricky part is to determine the most appropriate filtering between the first and fifth, as well as the second difference and fourth harmonics. Also, the sign of the correction of the phases should be in accordance with the sign used in the transport functions of the wavemaker.

From an engineering point of view, since the signal can be corrected to match any phase coherence between the waves components, wave packets of different shapes can be produced in order to determine the design wave for a particular application or structure. Moreover, the methodology was shown to produce the third order harmonics between the physical and numerical results with great accuracy, significantly superior to other techniques, see e.g., (Chen et al., 2014). This is crucial for studying the ringing phenomenon, which is of great concern for the survivability and life expectancy of offshore structures. The new methodology can also be effective for realistic ocean conditions that combine inline or opposing, sheared or ambient currents and waves (Stagonas et al., 2014; Buldakov et al., 2015).

On the downside, there are some limitations for the application of the new methodology. Similar to many other methods, it cannot be applied after the breaking of the wave

group, because the spectrum starts disintegrating. However, it can be used to the onset of breaking without any issues (Buldakov et al., 2017). Furthermore, the method cannot be used if reflections contaminate the wave signal at the focusing location. This is because reflections are freely propagating waves at the frequency range of the original free waves and thus included in the correction, but since they have opposite phases from the incident wave group, they can make the correction diverge[19]. Last but not least, to achieve accurate extraction of the free-wave spectrum, four simulations of groups of different phases are required per correction step. This can make the computational cost of the method a prohibitive factor for its application in large CFD domains. It should be noted, however, that for unidirectional waves the iterations can be performed in a two-dimensional domain and only the final solution should be applied in the three-dimensional domain. Moreover, once the wave group is focused, there is no need for additional iterations to generate groups of different phasing, since they can be readily produced by applying the desired phase shift (Vyzikas et al., 2018b).

Despite presenting various methodologies for focusing waves, an aspect that was not discussed until now is the essence of focusing. In the literature, the focusing criteria are not always the same between different studies. In many cases, the wave group is considered focused when it reaches its maximum crest elevation (Baldock et al., 1996; Ning et al., 2009b; Zhao et al., 2010; Adcock and Taylor, 2016a). In other cases, the focusing is evaluated based on the symmetry of the timeseries of the wave group around the main crest, i.e., the lateral troughs (Orszaghova et al., 2014). Another way to evaluate the focusing is by comparing the result visually (Schmittner et al., 2009) or with correlation coefficients (Fernández et al., 2014) with the target surface elevation. Another criterion, mostly associated with the energy concentration, refers to the contraction of the timeseries (Whittaker et al., 2017; Ning et al., 2009b), because the more compact the wave group is, the higher the energy concentration. The present focusing methodology, however, uses a more objective criterion to assess the focusing:

[19]Theoretically, one could apply a reflection analysis method to find only the incident signal, but due to the high nonlinearity of the problem near the focal point, such methods which rely on linear theory are not expected to be effective.

the group is considered focused when the desired phase coherence between the free wave components is achieved. This way not only the bias in assessing the focusing is reduced, but it also relates focusing to the physical mechanism of generating extreme waves, namely the zero phases between the components (for CF groups). Moreover, it can easily be expanded to study different phase shifts of the wave group. It should be noted that some of the aforementioned criteria to assess the focusing may coincide or depend on one another. For example, when a CF group is considered focused according to the present methodology, the phases of its underlying free-wave spectrum are zero. This leads to symmetry of the timeseries of the linear harmonics and subsequently symmetry of the nonlinear bound harmonics, and eventually, symmetry of the entire wave group.

Phase decomposition

A crucial part for the success of the focusing methodology is the accurate extraction of the linear harmonics. This is achieved by means of the four-wave decomposition method, which is here discussed in greater detail and compared with possible alternatives.

The phase or harmonic decomposition/separation methods used in ocean and coastal engineering are based on the principle that the free surface elevation can be expressed by a Stokes expansion (see Equation 5.9). This is a power series expansion and it assumes that each high order harmonic can be found from the envelope of the linear harmonics, by raising the latter to the corresponding order (Chen et al., 2014). A number of wave groups is simulated and their appropriate algebraic combination returns the harmonics of the signal[20]. Generally speaking, a larger number of wave groups with different phases shifts guarantees greater accuracy in the extraction of harmonics, with smaller need for frequency filtering.

[20]There exist other methods for separating the harmonic structure of wave groups, using for example cameras and the Morlet transform (Li and Ting, 2012).

The most widely used harmonic separation method is the two-phase decomposition, which requires a CF and a TF wave group to separate the signal in odd and even harmonics. The TF can be simply created by adding a phase shift of π at the CF group, or equivalently, by changing the sign of the wave equation. Odd harmonics contain the linear, third order and fifth order harmonics, while even harmonics contain the second sum, fourth and sixth order harmonics. The issue is that the linear harmonics can only be isolated by frequency filtering. This is only accurate for narrowbanded spectra, where the linear and third order harmonics do not overlap. However, this is rarely the case for realistic broadbanded spectra or for steep wave groups, whose free-wave spectrum may broaden considerably during focusing. As such, discrepancies due to this limitation are common. The two-wave decomposition has been used among others by Johannessen and Swan (2001); Ning et al. (2009a); Johannessen (2010); Chen et al. (2014).

By adding another two shifts of $\pi/2$ to the two-wave decomposition method, the set of the four wave groups for the four-wave decomposition method is obtained. The advantage of this method is that it separates mathematically the first and the third order harmonics. The former is only perturbed by fifth order terms, but in this case the filtering is more straight-forward. Moreover, the contribution of the fifth order harmonics is order of magnitudes smaller than that of the linear and the third order harmonics. In practice, this allows for accurate extraction of the free-wave spectrum even for broadbanded spectra. The third order harmonics are also perturbed by fifth order harmonics, but this is irrelevant for the application of the focusing methodology. The second order super-harmonics can be readily extracted, while the second order sub-harmonics require filtering, as seen later. The four-wave decomposition method was first suggested by Fitzgerald et al. (2012) and further elaborated in Fitzgerald et al. (2014) for forces on cylinders, in order to observe potential ringing effects. The method was extended to wave records by Stagonas et al. (2014), following the same principle. A similar method was used earlier by Siddorn (2012) to study wave-structure interaction problems and later by Zhao et al. (2017) and Mai et al. (2016). However, in these works it was

not combined with a focusing methodology and discrepancies were observed. It is noted that the usefulness of harmonic decomposition methods is not limited to focusing methodologies, but it can be proven valuable in understanding physical properties and structural responses related to specific harmonics.

The formulae for the four-wave decomposition are given in Equations 2.13 (Fitzgerald et al., 2014)[21]:

$$\text{Linear:} \qquad Af_{11}\cos\phi + A^3 f_{31}\cos\phi + O(A^5) = \frac{1}{4}\left(S_0 - S^H_{\pi/2} - S_\pi + S^H_{3\pi/2}\right) \tag{2.13a}$$

$$2^{nd}\text{ sum:} \qquad A^2 f_{22}\cos 2\phi + A^4 f_{42}\cos 2\phi + O(A^6) = \frac{1}{4}\left(S_0 - S_{\pi/2} + S_\pi - S_{3\pi/2}\right) \tag{2.13b}$$

$$\text{Third:} \qquad Af_{33}\cos 3\phi + O(A^5) = \frac{1}{4}\left(S_0 + S^H_{\pi/2} - S_\pi - S^H_{3\pi/2}\right) \tag{2.13c}$$

$$2^{nd}\text{ diff} + 4^{th}\text{:} \qquad A^2 f_{20} + A^4 f_{44}\cos 4\phi + O(A^6) = \frac{1}{4}\left(S_0 + S_{\pi/2} + S_\pi + S_{3\pi/2}\right) \tag{2.13d}$$

where f_{ij} are the coefficients in Fourier series, A the amplitude of the envelope and $S_{n\pi/2}$, $n = 0,1,2,3$ the timeseries of the surface elevation at the location of interest. The superscript H refers to the imaginary part of the conjugate of the Hilbert transform of the corresponding timeseries of the surface elevation.

As seen, the first, second and forth harmonics are perturbed by additional terms. The relative importance of the term f_{31} is small compared to the term f_{11}, because, despite of having the same frequency dependence, its amplitude dependence is at high order and thus much smaller. Similar is the case for the terms f_{42} and f_{22}. In general, this holds for all the difference terms f_{ij}, $i \neq j$, instead of the 2^{nd} difference terms f_{20}, which are important and they should be separated by frequency filtering from the 4^{th} order terms (f_{44}) (Fitzgerald et al., 2012). This is usually trivial to perform, because

[21] One should be alerted for potential misprints, in e.g., Mai et al. (2016), that can have significant effects on the results and lead to misinterpretations.

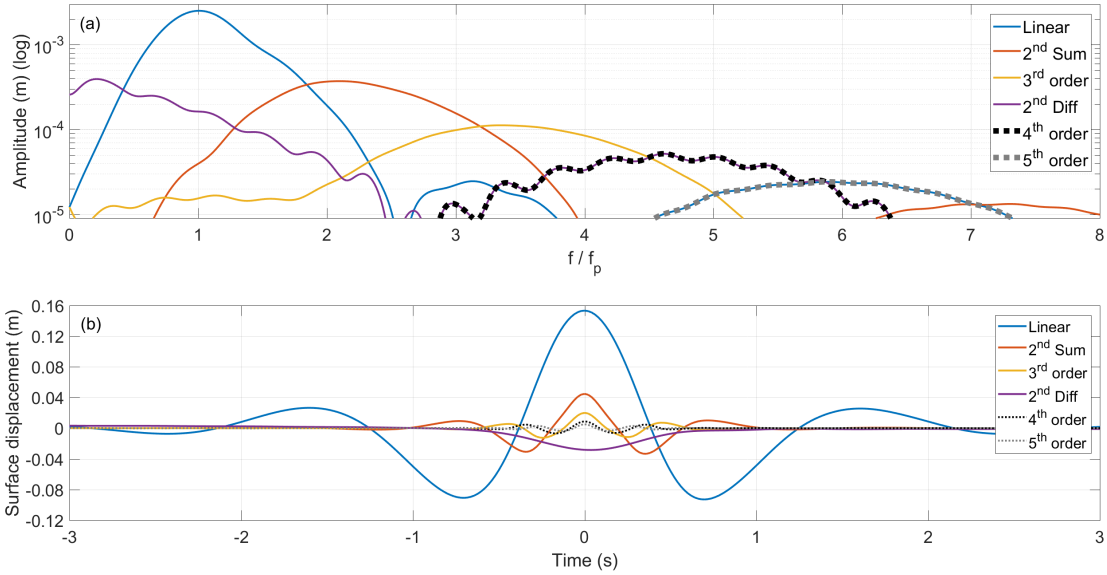

Figure 2.11: (a) Frequency bands for the selection of the harmonics after the four-wave decomposition and (b) timeseries of the harmonics using IFFT of the corresponding spectra.

they occupy distinctively different frequency bands. An example of the frequency filtering applied in the present study is shown in Figure 2.11a, where it is demonstrated how the 5^{th} and 4^{th} order harmonics are separated from the linear and 2^{nd} difference, respectively. The resulted timeseries at the focal location are also included in Figure 2.11b.

A more accurate separation of harmonics can be achieved by the twelve-wave decomposition of Hann et al. (2014), who considered phase shifts of an increment of $\pi/6$. This method practically eliminates the need for filtering for the separation of harmonics: the fourth order harmonics are readily separated from the second difference harmonics and the fifth order harmonics are calculated separately. The linear harmonics can be found by two different expressions, which serves as a verification of consistency. Nevertheless, for the wave group examined by Hann et al. (2014), the performance of the twelve-wave decomposition was similar to the four-wave decomposition for the surface elevation. Therefore, the twelve-wave decomposition seems that it will not increase the accuracy of the focusing methodology. However, the simulation of 8 additional

groups at every iteration step requires considerably more resources. Thus, respecting the "principle of proportionality" the four-wave decomposition is more appropriate for the present scope, offering improved accuracy for broadbanded spectra compared to two-wave decomposition at a minimum additional expense of resources.

Before closing the Chapter, it should be noted that the new focusing methodology as well as any analysis of focused waves in the frequency domain is performed by means of FFT. However, there are other available methods, such as the wavelet transform or the Stockwell transform (Gibson and Swan, 2007), which can be used to express the temporal spectral characteristics. In brief, the wavelet transform can offer interesting insights to the evolution of the energy spectrum over time, being able to describe the rapid wave-wave interactions and indicate ringing effects (Paulsen et al., 2013b). The wavelet transform is based on a "mother" function, which for the case of ocean waves takes the form of the Morlet function as the most appropriate (Zhao et al., 2009). Many features of the wavelet transform can be controlled by the selections of various parameters. The advantages of the wavelet transform are that it offers information about the dispersive properties of the group and it can be applied in non-periodic and non-stationary wave fields (Lin and Liu, 2004). All these are not possible with the FFT, but they come at the cost of the low resolution at the frequency domain and potential discrepancies. Overall, wavelet is a promising analysis method, but it appears to be heavily parameterized and to result in low frequency resolution, which makes it prohibitive for the present focusing methodology. Nevertheless, it could be used to examine the dispersion of wave groups during extreme wave formation. This was done by Ewans and Buchner (2008); Lin and Liu (2004), who showed that extreme waves appear to have a spectral signature, but later, the analysis of field records of Christou and Ewans (2011b) did not confirm any unique pattern.

Chapter 3

Validation of the models

THIS Chapter constitutes one of the two core elements of the present work. Here, the numerical models that are used to examine the physical processes of spectral changes due to wave-wave interactions are validated against experimental results and their strengths and weaknesses are highlighted. Through the validation of the models, the improvements achieved in the present study by using an accurate focusing methodology are also demonstrated. A qualitative comparison for HOS-ocean for the spectral evolution via Monte Carlo-type simulations is also performed.

3.1 The phase-resolving models

3.1.1 Characteristics of the models

On selecting the numerical models for simulating a physical phenomenon, the underlying physical process should be analysed and the modeller should examine whether the available numerical tools can reproduce them.

The present study concerns the spectral evolution during the propagation of very steep non-breaking unidirectional wave groups. Since, waves is a sub-category of free surface flows, the models should be able to treat the free surface with an appropriate algo-

Table 3.1: Physical processes simulated for focused waves per numerical model.

	Required	OpenFOAM	SWASH	HOS-NWT
Free surface modelling	✓	VoF	Grid stretching	as boundary cond.
Wave generation B.C.	✓	Linear superposition	Linear superposition	Linear; 2^{nd}; 3^{rd} order superp.
Wave absorption B.C.	✓	Active & passive	Passive	Passive
Finite depth	✓	Yes	Yes	Yes
Wave dispersion	✓	Yes	Yes	Yes
Resonant interactions	✓	Yes	Yes	Yes
Bound interactions	✓	Yes	Yes	Yes
Breaking waves	×	Yes	Bore-like	No
Directionality	×	Inefficient	Appropriate	Appropriate
Air modelling	×	Yes	Momentum transfer	No
FSI modelling	×	Yes	Weak	No
Turbulence	×	RANS, LES, DNS	Parameterized	No
Time scales (T_p)	10	1-10	1-100	1-1000
Spatial scales (L_p)	5	1-10	1-100	1-500
Computational cost	Low	Very high	Low	Very low

rithm. To produce and absorb waves, the models should include appropriate conditions for introducing an oscillatory flow in the domain and being able to control reflections, respectively. To replicate the nonlinear evolution of the wave field, the models should compute implicitly, via the governing equations of the flow, or explicitly, via analytical methods, the nonlinear resonant and bound wave-wave interactions. The wave groups examined here include wave components at any water depth regime, mainly intermediate water, and propagate for approximately 5 wavelengths. Thus, appropriate scales should be considered.

The essential characteristics that models should have for the present problem are listed in Table 3.1 and are marked with ✓. As seen, all the three models of the present study, namely OpenFOAM, SWASH and HOS-NWT, are appropriate for simulating the examined focused waves. If the scope of the present work was narrowed down to only non-breaking waves that do not interact with structures, then HOS-NWT would appear as the best option, thanks to its computational efficiency. Nevertheless, the present work aims to validate also operational coastal and ocean engineering models, e.g., SWASH, and CFD models, such as OpenFOAM, that can simulate accurately violent fluid-structure interaction (FSI) and wave breaking for realistic engineering applications. By achieving this, the ground for future research is prepared.

Table 3.2: Experimental conditions used for the validation of the phase-resolving NWTs (Vyzikas et al., 2013, 2014b, 2015, 2018b).

	Preliminary work	Initial validation	Dispersion study
Amplitude spectrum	JONSWAP-like	Pierson-Moskowitz	Gaussian
Peak frequency (f_p)	0.34 Hz	0.60 Hz	0.64 Hz
Depth (d)	2.5 m	0.5 m	1.0 m
Focal location	9.3 m	7.8 m	14.1 m
Measured crest elev. (η_c)	0.205 m	0.115 m	0.218 m
Facilities	COAST Lab	UCL	UCL
Focusing method	trial & error	Stagonas et al. (2014)	Stagonas et al. (2014)
Models tested	OpenFOAM	OpenFOAM; SWASH	OpenFOAM; SWASH; HOS-NWT

The three numerical models are presented in detail in the Appendix A and a more general table for their suitability is included (Table A.1). It is noted that the capabilities and computational efficiency of the models continuously improve and the reader should always consult the latest advances.

3.1.2 Experimental conditions for validation

The existing literature for the validation of OpenFOAM, SWASH and HOS-NWT with steep focused waves is either very limited, or it does not include an accurate focusing methodology and advanced techniques for analysing the results. Therefore, it was decided to use new experimental results and achieve accurate and consistent comparisons, aiming at performing a benchmark study.

The three main experimental campaigns used in the present work are summarized in Table 3.2. The most relevant characteristics of the wave groups are listed, including also the methods used for the analysis of the results. The studies of "Preliminary work", "Initial validation" and "Dispersion study" are presented in separate sections in this Chapter. The largest and most detailed part of the validation is devoted to the "Dispersion study", which was the most appropriate for examining the spectral evolution.

It can be seen from Table 3.2 that a wide range of conditions was tested at different facilities. Future work can further expand these conditions, for instance to deeper water and longer propagation.

3.2 Preliminary work for validation

3.2.1 Initial validation of OpenFOAM for extreme waves

The validation of the numerical models for the propagation of extreme waves started with the simulation of an extreme wave recorded at the Wave Hub site, replicated in the Ocean Basin of COAST Laboratory of the University of Plymouth and simulated in OpenFOAM using waves2foam (Jacobsen et al., 2012), the details of which are described in (Vyzikas et al., 2013). This part of the work led to the identification of the issues regarding the spectral evolution in the numerical models, which is the main subject of this Thesis, the employed approaches are similar to what has been used later and set the basis for the more sophisticated validation described in Section 3.3. For all studies in the present work, for consistency reasons, the version of the software was OpenFOAM 2.1.x, which was the newest at the time (2013) and any future versions that followed had improvements that were not relevant to the examination of the propagation of waves by the means that are used in this work.

Using the wave record from an Oceanor Seawatch II Buoy deployed in the area of the Wave Hub site (50.205380N,-5.363430E), an extreme event of $H = 9.57$ m occurred on 15/8/2012 was identified and replicated experimentally at $1:20$ scale in the Ocean Basin, where the wave depth was set at 2.5 m. After demonstrating that a long random-phase simulation could not capture the extreme wave in the experiment, the deterministic approach of the NewWave theory (Tromans et al., 1991) was used in order to generate a focused wave. As discussed in Section 2.4.4, due to the effect of the nonlinearities, the focal location was shifted and an empirical method for adjusting the phases of the wave components was used, similar to that of Ransley et al. (2013) that was first coined by Chaplin (1996). The success of the focusing was assessed by observing the highest crest between two symmetrical troughs.

The free surface displacement was recorded by five resistive wave gauges (WGs): one located close to the wave paddles, giving the input signal for the numerical inlet (N.I.),

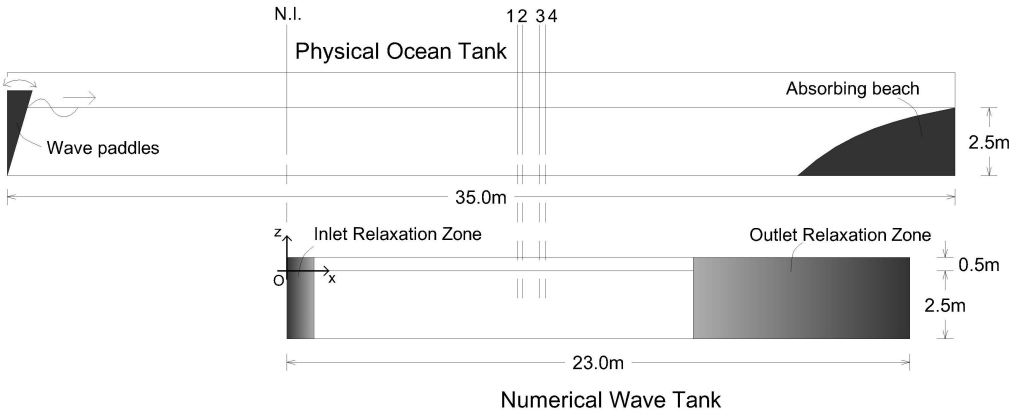

Figure 3.1: Experimental and numerical domain used for the replication of extreme wave at the Wave Hub site (Vyzikas et al., 2013).

and four close to the focal point, as seen in Figure 3.1. The focal location was WG3, located at 9.3 m downstream of N.I., and the focal time was 90.4 s. This way, the NWT was designed to be shorter than the physical model, in order to save computational resources, since the first part of the physical domain is not simulated in the model. Additionally, the technique of the truncated domain eliminates the complexity of the transport functions of the wave paddles and it uses a signal recorded far enough from them, which contains the undisturbed propagating waves without potential evanescence modes caused by the moving paddles. The input signal to the numerical model was a set of wave components with amplitudes, frequencies and phases obtained from FFT of the experimental signal at the N.I. locations. At that study, the signal was reproduced as a linear superposition of 243 wave components between 0.0039 Hz and 1 Hz, calculating the boundary conditions for the surface elevation and the velocity according to waves2Foam. This method guarantees that the surface elevation at the N.I. is identical between the physical and the numerical model. Provided that linear theory still holds, assuming low-amplitude wave components, the velocity profile under the free surface should be also the same, and thus, if the governing equations and the design of the NWT are accurate, the measurement at the focal location should be similar too.

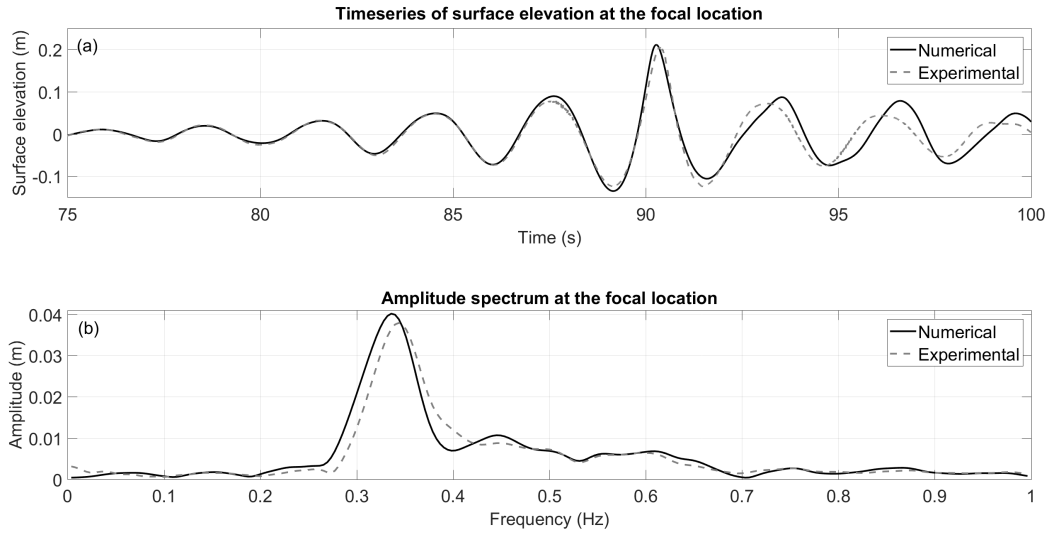

Figure 3.2: Comparison of the experimental and numerical results at the focal location of an extreme wave using empirical phase correction (Vyzikas et al., 2013).

The comparison at the focal location between the numerical and the physical model is given in Figure 3.2a. The main crest of the extreme wave is well reproduced, but there are clearly some phase anomalies following the main event. It should be noted that the timeseries of the numerical result were shifted in time in order for the main crest to coincide with the experimental one. This is common practice, since due to the nonlinearities, the focusing event is down-shifted in space or time and manual correction of the output of the model is required, as seen in many works, e.g., (Zhao et al., 2010; Gibson and Swan, 2007; Johannessen and Swan, 2003; Ning et al., 2009b; Westphalen et al., 2012; Johannessen and Swan, 2001). Nevertheless, this reveals a major drawback of the trial and error method. What is more alarming from the comparison between the physical and numerical is the shape of the spectrum shown in Figure 3.2b. The reason for these differences can be attributed to many factors, such as sufficient grid refinement, reflections from the outlet boundary, small preliminary wave breaking in the physical model etc., nevertheless, the fact that the spectral shape is different restricts this method from being used for in-depth validation of the spectral evolution.

The main conclusions from this preliminary study are:

1. A more sophisticated, less empirical, method should be used for the wave focusing.

2. Despite the relatively good reproduction of the main crest, the spectral evolution can deviate significantly.

3. OpenFOAM and waves2Foam have good potential for being used for extreme wave propagation, but fine-tuning is required.

4. Regarding the design of the NWT, some elements were considered successful implementations that were kept in the next studies: i) the wave generation, as linear superposition of wave components of a given amplitude spectrum; ii) the computational mesh as a 2D representation of the physical tank, and iii) the refinement of the mesh around the surface and the use of coarser towards the top and bottom of the NWT.

3.2.2 Initial validation of OpenFOAM using the focusing methodology

The first study where the methodology for the accurate focusing of wave groups of Stagonas et al. (2014) was used in a NWT was that of Vyzikas et al. (2014b). In that work, three wave groups of increasing steepness were examined, comprising a Pierson-Moskowitz (PM) spectrum. After a thorough convergence analysis of the NWT designed in OpenFOAM with waves2foam (see Figure 4 in (Vyzikas et al., 2014b)), the numerical results for the steepest wave group, which was the limiting breaking case in the experiment, were compared with the experimental results (see comment in footnote in Section 2.3.4).

The NWT comprised a "numerical mirror" of the physical wave flume of University College London (UCL) allowing for direct comparison at the exact same locations. The physical flume was 20x1.2x1 m and equipped with two piston-type wavemakers that were located at each end of the flume, capable of generating unidirectional waves and absorbing reflected waves with force feedback active absorption. The NWT is a

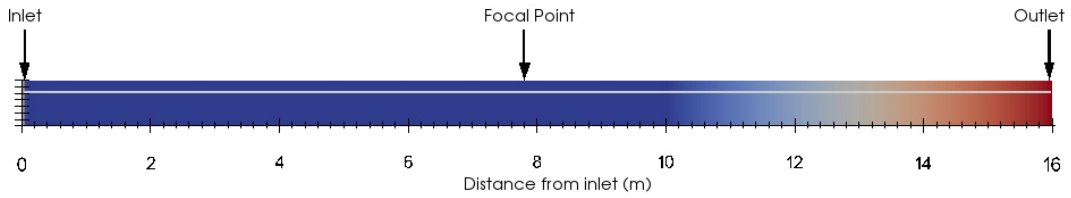

Figure 3.3: NWT in OpenFOAM showing the inlet boundary, focal location and outlet boundary as well as the free surface (white line) and the relaxation zone weighting (blue: nonlinear solution; red: target solution) (Vyzikas et al., 2014b).

shorter 2D cross section of the physical flume, designed as a 16x0.7m quasi-3D, one cell thick, domain. The focal location and the water depth were set at 7.8 m and 0.5 m respectively, identical in the numerical and physical model. The focal time is 64 s and the signal has a return period of 128 s. The signal is introduced at the inlet as a superposition of linear wave components that form the selected spectrum and it is absorbed by a relaxation zone at the outlet, similar to the first preliminary work (Section 3.2.1). The computational domain is shown in Figure 3.3, emphasizing to the exponentially increasing weighting of the relaxation zone expanding from 10 m to 16 m. The computational mesh is also designed with the same technique as before, using "cell grading", having the finest square cells surrounding the free surface and elongating cell height towards the top and bottom of the NWT, as seen in Figure 3.4. The minimum cell size selected for this mesh was 2.5 mm, being uniform in the $x-$direction, and the Courant number (C_o) was 0.1. Square cells are recommended for a highly distorted free surface (Jacobsen et al., 2012), while the grading of the cells results in significant savings of computational resources. The refinement around the interface of the two fluids is a common practice in CFD and in OpenFOAM is usually performed with the utility "snappyHexMesh" (Morgan and Zang, 2010), which however does not guarantee always as a smooth transition to the coarser part of the domain as the cell grading does (OpenCFD, 2012).

The main differences from the previous study (Vyzikas et al., 2013) are:

- The signal for the numerical input is taken from a theoretical spectrum and not

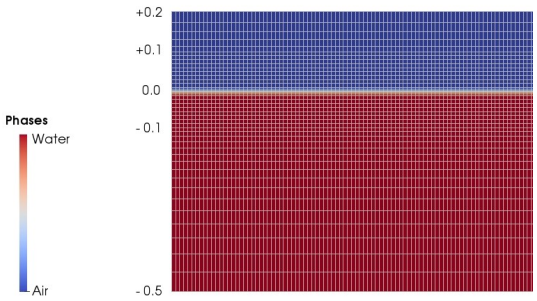

Figure 3.4: Computational mesh showing the cell shape. Square finer cells around the free surface (0.0 m) and coarser elongating cells at top and bottom (Vyzikas et al., 2014b).

from the recorded experimental signal.

- The signal is corrected independently in the numerical and physical flume using the methodology for focusing waves (Stagonas et al., 2014), as described in Section 2.4.5.

- The phases and the amplitudes of the wave components are corrected at the focal point.

- The validation is performed for each harmonic separately and not only for the total measured surface elevation.

The comparison with the experimental results presented here concerns only the strongly nonlinear group formed based on a PM spectrum with peak frequency $f_p = 0.6$ Hz, seen in Figure 3.5a. In Figure 3.5a, it is shown that the extracted linearised spectrum from the numerical model and the experiment are almost identical with the target spectra at the focal location, thanks to the application of the focusing methodology. Some discrepancies are observed in the amplitude spectrum only at the high-frequency wave components above $2f_p$. The same applies for the phases[1] of the linear components

[1] To be precise, the phase difference of the wave components are shown after subtracting the slope of the wrapped phases between $[0, 2\pi]$. Another way to present these results would be to plot the unwrapped phases from FFT of the linear harmonic, however that presentation makes it less straight-forward to see whether the wave components are in phase.

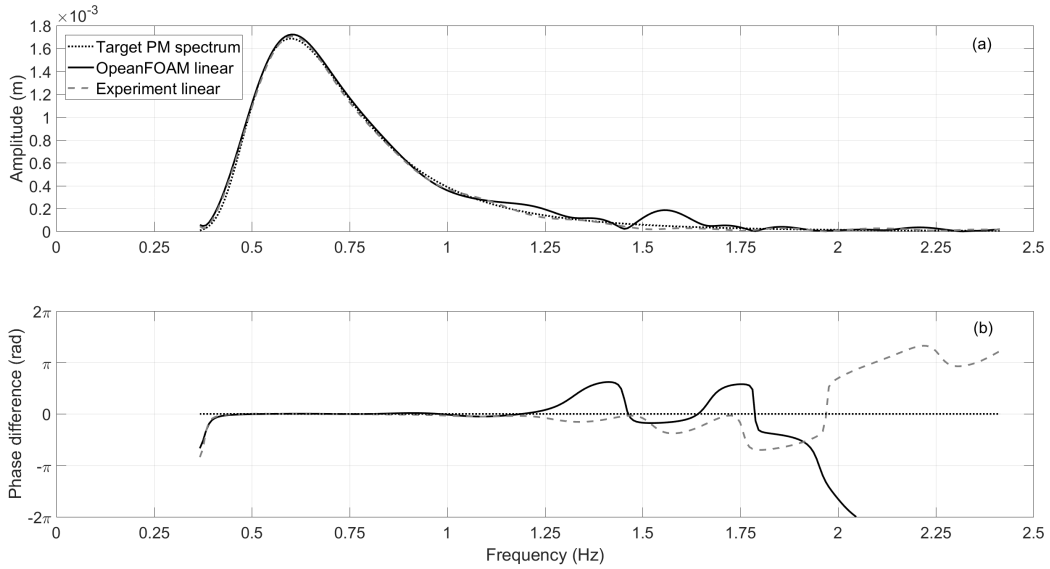

Figure 3.5: Spectral analysis of the numerical and physical results at the focal point: (a) Extracted linearised amplitude spectrum; (b) Phases of the linear wave components.

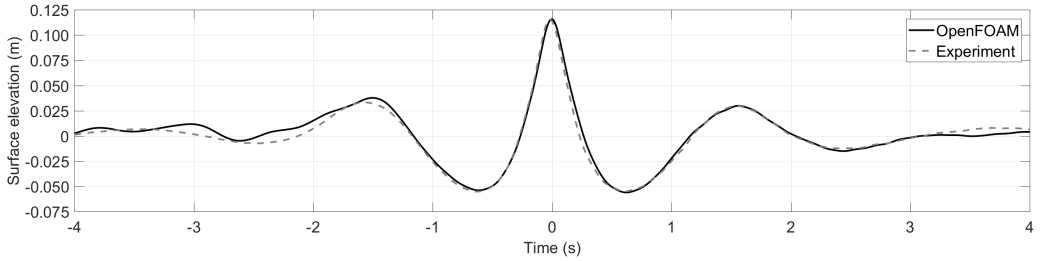

Figure 3.6: Measured surface elevation at the focal point in the numerical and physical flume.

plotted in Figure 3.5b. The analysis shows that the methodology has corrected and brought in phase the most energetic components of the spectrum, but it has been less effective for the high-frequency components. These components however have little energy content and contribute negligibly to the surface profile. The latter can be confirmed from Figure 3.6, where the surface profile of the numerical model and experiment are plotted. The main crest, two lateral troughs and two adjacent crests are in almost perfect agreement. Small discrepancies are only seen before and after the wave group. For all the results that follow, the timeseries have been shifted by 64 s, in order for the reference time to be the focusing event occurring at 0 s.

2-5 iterations of the focusing methodology are sufficient for the effective correction of the signal and any further iterations do not suppress the discrepancies observed. The nature of this discrepancies may be associated with the fact that the high frequency components of the linear harmonic may not follow exactly the linear dispersion, as shown with the spatio-temporal analysis of the wave field of Johannessen and Swan (2003); Gibson and Swan (2007); Taklo et al. (2015). This can reveal a limitation of the present correction method which uses the exact linear dispersion relation to propagate backwards the full extracted linearised harmonic. Another potential reason for the discrepancies might be reflections of long waves, that are linear and contaminate the signal causing modulations of the high-frequency components, or spurious waves caused by the wave generation and have not been separated from the main wave group at the focal location.

Next, the individual extracted harmonics are compared in Figure 3.7a, b, c and d for the linear, 2^{nd} sum, 3^{rd} order harmonics, which include also part of the 5^{th} order harmonics, and 2^{nd} difference harmonics (including the 4^{th} harmonics), respectively. The linearised harmonics are practically identical between the numerical model and the experiment, since they were corrected to match the target values with the methodology. This result simply confirms the effectiveness of the methodology in both physical and numerical flumes. All the simulated nonlinear harmonics are in good agreement between the numerical and physical wave tank having same phasing and similar amplitudes. The best agreement is achieved for the 2^{nd} sum harmonic, while the 3^{rd} order harmonics have approximately 20% higher crest in the experimental results. The most noticeable difference concerns the 2^{nd} difference harmonics, which exhibit a crest preceding the set-down. This is more than twice higher in the numerical model. The source of this crest is not predicted by 2^{nd} order theory and it is not expected by any underlying physical mechanism. More details about this set-up are given in Section 3.3.

To help understand the significance of the present findings, a comparison with the study of Chen et al. (2014) can be made, where a similar NWT in OpenFOAM was

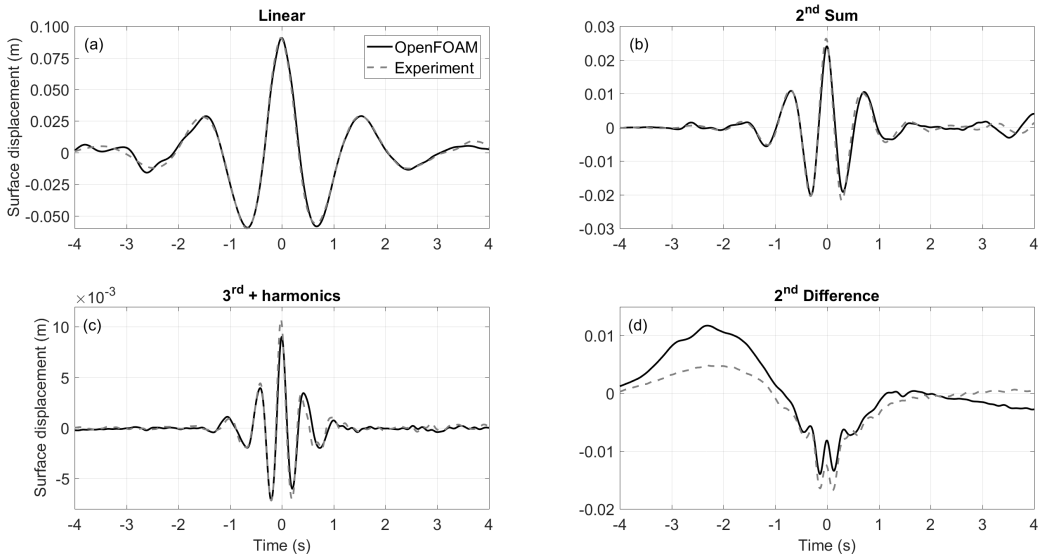

Figure 3.7: Comparison of the extracted nonlinear harmonics in the experiment and numerical model: (a) Linearised harmonics; (b) 2^{nd} sum; (c) 3^{rd} order; (d) 2^{nd} difference.

examined and the surface elevation was analysed in harmonics. It can be seen that in the absence of an effective correction methodology, important discrepancies are observed in the recorded signal of the focused wave. As seen in Figure 16 of (Chen et al., 2014), the higher order harmonics, which are of particular importance for the phenomenon of "ringing" (Fitzgerald et al., 2014), are hardly comparable with the experiment. Therefore, the present results show that appropriate correction of the sign is crucial for engineering purposes.

Attempting to improve the results and save computational resources, the same study was also performed using the boundary conditions of IHFOAM (Higuera et al., 2013a). As discussed in (Vyzikas et al., 2018b), IHFOAM seems to have a reduced computational time compared to waves2Foam (Jacobsen et al., 2012), thanks to the fact that relaxation zones are not required. On the downside, it introduces some discrepancies on the free surface near the inlet boundary (see Figure 3.8a) that fade quickly as the waves propagate, and downstream in the wave flume the results between the two boundary conditions are almost identical, as seen in Figure 3.8b. As shown in Figure 3.7d, a major difference between the numerical and the experimental results is the

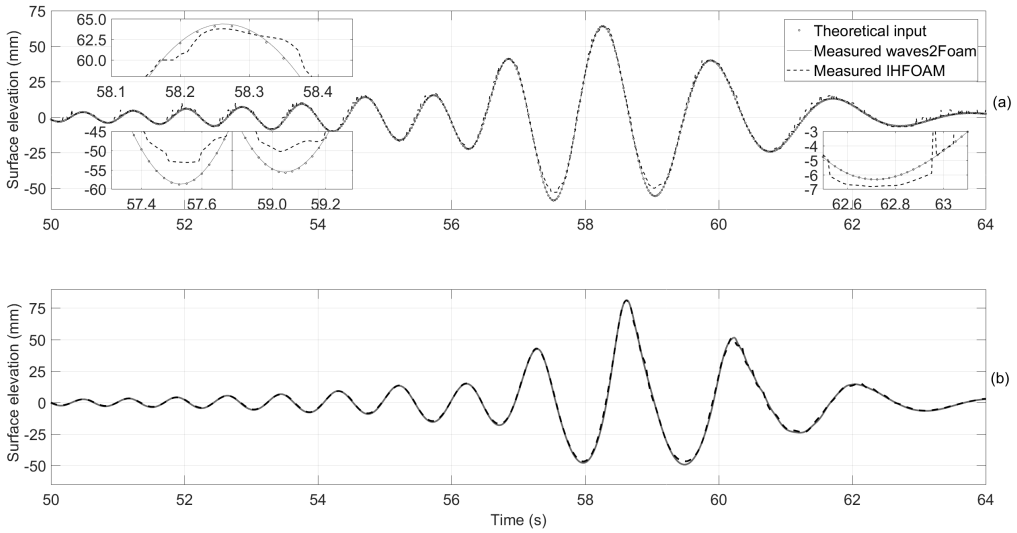

Figure 3.8: Comparison between the simulated surface elevation in waves2foam and IHFOAM: (a) At the inlet; (b) At first WG downstream (0.78 m).

evolution of the 2^{nd} difference harmonics. Based on the present findings, waves2foam and IHFOAM seem to both introduce a set-up preceding the wave group, which is slightly smaller when the boundary conditions of the former are used, as demonstrated in Figure 3.9.

The outcomes of this study can be mainly summarised to:

1. A NWT designed in OpenFOAM and waves2Foam or IHFOAM can replicate with very good accuracy an extreme wave event at a certain position and time.

2. The NWT is validated with experimental results for the total surface elevation and the extracted individual harmonics.

3. An appropriate correction methodology and a thorough convergence study is required to achieve the desired accuracy (Vyzikas et al., 2014b).

4. The employment of the focusing methodology increases significantly the computational burden, since 4 phases of the wave group must be simulated and at least 2-5 iterations are required to achieve high accuracy.

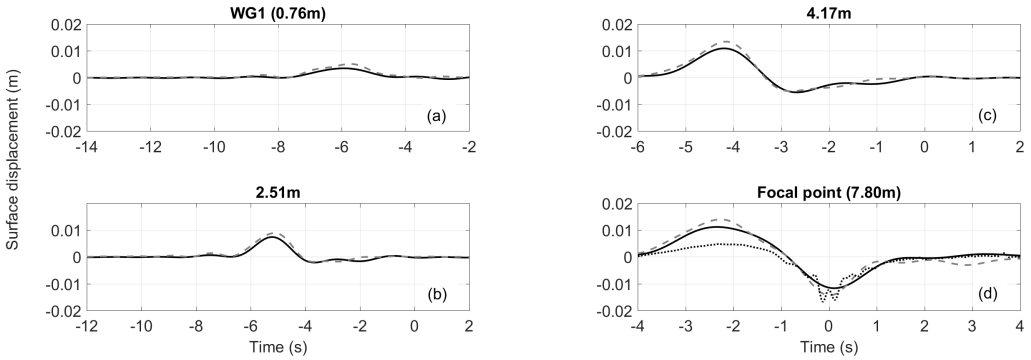

Figure 3.9: Comparison between waves2foam (—) and IHFOAM (- - -) for the evolution of the extracted 2^{nd} order difference harmonics at four locations from WG1 (0.76 m) to Focal point (7.80 m), where the experimental result is plotted as well ($\cdots$).

3.2.3 Initial validation of SWASH using the focusing methodology

Despite the successful initial validation of OpenFOAM with experimental results, using the correction methodology of Stagonas et al. (2014), the idea of employing other numerical solvers and validating them with the same consistent way was considered, since the computational cost of the two-phase CFD solver was very high. The scope is to identify a suitable faster solver that could be used to generate a corrected input signal with the focusing methodology and use CFD only for the final iteration. This can be possible only if the phases and amplitudes of the wave components at the inlet boundary are sufficiently similar after the application of the methodology in both models.

A promising numerical tool for such use is the nonlinear non-hydrostatic shallow water equation model SWASH, which is described in detail in Section A.2. The numerical approaches used in SWASH (Stelling and Zijlema, 2003) have shown good potential in simulating wave-wave interactions and wave transformation in coastal regions, nevertheless, to the best of the author's knowledge, SWASH has never been used for simulating extreme waves by other researchers.

The first study where a NWT in SWASH was examined for simulating extreme waves is that of Vyzikas et al. (2015). The results were compared with OpenFOAM and IH-

FOAM using the methodology of Stagonas et al. (2014). The same PM spectrum as in (Vyzikas et al., 2014b) was examined, seen in Figure 3.5a. For the sake of comparing the computational cost, a low resolution, not-fully-converged NWT in OpenFOAM (R2) was also examined, where the cell size was double than the converged (R1). In (Vyzikas et al., 2015) only results for the weakly nonlinear group were presented, while here, the analysis is focused on the strongly nonlinear group, which induces the strongest wave-wave interactions.

The NWT in SWASH was designed as an one-dimensional (1D) numerical mirror of the physical flume of the UCL laboratory having 0.5 m water depth. For practical engineering applications, SWASH is used commonly with one or two layers for the vertical discretization, which might be adequate for a crude estimation of the wave transformation in large coastal areas and for operational purposes, but it was shown not to be sufficiently accurate for the present study. Through an exhaustive convergence analysis, which included space and time discretization schemes, numerical schemes and levels of accuracy / iterations, SWASH was gradually optimised until its output was in good agreement with the CFD results. Over 40 combinations of the parameters available in SWASH were examined. These parameters are detailed in the manual of SWASH (The Swash Team, 2014) and since to the best of the author's knowledge no recommendations existed in the literature, the schemes were tested almost one by one. The final selection of the parameters is given in (Vyzikas et al., 2015), Briefly, the grid consisted of 6 layers of variable thickness of 5%, 10%, 15%, 20%, 25% and 25% of the water depth, calculated from the free surface to the sea bed, with finer layers towards the free water surface. The horizontal grid was uniform with a cell size of 40 mm. Considering the physics of the problem, SWASH was used in non-hydrostatic mode and the Keller-box scheme was employed for the calculation of the vertical pressure gradient using an implicit Euler scheme. A second order backward difference (BDF) numerical scheme was used for the discretization of the momentum and transport equations, as well as for the water depth at the points where the velocity is calculated. A semi-implicit Crank-Nicolson scheme was used for the time integration of the continuity equation and the

water level gradient, allowing the Courant number to take values greater than 1 and the stability not to depend only on the long wave celerity, which would slow down the computation. A high relative accuracy of the solvers was chosen (0.001) and a high number of maximum iterations (1000), which provide more accurate results compared to the default values of 0.01 and 100 respectively. The ILU preconditioner was used for the calculation of the non-hydrostatic pressure (Vyzikas et al., 2015).

The wave generation in SWASH is performed with a stationary boundary that calculates the surface elevation and the velocity for every layer. For the simulation of irregular waves, a "FOURIER" type inlet boundary was used, where the 263 wave components that synthesized the spectrum were linearly superimposed. The number of wave components is determined by the return time of the periodic signal, which was selected at 128 s, following the experiment. The frequency increment is thus found as $df = 1/128$ s and after windowing the spectrum between 0.37-2.41 Hz to keep only non-zero amplitudes, the 263 are selected. The surface displacement was recorded with virtual WGs at the exact same locations as in the CFD model and the experiment, having a sampling frequency of 100 Hz. A weakly reflective boundary condition was also used at the inlet to minimize any returning reflections. At the outlet of the numerical domain, the waves were absorbed by a 10 m sponge layer. It should be noted here that as observed with all the models that were used for simulating focused wave, the outlet boundary cannot absorb 100% of the incoming energy, resulting in reflections. This is partially due to the limitations of the techniques used as well as the complex velocity field incorporated in an focused wave group, which makes the employed absorption methods less effective than they are for regular waves. Thus, it is advised to keep the focal point sufficiently away from the outlet boundary in order to avoid contamination of the measured signal with reflections, which in this way will require more time to return from the outlet and be present at the time window of interest at the focal location.

The simulations were ran on a single core with an average computational time of 15-20' for the strongly nonlinear group. Different Linux desktops were used having processing

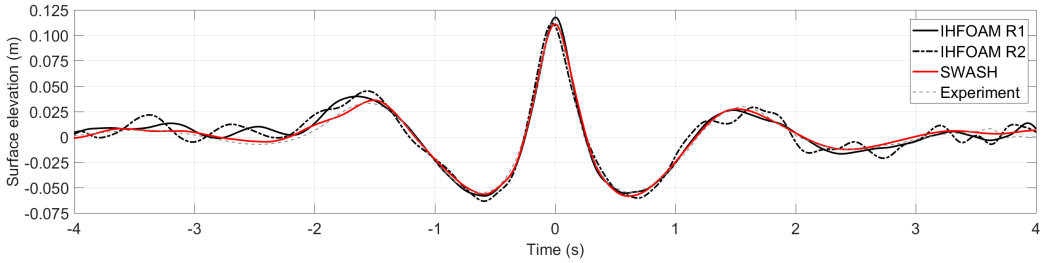

Figure 3.10: Measured surface elevation at the focal point in the numerical wave tanks and in the physical flume.

power of 1.8-2.2 GHz. Special scripts were written in MATLAB for the pre-processing, i.e. preparation of the input files, and the post-processing of the results, guaranteeing efficiency and consistency.

For the analysis of the strongly nonlinear wave group that follows, apart from the results of SWASH and experiment, also the results from the high (R1) and low (R2) resolution NWT designed in OpenFOAM and IHFOAM are included. Their computational meshes have a similar design as that in Figure 3.4. The minimum cell size of 2.5 mm and 5.0 mm for the R1 and R2 NWT, respectively, and the Courant number is the same ($C_o = 0.1$). The results of SWASH stand out with red colour in the figures. The same number of corrections (seven) was performed independently for each NWT, with the focusing of the wave group not showing any noticeable improvement after that point.

As seen in Figure 3.10, at the focal point, the general shape of the wave group is in very good agreement between the models with the most noticeable differences observed at the lateral crests. It is also observed that only the high resolution NWT in OpenFOAM (IHFOAM R1) resembles the main wave crest in the experiment, while IHFOAM R2 and SWASH have a similar and shorter crest (0.112 m) than that measured in the experiment (0.118 m). As a general shape of the total timeseries, SWASH seems to be closer to the experiment and have a smoother -fewer high frequency disturbances before and after the main troughs- time history of the free surface compared to OpenFOAM NWTs.

Next, the extracted harmonics at the focal point are examined in Figure 3.11. The linearised harmonics are practically identical in SWASH, IHFOAM R1 and experiment.

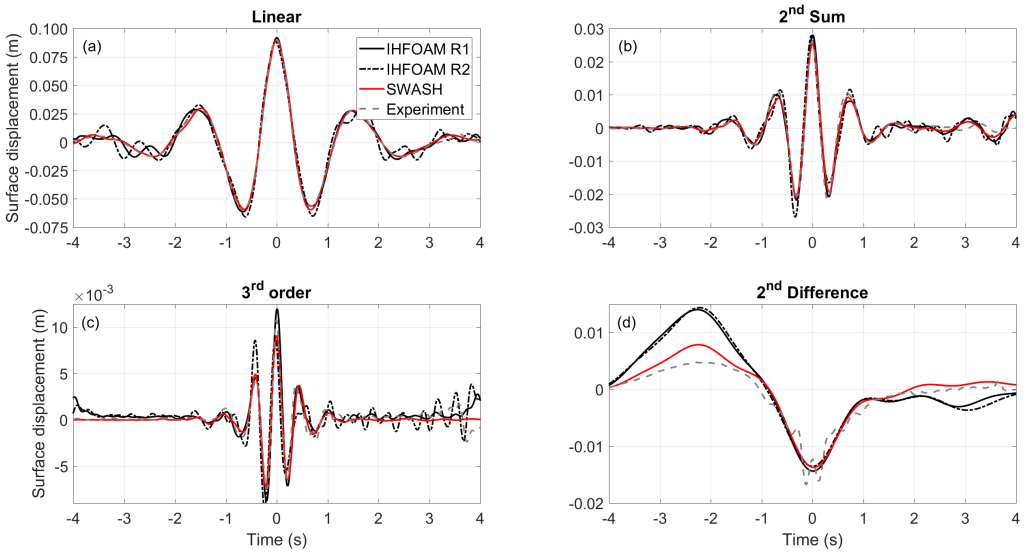

Figure 3.11: Comparison of the extracted nonlinear harmonics in the experiment and numerical models: (a) Linear harmonics; (b) 2^{nd} sum; (c) 3^{rd} order; (d) 2^{nd} difference.

Some discrepancies are observed in IHFOAM R2, where the adjacent troughs are deeper and the time history of the surface elevation before and after the lateral crests exhibits some anomalies. The 2^{nd} sum harmonics are practically identical in all the NWTs. As for the 3^{rd} order harmonics in Figure 3.11c, SWASH has the shortest main crest and left trough. The IHFOAM R2 NWT appears to handle less effectively these short waves. Nevertheless, the phasing is similar in all the models. The most important difference is shown for the 2^{nd} difference harmonics in Figure 3.11d. The preceding spurious crest, which is the same in IHFOAM R1 and R2, is noticeably shorter in SWASH, while the set-down is the same for all the models and experiment. Thus, for the 2^{nd} difference harmonics, SWASH is much closer to the experiment than CFD.

The spectral analysis in Figure 3.12a at the focal point shows that the main part of the extracted linearised spectrum matches the target amplitude spectrum for all the models. SWASH shows the best agreement with target spectrum at the high frequencies, while IHFOAM R2 demonstrates some bumps above $2f_p$. The peak of the amplitude spectrum is marginally lower in SWASH compared to IHFOAM R1 and R2 and it matches better the target spectrum. The reason for this is not yet clear. The phases

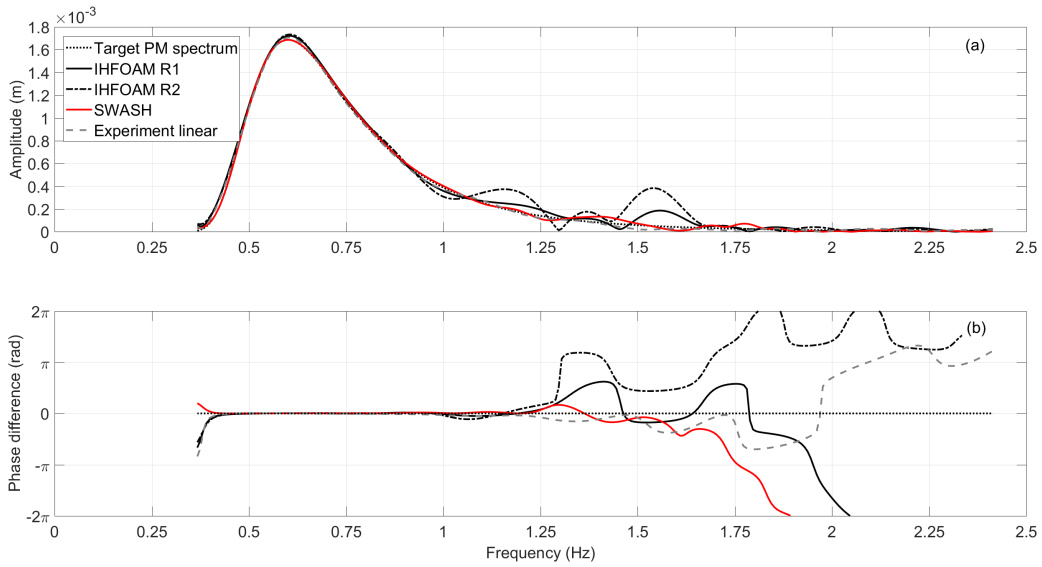

Figure 3.12: Spectral analysis of the numerical and physical results at the focal point: (a) Extracted linearised amplitude spectrum; (b) Phases of the linear wave components.

of the wave components in Figure 3.12b are zero for the main part of the spectrum, showing that the methodology has effectively focused the wave group, but above $2f_p$, the high frequency components are not well focused and have considerable differences between the models.

As mentioned, the main scope of the study of Vyzikas et al. (2015) was to examine potential use of SWASH or IHFOAM R2 for the iterations of the focusing methodology. For that, the input signals among the models are examined in Figure 3.13a, where it is seen that the input amplitude spectrum in IHFOAM R1 and IHFOAM R2 are very similar, apart from a discrepancy at 1.5 Hz, while the input spectrum in SWASH has considerably different shape in the main part of the spectrum and close to the spectral peak. This shows that the spectrum has been transformed differently in the NWTs despite the fact that at the focal point the results show almost excellent agreement. The phase differences, calculated as corrected input phases minus the linear theory prediction based on dispersion relation ($kx - \omega t$, where k is the wavenumber, x the distance between inlet and focal, ω the angular frequency and t the focal time), are shown in Figure 3.13b. For the main part of the spectrum, the NWTs have similar phases at the

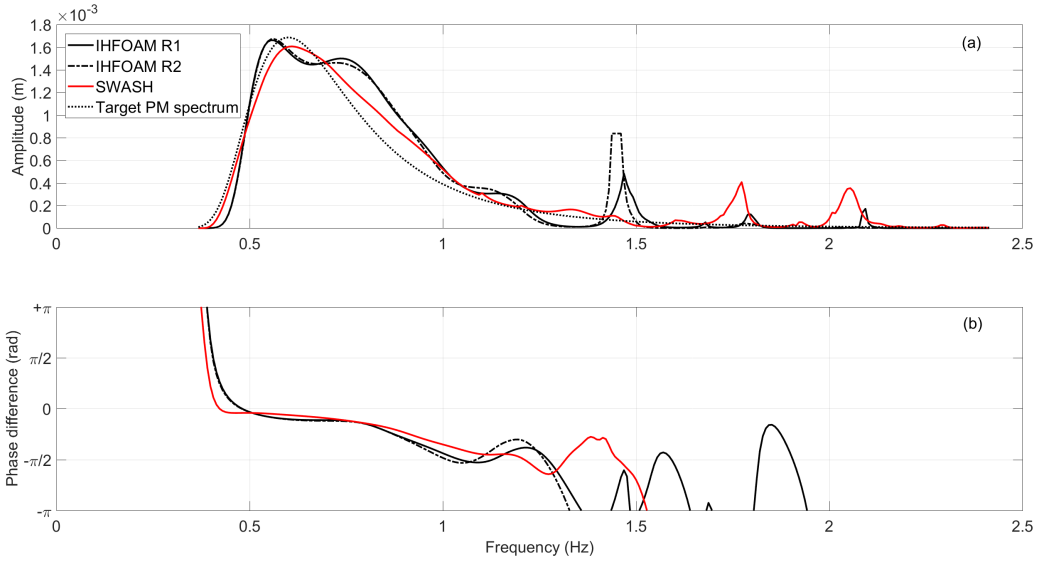

Figure 3.13: Spectral analysis of the numerical and physical results at the inlet: (a) Input linear amplitude spectrum; (b) Phases of the linear wave components between input phases and linear theory (dispersion relation).

inlet, but for higher frequencies above $1.5f_p$, the phases of the components exhibit important differences. In conclusion, it seems that, for both the amplitude spectrum and phases of the components, the low resolution NWT in OpenFOAM resembles better the behaviour of the high resolution NWT in OpenFOAM than SWASH does.

The outcomes of this study can be mainly summarised to:

1. A NWT designed in SWASH can replicate with very good accuracy steep wave groups, capturing the high-order nonlinear wave-wave interactions.

2. SWASH showed better agreement with the experiment than the CFD model for the reproduction of the 2^{nd} difference harmonics.

3. The input signal between SWASH and OpenFOAM is not sufficiently similar to allow for using SWASH for the preliminary iterations of the methodology. Instead, a low resolution NWT in OpenFOAM was proven effective for this scope, avoiding the complication of using two different models.

4. The comparisons among the models revealed noticeable deviations in the spec-

tral evolution, which requires further investigations into the dispersive properties of the NWTs.

3.3 Dispersion study

3.3.1 Description of the experiment

The observation of the transformation of the extracted linearised amplitude spectrum from the inlet to the focal location discussed in Section 3.2.3 led to the another set of experiments and consequently, to a more accurate and thorough validation of the numerical tools. The comparison with the experimental results is not performed only at the location of interest, namely the focusing location, but also along the flume, which gives a better insight for the evolution of the wave group and consequently the kinematics of the fluid, which are of practical engineering interest, since they are used for the calculation of the loading on marine structures. During the time of the present research, the methodology of focusing waves was fine-tuned and optimization of the NWTs was gradually performed as well.

The distinguishing characteristic of the validation presented in this section is that the amplitude spectrum is corrected at a different location (Amplitude Matching - AM) than the phases of the wave components (Phase Focal - PF). The AM location, where the amplitudes of the components are corrected to match the target spectrum, is selected to be close to the wave paddle, while the PF point, where the wave components are brought into phase, is located at a downstream location. In other words, the correction methodology is performed in two steps, independently for the phases and the linearised amplitude spectrum. The advantages of this approach are both practical and theoretical. By correcting the spectrum not at the inlet but downstream in the wave tank, the discrepancies from the wave paddle, such as linear transport functions and inconsistencies between different wave generation methods, are eliminated and the target spectrum is reproduced exactly in the nonlinear domain or physical wave tank.

At the same time, this method also enables the examination of the natural evolution of the amplitude spectrum from the AM location, where the wave group is dispersed, until the PF, where the strongest wave-wave interactions occur as the wave group takes its steepest form. Therefore, instead of forcing the wave group to take the target spectral shape at the focal point, as done in the initial validation of the models in Sections 3.2.2 and 3.2.3, the wave group is allowed to evolve freely from the AM to PF location according to the "dispersive" properties of the NWTs, which in physical terms are controlled by the third-order wave-wave interactions, as discussed in Section 2.2.

The experimental set-up and the comprehensive comparison between the NWT in OpenFOAM with IHFOAM and physical flume are described in (Vyzikas et al., 2018b). In that work, the focus was on the evolution of the harmonics up to the 4^{th} order and their contribution to the overall free surface profile. The measured results of the CFD model were compared with linear and the 2^{nd} order analytic solution of Sharma and Dean (1981), as formulated by Dalzell (1999). Here, the focus is on the validation of the models at specific locations in the NWTs, and for the sake of consistency with the analysis in the previous sections, only the evolution of up to 3^{rd} order harmonics is examined. As demonstrated in (Vyzikas et al., 2018b), the 4^{th} order harmonics exhibit similar properties and evolution to the 3^{rd} order harmonics.

The physical flume for the dispersion study is the wide wave flume of the UCL laboratory, which is 20 m long, 1.3 m deep and 2.5 m wide. For the experiments of this study, the working depth was set at 1 m. A schematic of the physical flume is shown in Figure 3.14. The wave generation is performed by seven flap-type computer-controlled absorbing wave paddles, which can produce a target surface elevation or spectrum based on linear transport functions. The wave paddles in this study have the same movement in order to act as one and produce a unidirectional wave group. The wave dissipation is achieved at the opposite end of the flume by a parabolic beach. The free surface displacement is recorded by seven resistive WGs along the tank, the locations of which are shown in Table 3.3. Their sampling frequency is 100 Hz and their accuracy

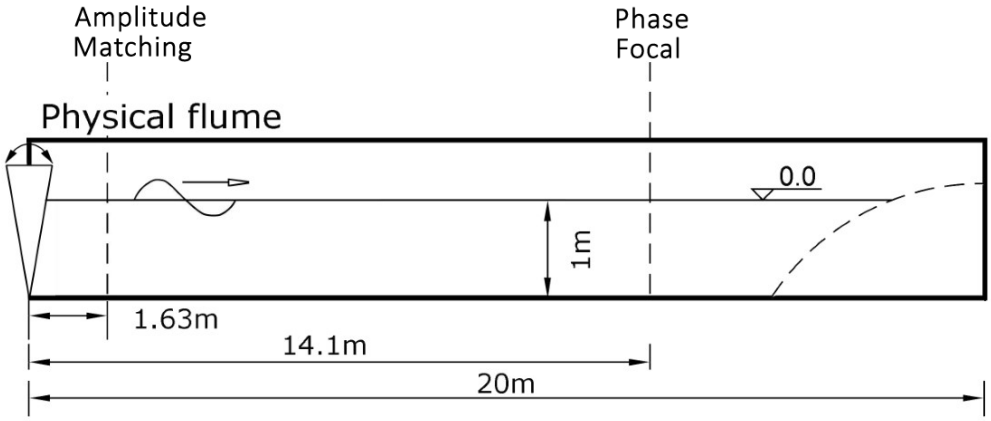

Figure 3.14: Schematic of the physical flume with the locations of the Amplitude Matching (AM) and Phase Focal (PF) points.

Table 3.3: Location of the wave gauges (AM: amplitude matching; PF: phase focal).

	WG1 (AM)	WG2	WG3	WG4	WG5	WG6	WG7 (PF)
Location (m)	1.63	5.17	9.40	11.50	13.80	13.90	14.10

is ± 1 mm. The AM point is at 1.63 m downstream of the wave paddles in order to be sufficiently close to the wave generation location and have minimum energy transfer to bound waves, but sufficiently far from the moving boundary in order to avoid contamination of the signal with spurious displacement waves (evanescent modes) caused by the moving paddles. It should be noted that for the steepest wave group, the experiments presented in (Vyzikas et al., 2018b) were performed again here with only WG7 in the physical flume, since the presence of the intrusive WGs marginally influences the wave profile. Thus, the comparison is further improved.

The examined wave group comprises a broadbanded Gaussian spectrum of 320 equidistant wave components in the range of frequencies 0.0078 Hz to 2.50 Hz, but practically any components with frequency higher than 1.5 Hz have zero energy. The selected target spectrum has several practical advantages compared with more realistic wave spectra such as JONSWAP. For experiments, the full range of frequencies included in the spectrum can be efficiently generated by the physical wavemaker, while for spectra with a high frequency tail, truncating the high frequency part at 2 or $3f_p$ is common practice and entails a rather sharp drop in the energy content of wave components with

unknown consequences in the spectral evolution. In contrast, the selected Gaussian spectrum is the broadest possible, spanning smoothly in frequencies from 0 to $2f_p$, and, as the wave group propagates in the flume, a high frequency tail is developed, as demonstrated by Vyzikas et al. (2018b). Additionally, a Gaussian spectrum has a compact shape of the timeseries of the free surface, consisting of 1 main crest and 2 deep troughs at focus, similar to PM spectra. On the other hand, the time history of the free surface for JONSWAP wave groups consists of many crests and troughs and it is wider, requiring a longer NWT for the simulation. The amplitude spectral shape is given by Equation 3.1, with standard deviation $\sigma_{SD} = 0.13$. The peak frequency of the amplitude spectrum is $f_p = 0.64$ Hz, which for the water depth of $d = 1$ m, corresponds to a wave group propagating in intermediate water depth; $k_p d = 1.75$, where k_p is the wavenumber of the peak frequency wave component. Wave groups of increasing steepness were tested in order to examine the effects of increasing nonlinearity. The steepness is controlled by multiplying all the amplitudes of the wave components of the linearised spectrum by the same factor and keeping all the other parameters identical. Here, only the strongly nonlinear limiting breaking wave group is examined, which has a linearly predicted amplitude of $A_{Th} = 0.154$ m, since it constitutes the most challenging case for the numerical models to replicate. The effects of steepness on the spectral evolution are discussed in Chapter 4.

$$E_a(f) = \frac{1}{\sigma\sqrt{2\pi}} e^{\left[\frac{-(f-fp)^2}{2\sigma^2}\right]} \tag{3.1}$$

3.3.2 OpenFOAM

Design of the NWT

The NWT was designed as a two-dimensional (2D) numerical mirror of the physical wave flume at UCL, described in the previous Section 3.3.1, as seen in Figure 3.15. The computational mesh had a similar design to that presented in Section 3.2.2, con-

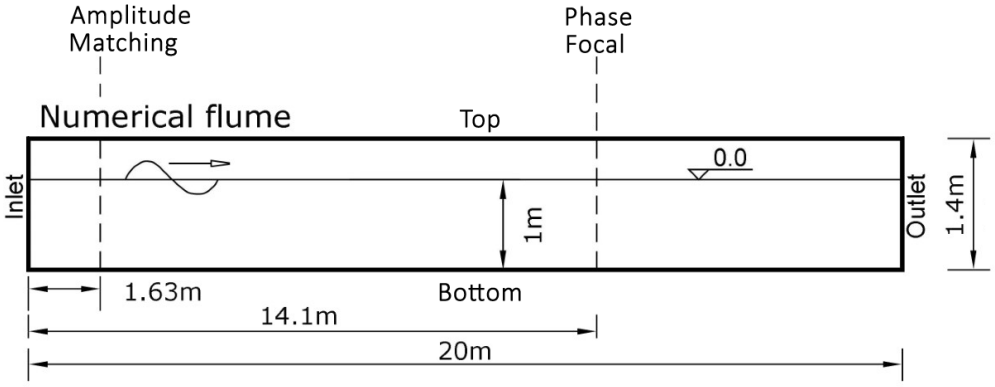

Figure 3.15: Schematic of the numerical flume in OpenFOAM.

sisting of three layers: a middle layer of square cells (aspect ratio, AR=1), which has the highest resolution and encapsulates the maximum and minimum free surface extending $\pm$ 0.2 m from the still water level (SWL); a top layer 0.2 m wide of maximum cell AR=2 extending to the atmospheric boundary; a lower layer 0.8 m wide of maximum cell AR=4 extending to the bottom of the NWT. This design was selected after trials ensuring highest accuracy and computational efficiency. WGs located at identical positions as in physical flume (see Table 3.3) recorded the free surface displacement at 100 Hz.

As discussed in Section 3.2.2, the most integrated and complete wave generation/absorption libraries in OpenFOAM, waves2Foam (Jacobsen et al., 2012) and IHFOAM (Higuera et al., 2013a), can practically produce similar results after the application of the focusing methodology (Stagonas et al., 2014). For the validation presented here, the selection between the two libraries is based on the absorption of the long spurious waves at the outlet boundary and the computational efficiency. As mentioned in Section A.1, the active wave absorption in IHFOAM is designed according to a SWE assumption and thus, it is expected to perform well with long waves that have a relatively uniform horizontal velocity profile. The effectiveness of the relaxation zones in waves2Foam increases with increasing their length. Here, two relaxation zones of 6 m and 8 m were tested. It was found that perfect absorption of the waves is neither achievable in waves2Foam, nor in IHFOAM, and therefore, the outlet boundary had to be suf-

ficiently far from the PF location in order for the reflected waves not to have enough time to return and contaminate the recorded signal. After tests of placing the outlet at different locations (note that for waves2Foam reflection can occur even from the beginning of the relaxation zones), it was observed that IHFOAM absorbed better the long waves and it was at least 30% more computationally efficient than waves2Foam, where the computational domain had to be elongated to accommodate the relaxation zone and additional computations take place in each cell of the relaxation zone. Accordingly, IHFOAM (Higuera et al., 2013a) was used for all simulations presented hereafter.

The computational domain is a 20 m long and 1.4 m high closed rectangular consisting of six wall with assigned appropriate boundary conditions for every variable as listed in Table 3.4 (Vyzikas et al., 2018b). Each wall is assigned with appropriate boundary conditions for every variable, namely γ_i, which refers to the dimensionless scalar field of the fluid phase fraction varying from $0 < \gamma_i < 1$, $Velocity$, which refers to the vector field of the velocity components (m/s) and $Pressure$, which corresponds to the scalar field of the total pressure minus the hydrostatic pressure $(Pa = kg/m/s^2)$. In Table 3.4, "IH_waves_InletAlpha" and "IH_Waves_InletVelocity" are the wave generation boundary conditions defined by IHFOAM. "IH_3D_2DAbsorbtion_Inlet Velocity" refers to the active absorption at the outlet boundary with a target value of zero. "zeroGradient" boundary condition defines the normal gradient of a quantity to the wall as zero. "buoyantPressure" specifies the normal gradient of pressure at the wall based as the atmospheric pressure gradient. "totalPressure" (p_o) is fixed on the boundary, but when velocity changes (U), pressure (p) is adjusted according to the relation $p_o = p + \frac{1}{2}\rho|U|^2$, where ρ is the density. The top boundary has "atmospheric" boundary conditions that allow air to come in and get out of the domain, but water can only leave the domain. This is achieved with "inletOutlet" and "pressureInletOutletVelocity" boundary conditions that switch U and p between fixed value and "zeroGradient" depending on the direction of U and evaluate U from the flux normal to the boundary when p is known. Care is taken so that the top boundary is sufficiently higher than the highest expected water elevation in order to avoid sinks of water from the top boundary of the NWT. The

Table 3.4: Boundary condition for the NWT in IHFOAM (OpenCFD, 2012).

	γ_i	*Pressure*	*Velocity*
Inlet	IH_Waves_InletAlpha	buoyantPressure	IH_Waves_InletVelocity
Outlet	zeroGradient	buoyantPressure	IH_3D_2DAbsorbtion_InletVelocity
Top	inletOutlet	totalPressure	presureInletOutletVelocity
Bottom	zeroGradient	buoyantPressure	fixedValue
Lateral walls	empty	empty	empty

velocity at the bottom of the NWT is specified by the a fixed value equal to zero; in other words as a no-slip condition. The lateral walls require boundary conditions that adjust the behaviour of the 3D mesh that OpenFOAM generates by default to a 2D mesh. This is achieved with "empty" boundary conditions that produce no solution for the variables normal to the third dimension (OpenCFD, 2012).

For the surface and the velocity profile reconstruction at the inlet, IHFOAM employs linear superposition (Dean and Dalrymple, 1991), as seen in Equation 3.2 and Equation 3.3, respectively. Although second order wave generation is available, it was not used due to its high computational cost; (320^2 wave interactions should be calculated at every time step at the inlet boundary). To further reduce the computational effort only a short part of the timeseries was simulated, when the wave group was present in the tank. Consequently, the experiments with a repeat period of 128 s were simulated between times 40 s and 70 s -including the focusing event at 64 s-, without inducing any errors in the dispersion of the wave group. This was achieved not by reducing the number of the wave components and thus the return period of the signal causing potential overlapping of consecutive wave groups, but simply by altering the starting and ending time of the numerical simulation. A large number of components guarantees adequate discretization of the spectrum, which can be crucial for the accurate reconstruction of the free water surface and the velocity profile at the inlet, because it affects later the dispersion of the wave group (Ning et al., 2009b). For periodic focusing wave groups, the number of components should be such that zero surface elevation before and after the wave group is achieved and thus, no wave-wave interactions occur (Shemer et al., 2001), especially when broadbanded spectra are simulated (Katsardi and

Swan, 2011). The initial discretization of the spectrum seems to be more crucial for spectral-based phase-resolving wave models, where the bound and resonant wave interactions become more pronounced with increasing spectral resolution (Shemer et al., 2001). Despite the fact that this is not strictly the case in CFD, some relevance may exist and high resolution of the input spectrum is in principle more accurate.

$$\eta = \sum_{i=1}^{N} \alpha_i cos(\kappa_i x - \omega_i t + \psi_i) \tag{3.2}$$

$$u = \sum_{i=1}^{N} \alpha_i \omega_i \frac{cosh(\kappa_i z)}{sinh(\kappa_i d)} cos(\kappa_i x - \omega t + \psi_i), \;\; w = \sum_{i=1}^{N} \alpha_i \omega_i \frac{sinh(\kappa_i z)}{sinh(\kappa_i d)} sin(\kappa_i x - \omega_i t + \psi_i) \tag{3.3}$$

where η is the free surface elevation; u and w the horizontal and vertical velocity components, (the normal to the NWT component $v = 0$); ψ the phase of each wave component i; z the distance from the bottom of the NWT; $x = 0$ m, horizontal distance from inlet boundary and t the time.

The numerical schemes for the spatial and temporal discretization of the partial differential equations (PDEs), which were selected after preliminary investigations being identical in the study of Vyzikas et al. (2018b) and are elaborated in (Ransley, 2015). "backward" second order, bounded, implicit time scheme is used for the time integration; "Gauss linear corrected" for the discretization of the Laplacian terms, which is a central differencing (linear interpolation) unbounded, second order, conservative scheme; second order Gaussian integration with linear interpolation for the gradient terms; Gauss second order unbounded with MUSCL (Monotonic Uwind-centered Scheme for Conservation Laws) and vanLeer limiters for the divergence terms. The GAMG (generalised geometric-algebraic multi-grid) solver with DIC smoother is used for the pressure equations and DILUPBICG (preconditioned bi-conjugate solver for asymmetric matrices with DILU (Diagonal Incomplete L unit lower triangular and U upper triangular) preconditioner) is used for the velocity equations. The MULES (multi-

dimensional limiter for explicit solution) is used to guarantee boundedness of scalar fields especially in phase or mass fractions (OpenCFD, 2012).

Convergence tests

The quality of a numerical simulation depends both on the equations and numerical schemes used, but also on the grid resolution. Convergence studies are essential when designing a NWT for simulating a specific problem and especially when advanced methods, such as the VoF, are employed, as highlighted by Kleefsman et al. (2005). Commonly, a convergence study is performed on the basis of increasing the resolution of the domain and comparing the consecutive outputs of the model. Here, convergence was performed both in spatial and temporal terms by evaluating combinations of cell size and Courant number (C_o), which controls dynamically the time step. Additionally, instead of comparing the recorded surface elevation only, the signal was analysed in harmonics and the discrepancies observed could be traced more effectively. For each combination of cell size and C_o, the methodology for focusing waves was applied separately in order to achieve consistent comparisons of the wave "dispersion" characteristics among the NWTs.

After preliminary investigations, some representative results are selected for the strongly nonlinear wave group and shown in Figure 3.16 as combinations of R and C, where R is the minimum cell size in mm and C is the value of C_o, which was selected to be the same as $alphaC_o$, referring to the C_o at the free surface (Vyzikas et al., 2017b). In general, it can be seen that coarser resolutions and higher C_o result in higher crest of the focused wave and slightly worse focusing (Figure 3.16A), which is mainly due to the overestimation of the 3^{rd} order harmonics (Figure 3.16c). This is the opposite case from that observed in Figure 3.11c, but in that case the AM and PF coincided. Normally, coarser resolution causes numerical dissipation and thus, decrease of the wave height along the tank. However, this is not the case here as the amplitude spectrum is corrected at AM, partially compensating for some energy losses. Similar issues with

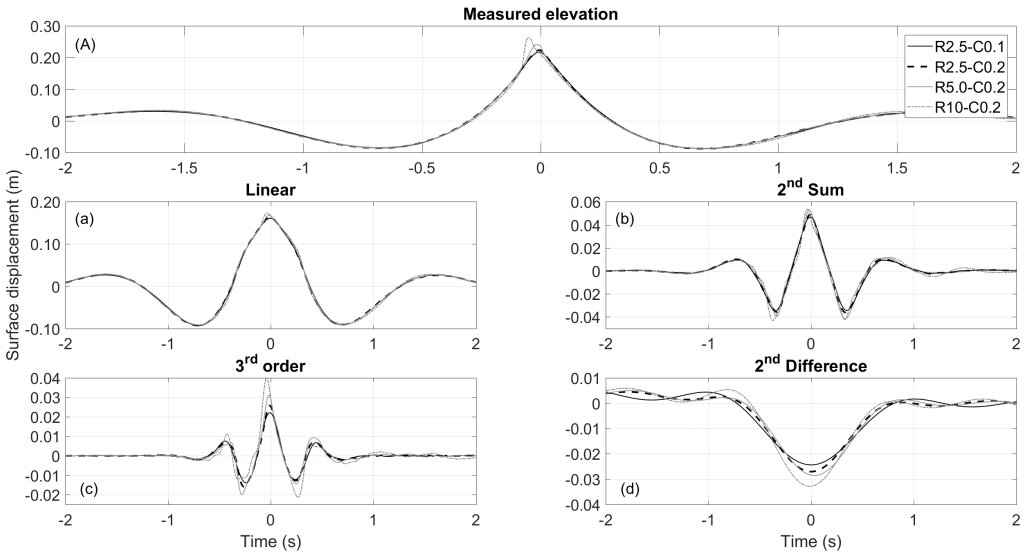

Figure 3.16: Convergence study for different grid resolutions (R in mm) and Courant numbers (C): (A) Total measured elevation at PF; (a) Extracted linear harmonic, (b) 2^{nd} sum, (c) 3^{rd} order harmonics, (d) 2^{nd} difference harmonic at PF.

overestimation of high order harmonics in focused waves simulated with OpenFOAM and waves2Foam were reported in (Yan et al., 2015). On the other hand, negligible differences are observed for the linearised harmonics (Figure 3.16a), which are corrected by the methodology for focusing waves and the 2^{nd} sum harmonics (Figure 3.16b). Considerable overestimation of the set-down, caused by the 2^{nd} difference harmonics, is observed for the more "relaxed" conditions (R10-C0.2) in Figure 3.16d.

Regarding the computational cost of the simulations, the time varied from approximately 1, 5, 35 and 50 hours for the R10-C0.2, R5.0-C0.2, R2.5-C0.2 and R2.5-C0.1 cases respectively for the steepest crest focused wave group. All simulations were conducted in parallel on a 16-core Intel Xeon E5-2650 @ 2.6GHz, using the simple decomposition method, since the cells were uniformly distributed in the $x-$direction. For the same grid resolution (R2.5), increasing the C_o from 0.1 to 0.2 results in approximately 35% faster simulations, but discrepancies are already noticeable for the 3^{rd} order harmonics and 2^{nd} difference harmonics. For the results that follow, the R2.5-C0.1 set-up was used, which discretizes the 20 m long domain with 2.48 M cells correspond-

ing to $L_p/dx = 1435$, where L_p is the wave length of the peak-frequency component and $dx = dy = 0.0025$ m, and $H_{PF}/dy = 120$ cells for the wave height at PF. It should be noted that this is an exceptionally high resolution and low C_o compared to that commonly used. e.g., C_o=0.5 and $L/dx = 240$ (Chen et al., 2014), but it was deemed necessary for performing a bench-mark study.

Validation

Before proceeding to the validation it is necessary to highlight the differences between the physical and the numerical flumes, which cause some inevitable discrepancies and explain better the obtained results, namely, the propagation of the individual harmonics. The main differences between the two flumes were:

(i) The wave generation was performed by a flap-type moving wave paddle in the laboratory and a stationary boundary in the numerical model, but both had linear transport functions.

(ii) The absorption of the waves was achieved by a parabolic beach in the physical flume and an outlet stationary boundary with active absorption in the NWT.

(iii) The recording of the free surface displacement in the physical flume had a measuring accuracy of $\pm$ 1 mm, while in the numerical model it was measured exactly at the location of the interface ($\gamma_i = 0.5$) by interpolation.

The comparison between the experimental and the numerical results is presented first as the total measured free surface elevation at the AM and PF locations and then separately for each harmonic at all the WGs listed in Table 3.3 apart from WG5, which is very close to WG6 and the conclusions from their results are similar. When validating a numerical model for the evolution of wave groups, it is crucial to perform the comparison with the experimental results at various locations in order to verify that the evolution of the group is consistent. It is possible to match the surface elevation at one location, but

this does not guarantee that the kinematics are similar, since this matching may be a result of cancellations of waves travelling to different directions.

The overall free surface elevation is shown in Figure 3.17a and 3.17b at the AM and PF location, respectively. The agreement between the numerical and the physical model is almost excellent for both locations, but more discrepancies are observed at the AM, where the first large waves in the group between -13 s and -11 s seem to be slightly ahead in the experiment and the two highest crests to be greater in the numerical model. Also, the free surface in the NWT seems to have some short waves (wiggles), which are probably an artefact of the boundary conditions of IHFOAM, initially seen in Figure 3.8a. These short waves eventually separate from the group, as explained in (Vyzikas et al., 2018b), and because of their smaller celerity they do not appear at PF, where the agreement is almost perfect. At PF the crest height and troughs are practically identical occurring at the same time without any adjustment of the recorded signal during the post-processing, as commonly done in most of the existing studies to achieve good comparison (see Section 2.2.1). The only observable differences are lateral of the adjacent crests and in the main crest which seems to be marginally steeper in the numerical model immediately after the focal time. These observations are supported with the error plot (dotted line in Figure 3.17b), which is calculated as the subtraction of the numerical from the experimental timeseries, and it demonstrates that the main discrepancy appears after the main crest.

The dispersion of the extracted linearised part[2] of the spectrum is the most important aspect in the propagation of the wave group as a whole, mainly because it constitutes the harmonics with the highest energy, but also because it determines the evolution of the associated bound waves. The extracted linearised harmonics in this study are considered to represent the free-wave regime, which propagate "freely" according to the linear dispersion relation. As explained in Section 2.2, during the focusing of the wave group there is a considerable transformation of the free-wave spectrum due to

[2]It is noted that the four-wave decomposition is performed using exactly the same parameters for the windowing of the signal and the necessary filtering for all the results that follow, done automatically for consistency.

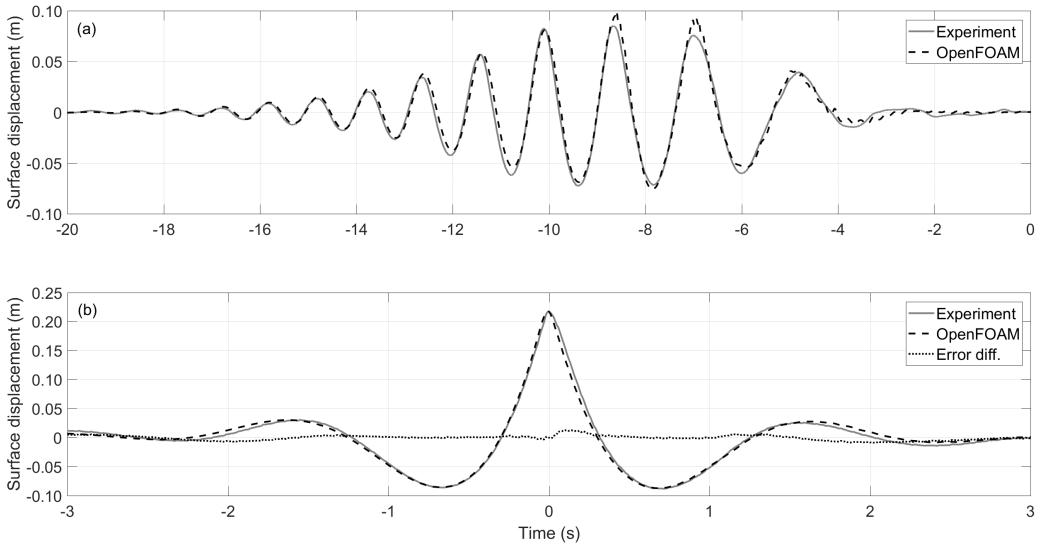

Figure 3.17: Comparison of the total measured surface elevation between the experiment and numerical model (OpenFOAM) at (a) at AM and (b) at PF location.

nonlinear wave-wave interactions, which for some cases may have a major role to the evolution of the wave group (see e.g., (Johannessen and Swan, 2003)). The minimum requirement for a numerical model in order to be reliable for the propagation of wave groups is its validation for the propagation of the linear waves, including the resonant / non-resonant interactions. The emergence of nonlinear bound harmonics then depends on the order of nonlinearity of the NWT. Figure 3.18 shows that excellent agreement between the numerical and the physical results regarding the evolution of the extracted linearised harmonics after the input signal is corrected with the methodology for focusing waves is achieved. Some negligible discrepancies are only observed before and after the main wave group. It is shown that the signal starts from a well-dispersed form in Figure 3.18a and gradually becomes compact towards focusing in Figure 3.18f. The scale of the $y-$axis is the same for all subplots in order to allow better observation of the increasing steepness.

Next, the extracted 2^{nd} order summation terms are presented in Figure 3.19. The first thing to observe is that the magnitude of the 2^{nd} sum harmonics is almost 5 times higher at PF than at AM, because the wave group becomes steeper at focus and there

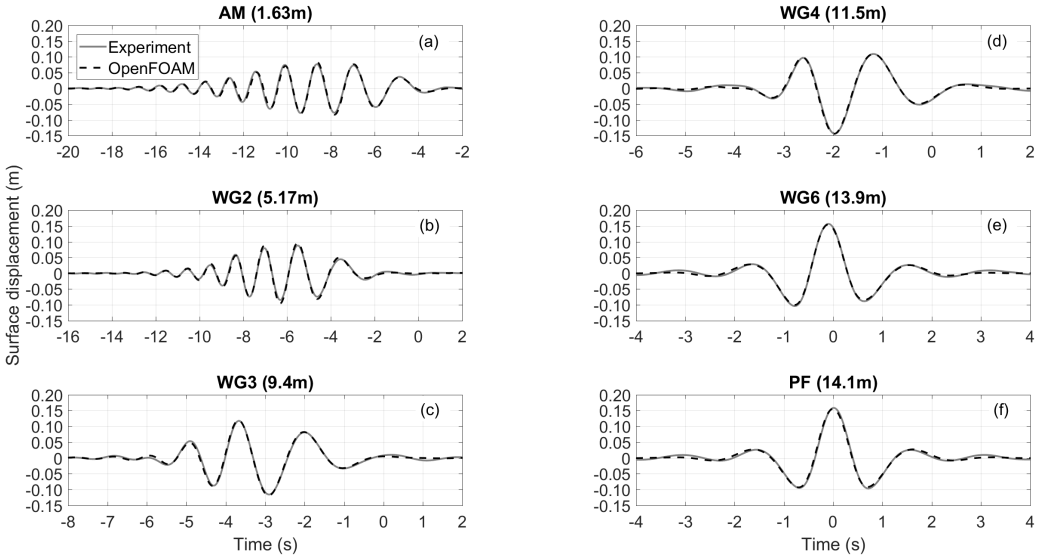

Figure 3.18: Comparison between the experiment and numerical model (OpenFOAM) of the timeseries of the extracted linearised harmonics at six locations from AM to PF.

is more energy transfer to bound waves. These energy transfers are also discussed in greater detail in Section 4.1. Comparing the corresponding subplots of Figures 3.18 and 3.19, it can be seen from the time scale that the 2^{nd} sum harmonics are bounded to the wave group and have double the frequency of the linearised harmonics (double number of crests in the same time range). Regarding the comparison of numerical and experimental results, it is seen that the agreement is almost perfect from WG3 until PF, but it is less impressive closer to the boundary at AM and WG2. This is due to a second group of waves existing at the tail of the signal. This group causes discrepancies close to the boundary (AM), but it appears to start separating from the main group at WG2 and eventually, it is left behind travelling at a lower celerity, despite the fact that its components have similar frequencies as the main 2^{nd} sum group. As discussed in (Vyzikas et al., 2018b), the reason for this is that this second group consists of spurious free waves that are not bounded to the linear group and thus travel slower than the 2^{nd} order bound waves. The creation of these waves is due to the linear wave generation, as explained in Section 2.2.2. Due to different wave generation between the physical and numerical tank, e.g., moving paddle and stationary boundary, the free

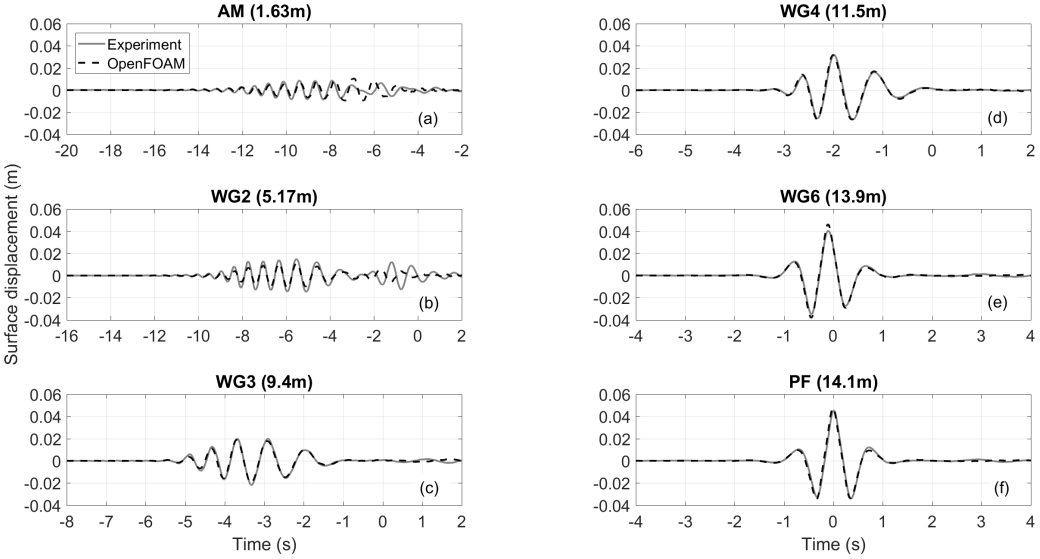

Figure 3.19: Comparison between the experiment and numerical model (OpenFOAM) of the timeseries of the extracted 2^{nd} order sum harmonics at six locations from AM to PF.

spurious waves are not identical, but the physical mechanism remains the same. Once the spurious waves are separated at $2L_p$ downstream of the inlet boundary, the agreement becomes excellent. The present results indicate that caution should be taken when simulating focused waves, in order to allow enough propagation for free spurious waves to separate from the group and not contaminate the result at the examined focal location.

The evolution of the 3^{rd} order harmonics in Figure 3.20 has similar characteristics to that of the 2^{nd} order sum harmonics. There are considerable discrepancies close to the inlet boundary at AM, but already at WG2 the spurious free waves separate from the main group and the agreement is nearly excellent at all the other locations until PF. These differences, close to the wave paddle, might be caused by the discrepancies induced by the wave generation mechanism of IHFOAM (see Figure 3.8a). Nonetheless, such impressive agreement at PF has not been observed in previous studies (Chen et al., 2014; Fitzgerald et al., 2014). By comparing the corresponding subplots of Figure 3.18 and 3.20, it can be seen that the 3^{rd} order harmonics are bounded to the linear

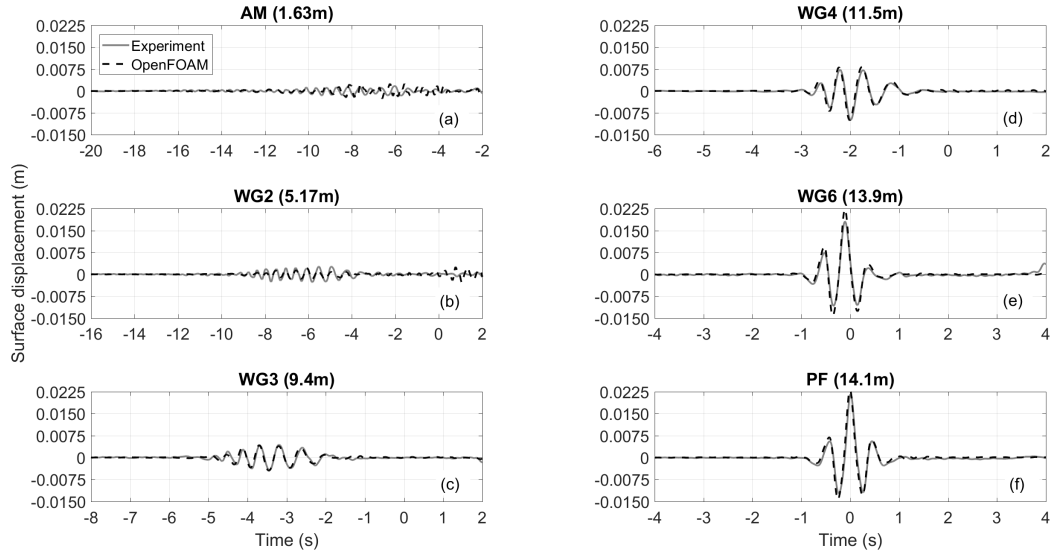

Figure 3.20: Comparison between the experiment and numerical model (OpenFOAM) of the timeseries of the extracted 3^{rd} order harmonics at six locations from AM to PF.

harmonic and they have approximately three times higher frequency (see for example the length of the timeseries that includes the corresponding harmonics at PF). It is also observed that the 3^{rd} order harmonics increase in amplitude only close to PF (WG6 and PF) where the group is sufficiently steep, while at AM and WG2 their energy is negligible.

Last, the evolution of the extracted 2^{nd} order difference harmonics is examined in Figure 3.21. The 2^{nd} order difference harmonics appear as a long bound wave causing a set-down under the wave group and having its maximum amplitude when the wave group is focused, as suggested by 2^{nd} order theory (Sharma and Dean, 1981). These general characteristics are observed here as the wave group approaches the PF location, where the numerical result reaches its best agreement with the experiment. However, as noted earlier in Figure 3.7d, there is a preceding long wave causing a surge in the NWT. Here, it can be seen that this surge is already created close to the boundary, at AM, and continues to travel ahead of the wave group. This suggests that the surge in the NWT may be an artefact of the boundary conditions of IHFOAM. As shown in Figure 3.9, the surge is slightly smaller when the boundary conditions of waves2Foam

are employed. At WG2 a small surge is also observed in the physical flume, but it does not seem to be present at downstream positions. This surge cannot be readily justified in the experiment, unless it is a free displacement wave from the moving paddle. The set-down becomes more noticeable from WG3 onwards and it becomes maximum at PF, where the difference between the numerical and the physical model is 3.8 mm, approximately 15 % of the maximum local surface displacement. At the last two WGs, a second wave is observed in the experiment at times 2-4 s that appears to have opposite direction of propagation of the main wave group, which is likely to be a sign of reflection. In the numerical model, the reflections arrive later, because in the experiment the mechanical beach extends upstream in the flume and thus, reflection is expected to begin earlier. The appropriate windowing of the signal in the analysis in the present study eliminated the influence of the reflection on the numerical results.

Previous studies also showed that the comparison of the long waves is very challenging, due to the different wave generation and absorption mechanisms in the physical and numerical tanks. The movement of the wave paddle can cause long spurious free waves in the physical model that are not present in the numerical model. At the same time, absorption of long waves in the numerical model is not a trivial issue. The analysis of the performance of the absorption of IHFOAM, either performed by pseudo-active absorption method (Higuera et al., 2013c) or by a moving wave paddle (Higuera et al., 2015), shows that reflections are present in the NWT and the long waves may not be accurately handled. Even when a damping layer, like a relaxation zone, is used for the wave energy dissipation at the end of the tank, an effective absorption of the long wave is nearly impossible (see Figure 2 in (Chen et al., 2014)). As discussed earlier, in the present study, the only remedy found for limiting the reflected waves was the placement of the outlet boundary far from the focal point, so that any reflected waves would require more time to reach the PF location.

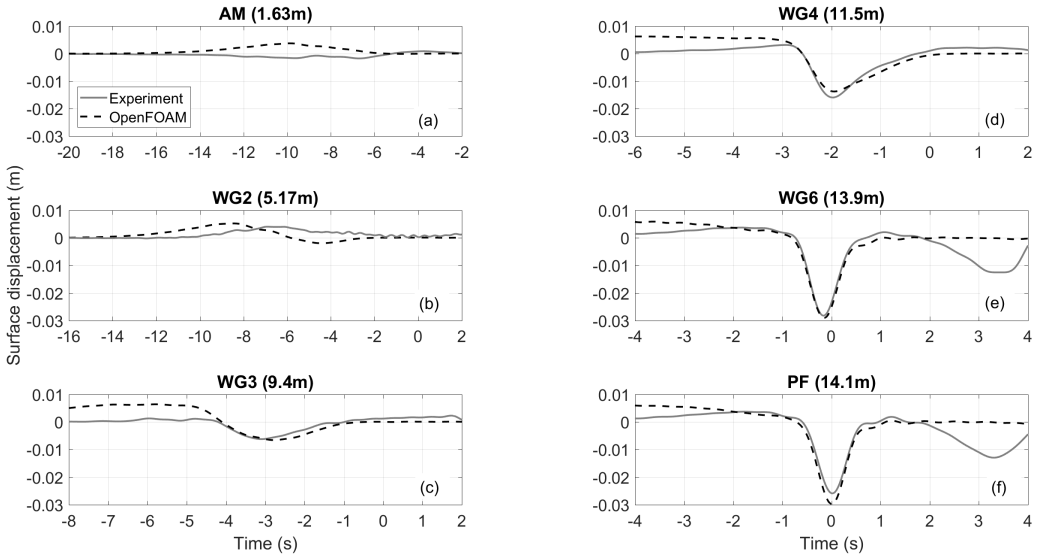

Figure 3.21: Comparison between the experiment and numerical model (OpenFOAM) of the timeseries of the extracted 2^{nd} order difference harmonics at six locations from AM to PF.

3.3.3 SWASH

The validation section of the NWT in SWASH, follows the same structure as that presented for OpenFOAM in the previous Section 3.3.2. At first a convergence analysis is presented, which is briefer than that of OpenFOAM and then, the comparison with experiments is shown for the measured surface elevation and for the individual harmonics.

Although the set-up for the SWASH NWT used in Section 3.2.3 (see the work of Vyzikas et al. (2015)) has much higher resolution and accuracy than those commonly used for engineering applications (1-2 layers), here, a further refinement is used to verify the accuracy of the NWT. In the convergence analysis for SWASH, the vertical resolution used in the initial validation (6 layers of 5, 10, 15, 20, 25, 25% thickness of the water depth) was compared to another higher resolution, where the number of layers was increased to 8 layers of 2, 4, 9, 15, 15, 20, 20% thickness of the water depth, because the water depth was increased from 0.5 m to 1 m (see Table 3.2). Additionally, a hyperbolic distribution for the horizontal velocity per layer was employed

instead of the default uniform distribution (The Swash Team, 2014) that was used in the initial validation (Section 3.2.3). The hyperbolic distribution induces higher accuracy, especially for the high frequency components in deep water. It should be noted that, similarly to the convergence of OpenFOAM (Section 3.3.2), for the new set-up of the SWASH NWT, all the corrections of the methodology were performed until the group was focused. The high resolution NWT is 30 m long following the design of the initial validation. The wave absorption is achieved by a 10 m long sponge layer starting at 20 m, which is sufficiently far from the PF, so that any reflections arrive with delay and do not contaminate the signal in the examined time window. The input signal comprised a discrete spectrum of 320 wave components between 0.0078 - 2.5 Hz, reproduced at the inlet as a summation of linear waves.

The convergence check for SWASH is presented in Figure 3.22. The difference at the measured surface elevation in Figure 3.22A is only 1 mm with the higher resolution giving a higher crest elevation, but, as the time history of the surface elevation shows, the shape of the wave group is practically identical. The linear harmonic in Figure 3.22a has the same amplitude and phase between the two resolutions. The case is similar for the 2^{nd} sum harmonics in Figure 3.22b. The 3^{rd} order harmonics are about 0.6 mm higher for the high resolution NWT (Figure 3.22c), but still the agreement is almost excellent. The greatest discrepancies are observed for the 2^{nd} difference harmonics, which are 1.7 mm lower (in absolute terms) for the low resolution NWT (Figure 3.22d), and also slightly wider. It is interesting to observe that the measured surface elevation is not identical to the sum of its harmonics, due to the filtering of very high and low frequencies during the separation of the harmonics. Nevertheless, this does not constitute an issue in the analysis, since there is consistency on the way the individual harmonics are extracted and compared for all the numerical models. For the validation of SWASH presented hereafter, high resolution NWT was used, which induces about 30% higher computational cost.

The total measured surface elevation of SWASH is compared with the experiment in

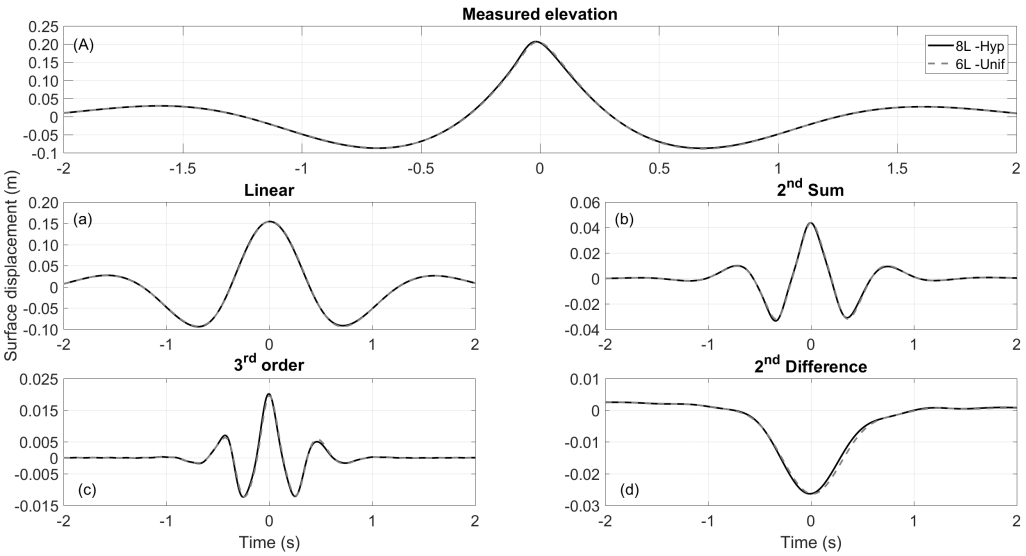

Figure 3.22: Convergence test for the SWASH NWT, where L refers the number of vertical layers and Hyp and Unif to hyperbolic and uniform horizontal velocity distribution per layer respectively.

Figure 3.23a and 3.23b at the AM and PF locations. In general, the agreement is very good, but more discrepancies are observed at the AM, especially at the highest crest and last trough, where SWASH overestimates the crest by 16.4 mm and underestimate the trough by 7.8 mm, corresponding to a 21.5% and 13% difference compared to the experiment, respectively. At PF, the shape of the simulated group is in good agreement with the experiment, however the latter is slightly steeper and higher by 10.5 mm, corresponding to 4.8% of the measured crest elevation. This result supports the conclusion for the initial validation of SWASH, showing that it cannot simulate a wave group as steep as in the experiment or OpenFOAM (see Figure 3.10). The error plot (dotted line in Figure 3.23b) also shows that the sole discrepancy is at the crest, where the experimental result is higher. The lateral crests are very well predicted with practically zero error.

Regarding the evolution of the individual extracted harmonics, very similar observation to that done for OpenFOAM can be made. Briefly, after the correction with the focusing methodology, the linearised harmonic is practically in perfect agreement with the

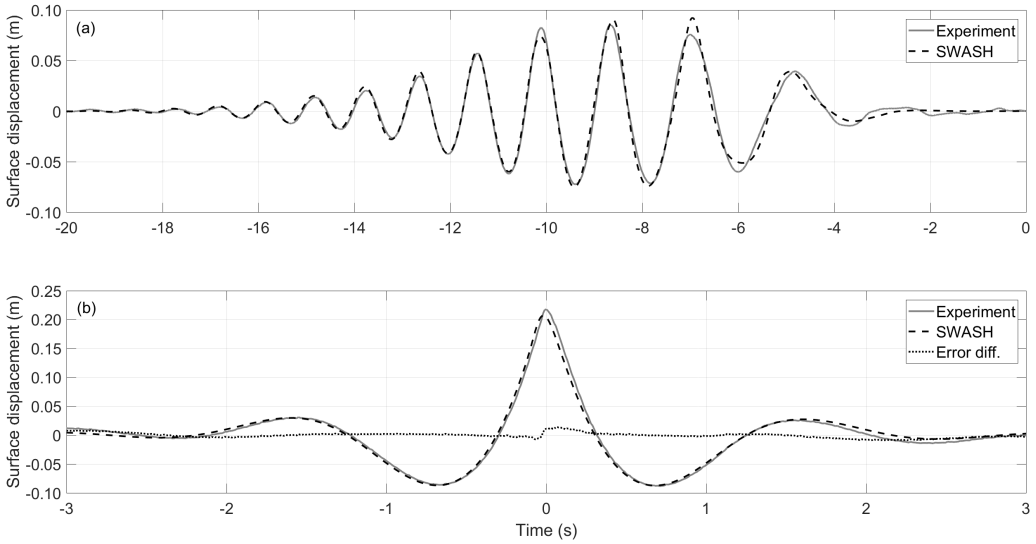

Figure 3.23: Comparison of the total measured surface elevation between the experiment and numerical model (SWASH) at (a) at AM and (b) at PF location.

experiment, as shown in Figure 3.24. For the 2^{nd} sum harmonics in Figure 3.25, the agreement improves as approaching the PF point, where it is almost excellent, since the spurious free waves that cause the discrepancies start separating from the group after WG2. The 3^{rd} order harmonics presented in Figure 3.26 are also in very good agreement, especially towards the PF point, where in this case the numerical model underestimates the crest by only 1.6 mm (7.3% of its crest height), confirming in a clearer manner the earlier observations (see Figure 3.11c). It is also interesting to note that, after careful examination of the results, close to the boundary at AM and WG2, 3^{rd} order harmonics have somewhat smoother timeseries compared to those reproduced in OpenFOAM, shown in Figure 3.20a and 3.20b, indicating that the inlet boundary of SWASH does not induce the high frequency spurious waves as that of IHFOAM. The 2^{nd} difference harmonic, presented in Figure 3.27, shows a very good agreement with the experiment, with the exception of WG2, where the experiment exhibits the unexpected crest. This comparison is better than that of OpenFOAM, since the spurious preceding crest is not present, confirming the earlier observation in Figure 3.11d. At PF, the trough of the 2^{nd} difference harmonic is practically the same as that extracted from the experiment.

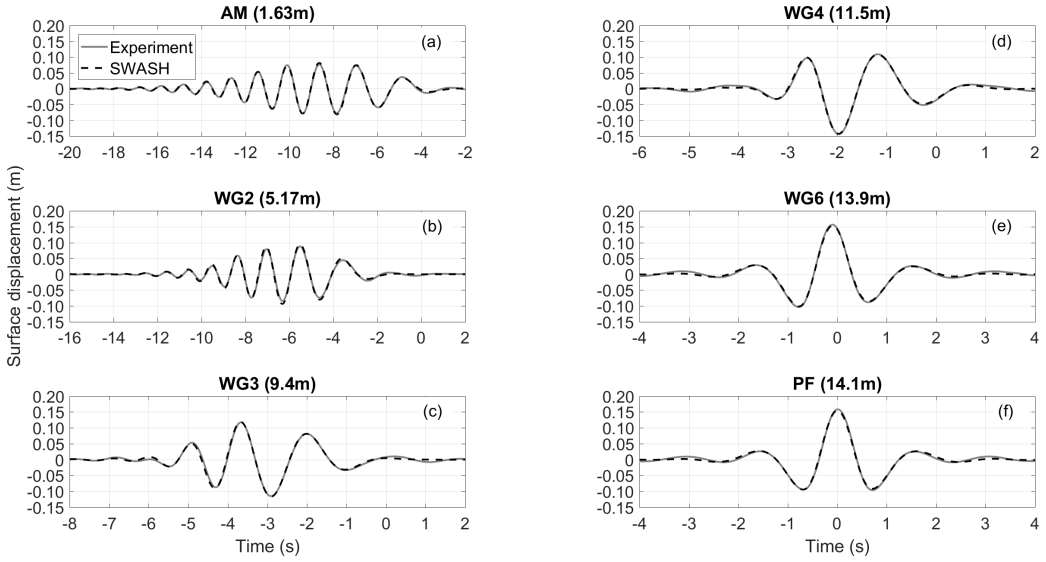

Figure 3.24: Comparison between the experiment and numerical model (SWASH) of the timeseries of the extracted linearised harmonics at six locations from AM to PF.

3.3.4 HOS-NWT

HOS is a high-order pseudo-spectral model, which is described in Section A.3. The main reason for deciding to employ the HOS-NWT for the simulation of focused waves is its computational efficiency, resulting in approximately 30-60 times lower computational cost compared to SWASH, which is already orders of magnitude faster than OpenFOAM. The validation of the HOS-NWT is also important in the present study for another aspect: to validate in detail the HOS method in order to employ the HOS-ocean version of the model for random phase simulations used for the Monte Carlo analysis with greater confidence. In this way, the Monte Carlo simulations can be used to compare the results for the spectral evolution produced from the phase-averaged models later in Chapter 4. Despite their efficiency, the HOS-NWT and HOS-ocean have an intrinsic limitation: only constant depth can be considered and as consequence, no submerged (or surface piercing) structures can be modelled. This is not an issue for the present study, but it can be a constraint for engineering applications.

HOS-NWT has been employed in previous studies for simulating extreme waves, but,

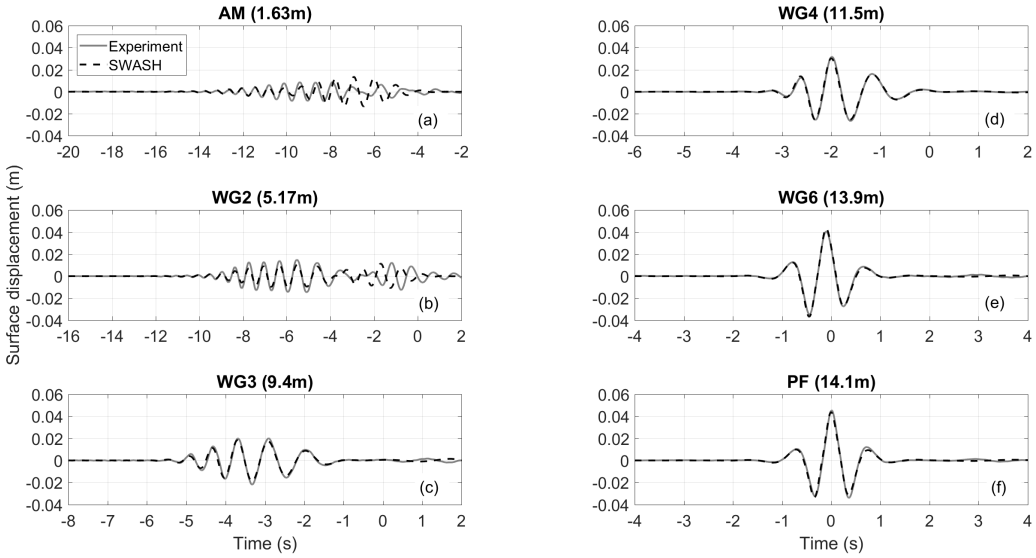

Figure 3.25: Comparison between the experiment and numerical model (SWASH) of the timeseries of the extracted 2^{nd} order sum harmonics at six locations from AM to PF.

to the best of the author's knowledge, it has never been validated against experimental results for steep focused wave groups, nor the individual harmonics have been examined prior to the present study. The available comparison with experimental results refers to a 3D focused wave group of low steepness and a unidirectional group of moderate steepness (Ducrozet et al., 2012b), showing relatively good agreement for the total surface elevation, but the wave groups are not well focused. Therefore, the validation of HOS-NWT is deemed necessary. In this section, the NWT is compared with the experimental results in the same fashion as before for OpenFOAM and SWASH, after performing a convergence analysis.

The version used here is the 2016 and until the moment of writing the present study, no major modifications were made to the code, apart from some bug fixes (see Section 4.7.1). It is important to note that apart from the predefined spectra included in the release of the code, namely JONSWAP and Bretschneider, there was no option of adding arbitrary spectra. A pre-processing tool was developed by the author in MATLAB that circumvents this constraint and allows for the definition of an arbitrary amplitude spectrum, providing more flexibility and enabling the use of the focusing methodology.

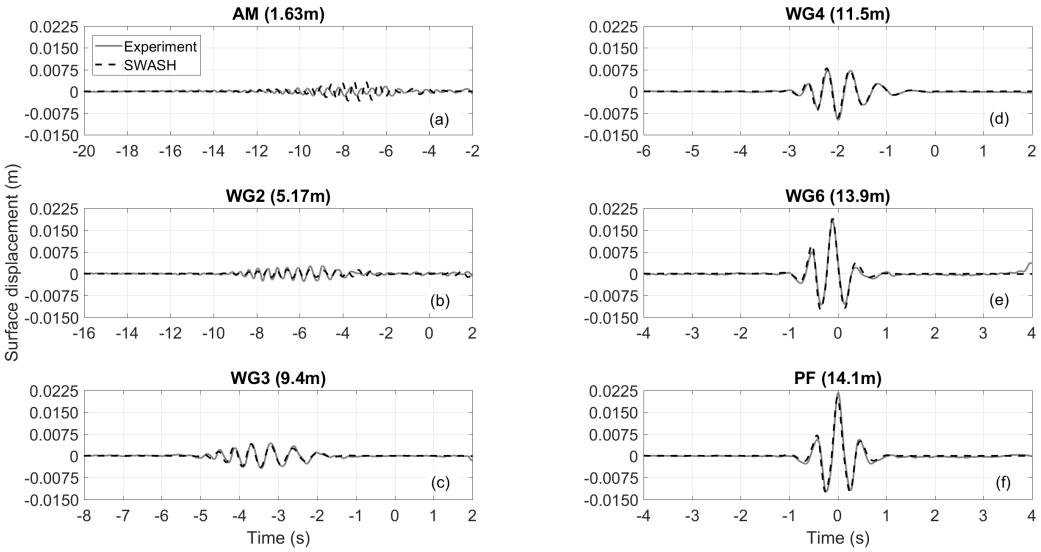

Figure 3.26: Comparison between the experiment and numerical model (SWASH) of the timeseries of the extracted 3^{rd} order sum harmonics at six locations from AM to PF.

The main parameters in the HOS-NWT are the number of nodes/modes in $x-$direction ($N1$), in $y-$direction ($N2$), at the wavemaker ($N3$), the dealiasing in $x-$ and $y-$direction ($p1$ and $p2$ respectively) and the HOS nonlinearity order ($mHOS$). These parameters are defined in the `common_vars.f90` and for every modification, the model has to be recompiled. For a 2D simulation of unidirectional wave groups, $N2 = p2 = 1$. As common practice suggests, full dealiasing was used by defining $p1 = mHOS$. HOS-NWT offers the possibility to simulate different types of wavemakers (hinge and piston of linear or higher order motion). Here, a linear piston wavemaker starting at the bottom of the flume was used. It is noted that for intermediate or deep water waves the use of a flap-type wavemaker is more appropriate, but the focusing methodology corrects any discrepancies. To allow for smooth starting of the simulation, a linear-type ramp-up time of 5 s is selected. The length of the NWT is 50 m and the depth is 1 m. An absorption zone (numerical beach) is set at the end of the NWT, starting at 40 m and occupying 20% of the numerical domain. Different lengths of the NWT were initially tested, in order to examine any potential reflections at the PF location, but the aforementioned set-up was deemed sufficient. The maximum sampling frequency of the WGs allowed in the model is selected (50 Hz) for the sampling of the free surface displacement,

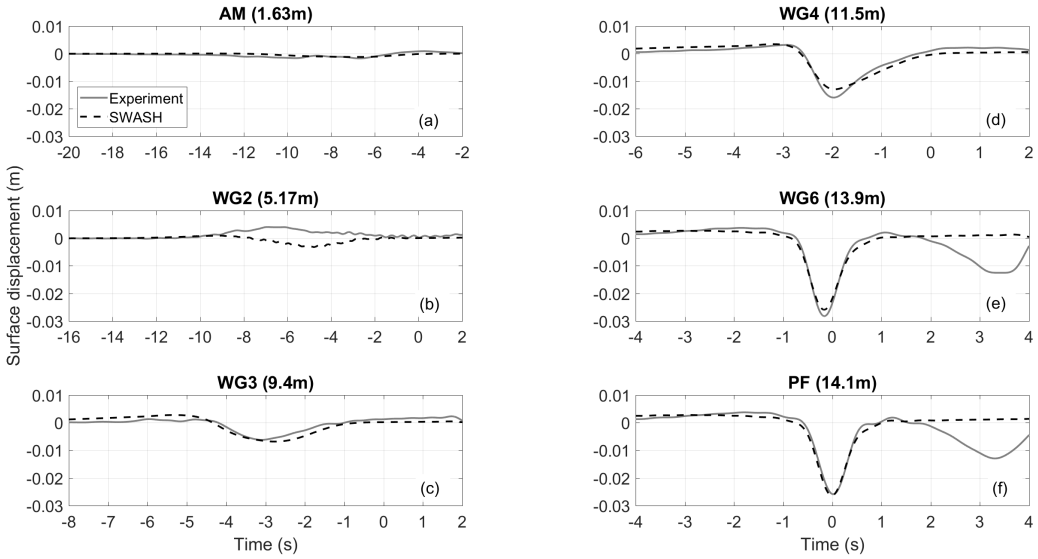

Figure 3.27: Comparison between the experiment and numerical model (SWASH) of the timeseries of the extracted 2^{nd} order difference harmonics at six locations from AM to PF.

with the WGs being at identical locations as in the physical flume[3]. The full length of the timeseries was simulated from 0 to 128 s. A Runge-Kutta 4^{th} order scheme is available for the integration in time, which tolerance is selected at 10^{-4} after tests. All the previous parameters are included in the `input_HOS-NWT.dat` file, where also the "type" of the examined case ($icase$) has to be defined. For the present NWT, $icase = 3$ was used as the basis, referring to a wavemaker with an amplitude-frequency spectrum as input, which, was prepared with MATLAB.

The convergence of the HOS-NWT is performed by examining the three main parameters of the model, i.e. $N1$, $N3$ and $mHOS$, using as input wave spectrum the final corrected spectrum from IHFOAM. Independent convergence with the focusing methodology was decided not to be performed because of the high number of combinations among the examined parameters. The values initially selected for the convergence test are taken from the tutorial cases: $N1$ is power of 2 plus one extra mode and $N3 = 33$, as suggested in the tutorial. The convergence analysis was planned according to the

[3]The results were interpolated to 100 Hz sampling frequency in the post-processing for consistency in the comparisons.

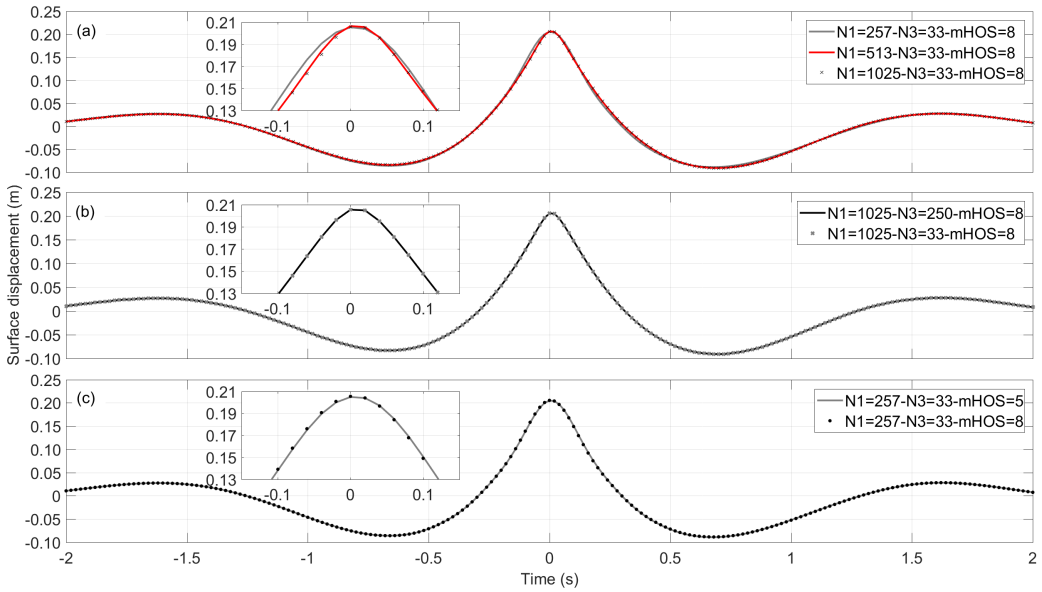

Figure 3.28: Convergence HOS-NWT: (a) Selection of $N1$; (b) Selection of $N3$ and (c) Selection of $mHOS$.

following strategy: for a high order of HOS, i.e., $mHOS = 8$, and the same $N3 = 33$, the value of $N1$ is examined (Figure 3.28a). Then, for $mHOS = 8$ and the selected $N1$ ($N1 = 1025$), the influence of $N3$ is examined. At the end, after selecting $N1$ and $N2$, the order of HOS is examined (Figure 3.28c). As it can be seen in Figure 3.28a, small discrepancies are observed for the lowest value of N1, but the agreement between $N1 = 513$ and $N1 = 1025$ is excellent. Thus, a value of $N1$ close to 513 can be selected. In Figure 3.28b, it can be seen that the increase of $N3$ does not improve the results of the simulation. Thus, any value of $N3$ higher than 30 is sufficient. Figure 3.28c, shows that the increase of the order of HOS does not cause any noticeable improvement on the results. $mHOS$ however is the parameter that increases the most the computational cost. For the results presented for the validation, the selected values of the HOS-NWT are $mHOS = 5$, $N1 = 500$ and $N3 = 40$ and with this selection, and the simulation is considered converged.

First, the comparison between HOS-NWT and the experiment is presented for the measured surface elevation in Figure 3.29. Similar to the observations for SWASH, at the AM point (Figure 3.29a), the last highest crest is overestimated by the numerical

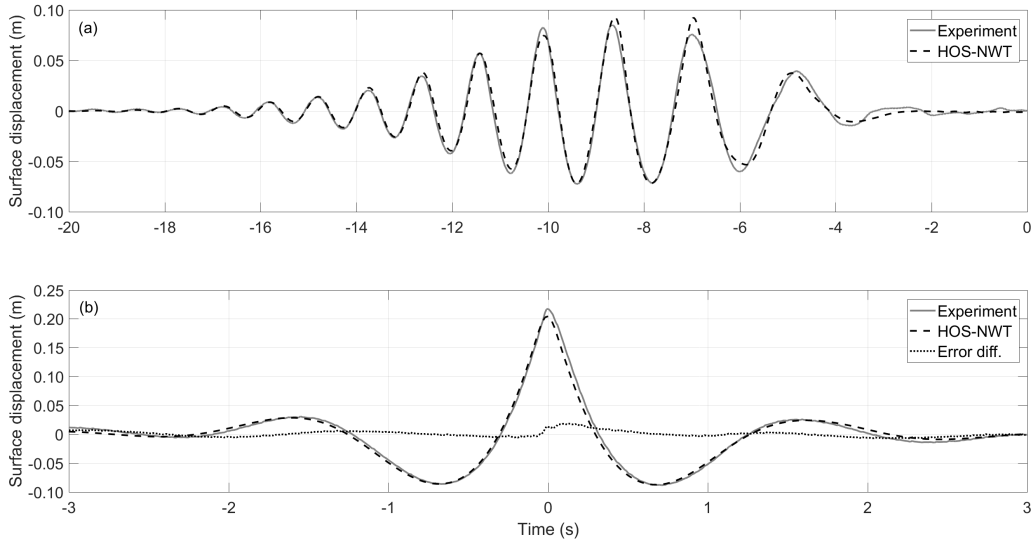

Figure 3.29: Comparison of the total measured surface elevation between the experiment and numerical model (HOS-NWT) at (a) at AM and (b) at PF location.

model, while the last trough is understimated. At PF (Figure 3.29b) the experimental crest is steeper and higher by 12.5 mm or 5.7% compared to the simulated wave group. The error plot in Figure 3.29b confirms that the main discrepancy is at the central crest and only minor differences are observed at its sides.

Similar to the other models, the extracted linearised harmonic of HOS-NWT is in excellent agreement with the experimental result, thanks to the application of the focusing methodology, as shown in Figure 3.30. The 2^{nd} sum harmonics in Figure 3.31 are also in very good agreement with those extracted from the experiment, especially after the spurious free waves are separated from the group beyond WG2. Similar is the case for the 3^{rd} order harmonics in Figure 3.32. These harmonics gain energy only when the wave group is close to focusing and, at PF, the numerical model underestimates the crest of the extracted harmonic by only 1.8 mm, corresponding to difference of 8.1% compared with the experiment. This is a remarkable agreement considering the computational efficiency of the model and the high steepness of the wave group. The greatest discrepancies between the numerical and physical results are observed for the 2^{nd} difference harmonic (Figure 3.33), as also noted for OpenFOAM and SWASH.

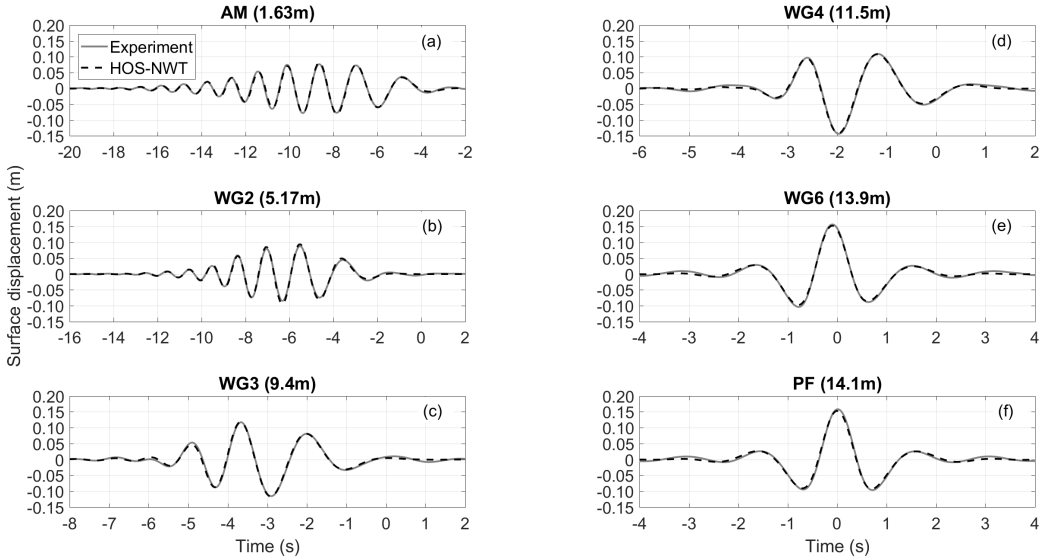

Figure 3.30: Comparison between the experiment and numerical model (HOS-NWT) of the timeseries of the extracted linearised harmonics at six locations from AM to PF.

Similar to SWASH and in contrast with OpenFOAM, HOS-NWT does not induce a spurious surge preceding the main trough. The results are similar, but slightly worse than those of SWASH. At PF, HOS-NWT overestimates the trough by 2.5 mm or 9.7%, with the shape of the trough being in very good agreement.

Even though not being part of the validation, another aspect referring to the order of the wavemaker is presented here. As it was observed in the previous sections, spurious waves were created from the linear motion of the wavemaker. HOS-NWT offers the possibility to examine, with low computational effort, the influence of the wavemaker at suppression of the spurious waves. It is expected that the use of a high order wavemaker will suppress the generation of the free spurious waves at the inlet; the 2^{nd} order wavemaker should decrease the spurious free long wave and the high frequency free waves of 2^{nd} order and the 3^{rd} order wavemaker should in addition not produce 3^{rd} order spurious waves. As seen in Figure 3.34a at WG3, where the high frequency free waves have separated from the main group, the magnitude of the 2^{nd} order free waves shown between 3-6 s is considerably smaller for the high order wavemakers. Also, the 3^{rd} order free waves following the wave group at 10-14 s seem

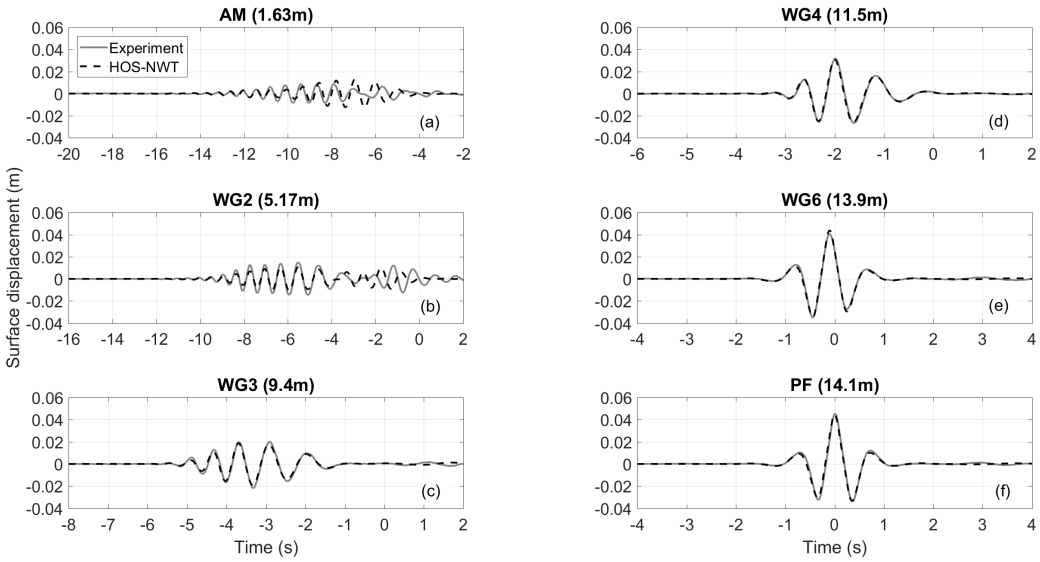

Figure 3.31: Comparison between the experiment and numerical model (HOS-NWT) of the timeseries of the extracted 2^{nd} order sum harmonics at six locations from AM to PF.

to be smaller for the 3^{rd} order wavemaker. At the PF location in Figure 3.34b, three things can be observed: a) the spurious long wave surge, shown between -8 s and -2 s, seems to be caused by the linear wavemaker, since it is decreased significantly for the high order wavemakers; b) the crest height seems to be 2 mm higher for the high order wavemakers and c) the spurious free waves of 2^{nd} order following the main group are smaller than that produced by the linear wavemaker. Note that at PF the 3^{rd} order spurious waves arrive after 15 s coinciding with the reflections from the outlet and for this reason are not presented here. Thus, the use of a high order wavemaker can be advantageous, but this does not imply that it will give better comparison with the experiment, especially if in the latter linear wave generation is used.

3.3.5 Intercomparison of phase-resolving models

Here a comparison among the numerical models that were validated in the previous sections is presented and the results are again compared with the experiments. This facilitates better interpretation of the numerical results and gives indications regarding

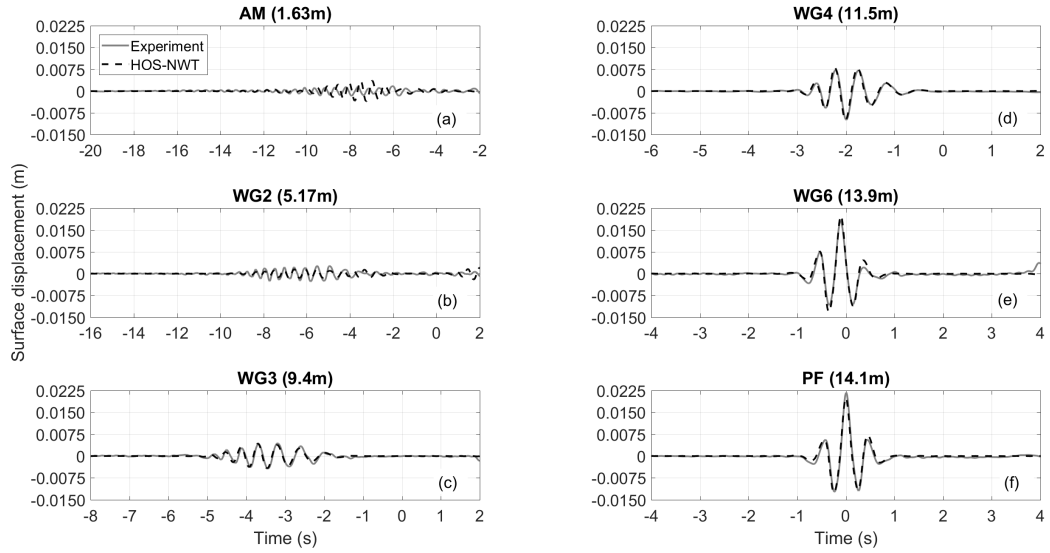

Figure 3.32: Comparison between the experiment and numerical model (HOS-NWT) of the timeseries of the extracted 3^{rd} order sum harmonics at six locations from AM to PF.

the possible use of an integrated approach of using a combination of high and low computational cost models.

The comparison is performed for the recorded free surface elevation at the PF location in Figure 3.35a and for the extracted individual harmonics at the same location, as shown in Figure 3.36. The quantitative comparison with the experiment is included in Table 3.5, as an absolute difference in mm and as a percentage (%) relative to the experiment. As seen in Figure 3.35a, all the numerical models have almost identical surface elevation and the only noticeable difference is at the crest height, where OpenFOAM produces a steeper crest, resembling better the experimental result. SWASH and HOS-NWT have practically the same crest height, being approximately 5% lower than the experimental result. Immediately after the focal time, the experimental crest is less steep, possibly because it is very close to breaking. This is not observed in SWASH and HOS-NWT, because wave breaking is not simulated properly, while for OpenFOAM, preliminary unpublished investigation showed that breaking occurs for slightly higher crests than in the physical model. Some differences between the numerical and experimental measurements are also observed before and after the lateral

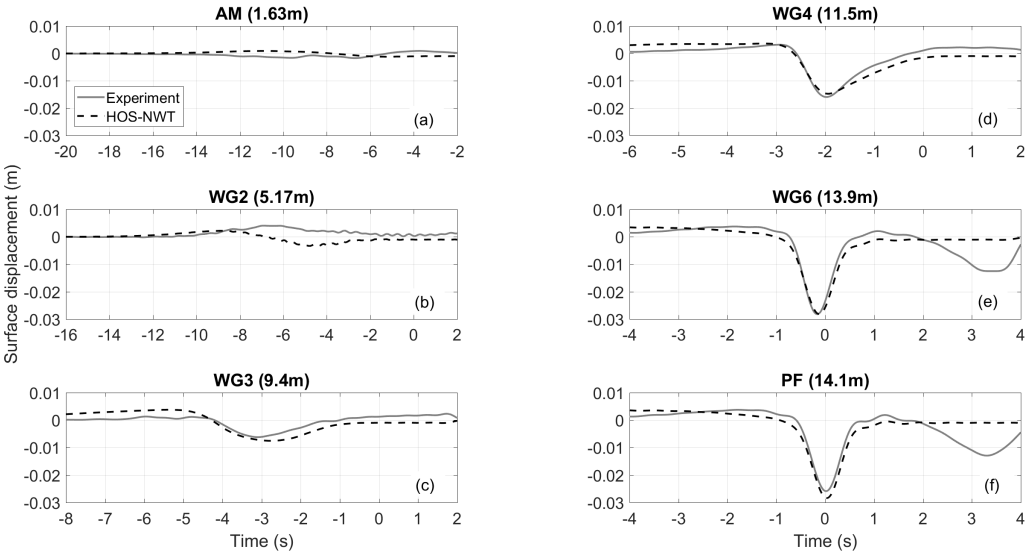

Figure 3.33: Comparison between the experiment and numerical model (HOS-NWT) of the timeseries of the extracted 2^{nd} order difference harmonics at six locations from AM to PF.

crests. To facilitate the comparisons, the error plots are included in Figure 3.35b, where it is seen that at the focal time ($t = 0$ s) only OpenFOAM has minimum practically zero difference, while SWASH and HOS-NWT have the same error. The greatest discrepancy is observed for HOS-NWT after the focal time.

Regarding the extracted harmonics, additionally to the linear, 2^{nd} sum, 2^{nd} difference and 3^{rd} order harmonics presented until now, the 4^{th} and 5^{th} order harmonics are also analysed here. The 4^{th} order harmonics are separated trivially by frequency filtering from the 2^{nd} difference, and 5^{th} order harmonics are taken out from the linearised harmonics in a similar manner[4]. The corresponding comparisons in Figure 3.36 and 3.37 confirm that OpenFOAM overestimates all the nonlinear harmonics. SWASH and HOS-NWT underestimate the high order harmonics up to 3^{rd}, but the 4^{th} and 5^{th} order harmonics are in almost excellent agreement with the experiment. A very good

[4]The 5^{th} order harmonics can be separated from the 3^{rd} and the linear harmonics and added together. However, this task requires very careful windowing in the spectral space and sometimes it may add bias, because there is overlapping of the harmonics. For the present case, the magnitude of the 5^{th} order harmonics within the extracted linearised harmonic is considerably greater than that included in the 3^{rd} harmonics. The former are always separated and the linearised harmonic is only considered up to 2.5 Hz, as seen in Figure 2.11.

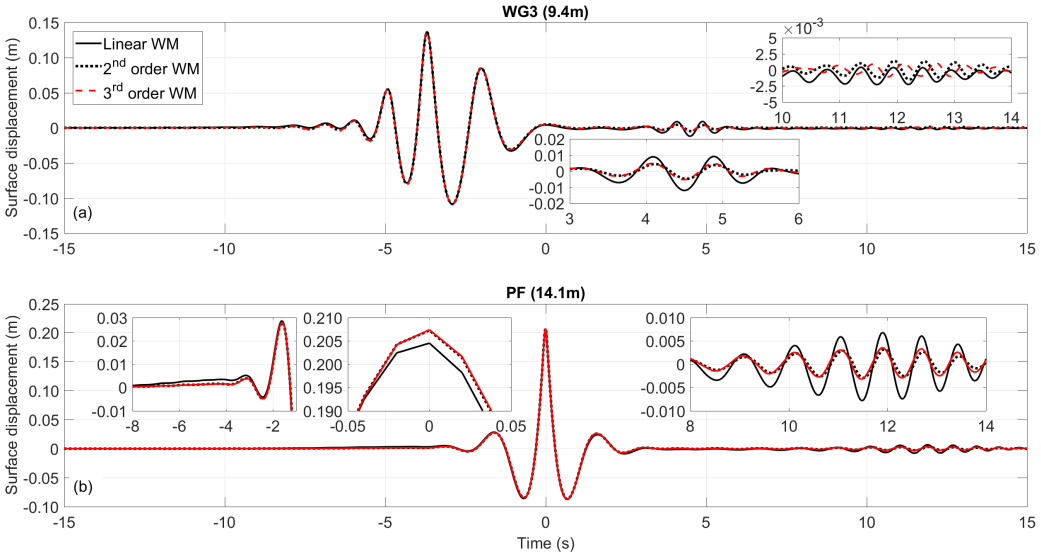

Figure 3.34: Comparison of the measured surface elevation at WG3 (a) and at PF (b) for the different orders of piston wavemakers (WM) at HOS-NWT with focus on the effects of high and low frequency waves.

agreement is achieved for the linear harmonics (Figure 3.36a), which amplitude spectrum was corrected by the methodology at the AM location, and the comparison at PF shows that all the NWTs can propagate the linear/free wave spectrum with sufficient accuracy. Nevertheless, the physical results have a higher crest than all the models, which seems to be one of the main reasons for the overall difference in the measured timeseries. As already demonstrated, the greatest discrepancies are observed for the 2^{nd} difference harmonics in Figure 3.36d, with OpenFOAM having a spurious crest before the main group and displaying similar trough as HOS-NWT. The best agreement in this case is observed for SWASH.

As seen in Table 3.5, most of the differences between the models are at the order of 1 mm. Apart from the fact that this is very close to the accuracy of the WGs in the experiment, it was observed that even the presence of WGs upstream of the PM marginally influences the wave profile for the steepest group, which can however alter considerably the (%) presented here. For this limiting case of the steepness of the wave group, and after taking into account the very good agreement between the models, one can even consider whether for these sub-millimetre differences the models' results should

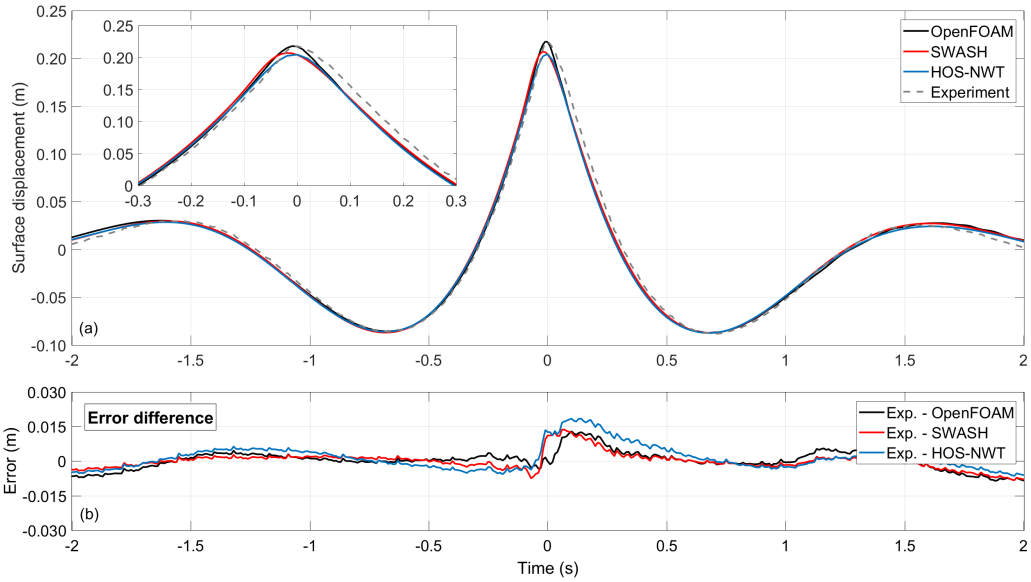

Figure 3.35: Comparison of the timeseries of the measured surface elevation at the PF location between the experiment and the phase-resolving numerical models (a) and error plots as difference between experiment and models (b).

be trusted more than the experiment. Moreover, it can be seen that the summation of the harmonics up to 5^{th} order is not exactly the same as the measured surface elevation, which implies that small amount of energy is also transferred at 6^{th} and higher harmonics that are filtered out in the present analysis. To the author's best knowledge this is the first time that 5^{th} order harmonics are analysed for three different NWTs and they show such a remarkable agreement.

Overall, the results show that OpenFOAM has the best agreement with the experiment

Table 3.5: Intercomparison of phase-resolving models at the PF location at the crest and through (2^{nd} diff). The experiment is used as the benchmark and the differences are expressed as absolute (mm) and percentage (%).

	Experiment	OpenFOAM		SWASH		HOS-NWT	
Total (measured)	217.5	0.2	0.1%	-10.5	-4.8%	-12.5	-5.7%
Linear	158.5	-3.3	-2.1%	-4.1	-2.6%	-5.3	-3.3%
2^{nd} sum	45.4	2.1	4.5%	-1.6	-3.4%	-0.7	-1.5%
2^{nd} difference	-25.9	-3.8	14.8%	-0.5	1.8%	-2.5	9.7%
3^{rd} order	21.7	1.5	6.7%	-1.6	-7.3%	-1.8	-8.1%
4^{th} order	8.8	1.8	20.2%	0.2	2.1%	0.1	1.6%
5^{th} order	5.3	1.4	26.1%	-0.2	-3.8%	-0.3	-4.8%
Sum of harmonics	213.9	-0.4	0.2%	-7.7	-3.6%	-10.3	-4.8%

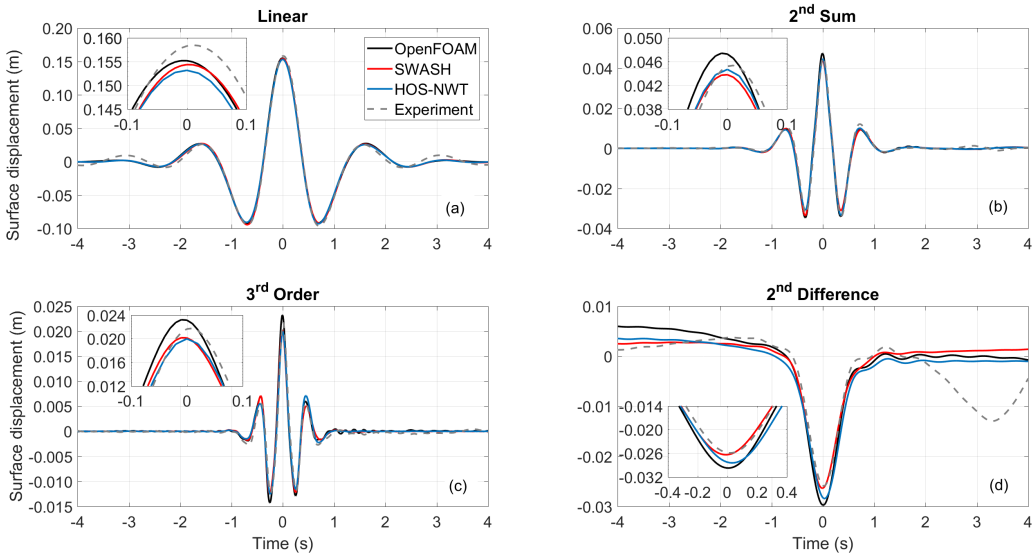

Figure 3.36: Comparison of the timeseries of the extracted surface elevation of each harmonics at the PF location between the experiment and the phase-resolving numerical models.

with only 0.1% difference at the crest. However, the advantage of this analysis is that it demonstrates that this may be a consequence of overestimation of all the nonlinear harmonics, whose effect on the dynamics of the wave group (kinematics) is yet to be examined. The other two models have considerably smaller differences for the individual harmonics, but an overall under-prediction of the wave crest.

The next part of the analysis concerns the comparison of the models in the frequency domain and it serves as a transitional step for the spectral evolution of the wave group,

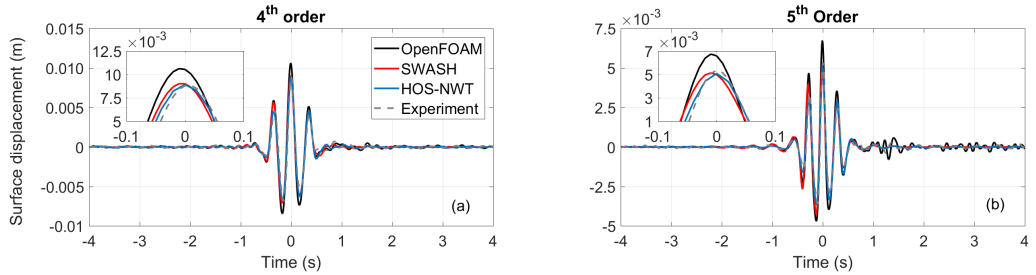

Figure 3.37: Comparison of the timeseries of the extracted surface elevation of the 4^{th} (a) and 5^{th} (b) order harmonics at the PF location between the experiment and the phase-resolving numerical models.

which will be discussed in the next chapter. In Figure 3.38, the spectral decomposition into individual harmonics is shown for the three numerical models and the experiment at the AM and PF locations, in the left and right column, respectively. Here, it is not deemed necessary to include the results of the 4^{th} and 5^{th} order harmonics. At AM, where the amplitude spectrum is corrected, there are not any noticeable differences among the models for the linearised spectrum (Figure 3.38a). The agreement for the 2^{nd} sum harmonics (Figure 3.38b) is good between SWASH and HOS-NWT, but OpenFOAM seems to be closer to the experiment, which does not have a smooth spectrum. It should be noted here that at AM the spurious free waves cannot be separated from the signal and they deteriorate the comparisons. The case is similar for the 3^{rd} order harmonics (Figure 3.38c), where SWASH and HOS-NWT are in good agreement and OpenFOAM is closer to the experiment with energy however spread in higher frequencies, possibly due to the artefacts of the IHFOAM wave generation (see Section 3.3.2). The 2^{nd} difference harmonics (Figure 3.38d) seems to be overestimated significantly by OpenFOAM, most likely as an effect of the spurious crest produced by the boundary. At the PF, the evolution of the extracted linearised spectrum is similar for all the numerical models, but slightly different from the experimental measurement, which exhibits the spectral peak at a higher frequency. Nevertheless, the energy transfer at higher frequencies is well reproduced (Figure 3.38e), resulting in a broadening of the spectrum. The energy content of the nonlinear harmonics at PF is very well reproduced by all the models, with OpenFOAM showing higher energy content at 3^{rd} order harmonics. Again, the greatest discrepancies appear for the 2^{nd} difference harmonics in Figure 3.38h. Overall, it can be concluded that the spectral evolution is well reproduced from AM to PF along the flume and the models are capable of reproducing the highly nonlinear wave-wave interactions occurring rapidly towards the focusing of a steep wave group, as discussed initially by Baldock et al. (1996) and demonstrated recently in OpenFOAM by Vyzikas et al. (2018b).

As discussed at the beginning of this chapter, the main motivation for studying SWASH and HOS-NWT was to explore the potential of efficient solvers to be used for the it-

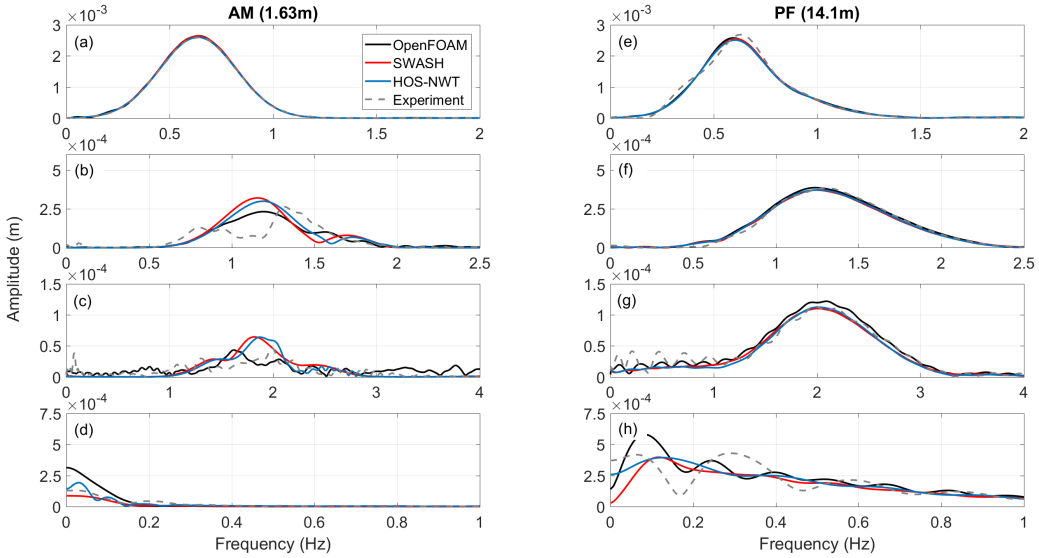

Figure 3.38: Comparison of the amplitude spectra extracted harmonics at the AM (left column) and PF (right column) location among the numerical models and the experiment.

erations of the focusing methodology in order to save computational resources from the expensive CFD model OpenFOAM. So far, it was shown that all the NWTs were capable of reproducing the nonlinear wave interactions and the spectral transformation towards focusing. Nevertheless, to answer the previous question, the input signal of the models, i.e. amplitudes and phases of the wave components, should be compared. This is shown in Figure 3.39.

As seen in Figure 3.39a, the input amplitude spectra of all the models has higher energy at its peak compared to the target spectrum. SWASH requires the highest input amplitude spectrum, while OpenFOAM and HOS-NWT have very similar input amplitude spectrum. There is also a small discrepancy observed for OpenFOAM at low frequencies, but the energy of these components is insignificant. The reason for this discrepancy at low frequencies cannot readily justified, but it can be related to the spurious long crest shown in 2^{nd} difference harmonics.

The corrected phases of the linearised wave components after the application of the methodology at PF are presented in Figure 3.39b, demonstrating the significant differ-

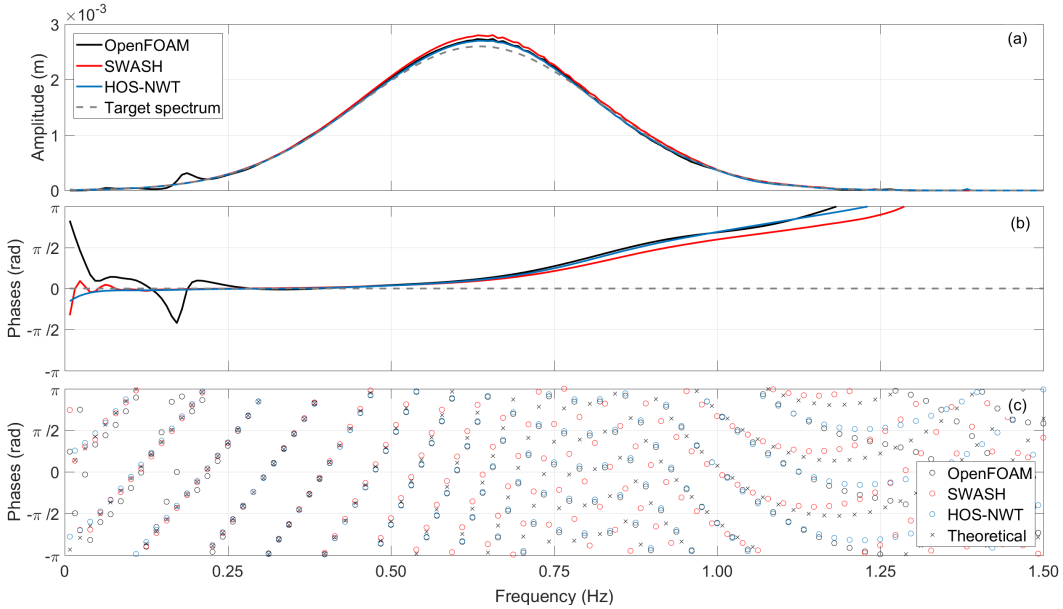

Figure 3.39: Comparison of the corrected linearised input amplitude spectrum (a), the phases of the wave components at the PF location (b) and the phases of the wave components at the inlet (c) for the numerical models used.

ence from the linear theory estimation of zero phases (- - -), especially for frequencies above 0.5 Hz and confirming emphatically that the dispersive properties of the wave group wave changed due to nonlinearities. Apart from the low frequency part of the spectrum, the three nonlinear models have similar input, with SWASH deviating the most, especially at high frequencies. It should be noted that when the nonlinear models run with this input, the output phases of the components of the linearised part of the spectrum at the PF are zero. To better observe the impact of the phase differences on the input signal at the inlet boundary, the phases at the inlet wrapped between $[-\pi, \pi]$ are presented in Figure 3.39c. These phases are calculated using the linear dispersion relation propagating the signal backwards for the distance between the PF location and the inlet boundary. The results are also compared with the theoretical phases of linear theory. Very good agreement is observed for all the models between frequencies 0.2 Hz to 0.5 Hz. Above 0.5 Hz, SWASH appears to deviate from the other two models, which results are even closer to linear theory. Above 1.25 Hz (approximately $2f_p$) the differences among the models are significant, however the energy of

these wave components is practically zero. This may be related to the fact that the high frequency components of the linearised harmonic may not propagate exactly as predicted by linear dispersion, as discussed in Section 3.2.2, and thus they are not corrected effectively by the focusing methodology.

The most interesting outcome of the comparison in Figure 3.39c is that the input signal of OpenFOAM and HOS-NWT seem to be quite similar, indicating the potential of HOS-NWT to be used for the iterations of the focusing methodology, saving computational resources (up to 2000 times). Therefore, the objective of using SWASH discussed in Section 3.2.3 can be at least partially achieved with HOS-NWT model. However, one should consider that SWASH has considerably more flexibility for engineering studies than HOS-NWT, being able to incorporate complex bathymetries and structures.

3.4 HOS-Ocean

Even though HOS-ocean (Ducrozet et al., 2016b) is a phase-resolving model, in the present section, it is validated qualitatively for the spectral evolution using simulations of random phases and not a focused wave group. The validation is performed for the spectral evolution against the published results of Benoit et al. (2015), who employed a Monte Carlo analysis with another HOS numerical model (COSMHOS code) and the Phase Averaged Equation (PAE) of Gramstad and Stiassnie (2013). Similar type of analysis, i.e., verifying PAE against random phase simulations with a fast phase-resolving numerical model, is common practice (Janssen, 2003).

The parameters of HOS-ocean are similar to that of HOS-NWT, with the latter have already been used for the initial validation of the HOS method (see Section 3.3.4). The difference between the two HOS models lies on the boundary conditions, as explained in Section A.3.3. HOS-ocean has periodic boundary conditions, simulating an infinite sea, thus the parameter $N3$ for the wavemaker of HOS-NWT does not exist here. In HOS-ocean, at the first time step, the simulation is initiated by a linear superposition

of waves, calculating the free surface elevation η and velocity potential at the free surface $\tilde{\phi}$. The calculated quantities are normalized by the wave length and the period of the peak frequency of the examined spectrum, L_p and T_p respectively. For the analysis that follows, the HOS nonlinearity order is $mHOS = 3$, corresponding to Zakharov equation (Onorato et al., 2007). This selection is consistent with the analysis of Benoit et al. (2015) and Gramstad and Stiassnie (2013) to allow for direct comparisons. Total dealiasing was achieved by selecting $p1 = mHOS = 3$. For the unidirectional simulations here, $N2 = p2 = 1$. The NWT was designed using $icase = 3$ for irregular wave simulation according to a predefined spectrum. The parameters $N1, p1, mHOS$ are selected in the `variables_3D.f90` file and for any modification the model has to be recompiled. The spectrum is defined in the `initial_condition.f90` file. A JONSWAP spectrum distribution was already included in the source code, but for the studies in the next chapter, the source code was altered to accommodate the Gaussian spectrum that was tested for the phase-resolving numerical models.

The convergence for HOS-ocean is performed in terms of $N1$. Different values were tested: $N1$ =32; 64; 128; 256; 512 for the same length of the domain (100L_p long). The free surface displacement was plotted along the NWT at a certain time instance for the simulations with different $N1$ and same initial conditions. It was observed that the results were identical for values of $N1 > 128$. As it was observed and confirmed with personal communication with G. Ducrozet (May, 2016), the accuracy of the NWT depends on the ratio of $xlen/N1$, where $xlen$ is the length of computational domain in the $x-$direction, which practically determines how many points/modes each wavelength is discretised with. When this ratio increases, the high frequency waves are not well resolved. To minimise any bias, it was decided to use $N1 = 512$ for the Monte Carlo simulations, since even high values of $N1$ do not induce considerable computational effort. The same selection was made by Benoit et al. (2015) and Gramstad and Stiassnie (2013). Directionality is controlled by the β parameter, which has a similar definition to that used in (Socquet-Juglard et al., 2005). For unidirectional seas $\beta \to 0$. For the time integration, a 4^{th} order Runge-Kutta Cash-Karp scheme is used with adaptive time step

(Cash and Karp, 1990) which is calculated automatically using a low tolerance of 10^{-7} to achieve good convergence (Ducrozet et al., 2016b). An additional control to avoid the simulation of unrealistic waves is included in HOS-ocean, referring to the maximum allowed slope of the free surface, defined as H/H_s. In practice, when this condition is violated, the simulation is terminated. After tests, the default value of $H/H_s > 10$ was finally used here.

For the analysis of the results, post-processing tools were developed performing FFT in space from the output of `2dpt.dat` file, which includes the 2D free surface elevation for each output time along the flume. The transformation from the $\kappa-$ spectrum to the $f-$ spectrum can be done with Equation 4.26. The wavenumber spectrum is smoothed using the Welch method and after trials it was decided to use it with division of the signal into 10 non-overlapping segments and thus, no use of Hamming window. To confirm the good initialization and convergence of the numerical schemes, as well as accurate post-processing of the results, a target spectrum was reproduced in a linear simulation ($mHOS = 1$) and it was confirmed that the spectral shape remains unchanged.

As mentioned, to confirm the applicability HOS-ocean for the spectral evolution, the results of Benoit et al. (2015) and Gramstad and Stiassnie (2013) were used. The former refer to 700 random runs of 1000 T_p of propagation and the latter to the PAE after being validated with 100 random runs using the Zakharov equation in deep water. In the work of Benoit et al. (2015), for the Monte Carlo simulations, 512 points/modes were used and a fixed time step of $\Delta t = T_p/200$. Here, the results that follow concern 800 random simulations for 1000 T_p duration of evolution of the corresponding spectra and an adjustable time step calculated by the Runge-Kutta 4^{th} order scheme of 10^{-7} tolerance. A larger number of random simulations was performed in order to increase confidence. $N1 = 512$ points/modes were used to discretise the domain, which had a length of 64 L_p. A code was written in Shell, combining MATLAB for the post-processing, that changes the $iseed$ number for the random phase generator in HOS-ocean and recompiles the code before every run. The output files of each run are assembled before the

post-processing.

Regarding the physical parameters, the gravitational acceleration is defined as g =9.81 m/s^2 and for deep water waves depth is set at a high value (5000 m). It is noted that the only available results in the literature consider infinite water depth and they are used here as a benchmark for validation. The initial conditions are defined by JONSWAP spectrum according to Equation A.40. The peak period is selected as T_p=2.006 s, resulting to a wave length of $L_p = 2\pi$ m in deep water. As such, the length of the simulated domain corresponds to 402 m ($64L_p$). For the parameters above $k_p = 1$ m^{-1}. The steepness of the generated sea is controlled by the significant wave height H_S, which here is H_s =0.3323 m and accordingly, a_j in Equation A.40 is calculated to scale the spectrum, as shown in (Benoit et al., 2015). The output (sampling) frequency is 0.1 T_p, corresponding to 0.05 s.

Based on the parameters described above, three unidirectional JONSWAP spectra are examined with different peak enhancement factors $\gamma =$ 1; 3.3; 20, as shown in Figures 3.40, 3.41 and 3.42 respectively. The spectra are plotted in $\kappa-$space to allow for comparison with the published results for $\kappa \in [0, 4\kappa_p]$. The confidence intervals are also plotted for the present results. As expected, stronger spectral changes occur for spectra with higher γ, which are farther from the equilibrium state, as discussed by Gramstad and Stiassnie (2013). In general, very good agreement is observed against the HOS code of Benoit et al. (2015) and the present results of HOS-ocean. The PAE is also shown to give very satisfactory prediction of the evolved wave field. It can also be seen that after the long propagation of the spectra, the equilibrium state approaches a PM-type distribution.

The results presented here for HOS-ocean demonstrate that the model has good accuracy in order to be used for Monte Carlo-type simulations. The only available results to compare the model was the three JONSWAP spectra in deep water and not the Gaussian spectrum in intermediate water depth that was used for the validation of OpenFOAM, SWASH and HOS-NWT. Having HOS-ocean validated is important, be-

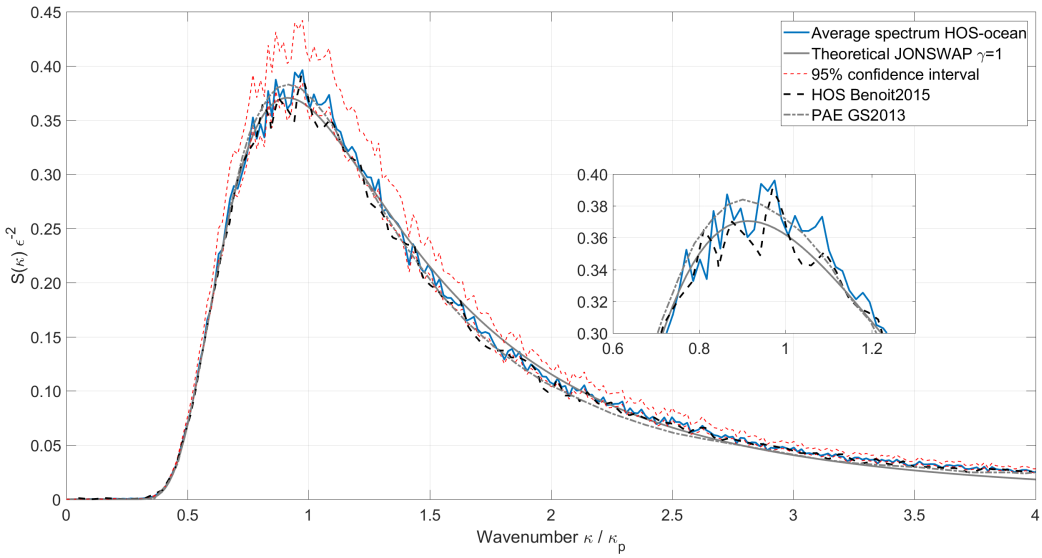

Figure 3.40: Comparison among PAE, HOS random simulations and Monte Carlo simulations against HOS-ocean (1000 T_p evolution of 800 runs) for JONSWAP spectrum $\gamma = 1$.

cause the model will be used in the next chapter for the propagation of the examined Gaussian spectrum and it will serve as a verification case for the phase-averaged General Kinetic Equation (GKE) model, which can provide the evolved free wave spectrum with a single run.

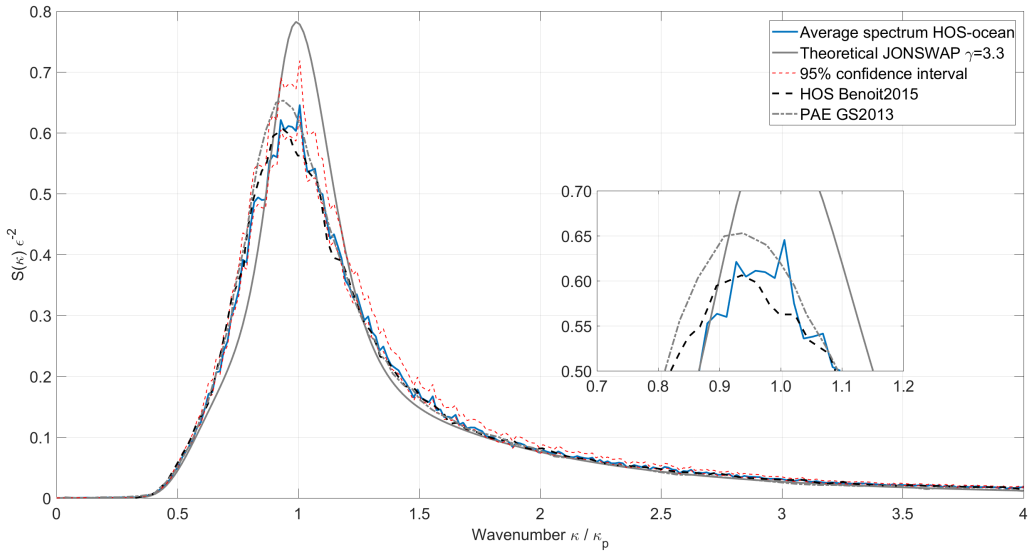

Figure 3.41: Comparison among PAE, HOS random simulations and Monte Carlo simulations against HOS-ocean (1000 T_p evolution of 800 runs) for JONSWAP spectrum $\gamma = 3.3$.

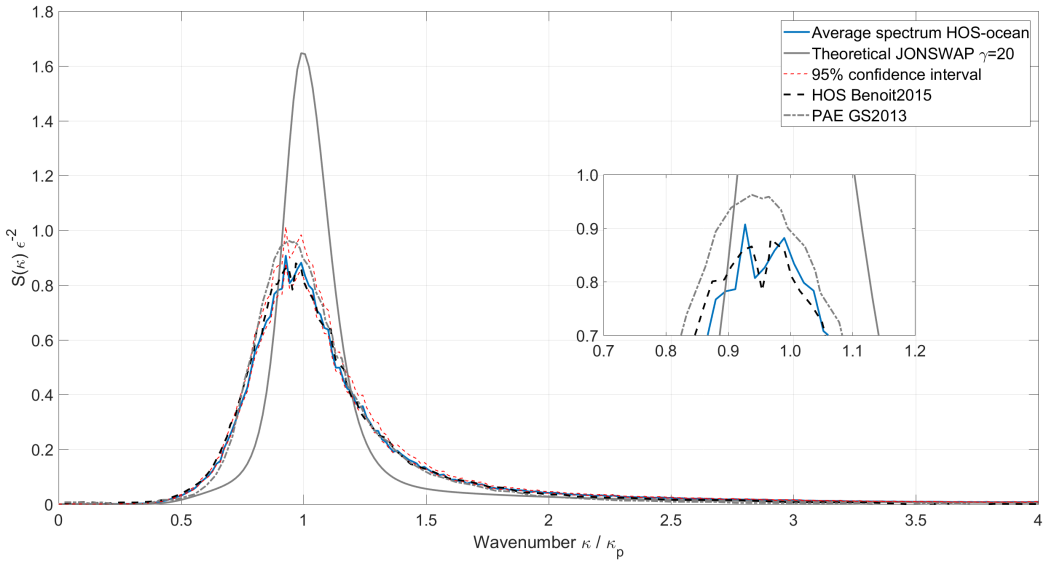

Figure 3.42: Comparison among PAE, HOS random simulations and Monte Carlo simulations against HOS-ocean (1000 T_p evolution of 800 runs) for JONSWAP spectrum $\gamma = 20$.

Chapter 4

Phase-averaged Vs Phase-resolving spectral evolution

THIS Chapter demonstrates the similarities of the spectral evolution in focused waves and in a phase-averaged approach. After analysing the spectral evolution of the phase-resolving numerical results, the most appropriate phase-averaged equation (PAE) is selected, which is able to replicate up to four-wave non-resonant interactions. The mathematical formulation and numerical implementation of the PAE are presented, as well as its application to focused waves. The latter includes investigations for the selection of the equivalent sea state characteristics. Various properties of the PAE are examined and, at the end of the chapter, the spectral evolution of the free-wave spectrum is computed for the wave groups of different steepness. The computed spectra are used in the following chapter for estimating the wave profile in a purely theoretical way.

4.1 Spectral changes in focused wave groups

4.1.1 Spectral evolution of the harmonics

In the present section, the spectral evolution of the harmonics of the Gaussian focused wave group examined in the previous Chapter 3 is presented by further analysing the results of the phase-resolving models. In that chapter, it was demonstrated that the three phase-resolving models tested in the present work (OpenFOAM, SWASH and HOS-NWT) have similar performance regarding the propagation of very steep non-breaking focused wave groups. As observed in Figure 3.38, the spectral analysis shows that all the models produce nearly identical results, especially regarding the evolution of the extracted linearised harmonic. This is very important because the linear harmonics determine the magnitude of the nonlinear bound harmonics (see Section 2.2.1). Consequently, any of the validated models can be used further for examining the spectral evolution.

The results presented in this section are produced using HOS-NWT, because, thanks to its low computational cost, a longer NWT of 50 m could be simulated. This allows for a wider window of timeseries of the surface elevation to be unaffected by the reflections coming from the outlet boundary. Additionally, the low computational cost of HOS-NWT makes simulation of the full range of the timeseries 0-128 s computationally efficient.

The separation of spectral harmonics presented herein is based on the four-wave decomposition method, discussed in Section 2.4.5. The results of the linear harmonic are presented after the exclusion of the 5^{th} order perturbations and also, the 4^{th} order harmonics are presented separately from the 2^{nd} difference harmonics. This analysis is consistent with that of Section 3.3.5. It is noted that no smoothing, nor frequency-shifting was applied to the spectral harmonics. Similarly, the time history of the harmonics was not time-shifted. However, a detail that should be discussed regarding the spectral analysis of evolution of the wave group along the NWT is the treatment of the spurious free waves created due to the imperfections of the wavemaker. These refer to

the 2^{nd} and higher order waves that, as shown in Section 3.3, separate from the main wave group only after WG2 (5.17 m) and thus, they are unavoidably included in the time window of the analysis at locations upstream of WG2. Since they are high order waves, their inclusion in the time window of the analysis affects only the nonlinear harmonics. This is manifested as fluctuations on the corresponding energy spectra of the harmonics. On the other hand, the linear harmonics obtained by the harmonic decomposition are independent of the length of the time window, provided that no reflections are included in the timeseries. After the spurious free waves start separating from the main wave group, they can be excluded from the analysis by selecting a narrow time window that includes only the main group, which after that stage consists of the free and bound waves. This can be achieved by visually selecting the appropriate range of the timeseries and replacing the surface elevation before and after the selected time window with zero elements, in order to keep always the same frequency resolution when when performing FFT. Care should be taken not to exclude accidentally part of the original free waves. It should be noted that using a high order wavemaker can minimize the spurious free waves, but as shown in Figure 3.34 it does not suppress completely the spurious waves, which is essential for this type of study. Also, for consistency with the experiment and the other numerical models, it was decided to use the linear wavemaker in HOS-NWT.

In the next paragraphs, the harmonics' evolution of the steepest wave group is discussed, since it exhibits the greatest spectral changes.

The evolution of the extracted linearised harmonic from the AM location at 1.63 m until the 14.10 m (PF) is presented in Figure 4.1, with the red arrow demonstrating its direction in space. This figure is similar to Figure 7a of Vyzikas et al. (2018b), which refers to results produced by OpenFOAM. It can be clearly seen that at 1.63 m the extracted linearised spectrum matches the Gaussian target spectrum, thanks to the application of the correction methodology. Then, the spectrum gradually evolves to a more broadbanded spectrum with more energy in higher frequencies and a down-

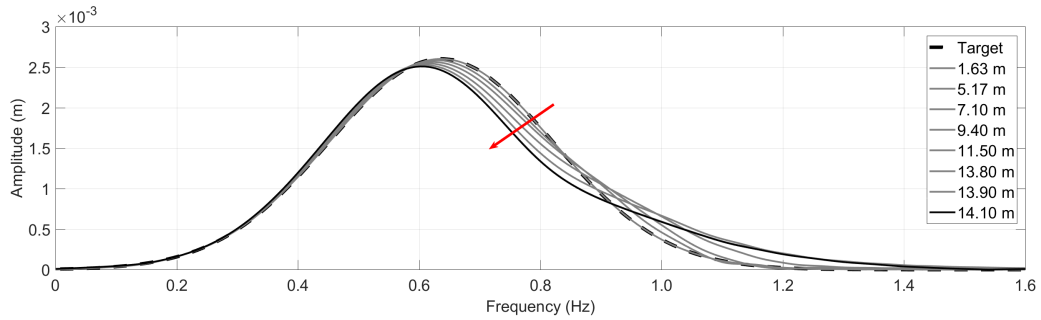

Figure 4.1: Spectral evolution of the extracted linearised harmonic at different locations from 1.63 m (AM), where the target initial Gaussian spectrum is reproduced, to 14.1 m (PF) in HOS-NWT ($d = 1$ m).

shifted spectral peak. Qualitatively, this behaviour was also observed in (Baldock et al., 1996; Shemer and Dorfman, 2008) for long-crested wave groups, as an effect of the nonlinearity. Here, however, thanks to the accurate separation of the harmonics, the linear part is clearly separated from the 3^{rd} order harmonics, which allows for more precise conclusions to be drawn for the involved wave-wave interactions. In fact, in many previous studies where the two-wave decomposition method was used (Johannessen, 2010; Gibson and Swan, 2007), it was indicated that important limitations arise when the linear and 3^{rd} order harmonics overlap, which is the case for broadbanded spectra or when high order interactions become strong, e.g, in shallow water (Katsardi and Swan, 2011).

The evolution of the nonlinear bound harmonics is shown in Figure 4.2. The results refer only to the wave group evolution from 6.10 m to 14.10 m, because, as discussed above, the WGs upstream of 6.10 m include also the high order spurious free waves. WGs were added in the NWT every 1 m in order to obtain measurements at equidistant locations and illustrate the rate of increase of the nonlinear bound harmonics. As seen in Figure 4.2a and 4.2c, the 2^{nd} order bound waves have already a considerable energy content at 6.10 m. Towards focusing, more energy is transferred to these harmonics at an increasing pace, which is demonstrated by the increasing distance of the curves near the peak for the 2^{nd} sum harmonics and the spreading of energy to higher frequencies for the 2^{nd} difference harmonics. Careful examination of these harmonics

also shows that their increase rate ceases at the last WG, which indicates some sort of energy saturation for the present case of limiting breaking wave group or a local static behaviour for the focused event (possible correlation with the "frozen" profile discussed in Section 2.3.2).

Similar behaviour with more intense characteristics is observed for the 3^{rd} and 4^{th}[1] order harmonics in Figures 4.2b and 4.2d, respectively. In contrast to the 2^{nd} order harmonics, at 6.10 m the energy content of the 3^{rd} and 4^{th} harmonics is negligible and they only gain considerable energy close to focusing. The latter indicates in a clear way the local and rapid spectral changes occurring when wave groups focus, described in past studies (Baldock et al., 1996; Gibson and Swan, 2007; Johannessen and Swan, 2003). Quantitatively, the energy of the 3^{rd} and 4^{th} almost doubles within the last 2-3 m of propagation, corresponding only to $0.5 - 0.8L_p$, with $L_p = 3.59$ m, which corresponds to a very short time scale. The present findings also show that steep focused wave groups may have high frequency harmonics with considerable energy to potentially excite offshore structures according to the ringing phenomenon (Fitzgerald et al., 2014).

4.1.2 The effect of the steepness

As mentioned in Section 3.3.1, three wave groups of increasing steepness were tested experimentally and numerically in the present work. The steepness was increased by multiplying the amplitude spectrum with the same factor. The linearly predicted amplitude at PF is calculated by adding the amplitudes of all the components, thus it is also called amplitude sum, denoted as $\Sigma\alpha_i$. A similar approach is used in the studies of Katsardi and Swan (2011) to estimate the evolution of the energy of wave groups and of Gibson and Swan (2007) and Adcock et al. (2015) to examine the effect of the steepness. The characteristics of the wave groups are listed in Table 4.1. To facili-

[1] The reason of the less smooth spectrum of the 4^{th} order harmonics is not clear, but it is assumed to be due to the less effective resolution of such high frequency waves in the NWT. The same behaviour was observed in OpenFOAM's results.

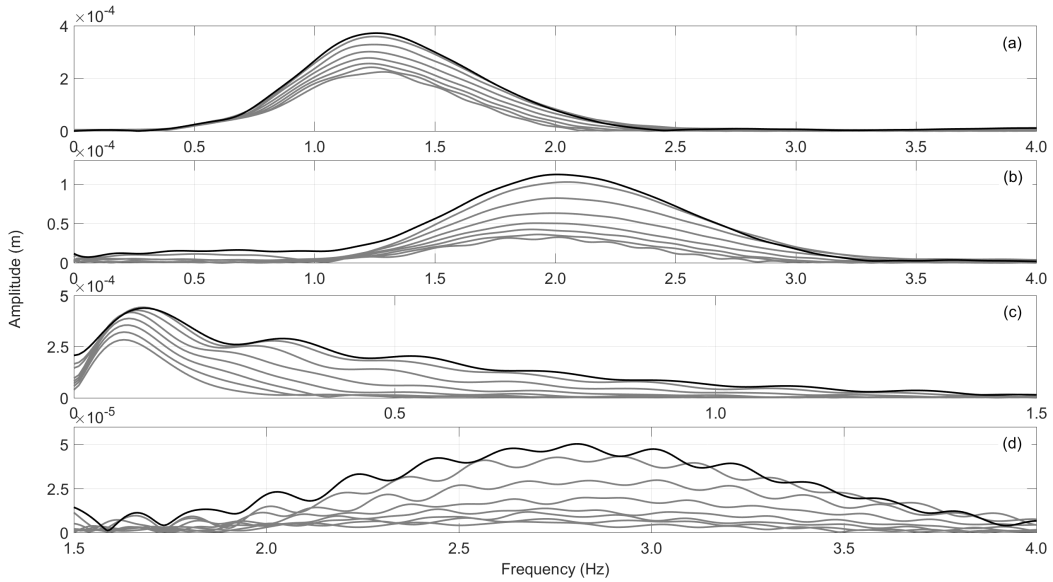

Figure 4.2: The evolution of nonlinear bound waves from in HOS-NWT from 6.10 m to 14.1 m (PF) every 1 m: (a) 2^{nd} order sum; (b) 3^{rd} order; (c) 2^{nd} difference; (d) 4^{th} order.

Table 4.1: Characteristics of wave groups of different steepness.

	Quasi-linear[a]	Weakly nonlinear	Strongly nonlinear
$\Sigma\alpha_i$ (m)	0.050	0.100	0.154
Factor[b]	1.00	2.00	3.08
Norm. factor	3.08	1.54	1.00

[a]The nonlinearity of the group is for naming only, not corresponding to turbulence characterization.
[b]Multiplication factor to increase steepness based on quasi-linear group.

tate comparisons, in the results that follow, the spectra and the harmonics have been normalized based on the strongly nonlinear wave group, which means that the results of the quasi-linear and weakly nonlinear groups have been multiplied by the normalization factor in Table 4.1, calculated as $\Sigma\alpha_i^{strongly\ nonlinear}/\Sigma\alpha_i^{wave\ group}$. The results of the wave groups of different steepness are only compared at the PF location in this section. Similar normalization is performed in the work of Adcock et al. (2015).

The spectral analysis of the extracted linearised harmonics at PF is presented in Figure 4.3. It can be clearly seen that the spectrum of the linear harmonics of quasi-linear group does not change almost at all, retaining the original shape of the target spectrum at AM. Very small change is observed for the weakly nonlinear group, which shows an

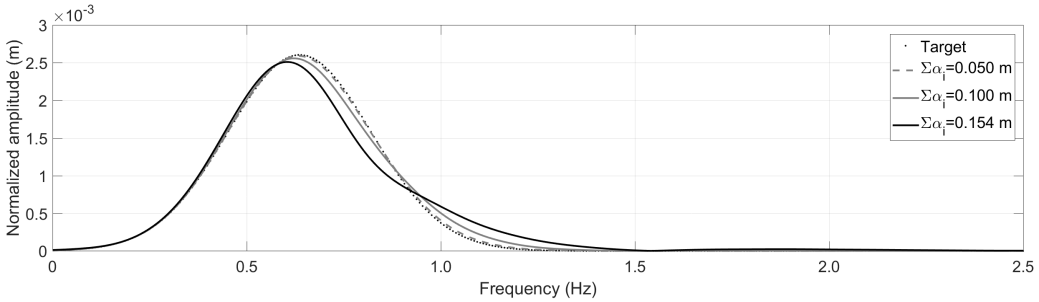

Figure 4.3: Extracted amplitude spectra of linear harmonics at 14.1 m (PF) for groups of different steepness.

incremental downshift and energy transfer to higher frequencies. As discussed for Figure 4.1 as well, the strongly nonlinear group exhibits a considerable downshift of the spectral peak and energy transfer to higher harmonics, losing its original Gaussian shape. The previous observations confirm quantitatively that the evolution of the free-wave spectrum is greater for steeper wave groups.

Similar analysis is performed for the nonlinear harmonics in Figure 4.4. Here however, it can be seen that the increase of the energy of the nonlinear harmonics is not equal to the increase of the amplitude sum, which was the case for the spectrum of the linear harmonics in Figure 4.3. Should that be the case, the spectra of the wave groups of different steepness would collapse to a single line or at least, they would have the same magnitude. The increase of the energy of the nonlinear harmonics is disproportionally large compared to the increase of $\Sigma\alpha_i$ and it is augmented with increasing order of the nonlinear harmonics. As a consequence, the energy of the 3^{rd} and 4^{th} harmonics is negligible for the quasi-linear wave group, but considerable for the strongly nonlinear group.

For the better quantification and illustration of the previously presented spectral analysis, the time history of the harmonics is presented in Figures 4.5 and 4.6 for the extracted linear and nonlinear harmonics, respectively. It can be seen that the time-sereies of the linear harmonics have practically identical crest. Only the harmonic of the strongly nonlinear group deviates at the adjacent troughs, which are shallower, and

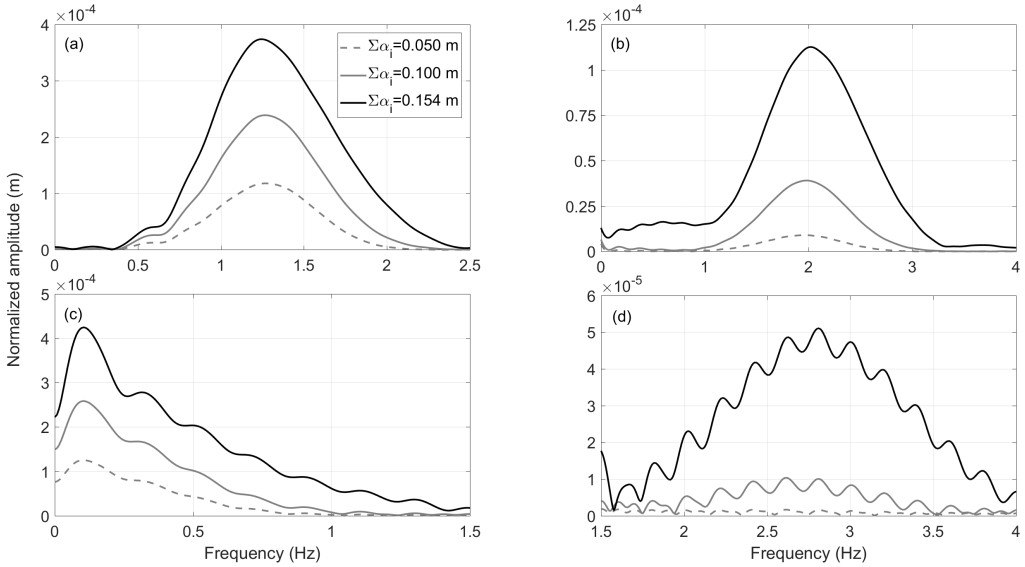

Figure 4.4: Extracted amplitude spectra of nonlinear harmonics at 14.1 m (PF) for groups of different steepness: (a) 2^{nd} order sum; (b) 3^{rd} order; (c) 2^{nd} difference; (d) 4^{th} order harmonics.

the lateral crests, which are shorter and wider. Similar results for OpenFOAM are presented in Figure 7b in (Vyzikas et al., 2018b). The shallowing of the troughs of steep groups has been reported in the past from experimental (Baldock et al., 1996) and numerical studies (Shemer et al., 2007). However, this was attributed mainly to the effect of the bound waves after being added to the free waves. Here, it is demonstrated that the spectral changes occurred at the strongly nonlinear group have an immediate effect on the timeseries of the free waves. These changes for the present case can only be attributed to the changes of the amplitudes of the wave components, since the phases were effectively corrected. In previous studies, the effects of amplitude and phase dispersion could not be accurately separated, due to the lack of an appropriate correction methodology, e.g., see (Katsardi and Swan, 2011; Gibson and Swan, 2007; Johannessen and Swan, 2003).

The timeseries of the extracted nonlinear harmonics (Figure 4.6) follow the observations made for Figure 4.4. Again, it is noted that if nonlinearity was increased proportionally to the increase of $\Sigma\alpha_i$, the timeseries would collapse into one, as shown for the

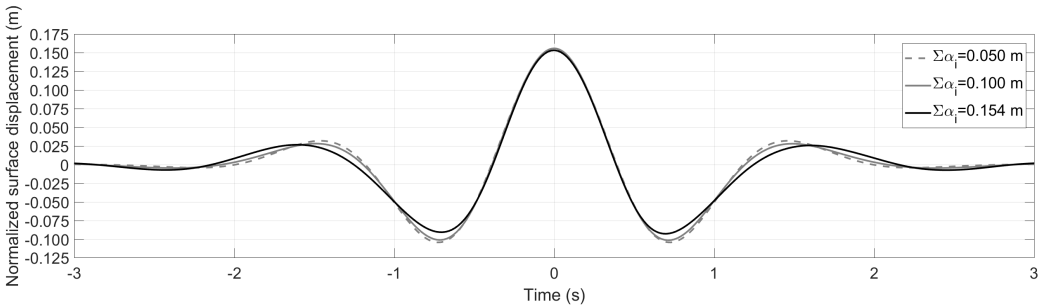

Figure 4.5: Timeseries of extracted linear harmonics at 14.1 m (PF) for groups of different steepness.

linear harmonic in Figure 4.5. The 2^{nd} order sum and difference harmonics seem to have already non-negligible contribution in the quasi-linear group and they have important contribution to the strongly nonlinear group. 3^{rd} order harmonics are negligible for the quasi-linear group, they have a small contribution for the weakly nonlinear group and certainly a contribution that cannot be ignored for the strongly nonlinear group. The 4^{th} order harmonics are practically zero for both quasi-linear and weakly nonlinear groups, but they seem not to be negligible for the strongly nonlinear group, being approximately 5.5% of the crest of the linear harmonic. It is reminded that the contribution of the high frequency nonlinear harmonics is expected to be even greater in OpenFOAM, as shown in Figure 3.36. These findings indicate that for nearly breaking unidirectional wave groups, the high order harmonics have an important role in determining the crest height and shaping the profile of the wave, as also noted by Johannessen and Swan (2003) for a JONSWAP-spectrum wave group.

The previous results are summarized in Figure 4.7, where the relative increase of the crest height of each harmonic, based on its value for the quasi-linear group, is presented. The markers "$\times$" represent the linear theory increase of $\Sigma\alpha_i$, indicated in Table 4.1 as "Factor". It is observed that the linear harmonic follows almost exactly the linear theory expectation. The crest of 2^{nd} sum and the trough of the 2^{nd} difference harmonics is approximately 4.5 times larger in the weakly nonlinear group and 13 times higher in the strongly nonlinear group. The weakly nonlinear group has 10 times higher 3^{rd} order harmonics and 60 times higher 4^{th} order harmonics than the quasi-linear group. What

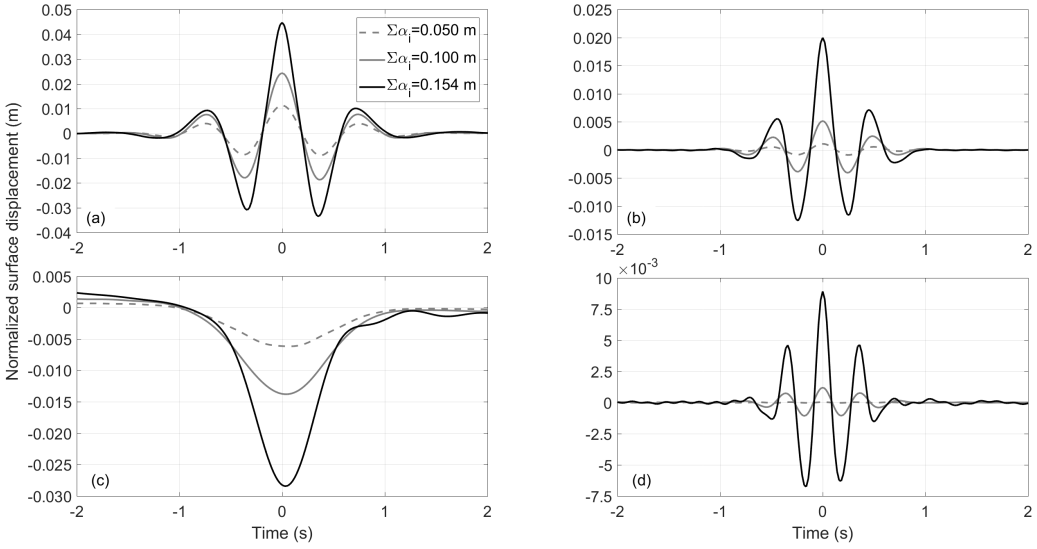

Figure 4.6: Timeseries of extracted nonlinear harmonics at 14.1 m (PF) for groups of different steepness: (a) 2^{nd} order sum; (b) 3^{rd} order; (c) 2^{nd} difference; (d) 4^{th} order.

is striking is the increase of the 3^{rd} and 4^{th} order harmonics for the strongly nonlinear group, where they seem to be approximately 73 and 850 times higher than their values for the quasi-linear group.

To summarise, the results of the phase-resolving models presented in this section show clearly that there are considerable spectral changes when the waves groups approach focusing, which increase with the steepness of the group. There is significant augmentation of bound nonlinear harmonics. Also, it was shown that the spectral evolution of the extracted linear harmonic is considerable, especially for the strongly nonlinear wave group. The latter is an effect of the nonlinearities that change the dispersive properties of the wave group and they cannot be predicted by linear theory. Assuming that the extracted linearised harmonic refers to the free waves, the nonlinear phase-resolving models used in the present study are shown to be capable of describing the spectral change of the free waves implicitly through the governing equations of the fluid flow. Another potential way to describe this spectral change is explicitly through the four-wave interaction theory, which is discussed in the next section.

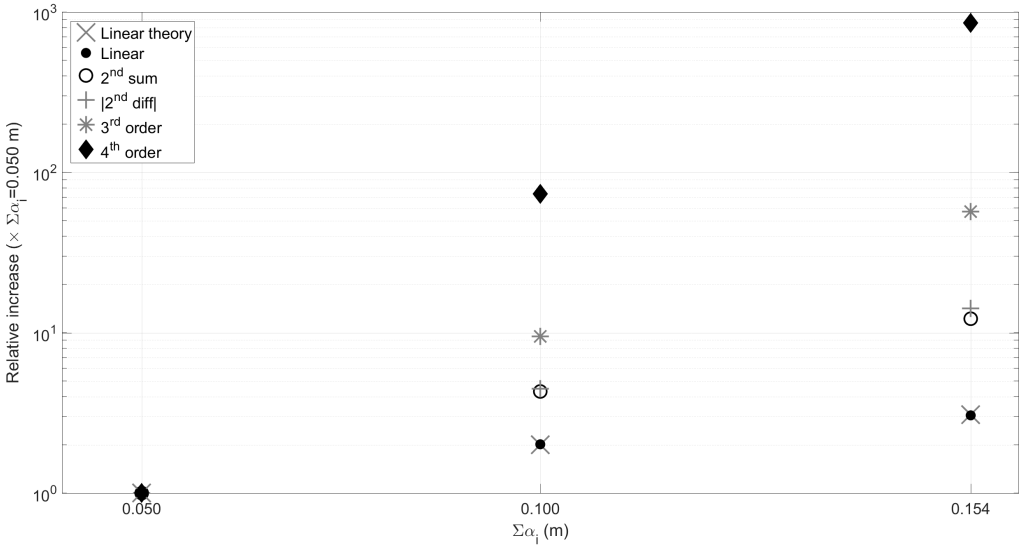

Figure 4.7: Relative increase of the crest or through of each harmonic at 14.1 m (PF) based on the corresponding recording of the quasi-linear wave group ($\Sigma\alpha_i = 0.050$ m) and comparison with linearly predicted increase. $y-$axis in log scale. Time window: [-4,4].

4.2 Stochastic approach of wave-wave interactions

4.2.1 Statistical description of an evolving wave field

For several applications, the exact characteristics of the individual waves are not relevant and instead the statistical characteristics of a sea state are more appropriate. This is because an ocean wave field is considered as a a superposition of infinite number of waves with different amplitudes and frequencies, travelling to different directions. This results in a system with infinite degrees of freedom that exhibits chaotic behaviour and can be better described by its statistical properties (Tanaka, 2007). Since gravity water waves interact with each other, changing their dispersive properties and producing new waves, the effects of nonlinearity further complicate the description of an evolving wave field. This problem is solved in the framework of wave turbulence, which is a robust mathematical theory to describe the evolution of nonlinear random wave fields and has applications to other fields of physics (Gramstad and Babanin, 2016). This theory refers to the chaotic behaviour developed in an initially Gaussian field, which

evolves according to the ZE, and is gradually weakly modulated leading to a turbulent signal (Fedele, 2008). To derive the equations for water waves, the assumption of weak turbulence is used and no breaking waves are considered.

The basic mathematical formulation is Hasselmann's kinetic equation (KE) (Hasselmann, 1962), which provides a statistical (phase-averaged) description of a wave field. The KE is widely used to present, especially in spectral models (Gramstad and Babanin, 2014). To verify its applicability, the results of the phase-averaged evolution of wave fields are commonly compared against a large number of realizations of phase-resolving models in Monte Carlo-type analyses that provide a more realistic representation of a wave field. For this scope, computationally efficient numerical models are used that can account for both resonant and bound high order wave-wave interactions. These models are based on the integro-differential form of the Zakharov equation (ZE) (Zakharov, 1968) using HOS methods, as in the present study, on the BST model (Bateman et al., 2001) and on the NLSE. Some of the main studies used HOS-type models to verify versions of the KE (Tanaka, 2001; Gramstad and Stiassnie, 2013; Benoit et al., 2015; Shemer et al., 2001; Tanaka, 2007; Janssen, 2005), and others to simulate focused waves (Gibson and Swan, 2007; Taklo et al., 2015; Adcock and Taylor, 2016a; Gibbs and Taylor, 2005; Katsardi and Swan, 2011). Studies with the NLSE (Dysthe et al., 2003; Socquet-Juglard et al., 2005; Trulsen et al., 2000) are also attractive thanks to their computational efficiency, but due to their inherent limitations regarding the spectral width (see Section 2.1), the NLSE is mainly used for narrow-banded wave groups, although the modified versions of these equations show better performance for broadbanded steep waves (Adcock and Taylor, 2016b).

As discussed, the nonlinearity of a wave field is associated with resonant and bound nonlinearities, which result in deviations from linear theory. The resonant nonlinearities can change the amplitudes and phases of the free wave spectrum, while the bound nonlinearities are "static" and refer to high order phase-locked harmonics (Taklo et al., 2015). The aforementioned phase-resolving equations constitute a good framework

to describe both types of nonlinearities. However, when referring to phase-averaged models, the essence of phasing and thus, phase-locked nonlinearities is lost (Tanaka, 2001). Therefore, for the KE is sufficient to describe the resonant wave-wave interactions, which can be achieved using a canonical transformation (Krasitskii, 1994). The problem then reduces to the assumptions in the derivation of the KE, the order of nonlinearity and the selection of the interacting wave components.

4.2.2 Selecting a phase-averaged model

As explained in Section A.4.4, the 3G spectral models use approximations of the standard KE with the main efforts being to reduce the computational cost for operational purposes. This is because, despite the concerns about the limits of the KE, e.g., rapid wind changes, it constitutes the most mathematically accurately described source term in ocean models (Cavaleri et al., 2007). Nevertheless, improved versions of the KE have been suggested (Annenkov and Shrira, 2006) to overcome these limitations. In this Section, the focus is more on the underlying assumptions in the KE, which determine its applicability and not on the reduction of the interacting quadruplets in order to increase the computational efficiency, which is the main concern for operational models.

The KE as suggested by Hasselmann (1962) assumes (as noted by Gramstad and Babanin (2016); Benoit et al. (2015) and Tanaka (2001)):

i) Spatial homogeneity of the wave field in scales shorter than $O(\varepsilon^4)$, where ε is the wave steepness.

ii) Constant water depth, unless examined on different grid points of a numerical model.

iii) A nearly Gaussian wave field, which implies weak nonlinearity and that the wave spectrum evolves on slow time scales $O(\varepsilon^4)$, aka the Hasselmann time scale and not in the fast scale, of BF nonlinearities.

iv) The wave field is random in the far past, meaning that the phases of the waves were uncorrelated long time ago, to enable time scale separation.

v) Broadbanded spectra with all the wave components having energy of the same order of magnitude, which is not the case for typical wind fields at their spectral tail.

A direct consequence of these assumptions is that the spectral evolution can be predicted by the KE only for long time scales of $> 1000T_p$ and that near-resonant (or non-resonant) are ignored, restricting the evolution due to exact resonant interactions. Nevertheless, the KE was shown to perform well for conditions that were violating these assumptions, giving good prediction of the wave field in short time scales $O(\varepsilon^2)$, see e.g., (Tanaka, 2001; Annenkov and Shrira, 2006) for the case of a rapid wind change.

For the scope of the present work of trying to replicate with a phase-averaged manner the spectral evolution observed in focused wave groups, the KE has two[2] unsurpassed shortcomings: a) It is not applicable (at least) in very short time scales of $\approx 5-10T_p$, which is typically the time horizon of the propagation of focused wave groups in experiments and numerical models. b) It cannot predict four-wave interactions in 1D, because exact resonant interactions are not possible in one direction[3]. However, this is a non-physical result, since many studies, including the present, demonstrate that there is spectral evolution in 1D.

Therefore, a different -less strict in its assumptions- model for the KE should be considered for the present study. The PAE of Gramstad and Stiassnie (2013), which is based on the derivation of Annenkov and Shrira (2006), is a good candidate for this scope. At present, the most advanced version of the PAE is the one suggested by Gramstad and Stiassnie (2013), which includes the effects of Stokes drift and has been tested in WW3 (Gramstad and Babanin, 2016). As described later in detail in Section 4.3, the PAE considers near-resonant interactions by relaxing the resonance conditions and is

[2]Additional restrictions may be the steepness of the wave group to cases where the bound nonlinearities are not significant and the correlation of the phases between the wave components.

[3]This was confirmed by trying DIA and WRT in a quasi-1D configuration in WW3, as described in Section A.4.4.

applicable for shorter time scales of $O(\varepsilon^2)$ for fast spectral evolution. As a result, the PAE can in principle have better performance than the KE in cases of rapid changes in the forcings of the wave field, such as changing wind conditions, and of unidirectional wave fields. Examples can be found in the literature in the works of Annenkov and Shrira (2015); Benoit et al. (2015); Gramstad and Stiassnie (2013); Gramstad and Babanin (2016) that demonstrate the better performance of the PAE compared to the KE or to operational algorithms based on the KE, such as DIA and WRT.

The literature also includes other versions of the KE that attempt to overcome the limitations especially regarding the consideration of the exact resonant interactions. Janssen (2003) suggested a version of the KE that includes non-resonant wave interactions, but it is still derived for slow time evolution of the spectrum. Tanaka (2007) shows that despite the slow time evolution assumption of the original KE and the arguments of Janssen (2003), the KE equation is capable, at least to some extent, to predict evolution of the spectrum in short time scale. Nonetheless, by not including non-resonant interactions, the applicability of the KE remains strictly in 2D evolution.

Taking into account the aforementioned considerations, in the present study it was decided to use the PAE of Gramstad and Stiassnie (2013), because it provides the framework to study spectral evolution in 1D and for short time scales. Additionally, it can be time marched with a straight-forward algorithm and it is expected to constitute an operational source term in future versions of spectral models (Gramstad and Babanin, 2016). However, there are other limitations[2] regarding the application of the PAE in focused wave groups, which make the present study particularly challenging. The literature with applications of the PAE is very limited and mainly produced by the authors that they developed it. As such, the present work endeavours to explore the limits of the PAE not only in the case of focused waves, but in finite water depth and very short time evolution of steep sea states.

4.2.3 The expected impact of resonant interactions

As mentioned, the literature regarding the PAE is very limited, but some general characteristics of the spectral evolution predicted by the PAE have been discussed in previous studies. On the other hand, the spectral evolution of unidirectional (1D) and directionally spread (2D) focused waves is better explored in the literature and there is more consensus about the behaviour of such wave groups. The issue in this case is more on the side of the techniques used to analyse the results and isolate the underlying physical processes. The main aspects of the spectral evolution in phase-averaged models and in focused wave groups are briefly discussed in the present section.

Focused wave groups

For focused wave groups, the result of nonlinear physics in 1D and 2D have considerable effects in the spectral evolution of the wave groups (Gibbs and Taylor, 2005). In ocean, a more realistic application of wave groups includes of course directional effects, but it was shown that extreme waves may be more likely to appear in swell-dominated seas (Gibson and Swan, 2007), and thus, the present 1D study is highly relevant to engineering applications. Arguably, wave groups of same steepness seem to undergo more significant spectral changes in 2D than in 1D. As a wave group focuses in 2D, there is a significant contraction of the along the mean direction and a long-crested behaviour in the transverse direction (Gibbs and Taylor, 2005; Adcock and Taylor, 2016b). Also a downshift of the peak frequency is observed together with energy transfer to high wavenumbers. The result is a focused wave group that can be usually well approximated by linear and second order theory for bound waves (Johannessen and Swan, 2003). On the other hand, unidirectional waves seem to undergo more modest changes of the underlying free-wave spectrum, but strong nonlinearity regarding the bound waves arises, resulting in steeper and taller waves at focus (Adcock and Taylor, 2016b). The free-wave spectrum becomes broader in 1D and there is a downshift of the peak frequency together with energy transfer to high frequencies (Bal-

dock et al., 1996; Johannessen and Swan, 2003). In both cases, the spectral changes take place relatively fast, which can be attributed to the local high energy concentration (Gibbs and Taylor, 2005). Despite the weaker spectral change of free waves in 1D, it was shown that the prediction of the NewWave model can be improved by considering the evolved and not the original free-wave spectrum (Johannessen and Swan, 2003; Vyzikas et al., 2018b). This is also supported by Gibson and Swan (2007), who argued that in 1D bound nonlinearities are not enough to predict accurately the focused wave group using a stationary spectrum.

The main issue with focused waves, experimentally or numerically, is the correct separation of the physical processes, since the result -although accurate and deterministic- includes both free and bound waves. Most of the studies to present used the two-wave decomposition method with frequency filtering to separate linear from third order harmonics, e.g., (Katsardi and Swan, 2011; Gibson and Swan, 2007; Johannessen, 2010; Gibbs and Taylor, 2005). This may include important discrepancies and it is restricted to applications with narrowbanded spectra, where the overlapping of linear and third order harmonics is minimum. However, decreasing the bandwidth can introduce BF-type nonlinearities that result in different spectral evolutions (Adcock and Taylor, 2016b). Moreover, in most of these studies, the limiting breaking case wave groups were used, but accurate focusing was not achieved due to the lack of an appropriate focusing methodology. The present study uses a four-wave decomposition and an effective method to focus the wave group making it superior overall compared to previous investigations. Still, it remains a potential issue to associate the extracted harmonics with the free and bound waves, as discussed in Section 4.7.3.

Attention should be also given to the effect of the water depth in the dispersion of the wave group. According to Katsardi and Swan (2011), for intermediate and shallow water depths, the dispersion is weakened and dispersive focusing ceases over more BF-type instabilities[4]. Recent studies have disproved this (Whittaker et al., 2016; Vyzikas

[4]To the author's view, the reason for the behaviour of the focused wave as a quasi-regular group with a high crest may be related to the initialization of the simulation very long time before the focusing event.

et al., 2018b), demonstrating that NewWave holds for finite water depth. This is of particular importance, because the spectral evolution is examined here in the context of finite water depth.

The spectral changes observed in 1D and 2D focused wave groups have been attributed to (only) non-resonant and resonant third-order (four-wave) interactions, respectively. This is discussed in the works of Gibbs and Taylor (2005) for 2D wave groups, Gibson and Swan (2007) for a spectrum with a small directional spreading, Janssen (2003) for 1D narrowbanded group attributing the changes to BF instabilities, Johannessen and Swan (2003) for 1D and 2D wave groups in deep water and Katsardi and Swan (2011) for 1D intermediate and shallow water. The most effective way to prove that four-wave interactions are the only possible mechanism that changes the free-wave spectrum is by isolating the physical processes in ZE-based models, as done by Gibson and Swan (2007) and Katsardi and Swan (2011)[5]. Assuming that only four-wave interactions change the free waves' dispersive properties, a phase-averaged model that accounts for the tri-spectrum (Cavaleri et al., 2007) should be adequate to predict the spectral change.

Random seas

The spectral change predicted by phase-averaged models refers to the case of wave fields with random phases and it is usually expressed in terms of integrated spectral parameters, such as skewness and kurtosis, which also give indications of probabilities of extremes (Gramstad and Trulsen, 2007). As discussed, the only model that can account for spectral evolution in 1D is the PAE with non-resonant wave-wave interactions. The first work that included non-resonant interactions is that of Janssen (2003), who observed in 1D a downshifting of the spectral peak accompanied with steepening of the

This creates a very dispersed wave field which evolution over long time may include different dynamics than that of a focused wave group with a time evolution of a few T_ps. Evidence for this can be found also in Figure 1b of Adcock and Taylor (2016a) which refers to deep water waves.

[5]This method needs attention before drawing robust conclusions, because it is based on the assumption that the free waves in the transformed and real world are the same. Recent findings (Aubourg et al., 2017), discussed at the end of the chapter, suggest other possible mechanisms as well.

low frequency part and broadening by energy transfer to higher wavenumbers. It was also highlighted that the spectrum undergoes a transitioning period of a few $\approx 5T_p$s, which is also confirmed by the direct computations of Tanaka (2001)[6]. The most recent studies in 1D were conducted with the PAE of Gramstad and Stiassnie (2013) and repeated by Benoit et al. (2015). JONSWAP spectra of different bandwidths were examined and it was shown that the narrowbanded spectra change significantly with the spectral peak being decreased and downshifted and the spectrum becoming broader with energy transfers to higher and lower wavenumbers. The spectrum is seen to undergo significant changes within the first few $10T_p$s, but after $200-300T_p$ it stabilises to a new form. This new state that the spectrum reaches is more stable.

It is argued that the role of four-wave interactions is to bring a spectrum which is far from equilibrium due to external forcing, such as wind, or due to an unstable initial shape, to a steadier state (Gramstad and Stiassnie, 2013; Gramstad and Babanin, 2016). Therefore, the impact of four-wave interactions becomes more apparent in cases where the spectrum is far from its equilibrium state[7], e.g., very narrowbanded spectrum (Tanaka, 2001). Theoretically, if the sea state chosen is close to the nonlinear equilibrium case, the action of four-wave interactions would be negligible (Janssen, 2003). This equilibrium condition is also referred to as "self-similarity" (Gagnaire-Renou et al., 2010) and it is also observed for 2D seas. It also seems to be an underlying physical process for the spectra of focused waves that are far from equilibrium, for which similar spectral changes to random wave fields were identified (Gibson and Swan, 2007).

In 2D, the spectral evolution includes directional spreading parameters and it can be more easily observed by integrating the energy of the wavenumbers over the directions. Having the possibility to expand to different directions, energy is transferred to directions far from the mean direction, which is somewhat opposite to what has been discussed for focused wave groups. The integrated energy spectra show similar qual-

[6] This transition period in the case of (Janssen, 2003) may be due to BF instabilities because the spectrum is sufficiently narrow in order to trigger them. Nevertheless, if a transition period to full nonlinearity exists, it may be an issue in the present study that focuses on the first few T_ps of evolution.

[7] This is well demonstrated by Gagnaire-Renou et al. (2010) where the initial unrealistic top-hat spectrum obtains a JONSWAP-type form after the action of four-wave interactions.

itative characteristics like in 1D, such as peak downshifting, energy transfer to high wavenumbers, steepening of the low-frequency and broadening (Dysthe et al., 2003). Simulations in 2D allow for comparisons between the PAE and other operational source terms, such as DIA and WRT. As a rule, PAE is closer to the more accurate WRT than to DIA that often overpredicts the directional spreading. The inclusion of non-resonant interactions in 2D seems not to have considerable impact, unless there is a strong change to the external forcing, such as the wind (Gramstad and Babanin, 2016). Such example is the case of a squall, for which it was shown that the non-resonant interactions cause a period of stronger transitions and narrower spectrum (Annenkov and Shrira, 2015)[8].

Direct or phase-averaged simulations predict considerable energy transfer to high wavenumbers. In real ocean, this energy would be dissipated due to effects of wave breaking, which is not modelled by the KE or potential flow models (Gramstad and Stiassnie, 2013). Thus, in some cases the KE may yield unrealistic spectral tails. Another aspect that is not often discussed is the effect of water depth. Although, in principle the KE can be derived for finite depth, it is mentioned by Tanaka (2007) that in shallower water, other effects, such as triads may arise, which can challenge the applicability of weak turbulence theory. In this sense, the present study contributes to expanding the bibliography by examining the spectral changes in finite water depth.

In the context of discussing the inclusion of non-resonant interactions in the KE, these also include the BF instabilities that where shown to arise under the condition of $k_p d > 1.36$ (Janssen and Onorato, 2007), where k_p is the wavenumber of the component of the f_p and d is the depth. The time scale of these interactions is very short, namely $O(\varepsilon^1)$ (Dysthe et al., 2003). However, for the present Gaussian spectrum which is broadbanded and $k_p d = 1.75$, no signs of side-band instabilities are observed indicating BF effects. It is interesting to note that there have been also efforts to build a global forecasting system for extreme waves by calculating the BF index (Janssen, 2005)

[8] In that study only the interactions that are not too far from resonance, i.e., $\Delta\omega/\omega_{min} \leq 0.25$, while in the present study all the interactions are considered.

from spectral models, but recent field studies do not support the argument that the mechanism for extreme wave generation is BF instabilities (Christou and Ewans, 2014; Fedele et al., 2016).

4.3 The mathematical formulation of the GKE

4.3.1 The derivation of the GKE

The derivation of the GKE follows the formulation of Gramstad and Stiassnie (2013), which is similar to that of Janssen and Onorato (2007). In the work of Gramstad and Stiassnie (2013), the GKE is mentioned as PAE, and the term GKE was first used in (Gramstad and Babanin, 2016). In the present study it was decided to use the term GKE in order to make distinction with the PAE of Benoit et al. (2015). In this section, the mathematical derivation of the GKE is presented, with the focus being on the numerical implementation of the GKE to a form that it can be time marched, as presented in Section 4.3.2. The simplifications and assumptions adopted in the derivation of the GKE are highlighted.

The derivation of the GKE begins from the Hamiltonian form of the ZE for the four-wave interaction of purely gravity waves, referring to Equation 2.23 in (Krasitskii, 1994). After the canonical transformation, discussed in Section 5.5.1, the generalized complex amplitude spectrum $b(k,t)$ of the free waves in the transformed space is given in Equation 4.1 for four interacting wave components vectors $\mathbf{k}_1, \mathbf{k}_2, \mathbf{k}_3, \mathbf{k}_4$.

$$i\frac{\partial b(\mathbf{k}_1)}{\partial t} = \omega(\mathbf{k}_1)b(\mathbf{k}_1) \; + \; \int T(\mathbf{k}_1,\mathbf{k}_2,\mathbf{k}_3,\mathbf{k}_4)b^*(\mathbf{k}_2)b(\mathbf{k}_3)b(\mathbf{k}_4)\times \\ \delta(\mathbf{k}_1+\mathbf{k}_2-\mathbf{k}_3-\mathbf{k}_4)\; d\mathbf{k}_2\; d\mathbf{k}_3\; d\mathbf{k}_4 \tag{4.1}$$

where t is time, $T(\mathbf{k}_1,\mathbf{k}_2,\mathbf{k}_3,\mathbf{k}_4)$ is the coupling coefficient for the KE (see Equation A.53), which corresponds to the coefficient $\tilde{V}^{(2)}_{0,1,2,3}$ in (Krasitskii, 1994) or to $T_{1,2,3,4}$ in

(Janssen and Onorato, 2007). In the present study, it was decided to use the formulation of Janssen and Onorato (2007), which, thanks to its more compact formulation, is simpler to program. The calculation of the coupling coefficients is presented in the Appendix B. $\omega(\mathbf{k}_i)$ is the angular frequency of a wave component given from the linear dispersion relation as $\omega(\mathbf{k}_i) = \sqrt{g|\mathbf{k}_i|\tanh(|\mathbf{k}_i|d)}$, with g being the acceleration due to gravity and d the water depth. The asterisk denotes the complex conjugation. Both $\omega(\mathbf{k}_i)$ and $T_{1,2,3,4}$ are calculated for finite water depth in the present study. Commonly, the deep water condition is used, because four-wave interactions are relevant to deeper water, since in very shallow water, the spectral evolution is dominated by triads (Holthuijsen, 2007).

The first step to solve the previous equation numerically is to assume a discrete spectrum (Equation 4.2) and replace Equation 4.1 by its discrete equivalent, which results in Equation 4.3.

$$b(\mathbf{k},t) = \sum_n b_n(t)\delta(\mathbf{k}-\mathbf{k}_n) \tag{4.2}$$

After that, the ZE can be replaced by the following expression:

$$\frac{db_1}{dt} = -i\omega_1 b_1 - i\sum_{2,3,4} T_{1234}\; b_2^*\; b_3\; b_4\; \delta_{12}^{34} \tag{4.3}$$

where a compact notation for the variables is adopted: $T_{1234} = T(\mathbf{k}_1,\mathbf{k}_2,\mathbf{k}_3,\mathbf{k}_4)$ and $\omega_1 = \omega(\mathbf{k}_1)$ (see also Appendix B). δ_{12}^{34} is the Kronecker delta, which determines the interacting components:

$$\delta_{12}^{34} = \begin{cases} 1 \text{ when } \mathbf{k}_1+\mathbf{k}_2 = \mathbf{k}_3+\mathbf{k}_4 \\ 0 \text{ otherwise} \end{cases} \tag{4.4}$$

Until this point, the phase information of the wave components is still retained, through the ZE. However, since the scope is to derive a phase-averaged equation, a stochastic

approach for b_i is considered, which is denoted as $\langle\cdot\rangle$, expressing the statistical average. To obtain the expression of the wave action $C_1 = \langle|b_1|^2\rangle$, which is the property that will be time marched, Equation 4.3 is multiplied by b_1^* and then the complex conjugate is added and the result is averaged. This process returns Equation 4.5. It should be noted that $\mathbf{k}_1$ refers to each discrete wavenumber of the spectrum that interacts with any possible combination of all the other wavenumbers $\mathbf{k}_2, \mathbf{k}_3, \mathbf{k}_4$.

$$\frac{dC_1}{dt} = -i \sum_{2,3,4} T_{1234} \ (\langle b_1^* b_2^* b_3 b_4\rangle - \langle b_4^* b_3^* b_2 b_1\rangle) \ \delta_{12}^{34} = 2Im \sum_{2,3,4} T_{1234} \ \langle b_1^* b_2^* b_3 b_4\rangle \ \delta_{12}^{34} \quad (4.5)$$

The next step for forming the time evolution of GKE includes the derivation with respect to time of the product $b_1^* b_2^* b_3 b_4$, which is substituted in Equation 4.3. This returns an equation $\frac{d}{dt}\langle b_1^* b_2^* b_3 b_4\rangle = i \ \Delta_{12}^{34} \langle b_1^* b_2^* b_3 b_4\rangle \ + \ high\ order\ cumulants$, as shown in Equation 2.6 of Gramstad and Stiassnie (2013). Δ_{12}^{34} is given by the angular frequencies of the interacting wave components as:

$$\Delta_{12}^{34} = \omega_1 + \omega_2 - \omega_3 - \omega_4 \quad (4.6)$$

It can be seen already from Equation 4.6 that the non-resonant components are allowed to interact through the expression of Δ_{12}^{34}, which is not forced to zero. This practically means that a less strict condition is adopted compared to the KE, where interactions are permitted only for the components that $\omega_1 + \omega_2 - \omega_3 - \omega_4 = 0$.

The expression of the statistical average of the low order cumulants includes contributions from high order cumulants (see Equation 2.8 in (Gramstad and Stiassnie, 2013)). This expression is derived under the assumption of statistical homogeneity and weak non-Gaussianity. The previous assumption also implies that the fourth and sixth order cumulants are smaller than the corresponding terms of C_i, as expressed in Equation 4.7. The variable k_{1234} was introduced after some substitutions and algebra and it is related to C_i, T_{1234} and b_i (see Equation 2.11 in (Gramstad and Stiassnie, 2013)).

$$C_1 = O(\varepsilon^2), \quad k_{1234} = O(\varepsilon^4), \quad k_{123456} = O(\varepsilon^6) \tag{4.7}$$

where $\varepsilon \ll 1$ the wave steepness.

The consequence of the connection between the low and high order cumulants is that the system of equations keeps expanding to higher orders and appropriate assumptions should be considered to close the set of equations to the desired order. Since the scope of the present work is to include third order nonlinearities, referring to the four-wave interactions, the Hamiltonian of order 4 is considered. For this, the sixth order terms $O(\varepsilon^6)$ can be considered zero, while the fourth order terms $O(\varepsilon^4)$ should be included. It can be shown that if one further sets $O(\varepsilon^4)$ terms to zero, the wave action remains constant $\left(\frac{dC_i}{dt} = 0\right)$ and the only thing that changes in the wave field is the phases of the components.

The previous consideration for the cumulants is mathematically consistent only if the sixth order cumulants are smaller than the products of C_i and the fourth order cumulants (Gramstad and Stiassnie, 2013). The derivation of GKE can account for up to five-wave interactions by including the corresponding coefficients presented in (Krasitskii, 1994). The inclusion of quintet interactions increases the computational cost significantly and for the present study only the quadruplet interactions are considered, as done also in (Gramstad and Stiassnie, 2013). Nevertheless, under certain conditions five-wave interactions may be important. However, taking into account that the literature is very recent and limited on the topic and the properties of this version of GKE are far from being explored sufficiently (Benoit et al., 2015; Gramstad and Babanin, 2016), considering five-wave interactions in the GKE is a very "risky" path to take at this stage.

In order to handle the stochastic approach $\langle\cdot\rangle$ in Equation 4.5, some new variables are introduced (e.g., k_{1234}), which are not discussed here for the sake of brevity. The reader is referred to (Gramstad and Stiassnie, 2013) for further details. Under the assumption

of a Gaussian initial condition, which means that the phases of the wave components were not correlated at $t = 0$, the GKE can be obtained in the form of Equation 4.8. In the expression suggested by Gramstad and Stiassnie (2013), the high order contributions of the orbits of the fluid particles, i.e., Stokes drift, were also included. However, for simplicity and since Gramstad and Stiassnie (2013) noted that the inclusion of Stokes drift did not make a noticeable difference in the results especially in 1D, it was decided not to include it in the present study; thus, $\beta_{1234} = 0$. The GKE of Equation 4.8 can be considered as an expansion of the KE of Hasselmann (1962), which can describe fast evolution at $O(\varepsilon^2)$ time scale and wave interactions at 1D. Since, the Stokes drift is ignored in the present work, the GKE is practically equivalent to the PAE suggested by Annenkov and Shrira (2006).

$$\frac{dC_1}{dt} = 4Re \sum_{2,3,4} T^2_{1234} \delta^{34}_{12} e^{i\theta_{1234}(t)} \int_0^t f_{1234}(\tau) e^{-i\theta_{1234}(\tau)}\, d\tau \tag{4.8}$$

where $f_{1234} = C_3 C_4 (C_1 + C_2) - C_1 C_2 (C_3 + C_4)$ and $\theta_{1234}(t) = \Delta^{34}_{12} t$

It can be demonstrated that the latter form of the GKE is conservative for the statistically averaged expressions of the invariants of the ZE (Gramstad and Stiassnie, 2013), namely:

Total wave action: $\tilde{N} = \sum_n C_n$;

Total momentum: $\tilde{\mathbf{P}} = \sum_n \mathbf{k}_n C_n$;

Total energy (Hamiltonian): $\tilde{H} = \sum_n \Omega_n C_n - \sum_{1,2,3,4} T^2_{1234} \delta^{34}_{12} Im\left(e^{i\theta_{1234}(t)} \int_0^t f_{1234}(\tau) e^{-i\theta_{1234}(\tau)}\, d\tau\right)$

4.3.2 The time evolution of the GKE

In this section, the numerical scheme for the time marching of the GKE is presented. Some additional calculations for the derivatives, which were not presented in the original publications (Gramstad and Stiassnie, 2013), are included here for clarity.

The GKE as expressed by Equation 4.8 can be marched in time using a Taylor expansion at time t. Such schemes are commonly employed for wave propagation problems.

Apart from its straight forward implementation, this numerical scheme is by definition conservative for the total wave action and momentum (Gramstad and Stiassnie, 2013). The Taylor expansion to third order, with a local truncation error of $O(\Delta t^4)$, is shown in Equation 4.9.

$$C_1(t+\Delta t) = C_1(t) + \Delta t C_1'(t) + \frac{\Delta t^2}{2} C_1''(t) + \frac{\Delta t^3}{6} C_1'''(t) + O(\Delta t^4) \tag{4.9}$$

What is left then is to calculate the derivatives of $C_1(t)$. The first $C_1'(t)$ derivative can be calculated from Equation 4.8 and it is given in (Gramstad and Stiassnie, 2013) as:

$$C_1'(t) = 4Re \sum_{2,3,4} T_{1234}^2 \delta_{12}^{34} e^{i\theta_{1234}(t)} I(t) \tag{4.10}$$

where $I(t)$ is the integral:

$$I(t) = \int_0^t f_{1234}(\tau) e^{-i\theta_{1234}(\tau)}\, d\tau \tag{4.11}$$

The second and third derivatives are not given in the original publication, but they can be calculated from the $C_1'(t)$. Considering T_{1234} and δ_{12}^{34} as constants, the derivation is reduced, as shown in Equation 4.12, which yields the $C_1''(t)$ in Equation 4.13.

$$\begin{aligned} &\left(e^{i\theta_{1234}(t)} I(t)\right)' = \left(e^{i\theta_{1234}(t)}\right)' I(t) + e^{i\theta_{1234}(t)} + I'(t) = \\ &i\theta_{1234}'(t) e^{i\theta_{1234}(t)} I(t) + e^{i\theta_{1234}(t)} I'(t) = i\theta_{1234}'(t) e^{i\theta_{1234}(t)} I(t) + f_{1234}(t) \end{aligned} \tag{4.12}$$

$$C_1''(t) = 4Re \sum_{2,3,4} T_{1234}^2 \delta_{12}^{34} \left[f_{1234}(t) + i\theta_{1234}'(t) e^{i\theta_{1234}(t)} I(t) \right] \tag{4.13}$$

To obtain the third derivative of $C_1(t)$, the derivation of $C_1''(t)$ has to be considered, which basically refers to the terms in brackets of Equation 4.13, as shown in Equation 4.14.

$$
\begin{aligned}
&\left[f_{1234}(t)+i\theta'_{1234}(t)e^{i\theta_{1234}(t)}I(t)\right]' = \\
&f'_{1234}(t)+\left(i\theta'_{1234}(t)\right)'e^{i\theta_{1234}(t)}I(t)+i\theta'_{1234}(t)\left(e^{i\theta_{1234}(t)}I(t)\right)' = \\
&f'_{1234}(t)+i\theta''_{1234}e^{i\theta_{1234}(t)}I(t)+i\theta'_{1234}(t)\left(i\theta'_{1234}(t)e^{i\theta_{1234}(t)}I(t)+f_{1234}(t)\right) = \\
&f'_{1234}(t)+i\theta''_{1234}e^{i\theta_{1234}(t)}I(t)-\theta'_{1234}(t)^2e^{i\theta_{1234}(t)}I(t)+i\theta'_{1234}(t)f_{1234}(t) = \\
&f'_{1234}(t)+\left(i\theta''_{1234}-\theta'_{1234}(t)^2\right)e^{i\theta_{1234}(t)}I(t)+i\theta'_{1234}(t)f_{1234}(t) \\
&\therefore Re\left[f'_{1234}(t)+\left(i\theta''_{1234}-\theta'_{1234}(t)^2\right)e^{i\theta_{1234}(t)}I(t)+i\theta'_{1234}(t)f_{1234}(t)\right] = \\
&Re\left[f'_{1234}(t)+\left(i\theta''_{1234}-\theta'_{1234}(t)^2\right)e^{i\theta_{1234}(t)}I(t)\right]
\end{aligned}
\tag{4.14}
$$

By considering only the real part of the derivative of Equation 4.14, $C'''_1(t)$ can be obtained from Equation 4.15:

$$
C'''_1(t) = 4Re\sum_{2,3,4}T^2_{1234}\delta^{34}_{12}\left[f'_{1234}(t)+\left(\theta''_{1234}(t)-\theta'_{1234}(t)^2\right)e^{i\theta_{1234}(t)}I(t)\right] \tag{4.15}
$$

By substitution of the derivatives of C_1 from Equations 4.10, 4.13 and 4.15 to Equation 4.9, the time-marching explicit scheme of Equation 4.16 is obtained, which constitutes the numerical implementation of the GKE in the present work.

$$
\begin{aligned}
C_n(t+\Delta t) = C_n(t)+4\Delta tRe\sum_{2,3,4}T^2_{1234}\delta^{34}_{12}\Bigg[&\frac{\Delta t}{2}f_{1234}(t)+\frac{\Delta t^2}{6}f'_{1234}(t)+ \\
&\left(1+\frac{i\Delta t}{2}\theta'_{1234}(t)+\frac{\Delta t^2}{6}\left(\theta''_{1234}(t)-\theta'_{1234}(t)^2\right)\right)I(t)e^{i\theta_{1234}(t)}\Bigg]+O(\Delta t^4)
\end{aligned}
\tag{4.16}
$$

The integral $I(t)$, shown in Equation 4.11 can be calculated iteratively, as seen in Equation 4.17.

$$\begin{aligned} I(t) &= I(t-\Delta t) + \int_{t-\Delta t}^{t} f_{1234}(\tau) e^{-i\theta_{1234}(\tau)}\, d\tau \\ &= I(t-\Delta t) + \frac{\Delta t}{2}\left[f_{1234} t - \Delta t e^{-i\theta_{1234}(t-\Delta t)} + f_{1234}(t) e^{-i\theta_{1234}(t)}\right] + O(\Delta t^3) \end{aligned} \tag{4.17}$$

Similarly, since $\beta_{1234} = 0$, $\theta_{1234}(t)$ is calculated from Equation 4.18.

$$\theta_{1234}(t) = \theta_{1234}(t-\Delta t) + \Delta_{12}^{34} \Delta t + O(\Delta t^3) \tag{4.18}$$

The derivatives of the variables can be calculated as:

$$\theta'_{1234}(t) = \Delta_{1234} t \tag{4.19a}$$

$$\theta''_{1234}(t) = \beta'_{1234}(t) = 0 \tag{4.19b}$$

$$f'_{1234}(t) = \frac{f_{1234}(t) - f_{1234}(t-\Delta t)}{\Delta t} + O(\Delta t) \tag{4.20}$$

The derivative of $I(t)$ can be calculated with with differentiation of Equation 4.11 as:

$$I'(t) = f_{1234}(t) e^{-i\theta_{1234}(t)} \tag{4.21}$$

To begin the time evolution of Equation 4.16 some initial values for the variables should be considered. Assuming that the initial condition is taken for $t = 0$, the values of the variables are given from Equation 4.22.

$$I(0) = 0 \tag{4.22a}$$

$$\theta_{1234}(0) = 0, \quad \theta'_{1234}(0) = 0 \tag{4.22b}$$

$$f'_{1234}(0) = 0 \tag{4.22c}$$

Similarly, an initial condition for the wave action spectrum $C_1(t=0)$ is required. This can be taken from measurements or from a theoretical spectrum. An appropriate transformation to obtain the wave action spectrum (C_n) from a given energy density spectrum in $\kappa-$space ($S(\mathbf{k})$) is shown in Equation 4.23. $D\mathbf{k}_1$ is the area of a bin in the wavenumber vector place that contains the energy of an arbitrary wave component with wavenenumber $\mathbf{k}_1$. This area is expressed by $D\mathbf{k}_n = Dk_xDk_y$. The 1D case for the spectrum is straight-forward to consider, by using $D\mathbf{k}_n = Dk_x$. After the time evolution of the GKE is finished, the opposite transformation of Equation 4.23 can be used to retrieve the spectrum $S(\mathbf{k})$.

$$C_1 = S(\mathbf{k}_1)\frac{D\mathbf{k}_1}{\omega_1}g \tag{4.23}$$

It is important to highlight that in (Gramstad and Stiassnie, 2013) a regularly spaced $\kappa-$grid is selected for the discretization. For the simple version of the numerical implementation of the GKE considered in the present study, this selection is crucial, because it allows interacting quadruplets to be defined. This aspect will be discussed later.

4.4 Verification of the GKE

The formulation of the GKE includes a large number of complex coefficients. Its programming for the formation of the 4^{th} order tensor T_{1234}, as well as the time marching, may induce potential errors and pitfalls. For this reason, verifying the code was con-

sidered essential before applying it to the present case. The verification of the GKE can be done based on the published results for the propagation of the 1D JONSWAP spectra published in (Gramstad and Stiassnie, 2013) and (Benoit et al., 2015). Another way to check the implementation and validity range of the GKE is comparison with Monte Carlo simulations with multiple realisations of random phases. This is commonly performed with HOS codes, as done in both of the aforementioned publications and in (Janssen, 2003), considering nonlinear order 3, which corresponds to the ZE. In the present study, HOS-ocean was used for Monte Carlo simulations, as discussed in Section 3.4.

For the verification of the GKE, the same JONSWAP spectra that were used in Section 3.4 will be employed. The expression of the JONSWAP spectrum in $\kappa-$space can be given by Equation 4.24.

$$S(\mathbf{k}) = \frac{\alpha}{2k^3} exp\left[-\frac{5}{4}\left(\frac{k}{k_p}\right)^{-2}\right] \gamma^{exp\left[-\left(\sqrt{k/k_p}-1\right)^2/(2\sigma^2)\right]} D(\theta) \tag{4.24}$$

$$\text{with } \sigma = \begin{cases} 0.07 \text{ for } \kappa \leq \kappa_p \\ 0.09 \text{ for } \kappa > \kappa_p \end{cases}$$

where $D(\theta)$ defines the directional distribution and for unidirectional propagation it is taken as $D(\theta) = 1$, α is a coefficient to determine the energy of the spectrum and γ is the peak enhancement factor.

For the verification of the present study, α and γ are taken from Table 4.2. The values are selected in such a way that the steepness, defined as $\varepsilon = k_p\sqrt{2\sum_n S_n}$ (Gramstad and Stiassnie, 2013) or $\varepsilon = \frac{k_p H_{m0}}{2\sqrt{2}}$ (Benoit et al., 2015), of the three examined spectra is the same, but the spectral width is different. k_p is the wavenumber of the component of f_p and $H_{m0} = 4\sqrt{m_0}$, where m_0 is the zeroth moment of the spectrum. H_{m0} is an estimate of the H_s calculated by the mean period (Holthuijsen, 2007). It becomes apparent that the three spectra have the same energy, but different spectral shape.

Table 4.2: Parameters for JONSWAP spectra for the verification of GKE.

α	0.0364	0.0238	0.0083
γ	1.0	3.3	20.0
Δk	0.066	0.050	0.040
Number of waves	60	80	100

For convenience, $k_p = 1$, which yields $L_p = 2\pi$ m in deep water and $T_p = 2.006$ s. Deep water is achieved by defining a large value for the water depth, e.g., 5000 m. An equidistant $\kappa-$grid with increment Dk is used ranging $[Dk,\ 4k_p]$. It is noted that considering $k(1) = 0$ instead of $k(1) = Dk$ may yield issues due to inclusion of infinitely long wavelengths.

For the results that follow, the resolution of the $\kappa-$grid is not constant for the three examined spectra, but it was chosen to be the optimum after convergence analysis, as seen in Table 4.2. This was done in order to save computational resources. As an approximate indication, for $1000T_p$ of propagation using a time step of $\Delta t = T_p/2$ as done in (Benoit et al., 2015), 60 waves require 0.5 h, 80 waves 3 h and 100 waves 7 h, on a single core of Intel i7 @ 3.0 GHz. Higher resolution was selected for the narrower spectra in order to allow for sufficient discretization of the main part of the spectrum and the spectral peak.

The results of the present implementation of the GKE are compared against the results of the PAE of Benoit et al. (2015), which seems to give similar qualitative results to that of Gramstad and Stiassnie (2013), as well as against Monte Carlo simulations of HOS-ocean using 800 random phase simulation and the COSMHOS Monte Carlo simulations of Benoit et al. (2015) using 700 simulations. As observed already in Section 3.4, the greatest spectral change occurs for the spectra with the highest γ, because they are far from equilibrium (see Section 4.2.3). These cases also, despite the overall good agreement, yielded the largest discrepancies between the predictions of HOS-ocean and PAE.

First, the long term evolution of the spectra is examined after $1000T_p$ in Figures 4.8, 4.9 and 4.10. As seen in Figure 4.8, the present results agree well for both the HOS

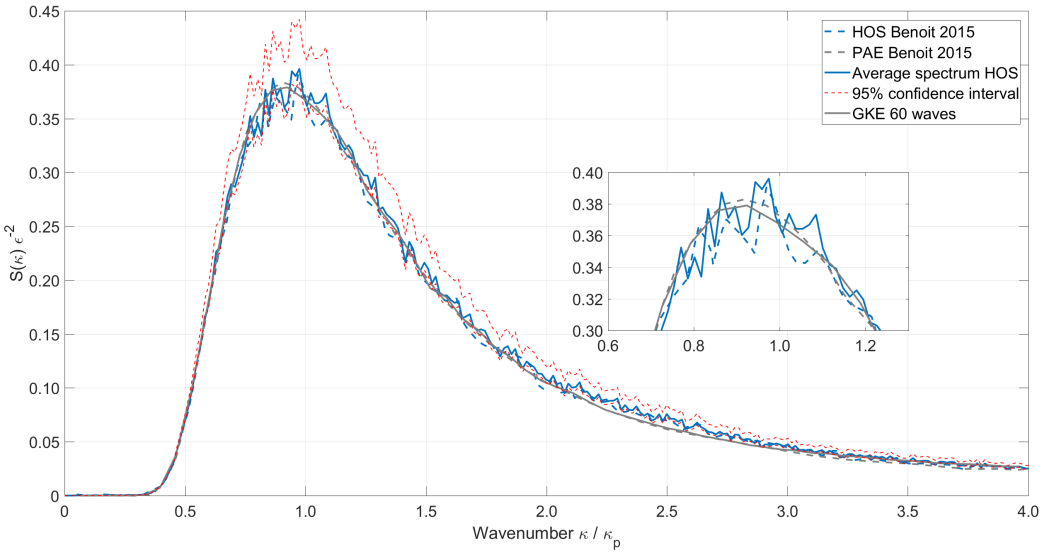

Figure 4.8: Comparison among the results of GKE, HOS-ocean and the published results of Benoit et al. (2015) for a JONSWAP spectrum of $\gamma = 1.0$ after evolution of $1000T_p$.

and PAE predictions for the broadbanded spectrum of $\gamma = 1$. In Figure 4.9, the overall agreement is very good for the spectrum of $\gamma = 3.3$, but noticeable discrepancies are observed near the spectral peak. Both GKE and PAE overpredict the evolved spectral peak compared with the HOS-ocean and COSMHOS results that are in good agreement between them. GKE seems also to predict a higher peak than PAE. The largest discrepancies appear for the spectrum of $\gamma = 20.0$[9], as shown in Figure 4.10. Clearly the two HOS codes that are in good agreement, yield a lower spectral peak than the GKE and PAE. Also, HOS simulations predict higher energy at around 0.5-0.7 κ/κ_p. Some small deviations from the HOS results can also be seen in higher wavenumbers, but the energy content is very low. What is important to observe is that the GKE have some local instabilities that were not present for at the beginning of the simulation. Also the predicted spectral peak is slightly wider than that of PAE and has a local deep. It is presumed that further increasing the resolution of the $\kappa-$grid would resolve these issues that appear only for very long evolution.

[9]A JONSWAP spectrum with $\gamma = 20.0$ can be rarely encountered in nature, however it is commonly used to examine spectral changes because it is far from equilibrium compared to more broadbanded spectra.

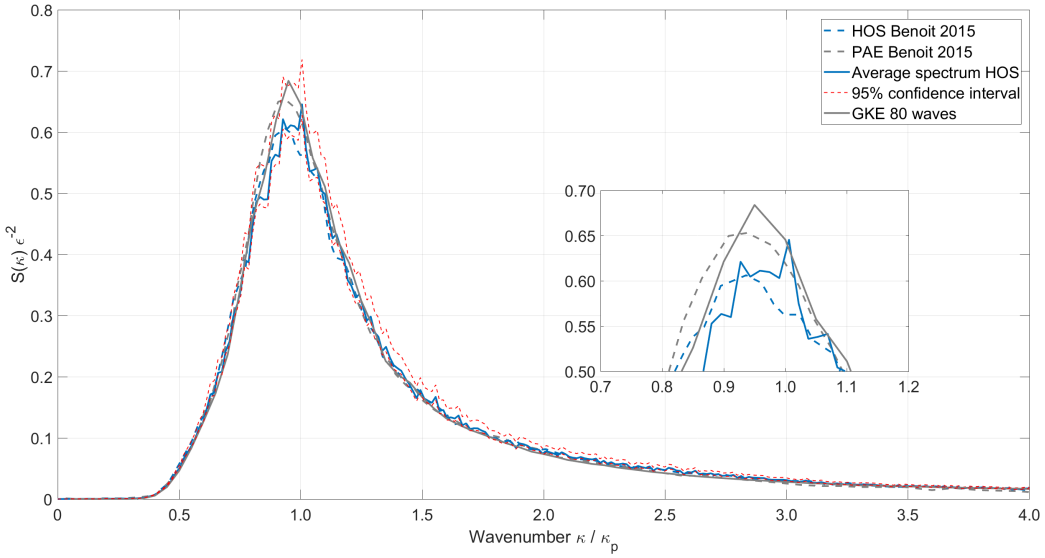

Figure 4.9: Comparison among the results of GKE, HOS-ocean and the published results of Benoit et al. (2015) for a JONSWAP spectrum of $\gamma = 3.3$ after evolution of $1000T_p$.

Trying to further analyse the discrepancy for the narrow JONSWAP spectrum after long evolution, additional tests were performed. As discussed, the role of the four-wave interactions is to stabilize the spectrum, bringing it to its equilibrium state, which means that after long evolution the spectral change should be minimal. This was also shown by Gramstad and Stiassnie (2013), Benoit et al. (2015) and (Tanaka, 2001), by examining the rate of spectral change, which was large for the first T_ps of evolution and decayed rapidly. In order to confirm this behaviour of the GKE, the spectra every $20T_p$s are presented in Figure 4.11a and 4.11b from the initial state at $t = 0$ to $t = 1000T_p$ and from $t = 800T_p$ to $t = 1000T_p$, respectively. The $x-$axis is truncated to facilitate observations. The initial and final spectra are indicated with black thick lines. It can be seen that the spectral peak is downshifted quickly and the energy is spread in lower and higher frequencies, only within $20 - 40T_p$. Afterwards, the energy of the wave components fluctuates within certain limits. The range of this fluctuation should decay with time, but here it is shown that even after long evolution $> 800T_p$ the values around the spectral peak continue to fluctuate considerably. As such, a stable situation has not been achieved for the very narrow spectrum of $\gamma = 20.0$. Therefore, the exact

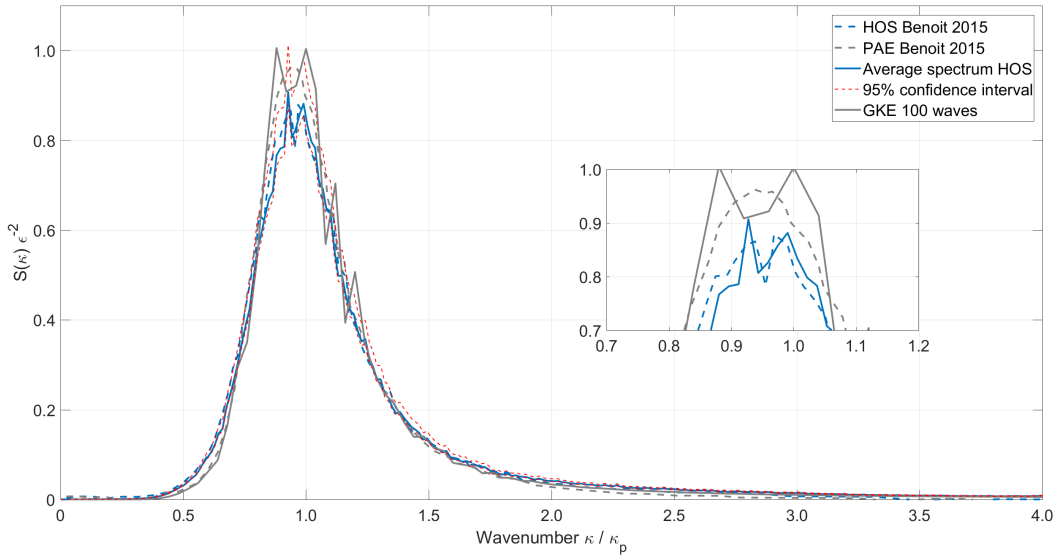

Figure 4.10: Comparison among the results of GKE, HOS-ocean and the published results of Benoit et al. (2015) for a JONSWAP spectrum of $\gamma = 20.0$ after evolution of $1000T_p$.

spectral shape obtained by the GKE for spectra very far from equilibrium cannot be predicted with confidence. Nevertheless, the general trend is very well estimated. It is also important to mention here the observation of Benoit et al. (2015) for the spectrum of $\gamma = 20.0$ that the error between PAE and Monte Carlo HOS simulations increases linearly with time, having a minimum at $300T_p$. Thus, these fluctuations should not be attributed to a potential wrong implementation of the GKE in the present study.

Apart from the long evolution, the short evolution of the wave spectrum should be considered, which is actually the main interest of the present study. To examine the behaviour of GKE for shorter time evolution, comparison with the only available results, to the author's best knowledge, found in (Benoit et al., 2015) is performed for the case of the spectrum with $\gamma = 20.0$. These results refer to evolutions of $30T_p$, $60T_p$, $200T_p$ and $300T_p$, as seen in Figures 4.12, 4.13, 4.14 and 4.15, respectively[10]. It can be seen that for the short evolution of $30T_p$ the GKE is in excellent agreement with the PAE and the small differences can be readily attributed to the lower resolution used

[10]To better illustrate the differences around the spectral peak, the $x-$axis is truncated to $2\kappa/\kappa_p$, even though the simulations were performed up to $4\kappa/\kappa_p$.

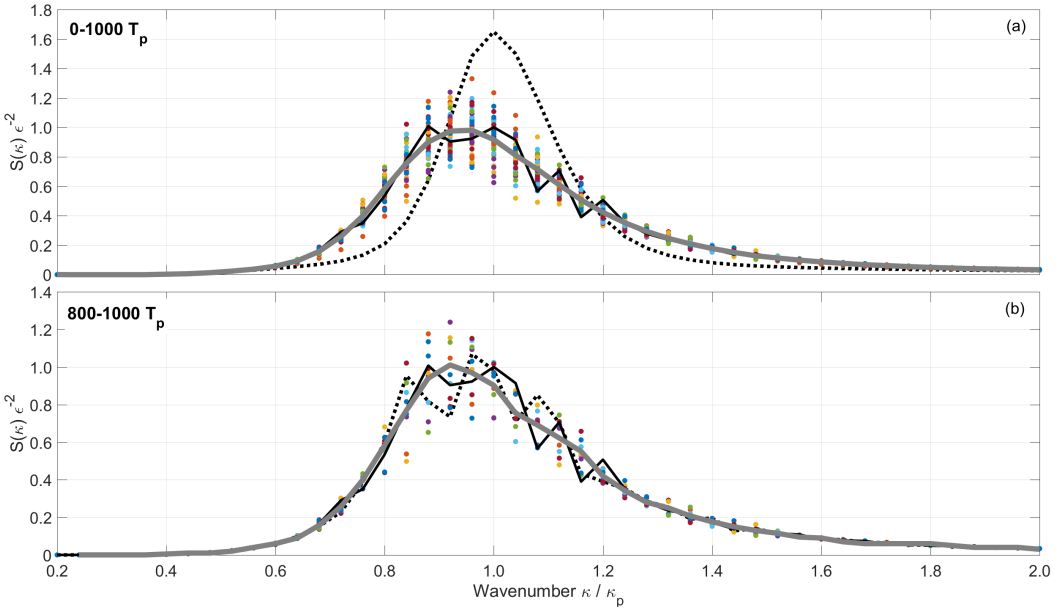

Figure 4.11: Spectral evolution every $20T_P$ for the spectrum of $\gamma = 20.0$ predicted by the GKE for time range of $0 - 1000T_p$ (a) and $800 - 1000T_P$ (b). Dots: intermediate times; Dotted black lines: initial time; Thick black lines: final time; Grey thick lines: mean of dots.

in the present study. However, both PAE and GKE exhibit important deviations from the result of the Monte Carlo predictions. The HOS-ocean result however is much closer to the PAE and GKE than the COSMHOS result of Benoit et al. (2015). Since the two HOS predictions are in good agreement for $60T_p$, $200T_p$ and $300T_p$, the present discrepancy may be attributed to the initialization of the HOS simulations. As discussed in Section A.3.3, the initial condition is selected according to linear theory and a ramp-up time is used in order to smoothly transit to the nonlinear simulation. In the present study with HOS-ocean, the smoothing time was selected as $1T_p$ in order to quickly obtain nonlinear evolution. The smoothing time may had been selected differently by Benoit et al. (2015). After evolution of $60T_p$ (Figure 4.13), it is seen that the two HOS predictions are in very good agreement. However, the results of GKE and PAE predict a bimodal behaviour of the spectrum, which cannot be easily explained. Since all the simulations were performed with the same time step as that of (Benoit et al., 2015), namely $T_P/2$, it was decided to examine the possibility that the discrepancies of the GKE are due to the selection of the time step, which is expected to have a greater

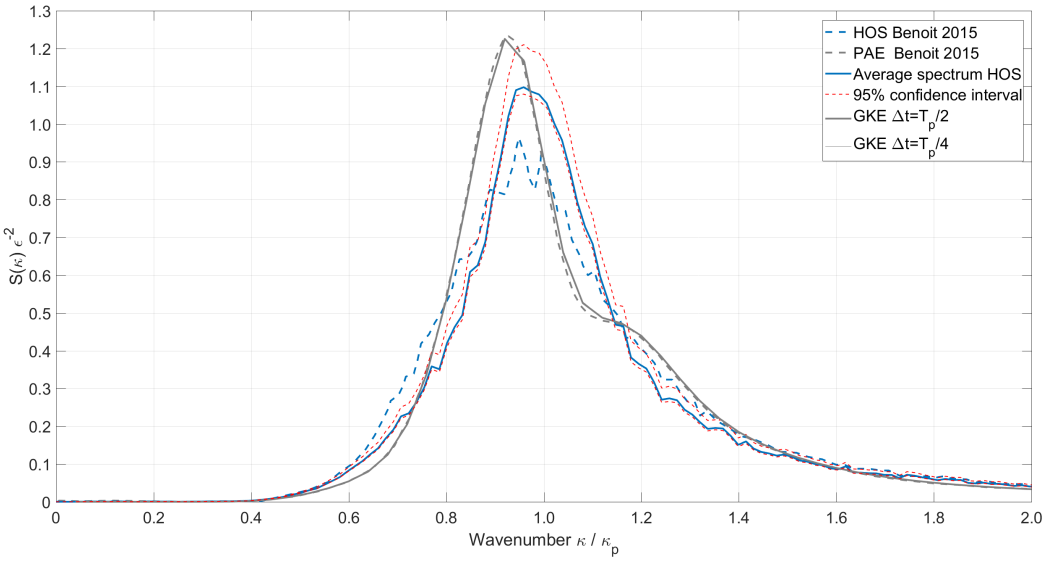

Figure 4.12: Comparison among the results of GKE, HOS-ocean and the published results of Benoit et al. (2015) for a JONSWAP spectrum of $\gamma = 20.0$ after evolution of $30T_p$.

impact for short term than for long term evolution. For that, a time step of $T_P/4$ was also used. As seen in Figures 4.12 and 4.13, the two results of different time steps exactly collapse to each other and it is concluded that the behaviour of the GKE cannot be attributed to a numerical error.

The bimodal behaviour of the GKE and PAE observed for short evolution seems to vanish after long propagation of $200T_p$, as seen in Figure 4.14, where the agreement is significantly improved. The spectral peak is well predicted, but PAE and GKE exhibit a wider and flatter peak. Finally, after $300T_p$, the best agreement is observed, as shown in Figure 4.15. The results of HOS models are close to PAE and GKE. There is still a difference near the peak though, which is predicted slightly downshifted and with higher energy by the phase-averaged equations.

Some important remarks can drawn for the behaviour of the GKE by examining details of the spectral evolution that require attention:

i) The selection of the interacting quadruplets is probably the most important aspect that influences the results. Even though a geometric frequency grid is used in

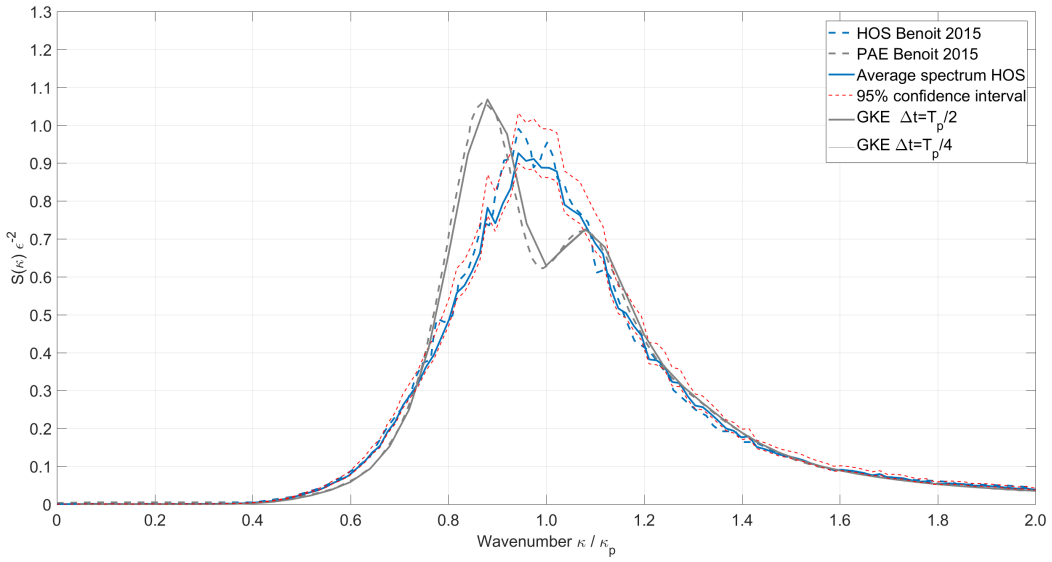

Figure 4.13: Comparison among the results of GKE, HOS-ocean and the published results of Benoit et al. (2015) for a JONSWAP spectrum of $\gamma = 20.0$ after evolution of $60T_p$.

practice (Gramstad and Babanin, 2016), in the present, study it revealed no spectral change even when the conditions of resonance were relaxed ($\delta k \neq 0$). Similarly, changing locally the $\kappa-$grid resolution reveals instabilities. Certainly, the selection of the interacting quadruplets requires further analyses and attention, especially for the 1D case where only non-resonant interactions are present.

ii) The present findings reveal potential non-convergence of the GKE for very narrow spectra in 1D after long time evolution. This may be a result of the selection of the interacting quadruplets and of insufficient $\kappa-$grid resolution. One can expect that if an infinitely high number of wavenumbers is used, the results will be smoother. On the other hand, the convergence of the GKE to a stabilized spectrum should not be taken for granted, because the existing results in the literature present the integrated properties of the spectrum instead of the exact spectral shape.

iii) The validity for the GKE for short term evolution, at least for the JONSWAP spectrum of $\gamma = 20.0$, should also be seen critically, since the results showed important deviations from HOS Monte Carlo simulations.

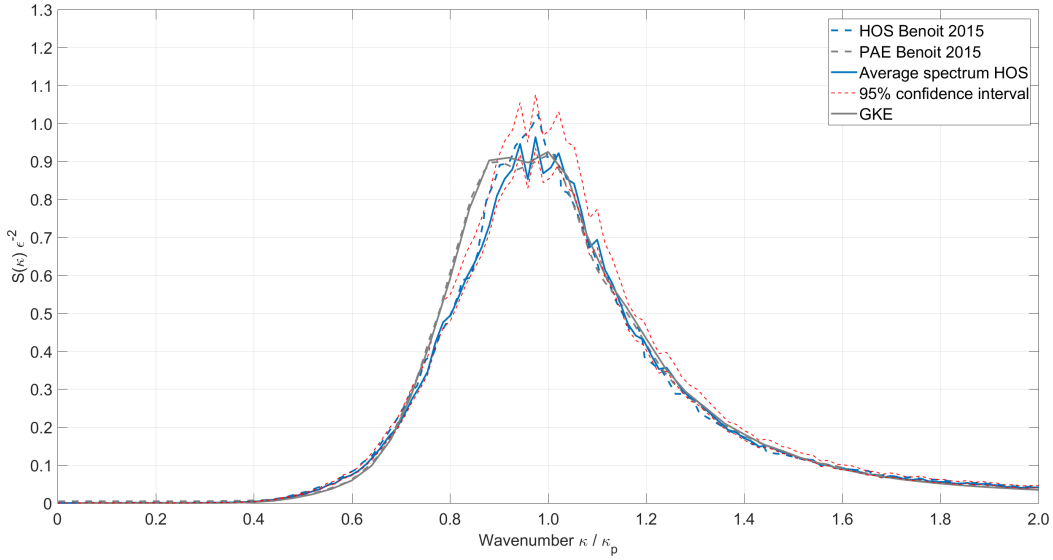

Figure 4.14: Comparison among the results of GKE, HOS-ocean and the published results of Benoit et al. (2015) for a JONSWAP spectrum of $\gamma = 20.0$ after evolution of $200T_p$.

To conclude however, the tests performed for the verification of the GKE in this section show that the behaviour of the GKE is qualitatively and quantitatively similar to that of PAE. Thus, the coupling coefficients and the numerical implementation of the GKE appear to be correct. Additionally, the GKE gives very good agreement with Monte Carlo HOS simulations, especially for long evolution and relatively broadbanded spectra. Differences were mainly observed for the very narrowbanded JONSWAP spectrum of $\gamma = 20.0$ and mainly for very short evolution. Since the present study aims at evaluating the spectral changes of the broadbanded Gaussian spectrum used for the focused waves, similar issues are not expected to appear. Nevertheless, it is still challenging to examine the spectral changes for short time evolution of a few T_ps using a stochastic approach, as discussed in the next section.

4.5 The use of the GKE for focused wave groups

Before applying the GKE in the case of focused waves, it is crucial to discuss some considerations about the potential equivalence of the sea state properties between

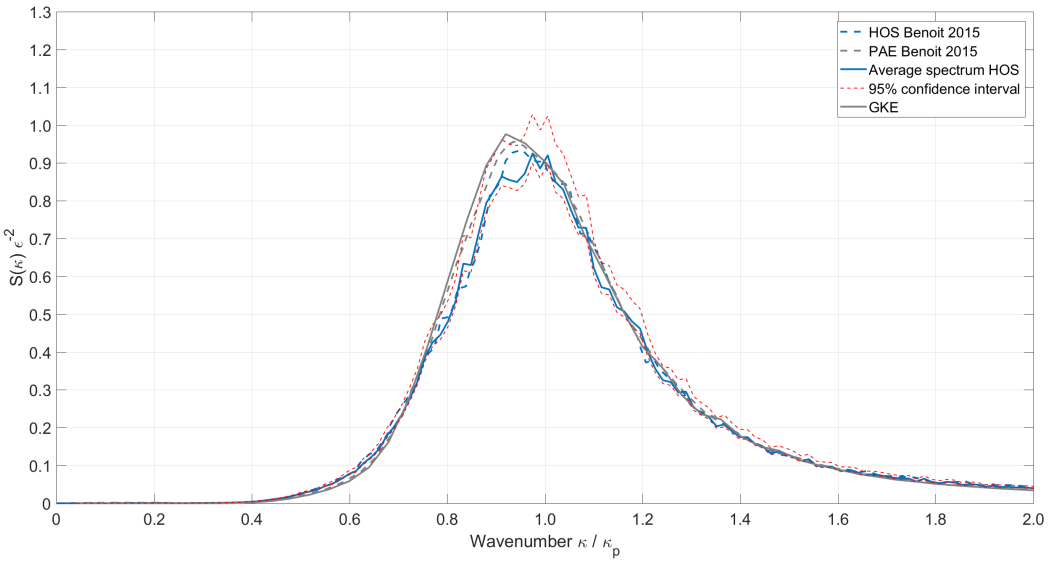

Figure 4.15: Comparison among the results of GKE, HOS-ocean and the published results of Benoit et al. (2015) for a JONSWAP spectrum of $\gamma = 20.0$ after evolution of $300T_p$.

phase-averaged and phase-resolving models. This can allow for better connecting the two approaches.

4.5.1 Selection of the $\kappa-$grid

In this section, the spectral evolution of the extracted linearised part of the spectrum, shown in Figure 4.5, that was found with the phase-resolving models for focused waves, will be examined in a stochastic manner using the GKE. For this, the Gaussian amplitude spectrum $S_\alpha(f)$ (Equation 3.1) of the dispersion study is employed, after it is firstly transformed to a variance (energy) density spectrum in the frequency domain $S(f)$, using Equation 4.25 (Holthuijsen, 2007).

$$S(f_i) = \frac{1}{2}\frac{\alpha(f_i)^2}{df} \tag{4.25}$$

where $\alpha(f_i)$ is the amplitude of each wave component i in the $f-$domain and df is the frequency increment.

Then, the obtained spectrum $S(f)$ has to be transformed from the $f-$domain to the $\kappa-$domain, since the GKE is derived for the wavenumber space. This can be achieved with the transformation described in (Holthuijsen, 2007) p. 49, using Equation 4.26.

$$S(k_i) = \frac{Cg_i}{2\pi} S(f_i) \tag{4.26}$$

where Cg_i refers to the group celerity, which can be calculated using the phase celerity C_i of each wave component, as seen in Equation 4.27 (Holthuijsen, 2007).

$$Cg_i = C_i \frac{1}{2} \left(1 + \frac{2kd}{\sinh(2kd)} \right) \tag{4.27}$$

where C_i is calculated using the wavenumber k from linear theory as $C_i = \sqrt{\frac{g}{k} \tanh(kd)}$.

The same transformation can be achieved using a discretised method and redistributing the energy from the frequency-bins to the wavenumber-bins, as show in Equation 4.28, which is possible since the employed spectra are density spectra.

$$S_i(k) = S_i(f) \frac{f_{i+1} - f_{i-1}}{k_{i+1} - k_{i-1}} \tag{4.28}$$

It is important to note here that since the GKE requires an equidistant $\kappa-$grid, first the wavenumbers are chosen and then the frequencies are calculated using the linear dispersion relation. The energy is distributed on the non-equidistant $f-$grid, following the definition of the desired spectrum, and then from Equation 4.26, $S(k_i)$ is calculated for the predefined equidistant $\kappa-$grid. This procedure was not needed for the verification of the GKE (Section 4.4), since the spectra were given directly in $\kappa-$space.

As described in Section 4.3.2, the obtained $S(k)$ spectrum should be transformed to a wave action spectrum $C(k)$ according to Equation 4.23 in order to be used in the GKE. To illustrate the transformations described above, the employed Gaussian spectrum of $f_p = 0.636$ Hz is shown in Figure 4.16. As seen, the $\kappa-$spectra are more spread

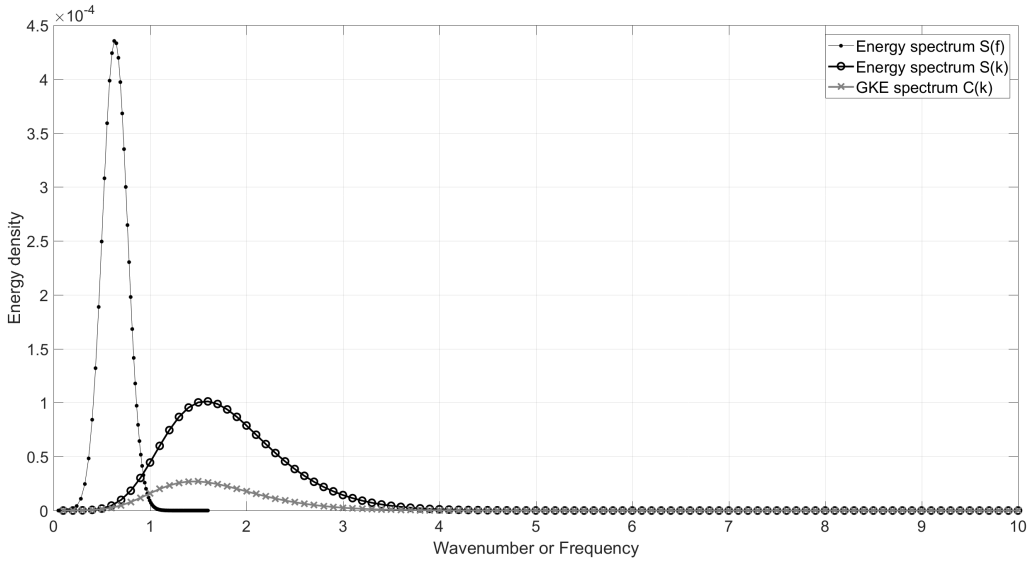

Figure 4.16: Comparison of the spectra in the $\kappa-$ and $f-$space using 100 wave components.

in high wavenumbers and, for their accurate calculation, the $\kappa-$grid should extend to wavenumbers of 5-6 m^{-1}, where there are still components with meaningful energy. It can also be observed that a regular $\kappa-$grid results in $f-$grid with relatively low resolution at low frequencies and very high resolution at high frequencies. As such, to capture the expected energy transfer up to 1.4-1.6 Hz seen in Figure 4.3, the $\kappa-$grid should extend up to 10 m $^{-1}$. Keeping in mind that sufficient resolution should be used in low frequencies, the total number of examined wave components should be relatively high. The challenge with the examined Gaussian spectrum is that it has a relatively low f_p and it is broadbanded, which results in energy at particularly low wavenumbers. This aspect will be discussed in Section 4.7.2 in more detail.

To ensure accurate implementation of the aforementioned transformations and correspondence with the phase-resolving models, the total energy of the spectrum was checked at almost all stages of the process. The total energy of the spectrum can be found by the integral of the curves $S(f)$ and $S(k)$. It can also be approximated from the significant wave height as $E_{tot} = \frac{H_s^2}{16}$, where H_s can be calculated from the timeseries of the surface displacement as $H_s = 4 \times SD(\eta(t))$, where SD is the standard deviation

(Holthuijsen, 2007). These definitions are employed throughout the present study.

4.5.2 Selection of the equivalent steepness

As observed in the spectral analysis in Section 4.1.2, the strongly nonlinear group ($\Sigma\alpha_i = 0.154$ m) is practically the only one that exhibits important spectral evolution of the extracted linearised harmonics. Thus, this group will be used for the analysis that follows. It is also reminded that the focused wave produced for the strongly nonlinear group referred to the limiting breaking case in the experiment. The significant wave height calculated for the strongly nonlinear group is $H_s = 0.0477$m. Preliminary investigation with the GKE for this H_s did not result in any spectral change even after very long evolution of $1000T_P$. This can be justified if one observes the timeseries of the surface elevation of the strongly nonlinear group and a random phase wave group that has the same E_{tot}, as presented in Figure 4.17a. Since the focused wave group has a return period of 128 s, the energy is concentrated only in the short time window of the focused group and the remaining long timeseries have zero energy. Thus, as seen from the timeseries, the steepness of a random phase group is much lower than the local steepness of the focused group. Consequently, the GKE does not predict any spectral change, since the overall steepness of the sea is relatively small.

At this stage, the first challenge in finding the equivalence between phase-resolving and phase-averaged models arises. The phase-averaged approach of random phases results in a sea state of much lower steepness than the local steepness of a focused wave group, since in the latter the energy is forced to be concentrated in a confined space. This low steepness sea state is in equilibrium and the interactions between the waves are weak. It becomes apparent that it is not "fair" to spread the energy of the focused wave over the entire timeseries of 0-128 s, but instead it would be more appropriate to find an equivalent energetic sea state that represents better the steepness of the focused wave. The only remote example discussed in the literature can be found in (Janssen, 2003), Figure 1, which refers to a focused group with a short

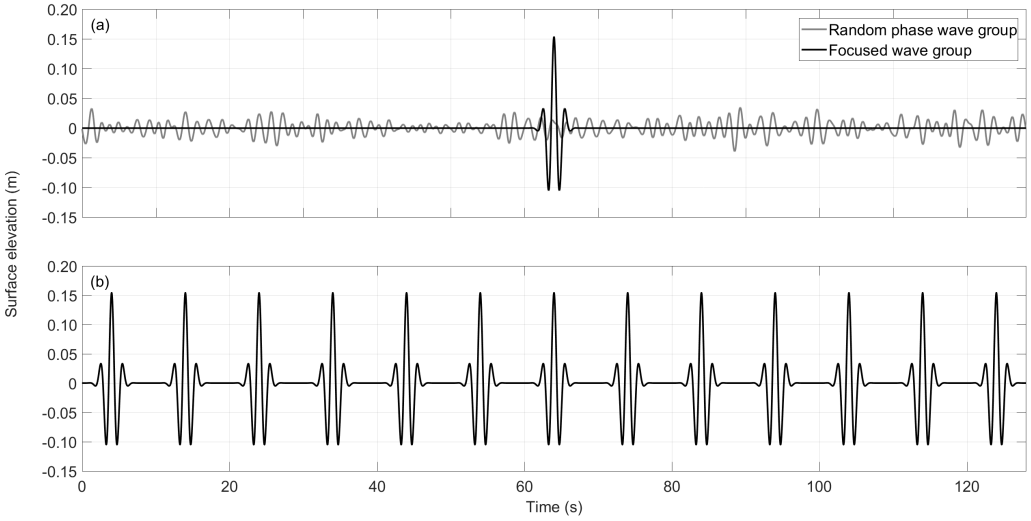

Figure 4.17: (a) Comparison of the timeseries of the of a focused wave group and random phase wave group generated by the same Gaussian spectrum used for the strongly nonlinear group ($\Sigma\alpha_i = 0.154$ m), based on linear theory. (b) Repetitive focused wave group.

return period that is repetitive in time. The result of a similar approach considered here is demonstrated in Figure 4.17b as an example, where the focused wave group is repeated with fixed time intervals. Of course, especially for the wave group examined here, this would imply a sea state of very high steepness, where wave breaking could potentially occur.

For focused wave groups, the return period can be determined by the frequency increment of the spectrum df. To achieve a return period of 128 s, $df \simeq 0.0078$ Hz (1/128=0.0078). Defining a larger df shortens the return period of the spectrum, making the event more repetitive in time. However, this approach was not preferred here, because it results in lower frequency resolution, which does not facilitates comparisons, and the return period is not the same for the different locations from AM (long dispersed group) to PF (compact focused group) in the tank. Instead of changing df, it was decided to truncate the timeseries and include only the time window that has waves inside. The energy of the wave group can be found by the H_s of the truncated timeseries of the surface elevation. Using linear theory to generate the timeseries, this

process returns an $H_s^{PF} \simeq 0.35$ m at the PF location and an $H_s^{inlet} \simeq 0.16$m near the inlet. Neither of these values is representative for all the locations in the tank, since they refer to two extreme cases of the wave group (dispersed and compact). One could instead select to use the average value H_s^{mean} calculated as the arithmetic or the geometric mean, $\simeq 0.25$ m and $\simeq 0.23$ m, respectively.

The previous approach of using a constant H_s is convenient, since the H_s can be easily approximated using the timeseries at the desired location. However, observation of the timeseries indicates that using H_s^{inlet} or H_s^{PF} is not representative, while using H_s^{mean} is still a crude approximation, since the H_s of the truncated timeseries does not increase linearly from the inlet to the PF location.

A solution to the above problem can be given by calculating a time dependent $H_s(t)$. To achieve that, the timeseries of the surface elevation were examined at locations $x = -1, -2, -3...n\ L_p$ m upstream of the PF location, where L_p is the wave length corresponding to the wave component at f_p. The generated timeseries were truncated automatically using a criterion based on their absolute maximum value divided by a desired tolerance. For example, at PF, where the linearly predicted maximum is 0.154 m, using a tolerance of 10, the timeseries before and after the group are truncated when the first value lower than 0.0154 m is encountered. Selecting a larger tolerance implies that longer timeseries are used, resulting to a lower value of H_s. In order to find the value of H_s at any location, the value of the H_S at the discrete locations x is firstly computed and a polynomial fitting is then used. An example of this process is given in Figure 4.18, where the truncated timeseries of the focused wave group are presented in the large plot at PF (top line) and at locations downstream. In the small subplot, the H_s calculated per location is presented with the fitted 2^{nd} order polynomial function.

To be precise, the previous approach for the H_s return a location related $H_s(x)$. However, since the H_s is calculated at locations relative to L_p, the same expression can be used in the GKE where the time integration is an increment of T_p. For this reason, $H_s(x)$ at x relative to L_p, is equivalent to $H_s(t)$ at t relative to T_p in the GKE.

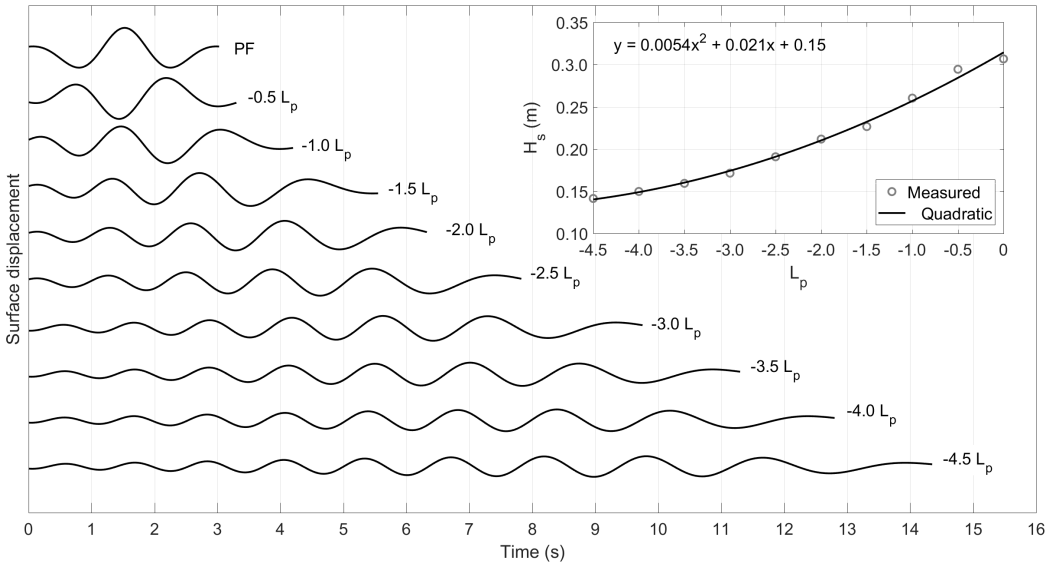

Figure 4.18: Example of truncated timeseries of the surface elevation used for the estimation of the $H_s(L_p)$ using tolerance=5.

Trying to explain the equivalence of the previous process between phase-resolving and phase-averaged models, one can consider the following: the GKE expresses the time evolution of a fixed sea area that does not propagate in space. On the other hand, focused waves with a moving time window represent a transient event in space, which steepness increases as a result of focusing. To do exactly the same for a random sea state, one would have to decrease the area of the sea keeping the same energy spectrum, which would increase its steepness. However, the strategy used here practically increases the energy of the sea state by simply increasing its H_s. This H_s is calculated from timeseries of the surface elevation of decreasing length. Thus, an equivalence between altering sea area in phase-averaged models and time in phase-resolving models is perceived.

An advantage of the method of defining $H_s(t)$ discussed above is that it allows for tracking the increasing steepness of the wave group at any time. In the algorithm of the GKE this can be implemented as such: at the end of each time step, when all the wave interactions are calculated and the new spectrum is computed, the energy of the latter is rescaled based on the H_s of the examined timestep. This is equivalent of

running the GKE for only one time step and then changing the spectrum and rerunning it. The flexibility of defining $H_s(t)$ using a polynomial function, is that it is independent of the magnitude of the time step. Care should be taken not to run the GKE for values of the H_s higher than H_s^{PF}. This can be easily implemented in the algorithm using a stopping condition. At the end of the calculation, the final spectrum is rescaled in order to have the H_s of the full timeseries, which corresponds to the original spectrum. This allows for direct comparison of the spectral evolution between phase-averaged and phase-resolving models for focused waves.

Results regarding the influence of the steepness in the present case are presented in Section 4.6.2.

4.5.3 Selection of the equivalent time evolution

As it became apparent from the verification of GKE in Section 4.4, the shape of the computed spectrum depends on the total time evolution. Thus, there is a second challenge for the transition from phase-resolving to phase-averaged models, which refers to the selection of the time.

There are two possible considerations for selecting the total evolution time in the GKE:

i) To use the exact time in the phase-averaged model as in the focused wave group. This can be done by finding how many T_ps the wave group has propagated from the wave paddle or AM location to the PF location. A way to calculate that is by finding how many L_ps the wave group has covered in this distance, in a similar manner as done in Figure 4.18. Instead of L_p, one could use L_{mean}, which corresponds to the mean frequency wave component, as a more representative value. f_{mean} can be calculated by the spectral moments as: $f_{mean} = \sqrt{m_1/m_0}$, where $m_n = \int_0^\infty f^n E(f) df$ (see (Holthuijsen, 2007) p. 61) [11].

ii) To assume that the free-wave spectrum has reached an equilibrium state and thus

[11] In the present work both the approaches were tried, but a only negligible difference was found.

use a very large evolution time of $100 - 1000T_p$.

The challenge with the former consideration is that since the waves are not randomly mixed within this time frame, the long waves that are just introduced at the inlet at $t = 0$, do not interact with the shorter waves that are already close to PF at that time. This is mentioned as a potential issue for calculating the wave-wave interactions by Shemer and Dorfman (2008) as well. Also, the GKE has shown some discrepancies for short propagation time, as discussed in Section 4.4. However, those results concerned the very narrowbanded JONSWAP spectrum of $\gamma = 20.0$ and it is not yet known if similar issues will appear for the broadbanded Gaussian spectrum used in focused waves. This is discussed later when the results of the GKE are compared with Monte Carlo simulations (see Section 4.7.1).

The issue with the latter approach is that it completely ignores the time evolution of the focused wave group and thus, it is totally decoupled from the phase-resolving aspect of the problem. Additionally, only a constant H_s can be used in the GKE and not the $H_s(t)$ consideration described previously. Last but not least, the equilibrium state of the spectrum is something to be proven, rather than something to be pre-assumed in order to start the analysis. For this reason, mainly the short time evolution will be considered, which is equivalent to the one derived the phase-resolving model or for convenience by linear theory, because the scope is not to run an expensive phase-resolving model before running the GKE.

The results of testing different time evolutions in the GKE for the present case are presented in Section 4.6.3.

4.5.4 Selection of the equivalent water depth

In the context of comparing focused waves and random waves, the effect of water depth should also be discussed. As explained in the derivation of the GKE (Section 4.3.1), the GKE was derived for finite water depth, which allows for its application at the

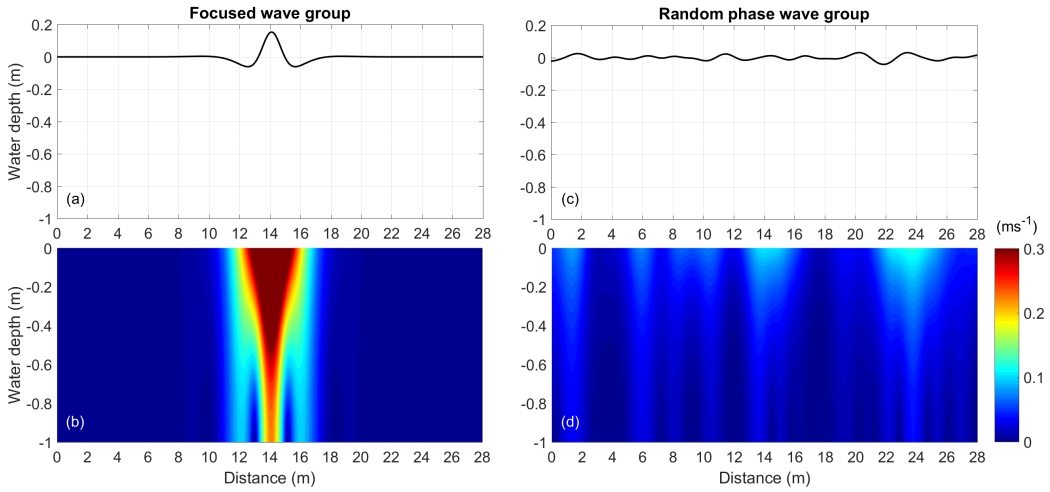

Figure 4.19: Effect of the focusing of the wave group on the kinematics. (a) (c) Surface displacement along the flume; (b) (d) Velocity magnitude beneath the SWL calculated by linear theory.

present study. Concerns for the use of the action of four-wave interactions and weak turbulence were also discussed in Section 4.2.3.

Considering a simple approach, the water depth can be taken as the actual water depth used in the phase-resolving models. However, one should be concerned whether, when the wave group focuses, the depth has an effect on the kinematics of the water particles near the bottom. To illustrate this, the velocity magnitude -calculated as $u_{mag} = \sum_{i=1}^{N} \sqrt{u_x^2 + u_z^2}$, for the N wave components, with horizontal velocity $u_x = \omega\alpha \frac{\cosh[k(d+z)]}{\sinh(kd)} \sin(\omega t - kx)$ and vertical velocity $u_z = \omega\alpha \frac{\sinh[k(d+z)]}{\sinh(kd)} \cos(\omega t - kx)$, with $z = 0$ at the SWL and pointing upwards (see Equation 3.3)- is presented for the focused wave group and a random wave group of the same energy spectrum is plotted in Figure 4.19. It can be clearly seen that the velocity field of a focused group is concentrated and it extends farther in the vertical. As a result, the wave group may be influenced by the finite water depth, since the waves start "feeling" the bottom of the flume when they become focused. Thus, it could be more relevant, instead of using the actual water depth, to define an equivalent water depth.

A way to perform the calculation of the equivalent water depth can be based on the

Ursell number, which gives an indication of the nonlinearities of the waves, combining the wave steepness and the water depth. For an irregular wave group, the Ursell number can be calculated by Equation 4.29 ((Holthuijsen, 2007) p. 273). To find the equivalence, a U_r can be calculated for the random wave group and one for the focused group using the truncated time history of the surface elevation. Then, the equivalent depth can be calculated in order to obtain the same U_r as for the random timeseries. This process results to a smaller water depth, which according to theory causes greater wave-wave interactions, see e.g. Section A.4.4.

$$U_r = \frac{gH_sT_m^2}{9\sqrt{2}\pi^2 d^2} \tag{4.29}$$

where $T_m = \sqrt{m_0/m_1}$[12], calculated using the spectral moments $m_n = \int_0^\infty f^n E(f)df$ (see (Holthuijsen, 2007) p. 61) .

Theoretically, an equivalent water depth can be calculated for different locations in the tank and define $d(t)$, in a similar way as for $H_s(t)$. However, contrary to H_s, the water depth cannot be updated in every timestep in the algorithm of the GKE, because the interaction coefficients are calculated using a specific water depth. For this reason, mainly, this approach was not examined in more detail, however, results considering different water depths are discussed in Section 4.6.4.

4.5.5 Phase mixing in the GKE

As described in (Gramstad and Stiassnie, 2013), the way the GKE is derived gives the option of mixing the phases, i.e. assuming uncorrelated phases at certain time intervals. In physical terms, phase mixing can be caused by a process, such as wave breaking. For this reason, in (Gramstad and Babanin, 2016) the phases are mixed at a time interval based on the wave breaking. In practical terms, mixing the phases is performed by setting $\theta(t)$ and $I(t)$ to zero (refer to Equations 4.18 and 4.17).

[12] It may be preferred to use the mean period T_m, instead of T_p, as a more representative parameter of the spectrum.

The impact of phase mixing for 1D and 2D spectra is discussed in section 8 of (Gramstad and Stiassnie, 2013). It is shown there that phase mixing has greater effect on 1D spectra than on 2D spectra, at least when comparing the integrated result over the directions. For the former, when phase mixing is performed, it causes a new period of fast evolution for the spectrum. The result in long term evolution is that the final spectrum deviates more from its original shape compared to the spectrum estimated by the GKE without phase mixing.

It becomes apparent that the inclusion of phase mixing in the GKE, as well as the selection of the mixing intervals, may influence the final shape of the spectrum. In the present study, since the wave group is very steep (limiting breaking), the effect of phase mixing was tested in intervals of every timestep. Of course, phase mixing at every timestep is a rather extreme case, but the overall scope here is to examine whether phase mixing has an impact on the spectral shape for short evolution times. The corresponding results are presented in Section 4.6.5.

4.6 Results of the GKE for focused waves

After discussing the potential ways to find the equivalent sea state characteristics between the phase-resolving and phase-averaged modelling in the previous section, here, the GKE is applied for the Gaussian spectrum of the steepest focused wave group. The characteristics of the original spectrum are: $f_p = 0.636$ Hz and $H_s^{orig} = 0.0477$ m. The wavelength of the component of the peak frequency is $L_p = 3.63$ m and the corresponding $k_p = 1.73$ m^{-1}.

Regarding the propagation distance of the focused wave, the focused wave travels $\Delta x = 14.1 - 1.63$ m from the AM to the PF location, which corresponds to $3.5L_p$. The distance between the inlet and the PF is $3.88L_p$. Consequently, the spectral evolution lasts for approximately $4T_p$ in the phase-resolving model.

The results are evaluated by comparing the evolved amplitude spectra, after the ap-

propriate transformations discussed in Section 4.5.1. Commonly, the $S(k)$ spectrum is compared, but since the analysis in the phase-resolving model in Section 4.1 was performed for the amplitude spectrum, for consistency reasons it was preferred to present the comparisons for the amplitude spectra. It is also noted, that a decreased frequency resolution is used for the spectrum in the GKE compared to the resolution of the original spectrum. To allow for direct comparison of the final amplitude spectra, the spectrum of GKE is interpolated using the same frequency increment df as the original spectrum. This is possible because all the spectra are expressed as density spectra, which means that their values are related to the df used. Therefore, the interpolation returns a spectrum with the same energy redistributed in different frequency bins.

4.6.1 Convergence analysis of the GKE

The parameters that control the accuracy of the numerical model of the GKE are the resolution of the $\kappa-$grid, the time step Dt and the maximum wavenumber k_{max} considered. Tests for the first two were also performed in the study of Gramstad and Stiassnie (2013) for a fixed range of the $\kappa-$grid. Here, it was also considered useful to check potential influence of the latter (k_{max}), since extending the $\kappa-$grid may add more interacting quadruplets, which can result in additional energy transfers.

The results of the convergence analysis of the GKE that follow refer to the evolved amplitude spectrum computed by the GKE after $25T_p$ of time evolution. This value was chosen in order to allow for noticeable spectral evolution to take place, but at the same time to prevent any smearing of the spectral shape as an effect of very long evolution. The energy of the sea state is determined by the value of the $H_s^{PF} = 0.35$ m in order to have sufficient steepness to cause noticeable spectral change.

Table 4.3: $\kappa-$grid resolution and number of waves (nodes) for convergence of GKE.

Dk (m^{-1})	Nodes
0.100	69
0.150	46
0.175	39
0.200	34
0.225	30
0.250	27

Convergence for Dk

The value of the Dk determines the resolution of the $\kappa-$grid. In the study of Gramstad and Stiassnie (2013) it was shown that the GKE exhibits very good convergence in respect to $\kappa-$grid resolution and, practically, already 16 nodes (or $Dk = 0.25$) are adequate to describe the evolution of a JONSWAP spectrum of $\gamma = 3.3$ after $1000T_p$ in 1D. On the other hand, Benoit et al. (2015) used a very high $\kappa-$grid resolution in order to be consistent with the wave nodes used in HOS model for the Monte Carlo simulations. For the 2D case, the results seem to be more sensitive to the $\kappa-$grid resolution, possibly due to the stronger spectral evolution.

The convergence analysis for Dk is done by keeping Dt and k_{max} constant. The latter is chosen as $Dt = T_p/2$, which is used in both the studies of Gramstad and Stiassnie (2013) and Benoit et al. (2015). The former was selected as $k_{max} = 5k_p$ after some preliminary investigations. As commented for Figure 4.16, a higher value for k_{max} should be used in order to cover all the possible interactions among wave components with meaningful energy, however the scope here is to identify whether the solution is converged after trying many values of Dk. These are listed in Table 4.3, together with the resulting number of wave components.

The evolved amplitude spectra for the different values of Dk are presented in Figure 4.20, where it can be observed that the spectral evolution is almost identical for all the tested $\kappa-$grid resolutions. The only noticeable -but still negligible- differences are observed bellow 0.4 Hz and at the spectral peak, but they should be rather attributed

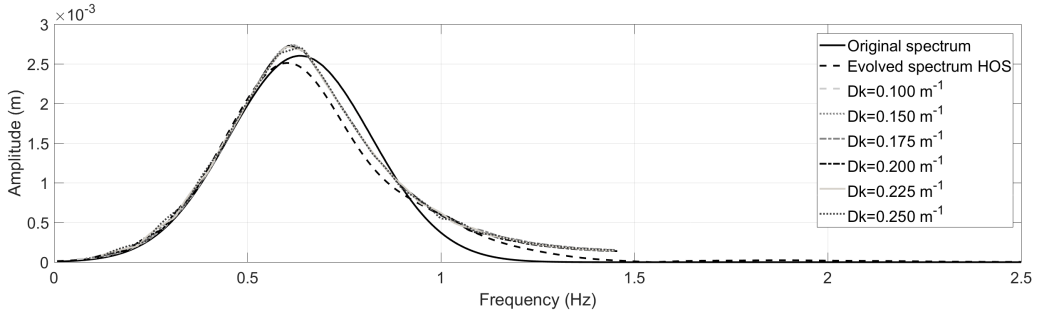

Figure 4.20: GKE predictions of the evolved amplitude spectrum after $25T_p$ for different $k-$grid resolutions Dk and constant $k_{max} = 5k_p$; $H_s = 0.35$ m; $Dt = T_p/2$.

to interpolation differences, because the $k(i)$ values are not at the same locations[13], rather than to convergence errors.

Since almost a perfect agreement is observed between $Dk = 0.200$ m^{-1} and $Dk = 0.100$ m^{-1}, it was decided to use the former resolution for the tests that follow in order to save computational resources.

An important observation that can be already made is that the evolved amplitude spectrum from the GKE is in general good qualitative agreement with the evolved spectrum from the phase-resolving model. The discrepancies and more in-detail analysis is done in the following sections.

Convergence for Dt

The integration in time for the GKE is controlled by the timestep Dt. In the study of Gramstad and Stiassnie (2013), different values of Dt were tested ranging from $T_p/200$ to $1T_p$, but the convergence was examined only in terms of total energy and not for the spectral shape. As also explained in (Gramstad and Stiassnie, 2013), the wave action and momentum are conserved independently of the timestep, thanks to the construction of the algorithm.

In the present tests, three values of the timestep ($Dt = T_p/8;\ T_p/4;\ T_p/2$) are compared

[13]This is because the $\kappa-$grid is regular and $k(1) = Dk$.

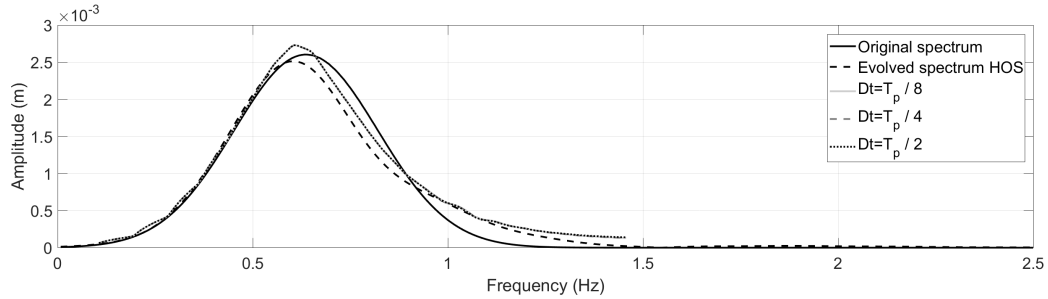

Figure 4.21: GKE predictions of the evolved amplitude spectrum after $25T_p$ for different timestep sizes Dt and constant $k-$grid resolution $Dk = 0.20$ m^{-1}; $k_{max} = 5k_p$; $H_s = 0.35$ m.

for the evolved amplitude spectral shape after $25T_p$, as shown in Figure 4.21. It can be observed that the results collapse to a single line, confirming that convergence is achieved irrespectively of the timestep. Some negligible differences can be seen in high frequencies around 1.4 Hz, but in practice they can be ignored.

For the results that follow, a timestep of $Dt = T_p/2$ was used to reduce the computational cost.

Convergence for k_{max}

As discussed at the beginning of this section, it was decided to perform convergence tests on the range of the $\kappa-$grid in order to check whether the additional interacting quadruplets have an influence on the main part of the spectrum. Using the Dt and Dk found from the previous sections, k_{max} was gradually increased from $k_{max} = 4k_p$ to $k_{max} = 10k_p$ in increments of $1k_p$. The results are shown in Figure 4.22.

Apart from the obvious difference that the lines of smaller k_{max} stop at lower frequencies, Figure 4.22 shows that below 1 Hz, where the main part of the energy is, the amplitude spectra are identical for all values of k_{max}. However, between 1-1.5 Hz there are some noticeable differences among the lines. In particular, at 1.2 Hz, there is a potential local discrepancy for $k_{max} = 6k_p$ and a smaller one for $k_{max} = 7k_p$.

For the remainder, $k_{max} = 10k_p$, corresponding to $f = 2.07$ Hz, is used in order to cover

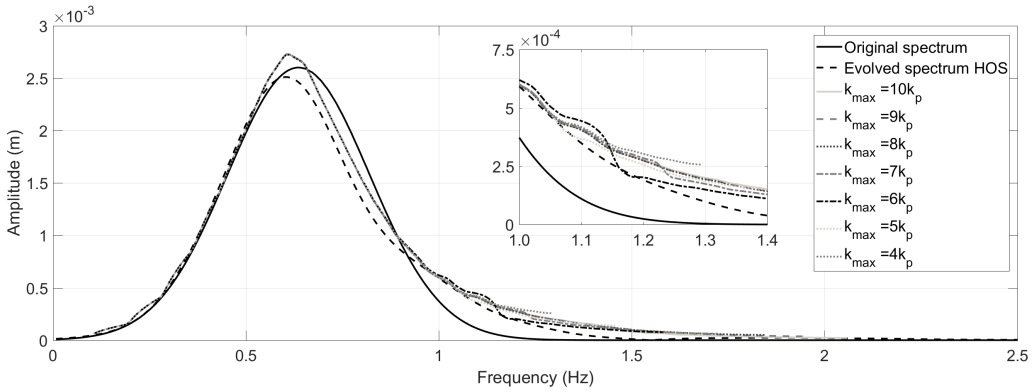

Figure 4.22: GKE predictions of the evolved amplitude spectrum after $25T_p$ for different maximum wavenumber k_{max} and constant $k-$grid resolution $Dk = 0.20$ m^{-1}; $H_s = 0.35$ m; $Dt = T_p/2$.

the spectral evolution at high frequencies, which extends up to 1.6 Hz in the phase-resolving model.

4.6.2 The impact of the steepness

In this section, the influence of the steepness of the sea state is examined, by controlling the energy of the spectrum through the H_s. The resulted energy spectra are rescaled based on a factor calculated by the ratio of the H_s^{orig}/H_s in order to match the energy of the original spectrum.

As discussed in Section 4.5.2, using the original $H_s^{orig} = 0.0477$ m of the full timeseries of the focused wave results in no difference. Instead, the timeseries were truncated and increased values of the H_s were determined. These values are calculated at the inlet ($H_s^{inlet} = 0.16$ m), the PF location $H_s^{PF} = 0.35$ m and their average $H_s^{mean} = 0.25$ m.

It was also shown that the algorithm of the GKE can be modified to include a time dependent $H_s(t)$, which can be determined by a polynomial function found by the values of the H_s calculated by the truncated timeseries of the focused wave (see Figure 4.18). Since the $H_s(t)$ is valid for only up to $4T_p$, referring to the time needed for the wave group to travel from the inlet to the PF location, the comparisons in the present section

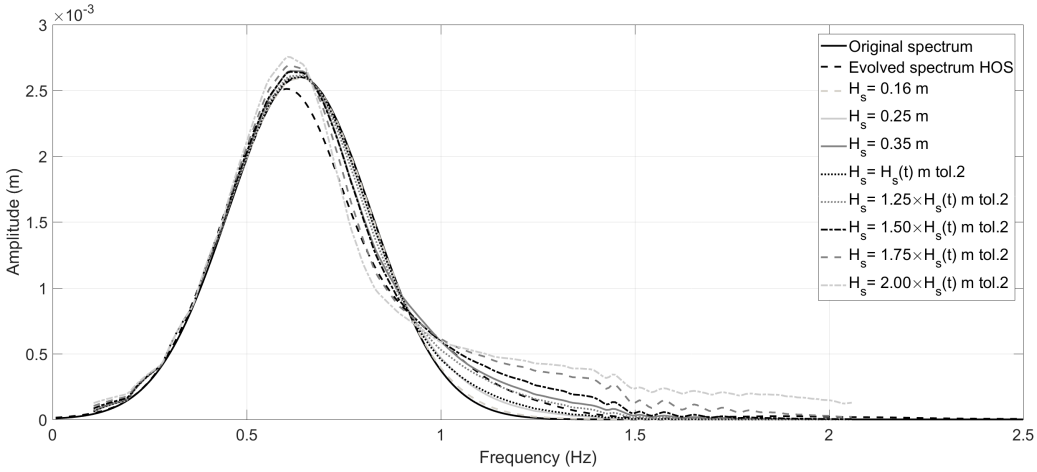

Figure 4.23: GKE predictions of the evolved amplitude spectrum after $4T_p$ for different values and expressions of H_s and constant $k-$grid resolution $Dk = 0.20$ m^{-1}; $k_{max} = 10k_p$; $Dt = T_p/2$.

are performed for a time evolution of $4T_p$.

The evolved spectra calculated by the GKE for the different values of H_s are shown in Figure 4.23. The parameters Dk, Dt and k_{max} are selected according to the convergence analysis in Section 4.6.1. Also, the expression used $H_s(t)$ is found for a tolerance $tol = 2$ of the timeseries based on the local maximum value, which polynomial fitting is $H_s(t) = (0.0089t)^2 + 0.022t + 0.17)$. Since, there was no considerable spectral evolution observed, additional expressions of $H_s(t)$ were tested, which are found by calculating $H_s(t)$ with an amplification factor >1.

Figure 4.23 shows that the part of the amplitude spectrum below 0.5 Hz remains practically unaffected by the increase of H_s. Increasing values of H_s mainly cause downshift and increase of the spectral peak and energy transfer to frequencies higher than 0.9 Hz. Using $H_s^{inlet} = 0.16$ m makes practically no change in the amplitude spectrum and after $4T_p$ the evolved spectrum is almost identical to the original spectrum. Using $H_s^{mean} = 0.25$ m, results to energy transfer between 0.9-1.5 Hz, while the amplitude spectrum at lower frequencies is practically unchanged. Similar behaviour is observed for $H_s(t)$ without an amplification factor. However, when the H_s is increased to $H_s^{PF} = 0.35$ m, considerable energy transfer is observed to frequencies higher than

0.9 Hz as well as a non-negligible spectral change between 0.5-0.9 Hz. Especially at the high frequency range of the spectrum, the results approach the evolved spectrum of HOS. Similar are the obtained results for $1.25 \times H_s(t)$, having a lower peak than those for $H_s^{PF} = 0.35$ m, a better agreement with the evolved spectrum of HOS at $f > 0.9$ Hz and an underprediction of the spectral change between 0.7-0.9 Hz. Increasing the amplification factor of $H_s(t)$ to values ≥ 1.5 causes more intense spectral changes, but always following the same trend: increasing and downshifting the spectral peak, energy transfer to $f > 0.9$ Hz and decrease of the energy between 0.7-0.9 Hz. Especially for the amplification factors of 1.75 and 2.00, the energy increase to higher frequencies is far from the evolved spectrum of HOS. Using an amplification factor of 1.5, results to a spectrum that is practically identical to that with $H_s^{PF} = 0.35$ m, except for $f > 1$ Hz, where the latter is closer to the evolved spectrum of HOS.

To sum up the previous findings, it is clear that H_s has an important role in the spectral evolution of the spectrum computed by the GKE. The general pattern of spectral evolution is consistent for the increasing steepness and it is similar to that found for the focused wave with HOS, apart from the spectral peak, which has always more energy than the original spectrum. The results that are closer to the evolved spectrum of HOS after time evolution of $4T_p$ are achieved for $H_s^{PF} = 0.35$ m and for $1.25 - 1.50 \times H_s(t)$. The general pattern of the evolved spectral shape is further investigated in the next sections.

4.6.3 The impact of the time evolution

As discussed in Section 4.5.3, the selection of an equivalent time evolution for the GKE may have important effects on the evolution of the spectrum. It is expected, based on the results of Section 4.4 for the JONSWAP spectrum of $\gamma = 20.0$, that for longer time evolutions, the spectral changes will be greater, since the quadruplets will interact for more time. It was also shown that after long time evolution, the spectrum may reach a quasi-steady state.

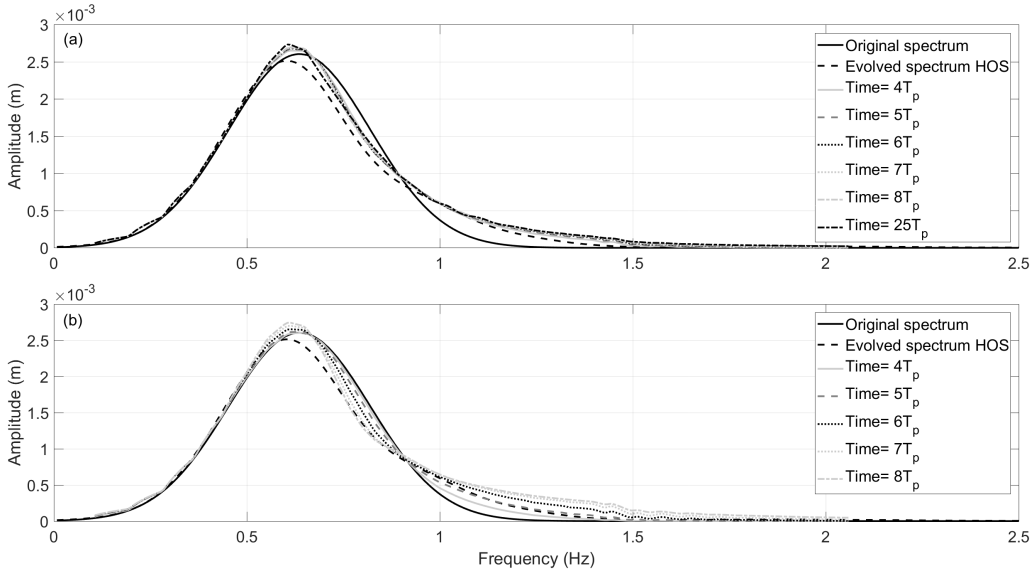

Figure 4.24: GKE predictions of the evolved amplitude spectrum at different times $N \times T_p$ and (a) constant value of $H_s = 0.35$ m and (b) expressions of $H_s(t)$ and constant $k-$grid resolution $Dk = 0.20$ m^{-1}; $k_{max} = 10k_p$; $Dt = T_p/2$.

The scope of this section is to examine whether a time evolution exists, which results in a spectral change similar to that of the HOS phase-resolving model for the focused wave. Based on the findings of Section 4.6.2, value of $H_s^{PF} = 0.35$ m is tested. Also, the behaviour of $H_s(t)$ is tested for time evolution higher than $4T_p$, by keeping the value of $H_s(t)$ constant after $T_p > 4$: $H_s(t > 4T_p) = H_s(4T_p)$. The consideration of $H_s(t)$ for longer time evolution is somewhat invalid, but the analysis was performed in order to examine if the spectrum of GKE will approach the evolved spectrum of the focused wave by having a small spectral change for the first periods and an increased change later.

The results of the amplitude spectrum for the cases of H_s discussed in the previous paragraph are presented in Figure 4.24 after time evolution of $4 - 8T_p$. The values of Dk, Dt and k_{max} are selected from the convergence analysis (Section 4.6.1).

For the case of a constant value of $H_s^{PF} = 0.35$ m in Figure 4.24a, it seems that for increasing time evolution from $4T_p$ to $8T_p$, the spectrum exhibits minimal differences with small energy increase at the spectral peak and at $f > 1.2$ Hz. Even after $25T_p$ of evolution, there is small spectral change resulting in a downshifting of the spectral peak

and increase of energy at $f > 1.2$ Hz. When the time dependent expression of $H_s(t)$ is used, the spectral changes after time evolution of $> 4T_p$ are more intense, as seen in Figure 4.24b. A higher energy transfer is predicted at $f > 0.9$ Hz and a lowering of the part of the spectrum between 0.7-0.9 Hz as well as an increase of the spectral peak. The more intense changes are assumed to be a result of the low tolerance of 2 that it is used, which results a $H_s(4T_p) \simeq 0.44$ m. However, it is out of the scope of the present work to further investigate this with other values of tolerance, because the spectral evolution pattern is persistent without approaching any better the evolved spectrum of HOS.

In conclusion, there was no obvious reason found until now to prefer the more complicated expression of $H_s(t)$ compared to a constant value of H_s. Using the latter, reveals a spectral evolution which is almost constant for the first $8T_p$ and follows the same pattern for longer time evolution of $25T_p$.

4.6.4 The effect of water depth in GKE

It was previously discussed (Section 4.5.4) that the effect of the depth on a focused wave may differ compared to a random phase wave group of the same steepness, because the energy is concentrated at a confined area and the kinematics are extended deeper in the vertical.

In this section, different values of water depth are examined in order to identify if the potentially shallower water depth that the focused wave experiences in phase-resolving model, should be accounted for as a smaller equivalent water depth in the GKE. This can be achieved, by simply changing the initial conditions in the GKE, which affects the interacting coefficients. It is expected that, since in shallower water the waves are weakly dispersive, and thus, they have similar wavelengths and wavenumbers, more interacting quadruplets can be identified. Also, since the depth dependent interacting coefficients have higher values, stronger spectral changes should occur for decreasing water depth.

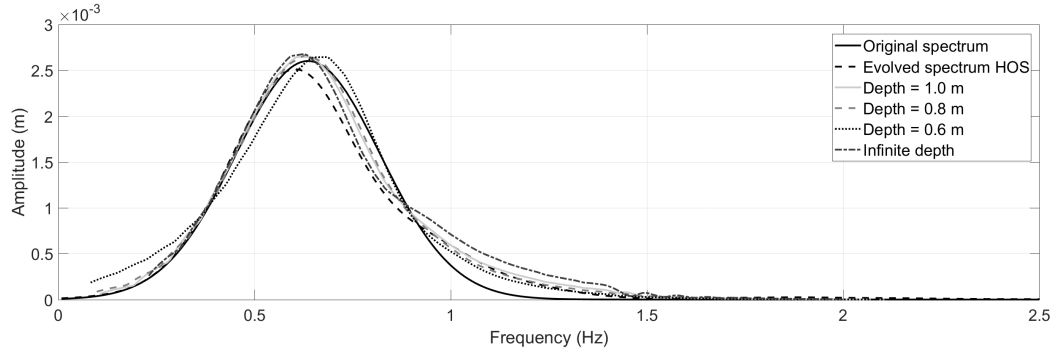

Figure 4.25: GKE predictions of the evolved amplitude spectrum after $4T_p$ for different values of water depth d and constant $k-$grid resolution $Dk = 0.20$ m^{-1}; $k_{max} = 10k_p$; $H_s = 0.35$ m; $Dt = T_p/2$.

The tests are performed here for the values of Dk, Dt and k_{max} found from the convergence analysis (Section 4.6.1). The results are presented in Figure 4.25 for decreasing water depth and also for the case of infinite water depth in order to observe the behaviour of GKE in almost all depth conditions.

The results in Figure 4.25 confirm that decreasing water depth results in stronger spectral changes. A water depth of $d = 0.8$ m results to negligible differences to the evolved spectrum after $4T_p$ compared to the original water depth of $d = 1$ m. Further decreasing the water depth to $d = 0.6$ m causes a significant spectral change: the spectral peak is forward-shifted and there is energy transfer to lower frequencies instead of higher frequencies. The evolved spectrum in fact moves to the opposite direction of the evolved spectrum from HOS. On the other hand, considering an infinite water depth results in a spectral shape which is similar around the spectral peak to the one for $d = 1$ m, has better agreement with the evolved HOS spectrum between 0.7-0.8 Hz, but it overestimates the energy for $f > 0.9$ Hz. It is also observed that the first frequency is approximately at 0.25 Hz, which corresponds to $k(1) = 0.20$ m^{-1} for infinite water depth.

The conclusion of the investigation for the equivalent water depth showed a spectral evolution almost opposite to what was initially suspected; instead of approaching the evolved spectrum from HOS for decreasing water depth, the evolved spectrum of GKE exhibited greater deviations. The infinite depth case showed only partial improvements

and greater disagreements for high frequencies. Consequently, there is no obvious reason to employ a different water depth, instead of the actual depth of the phase-resolving model $d = 1$ m.

4.6.5 The effect of phase mixing in the GKE

According to the discussion in Section 4.5.5, in the present study phase mixing is performed at every time step in order to identify its potential impact for short time evolution of the spectrum. Based on the observations of Gramstad and Stiassnie (2013), phase mixing is expected to result in stronger spectral evolution. It is also expected that the effects of phase mixing become more obvious for longer time evolution, simply because the phases have been mixed more times.

In this section, the effect of phase mixing is examined for a gradually increasing time evolution of $4T_p$, $6T_p$ and $8T_p$ examining both a constant $H_s = H_s^{PF}$ and a time dependent $H_s(t)$, since in the previous tests it was shown that H_s is one of the major factors that determine the spectral evolution. The results are included in Figure 4.26 and they are produced for the parameters Dk, Dt and k_{max} found through the convergence analysis (Section 4.6.1).

At first glance, it can be observed that phase mixing does not cause any dramatic changes to the evolved spectral shape. It is also confirmed that the differences at the resulted spectral shape are more noticeable for the longer time of $8T_p$ (Figure 4.26c). When the constant H_S is examined, all the examined times show that phase mixing results in a marginally lower spectral peak, which is closer to the evolved spectrum of the focused waves, but on the other hand there is smaller spectral change between 0.7-0.9 Hz, compared to the case without phase mixing. At frequencies higher than 1 Hz, noticeable change is observed only at $8T_p$, with phase mixing causing more energy transfer to these frequencies. For the expression of $H_s(t)$, it can be seen that at $4T_p$ (Figure 4.26a), there is practically no difference caused by phase mixing. Some deviations start to be observed in Figure 4.26b, showing that phase mixing slightly

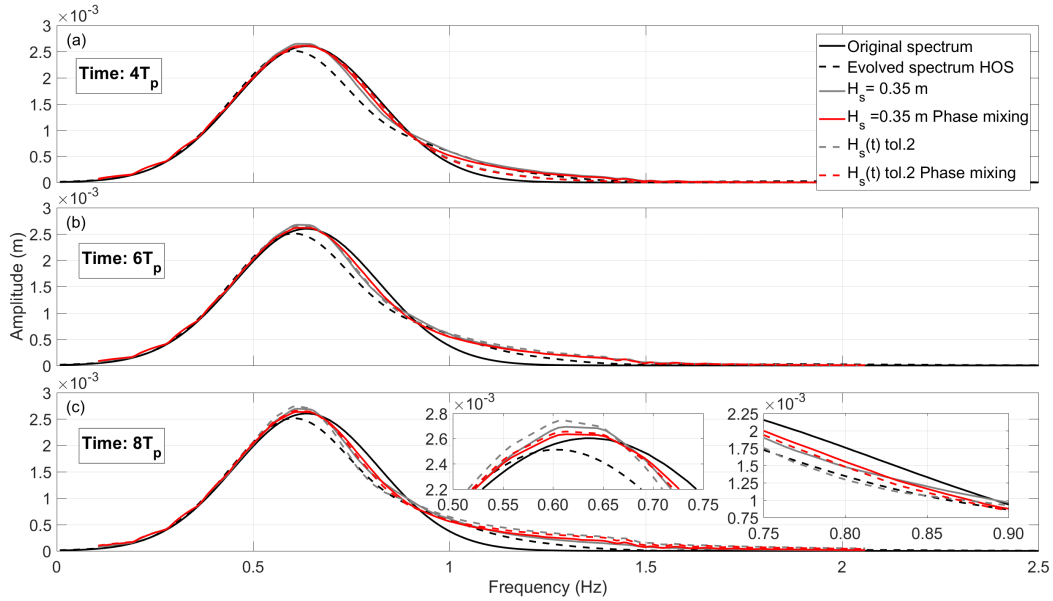

Figure 4.26: GKE predictions of the evolved amplitude spectrum after (a) $4T_p$, (b) $6T_p$, (c) $8T_p$ without (grey) and with phase mixing (red) every Dt for $H_s = 0.35$ m and $H_s(t)$ and constant $k-$grid resolution $Dk = 0.20$ m^{-1}; $k_{max} = 10k_p$; $Dt = T_p/2$.

unerestimates the spectral changes at frequencies higher than f_p. Similar is the trend for $8T_p$ in Figure 4.26c, where it is seen that phase mixing predicts a spectrum closer to the original, rather than the evolved spectrum. Further tests for $t = 25T_p$ (not presented here), show that indeed phase mixing causes important spectral changes, but mainly at $f > 0.9$ Hz, overpredicting considerable the energy there compared to the evolved HOS spectrum.

Summing up, phase mixing at every Dt has greater impact for longer time evolution, compared to the case without phase mixing. Nevertheless, the predicted spectral evolution, at least up to $8T_p$, shows more deviations compared to the evolved spectrum of focused waves in HOS for $f > f_p$, with an obvious improvement only around f_p. Consequently, phase mixing was not found to give an improved solution and since it adds bias in the study, due to the uncertainty of the selection of the phase mixing intervals, it was decided not to use it in the remaining tests.

4.7 Further investigations on GKE

The GKE seems to provide a reasonable spectral evolution compared that occurring during the focusing of wave groups. Nevertheless, despite the different trials performed in the previous section, the discrepancies seem to be persistent. Here, some more general issues are discussed and the validity of the methods employed is critically judged to a fundamental level.

4.7.1 Comparison of GKE with Monte Carlo simulations

In the previous sections, the spectral evolution for the Gaussian spectrum of the present study was examined purely with the GKE, after the latter has been verified for JONSWAP spectra (see Section 4.4). Although the resulted amplitude spectrum of GKE is in relatively good agreement with that predicted for focused waves by HOS -especially considering the assumptions taken into account in this process for finding the equivalent H_s- there are some noticeable discrepancies mainly at the spectral peak. Moreover, it should be noted that the GKE has never been examined for the Gaussian spectrum of the present study and additionally, it exhibited discrepancies with Monte Carlo HOS simulations for short time evolution, which is of the interest of the present work, for the JONSWAP spectrum of $\gamma = 20.0$. As such, it was deemed necessary to verify the GKE for the conditions used in the present study.

In this section, the behaviour of the GKE for the Gaussian spectrum is compared against HOS Monte Carlo simulations for short, mid-term and long-term time evolution, in order to investigate its validity. Different values of the H_s are also examined in HOS-ocean, which of course are constant. A challenge is that, since H_s determines the steepness in HOS-ocean and the code has stopping criteria to prevent simulation of unrealistic waves (see Section 3.4), not any values of H_s can be tested.

To be able to simulate the Gaussian spectrum of the present study, the source code of HOS-ocean had to be modified, in particular the `initial_condition.f90` file, in

order to include the expression of the desired spectral distribution (see Equation 3.1). Additionally, the HOS-ocean was not tested before the present work for Monte Carlo simulations in finite depth. After preliminary investigations, it was observed that the initial condition of the spectrum did not match exactly the desired one. Following the discussion with G. Ducrozet (personal communication, June 2016), the initialization of code was amended[14]. After the correction of the source code, the initial Gaussian spectrum at 1 m water depth matched exactly the theoretical spectrum.

The same setup of the HOS-ocean as in Section 3.4 was used for the simulations with the Gaussian spectrum. 800 random phase simulations were performed for a time evolution of up to $1000T_p$. The results are presented here for up to $509T_p$, which is already enough to identify the trend of the spectral change for long-term time evolution. Three values of the H_s were tested for finite depth of 1 m: $H_s = 0.35$ m, $H_s = 0.30$ m and $H_s = 0.20$ m, which results are shown in Figures 4.27, 4.28 and 4.29, respectively. The parameters for the GKE were chosen as $Dt = T_p/2$, $Dk = 0.15$ m^{-1} in order to have good resolution at the spectral peak, and $k_{max} = 4k_p$, in order to have approximately the same wavenumber range as that simulated in HOS-ocean. The results that follow refer to the normalized by the steepness ε energy spectra in $\kappa-$space, as done before in Section 3.4. The simulations in HOS-ocean require 12-18 hours on a single core intel i7 @ 3.0 GHz, depending on the value of H_s, while the GKE evaluates the spectrum in less than 20'.

The value of $H_s = H_s^{PF} = 0.35$ m that was initially tested seems to be exceptionally high and in some cases the stopping criterion of the code was activated. This can be also attributed to the numerical overflow of energy to high wavenumbers, since no dissipation mechanism is employed. In reality, wave breaking would take place (Tanaka, 2007). As such, the averaged spectra of the HOS-ocean in Figure 4.27 refer to an assembly of 138 simulations only. The first thing to observe is that before $16T_p$ the Monte Carlo simulations do not show noticeable spectral evolution apart from the spectral peak. On

[14] The calculation of the group celerity was corrected from
"$Cg = group\_velocity(omega\_n2(i1,1)/TWOPI * T, depth, grav)/(L/T)$" to
"$Cg = group\_velocity(omega\_n2(i1,1)/TWOPI/T, depth, grav)/(L/T)$"

the other hand, the GKE started deviating from the original spectrum already at $4T_p$. Between $16T_p$ and $64T_p$, significant deviation is observed for both the GKE and Monte Carlo simulations. However, the evolution trend at the peak is almost the opposite: the GKE predicts more energy at the peak than the original spectrum, while Monte Carlo simulations show less energy. Additionally, it is observed that there is energy transfer at very low and very high wavenumbers in HOS-ocean. From $128T_p$ and beyond, the spectral shape of GKE seems not to change considerably, while the energy of main part of the spectrum is HOS is further reduced with a significant energy transfer in higher wavenumbers. After long time, the spectrum in HOS eventually disintegrates. This is presumed to be due to energy transfer to high wavenumbers, which are cut-off in the FFT in HOS-ocean. As a result there is a leakage of energy to wavenumbers that are not resolved and the Monte Carlo spectrum loses appreciable amount of its original energy. Similar issue is discussed by Tanaka (2001), where energy leakage to higher wavenumbers was observed for a HOS-type model. On the other hand, the GKE is by definition conservative, since energy transfers occur only within the predefined $\kappa-$grid. To mitigate this issue in HOS-ocean, it was attempted to simulate 1024 nodes, but the simulation time was very high for a Monte Carlo approach. Since the case of $H_s = 0.35$ m appears to give unrealistic spectral evolution, no further discussion for the present results is done.

Lowering the value of H_s to $H_s = 0.30$ m does not activate the stopping criterion in HOS-ocean and the results of Figure 4.28 refer to an assembly of 800 simulations. Nevertheless, it can still be observed that energy cascade to high frequencies occurs after long-term evolution. As expected, the spectral changes here are less pronounced than for $H_s = 0.35$ m. Until $4T_p$ neither GKE nor Monte Carlo show any considerable spectral changes. At $8T_p$ however, the GKE starts deviating from the original spectrum by exhibiting an increase of the energy of the spectral peal and lowering of the energy between $k = 2 - 3$. Still the spectrum from Monte Carlo simulations is practically the same as the original and it starts only changing at $16T_p$. At mid-term evolution times between $32 - 128T_p$, it seems that both GKE and HOS retain a stabilized form of the

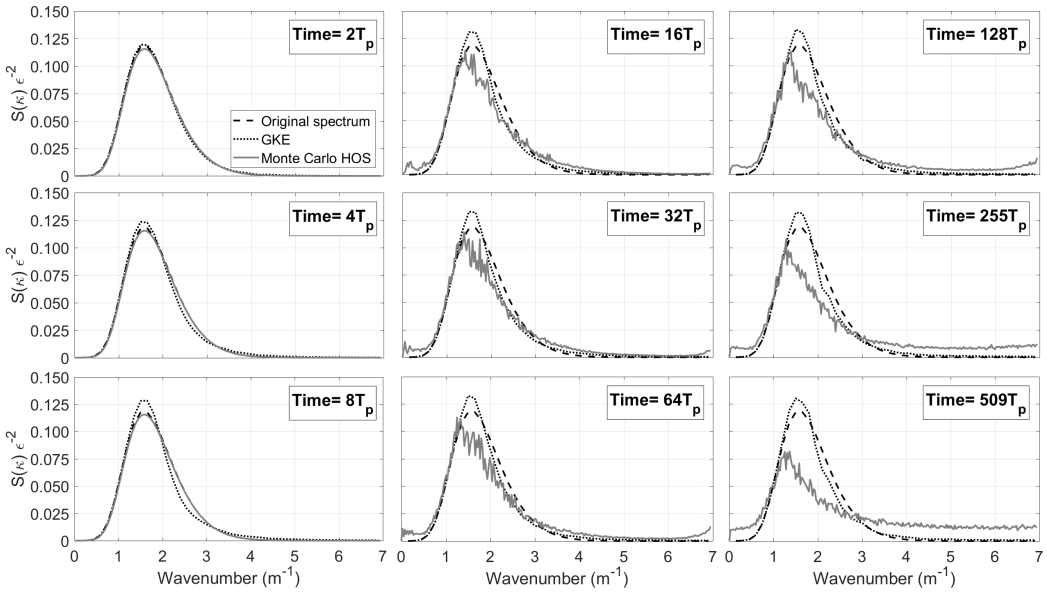

Figure 4.27: Comparison of the spectral evolution at different times between the GKE and Monte Carlo simulations for the Gaussian spectrum of $H_s = 0.35$ m at water depth of $d = 1$ m.

spectrum, which has increased energy in wavenumbers $k > 3$ m^{-1}. However, as observed for Figure 4.28, the energy of the spectral peak of HOS is lower that that of the GKE. Also, HOS shows a noticeable energy increase in low wavenumbers, which is not predicted by the GKE; a possible explanation for that is given in Section 4.7.4. For long-term time evolution of $255 - 509T_p$, it is seen that the spectrum of the GKE has minimal changes, while the spectrum of HOS starts losing energy to higher wavenumbers and its peak is further lowered, as also discussed for $H_s = 0.35$ m.

Further reducing the steepness with $H_s = 0.20$ m gives a almost stable spectrum, as seen in Figure 4.29. The GKE shows negligible deviation from the original spectrum even after long propagation of $509T_p$. The average spectrum of HOS is almost identical to the original spectrum until $16T_p$, when it starts exhibiting some differences mainly at the peak and a small gradual energy transfer to wavenumbers $k = 4 - 5$ m^{-1}. The spectrum is almost constant until $509T_p$ having only some local fluctuations.

Overall, the previous results show that meaningful comparisons between Monte Carlo simulations in HOS-ocean and the GKE can be performed only for 0.20 m $< H_s \leq 0.30$

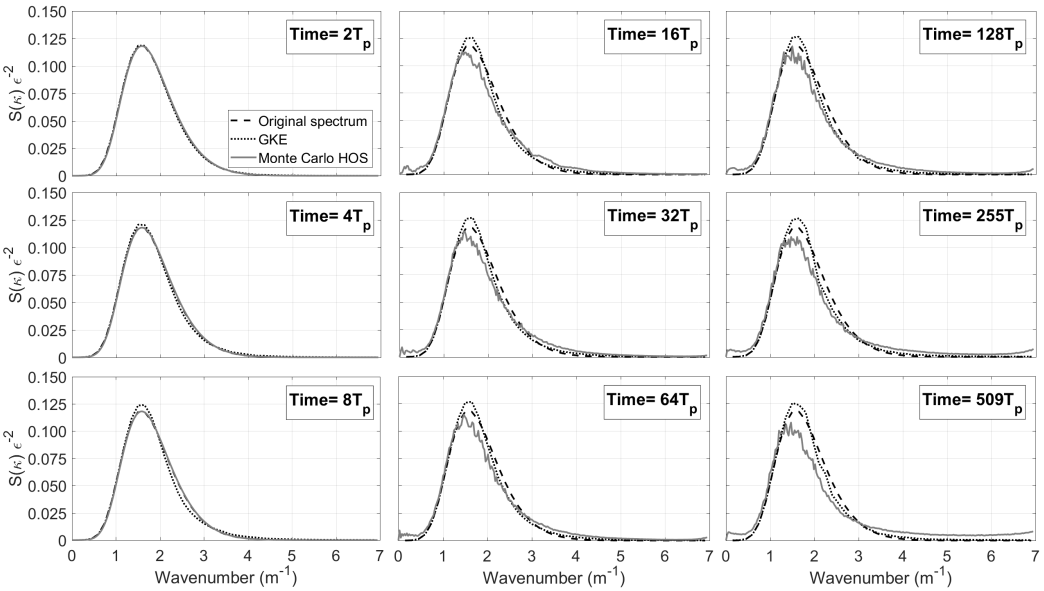

Figure 4.28: Comparison of the spectral evolution at different times between the GKE and Monte Carlo simulations for the Gaussian spectrum of $H_s = 0.30$ m at water depth of $d = 1$ m.

m, because $H_s = 0.20$ m results in clearly low steepness of the sea state to cause spectral evolution, while $H_s = 0.35$ m causes energy leakage in high wavenumbers in HOS that eventually disintegrate the spectrum. For the case of $H_s = 0.30$ m, relatively good agreement is observed between the evolved spectra of HOS and GKE at $k = 2-3$ m^{-1}, but consistently the spectral peak at HOS has lower energy than the original spectrum, which seems to be closer to the observation for the focused wave, while GKE predicts always higher energy at the peak compared to the initial state. Moreover, it is worth noting that for all the H_s examined, the Monte Carlo simulations exhibit almost no spectral change for time evolution shorter than $8T_p$. This cannot be readily justified, since the smoothing time in HOS-ocean was set only to $1T_p$ (see Section 4.4) and it implies that a "warm-up" time period in HOS-ocean may exist. Tanaka (2007) mentions that it takes approximately $10T_p$s for an initially linear wave field to evolve to a nonlinear field, but this is more related to the emergence of bound waves and not evolution of the free-wave spectrum.

To investigate if the previous conclusions are influenced by the water depth, infinite

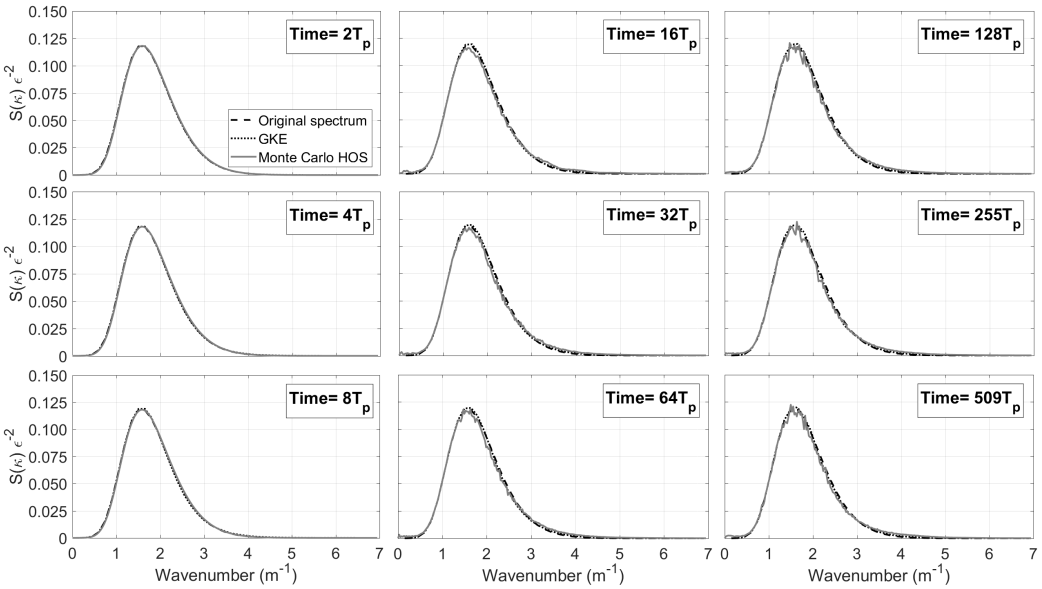

Figure 4.29: Comparison of the spectral evolution at different times between the GKE and Monte Carlo simulations for the Gaussian spectrum of $H_s = 0.20$ m at water depth of $d = 1$ m.

water depth was also tested for the case of $H_s = 0.30$ m, which gives appreciable energy transfer, but does not suffer from energy leakage. The results are presented for both GKE and Monte Carlo HOS simulations in Figure 4.30. The wavenumber spectrum for $d = 1$ m is also plotted in light grey to illustrate the difference in the initial conditions, since the values of wavenumbers are depth dependent.

As observed for the case of finite water depth, Figure 4.30 confirms that the GKE reacts faster and shows spectral evolution already for times shorter than $16T_p$. It is interesting however to observe that after long evolution the two evolved spectra converge predicting a downshifted and increased spectral peak, lower energy at $k = 2 - 3$ m^{-1} and energy increase at $k > 3$ m^{-1}.

Summing up the results of the present section, it seems that at short evolution times the HOS Monte Carlo simulations do not show spectral change, which does not agree with the GKE prediction. This may imply that there may be additional smoothing conditions in HOS-ocean for the initialization or that the wave interactions develop slower in deterministic models. For the cases of finite depth, the GKE and HOS predict a dif-

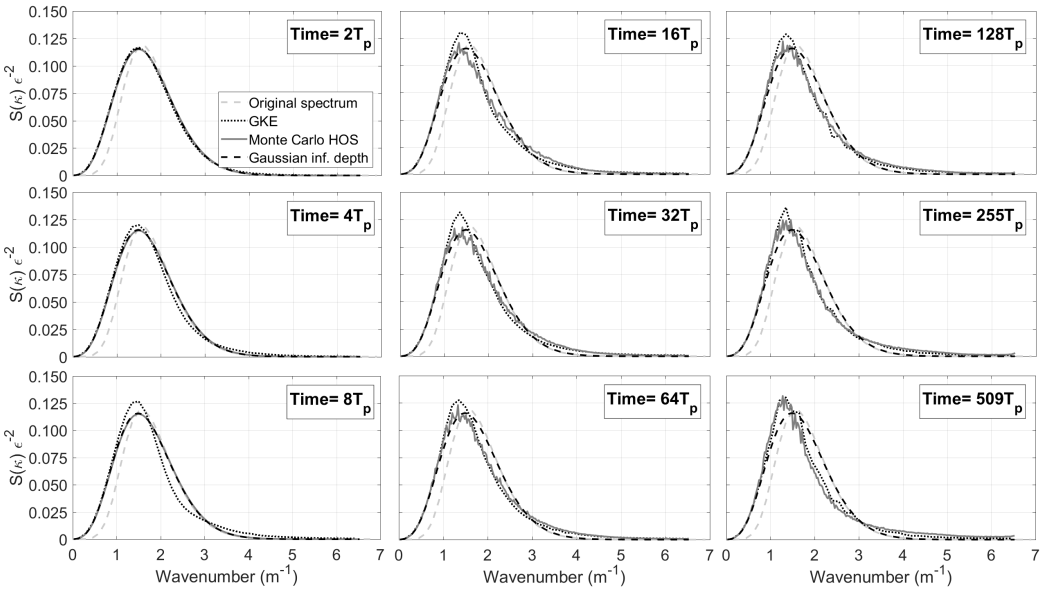

Figure 4.30: Comparison of the spectral evolution at different times between the GKE and Monte Carlo simulations for the Gaussian spectrum of $H_s = 0.30$ m at infinite water depth.

ferent spectral shape, mainly at the peak of the spectrum, for mid- and long-term time evolutions. For infinite water depth, it seems that the results of GKE and HOS start converging after long evolution. The latter observations about the water depth cannot be easily justified, since the GKE was derived for finite depth, but may have to do with additional bound interactions that are more pronounced in finite depth (see Section 4.2.3).

To the author's best knowledge, these are the first results in the literature that compare Monte Carlo simulations and the GKE at short evolution times and at finite depth. The conclusion of Benoit et al. (2015) is confirmed that more in-depth investigations are required to obtain a more complete view of the properties of the GKE.

4.7.2 Application of the GKE on another spectrum

As demonstrated in Section 4.7.1, there were some discrepancies observed in the spectral evolution of HOS and GKE even for short-term time evolution and finite water depth. The predicted spectral shape by the GKE seems to have higher energy

at the spectral peak compared to the evolved spectrum of the focused wave. Before concluding that this may a potential limitation of the GKE for the aforementioned conditions, different spectra should be tested. In the literature, the GKE was only tested for JONSWAP spectra and showed good agreement at least after long evolution.

In the present section, the PM spectrum used in the initial validation of the phase-resolving models in Section 3.2.2 and 3.2.3 is used in GKE. The rational for testing a spectrum with a more JONSWAP-type energy distribution is because the Gaussian spectrum has some characteristics that may pose limitations to its application in the GKE. The Gaussian spectrum is broadbanded and extends almost down to $k = 0.3$ m^{-1}, which is very close to $k(1)$. This may result in more interacting quadruplets in high wavenumbers and fewer at low wavenumbers with potential consequences for the spectral evolution. This can be well observed in Figure 4.16, where there seem to be more wave components in the high frequency part of the spectrum rather than in the main part. Moreover, the JONSWAP spectra already tested in the literature have a $k_p = 1$ m^{-1} and they are more "centred" on the $\kappa-$grid, which hypothetically could cause a more balanced interaction for low and high wavenumbers. A way to circumvent this potential issue, would be to test a Gaussian spectrum of higher f_p or smaller σ. However, there are no available experimental results for these cases and HOS or SWASH can simulate unrealistic focused waves that would break in reality. Similar issues, to a lesser extent also exist in OpenFOAM. Instead, it was preferred to adapt the PM spectrum already tested, as explained below.

The initial experiment for the PM spectrum in the phase-resolving models was performed again following the strategy of the dispersion study (see Section 3.3), according to which the amplitude spectrum was matched with the target spectrum close to the inlet (AM location) and it was let to evolve until the PF location, where the wave group was phase focused. The AM location is selected at 0.78 m and the PF at 7.80 m from the inlet. The water depth is $d = 0.50$ m. The peak of the spectrum is at $f_p = 0.60$ Hz, resulting to $L_p = 3.25$ m. Following the similar process as for the Gaussian spec-

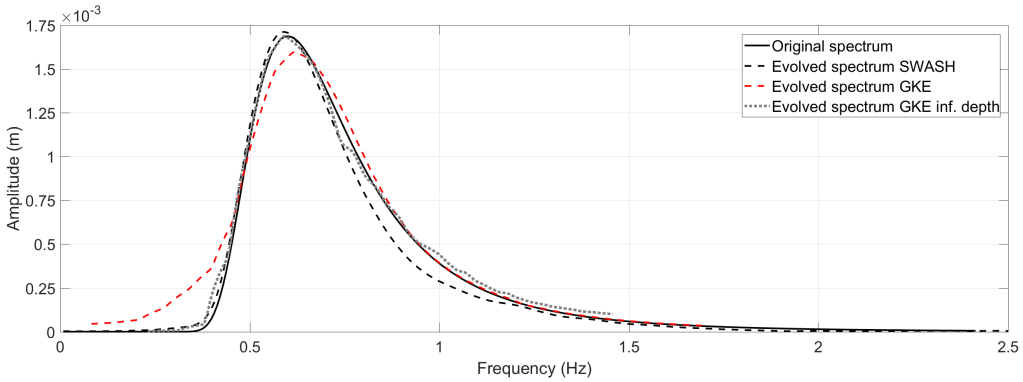

Figure 4.31: Comparison between the original and evolved PM amplitude spectrum computed with the GKE and the extracted linearised spectrum at PF in SWASH. For GKE: Time=$5T_p$ $H_s = 0.213$ m; $\Delta k = 0.20$ m^{-1}; $k_{max} = 5k_p$; $\Delta t = T_p/2$.

trum, described in Section 4.5.2, the original and the equivalent H_s are defined as $H_s^{orig} = 0.0277$ m and $H_s^{PF} = 0.210$ m, respectively. After some preliminary tests, the parameters chosen for the GKE are $Dk = 0.20$ m^{-1} and $Dt = T_p/2$. The wavenumber range is $k \in [Dk, 5k_p]$ and the spectrum is evolved for $t = 5T_p$, in order to observe better the spectral changes.

The focused wave tests of in this section are performed in SWASH, because the NWT was already setup and converged for the PM spectrum. A hyperbolic velocity distribution is used, with 8 vertical layers and $\Delta x = 0.04$ m, after the additional findings of Section 3.3.3. The wave was focused after two corrections using the focusing methodology.

The evolved spectra predicted by the GKE after $5T_p$ and by SWASH at the PF location are compared with the initial spectrum in Figure 4.31. Results of the GKE for infinite depth and long time evolution of $250T_p$ are also included.

The comparison of the evolved spectra shows that that the evolved spectrum of GKE for $d = 0.5$ m and $5T_p$ has a forward-shifted peak and increased energy at lower frequencies, which deviate significantly from the spectral evolution of the focused wave in SWASH. It does not predict neither the decrease of the energy at 0.7-1.2 Hz. The spectrum estimated after long evolution and infinite water depth by the GKE seems to

be rather closer to the initial spectrum than the evolved spectrum in SWASH.

On one hand, the results of this section demonstrate that the discrepancies found for the Gaussian spectrum are not related necessarily to the spectral distribution, but on the other hand indicate that the GKE may have limitations for applications in short time scales and/or on finite water depth.

Nonetheless, comparing the result of the GKE with the extracted linearised spectrum may include an inherent assumption itself. This concern is further investigated in the next sections.

4.7.3 The definition of the free-wave spectrum

In all the previous sections and in fact from the beginning of analysis of results with the focusing methodology, there is an underlying assumption in the present work that the extracted linearised harmonic corresponds to the free-wave spectrum. The only way that this was justified was by observing the timeseries of the harmonics and identifying visually which harmonics are bound and which are free (Vyzikas et al., 2018b). This however may be a crude approach since the dispersive properties of the underlying free-wave spectrum change due to the nonlinear wave-wave interactions. Thus, in order to be able to compare the evolved spectrum from the focused wave and the evolved spectrum of the GKE, which was derived for free waves only, a more robust way should be found to confirm that the extracted linearised spectrum through the four-wave decomposition is indeed the free-wave spectrum.

The previous concern is not discussed often in the literature or it is taken for granted. There is however a comment in the work of Tanaka (2001) (see conclusions), which may shed light to this problem. According to Tanaka (2001), the non-resonant wave-wave interactions, which at this case refer to bound waves, can be eliminated in a phase-resolving model by averaging many different random phase simulations. This is possible because bound waves emerge as phase related interactions of the free

waves. Therefore, the averaging over a sufficient number of random phase simulations can cancelled them out. As a result, this averaging can yield the free-wave spectrum. As mentioned in the paper of Tanaka (2001), this process does not constitute a proof that the spectrum estimated by the averaging is equivalent to that defined by ensemble averaging, which is the one computed by the GKE. An alternative way to identify the free-wave spectrum is to check whether it follows the linear dispersion relation by comparing the energy concentration at the wavenumbers in $f-k$ plots, as done by Shemer and Dorfman (2008), Taklo et al. (2015) and Johannessen and Swan (2003). However, potential issues may appear, since the dispersive properties of the wave group change in the nonlinear domain and the components of the free-wave "ridge" seem not to follow exactly the linear dispersion relation, as shown by Taklo et al. (2015).

The elimination of the bound interactions through averaging of random simulations explains exactly the concept behind the use of Monte Carlo simulations, which is not often discussed. The HOS-ocean of $mHOS = 3$ can resolve high order interactions and the simulations include bound waves. However, the averaging over a large number of random simultaions eliminates the bound waves and the free-wave spectrum can be retrieved. This legitimizes the comparison of the average spectrum of HOS-ocean with the GKE's free-wave spectrum.

The consideration of Tanaka (2001) triggered the idea to apply this method to the present study of focused waves in order to identify the free-wave spectrum. Of course here the phases cannot be random, because the interest is to observe the spectral change as the wave focuses. To achieve the cancelling out of the bound waves, groups of different phases shifts were simulated, similarly to those used for the four-wave harmonic decomposition method. Instead of simulating only four groups of phase shifting of $\pi/2$, 20 groups were simulated by changing the phases in increments of 0.1π between [0, 2π]. Tanaka (2001) found that 16 random simulations of high accuracy can be adequate to obtain the free-wave spectrum. The free-wave spectrum found through the averaging is compared with the extracted linearised harmonic at four locations in

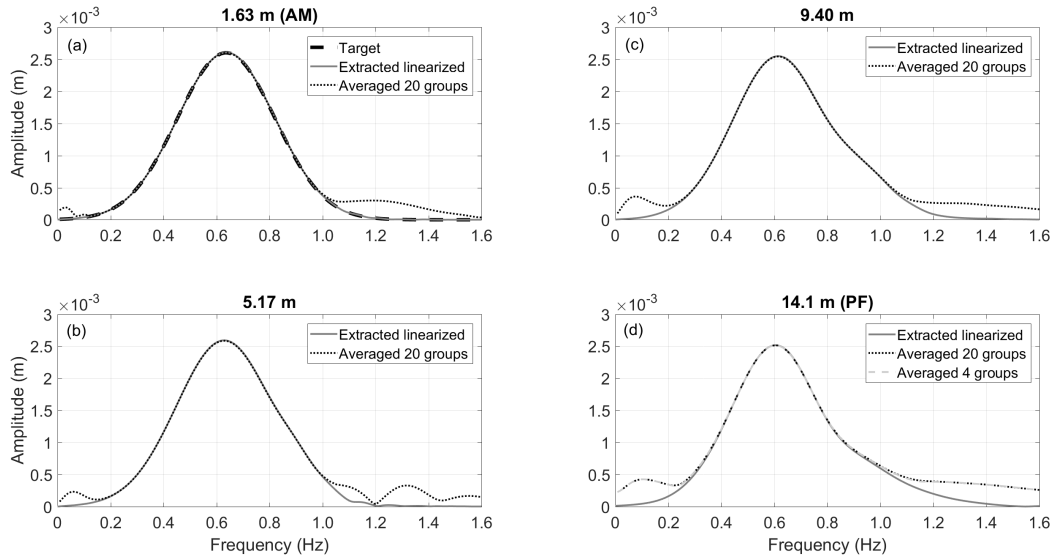

Figure 4.32: Comparison of the extracted linearised spectrum from the measured surface elevation using the four-wave harmonic decomposition and the free-wave spectrum from the averaging of different wave groups.

the NWT in HOS for the Gaussian spectrum, as seen in Figure 4.32.

The comparison of Figure 4.32 reveals a remarkably good agreement for the part of the spectrum between $f = 0.2 - 1.0$ Hz for all the examined locations. This suggests that the free-wave spectrum and extracted linearised spectrum are the same, which explains the rational for all the comparisons that preceded.

Deviations between the two free-wave spectra in Figure 4.32 are only manifested at low ($f < 0.2$ Hz) and high ($f > 1.0$ Hz) frequencies. A possible explanation for these differences can be the spurious low and high frequency waves created by the wave paddle, which are free. These waves can be eliminated by the four-wave decomposition, as they belong to 2^{nd} difference and 2^{nd} sum harmonics, but they are not eliminated by the averaging, since they are free components. Another explanation can be that due to the finite water depth and the increased local steepness of the focused wave some of the bound waves are not cancelled through the averaging.

Careful observation of the results of HOS-ocean in Figure 4.28 shows that some energy exists in low and high frequencies, which can be attributed to 2^{nd} order bound waves

that have not been effectively cancelled or to spurious free waves created by the linear initialiazation of the model, which continue to propagate in the periodic NWT.

In Figure 4.32d the result of the averaging of 4 phase-shifted wave groups is also plotted showing that excellent agreement with the result of 20 wave groups is achieved even using a small number of wave groups for focused waves.

In conclusion, the tests of the present section show that at least the main part of the extracted linearised spectrum from the four-wave decomposition is the free-wave spectrum, which gives confidence for the correct application of the methods of the present work.

4.7.4 The essence of wave-wave interactions in focused waves

Having verified in the previous section that the extracted linearised harmonics refer to the free-wave spectrum, the second fundamental assumption of the present work is examined. This refers to the consideration that the governing physical process that alters the spectrum of the free waves in 1D short propagation is the four-wave non-resonant[15] nonlinear wave-wave interactions, as described by the GKE. This assumption was considered since according to the available literature the non-resonant four-wave interactions is the only known mechanism that predicts spectral evolution of the free waves in 1D. This literature was discussed earlier in Section 4.2.3, together with the physical effects of the four-wave interactions.

To investigate the aforementioned assumption, the physical mechanism of the wave focusing is examined in greater detail. In the vast majority of publications, the focused wave group is examined until the focusing location and little is known to what happens beyond that point. In experiments, this is hard to examine, since very long flumes are required and in some cases friction of the walls may cause damping of the wave for

[15] In many publications non-resonant interactions may refer to bound wave interactions and the term near-resonant interactions is used to describe four-wave interactions for which $\Delta\omega_{12}^{34}$ is not necessarily zero (see Equation 4.6).

long propagation (Shemer et al., 2007). Even less is known about the evolution of the free wave spectrum because the four-wave decomposition method has been applied in a limited number of publications: in (Vyzikas et al., 2018b) for wave evolution and in (Chen et al., 2014) and (Fitzgerald et al., 2014) for analysis of forces. None of these works has examined the wave properties after focusing. The latter problem was investigated only experimentally (Baldock et al., 1996) for the measured timeseries and by (Adcock and Taylor, 2016b) using the two-wave decomposition. To do this in practice, the reversibility of the wave group is examined, which means that it is checked if the wave group returns to its original state after focusing. Two weaknesses of the studies refer to the fact that not the exact free-wave spectrum was examined, so that no robust conclusion can be made for the spectral evolution of the free waves, and that the focusing is not as accurate as in the present study, which does not allow for accurate comparisons at symmetric upstream and downstream locations of the focal point. In other studies, the term "reversibility" is used to examine the case of backward propagation of the group from the focal location to its initial state, but this mainly shows if the numerical model is robust and not what happens during the defocusing (Gibbs and Taylor, 2005; Adcock and Taylor, 2016a; Adcock et al., 2015). It is noted that there is not a consensus in the literature if the non-resonant interactions are reversible: in (Ducrozet et al., 2016c) reversibility of the envelope is not achieved, Katsardi and Swan (2011) mentions that the changes to the wave spectrum are permanent and in (Adcock and Taylor, 2016a) permanent changes of the spectral shape are observed; on the other hand, the works of Adcock and Taylor (2016b) and Baldock et al. (1996) show promising evidence of reversibility, despite the noticeable discrepancies.

Here, the problem of reversibility of the strongly nonlinear wave group is examined in HOS-NWT. For this scope the length of the numerical domain is extended to 65 m and WGs are added in symmetrical locations after the PF point. The results refer to the final iteration of the focusing methodology where the wave group is nearly perfectly focused. To compare the results at symmetrical locations the timeseries downstream of PF are flipped in time and they are overlaid on the timeseries upstream of the PF.

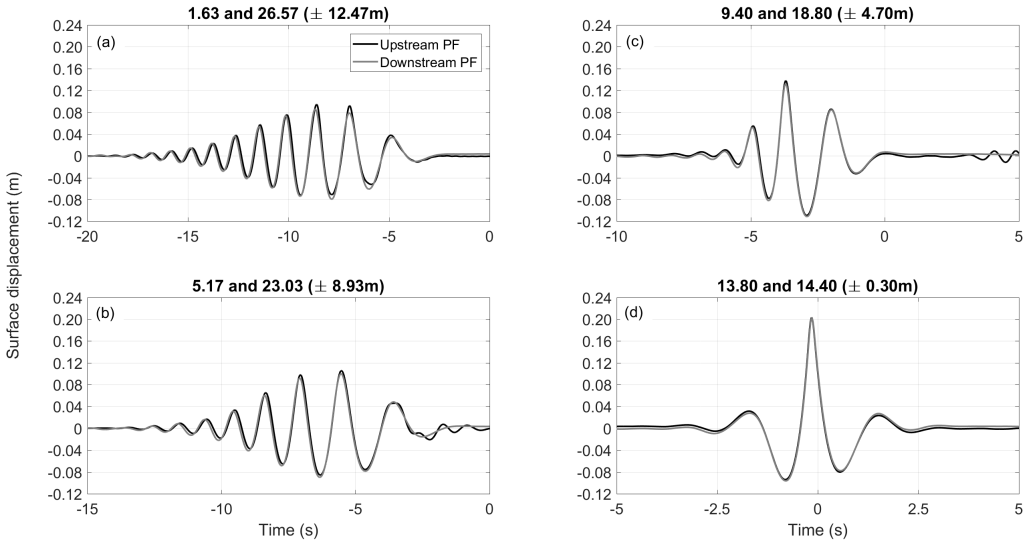

Figure 4.33: Timeseries of the measured surface elevation before and after focusing (flipped in time) in HOS.

The results for the measured timeseries are presented in Figure 4.33. It is noted that the results are not shifted in time to achieve better matching.

The results of Figure 4.33 indicate that the property of reversibility of wave-wave interactions seems to hold as the timeseries before and after focusing are in very good agreement. Small discrepancies are observed at the WGs at 1.63 m and 5.17 m in Figures 4.33a and 4.33b, respectively, possibly because the wave group near the inlet included the spurious free waves of the linear wave generation.

Next, the timeseries of the linear harmonics are isolated with the four-wave decomposition and filtering out of the 5^{th} order harmonics. The results are shown in Figure 4.34. It can be clearly seen that the matching of the timeseries in almost perfect. Only negligible differences can be observed for the high frequency free waves at the beginning of the timeseries in Figures 4.34a and 4.34b. The spectral analysis for the reversibility is shown in Figure 4.35. As show in Figure 4.35, the extracted linearised amplitude spectra before and after focusing are nearly identical at all the examined locations. A negligible discrepancy is only observed in Figure 4.35c at $f = 1.0 - 1.30$ Hz, which does not seem to be an artefact of the analysis, since different time windows were

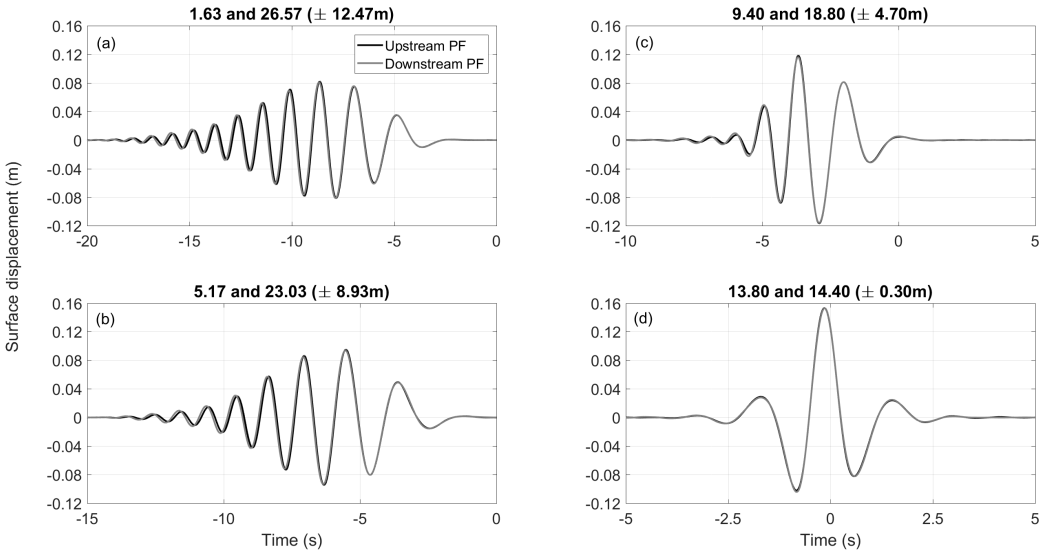

Figure 4.34: Timeseries of the extracted linearised harmonics from the measured surface elevation before and after focusing (flipped in time) in HOS.

tested and the extracted spectra remained the same. These results indicate that the free-wave spectrum are also reversible.

The present findings are of significant importance because they demonstrate that after 25 m of propagation and considerable spectral evolution on the way, the initial spectrum is exactly retrieved, as seen in Figure 4.35a. This proves that the wave interactions that change the free-wave spectrum are fully reversible.

The question is now what the full reversibility of the free waves imply for the nature of the occurring wave-wave interactions that change the free-wave spectrum during the focusing of the wave group.

On one hand, as discussed, according to the literature the only known mechanism that changes the free-wave spectrum in 1D is the non-resonant third order (or else referred as four-wave interactions) and the most appropriate model to describe them stochastically is the GKE. On the other hand, the nature of the four-wave interactions is to bring equilibrium to a spectrum, which obtains a stable form that should not change considerable ever after, unless disturbed by a physical mechanism such as wind input. The fact that the free-wave spectrum after focusing returns to its initial state contradicts

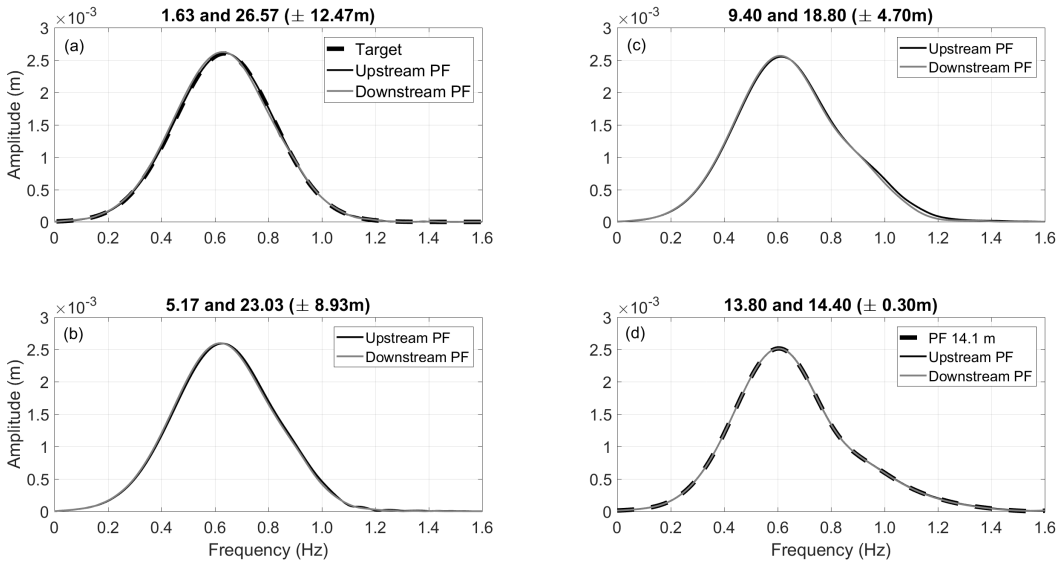

Figure 4.35: Extracted linearised spectrum from the measured surface elevation before and after focusing (flipped in time) in HOS.

the very nature of the four-wave interactions. However, if four-wave interactions is not the mechanism that changes the free-wave spectrum, then what this could be?

The spectral analysis of the bound nonlinear harmonics in Figure 4.2 shows that these harmonics obtain energy as the waves approach focusing. It is also expected that as the wave defocuses the energy of the bound waves will decrease. Based on the principle of energy conservation, since the energy of all the bound harmonics increases towards focusing, the only place that this energy can be taken from is the free-wave spectrum. This consideration may imply however, that the wave-wave interactions during focusing may be just bound interactions. According to the existing theories, bound wave harmonics are calculated based on a known free-wave spectrum and the do not alter the underlying spectrum. The energy of the free-wave spectrum was also tested and it was found that H_s decreases only by 5.5% from $H_s^{AM} = 0.0477$ m to $H_s^{PF} = 0.0450$ m, which does not justify the energy increase in all the nonlinear harmonics, This difference in H_S can be also justified to a small energy transfer in frequencies higher than 2.5 Hz in the extracted linearised harmonics that are filtered out as negligible. It is noted however that the 2^{nd} diff harmonics counteract pert of the effects of the high

order harmonics (see (Vyzikas et al., 2018b)).

The conclusion of the previous analysis is that the fact that four-wave interactions are the only mechanism that changes the underlying free-wave spectrum during the focusing of unidirectional wave groups should at least not been taken for granted. Further investigations are required on the nature of the occurring wave-wave interactions during focusing, since the present findings suggest that there might be bound wave interactions involved. If so, the GKE as derived should not be the appropriate way to model them. Instead, if only bound interactions are the driving mechanism of the spectral evolution, a model for the calculation of the estimation of the bound waves should be used that alters the underlying spectrum. This is done in a crude way with the LTA source term for triads, as discussed in Section A.4.4. Nevertheless, triads start dominate the spectral evolution only at very shallow water and some preliminary trials for focused waves in deep water, which are not presented here, showed similar spectral evolution to finite water depth. Also, according to the experiments of Beji and Battjes (1993), the bound waves developed by triads when the water depth decreases, become free when the water depth increases again. Similar behaviour for the wave-wave interactions was observed in the work of Li and Ting (2012) that examined the evolution of waves over a submerged step using spatio-temporal techniques. Thus, triads does not seem to be neither an appropriate mechanism to describe the spectral evolution in focused waves. Future work should focus on determining the true nature of the wave-wave interactions in focused wave groups.

A recent study (Aubourg et al., 2017) that was published after the present work was completed, used an advanced stereo imaging technique to map the free surface of random directional wave fields in a physical model, concluded that bound wave interactions may drive spectral change and the results do not agree with the theory for four-wave interactions. They suggest that in the short scale three-wave interactions are more important and four-wave interactions are more effective in the long term. These findings demonstrate that there may be gaps in the existing knowledge and methods

for predicting the spectral evolution and that the wave turbulence theory is still an active and unexplored field of research.

Before closing this section, it should be noted that despite the previous concerns, at present, four-wave interactions as modelled with GKE is the most appropriate way to replicate the spectral change. In this sense and based on the fact that in some cases an equilibrium state is not achieved for the examined spectrum, one could assume that there might be also other roles of four-wave interactions from just stabilizing the spectrum.

4.8 Final results for groups of different steepness

The discussion in the previous sections revealed potential errors and invalidity of the use of the GKE to describe the wave-wave interactions that take place during the focusing of a wave group or the role of the four-wave interactions in spectral changes. Nevertheless, the analysis of the results for the strongly nonlinear wave group ($\Sigma\alpha_i = 0.154$) in Section 4.6 demonstrated that the GKE can predict a shape of the free wave spectrum at short term time evolution that has to a good extent similar characteristics to the extracted linearised spectrum of the focused wave. Based on that and on the fact that at present the GKE is the most appropriate model yet existed to describe the evolution of 1D spectra for short time that includes non-resonant interactions, it is used in this section to calculate the spectral evolution for the wave groups of different steepness (see Table 4.1).

The parameters used in the GKE equation are selected based on the analysis of Section 4.6. As such, $Dk = 0.20$ m^{-1} is deemed adequate for the discretization of the spectrum in $\kappa-$space and the range of the $\kappa-$grid is $[Dk, 10k_p]$, since it was shown that interactions may occur at high wavenumbers. The timestep is set to $Dt = T_p/2$. To simplify the analysis and decrease the bias of selecting an equivalent time evolution for the spectrum, the actual evolution time of the focused wave group is used from the

inlet to the PF location, which is $t = 4T_p$. For this time evolution, phase mixing was shown to cause practically no difference to the evolved spectrum. Moreover, there is not necessarily any physical process in this theoretical case that may cause phase mixing and the selection of the mixing intervals may add bias to the analysis. For these reasons, phase mixing is not performed. Another parameter that was shown to have an important impact on the spectral evolution with the GKE was the equivalent water depth. Using an infinite water depth overpredicts the energy transfer to higher frequencies, while decreasing the water depth may cause a deviation of the results from the evolved spectrum of the focused wave. In addition, since the calculation of a reduced equivalent water depth through U_r can be rather complicated and may add bias in the analysis, it was decided to use the actual water depth $d = 1$ m.

After fixing all the other parameters in the GKE, probably the most important property of the sea state that controls the spectral evolution is its steepness, which is determined by the H_s. The analysis in Section 4.6.2 showed that for the present case there is no obvious advantage in using a timed dependent $H_s(t)$. Moreover, only values of $H_s > 0.25$ m caused appreciable energy transfer at $4T_p$. To avoid making the selection of H_s a trial and error exercise for achieving best comparison with the evolved spectrum of the focused wave, it was decided to apply the same objective method for estimating the H_s^{PF} for all the wave groups of different steepness. This is by truncating the linearly predicted timeseries of the surface elevation at PF using a tolerance of 4 for the amplitude sum ($\Sigma\alpha_i$). At the end of the calculation with the GKE, the results are rescaled based on the original value of H_s^{orig} from the full timeseries. The values of H_s^{orig} and H_s^{PF} are listed in Table 4.4 for the groups of different steepness. It is noted that the steepness ε of the strongly nonlinear is well bellow 1, as it is assumed for the derivation of the GKE.

The evolved amplitude spectra predicted by the GKE at $4T_p$ are compared with the extracted linearised spectrum of the focused wave at PF for the groups of different steepness in Figure 4.36. Here, it is again confirmed that the greatest spectral change

Table 4.4: Significant wave height (H_s) used in GKE and resulted steepness (ε) for the wave groups of the Gaussian spectrum.

	Quasi-linear	Weakly nonlinear	Strongly nonlinear
$\Sigma\alpha_i$ (m)	0.050	0.100	0.154
H_s^{orig} (m)	0.0155	0.0309	0.0477
H_s^{PF} (m)	0.1189	0.2378	0.3622
ε	0.073	0.146	0.222

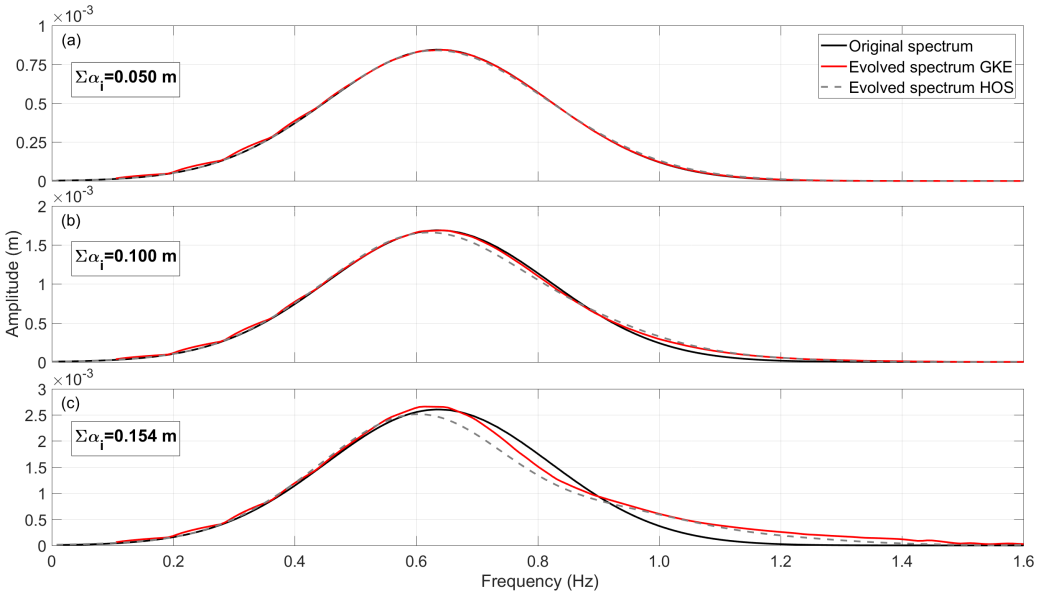

Figure 4.36: Comparison between the extracted linearised amplitude spectra at the PF in HOS and the evolved amplitude spectra after $4T_p$ in GKE for the three wave groups of different steepness.

occurs for the steepest wave group. More specifically, it can be seen that for the quasi-linear wave group (Figure 4.36a) there is practically no spectral change. The bumps of GKE at lower frequencies are artefacts of the interpolation. For the weakly nonlinear and strongly nonlinear groups, shown in Figure 4.36b and 4.36c, respectively, the GKE shows to predict very well the energy transfer to $f > 0.9$ Hz, the lowering of the energy at $f = 0.7 - 0.8$ Hz and the main discrepancy is at the spectral peak. There, the down-shift is captured to a good extent, but the GKE overestimates the energy compared to the evolved spectrum of the focused wave.

The amplitude spectra of Figure 4.36 are used in the next chapter to calculate the surface elevation.

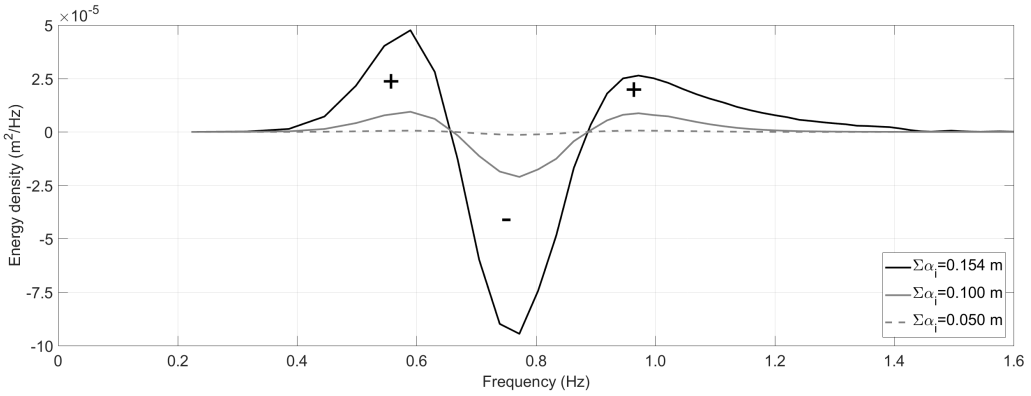

Figure 4.37: Comparison between the scaled source term S_{nl} calculated by GKE for the three wave groups of different steepness.

In the context of spectral modelling, it is interesting to present the corresponding source term S_{nl} for the four-wave interactions resulted from the GKE. This can be found by subtracting the initial energy density spectrum from the evolved spectrum. The S_{nl} are compared in Figure 4.37 for the groups of different steepness. To allow for a more appropriate comparison, the results have been scaled based on the strongly nonlinear group, in a similar way as in Section 4.1.2. For the S_{nl} however, the scaling factor was calculated by the ratio of the energy of the spectrum, being 2.383 for the weakly nonlinear group and 9.471 for the quasi-linear group. If the interactions were simply proportional to the steepness, all the lines would collapse to that for $\Sigma\alpha_i = 0.154$ m. However, it can be seen that the strongly nonlinear group results in a disproportionally greater S_{nl} and subsequently energy transfer compared to the other groups. The S_{nl} for the quasi-linear group is practically zero.

The pattern of the S_{nl} predicted by the GKE for the Gaussian spectrum agrees with the general three lobe pattern of the S_{nl} identified for JONSWAP spectra (Benoit et al., 2015). The first positive lobe implies downshifting of spectral peak, while the second positive lobe represents the energy transfer to high frequencies. The energy that is transferred to the positive lobes is pumped from the middle of the spectrum, which causes the lowering of the energy at $f = 0.7 - 0.9$ Hz.

4.9 Conclusions

The present section included an in-depth analysis of the spectral changes that take place during the focusing of a wave group. The results were analysed up to the 4^{th} order harmonics and emphasis was put to the evolution of the extracted linearised harmonics. The analysis of focused groups of different steepness showed that the spectral changes are disproportionally pronounced in the strongly nonlinear wave groups.

The evolution of the free-wave spectrum was then examined with a stochastic approach using the GKE, after confirming the applicability of the model and adapting it for the present case. Exhaustive tests were performed to detect the effects of the equivalent sea state parameters used in the GKE, as well as to identify the properties of the GKE for the different conditions tested. The results were also compared with Monte Carlo simulations. Since the literature on the topic is very recent and limited, the present findings can contribute to the better understanding of the properties of the GKE and the features of the four-wave nonlinear interactions.

Overall, good agreement was observed between the evolved spectrum of the GKE and the focused waves. The detected differences however should not be ignored since they may reveal flaws in the underlying theory, assumptions and derivation of the GKE. Further studies were performed to identify the potential sources of the discrepancies. The outcomes of these studies are very important because they prove for first time in a robust way that the wave-wave interactions in a focused wave group are fully reversible and that the main part of extracted linearised harmonics correspond to the free waves. These findings explain the rationality behind many works on focused waves that are rarely discussed.

On the other hand, the present studies provided indications that four-wave interactions may not be the physical mechanism -or at least not the only one- that controls the evolution of the free-wave spectrum during the dispersive focusing of unidirectional wave groups. This may be in contradiction to previous works, e.g., (Gibson and Swan,

2007; Katsardi and Swan, 2011), where these considerations were taken for granted.

Definitely, there are open issues and future work can go to different directions. First, experimental tests for the spectral evolution using the present method of Section 3.3 should be performed at different water depths, since the present findings show that the behaviour of the GKE is strongly dependent on the water depth and may converge to the spectral evolution of the focused waves if the depth is tuned appropriately. Secondly, tests with other JONSWAP-type spectra may be useful, since the distribution of the energy over the wavenumber grid can affect the spectral evolution. Also, although, logarithmic frequency grid is commonly applied in the literature to evaluate the source term for the four-wave interactions, here, for the 1D case, this type of grid revealed no spectral change. It is highlighted that the fashion that the interacting quadruplets are selected is one of the most crucial steps in the implementation of the GKE.

Additionally, despite the confirmation that the extracted linearised harmonics correspond to the free-wave spectrum, shown in this work, it would be very interesting to compare the results of the four-wave decomposition with that of spatio-temporal analysis. This analysis is performed by comparing the spectra in the $\kappa-$space with those in the $f-$space, as well as with the linear dispersion relation, and essentially identifying which part of the spectrum corresponds to the free wave components. The $\kappa-$spectrum is particularly hard to obtain in experiments, but easy in numerical models. Such experimental studies refer to those of Shemer and Dorfman (2008) using a CCD camera, Taklo et al. (2015) using a moving array of ultrasonic probes, Li and Ting (2012) using PIV and Aubourg et al. (2017) using stereo-PIV for a 2D wave field. In numerical models, Johannessen and Swan (2003); Gibson and Swan (2007) and Johannessen (2008) employed $\kappa - f$ plots to identify how the energy is distributed amongst waves following the linear dispersion and higher harmonics.

Last but not least, in terms of the physics described by the GKE, the present results support that the derivation of the GKE should be carefully revised in order to include quintet interactions or to further relax the underlying assumptions, as suggested by

Tanaka (2007) and Benoit et al. (2015). In addition, the author believes that the fundamental assumption that the free waves in the physical and transformed space are the same, should be investigated very critically. This is expected to influence the bound interactions, which in case of steep and focused waves are certainly not negligible. This consideration may also have effects on phase-resolving models that are based on the ZE. Also, an issue that needs further attention is the assumption that the phases of the waves are assumed uncorrelated, which poses a limitation to the application of the GKE for focused waves. Other assumptions that should be carefully re-examined in the derivation of the KE is the homogeneity of the wave field, since deviations from the Gaussian property were observed (Dysthe et al., 2003). To sum up, already from the work of Annenkov and Shrira (2006) open questions for the properties of the KE were identified that remain unanswered more than 10 years later, when deviations from the classic theory for wave-wave interactions were observed (Aubourg et al., 2017), supporting the author's belief that more complex physics are involved in the spectral evolution.

Despite the concerns and detected discrepancies in the applied methodology, the role of an engineer is to provide solutions making best use of the most appropriate tools available. Therefore, the results of the GKE for the evolved free-wave spectrum are used in the next chapter in order to compute the surface profile of the extreme waves studied, which, together with the kinematics, constitute the main interest from an engineering point of view.

Chapter 5

Reconstruction of the wave profile

THIS Chapter discusses the estimation of the free surface profile from the original and evolved free-wave spectra using analytical methods. The original spectra refer to the theoretical target spectra, while the evolved spectra are extracted from the fully nonlinear simulation using the four-wave decomposition or calculated by the GKE[1]. The scope is to examine whether the evolved free-wave spectra result in a better estimation of the wave profile when bound waves calculated by analytical methods are added to the linear harmonics. Such an analytical approach aims to reduce the computational cost of estimating a high order nonlinear NewWave profile by fully nonlinear numerical models. A previous study (Johannessen and Swan, 2003) demonstrated that knowing the evolved free-wave regime can improve significantly the linear and second order theory prediction[2]. Having achieved accurate focusing and using more advanced techniques to obtain the free-wave spectrum, this idea is examined here using linear theory, second order theory, fifth order approximation, the Creamer transform and Krasitskii's method. Part of this work was presented in (Vyzikas et al., 2018a).

[1] As discussed in Chapter 4, the final result of GKE was not identical to the extracted evolved spectrum. Future improvement in the GKE and better understanding of the physics will make the present methods even more relevant.

[2] It should be noted that the literature is not very rich in examples comparing individual harmonics because the four-wave decomposition has only been used in limited studies and in most cases the poor quality of the focusing can yield misleading results.

5.1 Linear theory

In this section, the results of linear theory in space and time are presented, but also its connection with the NewWave theory is discussed. Moreover, the validity of some "linear" methods used in the other sections is demonstrated.

Linear theory is the simplest way to calculate a wave profile. Hereafter, this refers to a time history of the surface elevation (timeseries) or a "snapshot" of the surface elevation in space at a specific time (spaceseries). Most importantly, linear theory is the basis of the NewWave theory, which, as explained in Section 2.4.1, gives the average shape of the largest waves in a Gaussian sea as the scaled autocorrelation function of the underlying free-wave spectrum. In practice, this refers to a superposition of the linear wave components that constitute the spectrum, with zero phase differences, to build an extreme wave crest. The NewWave is thus associated with focused waves (Walker et al., 2004).

Consequently, linear theory serves as a benchmark, and almost every study that uses focused waves compares the obtained nonlinear results with the linear theory estimation. Here, the focused wave profiles based on linear theory will be compared against the nonlinear numerical solutions of HOS-NWT using the original and evolved free-wave spectra for the wave groups of different steepness. Similar presentation is followed in the rest of the chapter for the other methods for reconstructing the wave profile.

5.1.1 Mathematical formulation

The linear theory estimation of the free surface elevation at a given time t and location x is given as the summation of N sinusoidal waves at the MWL, as shown in Equation 5.1. This expression is identical to Equation 3.2 that was given for wave generation at the inlet boundary.

$$\eta(x,t) = \sum_{i=1}^{N} \alpha_i \cos(k_i x - \omega_i t + \psi_i) \tag{5.1}$$

where $\eta(x,t)$ is the free surface elevation expressed as timeseries at a fixed location or as spaceseries at a given time. k_i is the wavenumber of a component i calculated for arbitrary water depth using the dispersion relation and its angular frequency ω_i. The phase of each wave component (ψ_i) is selected to be zero at the focal location and time.

Since the interest here is only in the wave profile, the kinematics are not discussed. For engineering purposes though, the interest is in the loading, which is directly linked to the kinematics. However, using potential flow theory, the kinematics underneath a given wave profile can be calculated (Slunyaev et al., 2013). Thus, obtaining an accurate description of the free surface is essential for calculating the loading analytically.

Linear theory works sufficiently well for low amplitude waves, but it deviates from the experimental or numerical measurements as the nonlinearity increases. Linear theory also assumes a constant free wave regime and cannot account for spectral changes and modulation of short waves and long waves, as shown by Longuet-Higgins (1978b) and Longuet-Higgins (1978a). This is also the case for all the methods for calculating bound waves hereafter, with the exception of the Creamer transform (Creamer et al., 1989), which is discussed in Section 5.4. The problem then reduces to finding an accurate description of the free-wave field. As noted by Johannessen and Swan (2001) and Johannessen and Swan (2003), there is evidence that the free-wave spectrum of focused waves changes by becoming broader in shorter timescales of a few wave periods, compared to Hasselmann's slow evolution (Hasselmann, 1962). They showed that the underlying linear spectrum has similar behaviour for both unidirectional and directionally spread focused waves when limiting breaking groups are examined, but for a given amplitude sum the spectral changes are more pronounced for long-crested groups, which makes the present work challenging. They also discuss that the change of the free-wave spectrum may explain the emergence of extremes in random ocean

background, which is of high relevance in the context of the present work.

The results in this thesis confirm the changing of the free-wave regime in short time scales, thanks to the four-wave harmonic decomposition, which allows for accurately isolating the free waves from the broadbanded spectrum. It can be therefore examined to what extent the solution can be improved when the evolved free-wave spectrum is used.

5.1.2 Results

In this section, a comparison between the wave profiles produced by the original and evolved free-wave spectra is presented. In Section 5.6, these results will also be compared against the fully nonlinear solution as well.

Figures 5.1, 5.2 and 5.3 compare the timeseries of the surface elevation at the PF location for the groups of different steepness. The presentation starts with the steepest group where the changes are more pronounced. The corresponding amplitude spectra were already presented in Figure 4.36.

It can be seen from Figure 5.1 that the timeseries of the evolved free waves give practically the same maximum crest elevation, but considerably shallower troughs and shorter and wider adjacent crests, than the original free waves. Similar behaviour has been noted by many authors, for example in the experimental studies of Baldock et al. (1996) and Johannessen and Swan (2001). In those studies, relatively narrowbanded spectra were examined, which allowed for the use of a two-wave harmonic decomposition. For broader spectra, as in the present work, the more accurate four-wave decomposition is required.

The differences at the timeseries are direct consequences of the spectral change of the free-waves, i.e. downshift of the peak and energy transfer to higher frequencies. Similar observations were also made in the numerical works of Zhao et al. (2010) and Ning et al. (2009a) that discuss the nonlinearities in focused waves.

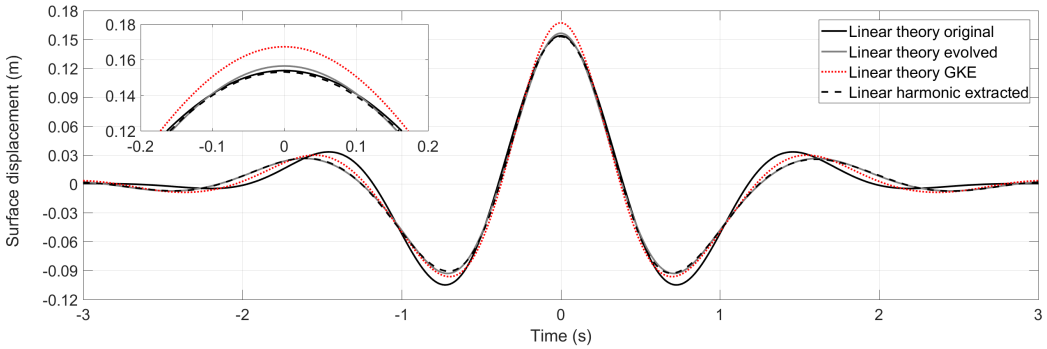

Figure 5.1: Comparison of the timeseries produced by linear theory using the original, evolved (HOS) and evolved GKE spectra with the extracted harmonic for the strongly nonlinear group ($\Sigma\alpha_i = 0.154$ m).

Careful observation shows that the extracted harmonics are in almost perfect agreement with the reconstructed harmonics using the evolved spectrum from HOS-NWT (gray line), but they are not identical, as one would expect, since the former is based on the spectrum of the latter. However, there are some small discrepancies at the crest. This cannot be justified by the definition of the spectra, since all the spectra used herein have been truncated to [0, 2.5 Hz], which was the definition of the original spectrum, and they have exactly the same df. The only explanations that can be given at this stage are that the difference between linear theory and extracted harmonic may be due to the fact that some high frequency waves of the linear harmonics may not travel according to linear dispersion, as discussed in Section 4.7.3, and that the phases of these high frequency components are not effectively corrected by the focusing methodology (see Figure 3.12) and thus, they may not be exactly zero as assumed for the reconstruction of the signal. It may also be the case that these two effects are in reality connected and consequences of one another.

Another noticeable aspect in Figure 5.1 is that the timeseries of the GKE spectrum has considerably higher crest and somewhat sharper adjacent crests. This is because the differences between the extracted spectra and those of GKE were not negligible as discussed before (see comment 1).

Regarding the wave groups of more moderate steepness, as seen in Figure 5.2, the

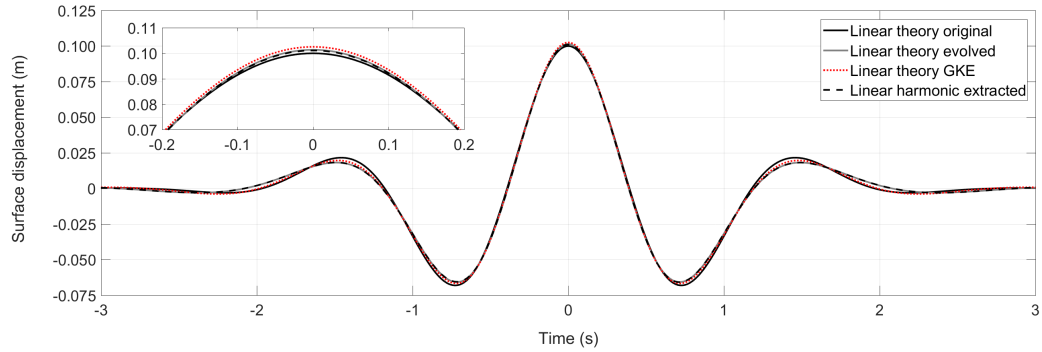

Figure 5.2: Comparison of the timeseries produced by linear theory using the original, evolved (HOS) and evolved GKE spectra with the extracted harmonic for the weakly nonlinear group ($\Sigma\alpha_i = 0.100$ m).

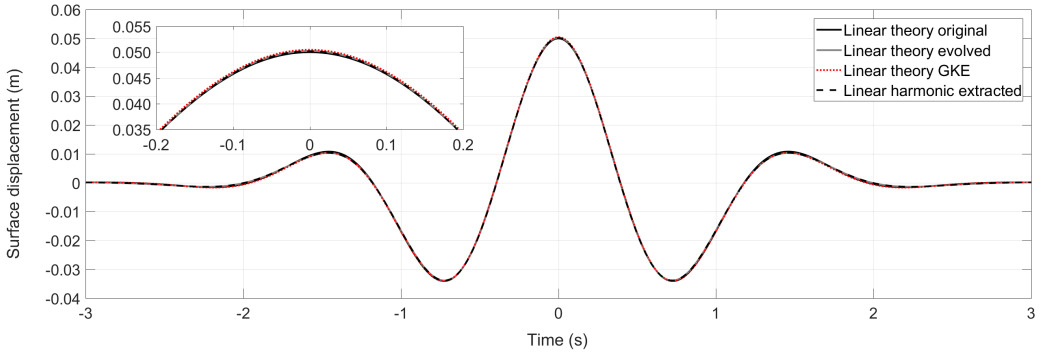

Figure 5.3: Comparison of the timeseries produced by linear theory using the original, evolved (HOS) and evolved GKE spectra with the extracted harmonic for the quasi-linear group ($\Sigma\alpha_i = 0.050$ m).

timeseries of the evolved weakly nonlinear group have noticeable differences only at the crest and troughs, where a marginal elevation is seen for the evolved spectra. The lateral crests are also lower. On the other hand, the evolved quasi-linear group seems to have practically identical timeseries to the original linear harmonics, as shown in Figure 5.3. This is expected since the free-wave spectrum remained almost unchanged.

The spaceseries of the surface displacement can be produced by linear theory for a given time t instance by Equation 5.1. Although, in general, from an engineering point of view, the spatial information is less interesting than the timeseries at the location of the structure, the spatial information can offer insights in the physics of the wave group. Also, if the structure is not slender compared to the wavelength (e.g. Pelamis

or long ships), the fluid-structure interaction problem should include spatial information of the wave dynamics. Figure 5.4 shows the snapshot of the free surface for the focal time $t = 0$ s for the groups of different steepness. The extracted harmonic is absent because the four-wave decomposition was applied in time and not in space. It is expected though to be very close to the result of the HOS spectrum. It can be seen that for the lowest (quasi-nonlinear group) the three underlying spectra produce practically identical spaceseries. However, as the steepness of the group increases and the underlying spectra begin to differ, the evolved spectra give a narrower and higher crest than that of the original spectrum. Also, the troughs become shallower and flatter. For the limiting breaking wave group, it can be seen that the linearly predicted surface profile based on the original spectrum is altered considerably when the evolved spectrum is used. The outlier, however, especially for the maximum crest elevation, is the linear wave group produced by the GKE spectrum, which seems to have a significantly higher crest.

It is interesting to notice that the ordinate $(y = 0)$ intersects the crest of the groups almost at the same locations ± 0.88 m. Applying the dispersion relation, it is found that 2×0.88 corresponds to approximately $L_p/2$ of the original spectrum. On the other hand, the distance between the local minima of the troughs is not the same between the wave groups. For the steepest group, the minima of the troughs are at ± 1.82 m for the evolved spectrum of HOS. Applying the dispersion relation, this distance corresponds to $L_p/2$ of the original spectrum. This geometric characteristic of the focused group is quite interesting and shows that despite the downshifting of the spectral peak at the evolved spectrum, the linear harmonics of the limiting breaking group have a wavelength which is that of the original L_p, and also, the zero upcrossing-downcrossing wavelength at the crest is half of the trough-to-trough wavelength. To the author's best knowledge, there is not a universal definition of the wavelength of a focused wave, but here it is shown that the three possible definitions, based on f_p, crest zero-crossings and trough-to-trough, can actually converge for the linear harmonic of the limiting breaking wave group and for the examined Gaussian amplitude spectrum.

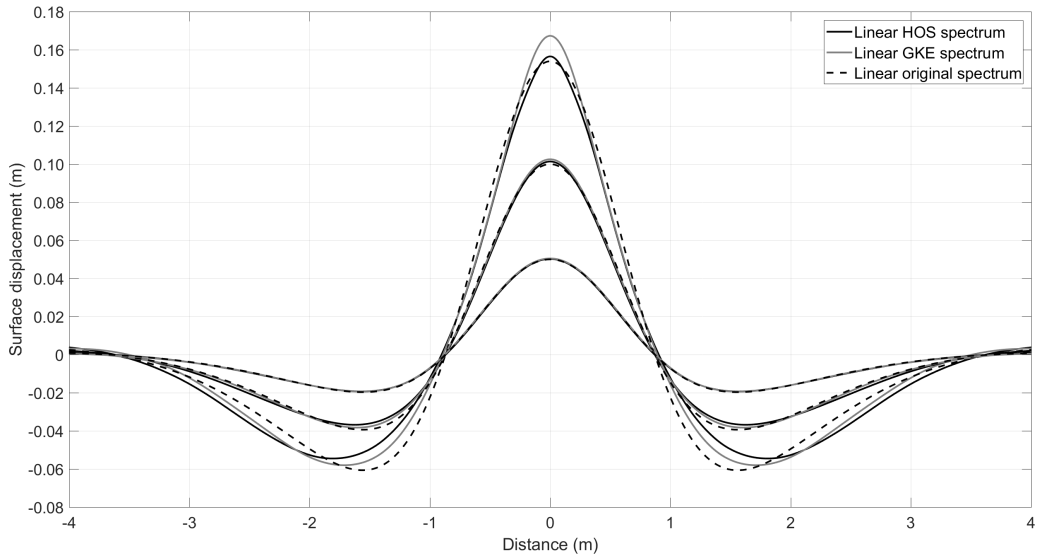

Figure 5.4: Comparison of the spaceseries produced by linear theory using the target, evolved (HOS) and evolved GKE spectra for the wave groups of different steepness.

The transition from timeseries to spaceseries, or else defined from $\kappa-$spectrum to $f-$spectrum, requires the assumption of linear wave theory, at least the way it is used in the present study (see Equation 4.26). Here, it would be useful to demonstrate the validity of transition from space to time, since it is used also later for the Creamer transform in Section 5.4. The first step towards that is to check the validity and accuracy of performing FFT in space and reconstructing the surface elevation. Figure 5.5 compares the result of reconstructed surface elevation with amplitude $\kappa-$spectra obtained from FFT of spaceseries of different spatial resolution Dx and same total length, which results in a same Dk. The latter is also calculated directly from the FFT, as a distance between two successive wavenumbers in the resulted regular $\kappa-$grid. The reconstructed spaceseries are also compared with the results of Inverse Fast Fourier Transform (IFFT) of given synthetic $\kappa-$spectra of similar characteristics. The obtained spaceseries are identical at the points of calculation and the only visual difference is because of the linear interpolation. This also shows that the selection of the initial Dx (or Dt) only influences the resolution and not the spaceseries (or timeseries), provided that the space-time operations are done correctly.

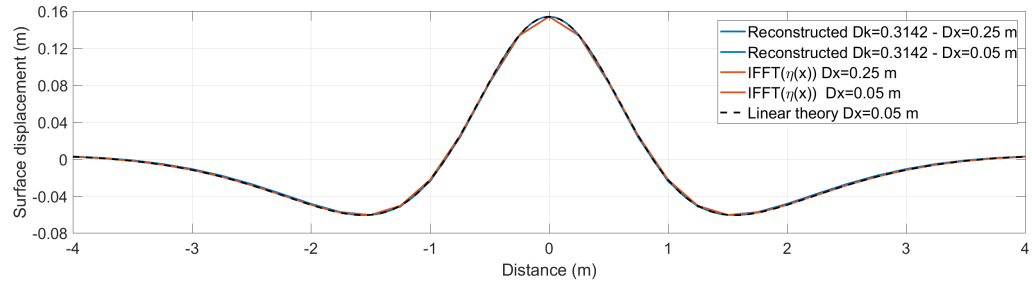

Figure 5.5: Comparison of the spaceseries obtained with different methods using the original amplitude spectrum.

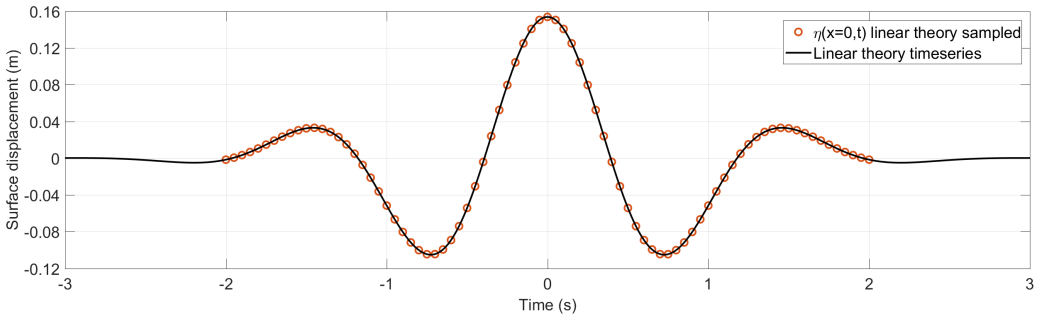

Figure 5.6: Comparison of the timeseries obtained by sampling the linear spaceseries at different t and the timeseries produced by the original amplitude spectrum.

In the case that timeseries are not available, but only the spatial information is known at different time instances, it is straightforward to show that the timeseries at the location of interest can be obtained by sampling on the spaceseries at that specific location at given times. Figure 5.6 shows the sampled timeseries from the spaceseries at a specific location, here $x =$PF. These correspond to the exact values of the original timeseries. This technique is used in Section 5.4.

5.1.3 Conclusions

The reconstruction of the timeseries of the surface elevation according to linear theory showed that the extracted linear harmonics can be rebuilt with very high accuracy. The use of the evolved free-wave spectrum results in a NewWave group that has very similar crest height, but considerably shallower and flatter troughs compared to the NewWave group based on the original free-wave spectrum. The differences are more

pronounced for the steepest wave group, following the larger differences between the original and evolved underlying spectra. The present results are in at least qualitative agreement with previous studies.

The consistency of the space-time transition based on linear theory was also confirmed and can be used in the following sections with confidence. The spaceseries of the wave profile revealed that increasing steepness of the group results in a NewWave spatial profile with shallower and flatter troughs and marginally higher crest.

5.2 Second order theory

Second order theory calculates the exact solution of the 2^{nd} order bound waves as the summation of any possible interactions between any two wave components of the free-wave spectrum. The interaction coefficients were given by Dalzell (1999) for finite depth by extending the existed solution of infinite depth. The formulation does not consider any pre-assumptions for the underlying spectrum, nor for the number of interacting components, but relies on a constant free-wave spectrum. The main issue with second order theory is the relatively high computational cost compared to linear theory.

For a given linear spectrum, second order theory adds 2^{nd} order sum and difference bound waves. The exact solution of Dalzell (1999) has been applied already in many studies, ranging from random simulations to derive statistics (Fedele and Tayfun, 2009) to steep focused wave groups (Shemer and Dorfman, 2008), or calculation of the 2^{nd} order boundary conditions in CFD NWTs (Hu et al., 2011; Westphalen et al., 2012; Hu et al., 2014)(see [1] in Appendix A). In the analysis of field data, the main challenge is to determine the underlying linear field (Slunyaev et al., 2011; Jonathan and Taylor, 1997), especially due to the potential directionality of the waves (Adcock et al., 2011). This process usually starts with a linear initial assumption of the wave field with added second order bound waves. Iterations are then performed until the calculated wave field matches the measured wave profile. In the present case, this is not required

because the original linear spectrum is defined theoretically and the evolved spectrum is extracted with accuracy.

5.2.1 Mathematical formulation

The second order summation was given for two waves by Dalzell (1999), who also applied it for an irregular wave signal. Here, the expressions presented refer to an arbitrary number of linear wave components (N), propagating in a single direction on finite water depth.

Before giving the final formulae, the assumptions and the derivation steps of Dalzell (1999) are presented. The problem of the wave-wave interactions was solved following a similar approach to that of Longuet-Higgins (1962), but Dalzell employed symbolic computations in Maple V for the coefficients. The derivation was based on potential flow theory, assuming irrotational, incompressible and inviscid flow, and applying the kinematic and dynamic boundary conditions at the free surface. The solution at the free surface was approximated by means of Taylor's expansion, truncated at the desired order. The first and second order terms were then grouped and coefficients were calculated. The linear and 2^{nd} order dispersion relation were satisfied for finding coefficients of the linear and second order interactions. The derivation was performed for finite water depth, but the deep water solution can be easily retrieved. Dalzell (1999) also showed that for only one wave interacting with itself, the solution reduces to a Stokes 2^{nd} order regular wave, while if two waves with opposite phases interact, the solution of a standing wave is obtained.

According to second order theory, the surface elevation η is given from the first harmonic and the matrix of the 2^{nd} order interactions with each free wave with all the rest, including the self-interaction, as shown in Equation 5.2. Commonly, the 2^{nd} order terms are grouped in 2^{nd} sum and 2^{nd} difference terms, at double and half the frequency of the wave group, respectively. The 2^{nd} order harmonics are calculated by Equations 5.3 and 5.4 and the coefficients are given in Equations 5.5 and 5.8 for any possible

combination of any wave component i with a component j.

$$\eta = \sum_{i=1}^{N} \alpha_i \cos\psi_i \; + \; 2^{nd} \text{ sum } + \; 2^{nd} \text{ difference} \tag{5.2}$$

where the phase function of a wave i, $\psi_i = k_i x - \omega_i t + \varepsilon_i$, with ε_i the arbitrary phase of a wave, α_i is the wave amplitude of first order.

$$\begin{aligned} 2^{nd} \text{ sum } \; = \; & \sum_{i,j=1}^{N} \frac{\alpha_i^2 |k_i|}{4\tanh(|k_i|h)} \left[2 + \frac{3}{\sinh^2(|k_i|h)} \right] \cos(2\psi_i) \\ & + \; \alpha_i \alpha_j B_p(k_i, k_j) \cos(\psi_i + \psi_j) \end{aligned} \tag{5.3}$$

$$2^{nd} \text{ difference } \; = \; \alpha_i \alpha_j B_m(k_i, k_j) \cos(\phi_i - \psi_j) - \sum_{i,j=1}^{n} \frac{a_i^2 |k_i|}{2\sinh(2|k_i|h)} \tag{5.4}$$

The solution above is given for non-zero MWL, which corresponds to the last term in Equation 5.4. In the present case, provided that the window of the timeseries is sufficiently wide to include the entire wave group, the MWL is negligible. Nevertheless, the wave-wave interaction coefficients are independent from the MWL and for their calculation only $B_p(k_i, k_j)$ and $B_m(k_i, k_j)$ are needed. As mentioned, unidirectional wave propagation is assumed for the present case, meaning that the angle between the components is zero and the $\cos(\phi_i - \phi_j) = 1$.

$$\begin{aligned} B_p(k_i, k_j) = & \frac{\omega_i^2 + \omega_j^2}{2g} - \frac{\omega_i \omega_j}{2g} \left[1 - \frac{1}{\tanh(|k_i|h)\tanh(|k_j|h)} \right] \\ & \times \left[\frac{(\omega_i + \omega_j)^2 + g|k_i + k_j| \tanh(|k_i + k_j|h)}{D_p(k_i, k_j)} \right] \\ & + \frac{\omega_i + \omega_j}{2gD_p(k_i, k_j)} \left[\frac{\omega_i^3}{\sinh^2(|k_i|h)} + \frac{\omega_j^3}{\sinh^2(|k_j|h)} \right] \end{aligned} \tag{5.5}$$

$$
\begin{aligned}
B_m(k_i,k_j) = & \frac{\omega_i^2+\omega_j^2}{2g} + \frac{\omega_i\omega_j}{2g}\left[1+\frac{1}{\tanh(|k_i|h)\tanh(|k_j|h)}\right] \\
& \times \left[\frac{(\omega_i-\omega_j)^2+g|k_i-k_j|\tanh(|k_i-k_j|h)}{D_m(k_i,k_j)}\right] \\
& + \frac{\omega_i-\omega_j}{2gD_m(k_i,k_j)}\left[\frac{\omega_i^3}{\sinh^2(|k_i|h)} - \frac{\omega_j^3}{\sinh^2(|k_j|h)}\right]
\end{aligned}
\tag{5.6}
$$

where the functions $D_p(k_i,k_j)$ and $D_m(k_i,k_j)$ are defined as:

$$
D_p(k_i,k_j) = (\omega_i+\omega_j)^2 - g|k_i+k_j|\tanh(|k_i+k_j|h) \tag{5.7}
$$

$$
D_m(k_i,k_j) = (\omega_i-\omega_j)^2 - g|k_i-k_j|\tanh(|k_i-k_j|h) \tag{5.8}
$$

As mentioned, the calculated 2^{nd} order solution is a summation of sum and difference harmonics. The former are high frequency terms that result in a steeper local wave profile, while the latter are low frequency terms causing a wider set-down under the wave group, virtually decreasing the MWL (Baldock et al., 1996). Consequently, the sum terms cause an asymmetry of the wave profile around the MWL, making shallower troughs and higher and narrower crests. These effects increase for higher values of steepness (H_s) (Dalzell, 1999).

In practice, second order theory was proven successful in representing the largest waves in real ocean, where directionality is an important factor (Gibbs and Taylor, 2005; Johannessen and Swan, 2003), and it is useful for producing statistical distributions for the wave crests. Nevertheless, if the underlying free-wave spectrum changes due to resonant third order interactions, deviations from second order theory are reported (Fedele and Tayfun, 2009). For unidirectional seas, on the other hand, 2^{nd} order harmonics are not adequate to capture the crest height if the steepness is high, as discussed later.

In the next section, the results of second order theory prediction are examined using the original and the evolved spectrum for unidirectional wave propagation.

5.2.2 Results

The second order theory prediction for the groups of different steepness is analysed in the spectral domain and in the time domain for the 2^{nd} order sum and difference harmonics produced based on the original and evolved linear harmonics. Also, the timeseries of the total surface elevation is presented for each group and compared with the result of the fully-nonlinear model HOS-NWT.

The presentation starts with the steepest wave group that results in greater spectral evolution and larger 2^{nd} order harmonics (Figures 5.7 - 5.9). The spectral analysis in Figure 5.7 shows that the 2^{nd} order sum and difference harmonics in Figures 5.7b and 5.7c[3], calculated based on the original free-wave spectrum, shown in Figure 5.7a, differ considerably from those calculated by the extracted evolved linear harmonics (gray line). As the free-wave spectrum broadens to higher frequencies, the calculated 2^{nd} order harmonics also become wider towards high frequencies and their peak value is lowered. The second order prediction based on the evolved spectrum from the NWT is closer to the extracted 2^{nd} order harmonics from the NWT than those calculated according to the original spectrum. However, there are some noticeable deviations: i) the peaks of the extracted harmonics are higher, ii) the extracted 2^{nd} difference harmonics seem to be more energetic at least in the part of the frequencies that were not filtered out and iii) the analytically calculated 2^{nd} difference harmonics seem to expand to higher frequencies. These differences cannot be justified at this stage and can be possibly associated with potential deficiencies of the harmonic decomposition. Somewhat surprisingly, the error of the free-wave spectrum of GKE seems to result in more realistic representation of the 2^{nd} order harmonics.

[3]The values of the 2^{nd} order harmonics have a local discrepancy at $f = 0$ Hz because the value of the amplitude spectrum below Dk was forced to zero, as it was not calculated by the GKE (see Figure 4.36).

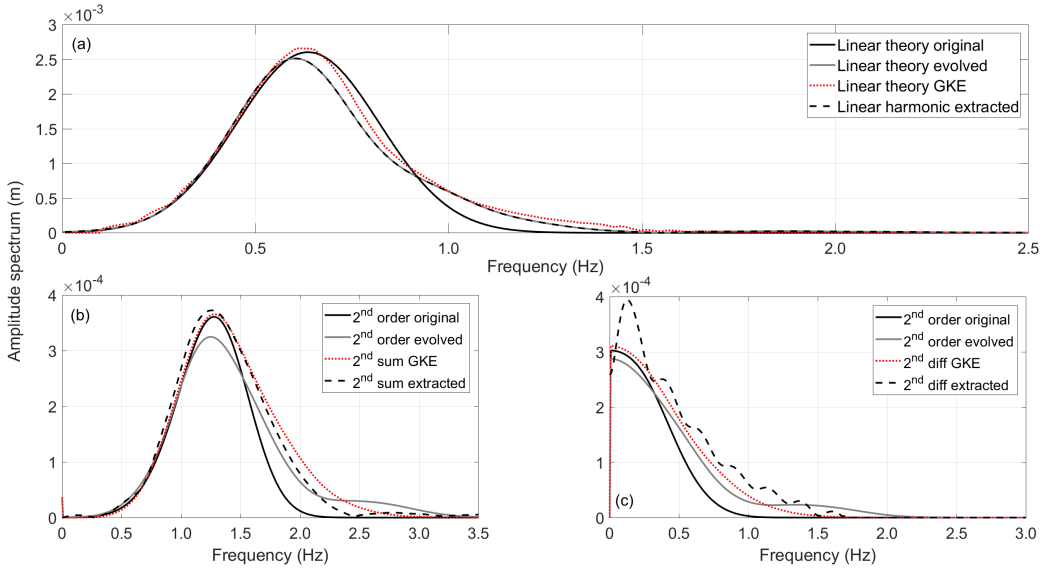

Figure 5.7: Comparison of the target, estimated evolved and extracted spectra at the PF location using 2^{nd} order theory: (a) Linear spectrum; (b) 2^{nd} order sum; (c) 2^{nd} order difference. Strongly nonlinear group.

The timeseries of the harmonics to second order are shown in Figure 5.8. It can be seen that the evolved linear harmonics with the shallower troughs and wider adjacent crests (Figure 5.8a) result in considerably different 2^{nd} order sum and difference harmonics in Figures 5.8b and 5.8c, respectively. Using the evolved linear harmonics from the NWT to calculate the 2^{nd} order harmonics gives a more realistic representation of the extracted 2^{nd} order harmonics from the four-wave decomposition. The analytically calculated crest of the 2^{nd} sum harmonic increases from 0.0341 m to 0.0403 m, approaching the crest of the extracted harmonic (0.0447 m). The adjacent crests are accurately calculated when the evolved spectrum is used, but the troughs, instead of becoming deeper, actually become shallower. It is interesting to note that using the evolved spectrum of the GKE, the 2^{nd} sum harmonics is very accurately computed. Regarding the 2^{nd} difference harmonics, using the extracted evolved spectrum results in a better represented set-down compared to the extracted harmonics, which is deeper and narrower. The solution is considerably improved with the trough getting deeper from -0.01796 m to -0.02288 m, with the value for the extracted harmonic being -0.02843 m. Again, the spectrum of the GKE offers a better solution for the 2^{nd} dif-

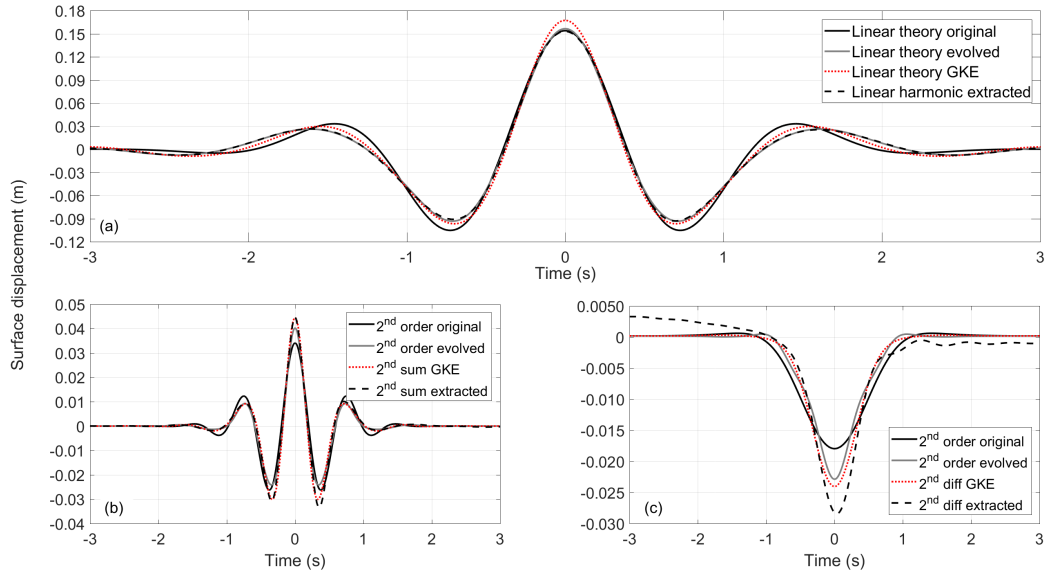

Figure 5.8: Comparison of the target, estimated evolved and extracted timeseries at the PF location using 2^{nd} order theory: (a) Linear harmonics; (b) 2^{nd} order sum; (c) 2^{nd} order difference. Strongly nonlinear group.

ference harmonics, but still without being able to match the extracted one. It is also interesting to note that before and after the main trough ($t \in [-1, 1]$ in Figure 5.8c) the analytical solution predicts almost zero surface displacement, while the extracted harmonic has a surge before the trough and set-down after. This is an indication of the issues of the NWT in reproducing well this low frequency harmonics.

The overall effect on the surface elevation of using the evolved free-wave spectra is presented in Figure 5.9, where it is compared with the fully nonlinear timeseries of HOS. It can be seen that the evolved spectra result in a more realistic shape of the wave group, which compares very well with the measurement at the adjacent crests and troughs, in contrast to the analytical solution based on the original spectrum. The main differences appear at the central crest where the second order solution underpredicts the crest height irrespectively of the underlying linear spectrum used. The extracted evolved spectrum combined with second order theory predicts a crest height of 0.1739 m, which is a marginal improvement towards the measured elevation of 0.2045 m. The use of the evolved spectrum of the GKE gives a value of 0.1877 m, which mainly comes

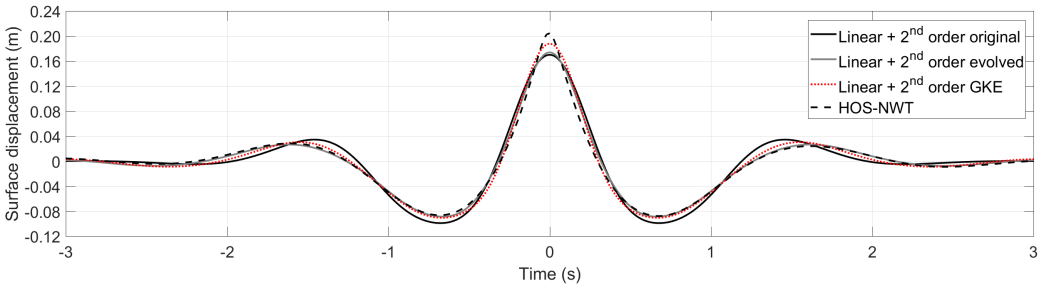

Figure 5.9: Comparison of measured timeseries and the timeseries up to 2^{nd} order based on the target, estimated evolved and extracted spectra at the PF location. Strongly nonlinear group.

from the overestimation of the timeseries of the linear harmonics, but it also induces some discrepancies at the lateral crests.

The same analysis is performed for the groups of moderate steepness. The results that follow show that as the steepness of the group decreases, the extracted 2^{nd} order harmonics are more similar to those analytically calculated.

For the weakly nonlinear group, Figures 5.10 and 5.11 show that the agreement between the extracted 2^{nd} order sum harmonics and the analytically calculated from second order theory is considerably improved when the evolved spectrum is employed. The timeseries show that crest height calculated by the extracted evolved and the spectrum of GKE are almost identical and marginally below the extracted 2^{nd} order sum harmonics. Some small differences at the lateral troughs of this harmonic are reported, with the GKE giving more realistic deeper troughs. The 2^{nd} difference harmonics of the evolved spectra are in better agreement with the extracted harmonics compared to the original spectra, but they still underestimate the depth of the trough.

The overall result of the surface timeseries in Figure 5.12 shows that the prediction of the crest height is improved from 0.1068 m to 0.1085 m when the extracted evolved free-wave spectrum is used and approaches better the fully nonlinear crest of 0.1123 m. The GKE spectrum predicts a crest of 0.1097 m, with this difference coming mainly from the overestimation of the linear harmonics.

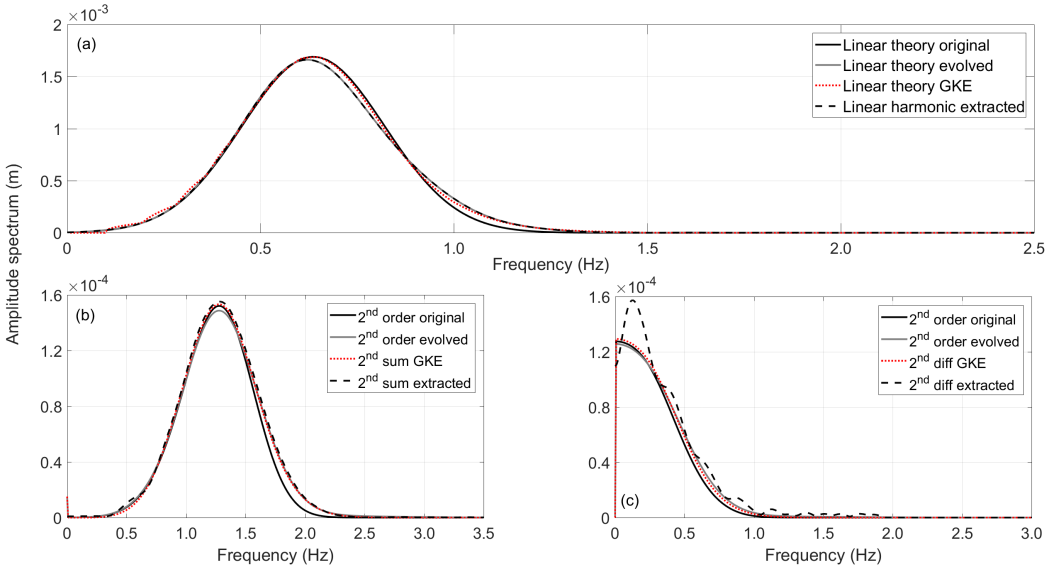

Figure 5.10: Comparison of the target, estimated evolved and extracted spectra at the PF location using 2^{nd} order theory: (a) Linear spectrum; (b) 2^{nd} order sum; (c) 2^{nd} order difference. Weakly nonlinear group.

The analysis of the quasi-linear group, which has practically no difference between the original and evolved free-wave spectra, shows that the spectra of the 2^{nd} order harmonics calculated from the second order theory are in very good agreement with the extracted harmonics (see Figure 5.13). This is also confirmed by the timeseries of the harmonics in Figure 5.14, with the only discrepancies seen in the 2^{nd} difference harmonics, where the extracted harmonics is deeper than the analytically calculated. The timeseries of the overall surface displacement in Figure 5.15 demonstrate that second order theory is adequate to describe the fully nonlinear solution of this group of low steepness. The crest height increases from 0.05168 m to 0.05194 m and to 0.05218 m when the evolved extracted and GKE spectra are used, respectively. The measured maximum elevation at the crest of the HOS-NWT simulation is 0.05219 m.

Similar qualitative conclusions were drawn from previous studies. Baldock et al. (1996) reported that increasing steepness of the group causes deviations from the second order theory of Longuet-Higgins and Stewart (1960). The deviations from analytical solutions of linear and second order theory were attributed to the local broadening of

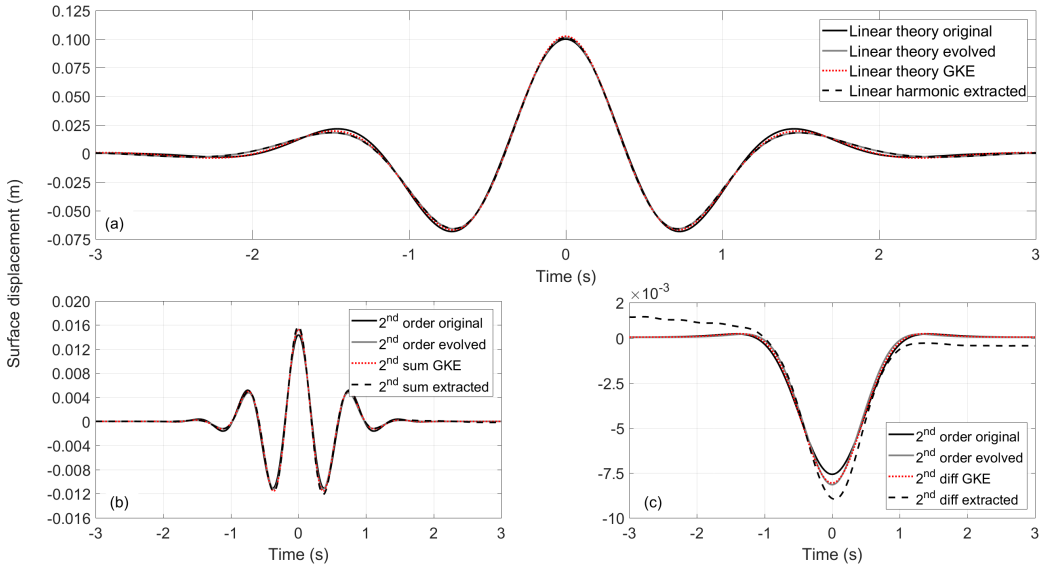

Figure 5.11: Comparison of the target, estimated evolved and extracted timeseries at the PF location using 2^{nd} order theory: (a) Linear harmonics; (b) 2^{nd} order sum; (c) 2^{nd} order difference. Weakly nonlinear group.

the free-wave spectrum that take place in short timescales of the propagation of the wave group towards focusing in the study (Johannessen and Swan, 2003). That work was later extended to examine kinematics, showing that knowing the evolved free wave regime improves the solution for the horizontal velocity profile even for nearly breaking unidirectional wave groups (Johannessen, 2010), which highlights the importance of the spectral evolution for engineering applications. Ning et al. (2008) and Ning et al. (2009b) also compared the results of fully nonlinear focused waves with the second order theory of Dalzell (1999). The results confirm that the asymmetries of the wave

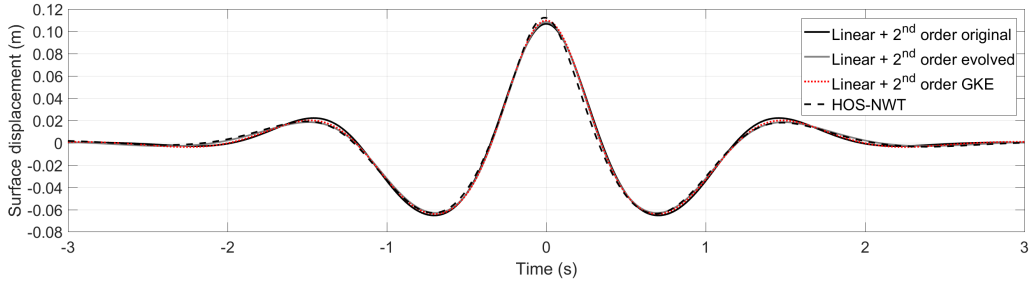

Figure 5.12: Comparison of measured timeseries and the timeseries up to 2^{nd} order based on the target, estimated evolved and extracted spectra at the PF location. Weakly nonlinear group.

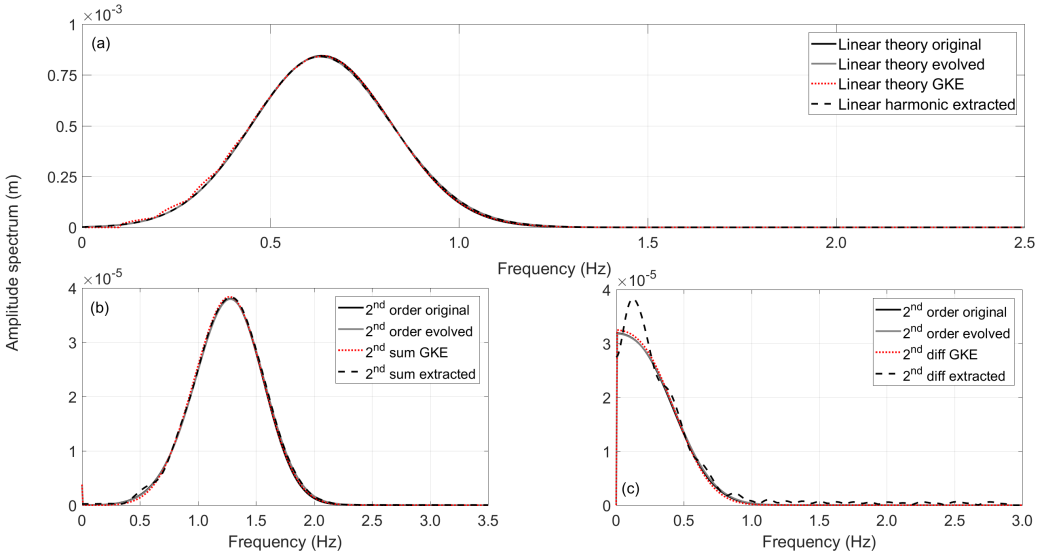

Figure 5.13: Comparison of the target, estimated evolved and extracted spectra at the PF location using 2^{nd} order theory: (a) Linear spectrum; (b) 2^{nd} order sum; (c) 2^{nd} order difference. Quasi-linear group.

profile increase with increasing steepness of the wave group, with the crests becoming higher and the troughs shallower. Compared to the fully nonlinear solution, the prediction of linear and second order theory produce a broader and lower crest and deeper and sharper troughs, indicating that energy is transferred to higher than 2^{nd} order harmonics. For the steeper groups, it was also seen that the dispersive properties of the wave profile were altered. The potential of second order theory to describe accurately steep wave groups when combined with the evolved free-wave spectrum was demonstrated by Gibbs and Taylor (2005) for directional waves, where the effects of higher than 2^{nd} order bound harmonics could be neglected. Therefore, the present methods for calculating the free-wave spectrum and combining it with 2^{nd} order bound waves may be even more relevant for realistic directionally spread focused waves.

When comparing with previous studies an issue is that the waves groups are not accurately focused and the results are commonly timeshifted, e.g., (Ning et al., 2009b). Despite the fact that the timeshifting manages to align the crests, the phases of the waves are not accurately corrected, which can result in considerable differences in the crest height and overall shape. Another equally important issue refers to the extrac-

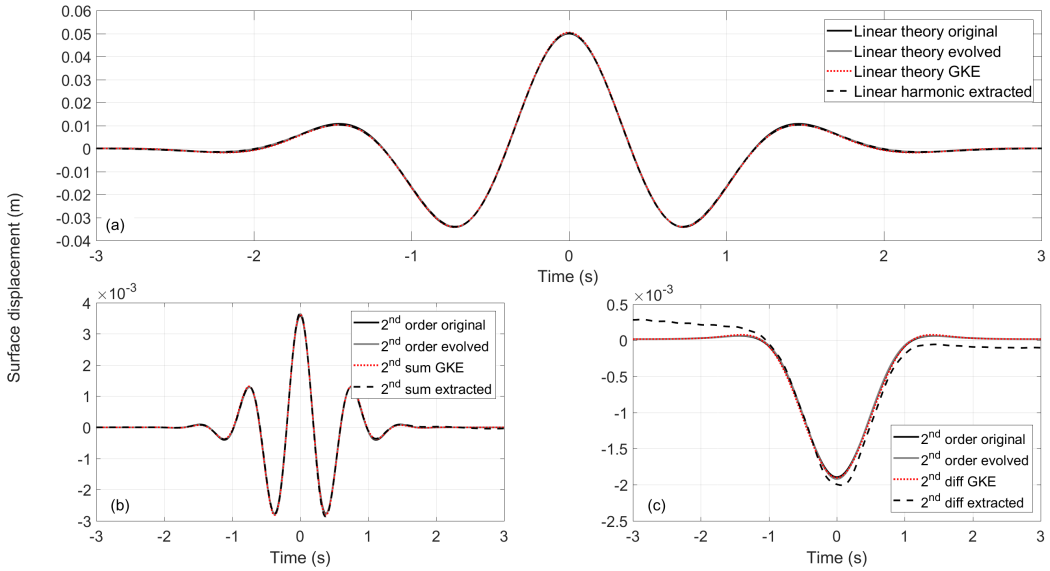

Figure 5.14: Comparison of the target, estimated evolved and extracted timeseries at the PF location using 2^{nd} order theory: (a) Linear harmonics; (b) 2^{nd} order sum; (c) 2^{nd} order difference. Quasi-linear group.

tion of the free-wave spectrum. The aforementioned studies (Johannessen and Swan, 2003; Ning et al., 2008, 2009b), among many others, employ a two-wave decomposition method, which is only accurate for narrowbanded spectra, because the 1^{st} and the 3^{rd} harmonics are only separated with frequency filtering. However, the analysis of this section demonstrated that both linear and 2^{nd} order analytical solutions are relatively sensitive to the definition of the free-wave spectrum, which here was obtained accurately by the four-wave decomposition.

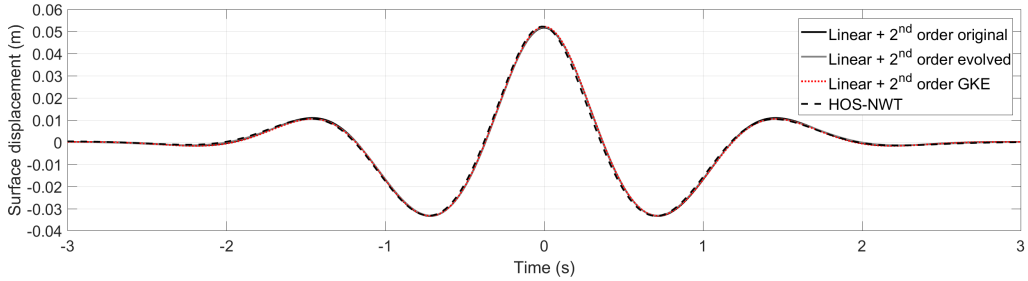

Figure 5.15: Comparison of measured timeseries and the timeseries up to 2^{nd} order based on the target, estimated evolved and extracted spectra at the PF location. Quasi-linear group.

Last but not least, to make realistic comparisons with fully nonlinear results, the wave group should propagate adequately long in the nonlinear numerical domain, in order to allow for both bound and resonant nonlinearities to develop. For example, the propagation from the inlet until the focal point is only $1.5L_p$ in the study of Ning et al. (2009b), which means that on one hand, the wave group is not well dispersed at the inlet in order for second order solution to be valid (at least for steep groups), and on the other hand, the resonant interactions may not have enough time to develop. Despite saving computational resources with shorter NWTs, these aspects should be examined carefully.

5.2.3 Conclusions

The present results show that second order theory can provide a good representation of focused waves, especially when the locally broadened free-wave spectrum is used. In particular, the overall shape of the group is better predicted compared to the results obtained by using the original spectrum. However, the maximum crest elevation shows a more gentle increase, which is not adequate to match that of the strongly nonlinear group from the fully nonlinear computation.

An important finding is the validity of second order theory by comparing the results with the extracted 2^{nd} order harmonics. The extracted 2^{nd} order harmonics of the fully nonlinear simulation are in good agreement with the analytically produced harmonics based on the evolved spectra. This agreement becomes excellent for waves of moderate steepness. The discrepancies between theoretical and extracted harmonics cannot be readily justified, but they may be related to limitations of analytical solution for very steep waves close to their breaking limit or to some deficiencies of the four-wave decomposition. It is noted that the focused wave crest obtains its maximum only locally and does not propagate at this extreme steepness. Thus, future work should examine whether such high steepness violates the underlying assumptions of second order theory. It is also reported that the discrepancies between the extracted and com-

puted harmonics are more pronounced for the 2^{nd} difference harmonic, which was also challenging to replicate in the numerical models, as shown in Chapter 3.

Another interesting result is that the 2^{nd} order harmonics produced based on the evolved spectrum of the GKE are in very good agreement with the extracted harmonics, which paradoxically is better than that when the extracted free-wave spectrum from HOS is used. This agreement is in particular remarkable for the 2^{nd} sum harmonics, but it may simply be a case specific finding.

5.3 Fifth order expansion

In this section, the result of the fifth order expansion of Walker et al. (2004) is examined for estimating the bound waves up to 5^{th} order. The formulation is based on the Stokes expansion of Fenton (1985) developed for a slowly modulated wave train. This is an approximate solution for the high order bound harmonics that, to the best of the author's knowledge, has been applied only for the case of the Draupner wave by Walker et al. (2004). The main issue of that study was that the characteristics of the underlying free-wave spectrum were not known and thus, any discrepancies can be associated with that limitation. Here, since the original and evolved free-wave spectra are known, the accuracy of the fifth order expansion for estimating the shape of focusing wave groups of varying steepness can be tested with accuracy.

The experimental work of Taklo et al. (2015) and the results presented in Chapter 3, identified bound wave harmonics up to 5^{th} order as the wave group approaches focusing, which makes the fifth order expansion an interesting approach for improving the linear NewWave solution.

5.3.1 Mathematical formulation

The derivation of the fifth order expansion is given in (Walker et al., 2004) and it uses the general formulation and coefficients of Fenton (1985). As mentioned, in the study of Walker et al. (2004) the linear part is not known and it has to be estimated from the fully nonlinear signal making some assumptions. Another consequence of that is that the value of kd needed for the expansion was not known and a large part of the study was devoted in estimating it. Here, the mathematical description of the expansion is given and the aforementioned limitations of the work of Walker et al. (2004) will be discussed in comparison to the present work.

To begin with, the underlying assumptions are discussed. The fifth order Stokes theory of Fenton (1985) assumes that waves propagate according to linear dispersion relation relative to any existent mean flow (current) in constant water depth. According to Stokes theory the wave is periodic and steady, and consequently, it can be expressed in Fourier series. These can be written as perturbation expansions that have parameters which satisfy the boundary conditions on the free surface, namely, the Bernoulli's equation for an incompressible and irrotational fluid that also satisfies the Laplace equation. The parameters used are the dimensionless wave height $k\frac{H}{2}$, which corresponds to the wave steepness, with H being the wave height, and the dimensionless water depth kd. Therefore, to expand the solution to fifth order, the wavenumber (k) and the water depth (d) should be known. For a regular wave k is related to d by the linear dispersion. The theory of Fenton (1985) can be used to expand the regular wave to high orders and it was found to be accurate for wavelengths that are sorter than ten times the water depth. There are however limits for the shallow and deep water that are discussed in the original paper.

The solution of the free surface profile ($\eta(x)$) can be given as a number of power series, truncated at fifth order, with the wave steepness as the expansion parameter. The free surface profile is calculated by Equation 5.9, which corresponds to Equation 14 in (Fenton, 1985).

$$\begin{aligned} k\eta(x) = kd &+ \varepsilon B_{11}\cos(kx) + \varepsilon^2 B_{22}\cos(2kx) + \varepsilon^3 B_{31}[\cos(kx) - \cos(3kx)] \\ &+ \varepsilon^4[B_{42}\cos(2kx) + B_{44}\cos(4kx)] \\ &+ \varepsilon^5[-(B_{53}+B_{55})\cos(kx) + B_{53}\cos(3kx) + B_{55}\cos(5kx)] + O(\varepsilon) \end{aligned} \tag{5.9}$$

where $\varepsilon = k\frac{H}{2}$, which is taken here as $\varepsilon = k\alpha$, since the individual waves that form the wave group are of low amplitude and thus, are considered linear waves.

The B_{ij} coefficients are given as hyperbolic functions of kd. These coefficients are also found in (Fenton, 1985)[4]. The values of B_{ij} coefficients are given for the specific value of $kd = 0.753981$ in the original paper, which served as a validation of the correct calculation of the coefficients for the present work.

$$B_{11} = 1 \tag{5.10a}$$

$$B_{22} = \frac{\coth(kd)(1+2C)}{2(1-C)} \tag{5.10b}$$

$$B_{31} = -\frac{3(1+3C+3C^2+2C^3}{8(1-C)^3} \tag{5.10c}$$

$$B_{33} = -B_{31} \tag{5.10d}$$

$$B_{42} = \frac{\coth(kd)(6-26C-182C^2-204C^3-25C^4+26C^5)}{6(3+2C)(1-C)^4} \tag{5.10e}$$

$$B_{44} = \frac{\coth(kd)(24+92C+122C^2+66C^3+67C^4+34C^5)}{24(3+2C)(1-C)^4} \tag{5.10f}$$

$$B_{51} = -(B_{53}+B_{55}) \tag{5.10g}$$

$$B_{53} = \frac{9(132+17C-2216C^2-5897C^3-6292C^4-2687C^5+194C^6+467C^7+82C^8}{128(3+2C)(4+C)(1-C)^6} \tag{5.10h}$$

$$B_{55} = \frac{5(300+1579C+3176C^2+2949C^3+1188C^4+675C^5+1326C^6+827C^7+130C^8}{384(3+2C)(4+C)(1-C)^6} \tag{5.10i}$$

[4]NB: In (Walker et al., 2004) there is a misprint for B_{31}, which has the opposite sign.

where $C = \mathrm{sech}(2kd)$.

The fifth order solution of Fenton (1985) provides a relatively simple way to calculate the high order bound waves of periodic waves. Based on this solution, Walker et al. (2004) provided an approximate solution for a periodic wave train, which corresponds to the NewWave profile and it is valid locally in space and time. The limitations of their work are discussed at the end of this section.

Equation 5.9 can be simplified by changing the original coordinate system from the bottom to the still water level (SWL) and by assuming that the SWL is defined at the MWL, the water depth d can be removed from the right hand side. Further, after dividing with the wavenumber and replacing the wave steepness with $\varepsilon = k\alpha$, Equation 5.11 is obtained.

$$\begin{aligned}\eta(x) = \quad & \alpha B_{11}\cos(kx) \\ & + k\alpha^2 B_{22}\cos(2kx) \\ & + k^2\alpha^3 B_{31}[\cos(kx) - \cos(3kx)] \\ & + k^3\alpha^4[B_{42}\cos(2kx) + B_{44}\cos(4kx)] \\ & + k^4\alpha^5[-(B_{53}+B_{55})\cos(kx) + B_{53}\cos(3kx) + B_{55}\cos(5kx)]\end{aligned} \tag{5.11}$$

An expression of Equation 5.11 can be presented based on the modified Stokes coefficients S_{ij} (see Equation A11 in the Appendix A of (Walker et al., 2004)). This results to Equation 5.12, which introduces the new variables D_{ij}.

$$\begin{aligned}\eta = & S_{11}D_{11} + \frac{S_{22}}{d}D_{22} + \frac{S_{31}}{d^2}D_{31} + \frac{S_{33}}{d^2}D_{33} + \frac{S_{42}}{d^3}D_{42} \\ & + \frac{S_{44}}{d^3}D_{44} + \frac{S_{51}}{d^4}D_{51} + \frac{S_{53}}{d^4}D_{53} + \frac{S_{55}}{d^4}D_{55}\end{aligned} \tag{5.12}$$

The variables D_{ij}, given in Equation 5.13, contain the phase and amplitude of the wave

form, being defined by the linear wave profile (η_L) and its Hilbert transform (η_{LH}), which practically changes the $\cos$ to $\sin$ function in the wave equation.

$$D_{11} = \eta_L = \alpha\cos(\theta) \tag{5.13a}$$

$$D_{22} = \eta_L^2 - \eta_{LH}^2 = \alpha^2\cos(2\theta) \tag{5.13b}$$

$$D_{31} = (\eta_L^2 + \eta_{LH}^2)\eta_L = \alpha^3\cos(\theta) \tag{5.13c}$$

$$D_{33} = (\eta_L^2 - 3\eta_{LH}^2)\eta_L = \alpha^3\cos(3\theta) \tag{5.13d}$$

$$D_{42} = (\eta_L^2 + \eta_{LH}^2)(\eta_L^2 - n_{LH}^2) = \alpha^4\cos(2\theta) \tag{5.13e}$$

$$D_{44} = (\eta_L^2 - \eta_{LH}^2)^2 - (2\eta_L\eta_{LH})^2 = \alpha^4\cos(4\theta) \tag{5.13f}$$

$$D_{51} = (\eta_L^2 + \eta_{LH}^2)^2\eta_L = \alpha^5\cos(\theta) \tag{5.13g}$$

$$D_{53} = (\eta_L^2 + \eta_{LH}^2)[\eta_L(\eta_L^2 - 3\eta_{LH}^2)] = \alpha^5\cos(3\theta) \tag{5.13h}$$

$$D_{55} = [(\eta_L^2 - \eta_{LH}^2)^2 - (2\eta_L\eta_{LH})^2]\eta_L - 4\eta_{LH}^2\eta_L(\eta_L^2 - \eta_{LH}^2) = \alpha^5\cos(5\theta) \tag{5.13i}$$

$$\tag{5.13j}$$

What is left to obtain the surface profile is to calculate the S_{ij} coefficients. This can be done by comparing Equation 5.11 with 5.12, after replacing in the latter the D_{ij} coefficients from Equations 5.13 with their form that contains the $\cos\theta$ function, where $\theta = kx$. The arguments of the $\cos$ functions indicate which products should be equated. The calculations of S_{ij} are shown in Equations 5.14 and they are not given in the paper of Walker et al. (2004).

$$\alpha B_{11} = S_{11}\alpha \Rightarrow S_{11} = B_{11} = 1 \tag{5.14a}$$

$$k\alpha^2 B_{22} = \frac{S_{22}}{d}\alpha^2 \Rightarrow S_{22} = kB_{22}d \tag{5.14b}$$

$$k^2\alpha^3 B_{31} = \frac{S_{31}}{d^2}\alpha^3 \Rightarrow S_{31} = k^2 B_{31}d^2 \tag{5.14c}$$

$$-k^2\alpha^3 B_{31} = \frac{S_{33}}{d^2}\alpha^3 \Rightarrow S_{33} = -k^2 B_{31}d^2 = k^2 B_{33}d^2 \tag{5.14d}$$

$$k^3\alpha^4 B_{42} = \frac{S_{42}}{d^3}\alpha^4 \Rightarrow S_{42} = k^3 B_{42}d^3 \tag{5.14e}$$

$$k^3\alpha^4 B_{44} = \frac{S_{44}}{d^3}\alpha^4 \Rightarrow S_{44} = k^3 B_{44}d^3 \tag{5.14f}$$

$$\begin{gathered} k^4\alpha^5[-(B_{53}+B_{55})] = \frac{S_{51}}{d^4}\alpha^5 \Rightarrow S_{51} = k^4[-(B_{53}+B_{55})]d^4 \\ \text{with } -(B_{53}+B_{55}) = B_{51} \end{gathered} \tag{5.14g}$$

$$k^4\alpha^5 B_{53} = \frac{S_{53}}{d^4}\alpha^5 \Rightarrow S_{53} = k^4 B_{53}d^4 \tag{5.14h}$$

$$k^4\alpha^5 B_{55} = \frac{S_{55}}{d^4}\alpha^5 \Rightarrow S_{55} = k^4 B_{55}d^4 \tag{5.14i}$$

(5.14j)

Equation 5.12 can be now solved. For better interpretation, the terms have be re-grouped in Equation 5.15, showing the different orders in separate lines in ascending order from first to fifth. For clarification, the first and second indices of the coefficients correspond to Stokes amplitude order and the harmonic of the frequency, respectively[5].

$$\begin{aligned} \eta = \quad & S_{11}D_{11} + \frac{S_{31}}{d^2}D_{31} + \frac{S_{51}}{d^4}D_{51} \\ & + \frac{S_{22}}{d}D_{22} + \frac{S_{42}}{d^3}D_{42} \\ & + \frac{S_{33}}{d^2}D_{33} + \frac{S_{53}}{d^4}D_{53} \\ & + \frac{S_{44}}{d^3}D_{44} \\ & + \frac{S_{55}}{d^4}D_{55} \end{aligned} \tag{5.15}$$

[5]Personal communication with P.H. Taylor, June 2016.

As mentioned, the fifth order expansion calculates only the high frequency harmonics. The calculation of the low frequency bound harmonics is more complex and in (Walker et al., 2004) a simple but crude approximation was suggested considering only the second order self interactions based on (Dean and Dalrymple, 1991)[5]. Since, for the present case the MWL is the same as the SWL, the Equation 14 in (Walker et al., 2004) reduces to Equation 5.16, considering $\overline{\alpha^2} = 0$. However, it is noted that in the end Walker et al. (2004) did not use this formula and calculated the 2^{nd} difference contribution by low-pass filtering and compared it with the exact second order solution of Dalzell (1999). Considerable differences were reported by Walker et al. (2004) for the case of Draupner wave, which exhibited a set-up instead of a set-down. This was explained later by Adcock et al. (2011) as an effect of directionality with two crossing sea states and thus, it was impossible to be explained under the unidirectional propagation considered by Walker et al. (2004).

$$\eta_{2-} = -\frac{\alpha^2 k}{2\sinh(2kd)} \tag{5.16}$$

Before presenting the application of the fifth order expansion on the present results, its application in the study of Walker et al. (2004) and their findings are briefly discussed. The scope of the work of Walker et al. (2004) was to provide an improved NewWave definition that includes bound harmonics to fifth order and to approximate the shape of the Draupner wave. The first step in doing that was to find a technique to estimate the underlying linear harmonics from the fully-nonlinear signal measured in the sea. This is a major challenge and it was done by assuming unidirectional waves and that the random signal consists of only linear and 2^{nd} order bound waves. The validity of this approach is tested by calculating the skewness of the estimated linear harmonic, which for a random linear Gaussian sea should be equal to 0. Despite finding a value which is close to that by excluding the Draupner wave from the record, the issue is that this criterion is not a priori valid, since the phases of the waves in the record are not necessarily Gaussianly distributed. A similar technique was used by Whittaker et al.

(2016) for recordings in shallower water. Another issue is that the fifth order expansion makes the assumption of a narrowbanded spectrum, which actually restricts it from application at the present case. However, the analysis of Whittaker et al. (2016) showed that it also works well for broadbanded spectra and $kd \geq 1$ and has almost identical results to the exact solution of Dalzell (1999). This gives confidence for applying the expansion at the present broadbadned spectrum of $k_p d \approx 1.7$.

A crucial step in this methodology is the selection of the kd, or practically k, since the depth d is known. In an irregular wave record, the selection of k is ambiguous because a representative wavenumber should be selected, which can be based on, e.g., the mean or peak frequency. Walker et al. (2004) found this wavenumber graphically by minimizing the difference between the calculated Stokes coefficient S_{22} with that estimated from the linearised wave record for zero skewness. However, a different approach is used in the present work that is believed to be more accurate, as explained in Section 5.3.2. Instead of trying to match the calculated value of S_{22} with an estimated one, the result of the exact second order solution is employed.

There are two other aspects that impose limitations to the fifth order expansion of Walker et al. (2004). As mentioned already, the 2^{nd} difference term is calculated separately and the suggested approximation of only the self interactions is crude. The exact second order solution can be used, but it is computationally expensive compared to the rest of the expansion. Moreover, it is somewhat paradoxical to use an approximate expansion of the 2^{nd} sum terms and the exact solution for the 2^{nd} difference. In the case of the Draupner wave record, the spectrum is relatively narrowbanded and the low frequency harmonics of the 2^{nd} difference can be extracted with filtering. However, this is not the case in the present study, and the overall scope is to produce a nonlinear profile, which is initially unknown. The second point of discussion is that the fifth order expansion was tested only for the Draupner wave and the amplitude of the linear NewWave was selected in order to match exactly the crest of the Draupner wave (see page 78 of (Walker et al., 2004)). Thus, it is no surprise that the crest elevations

matches the record, since the expansion was tuned to do so. Discrepancies are shown in the lateral crests and troughs (Figure 8 in (Walker et al., 2004)), indicating potential deficiencies of the method. For the results of the present work, the estimated crest elevation of the fifth order expansion was not tuned to match the fully nonlinear solution, and the result is based only on the original and evolved free-wave spectra and the selection of the representative wavenumber.

5.3.2 Results

Since in the present study the free-wave spectra are known, the only thing missing to apply the fifth order expansion is the definition of a representative wavenumber. The method suggested by Walker et al. (2004) using the skewness is irrelevant here, because on one hand the linear harmonic is known and on the other hand, the distribution of the phases is not Gaussian. Instead, it was decided, to use the original free-wave spectrum for finding the 2^{nd} sum harmonics of the Stokes expansion, as defined by the second line of Equation 5.15 for a wide range values of $kd \in [0.1, 4]$ and compare it with the exact solution of Dalzell (1999)[6].

This sensitivity-type analysis for the selection of k is shown in Figure 5.16a. Alongside, in Figure 5.16b, the results of the 2^{nd} difference harmonics are plotted for the same values of kd. It can be seen that the 2^{nd} sum harmonics of Stokes expansion has exactly the same crest height as the exact solution for the value of $kd = 2.5$ (marked with red). However, despite the almost excellent matching of the main crest and adjacent troughs, the lateral crests are overpredicted by the approximate solution. Instead, they are better described for the value of the wavenumber of the peak frequency component $k_p d$ marked with blue. For values $kd > 2.5$ and $kd < 2.5$, the 2^{nd} sum harmonic is overpredicted and underpredicted, respectively. It is worth mentioning that for values lower than $kd \leq 0.4$, the 2^{nd} sum harmonics change sign and become very large, as seen by the light gray line in Figure 5.16a. In general, the 2^{nd} sum harmonics are

[6] A similar concept was attempted in the study of Whittaker et al. (2016) for field data.

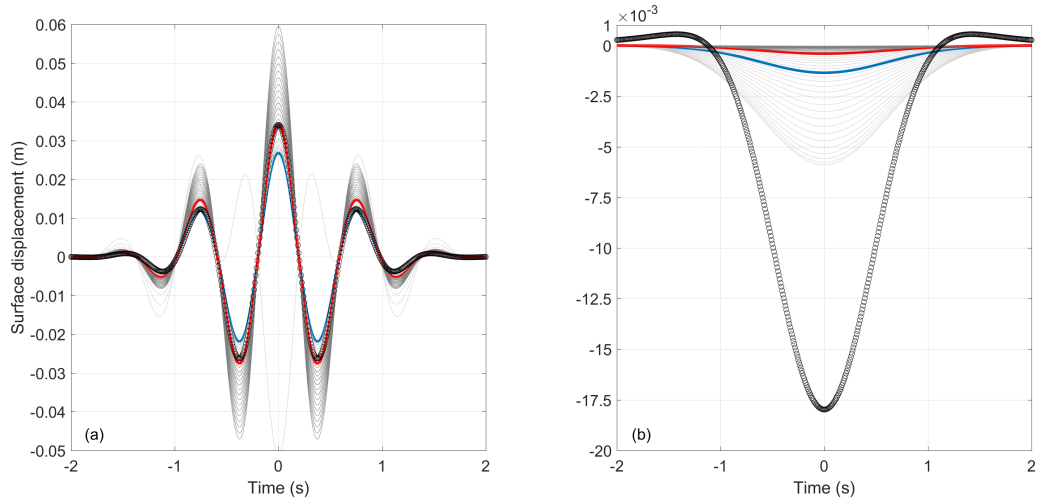

Figure 5.16: Sensitivity analysis for the selection of kd (a) 2^{nd} sum; (b) 2^{nd} difference. Red: $kd = 2.5$; Blue: $kd = k_p d$; Dark gray: $kd > 2.5$; Light gray: $kd < 2.5$; Black circles: exact solution (Dalzell, 1999).

relatively accurately predicted for $kd \in [0.5, 2.5]$. On the other hand, the 2^{nd} difference harmonics calculated by Equation 5.16 seems to be far from the exact solution. In particular, it is severely underpredicted by all values of kd and becomes negligible for $kd \leq 2.5$. In an attempt to improve the agreement for both the harmonics, different values of d were tested and the solution was seen to be very sensitive on the selection of the depth. To avoid adding extra bias in the analysis, the original water depth was used ($d = 1m$).

After the analysis of Figure 5.16, four representative values of kd were chosen for further tests on the behaviour of higher harmonics, as shown in Figure 5.17. The values of kd are: i) 2.5, because it matches exactly the crest of the 2^{nd} sum harmonic, ii) $k_p d \approx 1.7$, which showed good predictions and has the advantage that it can be directly selected from the spectrum, iii) 1.6, to see the sensitivity in comparison to $k_p d$ and because it is closer to the downshifted peak of the evolved spectrum. Moreover, this value of kd results in skewness closer to 0. iv) 0.9, as a compromise value for a sensible prediction of both the 2^{nd} sum and difference harmonics.

The results of Figure 5.17a show that the original linear harmonic is merely influenced

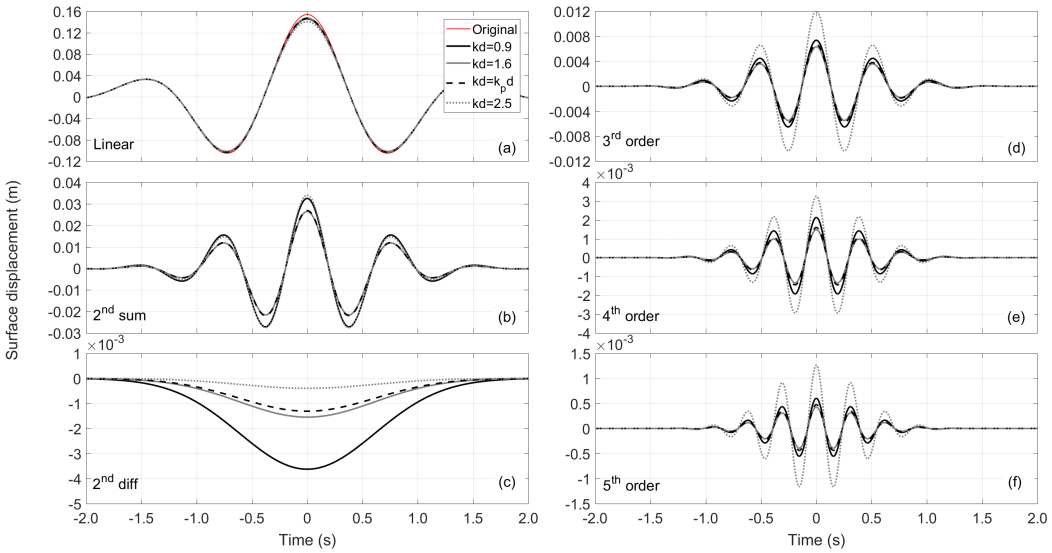

Figure 5.17: Comparison of the harmonics for the selected values of kd.

by the selection of kd, because the modified Stokes coefficient S_{11} is constant. The minor discrepancies at the crest are caused by the calculation of S_{31} and S_{51} that have however very small negative contributions. For almost all the harmonics, selecting a value close to $k_p d$, i.e., 1.6, has negligible effects. For the high frequency harmonics in Figure 5.17d,e,f, the high value of $kd = 2.5$ results in considerable overstimation of the surface elevation compared to the other values of kd, but to severe underprediction of the 2^{nd} difference harmonics in Figure 5.17c. The differences are the smallest for the 2^{nd} sum harmonics in Figure 5.17b, with $kd = 0.9$ and $kd = 2.5$ producing exactly the same result.

As a final check for the selection of the value of kd, the overall surface profile to fifth order is compared in Figure 5.18 for the selected values of kd. The variation amongst the profiles is in general little. As expected from the examination of the individual harmonics, $kd = 2.5$ produces the narrowest and highest crest, and the shallowest lateral troughs. The crest of the $k_p d$ is lower and marginally broader, being almost identical to the result for $kd = 0.6$. The lateral crests are identical for all the values of kd.

The sensitivity analysis for the selection of kd demonstrated that despite the differences

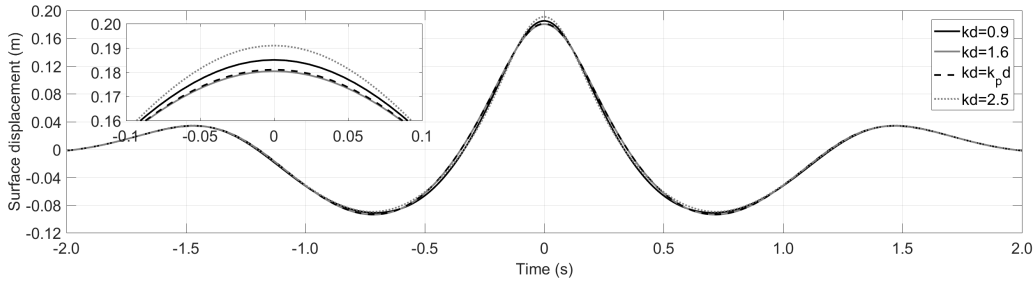

Figure 5.18: Comparison of the total surface elevation to 5^{th} order for the selected values of kd.

in the individual harmonics, the surface profile is similar for any of the four values tested, however none of these values could capture well the set-down of the 2^{nd} difference harmonics. For selecting the representative value of kd, it is noted that only the value k_pd can be selected without a sensitivity analysis and it is purely based on the spectral characteristics. Since there is no obvious advantage for selecting the values of $kd = 0.9$ and $kd = 2.5$ based on the previous findings, the more "natural" choice of k_pd is done. Due to the fact that the approximation of the 2^{nd} difference harmonics was not satisfying, at the end of this section the surface profile is also produced using the exact second order solution as well.

The surface profiles produced by the fifth order expansion based on the original and evolved free-wave spectra are presented for the wave groups of different steepnesses in Figures 5.19 - 5.21, starting with the strongly nonlinear group. The fully nonlinear solution of HOS-NWT is also plotted, as well as the linear solution based on the original spectra. For the fifth order expansion, the value of k_pd is calculated for each spectrum separately for the component that corresponds to the maximum of the amplitude spectrum. Comparisons were also performed using the k_pd value of the original spectrum (1.7186 m^{-1}) for the evolved spectra, with the results being very similar.

The results for the strongly nonlinear group in Figure 5.19 show that the fifth order solution provides an acceptable shape of the focused wave. Compared to the linear solution of the original spectrum, the fifth order expansion of the both the original and

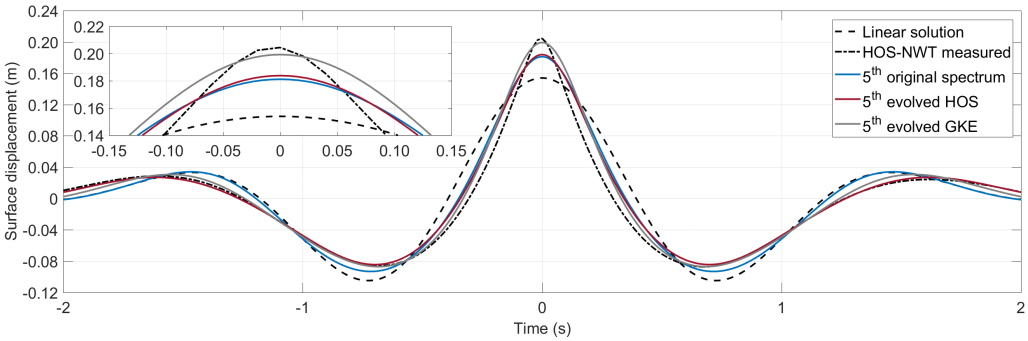

Figure 5.19: Calculated timeseries of the surface displacement for the strongly nonlinear group ($\Sigma\alpha_i = 0.154$ m) for $kd = k_p d$, using the original and the evolved linear harmonics.

evolved spectra produce a higher and steeper crest and shallower troughs. Improvement in approaching the fully nonlinear profile is observed when the evolved spectrum of HOS is used, with the lateral troughs becoming shallower and the lateral crests becoming lower and wider. A marginal increase of the crest height is observed from 0.1812 m to 0.1838 m. Using the evolved spectrum of GKE with the fifth order expansion produces a considerably higher crest of 0.1993 m ,which is very close to 0.2045 m of the fully nonlinear crest. The troughs are also in excellent agreement. However, the crest is broader than the measured, being close to that produced by the original spectrum and evolved spectrum of HOS.

The estimated surface profiles of the weakly nonlinear and quasi-linear wave groups are presented in Figures 5.20 and 5.21, respectively. As expected, the differences among the solutions for evolved and original underlying spectra are smaller. It can be seen that the approximated shape of the wave group is in very good agreement with the fully nonlinear solutions at any point of the timeseries. The maximum crest elevation of the weakly nonlinear group (0.1123 m) is marginally underestimated by the expansion using the original spectrum (0.1109 m) and overestimated by that of the GKE spectrum (0.1142 m), but it is the same as the expansion using the extracted linear harmonics of the HOS simulation. The results for the quasi-linear group are practically the same for all the spectra. The overall shape of the wave and the crest elevation are very well

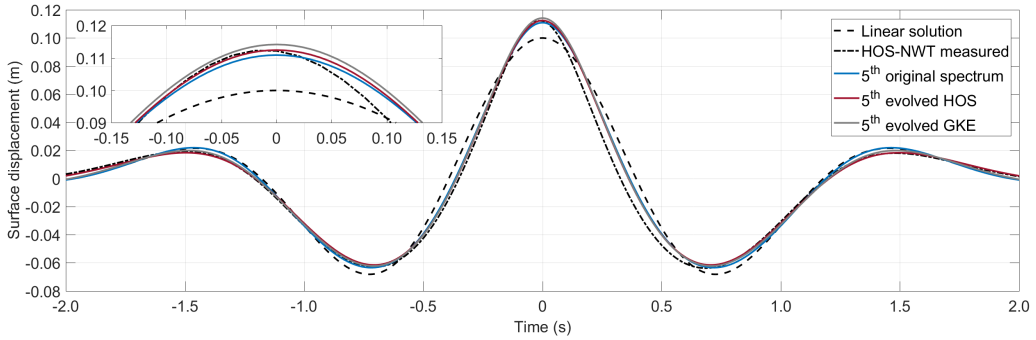

Figure 5.20: Calculated timeseries of the surface displacement for the weakly nonlinear group ($\Sigma\alpha_i = 0.100$ m) for $kd = k_p d$, using the original and the evolved linear harmonics.

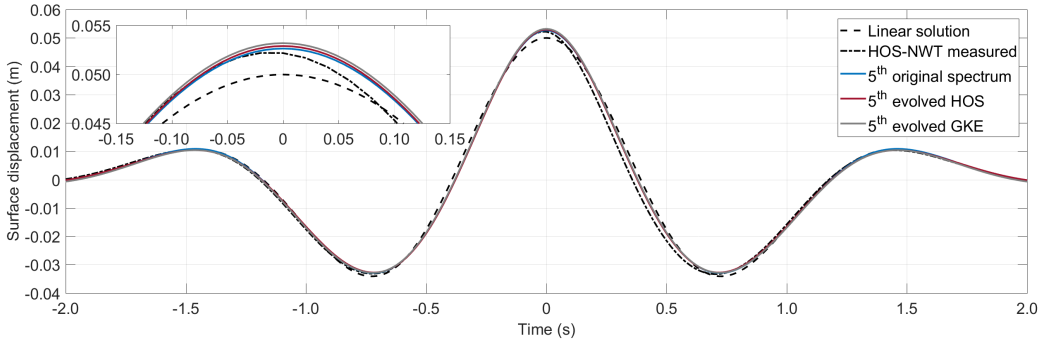

Figure 5.21: Calculated timeseries of the surface displacement for the quasi-linear group ($\Sigma\alpha_i = 0.050$ m) for $kd = k_p d$, using the original and the evolved linear harmonic.

predicted. The latter however is marginally overpredicted by all the expansions from 0.0522 m to 0.0526 m, 0.0529 m, 0.0532 m for the original, HOS and GKE spectra, respectively.

For the wave profiles presented so far, the 2^{nd} difference harmonics was approximated by the self interactions only. Here, since the underlying linear spectrum is available, the exact 2^{nd} order solution of Dalzell (1999) can be employed to examine the effect on the wave profile. This comparison is performed in Figure 5.22[7] for the spectrum of GKE, where "ex" indicates that the exact second order theory is used. The exact 2^{nd} order sum and difference harmonics are also plotted and compared with the corresponding approximated ones. It can be seen that the approximated 2^{nd} difference harmonics

[7]NB: The linear theory GKE solution in Figure 5.22 is based on the evolved spectrum of GKE, in contrast to the linear solutions in Figures 5.19 - 5.21, which are based on the original spectra.

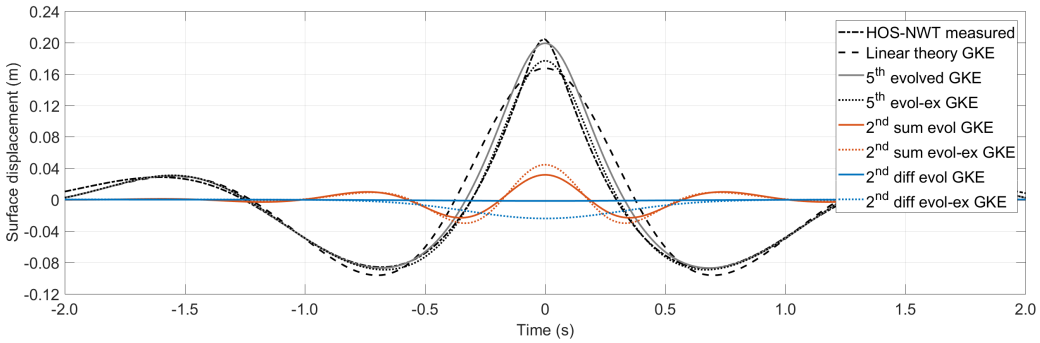

Figure 5.22: Comparison of the timeseries of the surface displacement for the strongly nonlinear group ($\Sigma\alpha_i = 0.154$ m) for $kd = k_p d$ using the self-interaction and the exact solution for the 2^{nd} diff harmonics for the evolved linear harmonic calculated by GKE.

is practically zero, while the exact 2^{nd} sum harmonics is considerably higher than the approximated. When the exact 2^{nd} difference harmonic (dotted blue line) is subtracted from the fifth order expansion, the maximum crest elevation decreases considerably to 0.177 m, but the shape of the crest becomes narrower, being in excellent agreement with the result of the HOS simulation. If instead of the approximated 2^{nd} sum, the exact harmonics was used, the crest elevation would rise to 0.1894 m. However, this was not done here, because it would start cancelling the entire principle of the fifth order approximation of using the modified Stokes coefficients.

It is also worth mentioning that the grouping of the terms of the fifth order expansion into frequency harmonics allows for comparisons with the individual harmonics extracted from the nonlinear simulation. This is not performed here for two main reasons: i) the results of Figure 5.17a suggest that the grouping may not be consistent with the harmonic decomposition, because the linear harmonics were not exactly retrieved and ii) the high order harmonics in Figure 5.17d,e,f are more sensitive to the selection of kd. A simple comparison with Figure 3.37, indicates that the extracted 4^{th} and 5^{th} order harmonics are almost an order of magnitude larger than that estimated by fifth order approximation. Thus, this method should be used only to approximate the total surface profile and not necessarily the individual harmonics.

5.3.3 Conclusions

The present results demonstrate that the fifth order expansion of Walker et al. (2004) can approximate with good accuracy the surface profile of nearly breaking NewWave-type wave group. Compared to the work of Walker et al. (2004), the present study has the advantage that the free-wave profile is known and the findings support the use of the method for improving the NewWave surface profile. To the author's best knowledge, this is the first study after the original paper that this method is employed.

Sensitivity analysis also showed that the final selection of the only unknown parameter, namely the representative wavenumber of the irregular group, can be done based on the k_p. Despite the good performance of the method, comparisons with the exact solution for the 2^{nd} order harmonics revealed underestimation of the individual harmonics, but with these differences almost cancelling the additional positive and negative contributions. Nevertheless, the discrepancies in the 2^{nd} difference harmonics were expected, since the fifth order approximation is based on the expansion of Fenton (1985), which accounts only for the high frequency bound waves and not for the long bound wave.

5.4 Creamer transform

The Creamer transform was suggested by Creamer et al. (1989) and it is based on the Hamiltonian expression for the water waves problem of weak nonlinearity. By employing a canonical transformation of the flow variables, the lowest order of nonlinearity is cancelled and this allows for the calculation of bound waves to infinite order through an integral representation of the amplitude spectrum. Essentially, the Creamer transform adds nonlinearity to a linear signal by incorporating bound waves. The original formulation of the transform was presented for spaceseries, but a simple technique using linear theory can be employed to obtain the timeseries of the surface elevation.

The Creamer transform is an efficient way to estimate a nonlinear wave profile by reproducing the expected nonlinear effects of steeper crests and shallower troughs. It has been used in a limited number of studies, showing good performance for up to 5^{th} order waves. As with all the previous methods for reconstructing the surface profile, the free-wave spectrum should be known, which imposes a considerable difficulty for applying the method to field data. Here, knowing the original and evolved spectrum, as well as the fully nonlinear results, gives the opportunity to assess the performance of the Creamer transform under controlled conditions for up to nearly breaking wave groups.

5.4.1 Mathematical formulation

The Creamer transform is based on the Hamiltonian representation of weakly nonlinear water waves. The basic assumptions dictate that the flow motion is irrotational and the effects of surface tension are excluded. The interior of the fluid follows the Laplace equation and appropriate conditions are applied on the boundaries. The water surface and velocity potential can be described by the ZE (Zakharov, 1968). The Hamiltonian, i.e., the energy of the fluid, can be expressed in power series that include integrals of the velocity potential at the free surface and the free surface elevation, which both can be expressed in the Fourier space for convenience. According to the theory, if the Hamiltonian can be expressed in power series and the leading order of nonlinearity does not include resonant interactions, it is possible to make a transformation and exclude the leading order of nonlinearity. Since for ocean gravity waves three-wave interactions are not resonant, a canonical transformation can be applied to the flow variables in order to eliminate the 3^{rd} order Hamiltonian ($H^{(3)}$). Through this transformation, the leading nonlinear terms of quadratic order can be removed, or more accurately be incorporated in the transformed variables, and the dynamics of the wave motion can be expressed by 1^{st} and 3^{rd} order terms. This is a very useful aspect, since the ocean waves can still be well approximated by ignoring 3^{rd} and higher order

nonlinearities (Creamer et al., 1989).

There are different ways to perform these transformations, which result in the same resonant wave interactions at 4^{th} order, but different non-resonant interactions at this order. At higher orders, both resonant and non-resonant interactions are different for the different transformations. This effectively controls the high order nonlinearities and it is upon the comparison of the various transformations to indicate which describes the fully nonlinear problem most appropriately. The general principle of using any transform is to derive a simpler form of the Hamiltonian and to obtain the dynamics of the motion that resemble better the fully nonlinear solution compared to the linearised solution of the original flow variables. In (Creamer et al., 1989), two transformations were examined and the Lie transform was preferred. This is because the Lie transform is practical to apply, gives a good approximation of Stokes waves, describes well the modulation of short waves on long waves and the Stokes drift is combined properly with the return flow (more details and examples in (Creamer et al., 1989)). Moreover, the Lie transform conserves the property of wave action, which guaranties minimal modification of the wave spectrum. A similar approach for describing the dynamics of the free surface by eliminating $H^{(3)}$ was followed also by Krasitskii (1994), with the canonical transform already discussed in Section 4.3.1 and been elaborated in Section 5.5.

A comparison between the Creamer and Krasitskii's canonical transforms is shown in Table 5.1. Both cancel the leading nonlinear terms by setting $H^{(3)} = 0$. Practically, this cancels the low order interactions and allows for obtaining the full solution to the higher order (4^{th}). The two canonical transformations are different only at $H^{(4)}$ and higher, due to their different formulation, which calculates differently the modified resonant and non-resonant interactions, indicated by $'$ and $''$ for Krasitskii and Creamer, respectively, as seen in Table 5.1. Thus, up to $H^{(3)}$ the result should be theoretically similar for the two methods. For the Creamer transform, the integral calculates the interactions to infinite order including both resonant and non-resonant interaction. The formulation of Krasitskii (1994) includes up to quintet interactions, corresponding to $H^{(5)}$, however, in

Table 5.1: Orders of Hamiltonian $H^{(n)}$ in Krasitskii and Creamer canonical transforms (R:Resonant; NR:Non-resonant; NA:Not applicable).

	$H^{(1)}$[a]	$H^{(2)}$	$H^{(3)}$	$H^{(4)}$	$H^{(5)}$
Real world	NA	Linear	NR	R + NR	NR
Krasitskii	NA	Linear	$\varnothing$	R′	R′
Creamer	NA	Linear	$\varnothing$	R″ + NR″	R″ + NR″

[a]The Hamiltonian of 1^{st} order ($H^{(1)}$) is not defined because it represents the energy, which is of 2^{nd} order expression of the surface displacement and velocity.

the present study, only up to four-wave interactions were considered. For comparison, the wave interactions before the transformations are also shown in Table 5.1 for the different orders of the Hamiltonian, referring to as the "Real world" case.

The Creamer transform for surface elevation refers to Equation 4.14a in the original paper of Creamer et al. (1989) and here it is given in Equation 5.17[8]. This equation calculates the amplitude spectrum of surface displacement in $\kappa-$space using the Hilbert transform of the spaceseries of the surface displacement ($\eta_H(x)$). The calculated nonlinear amplitude spectrum ($\eta_{NL}(k)$) includes the linear plus high order bound contributions. It is noted that the Creamer transform does not take into account wave dispersion (Slunyaev et al., 2013), which practically means that it is used for a harmonic signal which is static in space.

$$\eta_{NL}(k) = \frac{1}{|k|}\int e^{-ikx}\left(e^{ik\eta_H(x)} - 1\right)dx \tag{5.17}$$

The solution process followed in the present study is described next. Based on the known linear amplitude $f-$spectrum, the spaceseries of the surface elevation are constructed according to linear theory (Equation 5.1) for the focal time $t = 0$ s at a distance before and after the PF, so that the entire group is within the selected space range. The distance increment Dx is selected to be sufficiently small in order to provide good resolution of the signal. Decreasing the distance range around PF, i.e., the length of

[8]This simple form of the Creamer transform, strictly speaking, is valid for deep water waves. However, without this assumption the equation takes a more complex form. (Personal communication with M. Prevosto, January 2018).

the signal, increases Dk, while increasing Dx reduces k_{max}. By performing an FFT of the spaceseries, the amplitude $\kappa-$spectrum is obtained for the regular $\kappa-$grid resulted by the FFT. This process returns the positive and negative $\kappa-$spectrum and it is convenient because the phases of the components are incorporated in the imaginary part of the complex amplitudes and IFFT can be applied directly on the nonlinear spectrum after the transform. Alternatively, the $\kappa-$grid can be computed using the formula $Dk = \frac{2\pi}{(N-1)Dx}$, where N is the number of $x-$locations (Socquet-Juglard et al., 2005). These manipulations were discussed and verified in Section 5.1.2. The results of this process are the $\kappa-$grid and the linear spaceseries.

Next, the calculation of the Hilbert transform of the spaceseries is performed either using MATLAB' function or by changing the $\cos$ function to $\sin$ in Equation 5.1. Then, the integral of Equation 5.17 can be calculated by computing its argument for a specific wavenumber over the entire distance and taking the trapezoid of argument over the distance. This is done for all the wavenumbers and their summation returns the integral of Equation 5.17. To obtain the spaceseries, IFFT is applied to the result of the previous process, namely to $\eta_{NL}(k)$. The spaceseries can be plotted on the initially selected $x-$space.

A few remarks until this stage should be made: i) Care should be taken to exclude the contribution of $k = 0$, because it refers to an infinitely long wavelength and it creates singularity. This can be done by setting $\eta_{NL}(0) = 0$. ii) The nonlinear wave profile is not very sensitive to the selection of the limits of the spaceseries, provided that the entire linear group is included in the considered initial signal. iii) As a rule, the MWL should be extracted from the linear spaceseries. Here, since the linear spaceseries are wide enough that the surface displacement is zero before and after the group, the exclusion of the MWL results in negligible differences of approximately 0.03% at the crest of the steepest wave group.

To allow for comparisons with the other approaches for reconstructing the wave profile, the spaceseries should be converted to timeseries. An approach to do that was pro-

posed by Creamer et al. (1989), mentioning that the integration in time can be done by "just letting the linear variables evolve according to their quadratic Hamiltonian", or else stated by assuming linear dispersion. A formula to do that was suggested by Slunyaev et al. (2013) (Equation 20) for a deep water wave. The underlying principle is to apply the Creamer transform on linear profiles at different instances close to the time of interest. The linear profiles are found by propagating the wave group before and after the time of interest using the linear dispersion relation. The timeseries can then be obtained by sampling on the location of interest over the produced nonlinear snapshots of the wave profile for the various times. This approach was graphically verified in Figure 5.6. It is important to underline that this approach is only valid if the free-wave spectrum does not change significantly in the examined time range due to resonant interactions. Here, a short time window of ± 2 s of the focal time is examined, where it is assumed that the spectrum is not altered significantly.

The success of the Creamer transform, or any other transform for that matter, lies upon each efficiency to solve the wave motion problem in space and time compared to the classic approach of solving the PDEs of the fluid motion. Especially for short time scales and not very frequent time intervals, the Creamer transform can be very efficient, since it uses linear equations and thus, it is simpler than solving the PDEs (Creamer et al., 1989).

Hereafter, applications of the Creamer transformed are discussed. In the original paper, the Creamer transform demonstrated that it can replicate the effects of nonlinearity by making the wave profile steeper and approaching the exact stokes solution for the velocities of the water particles at the free surface. Also the problem of short waves riding on long waves was shown to be captured correctly. It is mentioned though, that the transformation is correct in unidirectional propagation and only approximate for directional waves. Other potential applications were also suggested for future studies, such as improved statistics of the free surface and the assessment of stochastic wave models that are based on the KE and include only four-wave interactions. It is worth

mentioning that Creamer et al. (1989) envisaged the potential of using their expansion to high orders in combination with the four-wave interactions in order to produce more realistic results. In other words, this suggestion seems similar to the approach of the present study of using the evolved spectra as input to the analytical models for calculating the bound waves.

Since its publication, the Creamer transform has been employed in a relatively small number of studies. Recognizing its efficiency over the classic Stokes expansion, Jonathan and Taylor (1997) used the Creamer transform to introduce nonlinearity to the linearised timeseries from the Tern platform and compared the results with the actual measurements finding satisfactory agreement for the statistics. The timeseries of a large wave produced by the Creamer transform was found to have a steeper and higher crest, and shallower troughs compared to its linear correspondant. Forristall (2002) also applied the Creamer transform to calculate bound waves and compared it with second order theory solution, finding that the former offers superior results and it has good potential for engineering applications. However, the limitations of the method are that the linear spectrum should be known and the timescales should be short, so that, during the transition from space to time, the underlying spectrum is not altered due to resonant interactions, as discussed above. The Creamer transform was also applied in the study of Prevosto and Bouffandeau (2002), who used linear Monte Carlo-type simulations based on a hindcast spectrum to reproduce the sea state in Draupner platform when the "New Year Wave" was measured. The idea was to induce nonlinearity locally by means of second order theory and Creamer transform at single large linear events and to examine if their crest height can reach that of the "New Year Wave" and ultimately find its exceedance probability. The Creamer transform gave a ten-time higher exceedance probability than second order theory, demonstrating that it induces higher than second order nonlinearity and in some cases it could also capture well the overall shape of the "New Year Wave". The results of Prevosto and Bouffandeau (2002) support that the Creamer transform is a good candidate for realistic ocean applications, which involve the effects of finite depth and directionality. That study reported that the

performance of the Creamer transform is similar to Stokes 5^{th} order waves.

Apart from deriving statistics, the Creamer transform was also used by Slunyaev et al. (2013)[9] to reproduce the single extreme wave events measured in the field. Under the assumption of unidirectional propagation and that the recorded waves were linearised using an iterative approach. Exact second order theory, NLSE to 2^{nd} and 3^{rd} order (considering a narrowbanded spectrum[10]) and Creamer transform were applied on the linearised spectrum. The results demonstrated that the Creamer transform resembles better the recorded spectrum by predicting a longer spectral tail than the other models. On the other hand, the results concerning the reconstructed kinematics indicate that the highest horizontal velocities are predicted by the 3^{rd} order NLSE. Fully nonlinear models (HOS and Dysthe (Dysthe, 1979)) were also applied without being able to capture the crest height of the recorded extreme wave, possibly due to the underlying assumptions. Nevertheless, it was claimed that Creamer transform can describe Stokes waves up to 4^{th} order[11]. In the paper of Slunyaev et al. (2013), the space-time transformation required to obtain the timeseries for the Creamer function is also described, by transforming the $f-$spectrum to $\kappa-$spectrum and assuming deep water conditions. Here, the transformation is expanded to finite depth by using the full linear dispersion relation and the transformation is not necessary because the linear spaceseries are known.

5.4.2 Results

In this section, the application of the Creamer transform is performed for the groups of different steepness and the original and evolved free-wave spectra.

First, an example of the application of the Creamer transform is presented in Figure

[9]The work of Slunyaev et al. (2013) is practically an extension of that of Slunyaev et al. (2011) and in the main text only the former reference is used.

[10]Although commonly applied in the literature, NLSE was not used in the present study because it assumes a narrowbanded spectrum. Also, as mentioned by Slunyaev et al. (2013), realistic extreme waves are strongly nonlinear and have a broad spectrum.

[11]There seems not to be a consensus regarding the order of Stokes waves that Creamer transform can capture among the cited studies.

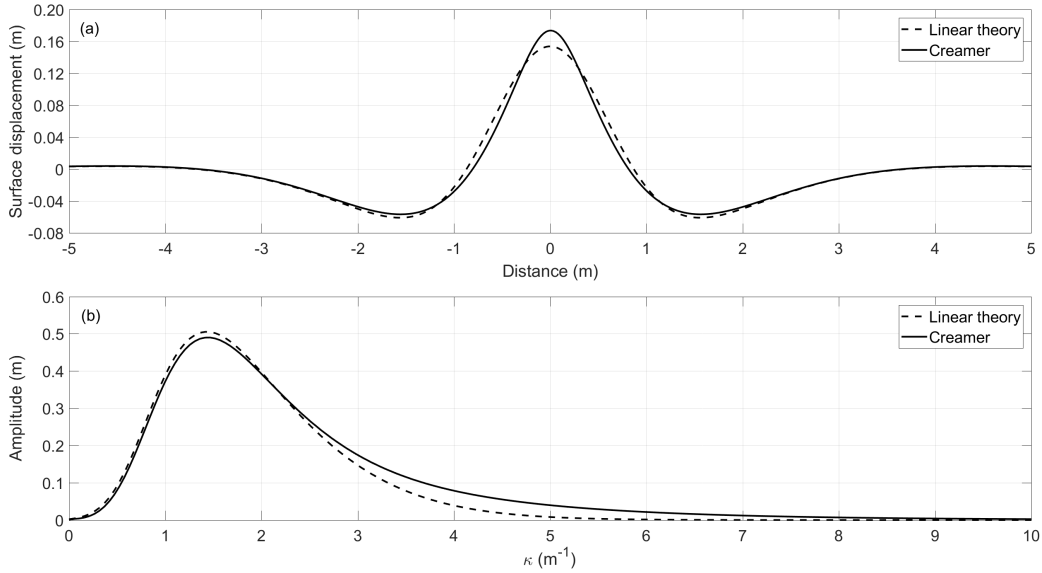

Figure 5.23: Comparison of the spatial profiles (a) and the amplitude $\kappa-$spectra (b) for the strongly nonlinear group ($\Sigma\alpha_i = 0.154$ m) between linear theory and Creamer transform using the original spectrum.

5.23 for the strongly nonlinear group, which exhibits the highest nonlinearity, allowing for better visualisation of the effects of the transformation. Figure 5.23a shows that the spatial profile of the wave becomes narrower and the maximum crest elevation is increased from 0.1540 m to 0.1737 m, corresponding to an increase of 12.8%. The troughs become shallower as well. Moreover, the original amplitude spectrum is seen to have a lower peak after the transform and significant energy transfer to higher wavenumbers, as seen in Figure 5.23b. These results constitute clear indications of good qualitative description of the effects of nonlinearity achieved by the Creamer transform. The spatial profiles of the water surface for the other wave groups are presented in Section 5.5 against the results of the Krasitskii transform.

For the remaining of the section, the results of the timeseries are presented, using the sampling technique at different time instances at the focal location $x =$PF. The results in Figure 5.24[12] for the strongly nonlinear group show that the selection of the underlying free-wave spectrum has considerable impacts on the wave profile produced by

[12]Notice in the subplot the lower time resolution for the Creamer transform result, which is sampled from the spaceseries every $Dt =$0.05 s.

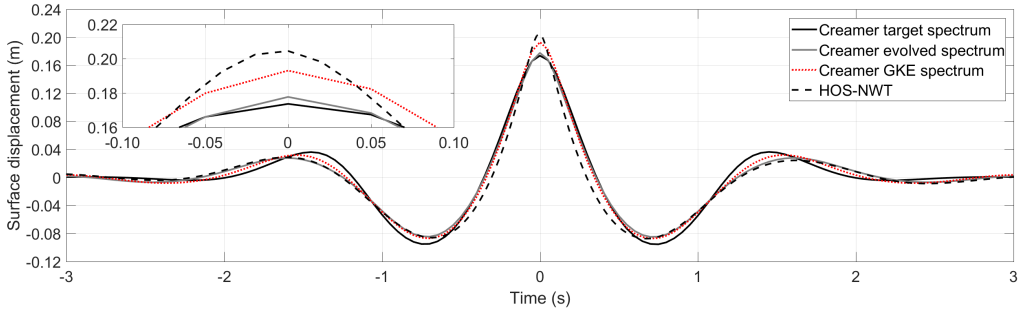

Figure 5.24: Comparison of the timeseries of surface displacement for the strongly nonlinear group ($\Sigma\alpha_i = 0.154$ m) produced by the Creamer transform using the original and evolved spectra.

the Creamer transform mainly at the lateral troughs and crests. The former become shallower and the latter wider and lower when the evolved spectra are used and they show very good agreement with the profile of the nonlinear simulation of HOS-NWT. Nonetheless, none of the different free-wave spectra produces a sufficiently narrow crest to match that of the fully nonlinear solution. Regarding the crest elevation, the Creamer transform, combined either with the original or the evolved spectra, underestimates the measured elevation. The use of the original spectrum results in the lowest crest elevation of 0.1737 m; the use of the evolved spectrum from HOS (gray line) marginally increases the elevation to 0.1777 m; and the spectrum of GKE predicts it at 0.1931 m. This behaviour is consistent with the findings of the other approaches, namely the second order and the fifth order expansion, indicating qualitatively good performance of the Creamer transform for a nearly breaking wave group.

Comparing Figure 5.24 with Figure 5.23a, it is interesting to notice some difference between the spatial and the temporal profile of the wave group. The spatial profile at $t = 0$ s has considerably shallower troughs than the time history of the surface elevation at $x =$PF. Also, the spatial profile does not have lateral crests. Similar observations were made by Tromans in the original paper of the NewWave theory (see Figure 4 in (Tromans et al., 1991)), who mentions that the spatial profiles of the wave decay faster from the main crest than the temporal profiles as a result of the dispersive nature of water waves.

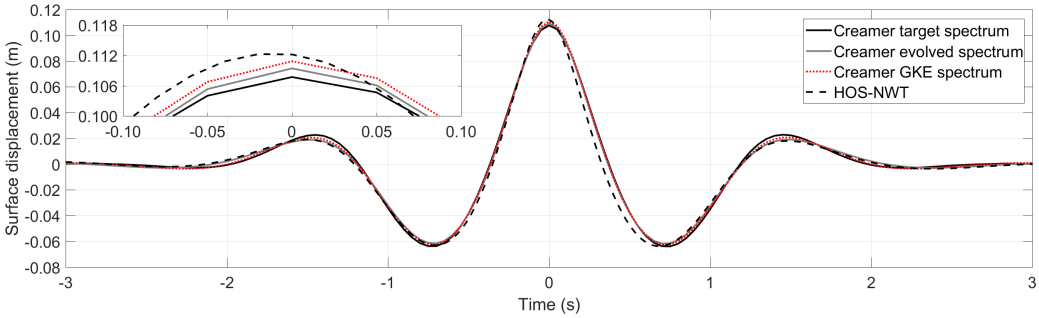

Figure 5.25: Comparison of the timeseries of surface displacement for the weakly nonlinear group ($\Sigma\alpha_i = 0.100$ m) produced by the Creamer transform using the original and evolved spectra.

The results for the weakly nonlinear and quasi-linear group are presented in Figures 5.25 and 5.26, respectively. With decreasing steepness of the group, the evolved spectra are more similar to the original and the differences among them vanish. For both the wave groups, the original and evolved HOS spectra underestimate the crest elevation. The exception is the spectrum of GKE for the quasi-linear group which marginally overpredicts the crest elevation. Consistently, the original spectrum gives a result farther from the fully nonlinear solution compared to the evolved spectra.

In quantitative terms, for the weakly nonlinear group, a crest elevation of 0.1077 m, 0.1094 m and 0.1108 m is predicted by the Creamer transform, for the original, HOS evolved and GKE evolved spectra, respectively. This shows a considerable improvement over linear theory prediction (0.100 m), but a noticeable deviation from the fully nonlinear results (0.1123 m). On the other hand, the different spectra of the quasi-linear group have only submillimetre deviations, with the original, HOS evolved and GKE evolved spectra predicting a maximum crest elevation of 0.05179 m, 0.05201 m, and 0.05233 m, respectively. Nevertheless, these still constitute a non-negligible improvement from the linear solution of 0.050 m to the fully nonlinear of 0.05219 m.

The comparisons between the results of the Creamer transform and the HOS-NWT fully nonlinear solution presented in this section demonstrate that the Creamer transform can predict the nonlinearities to a good extent, especially when the evolved free-wave spectrum is used, despite the aforementioned depth-related limitation of the for-

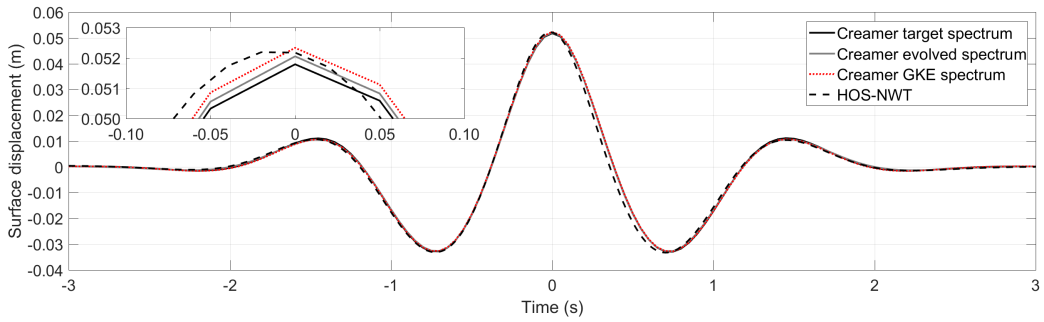

Figure 5.26: Comparison of the timeseries of surface displacement for the quasi-linear group ($\Sigma\alpha_i = 0.050$ m) produced by the Creamer transform using the original and evolved spectra.

mula used. Its performance compared to the other methods for calculating the bound waves is presented in Section 5.6.

5.4.3 Conclusions

The Creamer transform was examined in this section and its results were compared with fully nonlinear simulation for wave groups up to breaking limit. The results showed that this "surprising equation", as characterised by Forristall (2002), has appreciable performance for the focused wave groups of the present study. At the same time, it shows very good potential for practical applications thanks to its computational efficiency.

The main limitation of the Creamer transform is that it is formulated for calculating the spatial characteristics of the wave field and its application in time is hindered by linear theory. Nevertheless, if combined with a method that can predict evolution of the free-wave spectrum, the Creamer transform can become a very useful tool. The present study makes a step towards this direction.

At its present form, the Creamer transform, if applied strictly spatially, can still offer very important information of engineering interest, such as spatial kinematics and wave profiles that are relevant for large marine structure of the order of the wavelength. At the same time, it can be a useful method to linearize field measurements for further

applications with other modelling tools, as done in (Slunyaev et al., 2013), and to derive improved statistics for more accurate design of the marine structures (Prevosto and Bouffandeau, 2002). Future work should also examine the finite depth version of the Creamer transform formula.

5.5 Static Krasitskii

In this section, a method for calculating the bound waves of a known free-wave spectrum in $\kappa-$space based on the Hamiltonian description of surface waves is discussed. This method is similar to the Creamer transform, presented in the previous section, but the canonical transformation of the flow variables is different and thus, it results to different expressions of the Hamiltonian[13]. The derivation of the Hamiltonian was presented by Krasitskii (1994) and its coefficients were already employed in the GKE in Section 4.3. It is noted again that, the GKE was based on the "naive" assumption that the free waves in the real and transformed space are the same.

Building on that assumption, the idea of calculating the bound waves of the real space by the integral combinations of the free waves in the transformed space was coined. For the GKE, the coefficients of four-wave interactions were used in order to find the evolution of the spectrum in time, considering the resonant interactions between the waves in the transformed space. However, here, it is assumed that the spectra of the free waves before or after the time evolution are known and the bound waves are calculated using the coefficients of Krasitskii (1994). For this reason and to distinguish it from the time evolving KE, hereafter this method is referred to as "static Krasitskii".

[13]Acknowledgement: The author would like to thank M. Prevosto for suggesting the connection between the two methods and contributed to the derivation.

5.5.1 Mathematical formulation

Introduction

Before the mathematical derivation of the static Krasitskii method is presented, general information regarding the Hamiltonian representation of water gravity waves is discussed. For more details, the reader is directed to (Krasitskii, 1994) and references therein. Also, since the Creamer transform is also based on the Hamiltonian representation of free surface waves, relevant aspects and considerations were already discussed in Section 5.4.

The first description of the free surface waves in a Hamiltonian form was given by Zakharov (1968), which puts water waves in context with the general physical problem of nonlinear dispersive waves in continuous conservative media. In the case of ocean waves, the medium is water and the dispersion properties are defined by the linear dispersion relation. The previous generalization induces several advantages in the consideration of the problem, because the specific features of the medium are irrelevant and simple expressions of the perturbation expansions can be applied. In the core of the Hamiltonian expression is an integro-differential evolution equation of the complex wave amplitude, which is the Fourier transformation of the flow variables. For convenience in the derivation, the complex wave amplitude is transformed to an auxiliary variable. This process results to the reduced Hamiltonian equations, which are the well known ZE, and are the basis for the KE of wave evolution.

However, despite the fact that the flow equations for water waves are conservative, the reduced Hamiltonian equations are not, which results in a non-energy-conservative non-Hamiltonian system of equations. This issue has troubled researchers, who suggested that this may be due to the errors induced by considering only up to certain orders in the perturbation expansion. In reality, this inconsistency was proven to be a shortcoming of the derivation techniques used in ZE that do not guarantee symmetry conditions of the coefficients. This motivated Krasitskii to propose a new derivation of

the Hamiltonian that uses canonical transformations between the complex wave amplitude and the auxiliary variable, which results in a conservative system of equations (Krasitskii, 1994). The complex wave amplitude can then be expressed as integral power series of the auxiliary variable through a process that eliminates the unimportant non-resonant second, third and fourth order nonlinear terms from the Hamiltonian in the transformed space, where only free waves exist, and calculates only the modified resonant interactions (see Table 5.1). Provided that the kernels of the coefficients are symmetric, which is facilitated by the Hamiltonian expression of the problem, this process should lead to the same results as the original equations of hydrodynamics. In (Krasitskii, 1994), the Hamiltonian expression was presented up to fifth order ($H^{(5)}$), which corresponds to five-wave interactions. In the present study though, only up to four-wave interactions are included.

The canonical transformations

The description of the mathematical derivation of the Krasistkii formulation will start from the basic expressions of the flow variables, i.e., the vertical displacement of the free surface $\zeta(\mathbf{x},t)$ and the velocity potential $\psi(\mathbf{x},t)$ at the free surface, which are essential later on, because new canonical transformations will be considered for the specific problem of focused waves. Hereafter, in order to be consistent with the nomenclature in the rest of the thesis, $\zeta(\mathbf{x},t)$ is denoted as $\eta(\mathbf{x},t)$ and $\psi(\mathbf{x},t)$ as $\phi_s(\mathbf{x},t)$.

The classic assumptions for the fluid are considered: the flow is inviscid and irrotational; the velocity potential satisfies the Laplace equation ($\nabla^2\phi + \partial^2\phi/\partial z^2 = 0$) everywhere in the domain, following potential theory; appropriate boundary conditions are applied for an impermeable bottom; the kinematic and dynamic boundary conditions at the free surface are automatically satisfied by the construction of the Hamiltonian. As mentioned in Section 5.4.1, the Hamiltonian comprises the total energy (kinetic and potential) energy of the fluid, which is normalized here by the fluid density. The effects of surface tension are considered negligible, thus γ in the formulae of Krasitskii (1994)

is zero, and the waves propagate under the gravitational acceleration g. The Hamiltonian expression of the wave motion in space x and time t can be expressed by a pair of PDEs (Equations 5.18), which refer to the ZE (Zakharov, 1968). The procedure that follows is described in section 2 of (Krasitskii, 1994). Similar derivation of the canonical transformation can be also found in (Tanaka, 2001) and (Katsardi and Swan, 2011).

$$\frac{\partial \eta(\mathbf{x},t)}{\partial t} = \frac{\delta H}{\delta \phi_s(\mathbf{x},t)}, \quad \frac{\partial \phi_s(\mathbf{x},t)}{\partial t} = -\frac{\delta H}{\delta \eta(\mathbf{x},t)} \tag{5.18}$$

For finding the evolved spectrum or the bounded waves, the canonically conjugate variable $\eta(\mathbf{x},t)$ and $\phi_s(\mathbf{x},t)$ should be expressed in the Fourier space, according to Equations 5.19.

$$\hat{\eta}(\mathbf{x}) = \frac{1}{2\pi}\int \eta(\mathbf{k}) e^{i\mathbf{k}\cdot x} d\mathbf{k}, \quad \eta(\mathbf{k}) = \eta^*(-\mathbf{k}) \tag{5.19a}$$

$$\hat{\phi}_s(\mathbf{x}) = \frac{1}{2\pi}\int \phi_s(\mathbf{k}) e^{i\mathbf{k}\cdot x} d\mathbf{k}, \quad \psi(\mathbf{k}) = \psi^*(-\mathbf{k}) \tag{5.19b}$$

where $\mathbf{k} = (k_x, k_y)$ is the horizontal wavenumber vector, which is defined for both positive and the symmetric negative wavenumbers and $\mathbf{x}$ the location vector. t has been excluded for simplicity of the notation and the asterisks denote complex conjugates. The Fourier representation of the variables, which refers to amplitude spectra in $\kappa-$space, should not be confused with the variables in the physical space. The previous Fourier transformations can be simplified by considering unidirectional propagation with $\mathbf{k} = k_x = k$. The fraction $1/(2\pi)$ depends on the definition of the Fourier transform and for the unidirectional propagation, it can be $1/\sqrt{2\pi}$. For the remainder of the section, the variables are simply notated as $\eta(x)$ and $\phi_s(x)$, according to the unidirectional consideration.

Since the Fourier transformation is canonical, Equations 5.18 can be rewritten for the Fourier variables into the form of the canonical transformation of Equations 5.20, which

allow for the Hamiltonian to be a function of the variables in $\kappa-$space.

$$\frac{\partial \eta(k)}{\partial t} = \frac{\delta H}{\delta \phi_s^*(k)}, \quad \frac{\partial \phi_s(k)}{\partial t} = -\frac{\delta H}{\delta \eta^*(k)} \tag{5.20}$$

The pair of the canonical Equations 5.20 can be merged into one by considering a new pair of canonically conjugate variables $\alpha(k)$ and $i\alpha^*(k)$ which satisfy the following relations in Equation 5.21.

$$\eta(k) = M(k)[\alpha(k) + \alpha^*(-k)], \quad \phi_s(k) = -iN(k)[\alpha(k) - \alpha^*(-k)] \tag{5.21}$$

with

$$M(k) = \sqrt{\frac{q(k)}{2\omega(k)}}, \quad N(k) = \sqrt{\frac{\omega(k)}{2q(k)}} \tag{5.22}$$

According to the linear dispersion relation, $\omega = \sqrt{q(k)}$ and $q(k) = |k|tanh(|k|d)$, after considering zero surface tension ($\gamma = 0$).

The canonical transformation above allows for the transition of the initial variables $\eta(k)$ and $\phi_s(k)$ to the variable $\alpha(k)$ and merging of the two corresponding equations into one, as shown in Equation 5.23. As such, the Hamiltonian $H = H(\alpha, \alpha^*)$ becomes a function of $\alpha(k)$. This process facilitates the expression of the Hamiltonian into integral power series of variables, which for brevity are not given here. This is possible under the assumption of weakly nonlinear waves, i.e., waves of small amplitudes, and small steepness. The expansion can be truncated to the desired order, which in the original work of Krasitskii (1994) is regarded to fifth order, while in the present study only the terms up to and including fourth order are retained.

$$i\frac{\partial \alpha(\mathbf{k})}{\partial t} = \frac{\delta H}{\delta \alpha^*(\mathbf{k})} \tag{5.23}$$

To proceed further and simplify the integral power series of the Hamiltonian (Equations

2.11 and 2.13 in (Krasitskii, 1994)), an auxiliary new variable $b(k)$ is considered, which is connected with the Hamiltonian in a similar way as the variable $\alpha(k)$ in Equation 5.23, as seen in Equation 5.24. The gaining in introducing this new variable is that it allows for suppressing the non-resonant terms in the expression of the Hamiltonian and connecting $\alpha(k) \rightarrow b(k)$. This transformation must be canonical, implying that some canonicity conditions should be valid, which in (Krasitskii, 1994) refer to the Poisson brackets (Equation 2.15 - 2.16)[14].

$$i\frac{\partial b(k)}{\partial t} = \frac{\delta \tilde{H}}{\delta b^*(k)} \tag{5.24}$$

where $\tilde{H} = \tilde{H}(b, b^*)$ is the Hamiltonian $H = H(\alpha, \alpha^*)$ after considering the transformation $\alpha = \alpha(b, b^*)$.

To summarize, until now, the solution process of Krasitskii was followed almost step by step. This process aimed to transform the physical variables $\eta(x), \phi_s(x)$ to Fourier variables $\hat{\eta}(k), \hat{\phi}_s(k)$, which were expressed in Hamiltonian form, and after the canonical transformations, the Hamiltonian equations were reduced to expressions of the simple variables $\alpha(k)$ and $b(k)$.

To continue further and solve the present problem, a canonical transformation for $\alpha(k)$ to $b(k)$ should be considered that will allow for solving the final Equation 5.39 (Not presented in (Krasitskii, 1994)). It is repeated that $\eta(k)$ is the original amplitude spectrum in real space and $\alpha(k)$ is its transform. Since the real spectrum contains both free and bound waves, $\alpha(k)$ also does so. For this reason it is useful to associate it with the $b(k)$ spectrum that consists only of free waves in the transformed space. As mentioned, the assumption that the free waves in the real and transformed space are the same is considered ($\alpha_f(k) \equiv b(k)$), where $\alpha_f(k)$ corresponds only to the free waves of the $\alpha(k)$ spectrum, with the bound waves given by Equation 5.39. Thus, the only issue is now to define a canonical transformation for $\alpha(k)$.

[14] See also (Creamer et al., 1989) Equation 3.6.

Since only the free waves of the real space are considered ($\alpha_f(k)$), they should satisfy the expressions of the velocity potential and surface elevation of linear theory (Dean and Dalrymple, 1991). For simplicity, in the derivation that follows, the phase difference between the waves is considered zero ($\omega t + \theta = 0$), corresponding to a focused wave group, as shown in Equations 5.25 and 5.26 for the free surface elevation and velocity potential at the free surface respectively.

$$\eta(x) = \alpha_f(k)\cos(kx) \tag{5.25}$$

$$\phi_s(x) = \frac{\omega\alpha_f(k)}{k}\frac{\cosh(k(\eta+d))}{\sinh(kd)}\sin(kx) \tag{5.26}$$

where d is the water depth. Note that the focused wave is produced as a summation of every wave components of the Equations 5.25 and 5.26, and for convenience in the derivation, these formulae for a single wave component will be used without loss of generality. This consideration is also very convenient because it allows for simplifying the initial complex amplitude spectrum ($\eta(k)$), which consists of a real (η_R) and an imaginary (η_I) part, to a more compact form in the Fourier space, since $\theta(k) = 0$, as seen in Equation 5.27.

$$\begin{aligned} &\eta(k) = \eta_R(k) + i\eta_I(k) = |\eta(k)|e^{i\theta(k)} \\ &\therefore \quad \text{for} \quad \theta(k) = 0 \Rightarrow \eta(k) = |\eta(k)| \end{aligned} \tag{5.27}$$

In order to apply the canonical transformation for the variable $\alpha_f(k)$, Equations 5.25 and 5.26 should be expressed in Fourier space. For this, some basic formulae of the Fourier transforms ($\hat{F}$) of the trigonometric functions are employed (Bracewell, 1999).

The Fourier transform of the $\cos(kx)$ for the calculation of the surface elevation (Equation 5.25) is:

$$\begin{aligned}\hat{F}[1\cdot\cos(k_0x)](k) &= \int e^{-ikx}\left(\frac{e^{ik_0x}+e^{-ik_0x}}{2}\right)dx \\ &= \frac{1}{2}\int\left[e^{-i(k-k_0)x}+e^{-i(k+k_0)x}\right]dx \\ &= \frac{1}{2}\left[\delta(k-k_0)+\delta(k+k_0)\right]\end{aligned} \tag{5.28}$$

For discrete wavenumbers, the δ function can be only 1 when $k = k_0$ and 0 otherwise. Thus, the Fourier transform of $\eta(x)$ is simplified to the Equation 5.28:

$$\hat{F}[\eta(x)](k) = \eta(k) = \frac{\alpha_f(k)}{2} \tag{5.29}$$

The Fourier transform of the $\sin(kx)$ for the calculation of the velocity potential at the free surface (Equation 5.26) is:

$$\begin{aligned}\hat{F}[1\cdot\sin(kx)](k) &= \int e^{-ikx}\left(\frac{e^{ik_0x}-e^{-ik_0x}}{2i}\right)dx \\ &= \frac{1}{2}\int\left[-e^{-i(k-k_0)x}+e^{-i(k+k_0)x}\right]dx \\ &= \frac{1}{2}i\left[\delta(k+k_0)-\delta(k-k_0)\right]\end{aligned} \tag{5.30}$$

Note that the arguments of the $\cosh$ and $\sinh$ functions in Equation 5.26 can be simplified by considering that $\eta << d \Rightarrow \eta + d \simeq d$, which is valid for low amplitude linear waves in not very shallow water. Also, since the fraction $R_i = \frac{\cosh(kd)}{\sinh(kd)}$ is independent of x, it can be taken out of the integral of the Fourier transform as constant. Indeed, for a given water depth and wavenumber, R_i is constant and for the special case of infinite water depth, where $d/L > 1/2 \rightarrow kd > \pi$, $R_i = 1$. In the present study, R_i is used in the general form, but the canonical transformation is also given for the infinite water depth case.

Based on the previous considerations and the possible results of the δ functions in

Equation 5.30, the Fourier transform of $\phi_s(x)$ can be expressed by Equation 5.31[15].

$$\hat{F}[\phi_s(x)](k) = \phi_s(k) = -\frac{1}{2} i \frac{\alpha_f(k)\omega(k)}{k} R_i(k) \tag{5.31}$$

Next, the auxiliary variable $b(k)$ and its complex conjugate $b^*(k)$ are used in the canonical transformation of Equation 5.21 to substitute $\alpha(k)$ and $\alpha^*(k)$ (which more precisely refer to $\alpha_f(k)$ and $\alpha_f^*(k)$), respectively, resulting to Equations 5.32 and 5.33.

$$\frac{\eta(k)}{M(k)} = b(k) + b^*(-k) \tag{5.32}$$

$$i\frac{\phi_s(k)}{N(k)} = b(k) - b^*(-k) \tag{5.33}$$

Adding and subtracting the system Equations 5.32 and 5.33 by terms returns Equation 5.34 and 5.35, respectively.

$$\frac{\eta(k)}{M(k)} + i\frac{\phi_s(k)}{N(k)} = 2b(k) \tag{5.34}$$

$$\frac{\eta(k)}{M(k)} - i\frac{\phi_s(k)}{N(k)} = 2b^*(-k) \tag{5.35}$$

To find the relationship between $\alpha_f(k)$ and $b(k)$, $\eta(k)$ and $\phi_s(k)$ should be replaced in Equations 5.34 and 5.35 by their expressions in Equations 5.29 and 5.31, while $M(k)$ and $N(k)$ can be replaced by their expressions in Equation 5.22.

As such, using Equation 5.34 the relation of $b(k)$ and $\alpha(k)$ is obtained (Equation 5.36), which for infinite water depth, where $R_i(k) = 1$ and $q(k) = |k|$, reduces to the simplified Equation 5.37.

[15]The sign of the equation above is "-" for $k = k_0$ and "+" for $k = -k_0$. However, the equation is simplified by considering k with nonzero amplitude in the positive $\kappa-$plane only.

$$b(k) = \frac{\alpha_f(k)}{4}\left[\sqrt{\frac{2\omega(k)}{q(k)}} + \frac{R_i(k)}{k}\sqrt{2|\omega(k)|q(k)}\right] \tag{5.36}$$

$$b(k) = \frac{\alpha_f(k)}{2}\sqrt{\frac{2|\omega(k)|}{|k|}} \tag{5.37}$$

Moreover, doing the same substitutions in Equation 5.35 gives the expression of $b^*(k)$, as presented in Equation 5.38.

$$\begin{gathered} b^*(-k) = \frac{\alpha_f(k)}{4}\left[\sqrt{\frac{2\omega(k)}{q(k)}} - \frac{R_i(k)}{k}\sqrt{2|\omega(k)|q(k)}\right] \\ \text{expressed for } k \\ b^*(k) = \frac{\alpha_f(k)}{4}\left[\sqrt{\frac{2\omega(k)}{q(k)}} + \frac{R_i(k)}{k}\sqrt{2|\omega(k)|q(k)}\right] \end{gathered} \tag{5.38}$$

Comparing Equations 5.36 and 5.38, shows that the complex number $b(k)$ is equal to its complex conjugate $b^*(k)$, and thus its imaginary part is zero. This means that the phase of the waves is zero and this serves as a proof for the derivation of the special case of focused waves considered in this section (see Equation 5.27).

To conclude, this process of the canonical transformations relates the auxiliary variable $b(k)$ to the transformed spectrum of the free waves $\alpha_f(k)$ through Equation 5.36. $\alpha_f(k)$ is associated with the spectrum of the free waves of the real space ($\eta(k)$) via Equation 5.29. Therefore, when knowing the spectrum of the free waves in the real space, the aforementioned relations can be used to transform the variables in the space where the bound waves can be calculated. Then using the inverse process, the spectrum of the free + bound waves in the real space can be retrieved.

In the remainder of the section, the calculation of the bound waves from the transformed world is presented.

Calculation of the bound waves

The canonical transformations of the previous paragraphs resulted in the transition from the real space, where the free waves $\alpha_f(k)$ and their bound waves comprise the full spectrum $\alpha(k)$, to a transformed space, where there are only the free waves $b(k)$, under the assumption that $\alpha_f(k) \equiv b(k)$. Combinations of the free waves in the transformed space give raise to bound waves in real space through the canonical relations. Similarly to the Hamiltonian, the canonical transformations $\alpha(k) \rightarrow b(k)$ can be expressed in integral power series, which in (Krasitskii, 1994) is given up to fifth order in Equation 2.17. Here, the fifth order terms are discarder from Krasitskii's formula for simplicity, as seen in Equation 5.39. Note that the notation of the wavenumbers has been altered to correspond to the GKE of Chapter 4. Including the fifth order terms adds another five integrals with new coefficients in Equation 5.39 and induces considerable complication and computational cost.

$$\begin{aligned}\alpha_1 = b_1 &+ \int A^{(1)}_{1,2,3} b_2 b_3 \delta_{1-2-3}\, dk_{23} + \int A^{(2)}_{1,2,3} b_2^* b_3 \delta_{1+2-3}\, dk_{23} \\ &+ \int A^{(3)}_{1,2,3} b_2^* b_3^* \delta_{1+2+3}\, dk_{23} + \int B^{(1)}_{1,2,3,4} b_2 b_3 b_4 \delta_{1-2-3-4}\, dk_{234} \\ &+ \int B^{(2)}_{1,2,3,4} b_2^* b_3 b_4 \delta_{1+2-3-4}\, dk_{234} + \int B^{(3)}_{1,2,3,4} b_2^* b_3^* b_4 \delta_{1+2+3-4}\, dk_{234} \\ &+ \int B^{(4)}_{1,2,3,4} b_2^* b_3^* b_4^* \delta_{1+2+3+4}\, dk_{234}\end{aligned} \tag{5.39}$$

where δ is the Kronecker delta, with the notation

$$\delta_{1-2-3} = \begin{cases} 1 \text{ when } k_1 - k_2 - k_3 = 0 \\ 0 \text{ otherwise} \end{cases} \quad \text{and} \quad \delta_{1-2-3-4} = \begin{cases} 1 \text{ when } k_1 - k_2 - k_3 - k_4 = 0 \\ 0 \text{ otherwise} \end{cases}$$

As already discussed (see Table 5.1), the Krasitskii transformation to fourth order, as considered here, excludes all the non-resonant wave-wave interactions in the transformed space, which are "hidden" in the transformation. When expanding to integral power series, these interactions are expressed through the integrals and result in non-

resonant interactions (bound waves) in the real world. As such, the first three integrals in Equation 5.39 that include the A coefficients correspond to the second order bound waves, while the remaining four integrals that include the B coefficients refer to the third order bound waves.

The calculation of the coefficients in Equation 5.39 is done for the every possible quadruplet of the waves and their values are stored. To save computational time (up to 50-100 times), the values of the coefficients are calculated only for the corresponding non-negative δ functions. Similarly, the integrals in Equation 5.39 are calculated also for every possible combination of wavenumbers in four nested programming loops. The final values of integrals are the summations of the integrals for every set of wavenumbers.

Special care is taken for the singularities when the denominator of $b(k)$ or the coefficients becomes zero. For the former, this is taken into account by excluding the zero value from the $\kappa-$space, as discussed in Section 5.5.2. For the latter, the coefficient A or B are set to zero when the corresponding δ function is zero, e.g., if $\omega_1 - \omega_2 - \omega_3 = 0 \Rightarrow A^{(1)}_{1,2,3} = 0$.

The expressions of the A and B coefficients are shown in Equations 5.40 and 5.41, respectively, which are taken from the paper of Krasitskii (1994) with appropriate changing of the notation.

$$A^{(1)}_{1,2,3} = -\frac{U^{(1)}_{1,2,3}}{\Delta_{1-2-3}} = -\frac{U^{(1)}_{1,2,3}}{\omega_1 - \omega_2 - \omega_3} \tag{5.40a}$$

$$A^{(2)}_{1,2,3} = -2\frac{U^{(1)}_{3,2,1}}{\Delta_{1+2-3}} = -2\frac{U^{(1)}_{3,2,1}}{\omega_1 + \omega_2 - \omega_3} \tag{5.40b}$$

$$A^{(3)}_{1,2,3} = -\frac{U^{(3)}_{1,2,3}}{\Delta_{1+2+3}} = -\frac{U^{(3)}_{1,2,3}}{\omega_1 + \omega_2 + \omega_3} \tag{5.40c}$$

$$B^{(1)}_{1,2,3,4} = -\frac{Z^{(1)}_{1,2,3,4} + V^{(1)}_{1,2,3,4}}{\Delta_{1-2-3-4}} = -\frac{Z^{(1)}_{1,2,3,4} + V^{(1)}_{1,2,3,4}}{\omega_1 - \omega_2 - \omega_3 - \omega_4} \tag{5.41a}$$

$$B^{(2)}_{1,2,3,4} = -\frac{1}{4}\frac{3Z^{(2)}_{1,2,3,4} - Z^{(2)}_{2,1,3,4}Z^{(2)}_{3,4,1,2} - Z^{(2)}_{4,3,1,2}}{\Delta_{1+2-3-4}} = -\frac{1}{4}\frac{3Z^{(2)}_{1,2,3,4} - Z^{(2)}_{2,1,3,4}Z^{(2)}_{3,4,1,2} - Z^{(2)}_{4,3,1,2}}{\omega_1 + \omega_2 - \omega_3 - \omega_4} \tag{5.41b}$$

$$B^{(3)}_{1,2,3,4} = -\frac{Z^{(3)}_{1,2,3,4} + 3V^{(1)}_{4,3,2,1}}{\Delta_{1+2+3-4}} = -\frac{Z^{(3)}_{1,2,3,4} + 3V^{(1)}_{4,3,2,1}}{\omega_1 + \omega_2 + \omega_3 - \omega_4} \tag{5.41c}$$

$$B^{(4)}_{1,2,3,4} = -\frac{Z^{(4)}_{1,2,3,4} + V^{(4)}_{1,2,3,4}}{\Delta_{1+2+3+4}} = -\frac{Z^{(4)}_{1,2,3,4} + V^{(4)}_{1,2,3,4}}{\omega_1 + \omega_2 + \omega_3 + \omega_4} \tag{5.41d}$$

The coefficients A and B are functions of the coefficients U, Z and V, respectively, which can be calculated from the following relations (found in Section 4 of (Krasitskii, 1994)).

$$U^{(1)}_{1,2,3} = -U_{-1,2,3} - U_{-1,3,2} + U_{2,3,-1} \tag{5.42a}$$

$$U^{(3)}_{1,2,3} = U_{1,2,3} + U_{1,3,2} + U_{2,3,1} \tag{5.42b}$$

where $U_{1,2,3} = -N_1N_2M_2E^{(3)}_{1,2,3}$, with N and M being calculated from the canonical transformation 5.22.

$$V^{(1)}_{1,2,3,4} = \frac{1}{3}(-V_{-1,2,3,4} - V_{-1,3,2,4} - V_{-1,4,2,3} + V_{2,3,-1,4} + V_{2,4,-1,3} + V_{3,4,-1,2}) \tag{5.43a}$$

$$V^{(4)}_{1,2,3,4} = \frac{1}{3}(V_{1,2,3,4} + V_{1,3,2,4} + V_{1,4,2,3} + V_{2,3,1,4} + V_{2,4,1,3} + V_{3,4,1,2}) \tag{5.43b}$$

where $V_{1,2,3,4} = -2N_1N_2M_3M_4E^{(4)}_{1,2,3,4}$.

Note that in the original equations of Krasitskii (1994) for $V^{(1)}_{1,2,3,4}$ and $V^{(4)}_{1,2,3,4}$ include an additional a term $\Gamma_{1,2,3,4}$, which is omitted in Equations 5.43, because it is a product of the surface tension γ, which is zero ($\gamma = 0$) in the present study (see comment for

Equations 5.22).

It is worth mentioning that in (Krasitskii, 1994) the aspect of symmetry of the matrices of the coefficients is emphasized. This is because the coefficients should be symmetrical by their nature, but their calculation does not necessarily guarantee the symmetry. As such, Krasitskii (1994) suggests to impose the symmetry explicitly by equalizing the corresponding elements of the matrices. However, he refers to that for only one condition for the Hamiltonian, namely the $V^{(2)}$ coefficient (for more details see (Krasitskii, 1994) p. 5), which is not used in the calculation up to fourth order presented here. Thus, in the present work, the symmetry condition is not imposed to the other coefficients (U and V), assuming that they satisfy their natural symmetry conditions. Future work should examine in greater depth potential effects of imposed symmetries.

The coefficients of the energy (kinetic and potential) $E^{(3)}_{1,2,3}$ and $E^{(4)}_{1,2,3,4}$ can be calculated from Equations 5.44.

$$E^{(3)}_{1,2,3} = -\frac{1}{2\sqrt{2\pi}}[(k_1 \cdot k_2) + q_1 q_2] \tag{5.44a}$$

$$E^{(4)}_{1,2,3,4} = -\frac{1}{8(2\pi)}[2|k_1|^2 q_2 + 2|k_2|^2 q_1 - q_1 q_2 (q_{1+3} + q_{2+3} + q_{1+4} + q_{2+4})] \tag{5.44b}$$

where $q(k) = |k_i + k_j| \tanh(|k_i + k_j| d)$.

It should be noted that the original equation of $E^{(3)}$ in (Krasitskii, 1994) is derived for directional waves, and consequently its Fourier expression results in a denominator of 2π, because E comes from the integral is calculated for $dk_x\, dk_y$, which according to the Fourier definition gives $\frac{1}{\sqrt{2\pi}} \frac{1}{\sqrt{2\pi}} = \frac{1}{2\pi}$. For the unidirectional case considered here, the integral is defined only for dk_x and thus the denominator is $\frac{1}{\sqrt{2\pi}}$. Similarly for $E^{(4)}$, the original equation has $\frac{1}{(2\pi)^2}$, while here this is $\frac{1}{2\pi}$.

The expressions for Z, needed for the computations of B coefficients, can be found in the Appendix of (Krasitskii, 1994) as functions of the U and A coefficients. After

the appropriate changes in the notation, the Z terms used in the present study are presented here in Equations 5.45.

$$\begin{aligned} Z^{(1)}_{1,2,3,4} = \frac{2}{3}\Big[& U^{(1)}_{1,2,1-2}A^{(1)}_{3+4,3,4} + U^{(1)}_{1,3,1-3}A^{(1)}_{2+4,2,4} + U^{(1)}_{1,4,1-4}A^{(1)}_{2+3,2,3} \\ & + U^{(1)}_{2,1,2-1}A^{(3)}_{3,4,-3-4} + U^{(1)}_{3,1,3-1}A^{(3)}_{2,4,-2-4} + U^{(1)}_{4,1,4-1}A^{(3)}_{2,3,-2-3}\Big] \end{aligned} \tag{5.45a}$$

$$\begin{aligned} Z^{(2)}_{1,2,3,4} = -2\Big[& U^{(1)}_{1,3,1-3}A^{(1)}_{4,2,4-2} + U^{(1)}_{3,1,3-1}A^{(1)}_{2,4,2-4} + U^{(1)}_{1,4,1-4}A^{(1)}_{3,2,3-2} \\ & + U^{(1)}_{4,1,4-1}A^{(1)}_{2,3,2-3} - U^{(1)}_{1+2,1,2}A^{(1)}_{3+4,3,4} - U^{(3)}_{1,2,-1-2}A^{(3)}_{3,4,-3-4}\Big] \end{aligned} \tag{5.45b}$$

$$\begin{aligned} Z^{(3)}_{1,2,3,4} = 2\Big[& U^{(1)}_{4,1,4-1}A^{(1)}_{2+3,2,3} - U^{(1)}_{1+2,1,2}A^{(1)}_{4,3,4-3} - U^{(1)}_{1+3,1,3}A^{(1)}_{4,2,4-2} \\ & - U^{(3)}_{1,2,-1-2}A^{(1)}_{3,4,3-4} - U^{(3)}_{1,3,-1-3}A^{(1)}_{2,4,2-4} + U^{(1)}_{1,4,1-4}A^{(3)}_{2,3,-2-3}\Big] \end{aligned} \tag{5.45c}$$

$$\begin{aligned} Z^{(4)}_{1,2,3,4} = \frac{2}{3}\Big[& U^{(3)}_{1,2,-1-2}A^{(1)}_{3+4,3,4} + U^{(3)}_{1,3,-1-3}A^{(1)}_{2+4,2,4} + U^{(3)}_{1,4,-1-4}A^{(1)}_{2+3,2,3} \\ & + U^{(1)}_{1+2,1,2}A^{(3)}_{3,4,-3-4} + U^{(1)}_{1+3,1,3}A^{(3)}_{2,4,-2-4} + U^{(1)}_{1+4,1,4}A^{(3)}_{2,3,-2-3}\Big] \end{aligned} \tag{5.45d}$$

Finally, all the elements for the calculations for the integrals in Equation 5.39 are known and the transformed spectrum $\alpha(k)$, which includes both free and bound waves, can be calculated. This can be then transformed to the nonlinear spectrum in the real space using the canonical transformation of Equation 5.20. The process of the solution is summarized below, with the arrows referring to the transformations:

The original free-wave spectrum $\eta(k) \rightarrow \alpha_f(k)$, which contains free-waves in the transformed world. $\alpha_f(k) \rightarrow b(k)$, under the consideration that the transformed free wave $b(k) \equiv \alpha_f(k)$. The nonlinear spectrum $\alpha(k)$ is then calculated by the integrals of $b(k)$. Finally, $\alpha(k) \rightarrow \eta_{NL}(x)$, which is the spectrum in the real space, containing both free and bound waves, and corresponds to the desired solution.

5.5.2 Results

In this section, the results of the static Krasitskii method are presented after a brief description of the application of the solution process. Comparisons with the Creamer

transform are also shown for the strongly nonlinear wave group.

An important thing to note is that the surface profile is calculated only in space and not in time. The reason for this is that the calculations for the static Krasitskii method, similarly to the Creamer transform, are performed in the $\kappa-$space and thus, refer to spaceseries. However, in contrast to the Creamer transform, the timeseries for the static Krasitskii are not produced here. There are two main reasons for that: i) The nonlinear amplitude $\kappa-$spectrum cannot be transformed to a $f-$spectrum using Equation 4.26, because this equation assumes linear dispersion. Although for the free-wave part of the spectrum linear theory applies, for the bound waves added by the static Krasitskii method, application of Equation 4.26 would be inconsistent; ii) A method similar to that for producing the timeseries of the Creamer transform by applying the nonlinear transformation at spatial wave profiles some time instances before and after the focal time cannot be applied here because the canonical transformation for the derivation of the static Krasitkii method was performed assuming zero phases of the waves (see Equation 5.27). Thus, using such an approach would result in violation of the method and invalidity of the formulae for $b(k)$. A potential option for producing timeseries with static Krasitskii would be to extend the formula of Equation 4.26 using 2^{nd} and 3^{rd} order dispersion relation and treat the bound harmonics independently for producing a nonlinear $f-$spectrum. However, to the author's best knowledge, such method is not available at present and it can be subject of future work.

Next, the solution process for the static Krasitkii method as applied in the present study is briefly discussed with some considerations regarding the spatial and spectral resolution of the free-wave spectra used.

To begin with, from a known free-wave amplitude spectrum in the $f-$space, such as the original, the extracted evolved from the HOS simulation and the calculated by the GKE, the amplitude spectrum in $\kappa-$space is calculated. This can be done using the transformation of Equation 4.26, which is based on linear theory, or by performing FFT of the spaceseries produced by the application of linear theory (Equation 5.1) on the

amplitude spectrum in $f-$space. This process is described in Section 5.1.2. Here, the latter method is preferred, because the $\kappa-$grid is readily calculated by the FFT, both for positive and negative wavenumbers, and the complex amplitude spectrum is also directly calculated. Moreover, the obtained amplitude spectrum allows for application of the IFFT for reconstructing the wave profile. This method was also described in Section 5.4.1 for the application of the Creamer transform.

An issue when applying the static Krasitskii is the high computational cost for the calculation of the coefficients A and B. For this reason, a relatively coarse resolution is selected, namely $Dx = 0.25$ m and total distance of 20 m, which corresponds to 41 wavenumbers in the positive $\kappa-$space or 82 wavenumbers in the entire $\kappa-$grid that results from the FFT. The low resolution spaceseries that is afterwards produced, can be interpolated with a spline. To confirm the applicability of this method, the present resolution ($Dx = 0.25$ m) is compared with a high resolution signal ($Dx = 0.01$ m), as seen in Figure 5.27. In this figure, the original spaceseries based on linear theory produced by the Gaussian $f-$spectrum is given for high and low spatial resolution (black dashed line and dots, respectively). The signal for the low resolution is then reconstructed using an FFT - IFFT process (red line). Using the amplitude spectrum defined only on the positive $\kappa-$space and linear theory, the signal can also be reconstructed on an $x-$grid with Dx defined by Dk as $Dx = \frac{2\pi}{(N-1)Dk}$, where N is the number of points of $\kappa-$space from the FFT and Dk is the difference between two subsequent wavenumbers in the regular $\kappa-$space resulted from the FFT (green line). It is confirmed that the two latter lines are identical. A spline interpolation method can then be used in order to produce a higher resolution wave profile (gray line), which matches practically perfectly the high resolution signal of linear theory (dashed black line). Thus, the low resolution $\kappa-$spectrum can be used for static Krasitskii without loss of accuracy.

Also, this process demonstrates that the $\kappa-$grid can be constructed based on Dx and the results match those of the IFFT. This is useful, because the free-wave amplitude spectra $\eta(k)$, as used here, are real numbers defined in the positive $\kappa-$space. Thus,

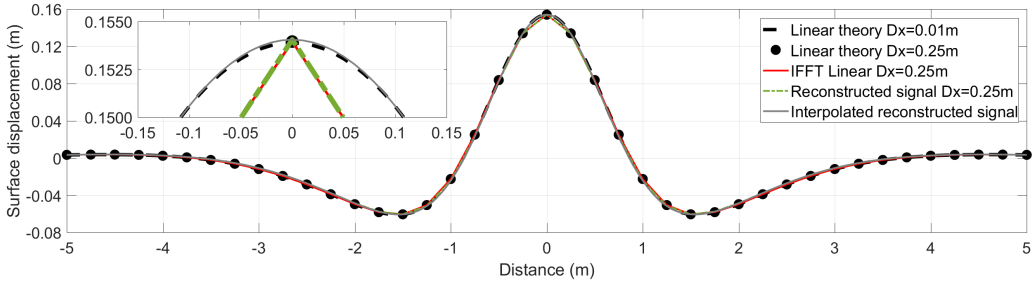

Figure 5.27: Initial spaceseries for the strongly nonlinear group ($\Sigma\alpha_i = 0.154$ m) produced by linear theory and IFFT. Depth=1 m.

also $\alpha_f(k)$ and subsequently $b(k)$ are initially defined for $k \geq 0$. However, since the solution takes place in the entire $\kappa-$plane, $b(k)$ should be extended with zero values in the negative wavenumbers, as seen in Figure 5.28a. As mentioned, for $k = 0$ there is singularity and thus, the new $\kappa-$grid is defined as: $k' = [-k_{max} : \Delta k : -\Delta k, \Delta k : \Delta k : k_{max}]$. Following the calculation of the integrals of Equation 5.39, which takes place in the entire $\kappa-$plane, the resulted nonlinear amplitude spectrum with both free and bound waves, expands in $[-k_{max}, k_{max}]$, as seen in Figure 5.28b. In the same plot, the effect of including nonlinear waves to the spectrum is observed to cause lowering of the peak, energy increase in high wavenumbers and small energy decrease at low wavenumbers. As expected, the inclusion of 3^{rd} order bound waves causes a small, but observable, enhancement of the aforementioned effects. These effects are shown later in greater detail.

As mentioned, an issue for the static Krasitskii method is the computational cost. For the results that follow, the values of $Dx = 0.25$ m and $x_{max} = 20$ m were chosen after preliminary tests, resulting in $Dk = 0.3142$ m^{-1} and $k \in [-12.566, 12.566]$, for either $d = 1$ m or $d = \infty$. Higher resolution than this has a considerable impact on the computational cost. The results for the strongly nonlinear group and the original spectrum are first compared with those of the Creamer transform. To the author's best knowledge such comparison was not performed in the past for the two methods that have common grounds in their derivation, but different expansion in high orders. As noted, the simple integral formula of the Creamer transform used here (Equation 5.17) assumes infinite

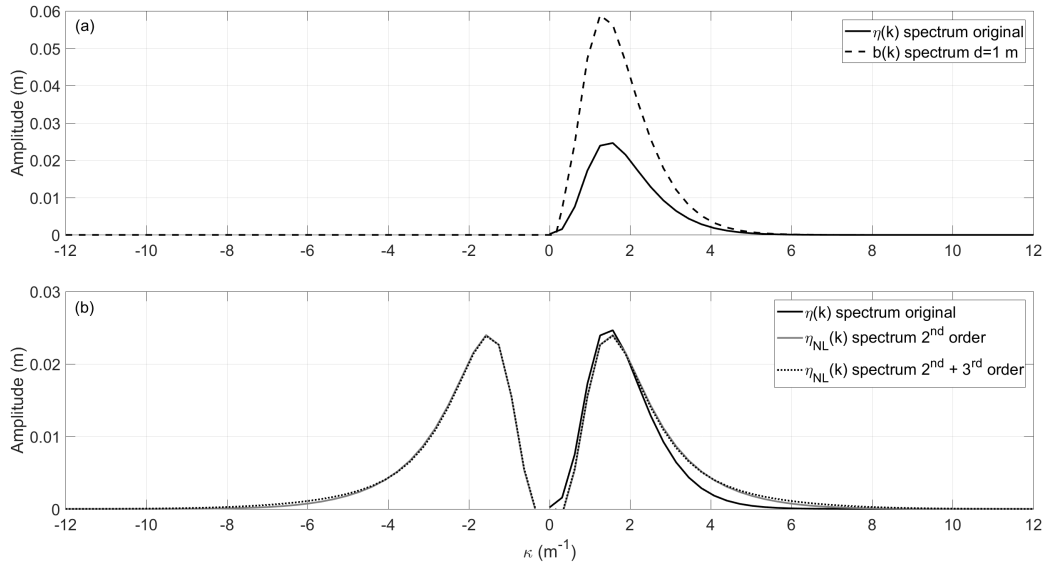

Figure 5.28: Amplitude spectrum and its canonical transformation (a) and comparison of the linear and nonlinear amplitude spectra (b) for the strongly nonlinear group ($\Sigma\alpha_i = 0.154$ m). Depth=1 m.

water depth. For this reason, the comparisons in Figures 5.29 and 5.30 are performed for both $d = 1$ m and $d = \infty$.

Figure 5.29 compares the original and the nonlinear amplitude density spectra produced by the static Krasitskii and Creamer methods. Note that only up to $k = 8$ m^{-1} are plotted for better comparisons. The same spectral resolution of $Dk = 0.3142$ m^{-1} is used for both methods for consistency. Also, the initial spectra are plotted and it is confirmed that they are identical for the two methods, which serves as a check for consistency of the comparisons that follow. First, it can be seen that the nonlinear spectra calculated by both methods are in very good agreement for $d = 1$ m (Figure 5.29a) and in almost excellent agreement for $d = \infty$ (Figure 5.29b). For $d = 1$ m, there are some discrepancies at low wavenumbers $k < 1$ and near $k = 0$, where the static Krasitkii predicts negative amplitudes. However, for the calculation of the spaceseries that follow, these values are set to zero. Moreover, at $k \in (2,4)$ the Creamer transform predicts lower amplitudes. Also note that the upwards line in Figure 5.29b is because the negative $\kappa-$space is considered, but only the positive is plotted. Another important aspect is that the addition of 3^{rd} order bound waves to the 2^{nd} order nonlinear spectra

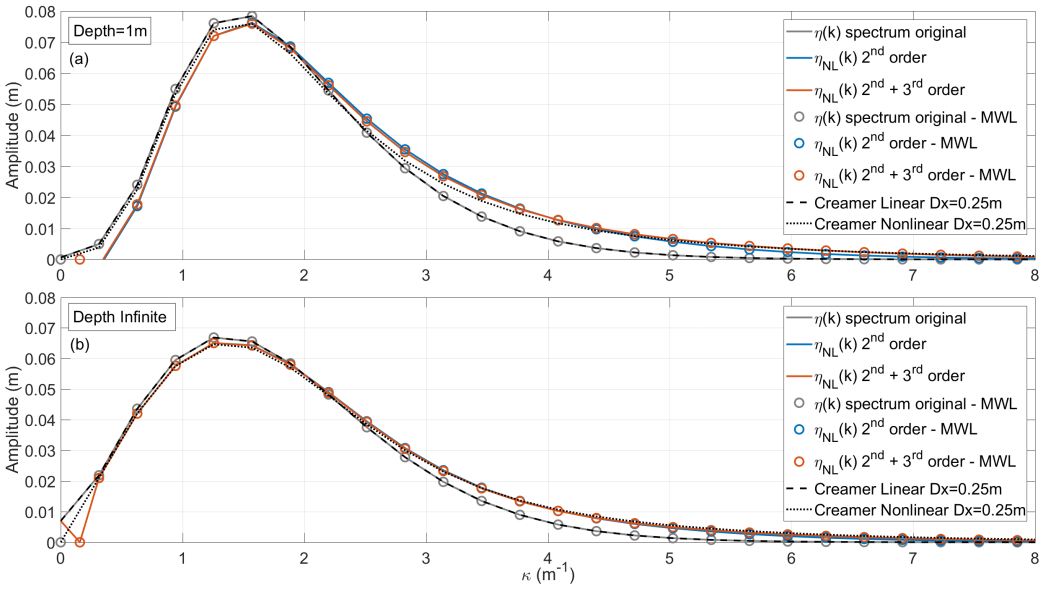

Figure 5.29: Amplitude density spectra of the strongly nonlinear group ($\Sigma\alpha_i = 0.154$ m) considering depth=1 m (a) and infinite depth (b). Comparison between original linear spectrum and nonlinear spectra using the static Krasitskii and Creamer methods.

of static Krasiskii reduces the energy in middle wavenumbers and increases the energy at high wavenumbers, confirming the previous observation of Figure 5.28b.

Figure 5.29 also examines the effect of the MWL. As mentioned, before application of the methods, the MWL should be subtracted (see remarks in Section 5.4.1), but for the present case, where sufficiently long spaceseries are selected and the depth is $d = 1$ m, the impact is negligible. This is confirmed here by Figure 5.29a, where the amplitude density spectrum produced after subtracting the MWL (gray circles) is the same as the linear spectra for static Krasitskii (gray line) and Creamer (black dashed line). Nevertheless, for the case of infinite depth (Figure 5.29b), where the spectrum is shifted to lower wavenumbers, subtracting the MWL results in setting the first value of the spectrum to zero with subsequent consequences in the results. For the spaceseries that follow, which most of the refer to $d = 1$ m, the MWL is not subtracted.

Based on the spectra of Figure 5.29, the corresponding spaceseries are plotted in Figure 5.29. The spline interpolation method is used due to the low space resolution of $Dx = 0.25$ m. In general, both static Krasitkii and Creamer reproduce the expected

effects of nonlinearity when bound waves are added to a linear profile, which refer to steepening of the main crest and increasing its height. For $d = 1$ m (Figure 5.29a), the Creamer transform has a wider main crest than the static Krasitskii method, while for $d = \infty$ (Figure 5.29b), the agreement is almost excellent. The results of the Creamer transform are plotted also for the high resolution used in Section 5.4.2 (black dotted line) and compared with the low resolution interpolated result (thin yellow line). It is seen that the main difference arises at the crest, where the low resolution result underestimates the crest height in comparison with the high resolution result. The crest height produced for the low resolution is very close to that of static Krasitkii of 3^{rd} order. Based on these observations, it is presumed that increasing the resolution for static Krasitkii should result in a higher crest elevation. The difference between 2^{nd} and 3^{rd} order static Krasitkii is more pronounced for $d = 1$ m, as expected, since bound interactions are stronger for finite water depth, and mainly concern the crest elevation.

It is also observed that for infinite depth there is merely visible discrepancy at the crest of the linear harmonics. Since the script for producing this harmonic is identical for both Creamer and Krasitskii methods, the most likely explanation is that the discrepancy is attributed to the discretization of the spectrum and the fact that the first element of the spectrum is disregarded. This is more visible for the spectrum in deep water, because it is shifted to lower wavenumbers and the omission of the first wavenumber, which has non-zero amplitude, has a greater effect compared to the spectrum at $d = 1$ m (see Figure 5.29).

For the wave groups of lower steepness, i.e., $\Sigma\alpha_i = 0.100$ m and $\Sigma\alpha_i = 0.050$ m, similar trends are identified, but the differences between the Creamer and static Krasitskii methods decrease as a consequence of the reduced nonlinearity. For the quasi-linear group, the nonlinear spaceseries are almost the same as the linear spatial harmonics. For brevity, these comparisons are not presented here.

Before presenting the results of the static Krasitskii for the groups of different steepness and the examined free-wave spectra, the linear spaceseries of the strongly nonlinear

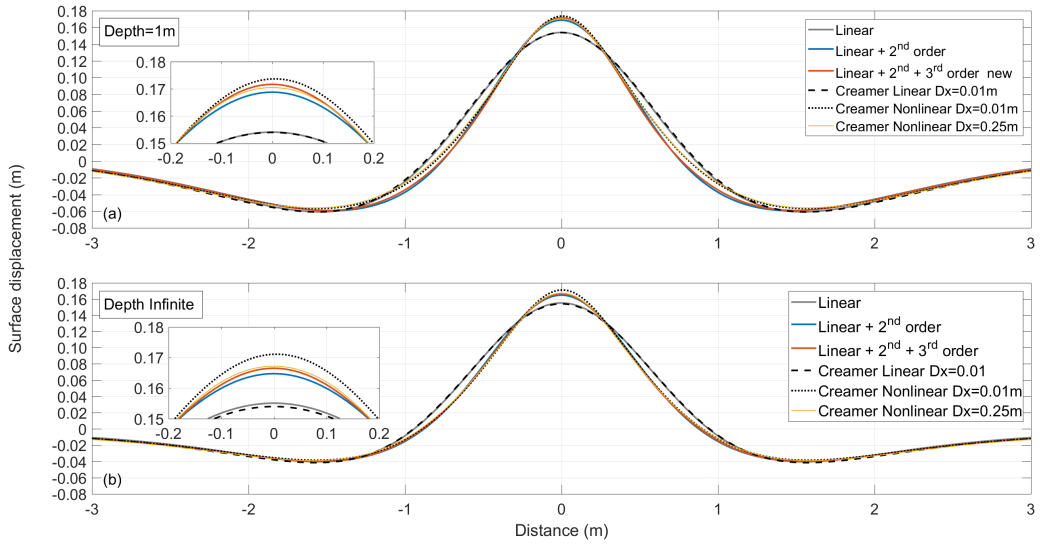

Figure 5.30: Spaceseries of the strongly nonlinear group ($\Sigma\alpha_i = 0.154$ m) considering depth=1 m (a) and infinite depth (b). Comparison between original linear signal and nonlinear signal using the static Krasitskii and Creamer methods.

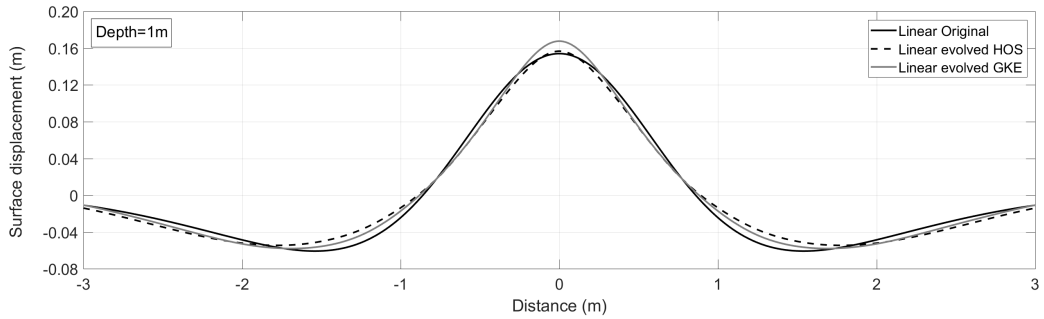

Figure 5.31: Spaceseries of the linear harmonics of the strongly nonlinear group ($\Sigma\alpha_i = 0.154$ m) for depth=1 m for the original and evolved underlying free-wave spectra.

group for the underlying free-wave spectra are presented in Figure 5.31. The same graphs were presented in Figure 5.4 for all the groups of different steepness, but at different scale. Plotting them at the same scale though, facilitates comparisons with the nonlinear solutions in Figure 5.32 of the present section.

The nonlinear spaceseries of the strongly nonlinear wave group calculated by static Krasitskii are presented in Figure 5.32. The linear spaceseries of the original free-wave spectrum are also included in the plot in order to examine the overall improvement of using an evolved spectrum and inducing up to 3^{rd} order bound wave nonlinearities. At

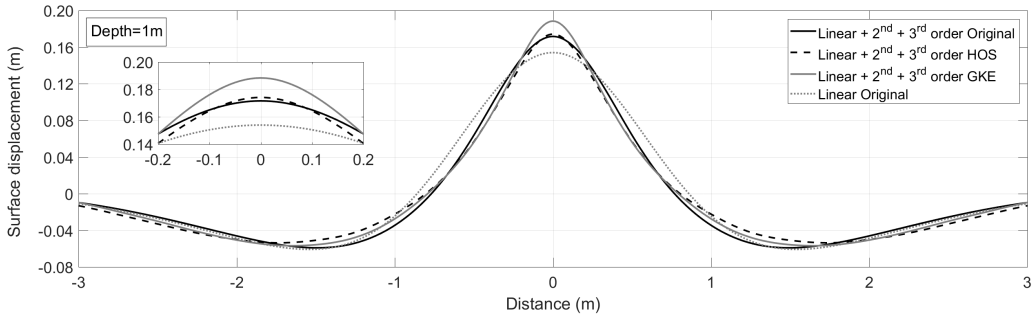

Figure 5.32: Spaceseries of the static Krasitskii solution for the strongly nonlinear group ($\Sigma\alpha_i = 0.154$ m) for d=1 m for the original and evolved underlying free-wave spectra.

this stage the spatial profile of the surface elevation from the nonlinear model is not available, but future studies will include it as a benchmark for the analytical methods. It can be seen that the evolved free-wave spectra result in a narrower crest above the MWL and flatter, shallower and wider troughs below the MWL compared to the original free-wave spectrum. The crest is also considerably narrower, steeper and higher (at least by 12%) than the linear solution, demonstrating the expected effects of the nonlinearity. The evolved free-wave spectrum of HOS marginally increases the nonlinear estimation of static Krasitskii compared to the original spectrum. The largest increase of the crest elevation is observed for the free-wave spectrum of the GKE, which is a direct consequence of the overestimation of the crest height of the linear harmonics of the GKE (see gray line Figure 5.31).

The results of the static Krasitskii for the weakly nonlinear and quasi-linear wave groups are presented in Figures 5.33 and 5.34, respectively. The inclusion of the bound waves for the weakly nonlinear group causes a noticeable narrowing of the main crest and an increase of the crest elevation by at least 7%. The effect of the narrowing in hardly visible for the quasi-nonlinear group, while the maximum crest elevation increases only by at least 3%. This confirms that for the quasi-linear group, the bound wave structure is very weak and practically the spectrum does not evolve.

Similar conclusions for the groups of different steepness were made by the previous methods for calculating the bound waves (second order theory, fifth order expansion

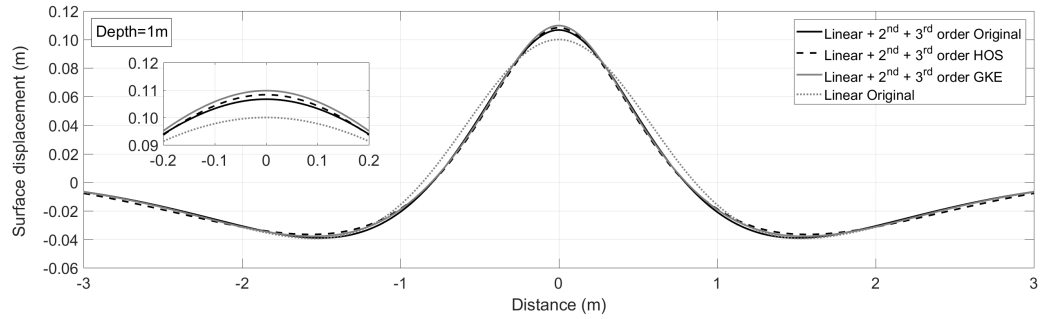

Figure 5.33: Spaceseries of the static Krasitskii solution for the strongly nonlinear group ($\Sigma\alpha_i = 0.100$ m) for d=1 m for the original and evolved underlying free-wave spectra.

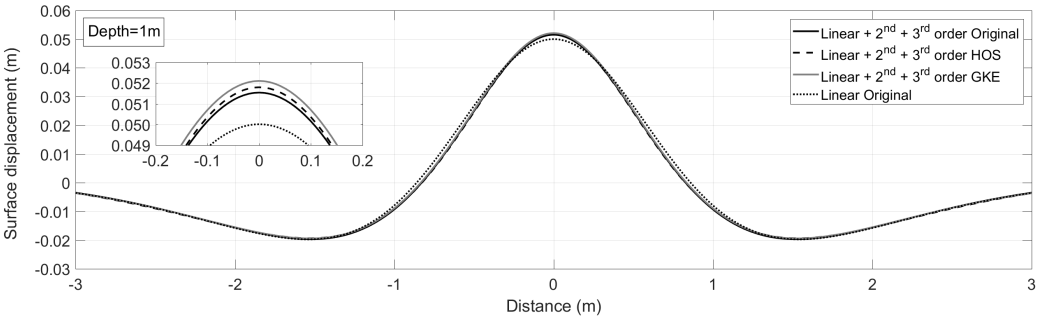

Figure 5.34: Spaceseries of the static Krasitskii solution for the quasi-linear group ($\Sigma\alpha_i = 0.050$ m) for d=1 m for the original and evolved underlying free-wave spectra.

and Creamer transform), but here the effects of using the evolved free-wave spectra are examined for the spatial profile of the focused wave and not the timeseries.

5.5.3 Conclusions

In this section, an original way to employ the canonical transformation of Krasitskii (1994) was presented to produce the bound nonlinear harmonics of second and third order based on a known free-wave spectrum. A similar assumption to that of the derivation of the GKE was made, which considers that the free waves in the real and transformed space are the same. This seems to be a natural choice since there is no way to know a priori the spectrum in the transformed space, as the only available information refers to the real space energy spectrum. As such, the aforementioned assumption is commonly used for the different versions of the KE (see Section 4.2.1), but it is not

necessarily the assumption that Krasitskii (1994) presented in the original paper. On the contrary, Krasitskii suggested that this is a "naive" consideration and recommended alternative derivations based on the Laplace equation (see p. 16 in (Krasitskii, 1994)), which however, to the author's best knowledge, they were not explored further since the original publication.

Regardless of the previous shortcoming on the derivation, the results for the space-series of a nonlinear wave profile exhibit the expected characteristics of nonlinearity: increase of the crest elevation, narrowing of the central crest and shallowing of the lateral troughs. The comparison with the results of the Creamer transform shows very good agreement, especially for the deep water case, where the Creamer transform is valid. It should be noted that the static Krasitskii method showed very good performance for up to the limiting breaking wave group, which is remarkable considering the underlying assumptions.

The main advantage of the static Krasitskii is that it is valid for both finite and infinite water depth, which brings it to a better position than the Creamer transform when examining broadbanded spectra that contain deep to shallow water wave components. However, a considerable handicap of the static Krasitskii method, as derived here, is that the canonical transformation is valid only for zero phases differences among the components. Consequence of that is that it cannot be applied to produce timeseries. Nevertheless, it is valid in the context of NewWave-type wave groups and thus, large waves in the ocean. Another disadvantage is the tedious derivation and the high computational cost of the method, which restricts it to a small number of wave components.

Future work can expand the present derivation to examine arbitrary phase differences among the wave components towards a more general version of the canonical transformation. Moreover, a mathematically and physically consistent way to produce timeseries should be explored, which will expand the applicability of the method for engineering purposes, where the local characteristics of the time evolving wave profile are the primary interest. Other aspects of the application of the method that should be

examined in greater depth are: i) the permitted interactions through the $\delta-$functions, which here are restricted to resonant interactions only when the differences between the wavenumbers are exactly zero. Relaxing this even to machine precision may have impact on the considered wave interactions and the calculated bound waves. ii) The effect of symmetries in the matrices of Krasitskii's coefficients. Krasitskii insisted to impose the symmetry for pairs of wavenumbers in the calculated coefficients, since the natural symmetry of the matrices should not be taken for granted. Which symmetries should be imposed and why can be subject of future work. iii) Revision on the calculation of Krasitskii's coefficients by employing the Laplace equation (see p. 16 in (Krasitskii, 1994)), which could save considerable computational cost.

Concluding, the examination of both the Creamer transform and the static Krasitskii method showed great potential for the calculation of nonlinear wave profiles by these two methods that might have been overlooked by the ocean engineering community, compared to more applied methods, such as the second order theory. It should be noted that for more consistent comparisons and benchmarking of the methods, deep water wave spectra should be examined, where both methods are valid. This can also set the course for new experimental campaigns in order to find the breaking limit and the spectral changes in deep water broadbanded wave spectra.

5.6 Intercomparison

In this section, comparisons among the different methods for reconstructing the time-series of the wave profile of Chapter 5 are performed[16]. Similar comparisons were made throughout this chapter, but here, the methods are compared using the same underlying free-wave spectra at each case. Graphs in this section are presented only for the strongly nonlinear group which exhibits the highest nonlinearity and the differences are more noticeable. Moreover, tables with the measured crest elevation and

[16]The spaceseries are not compared here, since the corresponding comparisons between the Creamer transform and static Krasitskii were performed in Section 5.5.2.

wave height as well as their comparison with the fully nonlinear solution are included. When relevant, comparisons with previous studies are discussed.

Some important remarks are made before presenting the results: i) The static Krasitskii's method results are not presented graphically, since, to present, there is no consistent method for producing the timeseries; ii) The Creamer transform results refer to the finite depth case, which is not strictly the case for the formulation used; iii) The results of the fifth order expansion in the graphs are produced using the exact 2^{nd} difference harmonics and the actual k_p of the corresponding spectra. This is because, as discussed in Section 5.3, using the self-interactions to calculate the 2^{nd} difference harmonics results in an artificial elevation of the entire central wave profile. Nevertheless, in the tables, both the exact and the approximate 2^{nd} difference harmonics are presented separately, using the k_p of the evolved and the original spectra, respectively; iv) The maximum crest elevation can be calculated from the spaceseries, since it refers to $t = 0$ s and thus, the static Krasitskii's method results are included in the tables. However, the surface profile at times $t \neq 0$ is not known and consequently the troughs cannot be estimated. As a result, the wave height by the static Krasitkii is not included in the tables.

The timeseries of the wave profile of the strongly nonlinear group at the PF location are presented in Figures 5.35, 5.36 and 5.37 for the original, extracted evolved and calculated evolved GKE amplitude spectra, respectively, using the surface profile reconstruction methods. To begin with, comparing the three figures shows that there is consistency in the behaviour of the profile reconstruction methods for all the underlying free-wave spectra and that the evolved spectra predict a more similar wave profile to the fully nonlinear simulation of HOS-NWT than when the original spectrum is used. Additionally, there is a considerable improvement from the linear theory prediction (blue line) when bound waves are added. The narrowing and increasing of the main crest are evident.

In more detail, Figure 5.35 demonstrates that despite the increase of the crest ele-

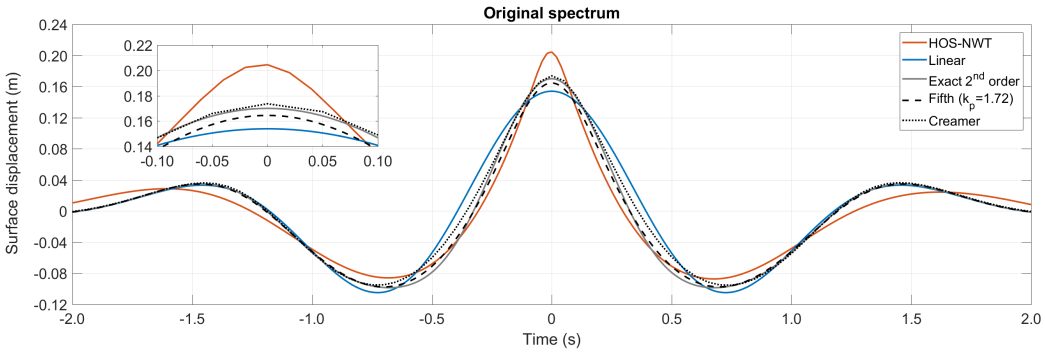

Figure 5.35: Free surface elevation timeseries of the strongly nonlinear group ($\Sigma\alpha_i = 0.154$ m) produced by the reconstruction methods of the wave profile, considering the original free-wave spectrum, and comparison with linear and fully nonlinear solution.

vation and shallowing of the neighbouring troughs resulted by the inclusion of bound waves, the central crest calculated using the original free-wave spectrum is still considerably wider than the simulated crest. The greatest discrepancy in these terms is observed for the Creamer transform. The prediction of the fifth order expansion for the troughs and width of the main crest is closer to the fully nonlinear simulation, but it underestimates the crest elevation compared to both Creamer transform and second order theory. Similar observations can be made for Figure 5.36. In this case however, the shape of the wave profile is better estimated thanks to the use of the evolved spectrum. All nonlinear analytical solutions provide a narrower crest compared with linear theory. Nevertheless, the Creamer transform estimation predicts a considerably wider crest compared to the fifth order expansion and second order theory, which both predict very similar lateral troughs. However, the fifth order expansion ceases reaching the crest elevation of the Creamer transform and second order theory. Last, Figure 5.37 shows that the crest elevation is increased for all the methods when the spectrum of the GKE is used. Again, the agreement at the troughs is better for the second order theory and fifth order expansion, but at the crest, the latter predicts a lower elevation compared to second order theory and the Creamer transform. Overall, with the exemption of the crest elevation, the fifth order expansion for the GKE spectrum shows a very good agreement of the central wave profile, which can be associated with the fine-tuning of the selection of the k_p used in the calculation.

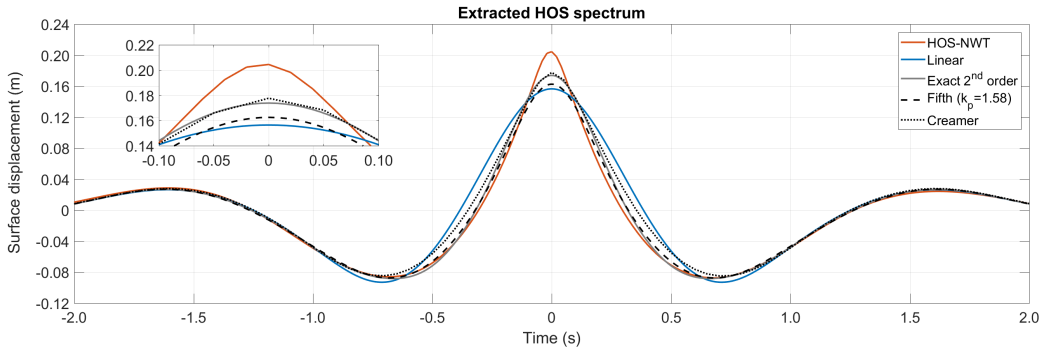

Figure 5.36: Free surface elevation timeseries of the strongly nonlinear group ($\Sigma\alpha_i = 0.154$ m) produced by the reconstruction methods of the wave profile, considering the extracted free-wave spectrum from HOS, and comparison with linear and fully nonlinear solution.

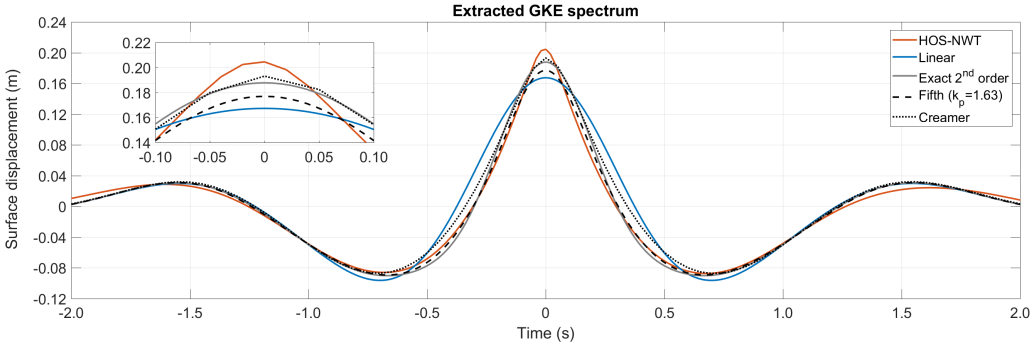

Figure 5.37: Free surface elevation timeseries of the strongly nonlinear group ($\Sigma\alpha_i = 0.154$ m) produced by the reconstruction methods of the wave profile, considering the calculated free-wave spectrum by the GKE, and comparison with linear and fully nonlinear solution.

Next, a quantitative comparison is performed for the analytically estimated maximum crest elevation for the wave groups of different steepness in Tables 5.2 - 5.3. For all cases, the measured maximum crest elevation in the fully nonlinear simulation is mentioned in the caption of the tables and the linear theory prediction with the original free-wave spectrum refers to the amplitude sum ($\Sigma\alpha_i$). It would be also useful if the tables are looked in two ways: as a whole ("full table" case) and by excluding the GKE spectrum and the "Fifth" order expansion ("excluded table" case). The GKE spectrum causes increased linear harmonics and thus, overall overestimation of the crest elevation, while the fifth order expansion uses the self-interactions for the 2^{nd} difference

Table 5.2: Crest elevation (m) calculated by the different methods for reconstructing the free surface profile of the strongly nonlinear group ($\Sigma\alpha_i = 0.154$ m). Measured in HOS-NWT: 0.2045 m.

	Linear theory	2^{nd} order	Fifth[a]	Fifth-Ex.[b]	Creamer	Krasitskii
Original spectrum	0.1540	0.1700	0.1812	0.1645	0.1737	0.1717
Evol. spectrum HOS	0.1565	0.1739	0.1838	0.1626	0.1777	0.1742
Evol. spectrum GKE	0.1673	0.1877	0.1993	0.1770	0.1931	0.1884

[a]The calculation is based on the k_p of the original spectrum and self-interactions for the 2^{nd} difference harmonics.

[b]The calculation is based on the actual k_p and the exact solution of the 2^{nd} difference harmonics.

Table 5.3: Crest elevation (m) calculated by the different methods for reconstructing the free surface profile of the weakly nonlinear group ($\Sigma\alpha_i = 0.100$ m). Measured in HOS-NWT: 0.1123 m.

	Linear theory	2^{nd} order	Fifth[a]	Fifth-Ex.[b]	Creamer	Krasitskii
Original spectrum	0.1000	0.1068	0.1109	0.1039	0.1077	0.1067
Evol. spectrum HOS	0.1013	0.1085	0.1124	0.1049	0.1094	0.1083
Evol. spectrum GKE	0.1025	0.1097	0.1142	0.1066	0.1108	0.1098

harmonics, which results in artificial elevation.

For the strongly nonlinear wave group (Table 5.2), the "full table" shows that the highest crest elevation is predicted by fifth order expansion and the GKE spectrum, while the lowest is predicted by fifth order expansion with the exact 2^{nd} difference harmonics and the original spectrum. A more realistic view is obtained when focusing on the "excluded table", showing that the second order theory, Creamer transform and static Krasitskii have similar predictions. Small improvement for the maximum crest elevation is noted when the evolved spectrum is used, with the highest proportional improvement shown for the second order theory.

For the weakly nonlinear wave group (Table 5.3), similar observations are made: highest crest elevations are observed when the GKE free-wave spectrum is used with the fifth order expansion, which overestimate the nonlinear simulation. It is worth noting that the predictions of the second order theory are higher here than the static Krasitskii. Further, examining only the "excluded table" and considering that the Creamer transform is not properly formulated for the finite water depth case, it seems that the best candidate to describe the crest elevation is the second order theory.

Table 5.4: Crest elevation (m) calculated by the different methods for reconstructing the free surface profile of the quasi-linear group ($\Sigma\alpha_i = 0.050$ m). Measured in HOS-NWT: 0.0522 m.

	Linear theory	2^{nd} order	Fifth[a]	Fifth-Ex.[b]	Creamer	Krasitskii
Original spectrum	0.0500	0.0517	0.0526	0.0509	0.0518	0.0515
Evol. spectrum HOS	0.0502	0.0519	0.0529	0.0511	0.0521	0.0518
Evol. spectrum GKE	0.0505	0.0522	0.0532	0.0514	0.0523	0.0521

For the quasi-linear wave group (Table 5.4), the differences in the crest elevation are marginal, especially when focusing on the "excluded table". In this case, the Creamer transform predicts the highest crest elevation. Looking at the "full table", similar to the weakly nonlinear group, the fifth order expansion overpredicts the maximum crest elevation, but here this applies even when the original free-wave spectrum is used, which indicates that the set-down of the wave group is ill-defined.

To facilitate comparisons with the fully nonlinear solutions, the results of Tables 5.2 - 5.3 are presented as (%) difference of the measured crest elevation of the nonlinear simulation of HOS-NWT, calculated as $\left(1 - \frac{\text{measured-analytical}}{\text{measured}}\right)$, in Tables 5.5 - 5.7.

For the strongly nonlinear wave group (Table 5.5), it is seen that the combination of the fifth order expansion with the GKE free-wave spectrum captures almost exactly the crest elevation of the nonlinear simulation. From the "excluded table", it is seen that the nonlinear solutions for the bound waves improve the linear theory estimation by almost 10%. Best estimation is achieved for the Creamer transform and the evolved spectrum of HOS. It is also observed that linear theory underestimates considerably the maximum crest elevation and the result improves marginally when the evolved free-wave spectrum is used.

Similar results were obtained in the experimental study of Baldock et al. (1996) for a strongly nonlinear narrowbanded wave group and the original free-wave spectrum (see Figure 6c in (Baldock et al., 1996)), where linear and second order theory deviated 30% and 20% from the measurements of the maximum crest elevation, respectively. Here, these differences are 25% and 17%. They also highlighted the fact that analytical solutions are much more successful in estimating the maximum crest elevation of

regular waves than of steep focused waves groups, which adds difficulty to the present challenges.

On the other hand, it should be also noted that the present findings are in contradiction with the study of Johannessen and Swan (2003)[17] who reported that for a unidirectional limiting breaking wave group in deep water the linear theory solution can account for only 65% of the crest elevation when the original spectrum is used and 81% when the locally broadened (evolved) free-wave spectrum is used (see Figure 13 in (Johannessen and Swan, 2003)). Similarly, for second order theory, it was reported that prediction of the maximum crest elevation was improved from 75% to 92%, while here the improvement is very moderate, only 2%, from 83% to 85%. Note that only the limiting breaking case is considered for the comparison here for consistency reasons, because it is impractical to try to match the same nonlinearity for wave groups of moderate steepness. There may be several reasons for these important deviations between the two studies: i) Physically, the amplitude spectra are different. In (Johannessen and Swan, 2003), $\alpha_i \propto f_i^{-2}$ is used, while in the present study a more natural broadbanded Gaussian distribution is used. ii) The focusing of the wave group in (Johannessen and Swan, 2003) is not performed using an advanced focusing methodology, as in the present study, and, as a consequence, the wave group is not accurately focused, as seen from the lateral asymmetries of the wave profile in Figure 13a of (Johannessen and Swan, 2003). iii) The two-wave decomposition is used in (Johannessen and Swan, 2003), compared to the more accurate four-wave decomposition method here, which may result in inaccuracies in the extraction of the linear harmonics with considerable consequences in using these harmonics for the analytical calculations with linear and second order theory. Therefore, at least for the latter two reasons, the analysis of the present study should be considered superior to that of Johannessen and Swan (2003).

Another study that examined limiting breaking unidirectional wave groups and compared with analytical predictions is that of Johannessen and Swan (2001). After dig-

[17] The reader should also consult the experimental campaign of Johannessen and Swan (2001) for a more complete view of the methods and testing conditions.

Table 5.5: Analytically calculated crest elevation as a percentage of the measured elevation in HOS-NWT (0.2045 m) for the strongly nonlinear wave group ($\Sigma\alpha_i = 0.154$ m).

	Linear theory	2^{nd} order	Fifth[a]	Fifth-Ex.[b]	Creamer	Krasitskii
Original spectrum	75%	83%	89%	80%	85%	84%
Evol. spectrum HOS	77%	85%	90%	80%	87%	85%
Evol. spectrum GKE	82%	92%	97%	87%	94%	92%

itizing Figure 7a of (Johannessen and Swan, 2001), it is found that linear and second order theory can account for only 65% and 75% of the maximum crest elevation, respectively, which is approximately 10% lower to the corresponding findings of the present study. Their explanation is that this may be a consequence of a changing free-wave regime. However, as suggested from the present findings, this should not be the reason, because the improvement is only marginal. The author believes that most likely the findings of Johannessen and Swan (2001) suffer from poor focusing of the wave group, which is supported from the lack of symmetry in the timeseries before and after the focal time and the considerable mismatch of the second order harmonics in Figure 17 of (Johannessen and Swan, 2001).

Last but not least, the findings of Katsardi and Swan (2011) are discussed. For intermediate and shallow water wave groups, they suggest that the nonlinear simulation results in lower prediction of the maximum crest elevation than linear theory. The present results contradict that and show that there is no weakening of the dispersive focusing in shallower water depth. The effects observed in that study are probably due to BF instabilities that may appear in a very dispersed wave train (see comment 4).

For the weakly nonlinear wave group (Table 5.6), it can be seen that, similarly to the strongly nonlinear group, the use of the evolved spectra has a negligible improvement on analytically calculated maximum crest elevation. In case of wave groups of moderate steepness however, linear theory accounts for 90% of the maximum crest elevation of the fully nonlinear simulation, while the best estimation of 97% is achieved by second order theory and Creamer transform, considering the "excluded table". Very good performance is also reported for the static Krasitskii method.

Table 5.6: Analytically calculated crest elevation as a percentage of the measured elevation in HOS-NWT (0.1123 m) for the weakly nonlinear wave group ($\Sigma\alpha_i = 0.100$ m).

	Linear theory	2^{nd} order	Fifth[a]	Fifth-Ex.[b]	Creamer	Krasitskii
Original spectrum	89%	95%	99%	93%	96%	95%
Evol. spectrum HOS	90%	97%	100%	93%	97%	96%
Evol. spectrum GKE	91%	98%	102%	95%	99%	98%

Table 5.7: Analytically calculated crest elevation as a percentage of the measured elevation in HOS-NWT (0.0522 m) for the quasi-linear wave group ($\Sigma\alpha_i = 0.050$ m).

	Linear theory	2^{nd} order	Fifth[a]	Fifth-Ex.[b]	Creamer	Krasitskii
Original spectrum	96%	99%	101%	98%	99%	99%
Evol. spectrum HOS	96%	100%	101%	98%	100%	99%
Evol. spectrum GKE	97%	100%	102%	98%	100%	100%

For the quasi-linear wave group (Table 5.7), it can be seen that linear theory already offers a very good estimation of the maximum crest elevation of 96% of the fully nonlinear solution, demonstrating that the bound waves have little energy content. When the analytical methods for calculating the bound waves are used, a perfect estimation of the maximum wave crest elevation is predicted. The use of fifth order expansion results in overestimations for any of the underlying free-wave spectra.

To conclude, the previous findings show that the maximum crest elevation is only marginally improved when using the evolved free-wave spectrum, nevertheless as found before, the overall shape of the wave profile is much more realistic. Moreover, linear theory is adequate for estimating the maximum crest elevation only for the quasi-linear group. For the wave groups of moderate and high steepness, $\Sigma\alpha_i = 0.100$ m and $\Sigma\alpha_i = 0.154$ m, a bound wave structure should be considered, which for the former results in very good estimation of the maximum crest elevation of 97%, while for the latter, the fully nonlinear result is still underestimated by approximately 15%. Therefore, for strongly nonlinear wave groups close to breaking, fully nonlinear solvers are definitely recommended.

Last but not least, another important aspect to consider, which is sometimes overlooked in similar studies, is the maximum wave height, measured as the vertical distance from the lowest elevation at the troughs to the highest elevation at the main crest.

The wave height is important for engineering purposes, because it refers to the total free surface displacement that a structure experiences and it is associated with the translation of a floating body caused by the waves. The results for the wave height are presented in Tables 5.8 and 5.9, only for the strongly nonlinear group for brevity purposes, as absolute values and as (%) estimation of the fully nonlinear solution (0.2913 m)[18], respectively. As discussed, results for the static Krasitskii are not included.

For convenience, the results of Table 5.8 and 5.9 are examined together and are directly compared with corresponding results for the crest elevation in Tables 5.2 and 5.5. It can be seen that the results for the wave height exhibit several differences compared those for the crest elevation. To begin with, for all the analytical calculations, the wave height is better predicted compared to the maximum crest elevation. This is possibly related to the fact that the effects of the bound nonlinearities are more prominent at the crest compared to the troughs and thus, the inclusion of the troughs proportionally improves the estimation. Additionally, focusing only on the "excluded table", it is seen that actually, the use of the evolved free-wave spectrum of HOS causes greater underestimation of the wave height compared to the free-wave spectrum. This is exactly the opposite case when maximum crest elevation is concerned. The reason for this is that the evolved linear harmonics have shallower troughs than the original and thus, the overall estimation of the wave height is lower. As a consequence, and in combination with the fact that the bound nonlinearities result in shallower troughs, the linear theory estimation of the wave height with the original spectrum is comparable and in some cases better than the evolved free-wave spectra with the bound nonlinearities. Of course, this is an artefact and the wave profile is considerably different, but it may be a useful observation when examining wave height statistics with random linear simulations. Moreover, it is noted that the fifth order expansion using the self-interactions for the set-down gives only an additional 2% increase of the wave heigh compared to the other methods, instead of 5-10% for the maximum crest elevation, because the

[18]It is remarkable to notice that the wave height of the focused wave group is approximately 1/3 of the water depth without the occurrence of wave breaking.

Table 5.8: Crest height (m) calculated by the different methods for reconstructing the free surface profile of the strongly nonlinear group ($\Sigma\alpha_i = 0.154$ m). Measured in HOS-NWT: 0.2913 m.

	Linear theory	2^{nd} order	Fifth[a]	Fifth-Ex.[b]	Creamer	Krasitskii
Original spectrum	0.2591	0.2687	0.2746	0.2622	0.2693	-
Evol. spectrum HOS	0.2497	0.2623	0.2684	0.2502	0.2627	-
Evol. spectrum GKE	0.2638	0.2780	0.2865	0.2664	0.2805	-

Table 5.9: Analytically calculated maximum wave height as a percentage of the measured wave height in HOS-NWT (0.2913 m) for the strongly nonlinear wave group ($\Sigma\alpha_i = 0.154$ m).

	Linear theory	2^{nd} order	Fifth[a]	Fifth-Ex.[b]	Creamer	Krasitskii
Original spectrum	89%	92%	94%	90%	92%	-
Evol. spectrum HOS	86%	90%	92%	86%	90%	-
Evol. spectrum GKE	91%	95%	98%	91%	96%	-

troughs are elevated and the entire wave profile is translated vertically, which increases considerably the crest elevation, but not necessarily the wave height.

Summing up, the previous results demonstrated that different conclusions may be drawn for the performance of the analytical methods and the underlying free-wave spectra depending on the examined parameters, e.g., maximum wave crest elevation or wave height. Therefore, the effects of nonlinearity should be examined from different angles in regard to the considered applications. Similarly, future work can expand the present methods to examine the effects of bound and resonant nonlinearities on the kinematics of focused wave groups, which determine the structural loads. Indeed, it is not known at this stage whether the maximum loads or the time history of the loads calculated based on the evolved free-wave spectra will be more appropriate than those calculated from the original spectra. For instance, the timeseries of the free surface elevation for the evolved HOS spectrum (Figure 5.36) are "smoother" with smaller abrupt changes between the crests and troughs compared to the timeseries based on the original spectrum (Figure 5.35) and may result in milder loads. Also, depending on the geometry of the structure and its degrees of freedom, different phasing of the extreme wave group may be used for the design load (see appendix of (Vyzikas et al., 2018b)).

Finally, as commented throughout the section and Chapter 4 (see Section 4.8), the

GKE overestimates the free-wave spectrum, especially near the peak, compared to the evolved spectrum extracted from the HOS simulation. Nonetheless, the paradox is that this overestimation, at least for the present Gaussian spectrum, results in a better prediction of the nonlinear wave profile. Therefore, it may result in a more conservative, at least safety-wise, estimation of wave profile and kinematics. To which extent this is case specific or it applies to other than Gaussian spectra should be part of future work. Thus, even if the reasons that the extracted and the GKE evolved spectra are different remain unknown, it would be interesting to see whether in the end the overall solution is more conservative for certain engineering applications.

On a final note, it is underlined that the present conclusions refer only to long-crested wave groups. However, the surface dynamics of directionally spread waves may be considerably different, and the additional bound wave elevation may be restrained only up to second order, see e.g., (Johannessen and Swan, 2001; Gibbs and Taylor, 2005). The broadening of the free-wave regime may also follow different patterns, as discussed by many authors, e.g., (Adcock and Taylor, 2016b), resulting in considerable deviations of the wave profile from the linear theory estimation.

Chapter 6

Conclusions

THIS last part of the Thesis summarizes the main achievements of the work conducted, highlights the remaining questions and suggests potential routes for future research. The present study is a balanced mixture of experimental, numerical and analytical methods aiming at accurate simulation of extreme waves and better understanding of the underlying physical process of wave-wave interactions during the formation of these waves. The conclusions are structured accordingly herein, but it is noted that for more information, the reader should refer to the conclusion sections of every chapter, where the corresponding considerations are discussed thoroughly.

Present challenges

A large part of the present work was devoted to an exhaustive multilateral literature review of extreme waves and numerical modelling techniques for ocean waves. The lack of consensus about the characteristics and the generation mechanisms of extreme waves, as well as the role of the nonlinear wave-wave interactions, impose an considerable challenge. At present, there are two competing "schools" in the field of extreme waves, namely, the MI and the dispersive focusing, who use different numerical models and methods of analysis. Thus, the literature is often contradictory and one should

consult carefully both approaches before drawing any conclusions for the examined problem. An additional difficulty comes from the numerical models and analysis techniques, which, due to the fact that they have different assumptions and limitations, may return considerably different results that can lead to misinterpretation of the underlying physical processes. To mitigate these challenges, the present work included a wide range of multi-purpose numerical models and analytical methods in order to tackle the problem of extreme waves from various perspectives. Based on the latest literature (Christou and Ewans, 2014; Fedele et al., 2016), which provides convincing evidence that dispersive focusing is a natural mechanism for the formation of extreme waves in the ocean, NewWave-type waves were used in the physical and numerical modelling. Moreover, the advanced focusing methodology of Stagonas et al. (2014) was employed for first time in NWTs, achieving great accuracy and minimising discrepancies between experimental and numerical results. The use of accurate techniques, i.e., four-wave decomposition, for the analysis of the results provided new insights into the evolution of the focusing wave groups. The analytical models, used or developed, contributed in supporting the interpretation of the physics of the problem.

Outcomes

Main achievements:

1. Insight in the nonlinear wave-wave interactions during the formation of NewWave-type extreme waves.
2. Development of a method using the GKE for estimating the evolution of the free-wave spectrum in focused wave groups.
3. Demonstration of the performance of analytical methods for reconstructing a nonlinear wave profile.
4. Validation of numerical models: OpenFOAM, SWASH, HOS-NWT and HOS-ocean.

Physics of focused waves

The evolution of waves in nonlinear media is associated with energy transfers among the wave components of the spectrum. In the context of water waves, these take the form of resonant and bound nonlinearities, which act at different scales and affect the spectrum in different ways, as explained in Section 2.2.

According to the theory, solely resonant interactions are capable of altering the free-wave spectrum and bound nonlinearities can only cause local changes to the wave profile. Previous experiments with focused waves (Baldock et al., 1996; Johannessen and Swan, 2003) provided some evidence that the free-wave regime changes in short scales and attributed this to resonant interactions. However, for unidirectional waves the conditions for resonant interactions cannot be satisfied (Janssen, 2003). To investigate this, the present study combined experimental and fully nonlinear numerical analysis of wave groups, using realistic broadbanded spectra that are not dominated by BF instabilities. With the help of the focusing methodology (Stagonas et al., 2014) and the four-wave decomposition, it was clearly demonstrated for first time that the free-wave spectrum gradually evolves towards focusing, with its spectral peak being downshifted

and its high frequency tail being broadened. To identify the nature of these changes, a code for the GKE based on the work of Gramstad and Stiassnie (2013) was employed. It was shown that there are strong correlations between the effect of near-resonant interactions and the observed changes on the free-wave spectrum.

The action of bound nonlinearities is better known: as the steepness of the group increases, energy is transferred locally and rapidly to higher and lower harmonics. For regular waves, harmonics can be easily identified by the multiple peaks at the spectrum (Zhao et al., 2009). However, for irregular waves, the distinction is more complicated, due to the overlapping of the harmonics. In such cases, the four-wave decomposition method becomes very useful. Employing this method to the focused wave groups of the present study revealed a strong harmonic structure with consistent characteristics, at least up to fifth order. The energy content of the harmonics reduces with increasing order. To study the effects of nonlinearities, wave groups of different steepness up to the breaking limit were examined. For groups of moderate steepness, the second order theory appeared adequate to describe the dynamics of the group, while, for very steep groups, third, fourth and fifth order harmonics became considerable. The magnitude of the nonlinear harmonics was shown to increase disproportionally to the increase of steepness of the wave groups, making limiting breaking groups particularly challenging to simulate. It is noted, however, that these observations may be different for directional waves (Latheef and Swan, 2013; Johannessen and Swan, 2001).

To present, the literature is not conclusive on the action of bound and resonant nonlinearities, especially in focused waves. The effects of the bound nonlinearities influence the wave group locally and are proven to be fully reversible. On the other hand, the reversibility of near-resonant nonlinearities depends on their nature; BF instabilities at short scales are reversible, while the long-term evolution leads to the stability of the spectrum at the Hasselmann's scale, without being reversible. The present study demonstrated with accuracy, using a long fully nonlinear numerical flume, that the near-resonant interactions are fully reversible for broadbanded spectra at the short

time scales of the focused wave events, sharing characteristics of both BF and Hasselmann's evolution processes.

Another important aspect that was also demonstrated refers to the validity of dispersive focusing in intermediate and shallow water depth. In contradiction to previous studies (Katsardi and Swan, 2011), where the weakening of dispersion in finite water depth hindered the focusing process, here it was shown, thanks to the effective focusing of the waves, that dispersive focusing holds also in shallower water, supporting the use of NewWave theory in coastal areas.

Numerical modelling

Probably the most quantifiable achievement of the present work is the accurate generation of focused wave groups in a range of NWTs and their validation against experimental results. Custom boundary conditions were prepared for each numerical model in order to best accommodate the application of the focusing methodology. The iterative corrections of the input signal with the methodology act as a self-calibration procedure that suppresses any particularities of the wave generation. This minimizes any discrepancies and gives the opportunity for consistent validation of the numerical models, which took place after optimization and thorough convergence of the NWTs.

Initially, OpenFOAM, with waves2Foam (Jacobsen et al., 2012) and IHFOAM (Higuera et al., 2013a) libraries, was employed in order to examine the capability of the solver to propagate very steep waves and prepare a CFD NWT that can handle strong fluid-structure interaction for future studies. Aiming at decreasing the computational cost, the operational model SWASH was used, followed by the HOS-NWT. Both solvers, despite their inherent assumptions and limitations, demonstrated very good agreement with the experimental results. Careful comparisons revealed that OpenFOAM and HOS-NWT have similar input boundary conditions, suggesting potential use of the computationally efficient HOS-NWT for the iteration of the focusing methodology, before the final run in OpenFOAM. It should be noted that it is the first time that the three

models of different governing equations, scales and purpose are compared under the exact same conditions. An overview of the applicability of these models is given in Table A.1, coming from a large literature review and working experience.

The comparison with experimental results demonstrated a remarkable performance of the OpenFOAM NWT, with an error of 0.1% for the crest of the limiting breaking wave group. SWASH and HOS-NWT also showed impressive performance, considering their underlying assumptions, with an average error of 5%. It is noted that no time-shifting or adjustment of the focal location were needed, thanks to the accurate focusing of the wave groups. The models were also validated for the evolution of each harmonic at consecutive locations in the NWTs. The evolution of the linear harmonic was replicated by the models with great accuracy, giving confidence for the reliable numerical dispersion of the wave groups. The greatest discrepancies were reported for the 2^{nd} difference harmonic, which shows a spurious elevation preceding the main wave group, probably created due to the linear wave generation. An interesting outcome of the intercomparison of the models (see Table 3.5) is that OpenFOAM seems to consistently overestimate almost all the nonlinear harmonics, with the approximate solvers giving actually closer results to the experiment. This implies that the impressive performance of OpenFOAM may be due to intercancellations of the individual harmonics, with potential unknown consequences to the kinematics. As such, the present study suggests that an in depth analysis of the results may reveal hidden discrepancies and the CFD models should not be treated with blind trust as the gold standard.

Good experience and best practice methods were reported for the numerical methods of the present study, which can have important value for practical engineering applications. For example, to the best of the author's knowledge, for CFD, it was the first time that direct comparison between the most widely used libraries, waves2Foam and IHFOAM, was performed, indicating higher computational efficiency, but with local discrepancies for the latter. Similarly, it was shown that SWASH has the best performance for the 2^{nd} difference harmonic, which is important for practical coastal engineering ap-

plications that include infragravity waves. Last but not least, it was shown that reflections could not be perfectly absorbed by any of the NWTs, with the only remedy found to be a long distance between the focal point and the outlet boundary.

Analytical methods

Analytical models were used in the present work in order to replicate the effects of nonlinear wave-wave interactions, aiming at both confirming the theory behind the physics of NewWave-type extreme wave formation, and suggesting an efficient way for estimating an extreme wave profile without the need for numerical simulations. The main issue of this part of the work was the very limited literature and the almost absolute lack of available codes.

The most challenging part was to estimate the near-resonant interactions for the change of the free-wave spectrum in long-crested seas. After confirming that the source terms of WW3 cannot account for spectral change in 1D, the GKE (Gramstad and Stiassnie, 2013) was programmed independently including the effects of near-resonant interactions. The GKE was validated against Monte Carlo simulations with the HOS-ocean for long timescales and its performance was tested for the first time in short timescales. A new method was then proposed for finding the equivalent sea state parameters in order to approach the spectral evolution of focused wave groups. After exhaustive investigations, it was demonstrated that the reproduced spectral change resembles to a good extent that of focused waves. Although discrepancies exist and may suggest deeper issues, this method constitutes one of the first efforts to "marry" the phase-averaged and phase-resolving spectral evolution.

The bound nonlinearities are always based on the underlying free-wave spectrum. The best established method is second order theory, which is routinely used in engineering practice. The present work went beyond the state of the art in two ways: i) By examining methods that are rarely used in the literature, such as the fifth order expansion (Walker et al., 2004) and the Creamer transform (Creamer et al., 1989), and by

proposing new methods, namely the "static Krasitskii" (Krasitskii, 1994). ii) By thoroughly examining the effects of using the original and the evolved free wave spectra. The results demonstrated that all the methods capture the nonlinear characteristics of the wave profile, namely the steepening and increase of the main crest, as well as the flattening of the troughs. The use of the evolved free-wave spectrum produces a more realistic profile, but without further increasing the crest elevation. Extensive comparisons with fully nonlinear simulations in Section 5.6 demonstrate the improvement of these analytical methods over the linear theory estimation and indicate the error margins. It is noted that for the steepest group, the crest height is underestimated by more than 10% by all the theories, which indicates the need for fully nonlinear simulations for such cases.

Overall, the use of an evolved free-wave spectrum accompanied by expansion to high order harmonics with analytical methods can provide an improved, more realistic, NewWave profile. Necessary elements for this approach, especially for very steep waves, are the experiments for finding the onset of breaking and fully nonlinear solvers for obtaining spatio-temporal information of the wave field. This constitutes a balanced use of tools towards an integrated modelling approach for extreme wave simulations.

Future work

The present study revealed the great potential of several numerical models and analytical methods for estimating an extreme wave profile. Most importantly, it suggested an integrated approach by preparing and employing an artillery of tools with known strengths and weaknesses. To advance the present findings, additional work would be welcomed in physical and numerical modelling, as well as in theoretical analysis.

On the general perspective, the target should be the better understanding of the physics of the formation of extreme waves and identification of the nonlinear physics that should be included in the design practice (Adcock and Taylor, 2016a). This process will con-

tribute to the de-rogueing of extreme waves and, consequently, decrease uncertainties and improve safety at sea. Key on achieving this is the clear understanding of the nonlinear wave-wave interactions, which, based on the present findings and recent research (Aubourg et al., 2017), seem to have a more complex role in the spectral evolution than that suggested by the traditional approaches of BF and Hasselmann. The spectral transformation under strongly nonlinear conditions is certainly an open field of research and new findings should be expected from multi-disciplinary studies that will have a greater impact in wave modelling, e.g., new source terms in spectral models.

The GKE was one of the first steps towards this goal. However, the properties of this equation are far from being properly explored, with the present work contributing to its validation at short and long timescales and finite water depth. An important aspect that requires addressing is the derivation of the GKE from the Boltzmann integral. More specifically, the naive consideration that the free waves in the real and transformed space are the same is not necessarily valid and the canonical transformation behind it should be carefully taken into account (Krasitskii, 1994). Moreover, on revisiting the GKE, the effects of quintet interactions should be examined. The present findings strongly support these concerns that have been already outlined by Tanaka (2007) and Benoit et al. (2015).

One of the main targets of the present study was to suggest ways to improve the estimation of extreme NewWave-type profiles. A way to achieve this is by using the evolved free-wave spectrum. Despite the fact that this does not seem to increase the crest height, it can affect considerably the wave profile, which can be of interest for the design of different structures. On this note, the shape variation of the wave profile with phase shifts of the NewWave profile can be of great engineering interest for determining the design wave. For such purposes, the analytical methods for building the nonlinear wave profile can be particularly useful. Extra work is required though to improve the functionality of some methods. For example, the finite depth version of the Creamer transform should be tested and effort should be made to derive static Krasit-

skii with more flexibility on the section of the phases in the canonical transformation.

As explained, the dynamics of directional waves may differ considerably from long-crested seas, which are less frequent in nature. To gain a holistic view of the problem, the present methods should be extended in 2D or even crossing seas. The complication of such an undertaking should not be underestimated. Before this venture, however, it would be advisable to test the methods of this work on different spectral distributions and water depths, as there are indications that these may alter the present picture of the problem. The role of experiments will be vital for finding the breaking limit of the wave groups and validating the numerical models for further studies. As suggested from the present analysis, a sensible start would be deep water conditions, in order to eliminate the bias of water depth.

Last but not least, from an engineering perspective, the inclusion of currents and the study of the kinematics is very important in order to find the loads on the structure. Some of the present tools have been already tested on wave-current regimes (Buldakov et al., 2015). Others, such as some of the analytical methods, can be modified to include the influence of uniform currents in a Doppler shift fashion. For sheared currents, however, numerical and experimental modelling seem to be the main trustworthy options at this stage. Moreover, an engineering design parameter that requires further attention is the ringing phenomenon. This high frequency excitation can be finally studied in a reliable way, using the present tools and methodologies that achieved accurate replication of the third and higher order harmonics of the wave group.

Exciting discoveries are expected in the near future in ocean and coastal engineering, thanks to the advanced tools and methods developed for field, experimental, numerical and analytical studies. The present work endeavoured to highlight the importance and contribute towards the integration of these approaches within the framework of extreme wave modelling.

Appendix A

Modelling tools

In this chapter all the numerical models used in the Thesis are presented in a consistent way: first an introduction to their development history and distribution of the software is given, followed by the mathematical description of the model, including the numerical schemes and the treatment of the forcing terms. The description of each tool includes also information regarding its efficiency and accuracy for the examined problem. The rationale for employing each specific model is discussed based on its advantages and drawbacks compared to other similar models.

A.1 OpenFOAM

A.1.1 Introduction to OpenFOAM

OpenFOAM (Open source Field Operation and Manipulation) is an extensive software package for solving continuous mechanics problems. It was initially developed in the late 1980s at Imperial College, London and it was later rewritten in C++, incorporating the advantages of object-oriented programming. To a large extent, OpenFOAM was based on the works of Jasak (1996) and Weller et al. (1998). Since 2012, the main distribution and maintenance of OpenFOAM is performed by the ESI group and "The

OpenFOAM Foundation" is the copyright holder of the code. Its latest version is 5.0 released in mid 2017 (OpenCFD_Ltd, 2015). A community-driven release is also available through the "foam-extend" project (OpenFOAM-Extend, 2015). Both releases are open-source and freely available under GNU General Public Licence. OpenFOAM can be compiled mainly in Linux operating systems, but a Windows version was recently developed as well as third party graphical user interfaces (GUI).

OpenFOAM is a generalized CFD platform organised as a set of C++ libraries that include solvers for complex fluid flows, chemical reactions, heat transfer, solid dynamics, electromagnetics or even astrophysics and financial problems. Hereafter, only aspects relevant to fluid flows are discussed. There are several reasons that OpenFOAM has gained popularity and it is now widely used for industrial and academic applications (Jasak et al., 2007):

1) The use of object-oriented programming in C++, which offers clarity and flexibility as well as maximum the code re-use. In this framework, adding new features in the software is straightforward and efficient, achieving both minimum impact on the existing part of the code, e.g., introduction of bugs, and making the expansion of its functionalities possible by taking advantage of the modularity of the programming language. Different solvers can be combined allowing for simulation of complex physics, such as fluid-structure interaction (FSI) simulations;

2) Mimicking the form of partial differential equations (PDEs) in the code, which makes the programming of the physics very intuitive by resembling the mathematical form of the equations, resulting in a user-friendly syntax;

3) Extended capabilities in simulating fluid dynamics through the large and growing set of libraries for solving the Navier-Stokes equations (NSE) are available, such as Reynolds Averaged Navier-Stokes (RANS), Large-Eddy Simulation (LES), Direct Numerical Simulation (DNS) and Detached-Eddy Simulation (DES) with relevant turbulence modes (OpenCFD_Ltd, 2015);

4) Pre- and post-processing tools are offered for mesh generation (blockMesh, snappy-

HexMesh) and sampling data (isosurfaces, gauges). More sophisticated post-processing can be performed with the third-party open-source software Kitware Paraview®;

5) Free-of-license and open-source code, which does not make the software a black-box toolbox and allows for user customization and optimization, unlike commercial software (Higuera et al., 2013a);

6) Theoretically unlimited parallelization using the OpenMPI implementation of the message passing interface (MPI) (OpenCFD, 2012), in contrast to commercial software that the level of permitted parallelization is an add-on to the cost;

7) Support from the growing users' community with a very active thematically split forum. New users can benefit from the large number of tutorials (OpenCFD, 2012) and the available basic documentation (Marić et al., 2014).

The dicretization of the governing equations is performed by the Finite Element Method (FEM) for structural mechanics and the Finite Volume Method (FVM) for fluid mechanics. OpenFOAM meshes consist of of points, faces, cells and boundary patches. The cell is defined as a closed volume from its faces having a centroid. The boundary faces of relevant cells are grouped to form patches, which simplifies the definition of the boundary conditions (Jasak et al., 2007). OpenFOAM meshes can be uniform or unstructured with convex polyhedral cells defined in such a way that form a continuous mesh without overlapping with one another. The variables are solved on the centroids of the cells and they are interpolated on the faces using the available interpolation schemes (Chen et al., 2014). OpenFOAM also offers a great variety of numerical schemes and methods for integrating the PDEs in space and time.

Regarding fluid flows, OpenFOAM can solve the 3-Dimensional (3D) NSE for single or multiphase flows including turbulence for complex 3D domains. This allows for employing the model for nonlinear problems with highly distorted free surface, such as wave breaking and interaction of waves and structures. As such, the code has been applied for coastal and ocean engineering studies (see Section A.1.2).

A.1.2 Mathematical formulation

The governing equations

The simulation of free surface waves in CFD often implies the modelling of two fluid phases for the water and the air, with an interface of the two fluid defining the free surface. RANS equations can be solved simultaneously for the two Newtonian fluids considering them as immiscible. Each fluid is characterized by a scalar variable, which is referred as phase fraction γ_i taking values between 0 and 1. For most cases regarding coastal and ocean engineering applications, the incompressibility assumption can be made. In this framework, the governing equations of the flow are the continuity equation (A.1) and momentum equations (A.2) (Versteeg and Malaskekera, 2007).

$$\nabla \mathbf{U} = 0, \tag{A.1}$$

$$\frac{\partial \rho \mathbf{U}}{\partial t} + \nabla \cdot (\rho \mathbf{U}\mathbf{U}) - \nabla \cdot (\mu_{eff} \nabla \mathbf{U}) = -\nabla p^* - g \cdot \mathbf{X} \nabla \rho + \nabla \mathbf{U} \cdot \nabla \mu_{eff} + \sigma_\tau \kappa_c \nabla \gamma_i \tag{A.2}$$

where **U** is the velocity vector, ρ is the density, p^* the pseudo-dynamic pressure, **X** the position vector, σ_τ the surface tension coefficient, κ_c the curvature of the interface, γ_i the fluid phase fraction and μ_{eff} the efficient dynamic viscosity. $\mu_{eff} = \mu + \mu_t$, with μ being the molecular dynamic viscosity ($10^{-3} m^2/s$ and $1.4810^{-5} m^2/s$ for water and air, respectively) and μ_t is the turbulent viscosity given by the turbulence model (Ferziger and Peric, 2002). It should be noted that for most of the civil engineering applications the surface tension is negligible (Jacobsen et al., 2012).

The governing equations can be discretized according to the FVM in order to allow for the numerical solution. This is performed over a control volume, which is the cell bounded by its faces, and the equations are integrated numerically on the faces (Ransley, 2015). Subsequently the equations can be written in a discretized form for a reference cell and its neighbours connected by the faces (Greaves, 2010).

To close the RANS equations a turbulence model should be used, as discussed in Section 2.1.2. In the present study, since no breaking waves or FSI were simulated, a "laminar" flow type was selected. The laminar model sets the eddy viscosity, turbulent kinetic energy and the Reynolds Stress to zero. Therefore, the the effective viscosity and the effective stress tensor is calculated by the fluid (laminar) viscosity and the laminar stress respectively. The laminar model was used by many authors even when wave-cylinder interaction was examined and it was proven to be stable compared with two-equation models that may be dissipative Elhanafi et al. (2017).

OpenFOAM simulates multi-phase incompressible fluid flows with the "interFoam" solver, which solves Equations A.1 and A.2 simultaneously for the two fluids using the FVM discretization and the Volume of Fluid Method (VoF), as described in the next paragraphs. A crucial issue in incompressible flows is that the pressure is not connected to the density. Thus, an appropriate coupling between the velocity and the pressure is required to ensure that the pressure field by the momentum equations results in a velocity field that satisfies the continuity equation (Versteeg and Malaskekera, 2007; Ferziger and Peric, 2002). OpenFOAM uses the PIMPLE algorithm, which is an iterative scheme based on a combination of the SIMPLE (Semi-Implicit Method for Pressure-Linked Equations) (Patankar and Spalding, 1972) and the PISO (Pressure Implicit with Splitting of Operators) (Issa, 1986) algorithms. The main structure of PIMPLE is inherited from PISO, but in order to achieve convergence of all the equations at each time step, it uses an under-relaxation (Jasak, 1996). According to the solution strategy in PIMPLE, the values of the velocity and pressure from the previous time step are used as a "guess" to solve the velocity equations, which is referred as momentum predictor. Then the velocity and pressure are corrected several times using pressure-velocity correctors until they satisfy the mass conservation equation to the desired tolerance. In similar CFD models, namely STAR CCM+ and Ansys CFX, the SIMPLE algorithm is used as a guess-and-correct method to compute pressure and velocity (Westphalen et al., 2008) (Westphalen et al., 2012) or the conservation equations are solved in a single linear system being fully coupled (Westphalen et al.,

2007).

Last but not least, stability issues have to be addressed, since numerical simulations of unsteady and rapidly changing numerical flows may suffer from instability, due to space-time integration. Instabilities can be suppressed with appropriate treatment of the time step, ensuring that a fluid particle does not move more than one cell at a time step. To achieve this in OpenFOAM, the time step can be adjustable and controlled by the Courant condition (C_o) (Courant et al., 1967), which represents the portion of the cell that the advective flow can cover in one time step (Chen et al., 2014), as seen in Equation A.3. This is common practice in CFD and it guarantees that the volume of fluid leaving a cell is exactly the amount that can be received by the neighbouring cells and vice versa (Westphalen et al., 2012). Although the Courant criterion is vital for the stability of explicit methods, it is also useful in transient nonlinear implicit methods to guarantee convergence (Jasak, 2006). An additional time-controller ($alphaC_o$) for the interface of multiphase flows based on the Courant condition is used in OpenFOAM. It is essentially a Courant number criterion, but only for the region of the interface of the two fluids. The global time step is the minimum calculated from the two criteria. The C_o should not exceed the value of 1 for stability, but commonly much lower values are used for wave propagation studies, typically 0.1-0.5.

$$C_o = \frac{\delta t |U|}{\delta x} \tag{A.3}$$

where δt is the maximum time step, δx is the cell size in the direction of the velocity $|U|$ at that location.

Another source of stability can arise from the coupling of pressure and velocity, especially when the two variables are solved at exactly the same locations on the computational grid. This is due to the fact that it is possible to obtain more than one possible solutions at the same location for the pressure. To mitigate this, staggered grids are used, meaning that the velocity and the pressure are not calculated at the same positions of the computational cell, e.g., one is calculated on the centre and the other on

the faces (Greaves, 2010).

The Volume of Fluid Method (VoF)

OpenFOAM employs the VoF method for the treatment of the free surface, as introduced in Section 2.1.2. Since Equations A.1 and A.2 are solved simultaneously for the two fluids, the algorithm for the volume fraction results in an additional advection equation (Equation A.4) without the need for explicitly solving for the interface (Greaves, 2010).

$$\frac{\partial \gamma_i}{\partial t} + \nabla \cdot [\mathbf{U}\gamma_i] + \nabla \cdot [\mathbf{U}_r \gamma_i (1-\gamma_i)] = 0 \tag{A.4}$$

where $\mathbf{U}_r \gamma_i (1-\gamma_i)$ is an artificial compression term with $\mathbf{U}_r$ being a relative compression velocity (Weller et al., 1998). This term lacks physical interpretation and it is added in order to tackle one of the known problems of VoF, which is the numerical smearing of the interface (Berberović et al., 2009).

With this consideration, the two-phase flow is simplified to a flow of a single mixed-fluid flow with density (ρ) and dynamic viscosity (μ), calculated by Equation A.5 respectively, using the properties of fluid 1 and 2 (Paulsen et al., 2014a). As such, very complex free surface flows can be modelled in a simple way, without requiring mesh motion (Higuera et al., 2013a).

$$\begin{aligned} \rho &= \gamma_i \rho_1 + (1-\gamma_i)\rho_2 \\ \mu &= \gamma_i \mu_1 + (1-\gamma_i)\mu_2 \end{aligned} \tag{A.5}$$

In OpenFOAM, the implementation of the VoF method follows an advanced two-phase flow technique (Berberović et al., 2009) based on the Volume of Fluid (VoF) method of Hirt and Nichols (1981). To tackle the issue with the smearing of the interface, which

can cause diffusivity and damping of the numerical solution, especially in the cases of low mesh resolution where the finite thickness of the free surface becomes more apparent (Rudman, 1997), OpenFOAM incorporated the advanced algorithm MULES (multi-dimensional limiter for explicit solution). MULES guarantees boundedness of scalar field γ_i in order to improve the accuracy of the representation of the free surface(OpenCFD, 2012) and vastly reduce the smearing.

The VoF implementation with MULES in OpenFOAM was proven to be an effective method for simulating highly distorted free surfaces, such as overturning breaking waves, splashing (Bredmose and Jacobsen, 2010) and green water effects rising by strong FSI (Ransley, 2015). Minor defects of the VoF have been reported in cases when surface tension increases; however in most coastal and ocean engineering applications the surface tension forces can be considered negligible due to the examined scale (Higuera et al., 2013a). Nevertheless, issues have been observed in OpenFOAM for the simulation of steep focused waves related to wave damping and premature breaking due to unrealistic air velocities at the interface caused by the great density difference between the two fluids (Higuera et al., 2015; Afshar, 2010; Jacobsen et al., 2012). Another issue with VoF may be the high mesh resolution required at the interface. On static meshes, this is done by refining the cell size around the free surface. More advanced approaches include adaptive meshes that follow quadtree-grid schemes for splitting the cells of the interface in four (Greaves, 2004). However, the latter induce additional computational cost and potentially spurious short waves on the interface. Thus, these methods were not preferred in the present work.

Wave generation and absorption

OpenFOAM has appropriate solvers for simulating free surface flows, and a special set of boundary conditions is further required to simulate water waves for coastal and ocean engineering problems (Jacobsen et al., 2012). These boundary conditions should provide the appropriate time dependent velocity field and surface elevation at

the inlet boundary for generating waves and a way to absorb the waves at the outlet boundary of the NWT.

Wave generation

The wave generation in numerical models is performed with three basic approaches, as outlined in (Higuera et al., 2015):

1) Internal sources: the wave generation is achieved by a mass and momentum source in an internal region of the NWT, where water is pumped in and out, following an oscillatory pattern which creates waves according to a mathematical description that is linked to a wave theory. The generated waves are radiated in all possible directions in the NWT and care should be taken to effectively dissipate the waves at the boundaries (Perez-Collazo, 2017). This method is associated with increased length of the domain and additional computational cost.

2) Static boundaries: the Dirichlet-type boundary conditions are applied on a static boundary wall by prescribing the free surface elevation and the velocity or the pressure field according to a wave theory. This is possibly the most common way to generate waves in Eulerian solvers, but care should be taken when comparing experimental results from physical wavemakers, since the numerical boundary suppressing the the displacement waves and the evanescent modes (Higuera et al., 2013a).

3) Moving walls: this method attempts to replicate the movement of a physical piston- or flap-type wavemaker using either a transport function for the paddle derived from a wave theory or the displacement time history of the actual paddle allowing for direct comparison with the experiment. The advantage compared to the previous methods is that the volume of the water in the NWT remains constant. On the downside, this method requires a moving mesh technique and remeshing at every time step, inducing additional computational cost. For this reason, it is not popular for Eulerian solvers. Ideally however, it should give the best comparison with the experimental results with-

out having the physical limitations of the paddles, such as mechanical inertia.

In the present study, wave generation was performed with a static boundary. Moving walls could be an alternative for better comparison with experimental results, however this method became available in OpenFOAM in the context of IHFOAM (Higuera et al., 2015) long after the simulations had been completed. Additionally, for comparison with other numerical models, the most convenient method to use is the static boundary with appropriate wave theories.

Historically, the most general method to generate waves in OpenFOAM employs the "GroovyBC" boundary condition, which was distributed independently from OpenFOAM and allows the user to specify a set of non-uniform boundary conditions of the variables' gradients. However, it is an elementary approach since it can be used only for simple wave theories (Stokes linear and 2^{nd} order theory) and can consider only wet and dry cells on the boundary, resulting to initial disturbances due to castellated timeseries of the surface elevation at the inlet (Higuera et al., 2013a). The first attempts to generate ocean waves based on realistic sea JONSWAP spectra in OpenFOAM with the "ras-InterFoam" solver were done by Morgan and Zang (2010), showing that OpenFOAM was a promising tool for coastal engineering problems. In a similar study (Morgan et al., 2010), Stokes waves were simulated with a static boundary, since it was found that the simulation of a moving wall to replicate a piston-type paddle was significantly more computationally expensive, due to remeshing and turbulent structures on the paddle. It was also observed that instabilities occurred for highly nonlinear waves. Prior to these works, Bredmose et al. (2006) used a Boussinesq-type boundary condition instead of linear theory to better control the flux on the static boundary with the input signal obtained from the experiment after filtering out the reflected waves.

A step change for the wave generation capabilities of OpenFOAM came with the almost simultaneous release of the libraries are waves2Foam (Jacobsen et al., 2012) and IH-FOAM (Higuera et al., 2013a). To present, they are the most advanced and widely used libraries in OpenFOAM for wave generation and absorption. In both, a range of wave

theories, such as Stokes waves up to 5^{th} order, cnoidal and stream function theory, is available. Irregular waves can be produced as the linear summation of the wave components of the desired energy spectrum. Second order wave generation for irregular waves is also possible (Higuera et al., 2013a). The wave generation is performed on a static boundary by calculating the vertical position of the free surface and imposing the velocity profile of the waves beneath it and setting the air velocities to zero. The pressure is not imposed, because the problem would be overspecified; instead, it is calculated by appropriate boundary conditions available in OpenFOAM, e.g., "buoyantPressure". In addition to the fixed boundary, the options of a stationary replica of a piston-type paddle (Higuera et al., 2013a) and a moving piston-type wavemaker are available in IHFOAM (Higuera et al., 2015). The latter is able to mimic real wave tanks with single-paddle or multi-paddle wave generation for directional waves. The movement of the paddles can be computed theoretically or defined by measurements of the motion of the physical paddles. Issues with meshing regarding differential movement of adjacent paddles are treated with transition zones, making the simulations robust. This formulation of the moving boundary was based on the previous work of IH2VOF (Lara et al., 2011) and it does not require additional assumptions in defining the fluid variables. On the other hand, waves2Foam gives greater flexibility to use customised spectra (Vyzikas et al., 2014b) and include uniform currents to the wave field through the "combinedWaves" method. A set of pre- and post-processing utilities customised for wave studies is offered in both libraries and their features are frequently updated. For the latest advances the reader should refer to the online wiki and manuals, e.g., (Jacobsen, 2017). The main difference between waves2Foam and IHFOAM lies on the wave absorption technique that is applied both at the inlet and outlet boundaries, as discussed in the next section.

For the static boundary generation examined in the present study, both waves2Foam and IHFOAM use a sophisticated approach to define accurately the free surface on the faces of boundary cells accounting for partially wet cells. As such, the volume fraction of the cell its given by the ratio of the wet area of its faces over the total area of its

faces, specified as A_w/A_f, for a given location of the free surface elevation relative to the centre of the cell (Jacobsen et al., 2012). This technique together with appropriate interpolation schemes allow for smooth free surface on the boundary, minimising any spurious oscillations. Nevertheless, the present tests show that IHFOAM reproduces a "spiky" surface elevation at the inlet, which is not observed in waves2Foam, thanks to the inlet relaxation zone (Vyzikas et al., 2015). A similar issue of "toothing" at the inlet for the steep waves has been reported by Ning et al. (2009b) for a high order boundary element method (HOBEM) numerical tank. Despite the discrepancies at the boundary though, the propagation and the final results are almost identical between waves2Foam and IHFOAM.

Another aspect to be discussed in the context of irregular wave generation with a fixed boundary, which is relevant for focused waves, is the accuracy of the wave definition, since any errors at the boundary condition propagate in the domain affecting the final results (Higuera et al., 2013a). Linear wave generation (see Equations 3.2 and 3.3) are applied for simplicity and for saving computational resources (Higuera et al., 2013a), however, it results in an unrealistic wave field contaminated with spurious waves. To mitigate this, the second order solution of Sharma and Dean (1981) can be used, but it can induce high computational cost for a large number of wave components. As one of the first attempts to include a second order wave generation in waves2Foam, an external library was suggested by Hu et al. (2014)[1], but it resulted in unrealistic computational times. Before that, Vyzikas et al. (2013) used a linear superposition of 2^{nd} order waves, which accounts only for self-interactions, attempting to introduce nonlinearity on the boundary at minimal extra computational cost. In IHFOAM, second order wave generation was included in the initial release and thanks to the fact that no inlet relaxation zone is included, the computational cost is significantly lower compared to waves2Foam.

Other wave generation methods in OpenFOAM were developed by Chen et al. (2014),

[1] Some typos were also pointed out from the author on this paper and the code has been adjusted and the loop of the code was optimised.

who included custom boundary conditions similar to waves2Foam in order to advance the NWT of Morgan and Zang (2010), and by Paulsen et al. (2012). The latter method is of particular interest because it employs domain decomposition methods combining a potential flow solver (PFS) (OceanWave3D) and a RANS NWT in OpenFOAM that run concurrently, with the PFS feeding the boundary conditions of the CFD model (Paulsen et al., 2013b). This method provides realistic wave conditions to the CFD solver, including all the developed nonlinearity by the wave-wave interactions, due to the propagation of the wave field. Thus, it is superior to second order generation (Paulsen et al., 2014a). A similar approach was recently presented by Gatin et al. (2017) using a HOS solver instead of PFS. In the present study, since focused waves propagate for short distance, the domain decomposition method was not deemed necessary.

Wave absorption

The problem of wave absorption arises in confined numerical or physical wave tanks where waves cannot be freely radiated as in open ocean (Higuera et al., 2013a). Wave absorption aims at dissipating the incident wave energy at the outlet of the NWT in order to prevent reflections that can propagate upstream. Wave absorption methods are also applied at the wave generation boundary in order to counteract the incoming returning reflections from the numerical domain and to continue producing the target solution of the wavemaker. Two are the main techniques to absorb waves: active and passive absorption. The former refers to a moving paddle which adapts its movement to cancel the unwanted waves and the latter to a numerical or physical beach which is designed to destroy the incoming energy.

Passive absorption can be achieved by different means, which are all based on the principle of extending the domain to accommodate the area of energy dissipation. For example, waves can be dissipated by increasing the fluid viscosity (Westphalen et al., 2008), by increasing the cell size causing numerical dissipation (Zhao et al., 2010), by modelling an inclined beach as a structure where waves break, by imple-

menting a porous material or by simply extending the length of the domain for transient wave groups (Morgan et al., 2010). Alternatively, a damping zone can be considered where an artificial damping is added in the momentum equation (Chen et al., 2014). In waves2Foam, relaxation zones are used as passive absorption, where a target solution is specified and the solution of the domain is gradually altered to match the target values at the end of the relaxation zone (Jacobsen et al., 2012). Such a technique was first used in OpenFOAM in the NWT of Afshar (2010), but required very high resolution. It was further developed in the waves2Foam library, where the solution for each flow variable Ψ in the relaxation zone is partially calculated by the governing equations for the fluid (Ψ_{com}) and by a target value (Ψ_{trg}). Depending on the location in the relaxation zone, there is different weighting w_r, ensuring a smooth transition from the fully nonlinear domain to the linearised boundary, as seen in Equation A.6. w_r is calculated by a chosen function, e.g., exponential weight.

$$\Psi = (1 - w_r)\Psi_{trg} + w_r\Psi_{com} \tag{A.6}$$

Such approach allows for the employment of relaxation zones both at the inlet and outlet boundary, with target values the wave components from each wave theory and zero velocities, respectively. At the inlet, relaxation zones "extend" the solution of the boundary in the nonlinear domain. On one hand, as observed in the present study, this prevents local instabilities, protects the boundary from returning waves and allows for generation of very steep (even non-physical waves). However, it becomes apparent that the region of the relaxation zone should not be considered as a fully nonlinear domain, but as a semi-linearised solution, which can have important consequences when considering the evolution of nonlinear waves. The effectiveness of the relaxation zones is proportional to their length (Wei and Kirby, 1995) and in general they are considered a good solution for absorbing high frequency waves. They also have the advantage that can take different shapes and be implemented anywhere in the domain (Jacobsen et al., 2012) (Paulsen et al., 2014a).

One of the drawbacks with some passive absorption methods is the artificial increase of the volume of water in the NWT after long time (Méndez et al., 2001). This is due to the fact that relaxation zones result in no conservation of mass at least at the beginning of the simulation. More specifically, it was demonstrated that during the first 5-10 wave periods the increase of the water volume is 1% and it reaches its maximum of 2% after long simulation times (Jacobsen et al., 2012).

Relaxation zones in OpenFOAM have been used in many studies. Before the release of waves2Foam, Bredmose and Jacobsen (2010) simulated steep and breaking focused waves on monopiles using long inlet and outlet relaxation zones. Long inlet relaxation zones were also used in the study of Hu et al. (2014) and Alford and Maki (2015). Instead, Vyzikas et al. (2014b) used a very short relaxation zone (5 cm) in order not to influence the nonlinear propagation of the waves, but to control the instabilities on the inlet when steep waves are generated. Relaxation zones were also used in the middle of the domain to absorb the diffracted waves from the cylinder in a domain decomposition method showing that only 1% of the reflected energy remains (Paulsen et al., 2014a). In REEF3D inlet and outlet relaxation zones were implemented for studying focused wave group, but in agreement with the opinion of the author, it is mentioned that since wave groups are compact events, the inlet relaxation zone can be avoided (Bihs et al., 2017).

To overcome the deficiencies of passive wave absorption, such as the increases computational cost due to the added length in the domain and the increment in the mean water level due to the added volume, Higuera et al. (2013a) introduced an active absorption method based on the one suggested by Lara et al. (2011). Active absorption was first developed for physical paddles to allow for modifying their motion based on a measured signal in front of them, which acts as feedback (force or surface elevation), allowing them to continue generating the target signal after cancelling the incoming waves. When the target signal is the mean water level, the paddle acts as an absorbing boundary. The same principle can be applied in a NWT, as detailed in (Higuera

et al., 2013a) for a fixed wall or a moving paddle (Higuera et al., 2015). It was demonstrated that latter method prevents an increase of the mean water level due to the unbalanced inflow and outflow between wave crests and it is computationally efficient since the remeshing occurs only locally.

The active absorption in IHFOAM is based on the Shallow Water Equation (SWE), assuming uniform distribution of the velocity in depth (U_c). This approximation is consistent with the motion of a piston wavemaker. The incoming waves are absorbed by imposing an opposite velocity field on the boundary, which is calculated as $U_c = -\sqrt{g/h}\eta_R$, where g is the gravitational acceleration, h the depth and η_R the surface elevation of the incoming wave, which is found by subtracting the measured surface elevation from the target solution. To perform this, the boundary is split into three zones, defined from the measured and the theoretical level of the free water surface, that are treated differently. The cells at the interface of the fluids are assigned to a specific zone and, depending on their location, different operations are performed (Higuera et al., 2013a) to allow for both generation and absorption of the waves[2]. The moving paddle described in (Higuera et al., 2015) absorbs the waves with a similar logic, but, since it is moving, U_c is integrated to provide the displacement of the paddle (ΔX) per time step (Δt) via a transport function considering that $\Delta X = U_c \Delta t$.

The active absorption of IHFOAM can be readily expanded in 3D domains to absorb waves with directionality. The principle is the same, but instead of the free surface, the mean velocity in the vertical is calculated with its mean direction. Then, the mean incident velocity vector is analysed to the normal and the tangential components and the correction is done by imposing the opposite mean velocity to the normal component according to SWE theory. In 3D, wavemaking boundary is decomposed to a number of slices representing independent wave paddles, where the absorption is performed. An issue with 3D active absorption is that the wave component parallel to the wavemaker is not absorbed and it results in tangential propagating waves along the inlet boundary

[2]Assigning the boundary cells to a specific zone is speculated to cause the discrepancies observed on the inlet in the present study (see Figure 3.8).

that can grow and create cross modes in the tank. Another issue is that the direction in complex wave fields cannot be calculated with accuracy.

Both in 2D and 3D, active wave absorption demonstrated good performance resulting to reflection coefficients under or about 10% for some typical waves tested. Best performance is observed for long waves than for intermediate and deep water conditions (Higuera et al., 2013a), due to the inherent assumption of the SWE. Thus, for the broadbanded irregular focused groups of the present work, it is not trivial to predict the performance of this active absorption method.

Working experience with the waves2Foam and IHFOAM has shown that IHFOAM can simulate very steep waves on the inlet boundary without instability issues, but waves2Foam requires even a thin relaxation zone (Vyzikas et al., 2014b). It should be underlined that none of the two methods can absorb 100% of the incident wave energy and care should be taken not to include reflections in the region of interest in the NWT.

The general design of a NWT

In this section, some general aspects regarding the design of a NWT in CFD, and specifically in OpenFOAM, are presented that were collected by relevant studies. The scope is to highlight commonalities referring to boundary conditions and mesh design.

A very common approach that was been used by the author as well (Vyzikas et al., 2013) when reproducing numerically physical results is to simulate a shorter version of physical wave tank in CFD in order to save computational resources. Additionally, when the problems is two-dimensional, the computational effort can be reduced significantly by designing a quasi-3D mesh that behaves as a 2D mesh. Such examples of truncated 2D domains can be found in the works of Zhao et al. (2010); Westphalen et al. (2008, 2012) and Bihs et al. (2017), which all refer to the simulation of focused waves.

Another commonly used technique in free surface flows, aiming at both reducing the

computational cost and increasing the accuracy, refers to the refinement of the mesh around the free surface. For example, Morgan et al. (2010), Ransley (2015) and Vyzikas et al. (2017b) used the utility of OpenFOAM "snappyHexMesh" to refine the mesh according to quadtree method. This refinement is also performed in the regions of interest, such as the wavemaker (Westphalen et al., 2008, 2012) and the structure. A mesh grading technique can be also used in order to achieve a smoother transition from the fine to the coarse cells, e.g., (Bredmose and Jacobsen, 2010; Vyzikas et al., 2013, 2014b; Chen et al., 2014). It is recommended not to exceed the size ratio of 1.1 between adjacent cells (OpenCFD, 2012).

When simulating highly distorted free surfaces, such as steep and breaking waves, it is recommended to use square cells with aspect ratio (AR) of their faces close to 1. This is because in elongated cells there is an artificial advection along the long side due to the nature of the VoF methods, resulting in unrealistic results for free surface flows. This was confirmed by Jacobsen et al. (2012) who tested breaking waves with meshes of different AR cells, finding that square cells perform the best. Square cells were also employed by Higuera et al. (2013b) at the breaking zone and by Bihs et al. (2017) who simulated breaking waves and wave-cylinder interaction. The same practice was used in all the works of the author for the cells around the free surface, as seen in Figure 3.4.

A commonality regarding the wave generation boundaries concerns the definition of zero air velocities at the inlet. This is easily achieved in two-phase flows by multiplying the velocities at the inlet with the phase fraction, which is zero for the air phase. This practice is used in waves2Foam and IHFOAM. Similar method was applied by Chen et al. (2014), Westphalen et al. (2008) and Morgan and Zang (2010). Other issues with unrealistic air velocities in the domain causing slow-down of the simulation have been reported (Jacobsen et al., 2012), which could be controlled by setting the air velocities zero everywhere in the domain. Such an approach however can lead to excessive momentum transfer from water to air and damping of the waves. In the

study of (Vyzikas et al., 2017b), it was shown that similar issues can be partially solved by setting different $alphaC_o$ and C_o.

The boundary conditions for the side and the top and bottom walls of the NWT have commonalities among different studies. For the top boundary, early works (Bredmose et al., 2006) used a solid wall resulting in additional forces when the wave hit the ceiling the NWT. OpenFOAM has appropriate conditions, e.g., "pressureInletOutletVelocity", that allow a replication of an "atmospheric" boundary, where air can flow in and out, but water permanently leaves the NWT when it reaches the top wall (Jacobsen et al., 2012; Chen et al., 2014). Similar, in NWTs designed in other CFD software, (Westphalen et al., 2012) the top boundary allows only air to leave and enter. For the other walls of the NWT (side walls and bottom) and the surface of the included structures, usually a no-slip condition is used, which means that all the components of the velocity on the wall are set to zero (Chen et al., 2014; Vyzikas et al., 2013; Hu et al., 2014). Alternatively, a free-slip -also referred as slip condition-, which means that the all the velocity components apart from the tangential are set to zero, can be applied at the bottom (Jacobsen et al., 2012) and the structure, resulting in omission of the shear force component (Paulsen et al., 2013b). Free-slip is also applied on solid surfaces, when the viscous boundary layer is to be neglected (Paulsen et al., 2014a).

The treatment of turbulence is also an important aspect in CFD. As mentioned, in the present study, a laminar flow model was used, because the waves were not breaking and there was no FSI. Nevertheless, even when wave-structure interaction is simulated, the laminar flow model was shown to give good results (Morgan and Zang, 2010; Chen et al., 2014), which justifies the present selection.

A.1.3 Application to nonlinear wave problems

In this section some representative works for the simulation of water waves in CFD and particular in OpenFOAM are listed.

Regarding the wave transformation in coastal areas, the ancestor of IHFOAM, IH2VOF, employed two-phase flow RANS equations to study infragravity waves generated by focused waves breaking on a slope and illustrated the advantage of using advanced solvers for simulating nearshore processes and overcoming the limitations of SWE and Boussineq models (Lara et al., 2011). In one of the first studies of waves in OpenFOAM (Morgan et al., 2010), the "rasInterFoam" solver was used to simulate wave propagation over a submerged bar in the classic experiment of Beji and Battjes (1993), examining for first time wave-wave interactions in a qualitative way. Chenari et al. (2015) used OpenFOAM and waves2Foam for performing a qualitative comparison of different types of breaking waves with the theory. In a more detailed approach, Jacobsen et al. (2012) demonstrated that OpenFOAM and waves2Foam are capable of reproducing the free surface and kinematics of breaking waves on a slope. The most complete work is that of Higuera et al. (2013b), which refers to the validation of OpenFOAM and IHFOAM for coastal engineering problems including wave breaking, wave-structure interaction, interaction of a long wave with a transient wave group on a slope, rip current development in a 3D beach, wave induced run up in the surf zone and run-up on a conical island, which is relevant for the simulation of tsunamis. This studies demonstrated that CFD can offer unique insight in coastal engineering problems and apart for comprehending the underlying physics, contribute to the better design of coastal structures.

The majority of studies using CFD however refers to wave-structure interaction, where there is high nonlinearity. Most of the studies refer to wave-cylinder problems, commonly representing monopile foundations for wind turbines. The early work of Bredmose et al. (2006) on loads on offshore wind turbines under extreme conditions of combined irregular seas and currents was followed by the use of "interFoam" solver to simulate steep and breaking focused waves on cylinders (Bredmose and Jacobsen, 2010), highlighting the deviations from the classic force estimation with the Morison's equations. More realistic cases of monopiles of wind turbines with inspection platforms were simulated trying to interpret some reported accidents (Bredmose and Jacobsen,

2011). Morgan and Zang (2010) also used OpenFOAM to simulate wave load on a cylinder with some noticeable deviation in the nonlinear harmonics of the waves from the experiment. OpenFOAM and waves2Foam was used to generate focused waves on cylinders with good accuracy (Ransley et al., 2013; Paulsen et al., 2013a). Paulsen et al. (2012, 2014a) applied an integrated modelling technique combining a PFS with waves2Foam to simulate realistic seas and model accurately the FSI on a cylinder focusing on the third order harmonics of forces, which are associated with ringing. A similar integrated modelling approach with a HOS model and OpenFOAM was suggested by Lu et al. (2017). The physics of wave-cylinder interaction deducted from simulations in OpenFOAM and waves2Foam were presented in (Paulsen et al., 2014b). Chen et al. (2014) also used OpenFOAM to calculate the force harmonics up to 4^{th} order for wave-cylinder interaction and study the wave run-up on the structure.

Studies relevant to MRE applications in OpenFOAM include simulations of Oscillating Water Columns (OWCs) (Iturrioz et al., 2015; Vyzikas et al., 2017b; Simonetti et al., 2015), floating bodies (Ransley, 2015), tidal turbines (Gebreslassie et al., 2013; Santo et al., 2017), offshore wind foundations (Paulsen et al., 2013b) and extreme waves at MRE deployment sites (Ransley et al., 2013; Vyzikas et al., 2013).

A.1.4 Conclusion

OpenFOAM is a very useful open-source tool for the industry and research community, thanks to its versatility and rapid expansion. The libraries for the generation and absorption of waves can make OpenFOAM an established tool for coastal and ocean engineering studies. Despite the already presented validation cases, more in-depth validation and optimization of the NWT is necessary in order to make OpenFOAM a trusted tool for practical civil engineering studies. The work in the present study is in line with these objectives, demonstrating OpenFOAM's capacity to accurately propagate very steep wave groups.

A.2 SWASH

A.2.1 Introduction to SWASH

SWASH (Simulating WAves till SHore) is a general-purpose numerical model for rapidly changing flows and wave transformation at arbitrary water depth which solves the non-linear shallow water equation (NLSWE) with a non-hydrostatic pressure assumption. SWASH was developed in TU Delft and it is an open-source software freely distributed under the GNU General Public License. The code is written in FORTRAN and its structure resembles the well-established spectral model SWAN. It can be compiled in Windows, Linux and Mac OS X operating systems for serial or parallel runs using the message passing environment MPI and a grid partitioning stripwise method to assign parts of the decomposed domain to different processors. Together with the solver, pre- and post-processing tools are provided in order to insert and extract the relevant flow variables. The first release of the model was in 2011, referring to version 1.02 and the latest release is version 4.01. For the simulations in the present work, version 3.14 was used, which had incorporated already all the physics and numerical techniques for the propagation of steep non-breaking waves over constant depth.

Thanks to its non-hydrostatic NLSWE formulation, SWASH can be used to simulate free-surface rapidly varying flows, without requiring special parameterizations. Such flows include coastal flooding, hydraulic jumps and in the context of waves, wave propagation over varying bathymetry, frequency dispersion, tsunamis, nonlinear wave-wave interactions, wave transformation in coastal areas (shoaling, refraction, diffraction and reflection), wave-current interactions, wave-induced currents, wave runup, surf and swash zone hydrodynamics, wave overtopping, turbulence and wave breaking with a bore similarity (The SWASH Team, 2017). SWASH was developed to be a flexible tool that can be applied to different space and time scales ranging from field to laboratory studies. As such, SWASH has been also validated against experimental results, as described later in this section.

The numerical implementation of the NLSWE is performed on a staggered grid for the calculation of the flow variables based on the FVM. The domain is bounded by the sea bed and the free surface. The computational efficiency of SWASH lies on the $\sigma-$transformed vertical grid, which forms layers of varying thickness, and on the Keller-box method, as elaborated below. A semi-implicit time integration is used to solve the incompressible NSE, averaged per layer, aiming for both numerical robustness as well as a good balance between computational efficiency and accuracy (Zijlema and Stelling, 2005). The development line of SWASH started with the preliminary studies of Stelling and Zijlema (2003), who used the Keller-box scheme in non-hydrostatic NLSWE; Zijlema and Stelling (2005), who developed the solver for the Poisson equation for the pressure; Stelling and Duinmeijer (2003) for conserving the momentum on staggered grids and Zijlema and Stelling (2008) that presented an efficient wet-drying algorithm for the prediction of the moving shoreline. SWASH was presented in (Zijlema et al., 2011) and since then developments for depth-induced wave breaking have been introduced (Smit et al., 2013). Especially, regarding the latter very challenging process of wave breaking, SWASH considers a single-value free surface and a bore analogy, modelling breaking as moving hydraulic jump with energy dissipation.

SWASH exhibits several advantages compared to other phase-resolving numerical models. Over RANS or SPH solvers that can describe the details of overturning flows, air-entrainment and wave-induced turbulence as well as realistic FSI, SWASH has the advantage of computational efficiency, which allows for real-life applications, while it can still replicate the bulk properties of breaking with reasonable accuracy. Compared to Boussinesq-type models, SWASH improves the accuracy of the wave dispersion by simply increasing the number of vertical layers, instead of increasing the order of derivatives. The latter is not trivial to implement numerically because it may cause potential instabilities due to short waves (The SWASH Team, 2017). The accuracy of Boussinesq models and SWASH is comparable for intermediate water depth (Zijlema et al., 2011) and, additionally, SWASH can be applied in deep water conditions by increasing the number of layers. Using one vertical layer essentially results in a hy-

drostatic (depth-averaged) model. All these advantages and flexibility make SWASH a favourable choice.

A.2.2 Mathematical formulation

Non-hydrostatic modelling

The first developments in non-hydrostatic modelling of water waves took place in the 90s, because there was a lack of accurate and efficient modelling practice, especially for the propagation of short waves or in cases where frequency dispersion and nonlinearities become considerable. The methods for the non-hydrostatic pressure computations are elaborated in (Zijlema and Stelling, 2005) and some necessary information that distinguish SWASH from other models are described here.

Non-hydrostatic modelling is based on the solution of the NSE or Euler equations by splitting the pressure into hydrostatic and non-hydrostatic. Commonly, the fractional step method is applied, which consists of two steps: first, the velocity field is obtained from the momentum equations and the free-surface conditions considering only hydrostatic pressure; at the second step, the velocity field is used to solve for the non-hydrostatic pressure a Poisson-like equation. However, this method has the drawback of introducing a splitting error, because the advection is not connected to the pressure gradient, making this scheme only first order accurate in time. Immediate impacts on the waves are inaccurate dispersion and significant damping. To mitigate this issue, a number of approaches have been proposed, such as performing a correction for the water level during the second fractional step by using a hydrostatic pressure assumption for the cells below the free surface or by solving first the Poisson equation for the non-hydrostatic pressure and then correcting the velocities, which are finally used to find the free surface.

The solution strategy in SWASH is different: instead of the fractional time step method, a projection method is used, which is referred as pressure correction technique, de-

composing the pressure into a hydrostatic and a non-hydrostatic part. Thus, there is no splitting error and the waves propagate without damping (The SWASH Team, 2017). According to this approach, the pressure and advection are not split, but a prediction-correction process is performed between the pressure and the velocity. This process first solves the momentum equations using the non-hydrostatic pressure from the previous timestep and hydrostatic pressure to obtain an estimate of the velocity field at the examined timestep. Next, the Poisson equation is solved using an efficient and stable preconditioned Krylov subspace technique to find the difference between the new and the old non-hydrostatic pressure by tanking the divergence of the momentum equations under the consideration of the incompressibility assumption. The advantage of this method is that the correct surface elevation is calculated by the pressure and that it is second order accurate in time. (Zijlema and Stelling, 2005).

The boundary conditions at the free surface consider automatically zero pressure, achieved by the continuity of the normal stresses. Thus, there is no need to specify artificial boundary conditions, thanks also to the fact that in incompressible flows there is no equation of state. An advantage is that the pressure is considered exactly at the free surface. SWASH uses the previously described method to find the velocity and pressure at the free surface, while other approaches enforce the non-hydrostatic pressure to zero and compute the velocity from the continuity equation, which can yield inaccuracies to the wave celerity (Zijlema and Stelling, 2005).

The governing equations of the flow are presented next, referring to he NLSWE, which can be derived from the incompressible NSE (Zijlema and Stelling, 2008). The vertical acceleration is induced as a result of the non-hydrostatic pressure gradient, calculated from the NLSWE, assuming that both advection and diffusion terms are negligible compared to it.

The governing equations of the one-dimensional (1D) depth-averaged non-hydrostatic free surface flow described by the non-conservative form of the NLSWE are presented in Cartesian notation in Equations A.7 and A.8. They are derived from the

two-dimensional form (Zijlema et al., 2011) after some substitutions by considering zero bottom friction ($c_f = 0$), no turbulent stresses ($\tau_{ij} = 0$) and negligible eddy viscosity ($v_t = 0$ and thus $\tau_{ij} = 0$), since non-breaking waves over a flat smooth bottom and in absence of strong sheared currents (Rijnsdorp et al., 2014) are considered in the present study.

$$\frac{\partial \zeta}{\partial t} + \frac{\partial hu}{\partial x} = 0 \tag{A.7}$$

$$\frac{\partial u}{\partial t} + u\frac{\partial u}{\partial x} + g\frac{\partial \zeta}{\partial x} + \frac{1}{2}\frac{\partial q_b}{\partial x} + \frac{1}{2}\frac{q_b}{h}\frac{\partial(\zeta - d)}{\partial x} = 0 \tag{A.8}$$

where t is time, x and z located at the still water level (SWL) and the $z-$axis pointing upwards, $\zeta(x,t)$ is the surface elevation measured from the SWL, $d(x)$ is the water depth calculated from the SWL, $u(x,t)$ is the depth averaged flow velocity in $x-$direction, g is the gravitational acceleration, $q(x,z,t)$ is the non-hydrostatic pressure (normalised by the density), which is calculated here from the non-hydrostatic pressure at the bottom q_b. $h = \zeta + d$ is the instantaneous water depth or total depth.

The non-hydrostatic pressure q_b can be computed by employing the Keller-box method (Lam and Simpson, 1976) (discussed later), as seen in Equation A.9. Note that the non-hydrostatic pressure at the free surface is zero, since the atmospheric pressure is disregarded. As such, the pressure p can be decomposed into a hydrostatic part p_h and the non-hydrostatic part q: $p = g(\zeta - z) + q = p_h + q$ (Stelling and Zijlema, 2003).

$$-\frac{q_b}{h} = \frac{1}{2}\frac{\partial q}{\partial z}|_{z=\zeta} + \frac{1}{2}\frac{\partial q}{\partial z}|_{z=-d} \tag{A.9}$$

Then, the velocity in $z-$direction at the free surface w_s and at the bottom w_b are calculated from Equations A.10 and A.11, respectively. This practically shows that the gradient of the pressure determines the vertical acceleration.

$$\frac{\partial w_s}{\partial t} = \frac{2q_b}{h} - \frac{\partial w_b}{\partial t} \tag{A.10}$$

$$w_b = -u\frac{\partial d}{\partial x} \tag{A.11}$$

The mass conservation at an infinitesimal water column can then be expressed from the vertical velocity averaged over the depth and horizontal velocity gradient, as seen in Equation A.12.

$$\frac{\partial u}{\partial x} + \frac{w_s - w_b}{h} = 0 \tag{A.12}$$

The expression for the free surface (Equation A.7) is also derived by considering a mass balance for a slice in the vertical for the water column (Rijnsdorp et al., 2014). It now becomes apparent that Equation A.8 refers to the momentum equation.

The governing equations are solved using the FVM and finite differences on a staggered grid in order to avoid de-coupling of the velocity and the pressure, which can cause non-physical oscillations and instabilities in colocated grids (Zijlema et al., 2011) (see also Section A.1.2 for OpenFOAM). The velocities are found at the center of the cell faces, while the pressure can be found at the cell centre (standard layout), or at the centre of the horizontal cell face at the intersection between to neighbouring layers (box layout, seen in Figure A.1) (The SWASH Team, 2017).

The Keller-box

The Keller-box method (Keller, 1971) gives accuracy and efficiency to SWASH for modelling waves. This scheme is also referred as Preissmann scheme and Hermitian or spline method (Lam and Simpson, 1976). It was implemented in SWASH for resolving the vertical pressure gradient, as described in (Stelling and Zijlema, 2003). According

to this scheme, the pressure is evaluated at the cell face -for this reason it is called edge-based scheme- and as a result, it can directly assure zero pressure at the free surface, which allows for accurate evaluation of the non-hydrostatic pressure using only a small number of vertical points. Such consideration is effective for simulating short waves with few or even one vertical point (depth averaged mode), which is almost impossible for the standard layout that requires 10-20 points for the same accuracy.

This compact differences scheme works in two steps using the values of the vertical pressure gradient ($\partial q/\partial z$) from two subsequent cells. For reference, see Figure A.2. At the first step, $\partial q/\partial z$ is approximated by the $w-$momentum equation at $z_{k-1/2}$ by means of forward differences and at $z_{k+1/2}$ by means of backward differences. At the second step, the average of the two calculated values is found, yielding $\partial q/\partial z$ at the cell centre located at k, as explained in (Zijlema and Stelling, 2005).

The Keller-box technique in NLSWE can be regarded as a discrete equivalent of the Boussinesq models by solving for the non-hydrostatic pressure simultaneously at a finite number of grid points. As a result, the accuracy of frequency dispersion in shallow water is similar to Boussinesq models by using only 1-3 layers. This discretization method, together with the $\sigma-$transformed grid allows SWASH to model the physics of nonlinear wave transformations in shallow water with a relative coarse vertical resolution and also have a small phase velocity error of 1% in deeper water (Rijnsdorp et al., 2014). For high vertical resolution of over 20 layers, however, the standard layout should be chosen for greater stability (Smit et al., 2013).

$\sigma-$transformed grid

The second characteristic that makes SWASH efficient and flexible is its vertical meshing technique: the transformable σ grid. This refers to a curvilinear grid, which can be stretched between the free surface and the bottom in order to represent the motion of the fluid. Assuming that the fluid elements are connected in a unique way in the vertical direction (no overturning waves), a σ-transformed grid can be advantageous from

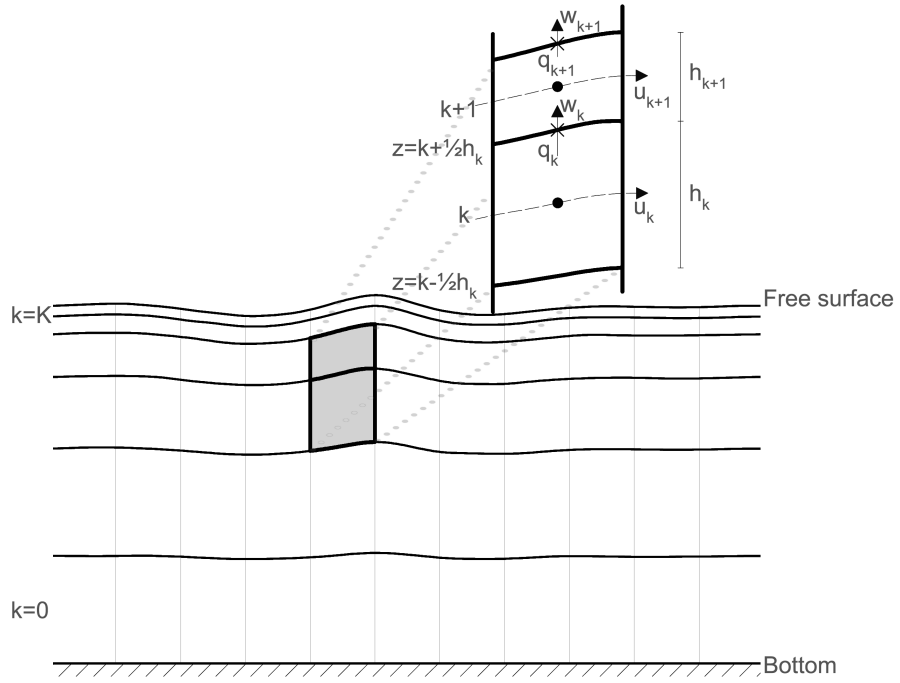

Figure A.1: Staggered grid for velocities and pressure used in SWASH on the $\sigma-$transfomed vertical grid. Layers' thickness and horizontal discretization are indicative.

a numerical point of view, because the grid follows the vertical expansion and contraction due to the waves without the need for remeshing. The computational nodes stay vertically aligned, which allows for implementation of high order numerical schemes for the calculation of the flow variables without smoothing. Such a method was employed initially for a finite element PFS (Turnbull et al., 2003), in a fashion similar to that used in SWASH, where new techniques were applied to minimize the truncation errors (Stelling and Zijlema, 2003). For operational applications, where there might be considerable variations of the water depth, the $\sigma-$transformed grid employed in SWASH exhibits an important advantage compared to fixed Cartesian grids. In the latter, the time step can become prohibitively short to satisfy the Courant condition. However, the flexible grid of SWASH can result in bigger cells and subsequently larger timesteps, offering computational efficiency. Moreover, the conservative character of the FVM in combination

with transformable layers guarantee accurate calculation of nonlinear waves when the vertical flow structure is important (Zijlema and Stelling, 2005).

In more detail, the computational grid of SWASH is structured consisting of non-overlapping cells that have the same number of neighbours (apart from the cells with faces at the boundaries). The vertical discretization is realized with a fixed number of layers that have absolute (constant) thickness or varying thickness relative to the water depth[3]. Figure A.1 shows an example of the grid used in the present study near the focal location. In the horizontal direction, a uniform distance between the grid points is used. In the vertical, the fluid domain is discretized with K layers ($k = 0...K$), with the bottom layer being $k = 0$ and the free surface $k = K$. The grid points (black dots) of the same layer form a streamline that defines the centre of the layer. The thickness of a layer k is defined as h_k. The interface between two adjacent layers k and $k+1$ is located at $z = k+1/2h_k$. The staggered arrangement of velocities and the hydrodynamic pressure (q_k) it becomes now apparent: the horizontal velocity u_k and vertical velocity w_k are defined at the middle of the the vertical and horizontal cell face, respectively, while q_k is defined at the same location as w_k according to the Keller-box scheme. The vertical velocity at the free surface and bottom is zero and the horizontal velocity can be found at the interface of two layers as the weighted average of the velocities at the adjacent cell centres: $u_k(z_{k+1/2}) \approx \frac{u_k h_{k+1} + u_{k+1} h_k}{h_k + h_{k+1}}$ (Zijlema and Stelling, 2005). For regions of tidal flats, special care is taken in SWASH so that the water depth does not become smaller than the layer's thickness by considering a drying and flooding procedure.

Time integration

The space-discretized governing equation yield a set of ordinary differential equations that should be time-marched using appropriate time integration schemes. A projection method is followed for the calculation of the pressure which requires the solution of the Poisson equation, which is done by employing BiCGSTAB (Biconjugate gradi-

[3]Note that at least one layer should be defined in a relative way in order to allow for changes of the water elevation.

ent stabilized method) with ILU preconditioner (Zijlema and Stelling, 2005). The time integration of the continuity and momentum equations can be performed using an explicit second-order leapfrog scheme, which prevents damping and results in accurate dispersion (The SWASH Team, 2017). As an alternative, which is favourable for large scale applications, an explicit time integration can be used for horizontal advective and viscosity terms and a semi-implicit for the pressure gradients and the free surface. The latter approach is unconditionally stable, since it is not limited by the wave celerity.

The explicit time integration schemes require additional stability criteria in order to control the magnitude of the time step. In SWASH, the well-known Courant condition is used, as expressed in Equation A.13 for 1D problems. Therefore, the timestep can be dynamically adjusted assuring accuracy and computational efficiency, using the optimum timestep size (The SWASH Team, 2017).

$$C_o = \frac{\Delta t(\sqrt{gd}|u|)}{\Delta x} \leq 1 \tag{A.13}$$

where $\sqrt{gd}$ is the wave celerity in shallow water.

The semi-implicit method uses a θ-scheme, which for stability should be selected as $\frac{1}{2} \leq \theta \leq 1$. Selecting $\theta = \frac{1}{2}$ yields the second-order accurate Crank-Nicolson scheme, while $\theta = 1$ results in the first-order backward Euler scheme.

In the present study an implicit time integration method was used for the continuity equation, water level gradient and vertical terms using the Crank-Nicolson scheme. The momentum equations were integrated using the second order backward difference (BDF) upwind scheme in both horizontal and vertical advective terms. More alternative can be found in the User's manual (The SWASH Team, 2017).

Wave-generation and absorption

SWASH requires an appropriate set of boundary conditions at the i) free surface, ii) bottom iii) offshore (wave generation and absorption) and iv) shoreline, for the velocity components and the stresses, which are calculated only by the pressure, since the viscous stresses are ignored (Zijlema and Stelling, 2005).

The kinematic and dynamic boundary conditions at the free surface and bottom dictate that no fluid particle can leave the free surface or penetrate the bottom (Rijnsdorp et al., 2014). At the free surface, the vertical velocity component w_s is found from the conservation of local mass (Equation A.12). The horizontal component can only be interpolated from the vertical cell face. The tangential and normal stresses are zero because the effects of wind and surface tension are neglected. At the bottom, the normal velocity w_b is found by Equation A.11 and the tangential stresses are ignored, while the normal stress are found using Equation A.9. The shoreline can be modelled as moving with wet and dry cells, ensuring non-negative water depth (The SWASH Team, 2017). At other closed boundaries in the domain, such as lateral walls, free-slip condition is used by enforcing the normal velocity and tangential stress to zero.

Wave generation is realised at the inflow boundary, where the normal velocity component from linear wave theory is imposed and the tangential velocity is set to zero. Since the momentum equation for the normal velocity is not solved at the inflow boundary, there is no need to define boundary conditions for both the water elevation and the non-hydrostatic pressure. A ramp-up time can be also used to prevent instabilities at an initially calm NWT (Stelling and Zijlema, 2003). The wave generation of SWASH can also account for irregular wave generation based on a predefined spectrum. In the present study, the free surface elevation is specified in terms of Fourier series. For the corrections of the focusing methodology, external tools were developed in MATLAB that prepare the input files and post process the output of SWASH to create files of timeseries per WG, position of the layers and velocity fields. Internal wave generation is not available in the main distribution of SWASH, however it has been implemented by

Zhang et al. (2016). A "partial" second order wave generation is available in SWASH, using the "ADDBoundwave" command, which can be used to add the bound long wave sub-harmonic and thus, minimize the spurious free long wave, but it does not account for the bound quadratic super-harmonics.

Wave absorption is performed at the outflow boundaries where the waves are dissipated or freely-radiated. Dissipation can be achieved by the inclusion of a sponge layer at the end of NWT and extending the computational domain by 1-3 times the typical wave length (The SWASH Team, 2017). At the end of the sponge layer the solution is prescribed to the SWL, i.e., the water level, the non-hydrostatic pressure and the horizontal velocity are set to zero (Stelling and Zijlema, 2003). Alternatively, the waves can be freely radiated by using the Sommerfeld radiation condition, which allows the waves to freely cross the boundary by prescribing a linear estimation for the wave kinematics on the outlet boundary. As such, the free surface elevation and the tangential velocity components are imposed based on Equation A.14 using the shallow water approximation for the wave celerity and the hydrostatic pressure assumption (Zijlema and Stelling, 2005). Consequently, this approach is more effective for long waves. Note that sponge layers and Sommerfeld boundary conditions can be used in combination to achieve better radiation of the outgoing waves. In this case, the damping coefficient of the sponge layers vanishes towards both ends of the sponge layer in order to allow for smooth transition between the waves in the NWT and defined kinematics at the outlet (Stelling and Zijlema, 2003).

$$\frac{\partial \psi}{\partial t} + \sqrt{gh}\frac{\partial \psi}{\partial t} = 0 \tag{A.14}$$

where ψ refers to either the free surface elevation and the tangential velocity component.

Apart from preventing reflections at the outlet boundary, the Sommerfeld condition can be applied on the inlet boundary in order to protect the wave generation from returning

waves from the NWT. For that, a weakly reflective boundary condition is used, which specifies a horizontal velocity distribution normal to the boundary. This is known as the Flather condition (Blayo and Debreu, 2005). As seen in Equation A.15, this condition is based on the shallow water approximation and calculates a corrected velocity u_{in} based on the difference between the incident target free surface elevation (ζ_{in}) and the measured one at the boundary. This technique resembles the active wave absorption of IHFOAM. On the other hand, sponge layers are equivalent to the relaxation zones used in waves2Foam, as discussed in Section A.1.2.

$$u_{in} = \pm\sqrt{\frac{g}{h}}(2\zeta_{in} - \zeta) \tag{A.15}$$

A.2.3 Applications

There is a wide range of applications in scientific publications that use SWASH. The up-to-date list of publications can be found at (SWASHweb, 2017). Some standard comparison cases with experimental results include standing waves, propagation of regular and transient waves, wave runup on a plane beach and propagation over submerged bars. Most of these tests were employed to test the gradual advances in non-hydrostatic modelling during the development process of SWASH. There are also studies of large scale applications.

Standing waves were used by Turnbull et al. (2003) to test the $\sigma-$transformed grid and the Keller-box for preventing wave dumping even for deep water waves (Stelling and Zijlema, 2003), showing its superiority to the standard layout for the non-hydrostatic pressure (Zijlema and Stelling, 2005). SWASH was tested for a regular progressive wave in a flume showing good accuracy in all water regimes, with a small phase velocity error in deeper water (Zijlema et al., 2011). The propagation of a bichromatic wave group (consisting of two wave components) was examined in SWASH for the emergence of second order bound waves, showing good agreement, but a small phase difference, with the analytical solution (Rijnsdorp et al., 2012). A solitary wave was

modelled using the Keller-box, but noticeable discrepancies in its shape were observed (Stelling and Zijlema, 2003). Turnbull et al. (2003) tested focused wave groups against the experiments of Baldock et al. (1996), showing some discrepancies due to high order nonlinearities. To the author's best knowledge, that was the only application of $\sigma-$transformed grids on focused waves before the study of Vyzikas et al. (2015) and the present Thesis.

Wave transformation over submerged obstacles, such as reefs or submerged breakwaters, is very relevant to coastal engineering studies. Stelling and Zijlema (2003) tested the non-hydrostatic model with Keller-box against the experimental results of Beji and Battjes (1993). Later, Zijlema and Stelling (2005) improved the solution with the Poisson equation, but both studies reported errors behind the bar. Stelling and Zijlema (2003) and Zijlema and Stelling (2005) also examined a similar case for the 2D problem of waves passing over a submerged shoal, testing the ability of the model to simulate refraction, diffraction and wave focusing behind the obstacle. A recent study employed SWASH to examine the optimum layout of two submerged breakwaters for the attenuation of regular and irregular waves in the presence of collinear and opposing currents, after validation with a single breakwater (Liang et al., 2015). In another study, SWASH was used with an internal wave generation in order to estimate the wave transmission coefficients over submerged breakwaters and build new empirical formulae for a JONSWAP spectrum, after validating a two-layer NWT with experimental results for a low-crested breakwater (Zhang et al., 2016).

The simulation of runup on a beach is also very important for coastal defence purposes. The wetting and drying algorithm of SWASH showed good performance in a number of studies, such as regular wave runup on a slope (Zijlema and Stelling, 2008), long wave (tsunami) runup on a plane beach and runup of solitary waves on a conical island (Zijlema et al., 2011). SWASH was also tested for the propagation of a tsunami over complex bathymetry against experimental and analytical solutions (Zijlema et al., 2011). The propagation of irregular waves over a slopping beach that includes a bar

demonstrated good agreement with experiments for the spectral evolution due to wave transformation (Zijlema and Stelling, 2008) as well as similar qualitative results to the phase-averaged model SWAN, which used the Lumped Triad Approximation (LTA) (see Section A.4.4).

SWASH was also compared against experimental results for irregular waves breaking on a slope of complex bathymetry (Zijlema et al., 2011), showing very good qualitative comparison for the transformation of the energy spectra (Suzuki et al., 2017). More detailed validation for breaking waves using the bore similarity was performed by Smit et al. (2013) for regular and irregular waves. Other tests include circulating flow for waves breaking over a submerged breakwater in a 2D basin (Smit et al., 2013) and wave-induced circulation in the case of rip currents, which are created due to wave breaking over a longshore varying bathymetry (Zijlema et al., 2011).

An important phenomenon in operational coastal engineering is the release of infra-gravity (IG) waves, as a consequence of wave breaking on a beach. IG waves are also known as surf-beats and have a period of 20-250 s. IG waves can cause harbour resonance, influence sediment dynamics and beach erosion (Rijnsdorp et al., 2012). SWASH was compared against experimental results for a wide range of IG waves propagating over plane and barred beach, showing good agreement with the measurements for the bulk parameters of the wave evolution, such as the root mean square (H_{rms}) wave height, mean wave period, wave dissipation, shoreline reflection and nonlinear wave-wave interactions (Rijnsdorp et al., 2014). The challenge from a numerical point of view is that while short waves are almost perfectly dissipated on a beach, IG waves are partially reflected to the inlet (Rijnsdorp et al., 2012). For such cases, the weakly reflective boundary and "ADDBoundwave" options of SWASH can be very useful (Rijnsdorp et al., 2014).

Overtopping is another very important parameter for the design of coastal defence structures, especially considering the sea level rise. Overtopping is challenging to measure experimentally and model numerically, due to intense wave breaking, sepa-

ration of the fluid from the bottom and spraying, which cannot be modelled by SWASH. However, the model can be used to capture the bulk properties of overtopping. SWASH was employed to study wave overtopping over a coastal dike and its performance was compared with experimental results for the surface elevation, but also for the kinematics obtained by the SPH model DualSPHysics, showing reasonable performance (St-Germain et al., 2014). In contrast with St-Germain et al. (2014) that used many layers, Suzuki et al. (2017) used SWASH in the depth-averaged mode (single layer) and demonstrated that it was still possible to capture bulk parameters of overtopping, at least as accurately as the existing empirical formulae, missing only single violent events that can however have a high impact on the discharge.

SWASH was employed for large scale applications, such as the storm events in Tramandai Beach in Brazil (Guimarães et al., 2015) that resulted in runup and inundation. SWASH was used in an integrated modelling approach combined with WAVEWATCH III and SWAN, in order to model the detailed wave transformation and runup close to the shore and at the urban region, offering important insights for coastal management and civil protection.

Other applications of SWASH refer to the modelling of vegetation, sediment transport, wind and porosity (The SWASH Team, 2017). The capabilities of SWASH keep expanding making the model more applicable for realistic studies. For example, Rijnsdorp et al. (2017) suggested an efficient subgrid approach to model the wave-induced currents, which are commonly under-resolved in coastal scale applications, despite their important role associated with sediment transport, dispersion of pollutants and generation of hazardous rip currents. Regarding the modelling of FSI, a new method was suggested by Rijnsdorp and Zijlema (2016) for simulating a fixed floating body in SWASH, using a coupled approach of a free surface and a pressurized fluid under the body. The advantage of implementing FSI in SWASH is that a single model can be used to simulate the evolution of the waves from the far-field as well as their interaction with the structure.

A.2.4 Conclusions

The developments in non-hydrostatic modelling, such as the $\sigma-$transformed vertical grids, the implementation of the Keller-box layout, the efficient calculation of the pressure from the Poisson equation as well as the representation of the wave breaking, resulted in the robust, accurate and computationally efficient numerical tool SWASH. Thanks to its characteristics, SWASH can be applied at different temporal and spatial scales and allow for modelling of both wave dispersion in deep water and surf zone.

SWASH comprises a valuable tool for operational coastal engineering applications as well as scientific research, showing several advantages over the NSE and Boussinesq solvers. In the present study, the merits of SWASH have been exploited to model strongly nonlinear wave-wave interactions in focused wave groups and validating the model and validate the model for this problem for first time.

A.3 High-order spectral method

A.3.1 Introduction to HOS

The HOS-ocean and HOS-NWT models have been developed at the LHEEA laboratory of Ecole Centrale de Nantes (ECN) and they are freely distributed under GNU General Public License. They were released in 2016 (Ducrozet et al., 2016b) and 2012 (Ducrozet et al., 2012a), respectively. These are the latest versions of a long line of development of similar codes for the propagation of waves, such as SWEET (spectral wave evolution in the ECN tank) (Bonnefoy et al., 2006a), SWENSE (Spectral Wave Explicit Navier-Stokes Equations) and HOST (High Order Spectral method Tank) (Ducrozet et al., 2006).

HOS is a pseudo-spectral method, because it evaluates the spatial derivatives of the flow variables in the Fourier space, but the products of the examined quantities are performed in the physical space (Ducrozet et al., 2016b). HOS-ocean and HOS-NWT

models share the same equations and solving techniques and essentially, they only differ at the treatment of the boundary conditions; HOS-ocean has periodic boundaries representing an infinite circulating ocean, while HOS-NWT has a bounded domain with wave generation and absorption boundary conditions and reflective walls elsewhere. At present, the models can simulate wave propagation on finite depth, but they cannot treat variable water depth and breaking waves. Also, there are restrictions to the wave steepness in order to prevent simulation of unrealistic waves. Together with the distribution of the codes come specially developed post-processing tools and routines to allow coupling with other models, such as SPH (Ducrozet et al., 2016a) or WAVEWATCH III.

A.3.2 Mathematical formulation

Traditionally, the modelling of nonlinear wave propagation without wave breaking is performed with PFS, usually employed with Boundary Element Methods (BEM). However, the computational cost of such approaches is restrictive for simulating large domains and long-term evolution of sea states. An alternative to that is the use of the fully nonliear ZE, as suggested by Dommermuth and Yue (1987) and West and Brueckner (1987). The formulation of West and Brueckner (1987) uses the full nonlinearity of the ZE and does not consider a truncation at 3^{rd} order in the mode amplitudes. The wave interactions are not restricted to those at or near resonance, as done originally by Zakharov (Zakharov, 1968), because the field quantities (surface displacement and velocity potential) and their gradients are evaluated without the need to distinguish between resonant and non-resonant interactions. This evaluation is performed in the spectral space using the FFT algorithm, making this approach fast to converge and very computationally efficient.

The HOS scheme is based on an expansion about the free surface, which is used as a reference, considering a continuous spectrum. Thus, this HOS approach is not valid if the reference surface is shifted or when very different wave lengths and amplitudes

are examined. Issues in HOS modelling can be caused if the waves are close to breaking and when large Courant numbers are encountered Dommermuth and Yue (1987). Other challenges refer to aliasing and the initialization of the nonlinear simulation with a linear condition, which have been carefully treated in HOS-ocean and HOS-NWT following Dommermuth (2000)

Since the mathematical formulation of HOS-ocean and HOS-NWT is identical in the domain and different only on the boundaries, an effort is done here to present the equations in a consistent manner from the relevant publications. As such, some variables have been changed. The reference coordinate system of the rectangular fluid domain is Cartesian and its beginning is located at one corner with $x-$ and $z-$ representing the horizontal and vertical axis respectively. The vertical axis is positive upwards and $z=0$ is located at the mean water level.

The fundamental assumption of potential flow theory is the consideration of an irrotational, inviscid, incompressible fluid allowing for the continuity equation to be expressed in the form of Laplace equation for the velocity potential ϕ, as seen in Equation A.16 (Ducrozet et al., 2016b).

$$\nabla^2\phi + \frac{\partial^2\phi}{\partial z^2} = 0 \tag{A.16}$$

where ∇ is the horizontal gradient operator (∂_x, ∂_y).

Next, the kinematic and dynamic boundary conditions at the free surface have to be defined (Equations A.17 and A.18) in order to close the system of equations following the formulation of Zakharov (1968). Since non-breaking waves are considered, the free surface is a single-valued variable at any location in the domain.

$$\frac{\partial\eta}{\partial t} = \left(1+|\nabla\eta|^2\right)W - \nabla\tilde{\phi}\cdot\nabla\eta \tag{A.17}$$

$$\frac{\partial \tilde{\phi}}{\partial t} = -g\eta - \frac{1}{2}|\nabla\tilde{\phi}|^2 + \frac{1}{2}\left(1+|\nabla\eta|^2\right)W^2 \tag{A.18}$$

where η is the free surface elevation, $\tilde{\phi}(x,t) = \phi(x,z=\eta(x,t),t)$ is the velocity potential at the free surface and W is the vertical velocity at the free surface $W = \frac{\partial\phi}{\partial z}(x,z=\eta,t)$ as expressed by West and Brueckner (1987).

The sea bed is considered impermeable and the bottom boundary condition reads:

$$\frac{\partial\phi}{\partial z}(x,z=-h,t) = 0 \tag{A.19}$$

The use of FFTs is the core of the solution process for the HOS method. Thus, the variables η and $\tilde{\phi}$ have to be expressed in the spectral domain. To achieve that a spectral basis ψ_m is defined, where the potential can be expanded on, as shown in Equation A.20.

$$\phi(x,z,t) = \sum_m A_m(t)\psi_m(x,z) = \sum_m A_m(t)\frac{\cosh[k_m(z+h)]}{\cosh(k_m h)}\exp(ik_m x) \tag{A.20}$$

where $k_m = m\Delta k_x = m\frac{2\pi}{L_x}$ the wavenumbers, demonstrating the expression of the of total length of the domain (L_x) according to the wave length.

After the previous transformation the examined variables can be expressed on the spectral basis as:

$$\tilde{\phi}(x,t) = \sum_m B_m^{\tilde{\phi}}(t)\exp(ik_m x) \tag{A.21}$$

$$\eta(x,t) = \sum_m B_m^{\eta}(t)\exp(ik_m x) \tag{A.22}$$

To solve Equations A.21 and A.22, the infinite expansion should be truncated to a finite number of modes N, which corresponds to the number of points along L_x in the physical

domain. For a given order of nonlinearity, the number of modes N is one of the main parameters that determines the accuracy of the solver. N has to be sufficiently high to account for the shortest wave lengths.

At this stage, the surface conditions η and $\tilde{\phi}$ are known and the only remaining unknown is the vertical velocity at the free surface, namely $W = \frac{\partial \tilde{\phi}}{\partial z}$, which is calculated according to the approach of West and Brueckner (1987). Then, the Equations A.17 and A.18 can be time marched. First, the velocity potential ϕ is expanded to a power series of components $\phi^{(m)}$ in wave steepness ε up to M, which refers to the HOS nonlinearity order ($mHOS$), as shown in Equation A.23.

$$\phi(x,z,t) = \sum_{m=1}^{M} \phi^{(m)}(x,z,t) \tag{A.23}$$

Next, the velocity potential at the free surface ($\phi^{(m)}$ at $z = 0$) is expanded in Taylor series around the mean water level ($z = 0$) up to order m at wave steepness ε^m.

$$\phi^{(1)}(x,0,t) = \tilde{\phi}(x,t) \tag{A.24}$$

$$\phi^{(m)}(x,0,t) = -\sum_{k=1}^{m=1} \frac{\eta^k}{k!} \frac{\partial^k \phi^{(m-k)}}{\partial z^k}(x,0,t) \quad \text{for} \quad m > 1 \tag{A.25}$$

These expansions of $\phi(x,z,t)$ and $\phi^{(m)}(x,0,t)$ form a triangular system, which simplifies the complicated Dirichlet problem of evaluating the potential on the free surface to M simpler problems of $\phi^{(m)}(x,0,t)$ calculated at mean water level. Similarly, another triangular system is formed by expanding in series the vertical velocity W, as seen in Equation A.26, which can be solved iteratively (Ducrozet et al., 2016b, 2012a).

$$W(x,t)^{(m)} = \sum_{k=0}^{m-1} \frac{\eta^k}{k!} \frac{\partial^{k+1} \phi^{(m-k)}}{\partial z^{k+1}}(x,0,t) \tag{A.26}$$

Consequently, the vertical velocity on the free surface at order M is computed as:

$$W(x,t) = \sum_{m=1}^{M} W^{(m)}(x,z,t) \tag{A.27}$$

The HOS method yields a fully nonlinear solution and solves the kinematic and dynamic boundary conditions exactly at the free surface. An interesting feature of the HOS models used here is that both solve the flow equations in a rectangular domain which has dimensions $L_x \times L_y$ corresponding to the natural eigenmodes of the wave tank, as explained in Equation A.20. Thus, the spectral expansion is based on the natural modes of the domain instead of the classic periodic expansions, resulting in normalising the modal wave number by the length of the domain L_x and the beam length of the tank L_y (Bonnefoy et al., 2006a). Moreover, to fully exploit this feature, all the quantities in the solution process are dimensionless. Thus, the depth of the tank h is set at $z = 1$ and the space and time scales are expressed as $[L] = h$ and $[T] = 1/\sqrt{g/h}$. At the end of the simulation, the quantities are transformed back to the physical space.

The time integration of the Equations A.17 and A.18 is done numerically with Runge-Kutta Cash-Karp scheme with adaptive step size (Cash and Karp, 1990). The time step is controlled by setting a desired tolerance, which typical values are $10^{-5} - 10^{-7}$, and it determines the number of internal iterations in the code for achieving convergence (Ducrozet et al., 2016b).

Another aspect that affects the accuracy in a pseudo-spectral formulation which uses FFTs is the aliasing phenomenon. When a physical quantity is expressed in spectral space, it is expanded to larger modes (N_d), which are equal to zero using a zero-padding approach and the computed quantities are then transformed to the original number of modes (N). For high accuracy, complete de-aliasing is recommended, which is achieved by using the halves rule of $M+1$ for the nonlinear order M, meaning that $N_d = \frac{M+1}{2}N$. Partial de-aliasing is also possible by using integers lower than M, which is useful to retain a reasonable cost at large 3D computations (Ducrozet et al., 2012a).

The high computational efficiency is also achieved thanks to the solution strategy of

solving the linear part of the equations analytically and the nonlinear numerically. In such approach, the CPU time can estimated from the parameters of the problem, according to the number of modes used (N) as $Nlog_2N$, for a given order of nonlinearity M (Ducrozet et al., 2012a). The simulation of a wavemaker in HOS-NWT induces some additional computational cost, but for a certain wavemaker it grows according to the aforementioned formula.

Another interesting aspect in the HOS method is the computation of the kinematics, namely the dynamic pressure and velocity, in the fluid domain e.g. (Ducrozet et al., 2016a,b). Since the HOS approach evaluates the quantities η and $\tilde{\phi}$ at the free surface only, the calculation of the kinematics in the fluid domain is performed during the post-processing at the desired area, using an approximation similar to that of the Dirichlet to Neumann Operator (DNO) models. Obtaining the kinematics allows also for coupling with other solvers, such as CFD and SPH (Ducrozet et al., 2016b).

A potential issue for nonlinear simulations is their initialization with linear conditions, which can create instabilities (Dommermuth, 2000). To mitigate this and avoid discontinuities, a relaxation period can be defined at the beginning of the simulation to facilitate the transition from the linear to the fully nonlinear solution by defining a smoothing time in Equations A.17 and A.18. This ramp-up time is defined at the wavemaker movement of HOS-NWT and at the first wave periods in HOS-ocean.

A.3.3 Boundary conditions and initial conditions

The definition of the boundary conditions is essentially the only difference between HOS-NWT and HOS-ocean. Common for the two models are the boundary conditions for the bottom and the free surface. As expressed in Equation A.19, the bottom boundary conditions impose impermeability. At the free surface, impermeability and pressure continuity are achieved through the kinematic and dynamic boundary conditions (Equations A.17 and A.18).

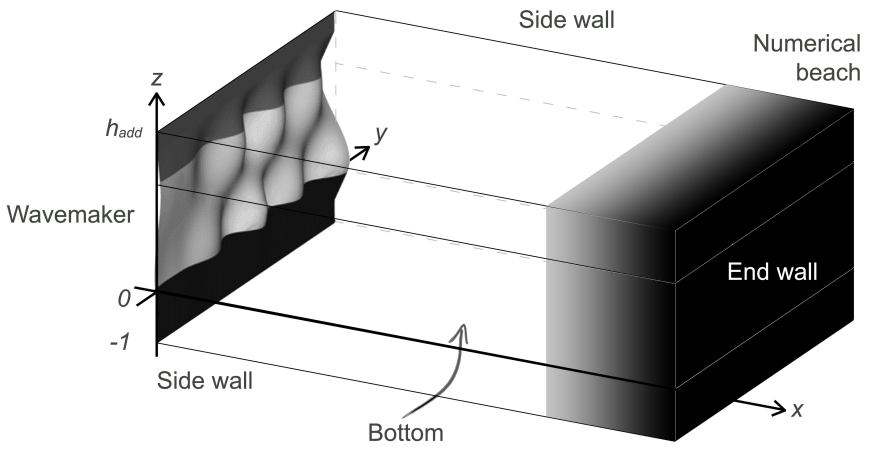

Figure A.2: Numerical domain used HOS-NWT, especially depicting the additional domain, the wavemaker and absorption zone.

The simulation of an infinite ocean with HOS-ocean requires periodic boundary conditions, which "recirculate" the computed quantities. For the simple case of an 2D domain this can be expressed as shown in Equation A.28 and it can be easily expanded in 3D domains for wave fields with directionality.

$$\left(\eta, \tilde{\phi}, W\right)(x=0,t) = \left(\eta, \tilde{\phi}, W\right)(x=L_x,t) \tag{A.28}$$

More complicated is the case for HOS-NWT, where special boundary conditions have to be set for the wave generation and absorption. A schematic of the domain is shown in Figure A.2 for HOS-NWT. All the vertical walls of the NWT are perfectly reflective and at the left wall ($x=0$) a wavemaker is modelled, while at the right wall ($x \to L_x$) a numerical beach is inserted for the dissipation of the wave energy (Ducrozet et al., 2012a).

The numerical beach at the end of the domain takes the form of a absorption zone, which imposes a local modification of the pressure in a similar way as the relaxation zones in OpenFOAM (see Section A.1). The weighting function of the relaxation was calibrated to match the physical absorption of the basin at ECN, using a third order

polynomial function (Ducrozet et al., 2012a).

The modelling of the wavemaker on the other hand requires special treatment. HOS-NWT follows the some principle as in SWEET (Bonnefoy et al., 2006a), but extended the 1^{st} and 2^{nd} order motion of the wavemaker to 3^{rd} order. Two types of wavemakers are modelled, namely piston and flap-type, with the hinge being at the bottom of the flume or detached. The wavemaker is assumed to have continuous geometry and a no-flow condition, as seen in Equation A.29:

$$\frac{\partial X}{\partial t} = \frac{\partial \phi}{\partial \phi} - (\nabla_v X) \cdot (\nabla_v \phi) \quad x = X(y,z,t) \tag{A.29}$$

with ∇_v is the vertical gradient.

To accurately model the movement of the wavemaker without increasing the energy and volume of fluid in the domain, the concept of the additional potential was introduced, coined by Bonnefoy et al. (2006a) following the work of Agnon and Bingham (1999). As seen in Figure A.2 the domain consists of three horizontal slices: the bottom black part, which corresponds to the actual physical domain; the top grey part, which refers to the additional potential; and the light grey transitional zone between the previous two. By employing the additional potential ϕ_{add}, the total potential is split into two parts $\phi = \phi_{spec} + \phi_{add}$, where ϕ_{spec} is the potential in the original computational domain, while ϕ_{add} is added to account for the nonhomogeneous conditions. As such, Equations A.17 and A.18 on $z = \eta(x,t)$ can be rewritten by including ϕ_{add} as a forcing term, with $\tilde{\phi}$ and W veing now defined with respect to ϕ_{spec}:

$$\frac{\partial \eta}{\partial t} = \left(1 + |\nabla \eta|^2\right) W - \nabla(\tilde{\phi} + \phi_{add}) \cdot \nabla \eta + \frac{\partial \phi_{add}}{\partial z} \tag{A.30}$$

$$\frac{\partial \tilde{\phi}}{\partial t} = -\eta - \frac{1}{2}|\nabla \tilde{\phi}|^2 + \frac{1}{2}\left(1 + |\nabla \eta|^2\right) W^2 - \nabla \tilde{\phi} \cdot \nabla \phi_{add} - \frac{1}{2}|\widetilde{\nabla} \phi_{add}|^2 - \frac{\partial \phi_{add}}{\partial t} - \nu \frac{\partial \eta}{\partial t} \tag{A.31}$$

A simple description of the approach is that the additional potential was added in order to have an opposite moving symmetrical wavemaker to the actual one and keep the quantities in the tank constant. The transitional region (light grey in Figure A.2) is introduced to balance the movement of the two opposite moving walls on the boundary in order to avoid discontinuities. This can be pictured as an elastic wall to balance the different deformations of the two layers and create a smooth transition resulting in a continuous wall on the boundary.

The governing Equations A.30 and A.31 have to be solved inside the domain and on the wave generation boundary as an expansion of perturbation series of the corresponding variable at each order $^{(i)}$ (Bonnefoy et al., 2006a), using the decomposition $\phi^{(i)} = \phi^{(i)}_{add} + \phi^{(i)}_{spec}$. As such, one obtains the following equations:

$$\Delta\phi^{(i)} = 0 \quad \text{inside the domain} \tag{A.32}$$

$$\frac{\partial\phi^{(i)}}{\partial n} = 0 \quad \text{on } x = L_x;\ y = 0,\ L_y;\ z = -1 \tag{A.33}$$

$$\frac{\partial\phi^{(i)}}{\partial x} - \frac{\partial X^{(i)}}{\partial t} = A_i \quad \text{on } x = 0 \tag{A.34}$$

$$\frac{\partial\eta^{(i)}}{\partial t} = \frac{\partial\phi^{(i)}}{\partial z} = B_i \quad on\ z = 0 \tag{A.35}$$

$$\frac{\partial\phi^{(i)}}{\partial t} + \eta^{(i)} + \nu\frac{\partial\phi^{(i)}}{\partial z} = C_i \quad on\ z = 0. \tag{A.36}$$

where n is the vector normal to the boundary.

For $(i = 1)$, the first order terms read:

$A_1 = 0, \quad B_1 = 0, \quad C_1 = 0.$

For $(i = 2)$, the second order terms read:

$$A_2 = -X^{(1)}\frac{\partial\phi^(1)}{\partial x^2} + \nabla_u X^{(1)} \cdot \nabla_u \phi^{(1)} \tag{A.37}$$

$$B_2 = -\eta^{(1)}\frac{\partial\phi^{(1)}}{\partial t \partial z} - \frac{1}{2}|\tilde{\nabla}\phi^{(1)}|^2 - \nu\left(\eta^{(1)}\frac{\partial\phi^{(1)}}{\partial^2 z} - \nabla\eta^{(1)} \cdot \nabla\phi^{(1)}\right) \tag{A.38}$$

$$C_2 = \eta^{(1)}\frac{\partial\phi^{(1)}}{\partial^2 z} - \nabla\eta^{(1)} \cdot \nabla\phi^{(1)} \tag{A.39}$$

To model a linear wavemaker the additional forcing term in Equations A.30 and A.31 is calculated as $\phi_{add} = \phi^{(1)}_{add}$, while for a second order wavemaker $\phi_{add} = \phi^{(1)}_{add} + \phi^{(2)}_{add}$ (Ducrozet et al., 2012a). This solution is similar to that used in the SWEET model (Bonnefoy et al., 2006a). The HOS-NWT includes also the expansion of the wavemaker to third order wave generation in order to minimize high order spurious free waves, using a similar approach as that of the previous orders and defining the term A_3. The solution of the third order problem requires the calculation of the previous orders, i.e. first and second order (Ducrozet et al., 2012b).

The HOS-NWT and HOS-ocean can simulate regular and irregular wave conditions. The difference is that in the former numerical model the wave definition is translated to a transport function to the wavemaker, while for the later it is imposed to the domain as an initial condition based on linear theory. The initial condition in HOS-NWT considers the fluid at rest. Nonlinear regular waves can be generated using the Stream Function Theory (Rienecker and Fenton, 1981). Irregular waves with directionality can be generated as a superposition of linear components, which amplitudes are defined by a predetermined spectrum for a given frequency discretization $F(\omega)$ and their direction are defined by a directional spreading $G(\theta)$. To apply the HOS scheme, the spectrum is translated to the Fourier domain B_{mn} by employing the modal discretization in $\kappa-$ space using Δk_x and Δk_y for the corresponding directions. The phases are uniformly distributed in $[0, 2\pi]$ and a randomly generated phase is assigned to each component. The free surface potential is computed in the Fourier space $B^{\tilde{\phi}}_{mn} = -i\frac{\omega_{mn}}{g}B^{\eta}_{mn}$, where ω_{mn} can calculated by the dispersion relation and then an inverse Fourier transform is used

to obtain the wave field.

The irregular wave spectrum available in both HOS-ocean and HOS-NWT is the JONSWAP directional spectrum form $S(\omega,\theta)=F(\omega)G(\theta)$, where the energy spectrum $F(\omega)$ is given in Equation A.40 for a given significant wave height H_s, the shape factor γ and peak period $T_p=\frac{2\pi}{\omega_p}$. The directional spreading $G(\theta)$ is defined in Equation A.41. Additional spectra were added in the code for the needs of the present study.

$$F(\omega)=a_J H_s^2 \omega_p^4 \omega^{-5} exp\left[-\frac{5}{4}\left(\frac{\omega}{\omega_p}\right)^{-4}\right]\gamma^{exp\left[-\frac{(\omega-\omega_p)^2}{2\sigma^2\omega_p^2}\right]} \tag{A.40}$$

with $\sigma=\begin{cases}0.07 \text{ for } \omega<\omega_p\\ 0.09 \text{ for } \omega\geqslant\omega_p\end{cases}$ and a_J chosen to obtain the correct H_s.

$$G(\theta)=\frac{1}{\beta}\left[\cos\left(\frac{\pi\theta}{4\beta}\right)\right]^2 \tag{A.41}$$

A.3.4 Applications

HOS-ocean and HOS-NWT were released relatively recently and there are not many applications that employ them, with most of them coming from ECN as part of the development of the models. For example, SWEET was compared against experiments for regular, irregular and focused wave groups, showing promising results and encouraging further developments (Bonnefoy et al., 2006b). Ducrozet et al. (2007) employed an unbounded version of the HOS model to examine freak waves "naturally" emerging extreme waves in a random 2-dimensional (2D) sea as well as "forced" extreme wave events with phase focusing. Thanks to its efficiency, HOS-NWT was also used to find the statistical properties of the sea state with random (Monte Carlo-type) simulations (Ducrozet et al., 2007). HOS-NWT was compared with experimental results for low and moderate steepness unidirectional and directional focused wave packets showing significant improvement over the SWEET (Ducrozet et al., 2012a). In the study of Ducrozet et al. (2016b), the calculation of the velocity and pressure field under a

freak wave, detected in a random sea, was examined and possible integration with HOS-NWT was suggested, which was performed in (Ducrozet et al., 2016a) for the reproduction the Draupner wave as well as a "naturally" occurring freak wave in a random simulation in HOS-ocean. HOS-NWT was also used to investigate the time-reversal of solitons and breathers in the context of nonlinear wave-wave interactions in the process of refocusing (Ducrozet et al., 2016c).

Similar HOS methods have been used by independent research groups to examine properties of nonlinear wave propagation, such as nonlinear spectral energy shifts, modulation instability, wave-wave interactions, the rate of change of sea spectra according to Hasselmann's theory, the evolution of bi-modal seas etc. Most of the studies employed the Zakharov Equation (ZE) (Zakharov, 1968) or similar approaches, which correspond to HOS nonlinearity order $mHOS = 3$ (Onorato et al., 2007). For example, Shemer et al. (2001) studied energy transfer due to wave-wave interactions in modulated wave trains. A focused wave group was simulated by Shemer et al. (2006), with the wavemaker signal being adjusted to match the experiment near the inlet, and by Shemer et al. (2007), who included bound waves, improving the agreement with the experiment. Two other benchmark studies for the evolution of focused waves (Gibson and Swan, 2007; Katsardi and Swan, 2011) also employed ZE and HOS-based methods. The BST model (Bateman et al., 2001), which is very similar to the HOS models of the present study, was used by Gibson and Swan (2007) to demonstrate that strong spectral changes take place close to the focal location mainly due to third-order resonant effects. Katsardi and Swan (2011) extended that study to intermediate and shallow water and, by exploiting the advantage of ZE to separate the bound and resonant wave-interactions, showed that the spectral evolution is subject to resonant four-wave interactions.

A.3.5 Conclusion

The HOS models used in the present work are characterized by fast convergence and computational efficiency, thanks to the fact that the HOS method takes into advantage the very nature of the waves, i.e. sinusoidal waves with frequencies and amplitudes, and expresses the problem in efficient Fourier series. On the other hand, the hydrodynamic models (OpenFOAM and SWASH) solve a type of the Navier-Stokes equations for any movement of fluid without necessarily examining waves. Moreover, the HOS method does not have the restrictions of the spectral bandwidth and the water depth, as the NLSE models.

In the present work, the HOS-NWT was chosen to examine focused wave groups and the HOS-ocean model to find the statistical properties of a sea with Monte Carlo-type simulations. For the present study, HOS serves as a bridge between phase-resolving and phase-averaged models, because, despite being a phase-resolving model, it evaluates the waves in the frequency domain using the Hamiltonian and FFT allowing for controlling the simulated wave-wave interactions through the selection of the nonlinearity order. It is important to note that it is the first time that the HOS models were not used to simulate very steep wave groups and they have been validated for the propagation of individual harmonics. For this, custom tools have been created in MATLAB and Shell and new spectra have been inserted in the source code by the author.

One of the greatest limitation of the HOS models at present is the constant water depth assumption. Recent attempts simulated variable depth (Gouin et al., 2015), and it is expected that thanks to that future releases of HOS models will gain popularity for practical engineering applications and allow for better coupling with other nonlinear solvers, such as CFD.

A.4 WAVEWATCH III

A.4.1 Ocean modelling

WAVEWATCH III (WW3) is based on the phase averaging approach for simulating the propagation of waves, which is a fundamentally different method than that used by the wave models described in the previous sections. As described in Section 2.1, there are two groups of wave modelling: phase-averaged and phase-resolving models. The latter simulate individual waves with known phases and result in a deterministic representation of the free water surface, while the former represent the evolution of a wave field in a statistical sense by dropping the phase information of the individual waves[4] and adopting a random phase approximation by calculating at every time step and at each geographical location the energy distribution in wave frequencies and directions. The underlying principle is that a random sea surface can be considered as a Fourier-type process of superposition of an infinite number of individual sinusoidal waves with their individual frequencies, amplitudes, phases and directions that form an energy spectrum. For this reason, these models are also called spectral models. As a consequence, phase-averaged models may miss the description of rapidly changing waves at scales shorter than the wave length, but they are still capable of retaining sufficient information for the evolution of a wave field as an evolving energy spectrum with its mean parameters, such as H_S, T_p, mean direction etc (Monbaliu and Lefèvre, 2005). The obtained spectrum is assumed to vary slowly in space and time and thus, the simulated sea state is assumed stationary and homogeneous at the model's mesh scale (Monbaliu and Lefèvre, 2005).

The advantage of the spectral approach is the significant gaining in computational efficiency compared to phase-resolving models and the fact that through this stochastic approach, the statistical parameters of interest are calculated directly without the need of random Monte Carlo-type simulations. Nonetheless, large errors can be introduced if

[4] There exist spectral models that retain the phase information carried in the bi-spectra, however these models are not commonly used for engineering purposes (Ardhuin and Roland, 2013).

the commonly assumed quasi-Gaussian statistical closure hypothesis is violated (Cavaleri et al., 2007). A considerable drawback is that phase-related effects, such as strong diffraction and generation of extreme waves (Babanin et al., 2012), cannot be replicated effectively and where possible they need to be parameterized.

Thanks to their computational efficiency, spectral models are used at large coastal and ocean scales and they are often coupled with atmospheric models to provide estimations of the global sea parameters. The simulated scales vary between tens of kilometres and time steps of one hour for ocean applications to tens of metres and seconds for nearshore modelling (Monbaliu and Lefèvre, 2005), but spectral models have also been applied at laboratory scale with spatial resolutions of 0.5 m (Ris, 1997). Spectral models are employed for wave forecasting, climate monitoring and navigation as well as long term assessment of the wave energy potential of a region (Sánchez et al., 2017). They are also useful tools for engineering purposes, providing the characteristics of the sea state that marine structures can be deployed (van Vledder, 2006). Popular spectral models, such as WW3, are continuously verified against in-situ records of wave buoys, HF radar measurements and altimetry data from satellites, which helps in tuning the models for more accurate predictions. This method of incorporating field measurements in a model to improve the results is called assimilation (Sánchez et al., 2017) and it is relatively new for wave models aiming to better understanding of the physical processes (Waters et al., 2013). Spectral models can estimate the sea parameters at areas that are not monitored with instrumentation and also simulate past events and provide long term statistics through hindcasting (Perez et al., 2017).

The development of spectral ocean models is a continuous effort that goes together with developments in atmospheric models and measuring in-situ techniques. The accuracy of the model is dependent on understudying and mathematically describing the relevant physical processes, on efficient numerics and coupling with weather and local models, which all constantly improve (Monbaliu and Lefèvre, 2005). These efforts resulted in three generations of wave models that are mainly characterised by the de-

scription of the nonlinear wave-wave interaction terms, which is the main subject of the present work. First generation models included only wind input and dissipation source terms (see next paragraphs A.4.4) that were tuned to match the available observed measurements. Second generation models distinguish between the swell and the wind generated sea. The energy transfer between wind sea and swell is performed in a parametric that represents the action of nonlinear wave-wave interactions. Third generation (3G) models, as described below, solve the wave action equation without making any assumption of the examined spectral shape and the nonlinear wave-wave interactions are solved using analytical algorithms that transfer energy among selected resonant combinations of waves (Monbaliu and Lefèvre, 2005). The flexibility and accuracy of ocean modelling was significantly improved with the 3G models, since the nonlinear transfers that alter the shape of the spectrum are no longer absent as in first generation models, nor heavily parameterized as in second generation models (Holthuijsen, 2007). Many 3G models were developed in the last two decades, with the best-known being WAM, WW3, SWAN, TOWAMAC and MIKE-21 SM (Yang et al., 2017). A good review touching all the aspects of spectral modelling is found in (Cavaleri et al., 2007) including contributions from almost all the "gurus" in ocean modelling.

Regarding the present study, it is noted that most of the available spectral models include similar source terms for the nonlinear wave-wave interactions and should theoretically produce similar results. In particular, WW3 is more applicable for ocean scale applications, while SWAN and TOMAWAC are more relevant for nearshore applications. Nevertheless, the last versions of SWAN are applicable also to offshore modelling (Gonçalves et al., 2014) and have also the advantage of the more efficient implicit time stepping method (Yang et al., 2017). Certainly, any of these models could be used in the present study, but WW3 was preferred thanks to the recent work of Gramstad and Babanin (2016) for the four-wave nonlinear interactions with the General Kinetic Equation (GKE).

A.4.2 Introduction to WAVEWATCH III

WW3 is 3G spectral model that was first released in the middle 90s and it was based on the principles of the first 3G spectral model, WAM (The WAMDI Group, 1988). The latter was designed for deep ocean and shelf sea applications, but it was also able to capture the transition to shallower water and refraction caused by currents (Monbaliu and Lefèvre, 2005). The first version of the model, "WAVEWATCH" (Tolman, 1989) was developed at TU Delft and the second version, "WAVEWATCH II", at NASA, Goddard Space Flight Center and included specific developments for use in super computers. In parallel, SWAN was being developed for coastal applications. The present version of WAVEWATCH, WW3, differs considerably from its predecessors in the numerics and the source terms that were previously tuned to replicate the nondimensional spectral characteristics for given fetches (Tolman and Chalikov, 1996). WW3 is maintained and distributed by NOAA/NCEP (National Oceanic and Atmospheric Administration / National Centers for Environmental Prediction) (NOAA, 2017) under an open-source password protected license. The users are allowed to modify the source code, but they are obliged by the license to provide NCEP with their developments, who then decides whether the developments will be included in the main distribution (Tolman, 2010). The code of WW3 is written in Fortran 90, in a modular format. The model can be parallelised using the OpenMP or MPI protocols. The selection of the physical processes and adopted parameterizations is performed at the compilation level, with the so called "switches". The grid generation program gridgenv3.0 is also provided with the source code of WW3.

The propagation of the wave field is linear and the nonlinear effects are included by source terms. The spectral evolution is formulated using a Eulerian approach, which for the spatial propagation on structured or unstructured grids is achieved by using a numerical scheme, such as FEM, FVM or FDM (Ardhuin and Roland, 2013). The wave spectrum is discretised uniformly in directions and logarithmically in frequencies. The latter is common practice in spectral models (van Vledder, 2006; Benoit, 2006;

Gagnaire-Renou et al., 2010; Gramstad and Babanin, 2016), because it allows for high resolution in the wavenumber space at lower frequencies, where the main part of the spectrum is, and sufficient resolution at high wave numbers that have little energy[5], resulting in more efficient computation. The time integration is achieved by implicit or explicit schemes. First and third order schemes are available for the wave propagation and a dynamic time stepping method can be used for the integration of the source terms. Some more specific features of WW3, refer to alleviation of the inter Garden Sprinkler Effect (GSE)[6], sub-grid representation of unresolved islands and dynamic ice coverage. In terms of numerical solution, one-way or more advanced two-way nesting schemes are possible, which can create a mosaic of multiple grids. Alternatively, a refined grid can move along a predefined path, following for example a cyclone.

Starting from the release WW3 v3.14, WW3 begun transitioning to a modelling framework, including a wide variety of physics, aiming at comprising a numerical tool for both operational and academic applications. v3.14 incorporated important developments regarding shallow water and surf zone phenomena, a dry grid method as well as spectral partitioning in the post-processing [7]. A landmark in the development of WW3 was version 4, which has important additions of curvilinear and unstructured grids, two-way nesting, developments in the source terms for wave generation, dissipation and bottom friction as well as outputting in the very handy structured NetCDF format (Ardhuin and Roland, 2013). WW3 v5.16 has some additional features relevant to possible extensions of the present work, such as the calculation of space-time extremes as well as the Two-Scale Approximation (TSA) and the Full Boltzmann Integral (FBI) source terms for nonlinear four-wave interactions (NOAA, 2017). It should be noted however that the non-resonant interactions are still not included in these formulations. Thus, for the examined problem of the present study, the v4.18 (Tolman, 2014) that was used

[5] The difference between the frequency and the wavenumber grid is a direct result of the linear dispersion relation.

[6] GSE is a numerical artefact referring to the geographical disintegration of the spectrum into distinct frequency-direction bins due to coarse resolution (Cavaleri et al., 2007).

[7] Spectral partitioning is a technique to separate a spectrum to its wave train components and treat them independently, without the need to average the statistics over the entire spectrum. It is useful for handling spectra consisting of wind sea and swells (Monbaliu and Lefèvre, 2005; Waters et al., 2013).

does not have any major differences from the latest version v5.16 (The WAVEWATCH III Development Group (WW3DG), 2016), released in late 2016.

A.4.3 Mathematical formulation

As a spectral model, WW3 solves the random phase spectral action density balance equation in the directional wavenumber space using FDM and an explicit time step through the Courant condition. The underlying assumption of the governing equation is that the local physical properties, such as the water depth, wave field and current, vary slowly in time and space compared to the individual wavelengths.

The derivation of the governing equation of the spectral evolution shown herein follows the description in the manual (Tolman, 2014). To begin with, an individual wave is considered, represented by a wavenumber vector **k** or the wavenumber k with direction θ. The intrinsic frequency of this wave is given by the linear dispersion relation (Equation A.42). In the case of ambient currents with a uniform velocity **U**, the absolute angular frequency of the wave ω should include the effect of current, in a Doppler-like equation, assuming that the wave and the currents have the same direction. As such the absolute observed frequency ω is the wave frequency σ altered by the current velocity, as seen in Equation A.43. The underlying assumption is that the diffraction of the wave due to the current is ignored, which is the case for slowly varying currents and bathymetry. Equation A.43 does not hold for strong nonlinearity and if the current has not a uniform vertical structure (Cavaleri et al., 2007) .

$$\sigma^2 = gk\ \tanh(kd) \tag{A.42}$$

$$\omega = \sigma + \mathbf{k}\cdot\mathbf{U} \tag{A.43}$$

where d is the mean water depth and g the gravitational acceleration.

When considering an arbitrary number of wave components to represent an irregular sea, the wave amplitude is not appropriate to represent the energy distribution of the sea, as in the case for a single wave, and instead the variance density spectrum is used (Holthuijsen, 2007). Here, it is denoted as F, being a function of wave parameters at each space location x and time t: $F(\mathbf{k},\sigma,\omega;\mathbf{x},t)$. Under the assumption of linear theory for the individual wave components of the spectrum, $\mathbf{k}$, σ and ω are connected, as seen in Equations A.42 and A.43, and thus, the variance density spectrum is expressed as $F(\mathbf{k},\theta)$. This expression in the $\kappa-$space is used in the solution process in WW3, because it is conservative for the wave growth and decay (Tolman, 2014). However, for practical applications, it is more useful to express the result in $f-$space . Thus, the output of WW3 is given as $F(f,\theta)$. This is performed with a simple Jacobian transformation (similar to Equation 4.26), as shown in Equations A.44 and A.45, for the relative (f_r) and absolute frequency (f_a), respectively. Integration over the $f-$ and $\theta-$space returns the total energy E of the spectrum and from that the significant wave heigh can be computed: $H_s = 4\sqrt{E}$ (Cavaleri et al., 2007).

$$F(f_r,\theta) = \frac{\partial k}{\partial f_r} F(k,\theta) = \frac{2\pi}{c_g} F(k,\theta) \tag{A.44}$$

$$F(f_a,\theta) = \frac{\partial k}{\partial f_a} F(k,\theta) = \frac{2\pi}{c_g}\left(1+\frac{\mathbf{k}\cdot\mathbf{U}}{kc_g}\right)^{-1} F(k,\theta) \tag{A.45}$$

where c_g is the so-called group velocity, given by Equation A.46.

$$c_g = \frac{\partial\sigma}{\partial k} = n\frac{\sigma}{k}, \quad n = \frac{1}{2} + \frac{kd}{\sinh 2kd} \tag{A.46}$$

There is however an issue with using the variance density spectrum in ocean models: in the presence of currents, the energy is not conserved, due to the work of the current transferring momentum to the waves. Nonetheless, the wave action, defined as $A \equiv E/\sigma$, is conserved for an individual wave, and, correspondingly, the action density

spectrum $N(k,\theta) \equiv F(k,\theta)/\sigma$ is conserved for an irregular sea. For this reason, the $N(k,\theta)$ is used in most of the present ocean models (Gonçalves et al., 2014).

The next step for determining the propagation of the wave spectrum is to find the evolution of the wave action density spectrum in space and time, i.e., $N(k,\theta;\mathbf{x},t)$, hereafter N. This can be achieved by building an equation with the time and space derivatives of N in a conservative form, which changes the total N according to the input of external forcings, namely the source terms S_{tot}. These source terms represent the parameterization of various physical processes that affect the spectrum. Attempting to make a rather far-fetched equivalence with phase-resolving models, the governing equations reproduce the motion of the fluid or the movement of the spectrum on the grid. The forcing terms refer to the wave generation and absorption in phase-resolving models and to the source terms in phase-averaged models.

The evolution equation in ocean models is called wave action balance or often energy balance equation, because it balances the affects of the source terms by modifying the spectrum. Here, it is expressed for a Cartesian grid in Equation A.47, but for large scale applications, a spherical grid is preferred (Tolman, 2014). It is noteworthy that ocean models evaluate the spectrum up to a cut-off frequency and above that a parametric tail is imposed.

$$\frac{\partial N}{\partial t} + \nabla_x \cdot \dot{\mathbf{x}} N + \frac{\partial}{\partial k}\dot{k}N + \frac{\partial}{\partial \theta}\dot{\theta}N = \frac{S_{tot}}{\sigma} \tag{A.47}$$

$$\dot{\mathbf{x}} = \mathbf{c}_g + \mathbf{U} \tag{A.48}$$

$$\dot{k} = -\frac{\partial \sigma}{\partial d}\frac{\partial d}{\partial s} - \mathbf{k} \cdot \frac{\partial \mathbf{U}}{\partial s} \tag{A.49}$$

$$\dot{\theta} = -\frac{1}{k}\left[\frac{\partial \sigma}{\partial d}\frac{\partial d}{\partial m} + \mathbf{k} \cdot \frac{\partial \mathbf{U}}{\partial m}\right] \tag{A.50}$$

where $\mathbf{c}_g$ is given by c_g and θ, s is a coordinate in the direction θ and m is a coordinate perpendicular to s.

As discussed, the known linear dispersion is considered for the propagation of N and thus, what is left to determine the spectral evolution is the action of the source terms. The source terms in WW3 include a wide range of processes, as shown in Equation A.51 and user defined sources (S_{xx}) can be added. In brief, wave generation by the wind is induced by S_{in}, deep water wave breaking (whitecapping) causes dissipation through S_{ds}, S_{nl} refers to nonlinear four-wave interactions, S_{ice} to wave-ice interactions and S_{ln} is used for linear initialization of the model. When water depth becomes small compared to the wavelength, the processes of wave-bottom interactions (S_{bot}), depth-induced breaking (S_{db}), triad wave-wave interactions (S_{tr}), wave scattering by the bottom (S_{sc}) and wave reflection by shorelines (or floating objects, e.g., icebergs) (S_{ref}) become important.

$$S \equiv \frac{S_{tot}}{\sigma} = S_{ln} + S_{in} + S_{nl} + S_{ds} + S_{bot} + S_{db} + S_{tr} + S_{sc} + S_{ice} + S_{ref} + S_{xx} \tag{A.51}$$

At present, significant efforts in ocean modelling focus on improving the source terms. Ideally, these terms would have a solid mathematical description, however this is not the case for most of them, because the corresponding physics are not sufficiently understood, for example whitecapping. The source term with the most robust mathematical description is S_{nl}, but it is very computationally expensive for operational purposes (van Vledder, 2006; Gagnaire-Renou et al., 2010).

As the present work is interested only in the nonlinear four-wave interactions, further simplifications on the equations presented so far can be made. At first, in order to examine only the impact of S_{nl} on the spectrum, a rather unconventional set-up of the model is considered. This refers to a single-point computation without allowing the spectrum to propagate on the grid. In this way, the spectrum evolves only in time as a result of the action of the source term. The definition of the grid used for the

```
 Status map, printed in  1 part(s)
-----------------------------------

 3333
 3213
 3333

 Legend :
-----------------------------
   0 : Land point
   1 : Sea point
   2 : Active boundary point
   3 : Excluded point
```

Figure A.3: Single-point grid definition in WW3.

present tests is shown in Figure A.3. In physical terms, the single-point definition of the spectrum corresponds to a spatially homogeneous infinite sea. This approach was employed by other researchers for the evaluation of S_{nl} (Benoit, 2006; Gagnaire-Renou et al., 2010; Gramstad and Babanin, 2016). Additionally, there is no action of current and all the other source terms are equal to zero.

Taking into account the aforementioned considerations, the balance equation used in the present study reduces to Equation A.52. As becomes apparent, integration of the spectrum is still performed over the wavenumbers and directions. The latter practically implies that 1D (unidirectional) propagation cannot be restricted in WW3. To circumvent this, it was found after trials that a spectrum can behave as one-dimensional if a very narrow directional distribution is considered and a high resolution for the directions. In this manner, the spectral energy is constrained in a single directional bin and if there is no other source terms to alter this, it stays in this bin even after long evolution of $> 100T_p$, behaving like a quasi-1D simulation.

$$\frac{\partial N}{\partial t} + \frac{\partial}{\partial k}\dot{k}N + \frac{\partial}{\partial \theta}\dot{\theta}N = S_{nl} \tag{A.52}$$

In the next paragraphs, the most commonly used models for the S_{nl} are discussed.

A.4.4 Wave-wave interactions source terms

The only mechanism known to alter the spectral shape in deep water, when input and dissipation terms are zero, is the nonlinear four-wave interactions (Holthuijsen, 2007), expressed by the S_{nl} source terms in spectral models. As discussed in (Babanin et al., 2012) and (Gramstad and Babanin, 2016), the existing expressions of S_{nl} are based on the Hasselmann's Kinetic Equation (KE) (Hasselmann, 1962)[8], which accounts only for resonant interactions in long time scales ($> 100T_p$) and thus, cannot describe fast evolution, nor spectral change in 1D. As a result, the existing source terms are not applicable for the unidirectional waves examined in the present work, which was proven by the single-point computations in WW3. Nevertheless, the present study would be incomplete if it did not include any description of the existing S_{nl} in ocean models, because more complete expressions of S_{nl} are expected to be added in the future (Gramstad and Babanin, 2016). Also, if one aims at examining short-crested (2D) extreme waves, which is a likely extension of this work, the existing expressions become relevant, since the resonant interactions are stronger than the non-resonant interactions for 2D broadbadned spectra in deep water (Janssen, 2003).

In brief, the scope of S_{nl} is to evaluate the KE, expressed by the Boltzmann integral (Equation A.53), for every wavenumber as a combination of the other three interacting wave numbers that make a resonant quadruplet (Hasselmann, 1962). The computation of the Boltzmann integral is not a simple task, because it includes a six-fold integral (three-fold integral over three wavenumbers). This is a very computationally expensive task, prohibitive for operational purposes (Monbaliu and Lefèvre, 2005; van Vledder, 2006). For this reason, the efforts in the last three decades are in finding approximate solutions that retain to an acceptable extent the basic characteristics of S_{nl} for practical applications (Holthuijsen, 2007). The inclusion of S_{nl} is important, because it is assumed that the four-wave interactions are vital for the spectral evolution of surface gravity waves generated by the wind in ocean and coastal areas (Benoit, 2006), as

[8] NB: all the expressions for the KE have the underlying assumption of weak nonlinearity and homogeneous conditions.

demonstrated by the JONSWAP experiment (Hasselmann, 1962), where a downshift of the spectral peak and a growth of the energy in high frequencies was observed (van Vledder, 2012). Nevertheless, a balance should be found between the accuracy of evaluating the Boltzmann integral and the computational efficiency depending on the applications (van Vledder, 2012).

$$S_{nl}(k_1) = \int\int\int G(\mathbf{k}_1,\mathbf{k}_2,\mathbf{k}_3,\mathbf{k}_4)\ \delta(\mathbf{k}_1+\mathbf{k}_2-\mathbf{k}_3-\mathbf{k}_4)\ \delta(\sigma_1+\sigma_2-\sigma_3-\sigma_4) \times [N_1N_2(N_3-N_4)+N_2N_4(N_3-N_1)]\ d\mathbf{k}_2\ d\mathbf{k}_3\ d\mathbf{k}_4 \tag{A.53}$$

where $\mathbf{k}_i$ is the wavenumber vector, N_i the wave action density per wavenumber, G is a coupling coefficient (see Section 4.3.1) and δ a Dirac function to ensure conservation of wave energy, action and momentum by defining the resonant quadruplets (van Vledder, 2012). Thus, interactions are permitted only among the wave components that fulfil the resonant conditions (Benoit, 2006). As a result, the δ functions reduce Equation A.53 to a three-fold integral (Cavaleri et al., 2007).

In the next paragraphs, a description of the most widely used S_{nl} will be discussed, as formulated in WW3 (Tolman, 2014).

Discrete Interaction Approximation (DIA)

DIA (Hasselmann and Hasselmann, 1985) was developed to tackle the issue of the high computational load of the exact solution of the Bolzmann integral (Equation A.53) and to preserve the dominant characteristics of the spectral evolution. The computational efficiency of DIA practically triggered the development of 3G spectral models (van Vledder, 2006) and it is still the most popular implementation of S_{nl} in operational models, despite its crude approximation (Benoit et al., 2015).

The formulation of the DIA was suggested by Hasselmann and Hasselmann (1985) for the $F(f_r,\theta)$ spectrum (see Equation A.44). DIA lies on the selection of a particular

interacting quadruplet and its symmetric set in the wavenumber vector space (Benoit, 2006; Holthuijsen, 2007). To select the resonant interactions, DIA considers that two out of the four examined components have the same wavenumber vectors ($\mathbf{k}_1 = \mathbf{k}_2$, corresponding to the self-interaction (Holthuijsen, 2007)) and the other two wave components have intrinsic frequencies dependent on the first wavenumber. This selection of wave components is shown in Equation A.54.

$$\mathbf{k}_1 + \mathbf{k}_2 = \mathbf{k}_3 + \mathbf{k}_4 \tag{A.54a}$$

$$\sigma_2 = \sigma_1 \tag{A.54b}$$

$$\sigma_3 = (1 + \lambda_{nl})\sigma_1 \tag{A.54c}$$

$$\sigma_4 = (1 - \lambda_{nl})\sigma_1 \tag{A.54d}$$

where λ_{nl} is a constant shape parameter, commonly taken as $\lambda_{nl} = 0.25$.

Under this considerations, the evolution of the Bolzmann integral (Equation A.53) reduces to Equation A.55 for the contribution of S_{nl} for each discrete wave component k_1 of the spectrum.

$$\begin{pmatrix} \delta S_{nl,1} \\ \delta S_{nl,3} \\ \delta S_{nl,4} \end{pmatrix} = D \begin{pmatrix} -2 \\ 1 \\ 1 \end{pmatrix} C_g^{-4} f_{r,1}^{11} \times \left[F_1^2 \left(\frac{F_3}{(1+\lambda_{nl})^4} + \frac{F_4}{(1-\lambda_{nl})^4} \right) - \frac{2F_1F_3F_4}{(1-\lambda_{nl}^2)^4} \right] \tag{A.55}$$

where the variables $_i$ refer to a discrete wave component with $(f_{r,i}, \theta_i)$ and C is a proportionality constant given by tuning of the source term, e.g., for WAM-3 cycle $C = 2.78 \times 10^7$ (Tolman, 2014), in order to obtain similar spectral changes to the empirical curves (van Vledder, 2012). D is a factor to account for the effect of water depth, since DIA was developed for deep water. The expression of D is takes into account the

mean water depth and the corresponding mean wavenumber (Hasselmann and Hasselmann, 1985). The latter approach for DIA is very economical, because the interaction coefficients do not need to be recalculated for shallower water, but instead, they are simply scaled (van Vledder, 2012). It should be mentioned however, that in reality the sets of resonance quadruplets change in shallower water, since the wavenumbers are depth dependent, and stronger interactions take place (Holthuijsen, 2007). The expression of D attempts to replicate only the latter effect.

Since DIA was tuned for specific set of spectra, it is able to estimate the "typical signature" of the four-wave energy transfer with S_{nl} having a three-lobe shape of (+ - +). The first positive lobe results in transfer of energy to frequencies lower than f_p, the second negative lobe pumps energy from the region around f_p and gives it to lower and higher frequencies (third lobe). These changes result in stabilization of the spectrum (Cavaleri et al., 2007). However, if the conditions differ significantly from the tuned parameters or unsteady situations occur, for example non-JONSWAP-like spectra (Gagnaire-Renou et al., 2010) and turning winds (Benoit, 2006) respectively, DIA may fail to reproduce the spectral evolution.

To give a perspective of the cost of the calculation of S_{nl}, even the very crude approach of DIA takes approximately 40% of the total computational cost of the spectral model, including the propagation and all the other source terms (van Vledder, 2012).

Full Boltzmann Integral (WRT)

DIA constitutes the crudest approximation of S_{nl}, which requires tuning of many other source terms in order to yield overall realistic results. The latter is certainly a deficiency of DIA, since it induces extended parameterizations (Cavaleri et al., 2007). On the other hand, higher level of accuracy can be achieved by considering a greater set of interacting quadruplets, of course at the price of high computational effort. In

WW3 there is the possibility to evaluate the exact[9] Boltzmann integral using the WRT method, which is named after its developers (Webb, 1978) (Tracy and Resio, 1982). WRT is based on the "EXACT-NL" source term derived by Hasselmann and Hasselmann (1985) assuming specific reference spectra (van Vledder, 2006).

According to WRT, the resonant quadruplets are defined by the more general -compared to DIA, Equation A.54- expression of Equation A.56.

$$\left.\begin{aligned} \mathbf{k}_1 + \mathbf{k}_2 &= \mathbf{k}_3 + \mathbf{k}_4 \\ \sigma_1 + \sigma_2 &= \sigma_3 + \sigma_4 \end{aligned}\right\} \tag{A.56}$$

The core of WRT is the selection of the integration space for each combination of wavenumbers $(\mathbf{k}_1, \mathbf{k}_3)$ and a number of transformations to treat the δ functions of Equation A.53. As such the Boltzmann integral can be expressed by Equation A.57 with the function $T(\mathbf{k}_1, \mathbf{k}_3)$ given by Equation A.58.

$$\frac{\partial N_1}{\partial t} = 2 \int T(\mathbf{k}_1, \mathbf{k}_3)\, d\mathbf{k}_3 \tag{A.57}$$

$$\begin{aligned} T(\mathbf{k}_1, \mathbf{k}_3) = \int\int G(\mathbf{k}_1, \mathbf{k}_2, \mathbf{k}_3, \mathbf{k}_4)\ \delta(\mathbf{k}_1 + \mathbf{k}_2 - \mathbf{k}_3 - \mathbf{k}_4) \\ \times\ \delta(\sigma_1 + \sigma_2 - \sigma_3 - \sigma_4)\ \theta(\mathbf{k}_1, \mathbf{k}_3, \mathbf{k}_4) \\ \times\ [N_1 N_2 (N_4 - N_2) + N_2 N_4 (N_3 - N_1)]\ d\mathbf{k}_2\ d\mathbf{k}_4 \end{aligned} \tag{A.58}$$

The function $T(\mathbf{k}_1, \mathbf{k}_3)$ includes an additional θ function, which is given by Equation A.59 and it determines the evaluated section of the integral by assuming that $\mathbf{k}_1$ is closer to $\mathbf{k}_3$ than to $\mathbf{k}_4$[10] and exploiting the symmetry properties.

[9] There are several approaches to solve the exact Boltzmann integral that have different internal assumptions for the elimination of the δ functions and the treatment of singularities, for example when $\mathbf{k}_1 = \mathbf{k}_2 = \mathbf{k}_3 = \mathbf{k}_4$ (van Vledder, 2006). These may affect the final "exact" solution (van Vledder, 2012).

[10] There is a misprint in Tolman (2014) mentioning $\mathbf{k}_2$ instead of $\mathbf{k}_4$, see (van Vledder, 2006).

$$\theta(\mathbf{k}_1,\mathbf{k}_3,\mathbf{k}_4) = \begin{cases} 1 \text{ when } |\mathbf{k}_1-\mathbf{k}_3| \leqslant |\mathbf{k}_1-\mathbf{k}_4| \\ 0 \text{ when } |\mathbf{k}_1-\mathbf{k}_3| > \mathbf{k}_1-\mathbf{k}_4| \end{cases} \tag{A.59}$$

The solution of WRT is then built by defining a new coordinate system in $\kappa-$space, where the resonance conditions are realised along a "locus". Since the resonant wavenumbers form circles with crossing points in $\kappa-$space, it is convenient to replace the (x,y) coordinate system with a new tangential and normal coordinate system (s,n) at the locus. The expression of $T(\mathbf{k}_1,\mathbf{k}_3)$ can then be written as a closed line integral along the closed locus, which can be solved in a discrete way be dividing the locus to a finite number of segments n_s, each having a coordinate s_i. As such, Equation A.58 becomes:

$$T(\mathbf{k}_1,\mathbf{k}_3) \simeq \sum_{i=1}^{n_s} G(s_i)W(s_i)P(s_i)\Delta s_i \tag{A.60}$$

where $P(s_i)$ is the product term at a point on the locus.

After the above considerations, the Boltzmann integral can be written in the form of Equation A.61, which is convenient because it evaluates the source term in absolute wavenumbers and directions, instead of wavenumber vectors.

$$\frac{\partial N_1}{\partial t} \simeq \sum_{i_{k_3}=1}^{n_k} \sum_{i_{\theta_3}=1}^{n_\theta} k_3 \; T(\mathbf{k}_1,\mathbf{k}_3) \; \Delta k_{i_{k_3}} \; \Delta\theta_{i_{\theta_3}} \tag{A.61}$$

The accuracy of WRT is of course superior to that of DIA, however, to give an indication of the computational cost, WRT is three to four orders of magnitude more expensive than DIA, which restricts its use to academic applications or to very limited spatial grids. In addition, it is recommended to include wavenumbers at frequencies at least between $[0.5f_p, 5f_p]$ in order to include a sufficient number of interacting quadruplets and retrieve the three-lobe shape of the S_{nl}. A useful feature of the computational strategy for WRT in WW3 is to pre-compute the coefficients of WRT for each local water depth, only

once at the beginning of the simulation and save it to a file that is accessible during the simulation. Further savings in the computational cost can be achieved by finding the coefficients of WRT for only rounded values of the water depth (van Vledder, 2006).

Other wave-wave interaction source terms S_{nl}

Aiming at finding a balance between computational efficiency and accuracy, or a half-way between DIA and WRT, various algorithms have been suggested to evaluate S_{nl}. There are two[11] main strategies to achieve that: extending DIA by including additional sets of quadruplets or find a way to reduce the computational cost of exact S_{nl} (van Vledder, 2012). Such methods have been developed and are available in operational models with a manageable computational cost of up to 200 times compared to DIA (Benoit, 2006).

The extension of DIA is not a simple task and requires a selection method to find the interacting configurations. On top of that, the inherent limitations of DIA remain, which refer to the validity only for particular spectra and the requirement for tuning (van Vledder, 2006). On the other hand, the computational cost of the exact methods can be reduced by efficient algorithms for the definition of locus and additional approximations, such as exclusion of quadruplets with small contributions. Exact methods do not require tuning, which seems to be a advantage (van Vledder, 2006), but it is not clear if their overall performance is better that that of extended DIAs (Cavaleri et al., 2007).

Examples of such methods for the evaluation of S_{nl} are, among others, the Generalized Multiple DIA (GMD), the Two-Scale Approximation (TSA) and the Full Boltzmann Integral (FBI) and the Gaussian quadrature method (GQM) (Gagnaire-Renou et al., 2010). GMD (Tolman, 2013) considers more interacting quadruplets than DIA, handles arbitrary spectra and interactions in very shallow water, but it has a much more complicated formulation. Its cost increases linearly with the number of quadruplets being two

[11] A third one refers to artificial neural networks, but it is not available in operational models yet (Sánchez et al., 2017).

times more expensive than DIA for one quadruplet configuration. TSA and FBI were implemented in the latest version of WW3 v5.16 (The WAVEWATCH III Development Group (WW3DG), 2016). FBI is equivalent to WRT, while TSA divides the spectrum into a broad-scale and residual spectrum, with the former being evaluated with exact methods (WRT) and the latter being approximated (van Vledder, 2012).

New expressions of S_{nl} were recently developed focusing on the physics of the four-wave interactions by including also non-resonant quadruplets in the form of the GKE (Gramstad and Babanin, 2016), as discussed in detail in Section 4.3.

Lumped Triad Approximation (LTA)

Another type of nonlinear wave-wave interactions is the triad wave interactions, which are relevant for very shallow water. Here, triads are briefly discussed because they are associated with bound wave nonlinearities. In phase-resolving models, as waves approach the shore, their profile becomes steeper and asymmetric. Phase-averaged approximations can be derived to replicate this effect from a phase-resolving model by applying a suitable close hypothesis (Cavaleri et al., 2007).

The effect of triad interactions on the spectral shape is the generation of sub- and super-harmonics at half and double frequencies of the original spectrum, resulting in a spectral shape with additional peaks at $\frac{1}{2}f_p$ and $2f_p, 3f_p...$ (Ris, 1997). In practical applications, sub-harmonics correspond to infra-gravity waves and the super-harmonics create a steeper wave profile. This behaviour was observed for waves passing over a submerged bar (Beji and Battjes, 1993).

In WW3, triads are included through a source term modelled by the LTA method, which, similar to its predecessor the Discrete Triad Approximation (Eldeberky and Battjes, 1995), considers only the self interactions that are dominant. According to LTA, energy is transferred from a component with frequency f_i to a component with frequency $2f_i$ only. Therefore, the sub-harmonics are not reproduced[12] and gradually multiple peaks

[12]WW3 has another source term for adding infra-gravity waves on top of a known linear spectrum in a

appear at the spectrum at high frequencies. LTA is conservative by definition, since the energy is pumped from one component to another with double frequency. This crude approximation can still describe the essential features of the spectral transformation in shallow water (Holthuijsen, 2007).

A.4.5 Applications

Spectral models are mainly used for ocean and coastal modelling at large spatial and temporal scales, but they can be also applied at laboratory scale to represent a wave transformation in a stochastic sense (Ris, 1997).

For wave forecasting, ocean models are coupled with atmospheric models. Such an example is the use of WW3 at global scale with nested regional domains (NOAA, 2017) and the PREVIMER operational forecast model, maintained at Ifremer in the framework of IOWAGA (Integrated Ocean Waves for Geophysical and other Applications) (Lecornu et al., 2008).

For hindcasting, spectral models are used to reproduce past events and long-term statistics. This is in particularly useful for complementing field observations, especially in places where the in-situ measurements are not available or continuous (Yang et al., 2017). For example, WW3 with multiple nested grids was used for the generation of a 30-year long global hindcast database (Chawla et al., 2013), as well as for HOMERE databased of Ifremer for the French coasts. Recently, the global wave hindcast database GOW2 was created with WW3 covering the world's coastline with over 40,000 locations from 1979 onwards (Perez et al., 2017).

Hindcast and forecasting are commonly used to study extreme weather events. The GOW2 database is used to identify extreme wave heights and tropical cyclones as well as to estimate the 50-year return period wave at every location of the globe for engineering applications (Perez et al., 2017). WW3 was also used, coupled with SWAN, to simulate severe storms at the Brazilian coast and to identify hazards for nearshore

non-energy conservative fashion (Tolman, 2014)

urban areas and extreme waves (Guimarães et al., 2014). The probability of extreme waves generation was examined via spectral kurtosis and skewness in SWAN under typhoon conditions (Mori, 2012). Similarly, (Cavaleri et al., 2012) employed WAM to examine if a ship accident was associated with rogue waves. The modelling of moving hurricanes can become efficient by employing nested grids, such as for the case of Lili hurricane (Tolman and Alves, 2005), or by using adaptive grids with automatic refinement (Popinet et al., 2010).

Regarding MRE studies, WW3 is mainly used for resource assessment, commonly for producing the far ocean boundary conditions for more detailed local models that are applied at the area of deployment of the device (Cornett et al., 2014; METOCEAN-SOLUTIONS-Ltd, 2008). For MRE resource characterization (IEC, 2015), at least 10 years of data is recommended, which highlights the importance of modelling in creating reliable long-terms statistics. Specifically, WW3 was used for wave energy resource assessment at the west coast of Vancouver Island, British Columbia, Canada (Kim et al., 2012), Uruguay (Alonso et al., 2015), Canary islands (Gonçalves et al., 2014) as well as for wind and wave resource characterization at East and South China sea (Zheng et al., 2011) and at the Red Sea (Langodan et al., 2016). In a recent study, the geometry of a wave point absorber was optimized in a potential flow model for the wave conditions estimated by WW3 for the coast of Brazil (Shadman et al., 2018). A hindcast database for MRE applications was created by Ifremer, covering the region from the North Sea to the Bay of Biscay and including relevant information to wave energy, currents, sediment dynamics etc for resource characterization as well as for examining engineering parameters, such as device optimization and survivability (Boudière et al., 2013).

A.4.6 Conclusions

Ocean modelling is an "art" of compromising among the existing human knowledge of very complicated global and local physical phenomena, computational resources and

the necessity to finally obtain an estimation of the atmospheric and wave climate. At a larger perspective, ocean modelling helps us understand better our natural world. Overall, great accomplishments have been achieved in the last decades thank to 3G models, allowing for very accurate description of the average behaviour of the ocean, yielding a bias of lower than 4% in predictions (Cavaleri et al., 2007). Taking into account climate change, trends show that wave height grows, as well as extreme events (Young et al., 2011). For such situations especially, present ocean models face certain shortcomings, as discussed in the complete review of the challenges in ocean modelling presented by Cavaleri et al. (2007).

The accuracy of ocean models depends mainly on three aspects: the forcing fields, namely the wind, currents and tides; the parameterization of the source terms; and the employed numerical schemes for discretization and integration of the physical parameters (Ardhuin and Roland, 2013).

To begin with, in the past, the atmospheric models had poorer representation of the wind field compared to present, and as a result, the accuracy of the ocean models was mainly affected by issues related to the wind input. The estimation of the wind fields has improved over the years and the challenge has moved mostly to how the corresponding source terms feed the waves with energy. The air-sea momentum transfer is generally well described, but in cases of hurricanes and gusty winds, which can cause effects like spray production, our understanding of the physical processes is still limited (Babanin et al., 2012). This is expected to improve by also obtaining better in-situ measurements of the wind. Probably the least understood physical process is the wave dissipation in deep water (whitecapping) and it ends up being the tuning knob for verifying ocean models with measurements. Dissipation in finite water is caused by bottom friction, which heavily depends on the local bottom topography and material that are not always known in sufficient detail. The propagation of waves in shallow water involves a high degree of nonlinearity, which stochastic representation is challenging. Connected to the shallow water effects is wave reflection by steep shores,

which has yield discrepancies in models. Also, modern spectral models treat wave-current interactions linearly, assuming uniform depth-integrated current profile, varying slowly in the horizontal dimension. This ideal case is far from reality especially in finite depth, where shear currents are present and highly nonlinear processes may take place, and it raises the challenge of building new governing equations that account for non-homogeneous media (Ardhuin and Roland, 2013). Regarding the spatial integration, the accuracy of the models' output can be improved by simply increasing the resolution globally or locally (with nested grids in coastal areas) or using subgrid approximations to represent small islands. Then the problem becomes an issue of higher computational cost, but moving grids and unstructured grids methods that have advanced considerably can mitigate this. Similarly, the representation of the spectrum can be improved by discretizing it in more frequencies and directions. However, this does not guarantee convergence, since the integration of the source terms is to an extent optimised to certain suggested values of frequency and direction increment[13].

The latter opens the floor to discuss issues regarding the nonlinear wave-wave interactions source terms. Arguably, four-wave interactions is the best-understood physical process, having a solid mathematical description, but, as discussed, due to the high computational cost of exact methods, at present only approximate methods are used in ocean modelling, mostly the DIA. The expected increase in processing power will be far from covering this shortcoming. As the description of the other source terms and efficiency of numerical schemes improve, DIA is expected to hinder the development of ocean models (Prabhakar and Uma, 2016), despite being the reason that 3G models were at first created. Therefore, extended DIAs or decreased exact S_{nl}s will eventually prevail. There are however considerable issues in replacing DIA in existing ocean models, since the other source terms, numerical schemes and discretization methods have been optimized according to DIA (Benoit, 2006). Thus, the replacement of DIA

[13]See for example Fig. 2 in (Gramstad and Babanin, 2016) where the solution of S_{nl} does not converge by increasing the directional discretization. The latter was noticed by simulations in the present work and it was confirmed in personal communication with O. Gramstad and it is implied in other publications as well, e.g., (Benoit, 2006), (van Vledder, 2006) and (Chawla et al., 2013). Each S_{nl} has its own optimum discretization.

should be performed in a holistic manner. At the same time, new source terms for the wind input should be tested with different S_{nl} methods, see for example the relevant comparisons between DIA and WRT (Zieger et al., 2015). This process is expected to yield better results in spectral evolution in extreme cases, such as hurricanes or turning winds, and to describe fast evolution time scales by including non-resonant interactions with the GKE (Gramstad and Babanin, 2016). As a result the comparison with in-situ measurements is expected to improve. However, it should be noted that wave buoys may underestimate extreme waves (Chawla et al., 2013), but other advances in field measurements, e.g., HF radars and SAR, can improve models via assimilation (Monbaliu and Lefèvre, 2005). These improvements may open the path for 4G models, where modelling will be done purely by physical principles (Babanin et al., 2012).

In the present work, WW3 is not examined in an operational setup, but the study is focused only on S_{nl} attempting to reproduce the observed spectral change during the focusing of wave groups due to nonlinear wave-wave interaction. By designing a special single-point configuration for the laboratory scale, all the available S_{nl}s were tested and it was confirmed that spectral change in 1D cannot be reproduced at present. However, the development of the GKE (Gramstad and Babanin, 2016) that is expected to be included in future versions of the software or the study of 2D spectra where the existing source terms should be sufficient, give value to the present tests.

A.5 Models' suitability

The various phase-resolving and phase-averaged models described in this chapter are based on different governing equations, which in practical terms result in differences in the scale of application, the physical processes involved in wave evolution, the modelling of turbulence and the interaction of waves with structures etc. Attempting to make a direct comparison of the models discussed in this chapter, their basic characteristics are listed in Table A.1. Their suitability can be readily deducted according to

Table A.1: Applicability of the numerical tools: simulated physical properties and models' characteristics.

	OpenFOAM	SWASH	HOS-NWT	HOS-ocean	Wavewatch-III
Model's Category	Two-phase CFD	NLSWE	Spectral PFS	Spectral PFS	Spectral Energy
Discretization	FVM	FVM	FFT	FFT	FDM
Hydrodynamics	Per cell	$\sigma-$layer	DNO	DNO	No
Variable depth	Yes	Yes	No[a]	No[a]	Yes
Turbulence	Yes	Approximated	No	No	Dissipation
Wave breaking	Yes	Approximated	No	No	Dissipation
Wave interactions	Implicit[b]	Implicit[b]	Explicit[c]	Explicit[c]	Approximated
Wave-current	Fully NL	Weakly NL	No	No	Linear
Wave-structure	Strong	Weak	No	No	No
Wave B.C.[d]	Yes	Yes	Yes	No	No
Mesh	Hexahedral	Grid-Layers	Fourier nodes	Fourier nodes	Un-/structured
Cell size (L_p)	$10^{-3} - 10^{-2}$	$10^{-2} - 10^{-1}$	1 / (64-512)	1 / (64-512)	$10^{1} - 10^{4}$
Comp. cost	Very low	Medium	High	Very high	Very high
Simulated scale	Device level	Coast	Flume	Ocean	Region-Globe
Time scale (T_p)	$10^{-8} - 10^{-3}$	$10^{-4} - 10^{-2}$	10^{-3}-10^{-2}	10^{-3}-10^{-2}	$10^{-1} - 10^{3}$

[a]The formulation for variable depth was presented by Gouin et al. (2015), but at present it is not included in the code's distribution

[b]Calculated as a result of the hydrodynamic equations.

[c]Explicit: depending on the order of $mHOS$. Implicit for $mHOS \geq 3$.

[d]Specific boundary conditions for wave generation and absorption in a NWT.

the involved physics, scale and computational resources. It should be underlined however, that this is a quite crude categorization and the capabilities of these open-source models are continuously expanding.

For the present study of non-breaking waves over a flat horizontal bottom, the phase-resolving models, OpenFOAM, SWASH and HOS-NWT, should produce similar results, once optimized and converged. On the other hand, for examining the spectral evolution stochastically, HOS-ocean can reproduce the underlying physics, while WW3 includes extended parameterizations.

Appendix B

Coupling coefficients for the GKE

The formulation of the GKE presented in chapter 4 is derived for finite water depth. To achieve this, the calculation of the angular frequency of a the wave component i is based on the linear dispersion relation: $\omega_i = \sqrt{g k_i \tanh(k_i d)}$, where d is the depth. The same also applies for the variables q_i that are used for the canonical transformation, as seen in Equation 2.9 of Krasitskii (1994). In fact, q_i are auxiliary variables used for the calculation of ω_i, as seen in Equation B.1, under the assumption that surface tension is zero. For deep water, as used in Janssen and Onorato (2007), $q_i = \omega_i^2/g$.

$$q_i = |\mathbf{k}_i| \tanh(|\mathbf{k}_i| d) \tag{B.1}$$

where $\mathbf{k}_i$ is the wavenumber vector, which is calculated iteratively for the wavelength L_i of a wave component with angular frequency ω_i, as seen from Equation B.2, which is based on the linear dispersion relation.

$$\mathbf{k}_i = \frac{2\pi}{L_i} = \frac{2\pi\omega_i^2}{g 2\pi \tanh(2\pi d/L_i)} \tag{B.2}$$

Similarly, the auxiliary variables $q_{i\pm j}$ for the combination of two wavenumbers $\mathbf{k}_i$ and $\mathbf{k}_j$ can be defined from Equation B.3.

$$q_{i\pm j} = |\mathbf{k}_i \pm \mathbf{k}_j| \tanh\left(|\mathbf{k}_i \pm \mathbf{k}_j| d\right) \tag{B.3}$$

The coupling coefficient T_{1234} for the GKE is found from Janssen and Onorato (2007), because it has a more compact form compared to that of the corresponding coefficient $\tilde{V}^{(2)}_{0,1,2,3}$ in (Krasitskii, 1994), which facilitates its programming. It can be easily proven that the two expressions are equivalent. T_{1234} is given from Equation B.4 as a combination of ω_i and the coefficients W, V^+ and V^- for the different combinations of the four wavenumbers $i = 1,2,3,4$.

$$\begin{aligned}
T_{1234} = W_{1,2,3,4} &- V^-_{1,3,1} V^-_{4,2,4-2} \left(\frac{1}{\omega_3 + \omega_{1-3} - \omega_1} + \frac{1}{\omega_2 + \omega_{4-2} - \omega_4} \right) \\
&- V^-_{2,3,2-3} V^-_{4,1,4-1} \left(\frac{1}{\omega_3 + \omega_{2-3} - \omega_2} + \frac{1}{\omega_1 + \omega_{4-1} - \omega_4} \right) \\
&- V^-_{1,4,1-4} V^-_{3,2,3-2} \left(\frac{1}{\omega_4 + \omega_{1-4} - \omega_1} + \frac{1}{\omega_2 + \omega_{3-2} - \omega_3} \right) \\
&- V^-_{2,4,2-4} V^-_{3,1,3-1} \left(\frac{1}{\omega_4 + \omega_{2-4} - \omega_2} + \frac{1}{\omega_1 + \omega_{3-1} - \omega_3} \right) \\
&- V^-_{1+2,1,2} V^-_{3+4,3,4} \left(\frac{1}{\omega_{1+2} - \omega_1 - \omega_2} + \frac{1}{\omega_{3+4} - \omega_3 - \omega_4} \right) \\
&- V^+_{-1-2,1,2} V^+_{-3-4,3,4} \left(\frac{1}{\omega_{1+2} + \omega_1 + \omega_2} + \frac{1}{\omega_{3+4} + \omega_3 + \omega_4} \right)
\end{aligned} \tag{B.4}$$

The notations with two wavenumbers are calculated as follows:

$\omega_{i\pm j} = \sqrt{g q_{i\pm j}} = \sqrt{g|\mathbf{k}_i \pm \mathbf{k}_j|}$.

The calculation of V^+ and V^- follows a similar fashion, for example:

$V^-_{3,2,3-2} = V^-(\mathbf{k}_3, \mathbf{k}_2, \mathbf{k}_3 - \mathbf{k}_2)$.

The calculation of the coefficients $V^\pm$ is given from Equation B.5.

$$V^{\pm}_{1,2,3} = \frac{1}{4\sqrt{2}}\Bigg[(\mathbf{k}_1\cdot\mathbf{k}_2 \pm q_1 q_2)\sqrt{\frac{g\omega_3}{\omega_1\omega_2}} + (\mathbf{k}_1\cdot\mathbf{k}_3 \pm q_1 q_3)\sqrt{\frac{g\omega_2}{\omega_1\omega_3}} + (\mathbf{k}_2\cdot\mathbf{k}_3 + q_2 q_3)\sqrt{\frac{g\omega_1}{\omega_2\omega_3}}\Bigg] \tag{B.5}$$

The calculation of the coefficients $W_{1,2,3,4}$ is given from Equation B.6.

$$W_{1,2,3,4} = U_{-1,-2,3,4} + U_{3,4,-1,-2} - U_{3,-2,-1,4} - U_{-1,3,-2,4} - U_{-1,4,3,-2} - U_{4,-2,3,-1} \tag{B.6}$$

where $U_{1,2,3,4}$ can be found from Equation B.7, using the appropriate signs.

$$U_{1,2,3,4} = \frac{1}{16}\sqrt{\frac{\omega_3\omega_4}{\omega_1\omega_2}}\left[2\left(k_1^2 q_2 + k_2^2 q_1\right) - q_1 q_2\left(q_{1+3} + q_{2+3} + q_{1+4} + q_{2+4}\right)\right] \tag{B.7}$$

Special care should be taken for the treatment of the obvious singularities. For these cases, $T_{1234} = 0$, and the calculation moves to the next combination of wavenumbers. Singularities arise in the cases that:

- $\mathbf{k}_1 = \mathbf{k}_2 = \mathbf{k}_3 = \mathbf{k}_4$
- $\mathbf{k}_1 = \mathbf{k}_3$ and $\mathbf{k}_2 = \mathbf{k}_4$
- $\mathbf{k}_1 = \mathbf{k}_4$ and $\mathbf{k}_2 = \mathbf{k}_3$

Another aspect that should be treated with care is the symmetry of T_{1234}. The coupling coefficient should to be "exactly" symmetric. This should arise as a result of the implicit computation for all the wavenumbers, however, issues may appear due to the truncation error of the machine, because the calculations include the π. For this reason, as well as to save computational resources, the symmetry condition can be taken explicitly, avoiding any potential rounding errors, with the use of Equation B.8.

$$T_{2134} = T_{1234} \tag{B.8}$$

A similar issue arises for the calculation of the Dirac δ functions, which allow interactions only when $\mathbf{k}_1 + \mathbf{k}_2 - \mathbf{k}_3 - \mathbf{k}_4 = 0$. However, since π is involved in the computation, the previous summation may be not be exactly zero. For this reason, instead of zero it is equalled to the precision of the machine, here 10^{-15}.

The programming of T_{1234} can be done in a relatively straight-forward way with four loops including all the possible combinations of four wavenumbers. The result is a 4-dimensional matrix consisting of four 2-dimensional layers of interacting wavenumbers vectors. For the simple case of 1D propagation, the layers collapse to arrays.

The computational effort for solving the GKE is consumed mainly on the calculation of the coefficients, at least for short spectral evolution time. For this reason, the calculation of T_{1234} can be performed before the time stepping and saved to a matrix. During the time marching of the GKE, the values of the required coefficients can be called from the 4-dimensional matrix. To further decrease the computational time, apart from taking into account the symmetry condition, T_{1234} should be calculated only for $\delta_{13}^{34} \neq 0$, since, as seen in the time marching equation (Equation 4.4), T_{1234} is multiplied by δ_{13}^{34}.

In the present work, the GKE is programmed in MATLAB. The required coefficients are programmed as functions that are called during the calculation of T_{1234}. The argument of these functions are the wavenumbers and the water depth.

Bibliography

Abanades, J., Greaves, D., and Iglesias, G. (2014). Coastal defence through wave farms. *Coastal Engineering*, 91:299–307.

Adcock, T. A. (2017). A note on the set-up under the Draupner wave. *Journal of Ocean Engineering and Marine Energy*, 3(1):89–94.

Adcock, T. A. and Draper, S. (2015). A note on the variation in shape of linear rogue waves in the ocean. *Underwater Technology*, 33(2):75–80.

Adcock, T. A. and Taylor, P. H. (2016a). Non-linear evolution of uni-directional focussed wave-groups on a deep water: A comparison of models. *Applied Ocean Research*, 59:147–152.

Adcock, T. A., Taylor, P. H., and Draper, S. (2016). On the shape of large wave-groups on deep water-The influence of bandwidth and spreading. *Physics of Fluids*, 28(10).

Adcock, T. a. a. and Taylor, P. H. (2014). The physics of anomalous ('rogue') ocean waves. *Reports on Progress in Physics*, 77(10):105901.

Adcock, T. A. A. and Taylor, P. H. (2016b). Fast and local non-linear evolution of steep wave-groups on deep water: A comparison of approximate models to fully non-linear simulations. *Physics of Fluids*, 28(1):016601.

Adcock, T. A. A., Taylor, P. H., and Draper, S. (2015). Nonlinear dynamics of wave-groups in random seas: unexpected walls of water in the open ocean. *Proceedings*

of the Royal Society A: Mathematical, Physical and Engineering Sciences, (471: 20150660).

Adcock, T. A. A., Taylor, P. H., Yan, S., Ma, Q. W., and Janssen, P. A. E. M. (2011). Did the Draupner wave occur in a crossing sea? *Proceedings of the Royal Society A: Mathematical, Physical and Engineering Sciences*, 467(2134):3004–3021.

Afshar, M. A. (2010). *Numerical Wave Generation In OpenFOAM*. PhD thesis, Chalmers University of Technology.

Agnon, Y. and Bingham, H. B. (1999). A non-periodic spectral method with application to nonlinear water waves. *European Journal of Mechanics - B/Fluids*, 18(3):527–534.

Alam, M. R. (2014). Predictability Horizon of Oceanic Rogue Waves. *Geophysical ResearchLetters*, 41:8477–8485.

Alberello, A., Chabchoub, A., Gramstad, O., Babanin, A. V., and Toffoli, A. (2016). Non-Gaussian properties of second-order wave orbital velocity. *Coastal Engineering*, 110:42–49.

Alford, L. K. and Maki, K. J. (2015). Generating Large Deterministic Water Waves for Numerical Simulation. In *Ann Arbor*, page 1001:48109.

Alonso, R., Solari, S., and Teixeira, L. (2015). Wave energy resource assessment in Uruguay. *Energy*, 93:683–696.

Annenkov, S. and Shrira, V. (2015). Modelling the Impact of Squall on Wind Waves with the Generalized Kinetic Equation. *Journal of Physical Oceanography*, 45(3):807–812.

Annenkov, S. Y. and Shrira, V. I. (2006). Role of non-resonant interactions in the evolution of nonlinear random water wave fields. *Journal of Fluid Mechanics*, 561:181.

Ardhuin, F. and Roland, A. (2013). The Development of Spectral Wave Models: Coastal and Coupled Aspects. In *Coastal Dynamics*, number May, pages 25–38, Arcachon, France.

Arena, F., Ascanelli, A., Nava, V., Pavone, D., and Romolo, A. (2008). Three-dimensional nonlinear random wave groups in intermediate water depth. *Coastal Engineering*, 55(12):1052–1061.

Arena, F. and Fedele, F. (2005). Nonlinear Space-Time Evolution of Wave Groups With a High Crest. *Journal of Offshore Mechanics and Arctic Engineering*, 127(1):46.

Astariz, S. and Iglesias, G. (2015). The economics of wave energy: A review. *Renewable and Sustainable Energy Reviews*, 45:397–408.

Aubourg, Q., Campagne, A., Peureux, C., Ardhuin, F., Sommeria, J., Viboud, S., and Mordant, N. (2017). 3-Wave and 4-Wave Interactions in Gravity Wave Turbulence. pages 1–18.

Aubourg, Q. and Mordant, N. (2015). Non local resonances in weak turbulence of gravity-capillary waves. *Physical Review Letters*, 114(144501).

Babanin, A. V., Onorato, M., and Qiao, F. (2012). Surface Waves and Wave-Coupled Effects in Lower Atmosphere and Upper Ocean. *Journal of Geophysical Research*, 117(January):1–10.

Bai, W., Feng, X., Taylor, R. E., and Ang, K. (2014). Fully nonlinear analysis of near-trapping phenomenon around an array of cylinders. *Applied Ocean Research*, 44:71–81.

Baldock, T. E., Swan, C., and Taylor, P. H. (1996). A laboratory study of nonlinear surface waves on water. *Philosophical Transactions of the Royal Society A: Mathematical, Physical and Engineering Sciences*, 354(1707):649–676.

Barthel, V., Mansard, E., Sand, S., and Vis, F. (1983). Group bounded long waves in physical models. *Ocean Engineering*, 10(4):261–294.

Bateman, W. J. D., Swan, C., and Taylor, P. H. (2001). On the Efficient Numerical Simulation of Directionally Spread Surface Water Waves. *Journal of Computational Physics*, 174(1):277–305.

Beji, S. and Battjes, J. A. (1993). Experimental investigation of wave propagation over a bar. *Coastal Engineering*, 19(1-2):151–162.

Benetazzo, A., Ardhuin, F., Bergamasco, F., Cavaleri, L., Guimarães, P. V., Schwendeman, M., Sclavo, M., Thomson, J., and Torsello, A. (2017). On the shape and likelihood of oceanic rogue waves. *Scientific Reports*, 7(1):8276.

Benjamin, T. B. and Feir, J. E. (1967). The disintegeration of wave trains deep water. *Journal of Fluid Mechanics*, 27(3):417–430.

Benoit, M. (2006). Implementation and test of improved methods for evaluation of nonlinear quadruplet interactions in a third generation wave model. In *Proc. 30th Int. Conf. on Coastal Eng.,*, pages 526–538, San Diego, California, USA.

Benoit, M., Elodie, G.-R., and Dumas-Primbault, S. (2015). On the modelling of non-resonant interactions in phase-averaged equations for water waves. In *Summer school "Wave propagation in complex media"*, number 17-28 August, Corsica, France.

Berberović, E., van Hinsberg, N. P., Jakirlić, S., Roisman, I. V., and Tropea, C. (2009). Drop impact onto a liquid layer of finite thickness: Dynamics of the cavity evolution. *Physical Review E*, 79(3):036306.

Bihs, H., Chella, M. A., Kamath, A., and Arntsen, Ø. A. (2017). Numerical Investigation of Focused Waves and Their Interaction With a Vertical Cylinder Using REEF3D. *Journal of Offshore Mechanics and Arctic Engineering*, 139(4):041101.

Bitner-Gregersen, E. M., Bhattacharya, S. K., Chatjigeorgiou, I. K., Eames, I., Ellermann, K., Ewans, K., Hermanski, G., Johnson, M. C., Ma, N., Maisondieu, C., Nilva, A., Rychlik, I., and Waseda, T. (2014). Recent developments of ocean environmental description with focus on uncertainties. *Ocean Engineering*, 86:26–46.

Bitner-Gregersen, E. M. and Gramstad, O. (2015). Rogue waves: Impact on ships and

offshore structures; DNV GL STRATEGIC RESEARCH & INNOVATION POSITION PAPER 05-2015. Technical report.

Blayo, E. and Debreu, L. (2005). Revisiting open boundary conditions from the point of view of characteristic variables. *Ocean Modelling*, 9(3):231–252.

Boccotti, P. (1982). On ocean waves with high crests. *Meccanica*, 17(1):16–19.

Boccotti, P. (1983). Some new results on statistical properties of wind waves. *Applied Ocean Research*, 5:134–140.

Bonnefoy, F., Haudin, F., Michel, G., Semin, B., Humbert, T., Aumaître, S., Berhanu, M., and Falcon, E. (2016). Observation of resonant interactions among surface gravity waves. *Journal of Fluid Mechanics*, 805:R3.

Bonnefoy, F., Touzé, D. L., and Ferrant, P. (2006a). A fully-spectral 3D time-domain model for second-order simulation of wavetank experiments. Part A: Formulation, implementation and numerical properties. *Applied Ocean Research*, 28(2):121–132.

Bonnefoy, F., Touzé, D. L., and Ferrant, P. (2006b). A fully-spectral 3D time-domain model for second-order simulation of wavetank experiments. Part B: Validation, calibration versus experiments and sample applications. *Applied Ocean Research*, 28(2):121–132.

Boudière, E., Maisondieu, C., Ardhuin, F., Accensi, M., Pineau-Guillou, L., and Lepesqueur, J. (2013). A suitable metocean hindcast database for the design of Marine energy converters. *International Journal of Marine Energy*, 3-4:e40–e52.

Boussinesq, J. (1872). Théorie des ondes et des remous qui se propagent le long d'un canal rectangulaire horizontal, en communiquant au liquide contenu dans ce canal des vitesses sensiblement pareilles de la surface au fond. *Journal de Mathématiques Pures et Appliquées*, pages 55–108.

Bracewell, R. N. (1999). *The Fourier Transform And Its Applications*. McGraw-Hill, New York, 3rd edition.

Bredmose, H., Dixen, M., Ghadirian, A., Larsen, T. J., Schløer, S., Andersen, S. J., Wang, S., Bingham, H. B., Lindberg, O., Christensen, E. D., Vested, M. H., Carstensen, S., Engsig-Karup, A. P., Petersen, O. S., Hansen, H. F., Mariegaard, J. S., Taylor, P. H., Adcock, T. A., Obhrai, C., Gudmestad, O. T., Tarp-Johansen, N. J., Meyer, C. P., Krokstad, J. R., Suja-Thauvin, L., and Hanson, T. D. (2016). De-Risk - Accurate Prediction of ULS Wave Loads. Outlook and First Results. *Energy Procedia*, 94(January):379–387.

Bredmose, H. and Jacobsen, N. G. (2010). Breaking wave impacts on offshore wind turbine foundations: focused wave groups and CFD. In *OMAE2010: Proceedings of the ASME 29th 2010 International Conference on Ocean, Offshore and Arctic Engineering*, Shanghai, China.

Bredmose, H. and Jacobsen, N. G. (2011). Vertical wave impacts on offshore wind turbine inspection platforms. In *OMAE2011: Proceedings of the ASME 30th 2010 International Conference on Ocean, Offshore and Arctic Engineering*, Rotterdam, The Netherlands.

Bredmose, H., Skourup, J., Hansen, E., Christensen, E. D., Pedersen, L., and Mitzlaff, A. (2006). Numerical reproduction of extreme wave loads on a gravity wind turbine foundation. In *International Conference on Offshore Mechanics and Arctic Engineering, OMAE*, pages 1–9.

Bredmose, H., Slabiak, P., Sahlberg-Nielsen, L., and Schlütter, F. (2013). Dynamic Excitation of Monopiles by Steep and Breaking Waves. Experimental and Numerical Study. In *Proceedings of the ASME 2013 32nd International Conference on Ocean, Offshore and Arctic Engineering*, number 2011, pages 1–10.

Brocchini, M. (2013). A reasoned overview on Boussinesq-type models : the interplay between physics , mathematics and numerics. *Proceedings of the Royal Society A: Mathematical, Physical and Engineering Sciences*, 469:20130496.

Brown, S., Greaves, D., Magar, V., and Conley, D. (2016). Evaluation of turbulence

closure models under spilling and plunging breakers in the surf zone. *Coastal Engineering*, 114:177–193.

Buldakov, E., Stagonas, D., and Simons, R. (2015). Lagrangian numerical wave-current flume. In *International workshop for water waves and floating bodies, IWWWFB30*, Bristol, UK.

Buldakov, E., Stagonas, D., and Simons, R. (2017). Extreme wave groups in a wave flume: Controlled generation and breaking onset. *Coastal Engineering*, 128:75–83.

Bunnik, T., Veldman, A., and Wellens, P. (2008). Prediction of Extreme Wave Loads in Focused Wave Groups. In *ISOPE-2008*, volume 8, pages 32–38.

Cash, J. R. and Karp, A. H. (1990). A variable order Runge-Kutta method for initial value problems with rapidly varying right-hand sides. *ACM Transactions on Mathematical Software*, 16(3):201–222.

Cavaleri, L., Alves, J. H. G. M., Ardhuin, F., Babanin, A., Banner, M., Belibassakis, K., Benoit, M., Donelan, M., Groeneweg, J., Herbers, T. H. C., Hwang, P., Janssen, P. A. E. M., Janssen, T., Lavrenov, I. V., Magne, R., Monbaliu, J., Onorato, M., Polnikov, V., Resio, D., Rogers, W. E., Sheremet, A., McKee Smith, J., Tolman, H. L., van Vledder, G., Wolf, J., and Young, I. (2007). Wave modelling - The state of the art. *Progress in Oceanography*, 75(4):603–674.

Cavaleri, L., Bertotti, L., Torrisi, L., Bitner-Gregersen, E., Serio, M., and Onorato, M. (2012). Rogue waves in crossing seas: The Louis Majesty accident. *Journal of Geophysical Research: Oceans*, 117(5).

CFD-Online (2018). CFD Online Wiki. URL: `http://www.cfd-online.com/Wiki/Main{_}Page`. Accessed: 20-Jan-2018.

Chaplin, J. R. (1996). On frequency-focusing unidirectional waves. *International Journal of Offshore and Polar Engineering*, 6(2):131–137.

Chaplin, J. R., Rainey, R. C. T., and Yemm, R. W. (1997). Ringing of a vertical cylinder in waves. *Journal of Fluid Mechanics*, 350:119–147.

Chawla, A., Spindler, D. M., and Tolman, H. L. (2013). Validation of a thirty year wave hindcast using the Climate Forecast System Reanalysis winds. *Ocean Modelling*, 70:189–206.

Chen, L. F., Zang, J., Hillis, A. J., Morgan, G. C. J., and Plummer, A. R. (2014). Numerical investigation of wave-structure interaction using OpenFOAM. *Ocean Engineering*, 88:91–109.

Chenari, B., Saadatian, S. S., and Ferreira, A. D. (2015). Numerical Modelling of Regular Waves Propagation and Breaking Using Waves2Foam. *Journal of Clean Energy Technologies*, 3(4):276–281.

Christou, M. and Ewans, K. (2011a). Examining a comprehensive dataset containing thousands of freak wave events. Part 1 - Description of the data and quality control procedure. In *OMAE2011: Proceedings of the ASME 30th 2010 International Conference on Ocean, Offshore and Arctic Engineering*, Rotterdam, The Netherlands.

Christou, M. and Ewans, K. (2011b). Examining a comprehensive dataset containing thousands of freak wave events. Part 2 - Analysis and findings. In *OMAE2011: Proceedings of the ASME 30th 2010 International Conference on Ocean, Offshore and Arctic Engineering*, Rotterdam, The Netherlands.

Christou, M. and Ewans, K. (2014). Field Measurements of Rogue Water Waves. *Journal of Physical Oceanography*, 44(9):2317–2335.

Cornett, A., Toupin, M., Baker, S., Piche, S., and Nistor, I. (2014). Appraisal of IEC Standards for Wave and Tidal Energy Resource Assessment. In *International Conference on Ocean Energy, ICOE 2014*, Halifax, Canada.

Courant, R., Friedrichs, K., and Lewy, H. (1967). On the Partial Difference Equations of Mathematical Physics. *IBM Journal of Research and Development*, 11(2):215–234.

Creamer, D. B., Henyey, F., Schult, R., and Wright, J. (1989). Improved linear representation of ocean surface waves. *Journal of Fluid Mechanics*, 205(-1):135.

Dalzell, J. F. (1999). A note on finite depth second-order wave - wave interactions. *Applied Ocean Research*, 21(December 1998):105–111.

Dean, R. and Dalrymple, R. (1991). *Water Wave Mechanics for Engineers and Scientists, Advanced Series on Ocean Engineering: Volume 2*. World Scientific.

Deng, Y., Yang, J., Tian, X., Li, X., and Xiao, L. (2016). An experimental study on deterministic freak waves: Generation, propagation and local energy. *Ocean Engineering*, 118:83–92.

Dommermuth, D. (2000). The initialization of nonlinear waves using an adjustment scheme. *Wave Motion*, 32(4):307–317.

Dommermuth, D. G. and Yue, D. K. P. (1987). A high-order spectral method for the study of nonlinear gravity waves. *Journal of Fluid Mechanics*, 184(-1):267.

Douglas, J. F., Gasiorek, J. M., Swaffield, J. A., and Jack, L. B. (2005). *Fluid Mechanics Fifth edition*. Pearson Education Limited, Essex, UK.

Ducrozet, G., Bingham, H. B., Engsig-Karup, A. P., Bonnefoy, F., and Ferrant, P. (2012a). A comparative study of two fast nonlinear free-surface water wave models. *International Journal for Numerical Methods in Fluids*, 69(11):1818–1834.

Ducrozet, G., Bonnefoy, F., and Ferrant, P. (2016a). On the equivalence of unidirectional rogue waves detected in periodic simulations and reproduced in numerical wave tanks. *Ocean Engineering*, 117:346–358.

Ducrozet, G., Bonnefoy, F., Le Touzé, D., and Ferrant, P. (2006). Implementation and validation of nonlinear wavemaker models in a HOS numerical wave tank. *International Journal of Offshore and Polar Engineering*, 16(3):161–167.

Ducrozet, G., Bonnefoy, F., Le Touzé, D., and Ferrant, P. (2007). 3-D HOS simulations of extreme waves in open seas. *Natural Hazards and Earth System Science*, 7(1):109–122.

Ducrozet, G., Bonnefoy, F., Le Touzé, D., and Ferrant, P. (2012b). A modified High-Order Spectral method for wavemaker modeling in a numerical wave tank. *European Journal of Mechanics, B/Fluids*, 34:19–34.

Ducrozet, G., Bonnefoy, F., Le Touzé, D., and Ferrant, P. (2016b). HOS-ocean: Open-source solver for nonlinear waves in open ocean based on High-Order Spectral method. *Computer Physics Communications*, 203:245–254.

Ducrozet, G., Fink, M., and Chabchoub, A. (2016c). Time-reversal of nonlinear waves: Applicability and limitations. *Physical Review Fluids*, 1(5):054302.

Dysthe, K. B. (1979). Note on a Modification to the Nonlinear Schrodinger Equation for Application to Deep Water Waves. *Proceedings of the Royal Society of London A: Mathematical, Physical and Engineering Sciences*, 369(1736).

Dysthe, K. B., Krogstad, H. E., and Müller, P. (2008). Oceanic Rogue Waves. *Annual Review of Fluid Mechanics*, 40(1):287–310.

Dysthe, K. B., Trulsen, K., Krogstad, H. E., and Socquet-Juglard, H. (2003). Evolution of a narrow-band spectrum of random surface gravity waves. *Journal of Fluid Mechanics*, 478:1–10.

Eldeberky, Y. and Battjes, J. A. (1995). Parameterization of triad interactions in wave energy models. In *Proc. Coastal Dynamics Conf. '95*, number January, pages 140–148, Gdansk, Poland.

Elhanafi, A., Fleming, A., Leong, Z., and MacFarlane, G. (2017). Effect of RANS-based Turbulence Models on Nonlinear Wave Generation in a Two-Phase Numerical Wave Tank. *Progress in Computational Fluid Dynamics*, 17(3):1–18.

Ewans, K. C. and Buchner, B. (2008). Wavelet analysis of an extreme wave in a model Basin. In *Proceedings of the 27th International Conference on Offshore Mechanics and Arctic Engineering*, pages 15–20.

Fedele, F. (2008). Rogue waves in oceanic turbulence. *Physica D: Nonlinear Phenomena*, 237(14-17):2127–2131.

Fedele, F., Brennan, J., Ponce De León, S., Dudley, J., and Dias, F. (2016). Real world ocean rogue waves explained without the modulational instability. *Scientific Reports*, 6(May):1–11.

Fedele, F. and Tayfun, M. A. (2009). On nonlinear wave groups and crest statistics. *Journal of Fluid Mechanics*, 620:221.

Fenton, J. D. (1985). A Fifth Order Stokes Theory for Steady Waves. *Journal of Waterway, Port, Coastal, and Ocean Engineering*, 111(2):216–234.

Fernández, H., Sriram, V., Schimmels, S., and Oumeraci, H. (2014). Extreme wave generation using self correcting method - Revisited. *Coastal Engineering*, 93:15–31.

Ferziger, J. and Peric, M. (2002). *Computational methods for fluid dynamics*. Springer, Berlin, 3rd editio edition.

Fitzgerald, C., Grice, J., Taylor, P. H., Eatock Taylor, R., and Zang, J. (2012). Phase manipulation and the harmonic components of ringing froces on a surface piercing column. In *International workshop for water waves and floating bodies, IWWWFB27*.

Fitzgerald, C., Grice, J., Taylor, P. H., Eatock Taylor, R., and Zang, J. (2014). Phase manipulation and the harmonic components of ringing forces on a surface piercing column. *Proceedings of the Royal Society of London A: Mathematical, Physical and Engineering Sciences*, 470(2168):20130847.

Forristall, G. Z. (1978). On the statistical distribution of wave heights in a storm. *Journal of Geophysical Research*, 83(C5):2353.

Forristall, G. Z. (2000). Wave Crest Distributions: Observations and Second-Order Theory. *Journal of Physical Oceanography*, 30(8):1931–1943.

Forristall, G. Z. (2002). Nonlinear Wave Calculations for Engineering Applications. *Journal of Offshore Mechanics and Arctic Engineering*, 124(1):28.

Gagnaire-Renou, E., Benoit, M., and Forget, P. (2010). Ocean wave spectrum properties as derived from quasi-exact computations of nonlinear wave-wave interactions. *Journal of Geophysical Research: Oceans*, 115(12).

Gatin, I., Vu Ceví C, V., and Jasak, H. (2017). A framework for efficient irregular wave simulations using Higher Order Spectral method coupled with viscous two phase model. *Journal of Ocean Engineering and Science*, 000:1–15.

Gebreslassie, M. G., Tabor, G. R., and Belmont, M. R. (2013). Numerical simulation of a new type of cross flow tidal turbine using OpenFOAM - Part I: Calibration of energy extraction. *Renewable Energy*, 50:994–1004.

Gibbs, R. H. and Taylor, P. H. (2005). Formation of walls of water in 'fully' nonlinear simulations. *Applied Ocean Research*, 27(3):142–157.

Gibson, R. and Swan, C. (2007). The evolution of large ocean waves: the role of local and rapid spectral changes. *Proceedings of the Royal Society A: Mathematical, Physical and Engineering Sciences*, 463(2077):21–48.

Giese, G. S., Chapman, D. C., Collins, M. G., Encarnacion, R., and Jacinto, G. (1998). The Coupling between Harbor Seiches at Palawan Island and Sulu Sea Internal Solitons*. *Journal of Physical Oceanography*, 28(12):2418–2426.

Gonçalves, M., Martinho, P., and Guedes Soares, C. (2014). Assessment of wave energy in the Canary Islands. *Renewable Energy*, 68:774–784.

Gouin, M., Ducrozet, G., and Ferrant, P. (2015). Development and validation of a non-linear spectral model for water waves over variable depth. *European Journal of Mechanics - B/Fluids*, 0:1–4.

Gramstad, O. and Babanin, A. (2014). Implementing New Nonlinear Term in Third Generation Wave Models. In *33rd International Conference on Ocean, Offshore and Arctic Engineering OMAE2014. Volume 4B: Structures, Safety and Reliability*, page V04BT02A057, San Francisco, California, USA. ASME.

Gramstad, O. and Babanin, A. (2016). The generalized kinetic equation as a model for the nonlinear transfer in third-generation wave models. *Ocean Dynamics*, 66(4):509–526.

Gramstad, O. and Stiassnie, M. (2013). Phase-averaged equation for water waves. *Journal of Fluid Mechanics*, 718:280–303.

Gramstad, O. and Trulsen, K. (2007). Influence of crest and group length on the occurrence of freak waves. *Journal of Fluid Mechanics*, 582:463–472.

Greaves, D. (2004). A quadtree adaptive method for simulating fluid flows with moving interfaces. *Journal of Computational Physics*, 194(1):35–56.

Greaves, D. (2010). Application of the finite volume method to the simulation of nonlinear water waves. In *Advances in Numerical Simulation of Nonlinear Water Waves*, chapter 8, page 357. The World Scientific Publishing Co.

Guimarães, P. V., Farina, L., Toldo, E., Diaz-Hernandez, G., and Akhmatskaya, E. (2015). Numerical simulation of extreme wave runup during storm events in Tramandaí Beach, Rio Grande do Sul, Brazil. *Coastal Engineering*, 95:171–180.

Guimarães, P. V., Farina, L., and Toldo, E. E. (2014). Analysis of extreme wave events on the southern coast of Brazil. *Nat. Hazards Earth Syst. Sci*, 14:3195–3205.

Hann, M., Greaves, D., and Raby, A. C. (2014). A new set of focused wave linear combinations to extract non-linear wave harmonics. In *International workshop for water waves and floating bodies, IWWWFB29*.

Hasselmann, K. (1962). On the non-linear energy transfer in a gravity-wave spectrum. *J. Fluid Mech*, 12(481-500):15.

Hasselmann, S. and Hasselmann, K. (1985). Computations and Parameterizations of the Nonlinear Energy Transfer in a Gravity-Wave Spectrum. Part I: A New Method for Efficient Computations of the Exact Nonlinear Transfer Integral. *Journal of Physical Oceanography*, 15(11):1369–1377.

Haudin, F., Cazaubiel, A., Deike, L., Jamin, T., Falcon, E., and Berhanu, M. (2016). Experimental study of three-wave interactions among capillary-gravity surface waves. *Physical Review E*, 93(4):1–12.

Haver, S. (2000). Evidences of the Existence of Freak Waves. In *Rogues Waves 2000*, pages 129–140, Brest, France.

Haver, S. (2004). Freak Waves : A Suggested Definition and Possible Consequences for Marine Structures. In *Rogue Waves 2004*, Brest, France.

Higuera, P., Lara, J. L., and Losada, I. J. (2013a). Realistic wave generation and active wave absorption for Navier - Stokes models Application to OpenFOAM®. *Coastal Engineering*, 71:102–118.

Higuera, P., Lara, J. L., and Losada, I. J. (2013b). Simulating coastal engineering processes with OpenFOAM. *Coastal Engineering*, 71:119–134.

Higuera, P., Lara, J. L., and Losada, I. J. (2013c). Simulating coastal engineering processes with OpenFOAM. *Coastal Engineering*, 71:119–134.

Higuera, P., Losada, I. J., and Lara, J. L. (2015). Three-dimensional numerical wave generation with moving boundaries. *Coastal Engineering*, 101:35–47.

Hirt, C. and Nichols, B. (1981). Volume of fluid (VOF) method for the dynamics of free boundaries. *Journal of Computational Physics*, 39(1):201–225.

Holthuijsen, L. H. (2007). *Waves in Oceanic and Coastal Waters*. Cambridge University Press.

Hu, Z. Z., Causon, D. M., Mingham, C. G., and Qian, L. (2011). Numerical simulation of floating bodies in extreme free surface waves. *Natural Hazards and Earth System Science*, 11(2):519–527.

Hu, Z. Z., Greaves, D., and Raby, A. C. (2014). Numerical wave tank study of extreme waves and wave structure interaction using OpenFOAM. In *Coastlab14: 5th Int Conf on the application of physical modelling to port and coastal protection*, pages 2, 243–252, Varna, Bulgaria.

Hunt, A. (2003). *Extreme waves, overtopping and flooding at sea defences*. PhD thesis, University of Oxford.

IEC (2015). Marine energy. Wave, tidal and other water current converters. Tidal energy resource assessment and characterization. Technical report, International Electrotechnical Commission.

Issa, R. (1986). Solution of the implicitly discretised fluid flow equations by operator-splitting. *Journal of Computational Physics*, 62(1):40–65.

Iturrioz, A., Guanche, R., Lara, J., Vidal, C., and Losada, I. (2015). Validation of OpenFOAM® for Oscillating Water Column three-dimensional modeling. *Ocean Engineering*, 107:222–236.

Jacobsen, N. G. (2017). waves2Foam Manual. Technical Report August.

Jacobsen, N. G., Fuhrman, D. R., and Fredsøe, J. (2012). A wave generation toolbox for the open-source CFD library: OpenFoam®. *International Journal for Numerical Methods in Fluids*, 70(9):1073–1088.

Janssen, P. A. E. M. (2003). Nonlinear four-wave interactions and freak waves. *Journal of Physical Oceanography*, 33:863–884.

Janssen, P. a. E. M. (2005). Nonlinear Four-Wave Interaction and Freak Waves. In *SOEST*, volume 33, pages 863–884.

Janssen, P. a. E. M. and Onorato, M. (2007). The Intermediate Water Depth Limit of the Zakharov Equation and Consequences for Wave Prediction. *Journal of Physical Oceanography*, 37(10):2389–2400.

Jasak, H. (1996). *Error Analysis and Estimation for the Finite Volume Method with Applications to Fluid Flows*. PhD thesis, Imperial College of Science, Technology and Medicine.

Jasak, H. (2006). Lecture notes in Numerical Solution Algorithms for Compressible Flows. Technical report, University of Zagreb, Croatia.

Jasak, H., Jemcov, A., and Tukovic, Z. (2007). OpenFOAM : A C ++ Library for Complex Physics Simulations. In *International Workshop on Coupled Methods in Numerical Dynamics*, Dubrovnik, Croatia.

Johannessen, T. B. (2008). On the Use of Linear and Weakly Nonlinear Wave Theory in Continuous Ocean Wave Spectra: Convergence With Respect to Frequency. In *ASME 2008 27th International Conference on Offshore Mechanics and Arctic Engineering: Volume 4: Ocean Engineering; Offshore Renewable Energy*, pages 211–217. ASME.

Johannessen, T. B. (2010). Calculations of kinematics underneath measured time histories of steep water waves. *Applied Ocean Research*, 32(4):391–403.

Johannessen, T. B. and Swan, C. (2001). A laboratory study of the focusing of transient and directionally spread surface water waves. *Proceedings of the Royal Society A: Mathematical, Physical and Engineering Sciences*, 457(2008):971–1006.

Johannessen, T. B. and Swan, C. (2003). On the nonlinear dynamics of wave groups produced by the focusing of surface-water waves. *Proceedings of the Royal Society A: Mathematical, Physical and Engineering Sciences*, 459(2032):1021–1052.

Jonathan, P. and Taylor, P. H. (1997). On Irregular, Nonlinear Waves in a Spread Sea. *Journal of Offshore Mechanics and Arctic Engineering*, 119(1):37.

Katsardi, V. and Swan, C. (2011). The evolution of large non-breaking waves in intermediate and shallow water. I. Numerical calculations of uni-directional seas. *Proceedings of the Royal Society A: Mathematical, Physical and Engineering Sciences*, 467(2127):778–805.

Keaney, I. (2015). *Evanescent Wave Reduction Using a Segmented Wavemaker in a Two Dimensional Wave Tank*. PhD thesis, National University of Ireland Maynooth.

Keller, H. B. (1971). A new difference scheme for parabolic problems. In *Numerical Solution of Partial Differential Equations-II*, pages 327–350. Elsevier.

Kharif, C. and Pelinovsky, E. (2003). Physical mechanisms of the rogue wave phenomenon. *European Journal of Mechanics, B/Fluids*, 22(6):603–634.

Kim, C.-K., Toft, J. E., Papenfus, M., Verutes, G., Guerry, A. D., Ruckelshaus, M. H., Arkema, K. K., Guannel, G., Wood, S. A., Bernhardt, J. R., Tallis, H., Plummer, M. L., Halpern, B. S., Pinsky, M. L., Beck, M. W., Chan, F., Chan, K. M. A., Levin, P. S., and Polasky, S. (2012). Catching the right wave: evaluating wave energy resources and potential compatibility with existing marine and coastal uses. *PloS one*, 7(11):e47598.

Kleefsman, K. M. T., Fekken, G., Veldman, a. E. P., Iwanowski, B., and Buchner, B. (2005). A Volume-of-Fluid based simulation method for wave impact problems. *Journal of Computational Physics*, 206(1):363–393.

Kofoed-Hansen, H., Kerper, D. R., Sørensen, O. R., and Kirkegaard, J. (2005). Simulation of long wave agitation in ports and harbours using a time-domain Boussinesq model. In *Proceedings of Fifth International Symposium on Ocean Wave Measurement and Analysis - WAVES 2005*, Madrid, Spain.

Kofoed-Hansen, H., Sloth, P., So/rensen, O. R., and Fuchs, J. (2001). Combined Numerical and Physical Modelling of Seiching in Exposed New Marina. In *Coastal Engineering 2000*, pages 3600–3614, Reston, VA. American Society of Civil Engineers.

Krasitskii, V. P. (1994). On reduced equations in the Hamiltonian theory of weakly nonlinear surface waves. *Journal of Fluid Mechanics*, 272:1–20.

Lam, D. C. and Simpson, R. B. (1976). Centered differencing and the box scheme for diffusion convection problems. *Journal of Computational Physics*, 22(4):486–500.

Langodan, S., Viswanadhapalli, Y., Dasari, H. P., Knio, O., and Hoteit, I. (2016). A high-resolution assessment of wind and wave energy potentials in the Red Sea. *Applied Energy*, 181:244–255.

Lara, J. L., Ruju, A., and Losada, I. J. (2011). Reynolds averaged Navier-Stokes modelling of long waves induced by a transient wave group on a beach. *Proceedings of the Royal Society A: Mathematical, Physical and Engineering Sciences*, 467(2129):1215–1242.

Latheef, M. and Swan, C. (2013). A laboratory study of wave crest statistics and the role of directional spreading. *Proceedings of the Royal Society*, 469:20120696.

Le Méhauté, B. (1976). *An Introduction to Hydrodynamics and Water Waves Volume 1: Fundamentals*, volume 1. Springer-Verlag.

Lecornu, F., Paillet, J., and Ravenel, H. (2008). PREVIMER - Coastal observations and forecasts 2 Years making-Up and future perspectives. In *SeaTechWeek Coastal Operational Oceanography*, volume 13, Brest, France.

Li, F. C. and Ting, C. L. (2012). Separation of free and bound harmonics in waves. *Coastal Engineering*, 67:29–40.

Liang, B., Wu, G., Liu, F., Fan, H., and Li, H. (2015). Numerical study of wave transmission over double submerged breakwaters using non-hydrostatic wave model. *Oceanologia*, 57(4):308–317.

Lin, E. B. and Liu, P. C. (2004). A discrete wavelet analysis of freak waves in the ocean. *Journal of Applied Mathematics*, 2004(5):379–394.

Lin, P. (2008). *Numerical Modeling of Water Waves*. Taylor & Francis.

Lindgren, G. (1970). Some Properties of a Normal Process near a Local Maximum. *The Annals of Mathematical Statistics*, 41(6):1870–1883.

Liu, P. C. and Pinho, U. F. (2004). Freak waves - more frequent than rare ! *Annales Geophysicae*, 22(5):1839–1842.

Liu, P. C. P. (2007). A chronology of freauqe wave encounters. *Geofizika*, 24(1):57–70.

Liu, P. L.-F. and Losada, I. J. (2002). Wave propagation modeling in coastal engineering. *Journal of Hydraulic Research*, 40(3):229–240.

Longuet-Higgins, M. S. (1962). Resonant interactions between two trains of gravity waves. *Journal of Fluid Mechanics*, 12(3):321–332.

Longuet-Higgins, M. S. (1978a). The Instabilities of Gravity Waves of Finite Amplitude in Deep Water I. Superharmonics. *Proceedings of the Royal Society A: Mathematical, Physical and Engineering Sciences*, 360(1703):489–505.

Longuet-Higgins, M. S. (1978b). The Instabilities of Gravity Waves of Finite Amplitude in Deep Water II. Subharmonics. *Proceedings of the Royal Society A: Mathematical, Physical and Engineering Sciences*, 360(1703):489–505.

Longuet-Higgins, M. S. (1980). On the distribution of the heights of sea waves: Some effects of nonlinearity and finite band width. *Journal of Geophysical Research*, 85(C3):1519.

Longuet-Higgins, M. S. and Stewart, R. W. (1960). Changes in the form of short gravity waves on long waves and tidal currents. *Journal of Fluid Mechanics*, 8(4):565–583.

Lu, X., Chandar, D. D. J., Chen, Y., and Lou, J. (2017). An overlapping domain decomposition based near-far field coupling method for wave structure interaction simulations. *Coastal Engineering*, 126(April):37–50.

Lynett, P. J., Liu, P. L.-F., Sitanggang, K. I., and Kim, D.-H. (2008). Modeling Wave Generation, Evolution, and Interaction with Depth-Integrated, Dispersive Wave Equations COULWAVE Code Manual Cornell University Long and Intermediate Wave Modeling Package v. 2.0. Technical report.

Mai, T., Greaves, D., Raby, A., and Taylor, P. H. (2016). Physical modelling of wave scattering around fixed FPSO-shaped bodies. *Physics Procedia*, 61:115–129.

Marić, T., Höpken, J., and Mooney, K. (2014). *The OpenFOAM Technology Primer*. sourceflux.

MARNET CFD (2002). Best practice Guidllines for Marine Applications of Computational Fluid Dynamics. Technical report.

Méndez, F. J., Losada, I. J., and Losada, M. a. (2001). Wave-Induced Mean Magnitudes in Permeable Submerged Breakwaters. *Journal of Waterway, Port, Coastal, and Ocean Engineering*, 127(1):7–15.

METOCEAN-SOLUTIONS-Ltd (2008). Marine energy resources. Ocean wave and tidal current resources in New Zealand. Technical report.

Moler, C. (2011). Shallow Water Equations. In *Experiments with MATLAB*, chapter Chapter 18, pages 241–246.

Monbaliu, J. and Lefèvre, J.-M. (2005). Measuring and analysing the directional spectrum of ocean waves. In *Measuring and Analysing the directional spectrum of ocean waves*, chapter Chapter 6: Spectral Wave Modelling, pages 189–200. COST Office.

Morgan, G. C. J. and Zang, J. (2010). Using the rasInterFoam CFD model for non-linear wave interaction with a cylinder. In *Proceedings of the Twentieth International Offshore and Polar Engineering Conference*, pages 418–423, Beijing, China.

Morgan, G. C. J., Zang, J., Greaves, D., Heath, A., Whitlow, C. D., and Young, J. R. (2010). Using the rasInterFoam CFD model for wave transformation and coastal

modeling. In *Proceedings of the International Conference of Coastal Engineering*, pages 418–423, Shanghai, China.

Mori, N. (2012). Freak waves under typhoon conditions. *Journal of Geophysical Research: Oceans*, 117(4):1–12.

Ning, D.-Z., Teng, B., Eatock Taylor, R., and Zang, J. (2008). Numerical simulation of non-linear regular and focused waves in an infinite water-depth. *Ocean Engineering*, 35(8-9):887–899.

Ning, D.-Z., Teng, B., Zang, J., and Liu, S. X. (2009a). An Efficient Model for Transient Surface Waves in Both Finite and Infinite Water Depths. *China Ocean Engineering*, 23(3):459–472.

Ning, D.-Z., Zang, J., Liu, S. X., Eatock Taylor, R., Teng, B., and Taylor, P. H. (2009b). Free-surface evolution and wave kinematics for nonlinear uni-directional focused wave groups. *Ocean Engineering*, 36(15-16):1226–1243.

NOAA (2017). Centre, National Weather Service - Environmental Modeling. URL: `http://polar.ncep.noaa.gov/waves/`. Accessed: 15-Oct-2017.

Onorato, M., Osborne, A. R., and Serio, M. (2007). On the relation between two numerical methods for the computation of random surface gravity waves. *European Journal of Mechanics, B/Fluids*, 26(1):43–48.

Onorato, M., Residori, S., Bortolozzo, U., Montina, A., and Arecchi, F. T. (2013). Rogue waves and their generating mechanisms in different physical contexts. *Physics Reports*, 528(2):47–89.

OpenCFD (2012). OpenFOAM: The Open Source CFD Toolbox User Guide Version 2.1.1. Technical report.

OpenCFD_Ltd (2015). The open source CFD toolbox. URL: `http://www.openfoam.com/`. Accessed: 28-Oct-2015.

OpenFOAM-Extend (2015). The OpenFOAM Extend Project website. URL: `http://www.extend-project.de/`. Accessed: 28-Oct-2015.

Orszaghova, J., Taylor, P. H., Borthwick, A. G. L., and Raby, A. C. (2014). Importance of second-order wave generation for focused wave group run-up and overtopping. *Coastal Engineering*, 94:63–79.

Patankar, S. and Spalding, D. (1972). A calculation procedure for heat, mass and momentum transfer in three-dimensional parabolic flows. *International Journal of Heat and Mass Transfer*.

Paulsen, B. T., Bredmose, H., and Bingham, H. B. (2012). Accurate computation of wave loads on a bottom fixed circular cylinder. In *International workshop for water waves and floating bodies, IWWWFB27*.

Paulsen, B. T., Bredmose, H., and Bingham, H. B. (2013a). Focused wave impact on a vertical cylinder: Experiment, numerical reproduction and a note on higher harmonics. In *International workshop for water waves and floating bodies, IWWWFB28*.

Paulsen, B. T., Bredmose, H., and Bingham, H. B. (2014a). An efficient domain decomposition strategy for wave loads on surface piercing circular cylinders. *Coastal Engineering*, 86:57–76.

Paulsen, B. T., Bredmose, H., Bingham, H. B., and Jacobsen, N. G. (2014b). Forcing of a bottom-mounted circular cylinder by steep regular water waves at finite depth. *Journal of Fluid Mechanics*, 755:1–34.

Paulsen, B. T., Bredmose, H., Bingham, H. B., and Schløer, S. (2013b). Steep Wave Loads From Irregular Waves on an Offshore Wind Turbine Foundation: Computation and Experiment. In *OMAE2013: Proceedings of the ASME 2013 32nd International Conference on Ocean, Offshore and Arctic Engineering*, Nantes, France.

Peregrine, D. H. (1967). Long waves on a beach. *Journal of Fluid Mechanics*, 27(04):815–827.

Perez, J., Menendez, M., and Losada, I. J. (2017). GOW2: A global wave hindcast for coastal applications. *Coastal Engineering*, 124:1–11.

Perez-Collazo, C. (2017). *Evaluation of the WEC sub-system of a hybrid wind-wave energy converter*. PhD thesis, University of Plymouth.

Pérez-Collazo, C., Greaves, D., and Iglesias, G. (2015). A review of combined wave and offshore wind energy. *Renewable and Sustainable Energy Reviews*, 42:141–153.

Phillips, O., Gu, D., and Donelan, M. (1993). Expected Sturcture of Extreme Waves in a Gaussian Sea. Part I: Theory and SWADE Buoy Measurements. *Journal of Physical Oceanography*, 23:992–1000.

Phillips, O. M. (1960). On the dynamics of unsteady gravity waves of finite amplitude Part 1. The elementary interactions. *Journal of Fluid Mechanics*, 9:193–271.

Popinet, S., Gorman, R. M., Rickard, G. J., and Tolman, H. L. (2010). A quadtree-adaptive spectral wave model. *Ocean Modelling*, 34(1-2):36–49.

Prabhakar, V. and Uma, G. (2016). A Polar Method using cubic spline approach for obtaining wave resonating quadruplets. *Ocean Engineering*, 111:292–298.

Prevosto, M. and Bouffandeau, B. (2002). Probability of occurrence of a "giant" wave crest. In *Proceedings of the International Conference on Offshore Mechanics and Arctic Engineering - OMAE*, volume 2, pages 483–490.

Ransley, E. (2015). *Survivability of Wave Energy Converter and Mooring Coupled System using CFD*. PhD thesis, University of Plymouth.

Ransley, E., Hann, M., Greaves, D., Raby, A. C., and Simmonds, D. (2013). Numerical and physical modeling of extreme waves at Wave Hub. *Journal of Coastal Research*, 29(65):1645–1650.

Rapp, R. J. and Melville, W. K. (1990). Laboratory Measurements of Deep-Water Breaking Waves. *Philosophical Transactions of the Royal Society A: Mathematical, Physical and Engineering Sciences*, 331(1622):735–800.

Reynolds, O. (1883). An Experimental Investigation of the Circumstances Which Determine Whether the Motion of Water Shall Be Direct or Sinuous, and of the Law of Resistance in Parallel Channels. *Philosophical Transactions of the Royal Society of London*, 174(0):935–982.

Rienecker, M. M. and Fenton, J. D. (1981). A Fourier approximation method for steady water waves. *Journal of Fluid Mechanics*, 104(-1):119.

Rijnsdorp, D. P., Smit, P. B., and Zijlema, M. (2012). Non-hydrostatic modelling of infragravity waves using SWASH. In *Coastal Engineering Proceedings*, Santander, Spain.

Rijnsdorp, D. P., Smit, P. B., and Zijlema, M. (2014). Non-hydrostatic modelling of infragravity waves under laboratory conditions. *Coastal Engineering*, 85:30–42.

Rijnsdorp, D. P., Smit, P. B., Zijlema, M., and Reniers, A. J. (2017). Efficient non-hydrostatic modelling of 3D wave-induced currents using a subgrid approach. *Ocean Modelling*, 116:118–133.

Rijnsdorp, D. P. and Zijlema, M. (2016). Simulating waves and their interactions with a restrained ship using a non-hydrostatic wave-flow model. *Coastal Engineering*, 114:119–136.

Ris, R. (1997). *Spectral modelling of wind waves in coastal areas*. PhD thesis, TU Delft, Delft University of Technology.

Roache, P. J. (1998). *Verification and Validation in Computational Science and Engineering*. Hermosa Pub.

Rudman, M. (1997). Volume-Tracking Methods for Interfacial Flow Calculations. *International Journal for Numerical Methods in Fluids*, 24(7):671–691.

Sánchez, A. S., Rodrigues, D. A., Fontes, R. M., Martins, M. F., Kalid, R. d. A., and Torres, E. A. (2017). Wave resource characterization through in-situ measurement followed by artificial neural networks' modeling. *Renewable Energy*.

Santo, H., Stagonas, D., Buldakov, E., and Taylor, P. H. (2017). Current blockage in sheared flow: Experiments and numerical modelling of regular waves and strongly sheared current through a space-frame structure. *Journal of Fluids and Structures*, 70(December 2016):374–389.

Schäffer, H. A. (1996). Second-order wavemaker theory for irregular waves. *Ocean Engineering*, 23(1):47–88.

Schmittner, C., Kosleck, S., and Janou, H. (2009). A Phase-Amplitude Iteration Scheme for the Optimization of Deterministic Wave Sequences. In *Proceedings of the ASME 2009 28th IInternational Conference on Ocean, Offshore and Arctic Engineering, OMAE2009*, pages 653–660, Honolulu, Hawaii, USA.

Shadman, M., Estefen, S. F., Rodriguez, C. A., and Nogueira, I. C. (2018). A geometrical optimization method applied to a heaving point absorber wave energy converter. *Renewable Energy*, 115:533–546.

Sharma, J. and Dean, R. (1981). Second-Order Directional Seas and Associated Wave Forces. *Society of Petroleum Engineers Journal*, 4:129–140.

Shemer, L. and Dorfman, B. (2008). Experimental and numerical study of spatial and temporal evolution of nonlinear wave groups. *Nonlinear Processes in Geophysics*, 15(6):931–942.

Shemer, L., Goulitski, K., and Kit, E. (2006). Steep Waves in Tanks: Experiments and Simulations. In *OMAE2006: Proceedings of the ASME 25th 2010 International Conference on Ocean, Offshore and Arctic Engineering*, pages 1–9, Hamburg, Germany.

Shemer, L., Goulitski, K., and Kit, E. (2007). Evolution of wide-spectrum unidirectional

wave groups in a tank: an experimental and numerical study. *European Journal of Mechanics, B/Fluids*, 26(2):193–219.

Shemer, L., Jiao, H., Kit, E., and Agnon, Y. (2001). Evolution of a nonlinear wave field along a tank: experiments and numerical simulations based on the spatial Zakharov equation. *Journal of Fluid Mechanics*, 427:107–129.

Shi, F., Kirby, J. T., Tehranirad, B., Harris, J. C., and Grilli, S. (2012). FUNWAVE-TVD Fully Nonlinear Boussinesq Wave Model with TVD Solver Documentation and User's Manual. Technical report.

Siddorn, P. D. (2012). *Efficient Numerical Modelling of Wave-Structure Interaction*. PhD thesis, University of Oxford.

Simonetti, I., Cappietti, L., El Safti, H., and Oumeraci, H. (2015). Numerical Modelling of Fixed Oscillating Water Column Wave Energy Conversion Devices: Toward Geometry Hydraulic Optimization. In *Proceedings of the ASME 34th International Conference on Ocean, Offshore and Arctic Engineering OMAE2015*.

Slunyaev, A., Pelinovsky, E., and Guedes Soares, C. (2011). Reconstruction of extreme events through numerical simulations. In *Proceedings of the International Conference on Offshore Mechanics and Arctic Engineering - OMAE 2011*, volume 2, pages 935–943, Rotterdam, The Netherlands. ASME.

Slunyaev, A., Pelinovsky, E., and Guedes Soares, C. (2013). Reconstruction of Extreme Events Through Numerical Simulations. *Journal of Offshore Mechanics and Arctic Engineering*, 136(1):011302.

Smit, P. B., Zijlema, M., and Stelling, G. S. (2013). Depth-induced wave breaking in a non-hydrostatic, near-shore wave model. *Coastal Engineering*, 76:1–16.

Socquet-Juglard, H., Dysthe, K. B., Trulsen, K., Krogstad, H. E., and Liu, J. (2005). Probability distributions of surface gravity waves during spectral changes. *Journal of Fluid Mechanics*, 542:195–216.

St-Germain, P., Nistor, I., Readshaw, J., and Lamont, G. (2014). Numerical modeling of coastal dike overtopping using SPH and Non- hydrostatic NLSW equations. In Lynett, P., editor, *Proc. 34th Int. Conf. on Coast. Eng.*, pages 1(34), structures–10.

Stagonas, D., Buldakov, E., and Simons, R. (2014). Focusing unidirectional wave groups on finite water depth with and without currents. In *Coastal Engineering Proceedings*, Seoul, South Korea.

Stagonas, D., Higuera, P., and Buldakov, E. (2018). Simulating Breaking Focused Waves in CFD : Methodology for Controlled Generation of First and Second Order. 144(2):1–8.

Stelling, G. S. and Duinmeijer, S. P. (2003). A staggered conservative scheme for every Froude number in rapidly varied shallow water flows. *International Journal for Numerical Methods in Fluids*, 43(12):1329–1354.

Stelling, G. S. and Zijlema, M. (2003). An accurate and efficient finite-difference algorithm for non-hydrostatic free-surface flow with application to wave propagation. *International Journal for Numerical Methods in Fluids*, 23(May 2002):1–23.

Stokes, G. (1847). On the theory of oscillatory waves. *Transactions of the Cambridge Philosophical Society*, 8:197–229.

Sun, Z. C., Zhao, X. Z., Zhang, Y. F., and Shen, J. F. (2008). Focusing Models for Generating Freak Waves. In *Proceedings of the Eighth (2008) Isope Pacific/Asia Offshore Mechanics Symposium: Pacoms-2008*, pages 222–228.

Sutherland, J. and Barfuss, S. (2011). Composite Modelling, combining physical and numerical models. *34th IAHR World Congress, Brisbane, Australia*, (June).

Suzuki, T., Altomare, C., Veale, W., Verwaest, T., Trouw, K., Troch, P., and Zijlema, M. (2017). Efficient and robust wave overtopping estimation for impermeable coastal structures in shallow foreshores using SWASH. *Coastal Engineering*, 122(September 2016):108–123.

Swan, C. and Sheikh, R. (2015). The interaction between steep waves and a surface-piercing column. *Philosophical transactions. Series A, Mathematical, physical, and engineering sciences*, 373(2033):20140114.

SWASHweb (2017). SWASH Webpage. URL: `http://swash.sourceforge.net/`. Accessed: 10-Oct-2017.

Taklo, T. M. A., Trulsen, K., Gramstad, O., Krogstad, H. E., and Jensen, A. (2015). Measurement of the dispersion relation for random surface gravity waves. *Journal of Fluid Mechanics*, 766:326–336.

Tanaka, M. (2001). Verification of Hasselmann's energy transfer among surface gravity waves by direct numerical simulations of primitive equations. *Journal of Fluid Mechanics*, 444:199–221.

Tanaka, M. (2007). On the Role of Resonant Interactions in the Short-Term Evolution of Deep-Water Ocean Spectra. *Journal of Physical Oceanography*, 37(4):1022–1036.

Tayfun, M. A. (1980). Narrow-band nonlinear sea waves. *Journal of Geophysical Research*, 85(C3):1548.

Taylor, P. H., Adcock, T. A. A., Borthwick, A. G. L., Walker, D. A. G., and Yao, Y. (2006). The nature of the Draupner giant wave of the 1st January 1995 and the associated sea-state, and how to estimate directional spreading from an Eulerian surface elevation time history. In *9th International Workshop on Wave Hindcasting and Forecasting*.

Taylor, P. H. and Swan, C. (2000). NewWaves, Solitons and Spreading. In *Rogue Waves 2000*, Brest, France.

Taylor, P. H. and Williams, B. A. (2004). Wave Statistics for Intermediate Depth Water-NewWaves and Symmetry. *Journal of Offshore Mechanics and Arctic Engineering*, 126(1):54.

The Swash Team (2014). USER MANUAL SWASH version 2.00 AB.

The SWASH Team (2017). SWASH User Manual version 4.01A. Technical report, Delft University of Technology.

The WAMDI Group (1988). The WAM model - A third generation ocean wave prediction model.

The WAVEWATCH III Development Group (WW3DG) (2016). User manual and system documentation of WAVEWATCH III Version 5.16 Tech. Note 329. Technical report, NOAA/NWS/NCEP/MMAB, College Park, MD, USA.

Tolman, H. L. (1989). The numerical model WAVEWATCH: a third generation model for the hindcasting of wind waves on tides in shelf seas. *Communications on Hydraulic and Geotechnical Engineering*, (89-2):72.

Tolman, H. L. (2013). A Generalized Multiple Discrete Interaction Approximation for resonant four-wave interactions in wind wave models. *Ocean Modelling*, 70:11–24.

Tolman, H. L. (2014). User manual and system documentation of WAVEWATCH III. Technical report.

Tolman, H. L. and Alves, J.-H. G. (2005). Numerical modeling of wind waves generated by tropical cyclones using moving grids. *Ocean Modelling*, 9(4):305–323.

Tolman, H. L. and Chalikov, D. (1996). Source Terms in a Third-Generation Wind Wave Model.

Tolman, I. H. (2010). WAVEWATCH III development best practices. Tech. Note 286, Ver. 0.1. Technical report, NOAA/NWS/NCEP/MMAB.

Tracy, B. A. and Resio, D. T. (1982). Theory and Calculation of the Nonlinear Energy Transfer between Sea Waves in Deep Water. WIS Technical Report 11. Technical report, US Army Engineer Waterways Experiment Station, Vicksburg, Mississippi, USA.

Tromans, P. S., Anatruk, A. H. R., and Hagemeijer, P. (1991). New model for the kinematics of large ocean waves application as a design wave. In *Proceedings of*

the First International Offshore and Polar Engineering Conference, August 11, 1991 - August 16, pages 64–71.

Trulsen, K., Kliakhamdler, I., Dysthe, K. B., and Velarde, M. G. (2000). On weakly nonlinear modulations of waves in deep water. *Phys. Fluids*, 12(10):2432–2437.

Trulsen, K., Tobias, O., and Velarde, M. G. (2001). The nonlinear Schrödinger method for water wave kinematics on finite depth. *Wave Motion*, 33:379–395.

Tsai, C.-H., Su, M.-Y., and Huang, S.-J. (2004). Observations and conditions for occurrence of dangerous coastal waves. *Ocean Engineering*, 31(5-6):745–760.

Tucker, M. J. (1999). The Shape, Period and Wavelength of High Storm Waves. *Underwater Technology*, 23(4):169–179.

Turnbull, M. S., Borthwick, A. G. L., and Eatock Taylor, R. (2003). Numerical wave tank based on a sigma-transformed finite element inviscid flow solver. *International Journal for Numerical Methods in Fluids*, 42(April 2002):641–663.

van Vledder, G. P. (2006). The WRT method for the computation of non-linear four-wave interactions in discrete spectral wave models. *Coastal Engineering*, 53(2-3):223–242.

van Vledder, G. P. (2012). Efficient algorithms for non-linear four-wave interactions. In *ECMWF workshop on Ocean Waves*, number June, pages 97–112, Reading, UK.

Versteeg, H. K. and Malaskekera, W. (2007). *An Introduction to Computational Fluid Dynamics, The Finite Volume Method (Second edition)*, volume M. Pearson Prentice Hall.

Vyzikas, T., Deshoulieres, S., Barton, M., Giroux, O., Greaves, D., and Simmonds, D. (2017a). Experimental investigation of different geometries of fixed oscillating water column devices. *Renewable Energy*, 104:248–258.

Vyzikas, T., Deshoulieres, S., Giroux, O., Barton, M., and Greaves, D. (2017b). Numerical study of fixed Oscillating Water Column with RANS-type two-phase CFD model. *Renewable Energy*, 102:294–305.

Vyzikas, T. and Greaves, D. (2018). Chapter 8: Numerical Modelling. In *Wave and Tidal Energy*, pages 289–363. Wiley-Blackwell publishing.

Vyzikas, T., Greaves, D., Simmonds, D., Maisondieu, C., Smith, H., and Ranford, L. (2014a). Application of numerical models and codes - Task 3.4.4 MERiFIC project. Technical report, University of Plymouth.

Vyzikas, T., Prevosto, M., Maisondieu, C., Tassin, A., and Greaves, D. (2018a). Reconstruction of an extreme wave profile with analytical methods. In *International workshop for water waves and floating bodies, IWWWFB33*, Guidel-Plages, France.

Vyzikas, T., Ransley, E., Hann, M., Magagna, D., Simmonds, D., Magar, V., and Conley, D. (2013). Integrated Numerical Modelling System for Extreme Wave Events at the Wave Hub Site. In *ICE Conference: Coasts, Marine structures and Breakwaters*, Edinburgh, UK.

Vyzikas, T., Stagonas, D., Buldakov, E., and Greaves, D. (2014b). On the simulation of focused waves with OpenFOAM & waves2Foam. In *Coastlab14: 5th Int Conf on the application of physical modelling to port and coastal protection*, pages 2, 237–282, Varna, Bulgaria.

Vyzikas, T., Stagonas, D., Buldakov, E., and Greaves, D. (2015). Efficient numerical modelling of focused wave groups for freak wave generation. In *ISOPE-2015: 25th International Offshore and Polar Engineering Conference*.

Vyzikas, T., Stagonas, D., Buldakov, E., and Greaves, D. (2018b). The evolution of free and bound waves during dispersive focusing in a numerical and physical flume. *Coastal Engineering*, 132:95–109.

Walker, D., Taylor, P., and Taylor, R. E. (2004). The shape of large surface waves on the open sea and the Draupner New Year wave. *Applied Ocean Research*, 26(3-4):73–83.

Wang, H., Draper, S., Zhao, W., Wolgamot, H., and Cheng, L. (2017). Development of a CFD Model to Simulate Three-Dimensional Gap Resonance Applicable to FLNG Side-by-Side Offloading. In *36th International Conference on Ocean, Offshore and Arctic Engineering OMAE2017*, Trondheim, Norway. ASME.

Waters, J., Wyatt, L. R., Wolf, J., and Hines, A. (2013). Data assimilation of partitioned HF radar wave data into Wavewatch III. *Ocean Modelling*, 72:17–31.

Webb, D. (1978). Non-linear transfers between sea waves. *Deep Sea Research*, 25(3):279–298.

Wei, G. and Kirby, J. T. (1995). Time-Dependent Numerical Code for Extended Boussinesq Equations. *Journal of Waterway, Port, Coastal, and Ocean Engineering*, 121(5):251–261.

Weller, H. G., Tabor, G., Jasak, H., and Fureby, C. (1998). A tensorial approach to computational continuum mechanics using object-oriented techniques. *Computers in Physics*, 12(6):620–631.

West, J. and Brueckner, K. A. (1987). A New Numerical Method for Surface Hydrodynamics. *Journal of Fluid Mechanics*, 92(CII):11,803–11,824.

Westphalen, J., Greaves, D., and Chris, W. (2007). Comparison of free surface wave simulations using STAR CCM+ and CFX. In *Proceedings of the 10th Numerical Towing Tank Symposium*, pages 47–88.

Westphalen, J., Greaves, D., Chris, W., Zang, J., and Taylor, P. H. (2008). Numerical simulation of extreme free surface waves. In *Proceedings of the 8th International Offshore (Ocean) and Polar Engineering Conference & Exhibition*.

Westphalen, J., Greaves, D., Williams, C. J. K., Raby, A. C., and Zang, J. (2012). Focused waves and wavestructure interaction in a numerical wave tank. *Ocean Engineering*, 45:9–21.

Whittaker, C., Fitzgerald, C., Raby, A., Taylor, P., Orszaghova, J., and Borthwick, A. (2017). Optimisation of focused wave group runup on a plane beach. *Coastal Engineering*, 121:44–55.

Whittaker, C., Fitzgerald, C., Raby, A., and Taylor, P. H. (2016). The shape of large waves in the coastal zone. *Coastal Engineering*, 114:253–264.

Yan, S., Ma, Q. W., Sriram, V., Qian, L., Ferrer, P. J. M., and Schlurmann, T. (2015). Numerical and Experimental Studies of Moving Cylinder in Uni-directional Focusing Waves. In *ISOPE-2015: 25th International Offshore and Polar Engineering Conference*.

Yang, Z., Neary, V. S., Wang, T., Gunawan, B., Dallman, A. R., and Wu, W.-C. (2017). A wave model test bed study for wave energy resource characterization. *Renewable Energy*, 114:132–144.

Young, I. R., Zieger, S., and Babanin, A. V. (2011). Global trends in wind speed and wave height. *Science (New York, N.Y.)*, 332(6028):451–5.

Zakharov, V. E. (1968). Stability of periodic waves of finite amplitude on the surface of a deep fluid. *Journal of Applied Mechanics and Technical Physics*, 9(2):190–194.

Zakharov, V. E. and Ostrovsky, L. A. (2009). Modulation instability: The beginning. *Physica D*, 238:540–548.

Zang, J. and Taylor, P. H. (2010). Steep wave and breaking wave impact on offshore wind turbine foundations - Ringing re-visited. In *International workshop for water waves and floating bodies, IWWWFB25*.

Zhang, H., Schäffer, H. A., and Jakobsen, K. P. (2007). Deterministic combination of numerical and physical coastal wave models. *Coastal Engineering*, 54(2):171–186.

Zhang, N., Zhang, Q., Zou, G., and Jiang, X. (2016). Estimation of the transmission coefficients of wave height and period after smooth submerged breakwater using a non-hydrostatic wave model. *Ocean Engineering*, 122:202–214.

Zhao, W., Wolgamot, H. A., Taylor, P. H., and Eatock Taylor, R. (2017). Gap resonance and higher harmonics driven by focused transient wave groups. *Journal of Fluid Mechanics*, 812:905–939.

Zhao, X.-z., Hu, C. H., and Sun, Z. C. (2010). Numerical simulation of extreme wave generation using VOF method. *Journal of Hydrodynamics*, 22(4):466–477.

Zhao, X. Z., Sun, Z. C., and Liang, S. X. (2009). A numerical study of the transformation of water waves generated in a wave flume. *Fluid Dynamics Research*, 41(3):035510.

Zheng, C., Zhuang, H., Li, X., and Li, X. (2011). Wind energy and wave energy resources assessment in the East China Sea and South China Sea. *Science China Technological Sciences*, 55(1):163–173.

Zieger, S., Babanin, A. V., Erick Rogers, W., and Young, I. R. (2015). Observation-based source terms in the third-generation wave model WAVEWATCH. *Ocean Modelling*.

Zijlema, M. and Stelling, G. S. (2005). Further experiences with computing non-hydrostatic free-surface flows involving water waves. *International Journal for Numerical Methods in Fluids*, 48(2):169–197.

Zijlema, M. and Stelling, G. S. (2008). Efficient computation of surf zone waves using the nonlinear shallow water equations with non-hydrostatic pressure. *Coastal Engineering*, 55(10):780–790.

Zijlema, M., Stelling, G. S., and Smit, P. B. (2011). SWASH: An operational public domain code for simulating wave fields and rapidly varied flows in coastal waters. *Coastal Engineering*, 58(10):992–1012.